Elif Ağcakoca, Civil Engineering, Sakary Apllied Science University (Turkey)

Elif Eker Kahveci, Mechanical Engineering, Sakarya University (Turkey)

Erman Aslan, Mechanical Engineering, Kocaeli University (Turkey)

Fahrettin Horasan, Computer Engineering, Kırıkkale University (Turkey)

Faruk Fırat Çalım, Civil Engineering, Alparslan Türkeş University (Turkey)

Feyza Gurbuz, Industrial Engineering, Erciyes University (Turkey)

Francesco de Paulis, Electrical and Electronics Enginering, University of L'Aquila (Italy)

Gökhan Dok, Civil Engineering, Sakary Apllied Science University (Turkey)

Grazyna S Martynkova, Nanotechnology Centre, VŠB-Technical University of Ostrava · Nanotechnology Centre (Czech Republic)

Grzegorz Jaworski, Physics, Heavy Ion Laboratory, University of Warsaw (Poland)

H. F. Nied, Department of Mechanical Engineering and Mechanics, Lehigh University (U.S.A.)

Hakan Alp, Geophysical Engineering, Cerrahpaşa University (Turkey)

Hatice Esen, Industrial Engineering, Kocaeli University (Turkey)

Hüseyin Aksoy, Biology, Sakarya University (Turkey)

Issa Al-Harty, Civil and Architectural Engineering, Sultan Qaboos University (Oman)

İbrahim Bahadır Başyiğit, Electrical and Electronics Engineering, Isparta Apllied Science University (Turkey)

İsmail Hakkı Demir, Architecture, Sakarya University (Turkey)

Kamaruzzaman Sopian, Renewable Energy, Universiti Kebangsaan Malaysia (Malaysia)

Khalifa Al-Jabri, Civil and Architectural Engineering, Sultan Qaboos University (Oman)

Luan Thach Hoang, Mathematics, Texas Tech University (U.S.A.)

Luis A. Materon, Biology, The University of Texas Rio Grande Valley (USA)

M. Hilmi Nişancı, Electrical and Electronics Engineering, Sakarya University (Turkey)

Mahmud Tokur, Metallurgical and Materials Engineering, Sakarya University (Turkey)

Mehmet Emin Aydın, Industrial Engineering, University of Bedfordshire (UK)

Mehmet Uysal, Metallurgical and Materials Engineering, Sakarya University (Turkey)

Mesut Baran, Electrical and Computer Engineering, FREEDM Systems Center, North Carolina State University (U.S.A.)

Miraç Alaf, Metallurgical and Materials Engineering, Bilecik Şeyh Edebali University (Turkey)

Mohammad Sukri bin Mustapa, Faculty of Mechanical & Manufacturing Engineering, Universiti Tun Hussein Onn Malaysia (Malaysia)

Muhammed Fatih Adak, Computer Engineering, Sakarya University (Turkey)

Muhammed Maruf Öztürk, Computer Engineering, Süleyman Demirel University (Turkey)

Murat Güzeltepe, Mathematics, Sakarya University (Turkey)

Murat Sarduvan, Mathematics, Sakarya University (Turkey)

Murat Tuna, Chemistry, Sakarya University (Turkey)

Technical Editor

Hatice Vural, Electrical and Electronics Enginering, Amasya University (Turkey)

Editorial Assistant

Ahmet Erhan Tanyeri, Sakarya University (Turkey)

Evrim Yüksel, Sakarya University (Turkey)

RESEARCH ARTICLES

Title: On Fibonaccı (k,p)-Numbers and Their Interpretations

Authors: Yasemin TAŞYURDU, Berke CENGİZ

On Fibonacci (k, p)-Numbers and Their Interpretations

Yasemin TAŞYURDU [*1] ID, Berke CENGİZ[1] ID

Abstract

In this paper, we define new kinds of Fibonacci numbers, which generalize both Fibonacci, Jacobsthal, Narayana numbers and Fibonacci p-numbers in the distance sense, using the definition of a distance between numbers by a recurrence relation according to a new parameter k. Tiling and combinatorial interpretations of these numbers are presented, and explicit formulas that allow us to calculate the nth number are given. Also, their generating functions are obtained and sums formulas of these numbers with special subscripts are given by tiling interpretations that allow the derivation of their properties.

Keywords: Combinatorial identities, Fibonacci p-numbers, generalized Fibonacci numbers, tilings

1. INTRODUCTION

Fibonacci numbers are given by recurrence relation $F_n = F_{n-1} + F_{n-2}$ for $n \geq 2$ with initial terms $F_0 = 0$, $F_1 = 1$. These numbers have many generalizations, applications and interpretations presented in different ways [1]. Most of generalizations are obtained by changing the coefficient and distance between the added terms in the recurrence relation of the Fibonacci numbers and their initial terms. For instance, k-Fibonacci numbers are defined by recurrence relation $F_{k,n} = kF_{k,n-1} + F_{k,n-2}$ for $n \geq 2$ with initial terms $F_{k,0} = 0$, $F_{k,1} = 1$ by generalizing Fibonacci numbers according to the value of a new parameter k for the coefficient of the $(n-1)$th term in recurrence relation [2]. Then, a new family of k-Fibonacci numbers is defined and its

period and many properties of this family are presented [3-7].

On the other hand, taking into account the parameter p for distance between the added terms in the recurrence relation of the Fibonacci numbers, Fibonacci p-numbers are determined the by recurrence relation

$$F_p(n) = F_p(n-1) + F_p(n-p-1), \ n > p+1$$

with initial terms $F_p(1) = F_p(2) = \cdots = F_p(p+1) = 1$ for $p \geq 0$, and presented $(p \times 1) \times (p \times 1)$ companion matrix for these numbers [8, 9]. Some authors have presented fundamental identities of the Fibonacci p-numbers that are similar to well-known properties of the Fibonacci numbers and have provided various general formulas for these numbers. Using various properties of Pascal's triangle, the Fibonacci

p-numbers can be derived and their matrix representations are given [10, 11].

The Fibonacci p-numbers have led to the discovery of an infinite amount of the number sequences presented by recurrence relations called generalized or distance Fibonacci numbers. For instance, generalized Fibonacci numbers are defined by recurrence relation $F(k,n) = F(k,n-1) + F(k,n-k)$ for $n \geq k+1$ and with initial terms $F(k,n) = n+1$ for $0 \leq n \leq k$, the integer $k \geq 1$ by considering different parameters for both the initial terms and the distance between the added terms in the recurrence relation of the Fibonacci numbers [12]. In [13], distance Fibonacci numbers are introduced by recurrence relation $Fd(k,n) = Fd(k,n-k+1) + Fd(n-k)$ for $n \geq k$ and with initial terms $Fd(k,n) = 1$ for $0 \leq n \leq k-1$, integers $k \geq 2$ and $n \geq 0$. Then $(2,k)$-distance Fibonacci numbers are given by $F_2(k,n) = F_2(k,n-2) + F_2(k,n-k)$ for $n \geq k$ and with initial terms $F_2(k,i) = 1$ for $i = 0,1,\ldots k-1$, integers $k \geq 1$ and $n \geq 0$ as a new kind of the distance Fibonacci numbers [14].

Combinatorial and tiling interpretations are extensively used in researching generalized Fibonacci numbers and their properties. These numbers are interpreted as the number of tiling of a board of length n, a $1 \times n$ grid with cells labeled $1, 2, \ldots, n$, using squares and dominoes of various lengths. For instance, the nth Fibonacci number counts the number of distinct ways to tile a $1 \times n$ board using 1×1 squares and 1×2 dominoes. Then, many well-known relationships among Fibonacci numbers are provided via combinatorial and tiling proofs [15-17]. In [18], the tiling representations of Fibonacci p-numbers are introduced.

The aim of this study is to generalize the well-known Fibonacci, the Fibonacci type and the distance Fibonacci numbers and define new kinds of the Fibonacci, the Jacobsthal, the Narayana numbers and the

Fibonacci p-numbers generalized in the distance sense using many generalization criterion used to generalize recurrence sequences presented by recurrence relations, as in the studies cited above. It is to derive the general formulas, generating functions and some identities for these generalized Fibonacci numbers. It is also to express these numbers with set decomposition, combinatorial, tiling interpretations, and give their special cases and generalize all the results.

2. FIBONACCI (k,p)-NUMBERS

In this section, new generalizations of the well-known Fibonacci, the Fibonacci type and the distance Fibonacci numbers, called Fibonacci (k,p)-numbers, are presented according to a new parameter k. The nth Fibonacci (k,p)-number is expressed by set decomposition, combinatorial and tiling interpretations that allow the derivation of its properties.

Definition 1. For integers $k, p \geq 1$ and $n \geq p$, the nth Fibonacci (k,p)-number is defined by recurrence relation

$$F_p^{(k)}(n) = F_p^{(k)}(n-1) + kF_p^{(k)}(n-p) \quad (1)$$

with initial terms $F_p^{(k)}(n) = 1$ for $n = 0,1,2,\ldots,p-1$. The sequences of the Fibonacci (k,p)-numbers are denoted by $\left\{F_p^{(k)}(n)\right\}_{n \geq 0}$.

Sequences of the Fibonacci (k,p)-numbers for $p = 1,2,3,4,5,6$:

$$\left\{F_1^{(k)}(n)\right\}_{n \geq 0} = \{1, 1+k, 1+2k+k^2,$$
$$1+3k+3k^2+k^3, 1+4k$$
$$+6k^2+4k^3+k^4, \ldots\}$$

$$\left\{F_2^{(k)}(n)\right\}_{n \geq 0} = \{1,1,1+k,1+2k,1+3k$$
$$+k^2,1+4k+3k^2,1+5k$$
$$+6k^2+k^3,\ldots\}$$

$$\left\{F_3^{(k)}(n)\right\}_{n\geq 0} = \{1, 1, 1, 1+k, 1+2k,$$
$$1+3k, 1+4k+k^2, 1+5k+3k^2,$$
$$1+6k+6k^2, \dots\}$$

$$\left\{F_4^{(k)}(n)\right\}_{n\geq 0} = \{1, 1, 1, 1, 1+k, 1+2k,$$
$$1+3k, 1+4k, 1+5k+k^2,$$
$$1+6k+3k^2, \dots\}$$

$$\left\{F_5^{(k)}(n)\right\}_{n\geq 0} = \{1, 1, 1, 1, 1, 1+k, 1+2k,$$
$$1+3k, 1+4k, 1+5k,$$
$$1+6k+k^2, 1+7k+3k^2, \dots\}$$

$$\left\{F_6^{(k)}(n)\right\}_{n\geq 0} = \{1, 1, 1, 1, 1, 1, 1+k,$$
$$1+2k, 1+3k, 1+4k, 1+5k,$$
$$1+6k, 1+7k+k^2, \dots\}$$

Definition 1 is the general form of many generalized Fibonacci numbers defined by well-known recurrence relations and the distance sense. Special cases of the Fibonacci (k, p)-numbers obtained according to parameters k and p are given in the Table 1. Therefore, any result obtained throughout the study for the Fibonacci (k, p)-numbers is valid for all numbers mentioned in Table 1.

Table 1 Special cases of the Fibonacci (k, p)-numbers

k	p	Symbol	nth Fibonacci (k, p)-number
1	2	$F_2^{(1)}(n) = F_{n+1}$	F_n, nth Fibonacci number [1]
1	$p+1$	$F_{p+1}^{(1)}(n) = F_p(n+1)$	$F_p(n)$, nth Fibonacci p-number [8]
2	2	$F_2^{(2)}(n) = J_{n+1}$	J_n, nth Jacobsthal number [19]
1	3	$F_3^{(1)}(n) = N_{n+1}$	N_n, nth Narayana number [20]

For some values of k and p, the sequences of the Fibonacci (k, p)-numbers, $\left\{F_p^{(k)}(n)\right\}_{n\geq 0}$ indexed in The On-Line Encyclopedia of Integer Sequences [21], from now on OEIS, are:

- $\left\{F_1^{(1)}(n)\right\}_{n\geq 0}$ in A000079

$\{1, 2, 4, 8, 16, 32, 64, 128, 256, 512, 1024, \dots\}$

- $\left\{F_2^{(1)}(n)\right\}_{n\geq 0}$ in A000045

$\{1,1,2,3,5,8,13,21,34,55,89,144,233,377, \dots\}$

- $\left\{F_6^{(1)}(n)\right\}_{n\geq 0}$ in A005708

$\{1,1,1,1,1,1,2,3,4,5,6,7,9,12,16,21, \dots\}$

- $\left\{F_2^{(2)}(n)\right\}_{n\geq 0}$ in A001045

$\{1, 1, 3, 5, 11, 21, 43, 85, 171, 341, 683, \dots\}$

- $\left\{F_2^{(4)}(n)\right\}_{n\geq 0}$ in A006131

$\{1,1,5,9,29,65,181,441,1165, \dots\}$

- $\left\{F_2^{(8)}(n)\right\}$ in A015443

$\{1,1,9,17,89,225,937,2737,10233, \dots\}$

More generally, for $p = 1,2$ the Table 2 and Table 3 are obtained:

Table 2 Fibonacci $(k, 1)$-numbers

$F_p^{(k)}(n)$ $\backslash$ n	0	1	2	3	4	5	6	7	8
$F_1^{(1)}(n)$	1	2	4	8	16	32	64	128	256
$F_1^{(2)}(n)$	1	3	9	27	81	243	729	2187	6561
$F_1^{(3)}(n)$	1	4	16	64	256	1024	4096	16384	65536
$F_1^{(4)}(n)$	1	5	25	125	625	3125	15625	78125	390625
$F_1^{(5)}(n)$	1	6	36	216	1296	7776	46656	279936	1679616
$F_1^{(6)}(n)$	1	7	49	343	2401	16807	117649	823543	5764801
$F_1^{(7)}(n)$	1	8	64	512	4096	32768	262144	2097152	16777216
$F_1^{(8)}(n)$	1	9	81	729	6561	59049	531441	4782969	43046721
$F_1^{(9)}(n)$	1	10	100	1000	10000	100000	1000000	10000000	100000000
$F_1^{(10)}(n)$	1	11	121	1331	14641	161051	1771561	19487171	214358881

Table 3 Fibonacci $(k, 2)$-numbers

$F_p^{(k)}(n)$ $\backslash$ n	0	1	2	3	4	5	6	7	8
$F_2^{(1)}(n)$	1	1	2	3	5	8	13	21	34
$F_2^{(2)}(n)$	1	1	3	5	11	21	43	85	171
$F_2^{(3)}(n)$	1	1	4	7	19	40	97	217	508
$F_2^{(4)}(n)$	1	1	5	9	29	65	181	441	1165
$F_2^{(5)}(n)$	1	1	6	11	41	96	301	781	2286
$F_2^{(6)}(n)$	1	1	7	13	55	133	463	1261	4039
$F_2^{(7)}(n)$	1	1	8	15	71	176	673	1905	6616
$F_2^{(8)}(n)$	1	1	9	17	89	225	937	2737	10233
$F_2^{(9)}(n)$	1	1	10	19	109	280	1261	3781	15130
$F_2^{(10)}(n)$	1	1	11	21	131	341	1651	5061	21571

For $k = 1,2$ the Table 4 and Table 5 are obtained:

Table 4 Fibonacci $(1, p)$-numbers

$F_p^{(k)}(n)$ $\backslash$ n	0	1	2	3	4	5	6	7	8
$F_1^{(1)}(n)$	1	2	4	8	16	32	64	128	256
$F_2^{(1)}(n)$	1	1	2	3	5	8	13	21	34
$F_3^{(1)}(n)$	1	1	1	2	3	4	6	9	13
$F_4^{(1)}(n)$	1	1	1	1	2	3	4	5	7
$F_5^{(1)}(n)$	1	1	1	1	1	2	3	4	5
$F_6^{(1)}(n)$	1	1	1	1	1	1	2	3	4
$F_7^{(1)}(n)$	1	1	1	1	1	1	1	2	3
$F_8^{(1)}(n)$	1	1	1	1	1	1	1	1	2
$F_9^{(1)}(n)$	1	1	1	1	1	1	1	1	1
$F_{10}^{(1)}(n)$	1	1	1	1	1	1	1	1	1

Table 5 Fibonacci $(2,p)$-numbers

$F_p^{(k)}(n)$ \ n	0	1	2	3	4	5	6	7	8
$F_1^{(2)}(n)$	1	3	9	27	81	243	729	2187	6561
$F_2^{(2)}(n)$	1	1	3	5	11	21	43	85	171
$F_3^{(2)}(n)$	1	1	1	3	5	7	13	23	37
$F_4^{(2)}(n)$	1	1	1	1	3	5	7	9	15
$F_5^{(2)}(n)$	1	1	1	1	1	3	5	7	9
$F_6^{(2)}(n)$	1	1	1	1	1	1	3	5	7
$F_7^{(2)}(n)$	1	1	1	1	1	1	1	3	5
$F_8^{(2)}(n)$	1	1	1	1	1	1	1	1	3
$F_9^{(2)}(n)$	1	1	1	1	1	1	1	1	1
$F_{10}^{(2)}(n)$	1	1	1	1	1	1	1	1	1

2.1. Generating Functions for $F_p^{(k)}(n)$

In this section, generating functions are constructed for the sequences of the Fibonacci (k,p)-numbers, $\left\{F_p^{(k)}(n)\right\}$ that generalize the well-known Fibonacci, the Fibonacci-like and the distance Fibonacci sequences.

We define $G_p^{(k)}(x)$ the generating functions of the sequences $\left\{F_p^{(k)}(n)\right\}$ such that

$$G_p^{(k)}(x) = \sum_{n=0}^{\infty} F_p^{(k)}(n)\, x^n \qquad (2)$$

where integers $k, p \geq 1$. Then the generating functions of the sequences $\left\{F_p^{(k)}(n)\right\}$ are given in the following theorem.

Theorem 2. Let $k, p \geq 1$ be integers. Generating functions for the sequences of the Fibonacci (k,p)-numbers, $\left\{F_p^{(k)}(n)\right\}$ are

$$G_p^{(k)}(x) = \frac{1}{1 - x - kx^p}.$$

Proof. Using equations (1) and (2), we have

$$G_p^{(k)}(x) = \sum_{n=0}^{\infty} F_p^{(k)}(n)\, x^n$$

$$= F_p^{(k)}(0) + F_p^{(k)}(1)x^1 + F_p^{(k)}(2)x^2$$

$$+ \cdots + F_p^{(k)}(n)x^n + \cdots$$

and

$$G_p^{(k)}(x) - xG_p^{(k)}(x) - kx^p G_p^{(k)}(x)$$

$$= \sum_{n=0}^{\infty} F_p^{(k)}(n)\, x^n - \sum_{n=0}^{\infty} F_p^{(k)}(n)\, x^{n+1}$$

$$- k\sum_{n=0}^{\infty} F_p^{(k)}(n)\, x^{n+p}$$

$$= \sum_{n=0}^{p-1} F_p^{(k)}(n)\, x^n + \sum_{n=p}^{\infty} F_p^{(k)}(n)\, x^n$$

$$- \sum_{n=0}^{p-2} F_p^{(k)}(n)\, x^{n+1} - \sum_{n=p-1}^{\infty} F_p^{(k)}(n)\, x^{n+1}$$

$$- k\sum_{n=0}^{\infty} F_p^{(k)}(n)\, x^{n+p}$$

$$= \sum_{n=0}^{p-1} F_p^{(k)}(n)\, x^n - \sum_{n=0}^{p-2} F_p^{(k)}(n)\, x^{n+1}$$

$$+ \left(\sum_{n=0}^{\infty} F_p^{(k)}(n+p)\, x^{n+p}\right.$$

$$-\sum_{n=0}^{\infty} F_p^{(k)}(n+p-1)\,x^{n+p}$$

$$\left.-k\sum_{n=0}^{\infty} F_p^{(k)}(n)\,x^{n+p}\right)$$

$$=\sum_{n=0}^{p-1} x^n - \sum_{n=0}^{p-2} x^{n+1}$$

$$+\sum_{n=0}^{\infty}\left(F_p^{(k)}(n+p) - F_p^{(k)}(n+p-1)\right.$$

$$\left.-kF_p^{(k)}(n)\right)x^{n+p}$$

$$=1$$

with $F_p^{(k)}(n) = 1$ for $n = 0,1,2,\dots,p-1$ and the generating functions of the sequences $\left\{F_p^{(k)}(n)\right\}$ are

$$G_p^{(k)}(x) = \frac{1}{1-x-kx^p}.$$

Thus, the proof is completed.

Using parameters k and p given in Table 1 in Theorem 2, the generating functions for the special cases of the sequences of the Fibonacci (k,p)-numbers are given in the following corollary.

Corollary 3. The generating functions of the sequences given in Table 1 are:

- $G_2^{(1)}(x) = \frac{1}{1-x-x^2}$ for the Fibonacci sequences, $\{F_{n+1}\}$ with $k = 1, p = 2$, [22]

- $G_{p+1}^{(1)}(x) = \frac{1}{1-x-x^{p+1}}$ for sequences of Fibonacci p-numbers, $\{F_p(n+1)\}$ with $k = 1, p = p+1$, [10]

- $G_2^{(2)}(x) = \frac{1}{1-x-2x^2}$ for the Jacobsthal sequences, $\{J_{n+1}\}$ with $k = 2, p = 2$, [22]

- $G_3^{(1)}(x) = \frac{1}{1-x-x^3}$ for Narayana sequences, $\{N_{n+1}\}$ with $k = 1, p = 3$.

3. INTERPRETATIONS OF THE FIBONACCI (k,p)-NUMBERS

In this section, the Fibonacci (k,p)-numbers are expressed with different interpretations such as set decomposition, combinatorial and tiling interpretations. Using these interpretations, general formulas and identities for the Fibonacci (k,p)-numbers are obtained.

3.1. Set Decomposition for $F_p^{(k)}(n)$

We now represent numbers $F_p^{(k)}(n)$ according to special decompositions of the set of n integers. Assume that $k \geq 1$ and $p > 1$ are integers and $S_n = \{1,2,\dots,n\}$ is the set of n integers. Let $\mathcal{A} = \{A_i : i \in I\}$ be the family of subsets of the set S_n such that each subset A_i contains consecutive integers and satisfies the following conditions

  i. $|A_i| = 1$ or $|A_i| = p$ for $i \in I$,

  ii.   If $|A_i| = p$, it may be colored with one of k different colors,

  iii. $A_i \cap A_j = \emptyset$ for $i \neq j$, $i,j \in I$,

  iv. $\left|\bigcup_{i \in I} A_i\right| = n$

for $n \geq 1$.

Each the family $\mathcal{A}$ is a color decomposition of the set of n integers related to k different colors and is called as a (k,p)-decomposition of the set S_n.

Theorem 4. Let $k, n \geq 1$ and $p > 1$ be integers. Then the number of all (k,p)-decompositions of the set S_n is equal to $F_p^{(k)}(n)$.

Proof. By induction. Let $k, n \geq 1$ and $p > 1$ be integers and $S_n = \{1, 2, \ldots, n\}$. Indicate by $s(k,p)_n$ the number of all (k,p)-decompositions of the set S_n. To complete the proof, we show that $s(k,p)_n = F_p^{(k)}(n)$. For $n < p$, $\mathcal{A}$ the family can be obtained in exactly one way with $|A_i| = 1, i \in I$ for each subset, so S_n has 1 such family and $s(k,p)_n = 1 = F_p^{(k)}(n)$. For $n \geq p$, either $\{1\} \in \mathcal{A}$ or $\{1, 2, \ldots, p\} \in \mathcal{A}$, and suppose that $s(k,p)_n = F_p^{(k)}(n)$ holds for n. We show that it is true for $n + 1$ which means $s(k,p)_{n+1} = F_p^{(k)}(n+1)$. Let $s_1(k,p)_{n+1}$ be the number of all (k,p)-decompositions of the set S_{n+1} such that $\{1\} \in \mathcal{A}$ and let $s_p(k,p)_{n+1}$ be the number of all (k,p)-decompositions of the set S_{n+1} such that $\{1, 2, \ldots, p\} \in \mathcal{A}$. Since these two cases are mutually exclusive, by the addition principle $s(k,p)_{n+1} = s_1(k,p)_{n+1} + s_p(k,p)_{n+1}$. If $\{1\} \in \mathcal{A}$, then the number of all (k,p)-decompositions of the set $S_{n+1-1} = \{2, 3, \ldots, n+1\}$ is $s(k,p)_{n+1-1}$. Add $\{1\}$ to each of the families of subsets of the set S_{n+1-1}. Then we have $s(k,p)_{n+1-1} = s_1(k,p)_{n+1}$ the families. If $\{1, 2, \ldots, p\} \in \mathcal{A}$, then the number of all (k,p)-decompositions of the set $S_{n+1-p} = \{p+1, p+2, \ldots, n+1\}$ is $s(k,p)_{n+1-p}$. Add $\{1, 2, \ldots, p\}$ to each of the families of subsets of the set S_{n+1-p} with a choice of k different colors. Then we $ks(k,p)_{n+1-p} = s_p(k,p)_{n+1}$ the families. On the other hand, using the induction's hypothesis and the recurrence relation (1), we obtain

$$
\begin{aligned}
s(k,p)_{n+1} &= s_1(k,p)_{n+1} + s_p(k,p)_{n+1} \\
&= s(k,p)_n + ks(k,p)_{n+1-p} \\
&= F_p^{(k)}(n) + kF_p^{(k)}(n+1-p) \\
&= F_p^{(k)}(n+1)
\end{aligned}
$$

and the theorem is proved.

This interpretation of set decomposition allows a tiling approach for the Fibonacci (k,p)-numbers.

3.2. A Tiling Approach to $F_p^{(k)}(n)$

We now give the tiling interpretations for the sequences of the Fibonacci (k,p)-numbers and show that the nth Fibonacci (k,p)-number counts the number of distinct ways to tile a board of length n, called a $1 \times n$ board, using boards of lengths 1 and different colored p.

Assume that $k \geq 1$ and $p > 1$ are integers. Let us represent the numbers $F_p^{(k)}(n)$ as the number of distinct ways to tile a $1 \times n$ board using 1×1 boards (squares) and colored $1 \times p$ boards (p-ominoes), where there are k different colors for p-ominoes. Suppose we begin from the leftmost when placing cells and a $1 \times n$ board is splinted as follows:

$$\boxed{1 \times c_1} \boxed{1 \times c_2} \boxed{\cdots} \boxed{1 \times c_i}$$

Where each $1 \times c_i$ board satisfies the following conditions

  i. $c_i \in \{1, p\}$ for $i \in I$,

  ii.   If $c_i = p$, it may be colored with one of k different colors,

  iii. $\sum_{i \in I} c_i = n$.

Theorem 5. For integers $k, n \geq 1$ and $p > 1$, $F_p^{(k)}(n)$ counts the number of distinct ways to tile a $1 \times n$ board with 1×1 squares and colored $1 \times p$, p-ominoes, where there are k different colors for p-ominoes.

Proof. By induction. Let $k, n \geq 1, p > 1$ be integers. Indicate by $(k,p)_n$ the number of distinct ways to tile a $1 \times n$ board using 1×1 squares and colored $1 \times p$, p-ominoes, where there are k different colors for p-ominoes. To complete the proof, we show that $(k,p)_n = F_p^{(k)}(n)$. For $n < p$, all cells in tilings are 1×1 square and it can be obtained in exactly one way, so $(k,p)_n = 1 = F_p^{(k)}(n)$. For $n \geq p$, the first cell in the tilings is either a 1×1 square or a $1 \times p$, p-omino, and suppose that $(k,p)_n = F_p^{(k)}(n)$

holds for n. We show that it is true for $n + 1$ which means $(k, p)_{n+1} = F_p^{(k)}(n + 1)$. From now on, according to two options of the first cell, there are $(k, p)_{n+1-1}$ distinct ways to tile a $1 \times n$ board whose first cell is a 1×1 square, and there are $k(k, p)_{n+1-p}$ distinct ways to tile a $1 \times n$ board whose first cell is a $1 \times p$, p-omino with a choice of k different colors. Since these two cases are mutually exclusive, by the addition principle $(k, p)_{n+1} = (k, p)_n + k(k, p)_{n+1-p}$. On the other hand, using the induction's hypothesis we have $(k, p)_n = F_p^{(k)}(n)$ and $(k, p)_{n+1-p} = F_p^{(k)}(n + 1 - p)$. By the recurrence relation (1), we have

$$\begin{aligned} (k, p)_{n+1} &= (k, p)_n + k(k, p)_{n+1-p} \\ &= F_p^{(k)}(n) + kF_p^{(k)}(n + 1 - p) \\ &= F_p^{(k)}(n + 1) \end{aligned}$$

and the theorem is proved.

We now give another general formula that directly presents the nth Fibonacci (k, p)-number.

3.3. Combinatorial Representation of $F_p^{(k)}(n)$

We now present combinatorial formulas for the Fibonacci (k, p)-numbers. An explicit formula that allows us to calculate the nth Fibonacci (k, p)-number, $F_p^{(k)}(n)$ are given in the following theorem.

Theorem 6. Let $k, p \geq 1$ and $n \geq 0$ be integers. Then

$$F_p^{(k)}(n) = \sum_{i=0}^{\left\lfloor \frac{n}{p} \right\rfloor} \binom{n - i(p - 1)}{i} k^i$$

Proof. By induction. Let $k, p \geq 1$ and $n \geq 0$ be integers. If $n < p$, then $\left\lfloor \frac{n}{p} \right\rfloor = 0$. Using Definition 1, we have

$$F_p^{(k)}(n) = \sum_{i=0}^{\left\lfloor \frac{n}{p} \right\rfloor} \binom{n - i(p - 1)}{i} k^i = 1$$

for $n < p$. Assume that $n \geq p$. Let us suppose this formula is true until n. Then

$$F_p^{(k)}(n + 1) = F_p^{(k)}(n) + kF_p^{(k)}(n + 1 - p)$$

$$= \sum_{i=0}^{\left\lfloor \frac{n}{p} \right\rfloor} \binom{n - i(p - 1)}{i} k^i$$

$$+ \sum_{i=0}^{\left\lfloor \frac{n+1-p}{p} \right\rfloor} \binom{n + 1 - p - i(p - 1)}{i} k^{i+1}$$

$$= \binom{n}{0} + \sum_{i=1}^{\left\lfloor \frac{n}{p} \right\rfloor} \binom{n - i(p - 1)}{i} k^i$$

$$+ \sum_{i=0}^{\left\lfloor \frac{n+1}{p} \right\rfloor - 1} \binom{n + 1 - p - i(p - 1)}{i} k^{i+1}$$

$$= 1 + \sum_{i=0}^{\left\lfloor \frac{n}{p} \right\rfloor - 1} \binom{n - (i + 1)(p - 1)}{i + 1} k^{i+1}$$

$$+ \sum_{i=0}^{\left\lfloor \frac{n+1}{p} \right\rfloor - 1} \binom{n - (i + 1)(p - 1)}{i} k^{i+1}$$

$$= 1$$

$$+ \sum_{i=0}^{\left\lfloor \frac{n+1}{p} \right\rfloor - 1} \binom{n - (i + 1)(p - 1) + 1}{i + 1} k^{i+1}$$

$$= 1 + \sum_{i=1}^{\left\lfloor \frac{n+1}{p} \right\rfloor} \binom{n + 1 - i(p - 1)}{i} k^i$$

$$= \sum_{i=0}^{\left\lfloor \frac{n+1}{p} \right\rfloor} \binom{n + 1 - i(p - 1)}{i} k^i$$

which completes the proof.

Note that in the proof of Theorem 6, $a < b \Rightarrow \binom{a}{b} = 0$, $a < 0 \Rightarrow \binom{a}{b} = 0$ and $\binom{a}{0} = 1$ for $\forall$ a are considered.

Using parameters k and p given in Table 1 in Theorem 6, well-known combinatorial formulas that allow us to calculate the nth terms of the special cases of the sequences of the Fibonacci (k, p)-numbers are given in the following corollary.

Corollary 7. The combinatorial formulas of the sequences given in Table 1 are:

- $F_{n+1} = \sum_{i=0}^{\lfloor \frac{n}{2} \rfloor} \binom{n-i}{i}$ for the Fibonacci numbers, $F_2^{(1)}(n) = F_{n+1}$ with $k = 1$, $p = 2$, [22]

- $F_p(n+1) = \sum_{i=0}^{\lfloor \frac{n}{p+1} \rfloor} \binom{n-ip}{i}$ for the Fibonacci p-numbers, $F_{p+1}^{(1)}(n) = F_p(n+1)$ with $k = 1$, $p = p + 1$, [11]

- $J_{n+1} = \sum_{i=0}^{\lfloor \frac{n}{2} \rfloor} \binom{n-i}{i} 2^i$ for the Jacobsthal numbers, $F_2^{(2)}(n) = J_{n+1}$ with $k = 2$, $p = 2$,

- $N_{n+1} = \sum_{i=0}^{\lfloor \frac{n}{3} \rfloor} \binom{n-2i}{i}$ for the Narayana numbers, $F_3^{(1)}(n) = N_{n+1}$ with $k = 1$, $p = 3$.

3.4. Identities for $F_p^{(k)}(n)$

We now give the identities and the sums formulas of the Fibonacci (k, p)-numbers with special subscripts via tiling proof in the following theorems.

Theorem 8. Let $k, p \geq 1$ and $n \geq 2p - 1$ be integers. Then

$$F_p^{(k)}(n) = (k-1)F_p^{(k)}(n-p)$$
$$+ F_p^{(k)}(n-1) + F_p^{(k)}(n-p+1)$$
$$- kF_p^{(k)}(n-2p+1).$$

Proof. This result is obtained directly from the equation (1).

Theorem 9. Let $k, p \geq 1$ and $n \geq 0$ be integers. Then

$$F_p^{(k)}(n+p) = \sum_{i=0}^{n} kF_p^{(k)}(i) + 1.$$

Proof. From Theorem 5, the number of distinct ways to tile a $1 \times (n + p)$ board using 1×1 squares and k different colored $1 \times p$, p-ominoes is equal to $F_p^{(k)}(n + p)$. Thus, the left-hand side of this identity is counted. If we show that the right-hand side of the identity gives the same count, the proof is completed. Suppose that we have a $1 \times (n + p)$ board and place the cells beginning from the leftmost cell. There is exactly a tiling where all the cells are 1×1 square. In the other cases there is at least a $1 \times p$, p-omino. Tilings containing only a $1 \times p$, p-omino can be partitioned according to the location of the first $1 \times p$, p-omino, counting from the left. There are $kF_p^{(k)}(n)$ distinct ways to tile $1 \times (n + p - p)$ board if $1 \times p$, p-omino appears for the first time in the first cell, and $kF_p^{(k)}(n - 1)$ distinct ways to tile $1 \times (n + p - p - 1)$ board if $1 \times p$, p-omino appears for the first time in the second cell where there are k different colors for p-ominoes. Similarly, if $1 \times p$, p-omino appears for the first time in the last cell, there are n times 1×1 square before the location of $1 \times p$, p-omino and we get $kF_p^{(k)}(0)$ distinct ways to tile $1 \times (n + p - p - n)$ board where there are k different colors for p-ominoes. The desired result is the sum of all the tilings and $\sum_{i=0}^{n} kF_p^{(k)}(i) + 1 = F_p^{(k)}(n + p)$ is obtained. So, the proof is completed.

Theorem 10. Let $k, p \geq 1$ and $n \geq 0$ be integers. For $0 \leq r \leq p - 1$, we have

$F_p^{(k)}(np + r + 1)$

$$= \begin{cases} k^{n+1} + \sum_{i=0}^{n} k^{n-i} F_p^{(k)}(ip + r), & r = p - 1 \\ \sum_{i=0}^{n} k^{n-i} F_p^{(k)}(ip + r), & r < p - 1 \end{cases}$$

Proof. From Theorem 5, the number of distinct ways to tile a $1 \times (np + r + 1)$ board using 1×1 squares and k different colored $1 \times p$, p-ominoes is equal to $F_p^{(k)}(np + r + 1)$. Thus, the left-hand side of this identity is counted. If we show that the right-hand side of the identity gives the same count, the proof is completed. Suppose that we have a $1 \times (np + r + 1)$ board and place the cells beginning from the leftmost cell. If $r < p - 1$, then all tilings have at least a 1×1 square. Tilings containing only a 1×1 square can be partitioned according to the location of the first 1×1 square, counting from the left. There are $F_p^{(k)}(np + r)$ distinct ways to tile $1 \times (np + r + 1 - 1)$ board if 1×1 square appears for the first time in the first cell, and $k F_p^{(k)}((n-1)p + r)$ distinct ways to tile $1 \times (np + r + 1 - 1 - p)$ board if 1×1 square appears for the first time in the second cell where there are k different colors for p-ominoes. Similarly, if 1×1 square appears for the first time in the last cell, there are i times $1 \times p$, p-omino before the location of 1×1 square and we get $k^i F_p^{(k)}(p(n-i) + r)$ distinct ways to tile $1 \times (np + r + 1 - 1 - ip)$ board where there are k different colors for p-ominoes. The desired result is the sum of all the tilings and $\sum_{i=0}^{n} k^{n-i} F_p^{(k)}(ip + r) = F_p^{(k)}(np + r + 1)$ is obtained. Otherwise, if $r = p - 1$, there is exactly one more tiling where all tilings are $1 \times p$, p-omino and the number of such tilings is k^{n+1} with a choice of k different colors. So $\sum_{i=0}^{n} k^{n-i} F_p^{(k)}(ip + r) + k^{n+1} = F_p^{(k)}(np + r + 1)$ is obtained. So, the proof is completed.

4. CONCLUSION AND SUGGESTION

The generalizations and applications of the Fibonacci and the Fibonacci-type numbers have been presented in many ways. Most of generalizations are related to arbitrary parameters for initial terms, the coefficient and distance between the added terms in the recurrence relation of the Fibonacci numbers. In this paper, we define new generalizations of the well-known Fibonacci, the Fibonacci-type and the distance Fibonacci numbers, called Fibonacci (k, p)-numbers, according to a new parameter k. Thus, we have generalized the well-known Fibonacci, the Jacobsthal, the Narayana numbers and the Fibonacci p-numbers in the distance sense given in [1, 8, 19, 20]. Then the Fibonacci (k, p)-numbers are expressed by set decomposition, combinatorial and tiling interpretations which allow to derive properties of them via set decomposition, combinatorial and tiling proofs. Also, explicit formulas that allow us to calculate the nth terms of the sequences of the Fibonacci (k, p)-numbers are given. Finally, generating functions, sums formulas and identities for these numbers are obtained.

It would be interesting to study these numbers in matrix theory. More general formulas that allow us to calculate the nth Fibonacci (k, p)-number and relations like the known relations between the well-known Fibonacci and Fibonacci type numbers can be explored.

The Declaration of Conflict of Interest/ Common Interest

No conflict of interest or common interest has been declared by the authors.

Authors' Contribution

The first author contributed 60%, the second author 40%.

The Declaration of Ethics Committee Approval

This study does not require ethics committee permission or any special permission.

The Declaration of Research and Publication Ethics

The authors of the paper declare that they comply with the scientific, ethical and quotation rules of SAUJS in all processes of the paper and that they do not make any falsification on the data collected. In addition, they declare that Sakarya University Journal of Science and its editorial board have no responsibility for any ethical violations that may be encountered, and that this study has not been evaluated in any academic publication environment other than Sakarya University Journal of Science.

REFERENCES

[1] A. F. Horadam, "A Generalized Fibonacci Sequence," The American Mathematical Monthly, vol. 68, no. 5, pp. 455-459, 1961.

[2] S. Falcon, A. Plaza, "On the Fibonacci k-Numbers," Chaos, Solitons & Fractals, vol. 32, no. 5, pp. 1615-24, 2007.

[3] M. El-Mikkawy, T. Sogabe, "A New Family of k-Fibonacci Numbers," Applied Mathematics and Computation, vol. 215, no. 12, pp. 4456–4461, 2010.

[4] V. K. Gupta, Y. K. Panwar, O. Sikhwal, "Generalized Fibonacci Sequences," Theoretical Mathematics & Applications, vol. 2, no. 2, pp. 115-124, 2012.

[5] Y. Taşyurdu, N. Çobanoğlu, Z. Dilmen, "On the a New Family of k-Fibonacci Numbers," Erzincan University Journal of Science and Technology, vol. 9, no. 1, pp. 95-101, 2016.

[6] O. Deveci, Y. Aküzüm, "The Recurrence Sequences via Hurwitz Matrices," Annals of the Alexandru Ioan Cuza University-Mathematics, vol. 63, no. 3, pp. 1-13, 2017.

[7] Y. K. Panwar, "A Note on the Generalized k-Fibonacci Sequence," MTU Journal of Engineering and Natural Sciences, vol. 2, no. 2, pp. 29-39, 2021.

[8] A. P. Stakhov, "Introduction into Algorithmic Measurement Theory," Soviet Radio, Moskow, Russia, 1977.

[9] A. P. Stakhov, "Fibonacci Matrices, a Generalization of the Cassini Formula, and a New Coding Theory," Chaos, Solitons & Fractals, vol. 30, no. 1, pp. 56-66, 2006.

[10] E. Kiliç, "The Binet formula, Sums and Representations of Generalized Fibonacci p-numbers," European Journal of Combinatorics, vol. 29, no. 3, pp. 701–711, 2008.

[11] K. Kuhapatanakul, "The Fibonacci p-Numbers and Pascal's Triangle," Cogent Mathematics, vol. 3, no. 1, 7p, 2016.

[12] M. Kwasnik, I. Włoch, "The Total Number of Generalized Sable Sets and Kernels of Graphs," Ars Combinatoria, vol. 55, pp. 139-146, 2000.

[13] U. Bednarz, A. Włoch, M. Wołowiec-Musiał, "Distance Fibonacci Numbers, Their Interpretations and Matrix Generators," Commentationes Mathematicae, vol. 53, no. 1. pp. 35-46, 2013.

[14] I. Włoch, U. Bednarz, D. Brod, A. Włoch, M. Wołowiec-Musiał, "On a New Type of Distance Fibonacci Numbers," Discrete Applied Mathematics, vol. 161, no. 16-17, pp. 2695-2701, 2013.

[15] R. C. Brigham, R. M. Caron, P. Z. Chinn, R. P. Grimaldi, "A Tiling Scheme for the Fibonacci Numbers," Journal Recreational Mathematics, vol. 28, no. 1, pp. 10–17, 1996-97.

[16] A. T. Benjamin, J. J. Quinn, "Proofs that Really Count: The Art of Combinatorial Proof," Mathematical Association of America, Washington D. C., 2003, 194p.

[17] Y. Taşyurdu, N. Ş. Türkoğlu, "A Tiling Interpretation for (p,q)-Fibonacci and (p,q)-Lucas Numbers," Journal of Universal Mathematics, vol. 5, no. 2, pp. 81-87, 2022.

[18] Y. Taşyurdu, B. Cengiz, "A Tiling Approach to Fibonaccı p-Numbers," Journal of Universal Mathematics, vol. 5, no. 2, pp.177-184, 2022.

[19] A. F. Horadam, "Jacobsthal and Pell Curves," The Fibonacci Quarterly, vol. 26, no. 1, pp. 79-83, 1988.

[20] J. P. Allouche, T. Johnson, "Narayana's Cows and Delayed Morphisms," In: Articles of 3rd Computer Music Conference JIM96, France, 1996.

[21] N. J. A. Sloane, The On-Line Encyclopedia of Integer Sequences, The OEIS Foundation, 2006, www.research.att.com/~njas/sequences/.

[22] T. Koshy, "Fibonacci and Lucas Numbers with Applications," vol. 1, 2nd Edition, Wiley-Interscience Publications, New York, 2017, 704p.

Title: Socio-Economic Effects of Covid-19 on Construction Sector in Turkey

Authors: Asena KARSLIOĞLU, Mehmet Hanifi ALKAYIŞ, Eren BALABAN,Mehmet İnanç ONUR

Socio-Economic Effects of Covid-19 on Construction Sector in Turkey

Asena KARSLIOĞLU KAYA[*1] iD, Mehmet Hanifi ALKAYIŞ[2] iD, Eren BALABAN [*2] iD,

Mehmet İnanç ONUR[1] iD,

Abstract

The world has been living tough times both socially and economically because of the novel coronavirus. Social effects of Covid-19 have seen right after precautions taken by governments all around the world. However, precautions brought economical problems. Construction industry is also affected from this situation. To better understand the effect of Covid-19 on construction industry, questionnaire is carried out among people from construction industry. Questions are selected specifically for targeted people in construction industry. Survey is conducted electronically. Participants remained anonymous during survey. Totally 598 participants took part in questionnaire voluntarily. Survey questions are about job safety, finding a new job and precautions. Results indicated that, Covid-19 caused increase in unemployment in construction industry, making it harder to find a new job. This study proves that ordinary workers in the construction industry are the most vulnerable part for Covid -19 pandemic.

Keywords: Construction sector, covid-19, unemployment, job safety

1. INTRODUCTION

The world is facing a situation that it has not encountered for a long time. This situation caused by a novel type of virus. This virus is in the family of coronavirus. Coronavirus can cause common cold [1]. However, new kind of corona virus caused a new disease called severe acute respiratory syndrome in 2002. That virus is called as Sars CoV. Another type of corona virus caused a new outbreak in Saudi Arabia in 2012. This illness is named as Middle East Respiratory

Syndrome. Those two corona viruses claimed 1632 lives around the world [2]. In late December 2019, Dr. Li Wenliang and his colleagues identified new group of patients in Wuhan, Hubei Province, China with atypical pneumonia with severe features [1, 3]. This new disease is called as corona virus disease-19 (Covid-19) by World Health Organization (WHO) [2] and the novel virus is named as Sars-CoV-2 by International Committee on Taxonomy of Viruses [4]. Initial twenty-seven cases were tracked down to Huanan seafood market [1,

5]. After the initial cases, Covid-19 started to spread all around the world very quickly. WHO declared new outbreak as public health emergency of international concern on 30th January of 2020 [6, 7]. There were 7818 reported confirmed cases all around the world on 30th January 2020 [7].

Covid-19 is declared as pandemic because of high degree of spread and severity by WHO on 11th of March. The reported Covid-19 cases are stated as 118000 on same statement of WHO. Since Covid-19 can infect the society easily and rapidly, governments all around the world started to take precautions to control pandemic infection inside the country. Those measures include international and domestic travel bans, partial or total lockdowns, cancelling social gatherings like cultural and religious activities, sports games, scientific and political events [2]. Those precautions helped to contain the virus however, they yielded economical problems in society. Those precautions affected to people especially who are working in tourism and transportation sectors [2]. Decline in hotel reservation resulted decrease in prices of agriculture commodities by 20%. Survey conducted among the British Plastic Federation revealed that, 98% of participants are concerned with negative impact of the pandemic on business operations and 80% of the participants are expecting decline in turnover over the next two quarters. The chemical production is estimated to decline by 1.2% globally. Education system is also affected from ban on public gatherings. 900 million learners affected from closing education facilities all around the world [6].

Finance markets are also affected from Covid-19 outbreak globally. World Trade Organization (WTO) and Organization for Economic Cooperation and Development (OECD) announced that the pandemic is the largest threat to global economy since 2008-2009 [2]. Pandemic damaged the supply and demand chain [6]. A recession is expected during and after outbreak which will yield high unemployment rate and lost income and high inflation [2, 8]. Precarious countries are more susceptible to economical effects of the pandemic [8]. US stock markets fell dramatically. Other stock markets around the globe followed US stock market. In order to stop decrease in stock markets, monetary and fiscal policies are implied quickly. Those policies include lowering interest rates and announcing rescue packages. For example, US Federal Reserves lowered interest rates to 0% while Bank of England has cut the interest rate to 0.1%. Those precautions caused an increase in the stock markets. Meanwhile, G20 countries promised 5 trillion dollars to protect global economy and UN started humanitarian response plan [6, 9, 10). According to those data, it is clear that, Covid-19 possesses great risks and uncertainty globally in financial markets and recovery time might be as long as two decades [9, 10]. Timothy Laing investigated how Covid-19 effected mining industry.

When it comes to studies regarding how Covid-19 affects construction industry, there is not so many studies available currently. In one of those studies, Ubaidillah and Riyanto investigated effect of work culture and extrinsic work motivation on construction company strategy to deal with Covid-19. Their study is conducted by making observations and supporting interviews. According to their results, work culture and extrinsic work motivation play a key role on company strategy [11].

Department of Labor, Occupational Safety and Health Administration (OSHA) issued some tips for people who are working in construction industry to prevent from Covid-19 [12]. Those tips include encouraging workers to stay at home if they are sick, wearing masks over nose, avoiding physical contact with others. Osha also gives some responsibilities to construction company to keep workers uninfected. Those

precautions include training workers how to properly put on and take off protective clothing and equipment, promoting personal hygiene, providing alcohol-based hand rubs containing at least 60% alcohol when workers are not able to reach to soap and water. OSHA also states keeping in-person meetings as short as possible, limiting the number of workers in attendance. Encouraging workers to report any safety and health concerns are also encouraged. Similar precautions are also issued by the Ministry of Environment and Urbanization. Those precautions forbid usage of same equipment mutually, entering construction site without body temperature measurement, limiting unnecessary personnel entrance to construction site.

According to same document, office workers should either work from home or take shifts. Those precautions are necessary to take; however, it might cause losing jobs. According to survey conducted by Adams-Prassl et al. working from home rates are 35% and 25% in USA and UK respectively in construction industry. 60% of participants stated that they will have economical struggles in the future due to Covid-19 [13].

Ogunnusi et al. (2020) conducted 71 surveys from employees in the construction industry to examine the changes and new opportunities created by the Covid-19 pandemic on the current construction industry. By analyzing the survey data in SPSS statistical analysis program; procurement process, worker safety, time, cost etc. It was concluded that the pandemic affected the construction sector by 90%. In addition, it has been observed that sudden modernization and digitalization in the construction sector create job opportunities in the sector [14].

Alsharef et al. (2021) investigated the early effects of Covid-19 on the construction industry, according to a survey of thirty-four phone calls conducted in the United States. According to the interviews, project delays and cost increases were stated as the most negative features. In addition, there were complaints about the decrease in material supply and production. Furthermore, the study sheds light on the negative aspects of the sector during the pandemic process and presents findings to intervene in the sector and government institutions [15].

Pamidimukkala and Kermanshachi (2021) conducted research on articles, industry publications and reports to identify the problems faced by construction workers in the field of health and safety during the Covid-19 process and to find solutions. As a result of the study, seventeen main problems caused by Covid-19 were identified and categorized. As a result of the study, it was observed that health concerns have a psychologically devastating effect on workers. Moreover, strategies for worker problems were presented by presenting sterilization etc. suggestions for the problems identified in the study [16].

Rokooei et al. (2022) examined the effects of Covid-19, which has taken a negative place in world trade since 2020. For this reason, a total of 567 responses were collected by conducting a Likert scale survey with the experts in the construction sector 3 times (once every 6 months) on different dates. The survey results were analyzed statistically, and the change in the pandemic perceptions of civil engineers over time was examined. As a result, it has been observed that despite the decrease in the effects of Covid-19 in the construction sector in the group responses over time, its effect is remarkably high, and the sensitivities have changed, albeit slightly, according to the difference in experience [17].

Alfadil et al. (2022) searched the environmental factors of the Covid-19 pandemic on the construction sector by using the systematic review method,

making use of the publications in the literature. After 2010, studies with risks similar to pandemics were examined worldwide and it was observed that Malaysia and Egypt were most affected by these risks. As a result of the research, it has been suggested that the financial and supply chain factors are restricted in the contracts and that the specified costs and durations will reduce the quality of the project [18].

Elnaggar and Elhegazy (2022) studied the financial effects of the Covid-19 pandemic on Egypt's construction sector by conducting a 16-question survey. In this survey, factors such as cost items, human and machine effects, and facilities were examined and analyzed, and measures were proposed for different periods. These recommendations include strengthening infrastructure, rapid response to problems, improving workers' health and safety, and increasing digitization [19].

Effects of Covid-19 on various economic markets such as mining, financial markets, production and chemistry industries are already started to be investigated by several researchers. However, studies regarding its effects to construction industry are quite limited until now according to the best knowledge of the authors. Therefore, a questionnaire is conducted to field and office engineers and workers in order to reveal direct effects of Covid-19 to construction industry in Turkey. Results of this study provide insight to current situation of the participants and their future expectancy after Covid-19 pandemic.

2. METHOD

A questionnaire is a systematic method of data collection. It is possible to collect many diverse types of data with the questionnaire method. In this study, job performances, knowledge levels, preferences, etc. such data are collected. The purpose of the survey is to determine the socio-economic effects of Covid-19 on construction sector in Turkey. The questions used in the survey form are closed-ended questions. Question types are two options (yes / no), best answer, scaled answers (Likert scale) and sequential options.

The survey is prepared between April 2020 and May 2020 to determine the first effects of the Covid-19 pandemic on the construction industry. Online data are collected by preparing a google form for the survey. At the beginning of the survey, the participants are used to categorize them into smaller and more specialized groups based on demographic questions and criteria such as age, education level, and marital status. One of the aims of the study is to determine the crucial differences between the answers given by the five different groups. Engineers in the public sector, construction workers, construction site engineers and project engineers are selected as the audience of this study. In addition, the survey conducted in employers. The questionnaire is prepared and electronically distributed to people. All participants are volunteered for this study. Participants are informed about their answers will be used for research purposes.

After preparing the draft questionnaire, it is assessed to improve the questionnaire and identify possible errors. Testing is conducted to ensure the reliability and validity of the questionnaire before it is distributed to the masses. The survey firstly is applied to a smaller group representing the larger group. In this study, Comrey and Lee (1992) guidelines are used for the sample size. They suggested that 50 samples are poor, 300 samples are good, 500 samples are very good, and 1000 samples are perfect [20]. A total of 598 people participated in this questionnaire.

Since construction industry is composed of many components when human resources are considered. Those components can be given as field engineers, design engineers, workers and foremen in the site, contractors

and engineers working in state institutions. Due to different jobs, they perform, they are susceptible and affected by Covid-19. In order to take this fact into consideration, different surveys are prepared for different groups. All groups are asked about the future of construction industry in common. Balance of payments are considered for site engineers, office engineers and contractors. In order to correlate the answers about payments from engineers, contractors are asked if they can pay regularly to their personnel. It is also asked if engineers lost their jobs and if contractors fired some of their employees. It is also questioned that if the engineers had to get a new job other than construction. Answers to those questions will be given provided in next section.

The data filled in by the participants are automatically saved to the Google Excel page and the data is transferred to the Microsoft Excel program. Percentage distributions are made in the Microsoft Excel program. The data is analyzed using SPSS Statistics software. Values are assigned as "None=1", "Little=2", "Moderate=3", "Very=4" and "Too much=5" in SPSS. When analyzing data with SPSS, the data we are working on should be distributed normally or close to normal. Kolmogorov-Smirnov test is conducted to control the normality of the distribution. According to the test results, it is seen that the distribution of the data is suitable.

3. RESULTS

A total number of 598 people from Turkey participated in our survey. 52 people work in state institution, 81 people are employers, 139 people are project engineers, 276 people are field engineers and remaining participants are foreman who work in construction industry and employers. 508 participants are male while only 90 participants are female only. Newly graduated civil engineers and engineers

working for state institutions take part in this study.

3.1. Social Backgrounds of Participants

In order to determine the social background of the participants, information about their age, their marital status, their level of education and where they live are collected. 51% of participants stated they are single. Majority of participants stated their age between 26 – 35. Those people constitute 56% of all participants. Second largest groups' age is between 36 – 45. Age distribution of participants are given on Fig.1.
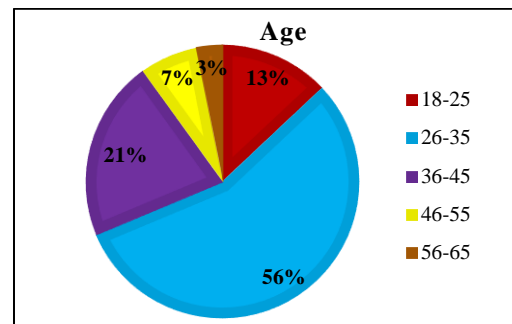
Figure 1 Age distribution of participants

69% of participants hold undergraduate degree, 20% holds Master of Science (M.Sc.) degree and 1% has Ph.D. degree. The remaining participant are either graduated from high school or primary school. Those people mostly work in private companies. Percentages related to where those people work are given on Figure 2 below.
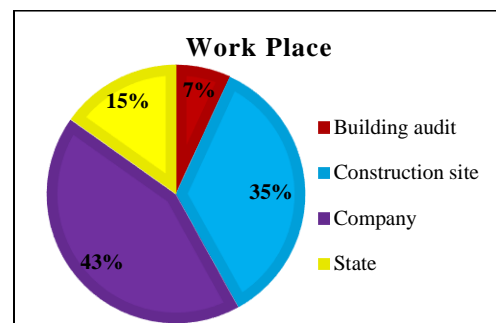
Figure 2 Workplaces' of participants

When current accommodation status is asked to participants, it is seen that 65% of

participant gave the answer with family which corresponds to 391 people. The ratio of people living with family is well above the sum of married participants. If we consider 9% of participants stated living on construction site, some part of the students and newly graduated engineers are living alone or with flat mates. Those people have not thought to move into their family due to economic difficulties. Although only 17% of foreigners are married and 33% are student, 37% are living with their family.

3.2. Effect of Covid – 19 in General

In order to determine and evaluate the general effect of Covid-19 pandemic to participants' daily life, questions were asked regarding if they or someone around them had Covid-19, if they take necessary precautions, and if they believe those precautions prevents them to get infected, what they think about change of solidarity in society, source of the news, if they support 14-day curfew and when they expect the end of pandemic.

25% of participants answered that their lives are seriously affected from corona virus disease. However, 20% of participants reported that they are taking too much personal precautions. Figure 3 and Figure 4 provides more detailed information about participants' reactions to effect of Covid-19 and how seriously they take precautions to prevent from Covid-19. However, results show that, majority of participants take necessary precautions at distinct levels.
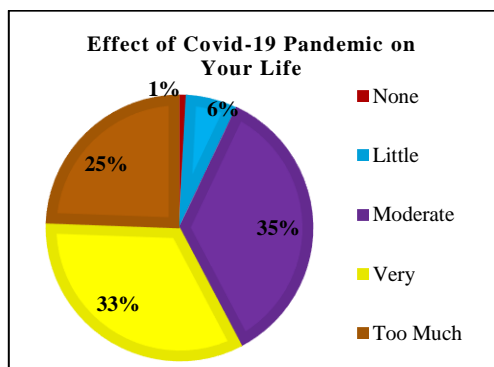
Figure 3 Effect of Covid-19 to lives of participants
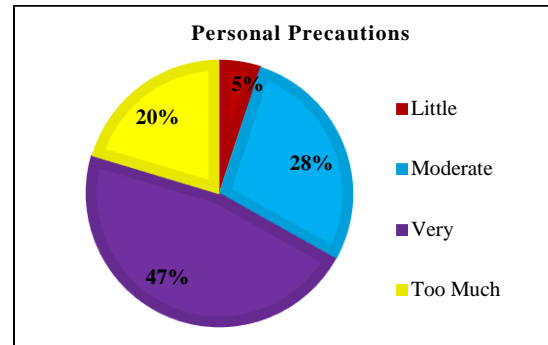
Figure 4 How seriously participants take precautions

As stated earlier in this paper, governments took some decisions to stop spread of Covid-19 in society. Participants are asked if they are satisfied with these regulations. 6% of participants said they are not satisfied with the precautions by government. The answers to these questions can be seen in detail on Figure 5 below.
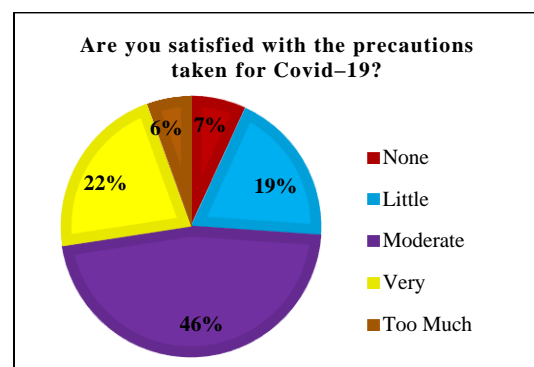
Figure 5 Level of satisfaction of participants against measures taken by government

1% of participants had Covid-19 in Turkey during this survey carried out. This could be due to related to the Figure 4 given above. According to Figure 5, only 5% of participants stated that, they take little precautions. 83% of participants reported that no one around their selves had Covid-19. However, 1% of them reporting that there are 11 or more people they know had Covid-19.

3.3. Social Effects of Covid-19

Covid-19 has changed our lives and our behaviors. In order to understand these changes several questions are asked to

participants. Participants are asked if they see any change in the solidarity between people after Covid-19. Majority of participants answered this question with yes. However, 44% of participants between people did not change.

This study also reveals that; people are changing their way of getting news. Most of the participants in our study group said that they get news related Covid-19 from social media. 1% of participants from said that they are getting news related to Covid-19 from all resources available.

Countries like Italy issued complete lockdowns and some other countries like Turkey issued partial curfews to stop spread of Covid-19. Therefore, it was important to determine if construction industry supports or does not support these decisions. Therefore, participants are asked if they support 14-day curfew or not. 58% of the participants supported curfew, however, 22% of them are against 14-day long curfew.

The last question in this section of the study is to learn prediction of participants about when pandemic will be over. 5% of participants think that Covid-19 will never end. 30% of participants think that pandemic will end in July or August. Figure 6 gives all ratios given in this question.
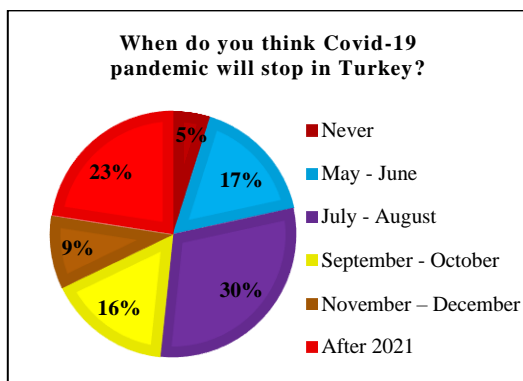
Figure 6 Predictions of participants about when the pandemic will end

3.4. Effect of Covid-19 on Construction Industry

To determine the satisfaction degree with the current status of construction industry, a question is asked. The majority of the participant expressed that they are happy with the current status of construction industry. However, as it may be seen from Figure 7 below, there are substantial amount of people who are not happy or satisfied with the current status of construction industry.
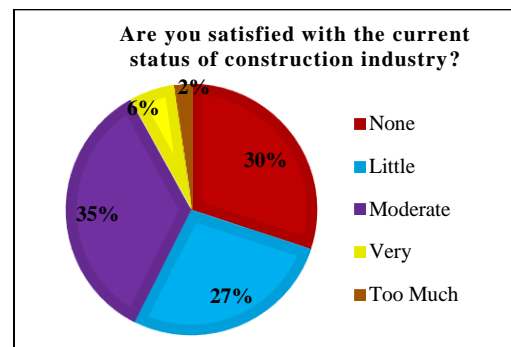
Figure 7 Satisfaction Ratios of Participants about Construction Industry

The second question is asked if the participants think construction industry is affected or not from Covid-19. These answers are provided in Figure 12. To sum up Figure 8, it is seen that 50% of participants think Covid-19 highly affected construction industry, while only 4% of them said Covid-19 did not have influence on construction industry.
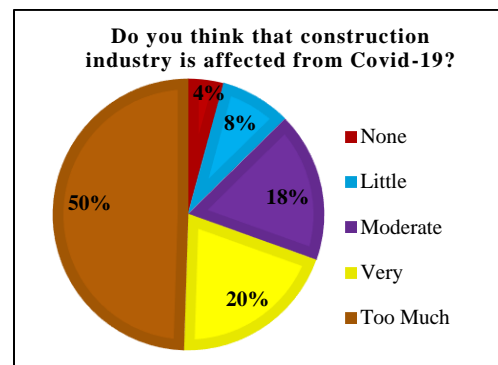
Figure 8 Thoughts of participants about Effect of Covid-19 in Construction Industry

The most important factor to determine the economical effect of Covid-19 is to ask participants about their employment status during time of survey and ask them if they lost their job due to Covid-19. Results showed that there are 62% and 61% employment rate in field engineers and project engineers in private sector. Only 3% of field engineers and 1% of project engineers lost their job due to Covid-19. However, this ratio increases enormously for foreman which becomes 22%. These numbers suggest that ordinary workers are more susceptible to effects of Covid-19. Figure 9 provides figures for construction sector below. 26% of foreman had to take unpaid holiday. It should be noted that 24% of them were already unemployed.
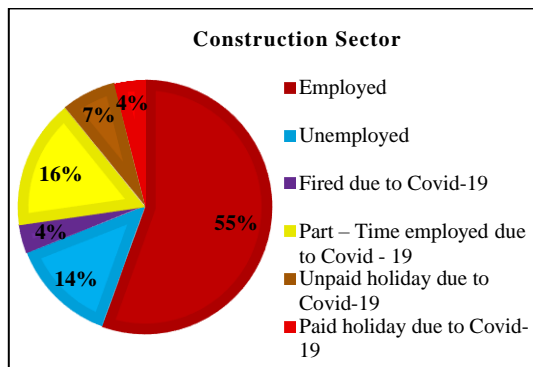
Figure 9 Employment Status' of Construction Sector

Engineers working on state institutions are relative in a good condition rather than other participants of this study. Only 2% of participants from Turkey took unpaid holidays, 52% started to work part-time. Engineers working in state institutions in other countries did not take any holiday but half of them started to work part time.

In order to properly determine the effect of Covid-19 in job market of construction industry, employers were asked how they manage this extraordinary situation. 16% of employers said that they had to ask their employees to take unpaid holidays, 55% of them said they asked their employees to come to office on specified days and 20% said employees are on paid holidays.

It is important to control approval process of the new projects. 87% of participants said time needed for approval process is longer after Covid-19.

Contracts are made for a time interval which means that, contractors should finish the work in a given time period. It is also important if the contractor decided to stop construction or continue. The answers of field engineers are quite important to this question because it directly affects if they keep or lose their jobs. Those answers are provided in Figure 10.
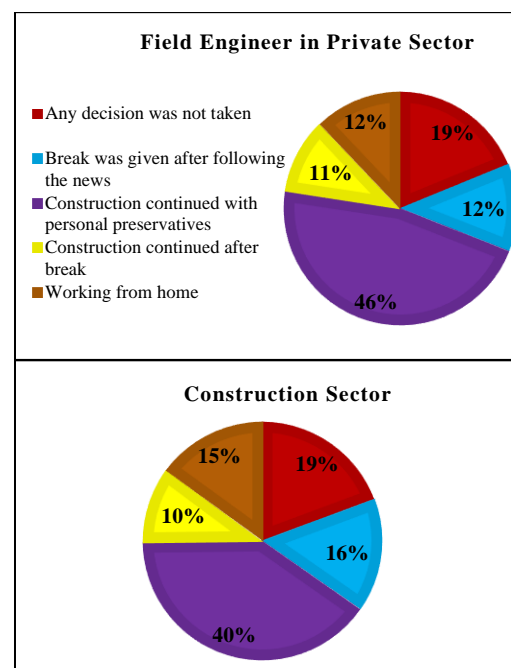
Figure 10 Answers to question regarding decision to continue construction by field engineers

It is seen that half of participants said that they were given personal preservatives in order to prevent from Covid-19 and continue construction. 19% of participants said that no decision is taken. When the same question is asked to the project engineers, following results are obtained. 33% of participants said that they continued to work after personal preservatives are distributed. Significant amount of project engineers can work from home in Turkey.
It is also important to determine if the new construction projects are about the begin or

not during Covid-19. Therefore, question of if you are able to get a new contract after Covid-19 is asked to project engineers and workers. Their answers are provided in Figure 11.

It is also important to get a regularly paychecks for each person in construction industry. Therefore, to reveal current status of payments we also asked if they are able to get their pay checks regularly. When the engineers are considered, most of them were able to get their paychecks regularly. Only small amount of them were able to get it partially while, few of them told they do not get their paychecks. In case of project engineers, higher amount of them reported either they get partial paychecks, or they do not get their paychecks. When the same question is asked to workers, only 28% of them said they get their paychecks regularly, 60% said they get it partially.
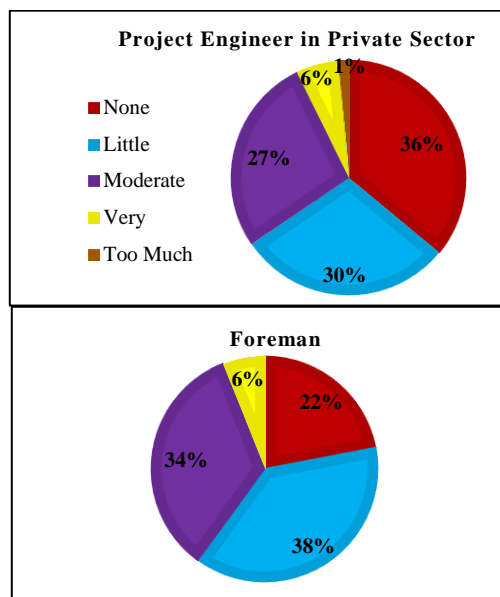
Figure 11 Answers given if project engineers, and workers are able to get a new contract

When the participants are asked if they had to work in another industry, 10% of field engineers and 12% of project engineers answered this question as yes. However, answers of ordinary workers are quite higher than these values. 22% of workers said they had to work in other industries.

In order to conclude this section, we asked the question if the participants are optimistic about future of the construction. 55% of participants are found to be optimistic about future of construction industry. They think that conditions of construction industry will be better in the future.

One-way analysis of variance ANOVA test is used for statistical analysis. One-way ANOVA is used to calculate the significance of the difference between three or more independent means in a normally distributed series. $P < 0.005$ is obtained in results of one-way ANOVA, for the answer to the question of "Do you think that construction industry is affected from Covid – 19?" in all occupational groups. Since the p value is less than 0.001, there is a very high level of statistically significant difference between the groups.

3.5. Effect of Covid-19 into Construction Companies on Stock Markets

It is known that construction industry is very prone to economical and social crisis. This is validated by a study conducted by Chen et al [21]. Researchers investigated the Japanese construction companies on US stock markets during global financial crisis. This study concluded that those companies were affected from that crisis. Therefore, in this study, change of prices of these companies are considered during Covid-19. It is seen that prices of shares of these companies were affected Covid -19. When world health organization declared pandemic, sharp decreases observed on those same companies. However, with the measures taken by several governments, prices of these shares increased. These changes proved that stake prices of construction companies are susceptible to health crisis.

4. CONCLUSION

A detailed survey is prepared in order to determine how Covid-19 affected construction industry. Survey targeted all people working in construction industry. Results provided us some important aspects about effects of Covid-19 outbreak. A total number of 598 people participated in our survey. Following results can be drawn according to answers given to our survey.

- Majority of the participants expressed that Covid-19 has influenced their lives. Exceedingly small amount of people said their life does not change after pandemic.

- Participants are very keen on taking necessary precaution not to get Covid-19 and prevent spread of it between co-workers. Answers also revealed that, employers also take necessary precautions at workplace. However, workers/foreman believe that more precautions may be taken by the employers.

- Only 1% of participants from Turkey diagnosed with Covid-19. Most of the participants stated that, no one they know had Covid-19. However, there are participants who told that they know people diagnosed with Covid-19.

- In order to stop spread of Covid-19, most of participants supports 14-day long curfew. However, participants are not willing to take unpaid holiday.

- People in construction industry lost their jobs due to Covid-19. Role in the industry affects the chance of losing job. These observations are also valid in case of getting paychecks. Engineers are more likely to keep their job and get regular payments while, foreman/workers are more vulnerable to losing job or losing income even though they work. Workers also has the highest ratio for changing working industry.

- Newly graduated engineers think that finding job is harder during Covid-19.

- Half of the construction works continued by providing engineers and workers take necessary precautions.

- Stake prices of construction companies are also susceptible to global health issues encountered.

- The construction industry was seen unprepared for global pandemics. To being prepared for future pandemics, the construction industry needs several research in this area.

- Since the construction industry has many different stakeholders, separate studies should be conducted for each one.

- Due to much of the work area in the construction sector is face-to-face, occupational health should be given more importance.

- To prevent the losses caused by such pandemics on the construction sector, the insurance system should be better supervised by the authorized institutions.

REFERENCES

[1] M. Baghchechi, J. Dunn, N. Jaipaul, & S. E. Jacob. "Art of prevention: Life in the time of coronavirus," International journal of women's dermatology, 6(3), 137-141, 2020.

[2] I. Chakraborty, & P. Maity, "COVID-19 outbreak: Migration, effects on society, global environment and prevention," Science of the Total Environment, 728, 138882, 2020.

[3] European Centre for Disease Prevention and Control, https://www.ecdc. europa.eu/en/covid-19-pandemic, 2020.

[4] A. E. Gorbalenya, S. C. Baker, R. Baric, R. J. D. Groot, C. Drosten, A. A. Gulyaeva, ... & J. Ziebuhr, "Severe acute respiratory syndrome-related coronavirus: The species and its viruses–a statement of the Coronavirus Study Group", 2020.

[5] C. Huang, Y. Wang, X. Li, L. Ren, J. Zhao, Y. Hu, ... & B. Cao, "Clinical features of patients infected with 2019 novel coronavirus in Wuhan, China", The lancet, 395(10223), 497-506, 2020.

[6] M. Nicola, Z. Alsafi, C. Sohrabi, A. Kerwan, A. Al-Jabir, C. Iosifidis, C., ... & R. Agha, "The socio-economic implications of the coronavirus pandemic (COVID-19): A review", International journal of surgery, 78, 185-193, 2020.

[7] World Health Organization (WHO), https://www.who.int/news-room/detail/27-04-2020- who-timeline—covid-19, 2020.

[8] K. Bozorgmehr, V. Saint, A. Kaasch, D. Stuckler, & A. Kentikelenis, "COVID and the convergence of three crises in Europe", The Lancet Public Health, 5(5), e247-e248, 2020.

[9] D. Zhang, M. Hu, & Q. Ji, "Financial markets under the global pandemic of COVID-19", Finance Research Letters, 36, 101528, 2020.

[10] R.Djalante, J. Lassa, D. Setiamarga, A. Sudjatma, M. Indrawan, B. Haryanto, B., ... & H. Warsilah, "Review and analysis of current responses to COVID-19 in Indonesia:

Period of January to March 2020", Progress in Disaster Science, 6, 100091, 2020.

[11] R. Ubaidillah, & S. Riyanto, "The Influence of Work Culture and Extrinsic Work Motivation on Construction Company Strategies in Facing the COVID-19 Pandemic", 2020.

[12] OSHA, "Covid-19 guidance for the construction workforce." Occupational Safety and Health Administration, 2020.

[13] A. Adams-prassl, et al., "The large and unequal impact of COVID-19 on workers. VoxEU. org. Library Catalog: VoxEU", url: https://voxeu.org/article/large-andunequal-impact-covid-19-workers, 2020.

[14] M. Ogunnusi, M. Hamma-Adama, H. Salman, & T. Kouider, "COVID-19 pandemic: the effects and prospects in the construction industry", International journal of real estate studies, 14(Special Issue 2), 2020.

[15] A.Alsharef, S. Banerjee, S. J. Uddin, A. Albert, & E. Jaselskis, "Early impacts of the COVID-19 pandemic on the United States construction industry", International journal of environmental research and public health, 18(4), 1559, 2021.

[16] A. Pamidimukkala, & S. Kermanshachi, "Impact of Covid-19 on field and office workforce in construction industry", Project Leadership and Society, 2, 100018, 2021.

[17] S. Rokooei, A. Alvanchi, & M. Rahimi, "Perception of COVID-19 impacts on the construction industry over time", Cogent Engineering, 9(1), 2044575, 2022.

[18] M. O. Alfadil, M. A. Kassem, K. N. Ali, & W. Alaghbari, "Construction industry from perspective of force majeure and environmental risk compared to the CoViD-19 outbreak: a systematic literature review", Sustainability, 14(3), 1135, 2022.

[19] S. M. Elnaggar, & H. Elhegazy, H. "Study the impact of the COVID-19 pandemic on the construction industry in Egypt", In Structures (Vol. 35, pp. 1270-1277). Elsevier, 2022.

[20] A. L. Comrey, & H. B. Lee, "Interpretation and application of factor analytic results", Comrey AL, Lee HB. A first course in factor analysis, 2, 1992.

[21] K. Chen, & C. Hsiao, "The Impact of Global Financial Crisis on Japan's Construction Industry", Available at SSRN 3021651, 2017.

Title: Feature Analysis For Motor Imagery EEG Signals With Different Classification Schemes

Authors: Esra KAYA, Ismail SARITAS

Feature Analysis for Motor Imagery EEG Signals with Different Classification Schemes

Esra KAYA *1 ID, Ismail SARITAS1 ID

Abstract

A Brain-Computer Interface (BCI) is a communication system that decodes and transfers information directly from the brain to external devices. The electroencephalogram (EEG) technique is used to measure the electrical signals corresponding to commands occurring in the brain to control functions. The signals used for control applications in BCI are called Motor Imagery (MI) EEG signals. EEG signals are noisy, so it is important to use the right methods to recognize patterns correctly. This study examined the performances of different classification schemes to train networks using Ensemble Subspace Discriminant classifier. Also, the most efficient feature space was found using Neighborhood Component Analysis. The maximum average accuracy in classifying MI signals corresponding to right-direction and left-direction was 80.4% with a subject-specific classification scheme and 250 features.

Keywords: BCI, classification scheme, eeg, feature selection, subject-specific, subject-independent

1. INTRODUCTION

Everything that occurs with the transfer of information through different mediums occurs in the communication field. In human physiology, the main communication organ is the brain. In realizing any function, the first message emerges in the brain as electrical signals and is transmitted to the whole body through neurons. Functions can be performed without body parts if the electrical signals arising from the messages formed in the brain are measured and decoded [1]. Brain-Computer Interface (BCI) systems replace the place of neurons by directly transferring information from the brain to external devices [2]. Electroencephalogram (EEG) is the technique BCIs generally use to measure electrical signals of the brain because it is non-invasive and harmless and can be portable and low-cost. Thus, BCI can decode EEG signals for different brain activities [1]. BCI technology can provide many applications, especially for people who suffer from stroke, spinal cord injury, amyotrophic lateral sclerosis, or are amputated, by helping them to control external devices such as wheelchairs and robotic arms [2, 3]. BCIs can also improve healthy people's quality of life by assisting them in different activities. Decoding the

* Corresponding author: esrakaya@selcuk.edu.tr (E.KAYA)
1 Selcuk University
E-mail: isaritas@selcuk.edu.tr
ORCID: https://orcid.org/0000-0003-1401-9071, https://orcid.org/0000-0002-5743-4593

movement intention from the brain is essential to control an external device. EEG signals generated in response to movement intentions are called Motor Imagery (MI) signals [3]. Due to the noisy nature of EEG signals (environmental noise, Electrocardiography (ECG), Electrooculography (EOG), and Electromyography (EMG)), it is hard to discriminate the class samples [1, 2]. Thus, it is important to choose the best classification scheme to train a network and to determine the most efficient feature space.

If we examine the literature studies using different classification schemes, Zhu et al. proposed a CNN structure based on CSP to preserve temporal information for the subject-specific scheme. They obtained 73.0% for right-hand and left-hand MI EEG signals of 25 healthy subjects between the ages of 18 and 25 [4]. In another study, Xu et al. used VGG16 CNN architecture as a transfer learning method for the subject-specific classification of right-hand and left-hand MI EEG signals of 9 subjects. They have used the STFT output spectrogram of the signals as inputs for the CNN. The obtained mean accuracy was 74.2% [5]. Zhao et al. used a multi-Branch 3D CNN architecture for subject-specific classification of right-hand and left-hand MI EEG signals of 9 subjects. The 3D input of the CNN was the signals' time steps with the electrode positions where zero value was used for the nonexistent electrodes. The average accuracy was %75 [6]. Ha and Jeong proposed a Capsule Network for a more robust subject-specific classification of right-hand and left-hand MI EEG signals obtained from 9 subjects. They used spectrograms of the STFT method as inputs and obtained a 77.0% average accuracy [7]. Jin et al. aim to control the complexity of the Extreme Learning Machine (ELM) network model by excluding redundant hidden neurons using sparse Bayesian learning for the subject-specific classification of right-hand and left-hand MI EEG signals of 9 subjects. The obtained mean accuracy was

78.5% [8]. Kwon et al. generated a new input based on spectral-spatial filtering using mutual information for a CNN structure with a feature fusion process to develop a calibration-free BCI system. The data belong to 54 subjects of right-hand and left-hand MI EEG signals. They obtained 74.2%, and 71.3% mean accuracy for subject-independent and subject-specific classifications, respectively [9]. Zhang et al. tried a deep CNN architecture for subject-specific, subject-independent, and subject-adaptive classification schemes by adapting the network parameters on different levels. They obtained 63.5%, 84.2%, and 86.8% accuracies with the related schemes for the right-hand and left-hand MI EEG signals of 54 healthy subjects between 24 and 35 years of age [10]. Perez-Velasco et al. proposed a new CNN structure called EEGSym, which employs the use of inception modules and residual connections for the Subject-Independent classification of right-hand and left-hand MI EEG signals. They used the mid-sagittal plane of the brain as the symmetry line. They obtained 84.7% mean accuracy for 54 subjects [11]. Dolzhikova et al. proposed a Multi-Subject Ensemble Deep CNN (MS-En-CNN) approach for the subject-independent classification of right-hand and left-hand MI EEG signals of 54 subjects based on trial sessions. They achieved an 85.4% average accuracy with the offline and online phases of session 2 [12].

There are also feature extraction and analysis studies for a BCI to recognize patterns in EEG signals more effectively. In a study realized by Raza et al., a method was proposed called Transductive Learning with Covariate Shift Detection (TLCSD) to detect covariate shifting in the distribution of features between training and testing phases of right-hand and left-hand MI EEG signals. The average mean accuracy was 74.92% for nine subjects [13]. Xie et al. proposed an algorithm for classifying right-hand and left-hand MI EEG signals by employing sub-manifold learning of multidimensional

Riemannian space of symmetric positive-definite covariance matrices called Tangent Space of Sub-Manifold (TSSM). The method gives a 75.5% mean accuracy for nine subjects with a Linear Discriminant Analysis (LDA) classifier [14]. Sakhavi et al. used the Filter Bank Common Spatial Pattern (FBCSP) method to extract temporal features of right-hand and left-hand MI EEG signals as inputs to the CNN architecture. They realized the classifications with three different scenarios for CNN: convolution only over time, convolution only over channels, and convolution over both time and channel. They obtained a maximum average accuracy of 74.5% for nine subjects using convolution over time and channel [15]. Fu et al. proved that mu rhythms are more effective for the binary classification of MI EEG signals using CSP features and a regularized LDA (RLDA) classifier. The average accuracy was 77.0% for seven subjects [16]. You et al. used a Flexible Analytic Wavelet Transform (FAWT) to obtain time-frequency features. They reduced the feature space dimension using Multidimensional Scaling (MDS) to classify four subjects' right-hand and left-hand MI EEG signals. The average accuracy was 85.3% [17]. Liang and Ma proposed a Multi-source Fusion Transfer Learning (MFTL) based on covariance matrices of Riemannian space to choose features of source subjects similar to the current subject. Thus, the features of the BCI system are always calibrated. They obtained 72.5% accuracy for the right-hand and both feet MI EEG signals of 12 subjects [18].

As seen from the literature, there are many studies about feature extraction and analysis studies to improve the classification of EEG signals. The studies show that there is still a need for improvement. However, the studies about the classification schemes generally belong to the subject-specific scheme, which is used without determining the best classification scheme. In this study, we have used four classification schemes to determine which scheme yields the best

performance on our data. We evaluated the BCI-dependent scheme, which there is no study we have come across, as well as subject-specific, subject-independent, and subject-adaptive. Also, we determined the more efficient minimum feature space through several procedures to classify right-direction and left-direction MI EEG signals.

2. MATERIAL AND METHODS

2.1. Dataset

We obtained MI EEG signals related to the movements to the right and left direction from five healthy subjects. Before the recordings, necessary ethical permissions and informed consent forms were obtained. The signals were recorded in one session with two runs with a short break between them. The demographic properties of the subjects are given in Table 1.

Table 1 The demographic properties of the subjects EEG recordings belong to.

Subject	Gender	Age	Total Samples	BCI Training
S1	Female	37	160	Yes
S2	Female	26	160	No
S3	Male	22	80	No
S4	Male	52	80	No
S5	Female	33	80	No

The EEG signals were obtained using a 14-channel Emotiv Epoc+ headset. The sampling frequency was adjusted to 256 Hz. The advantage of this EEG headset is that it allows the user to realize cognitive tasks outside a medical facility, making it more suitable for daily use. The study paradigm was created using PsychoPy software, which works with EmotivPRO synchronously. EmotivPRO does not allow us to label signal epochs by itself while obtaining EEG signals. However, PsychoPy makes it possible to label the epochs of the EEG signal.

The paradigm starts with a 10s blank screen where the subjects look at it while not doing

anything to create the baseline signal of the study. Then, a 2s part with a cue starts with a ding sound, which shows the right or left direction MI task with a command of direction. After the cue part, the subjects think of the movement associated with the command of the direction for 5s with a fixation cross appearing on the related direction of the screen. The trial ends with a ding sound, and the subjects close their eyes to rest until another ding sound starts. The paradigm is based on thinking of the movement in the desired direction, not on thinking of the movement of a limb. The timing of the cue-guided paradigm of the study is shown in Figure 1.
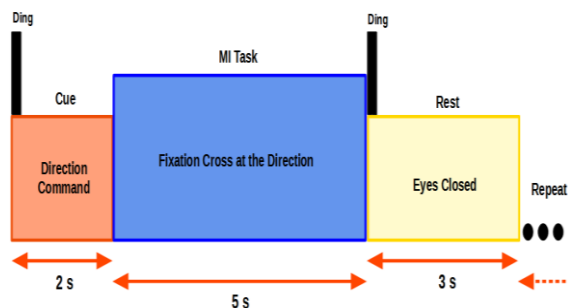
Figure 1 The BCI paradigm of the study.

2.2. Preprocessing and Feature Extraction

The signals were filtered with a 50 Hz Notch filter to eliminate the power noise. Common Average Reference (CAR) was applied for signal-to-noise optimization. Also, we used baseline correction to retract the signal distribution around the 0 amplitude position to ensure consistency among the signals. The 3% minimum and maximum outliers of the signals were discarded. Finally, the epoch signals related to the MI task were extracted. The baseline signal, where the subject does not realize any cognitive task, was subtracted from the epochs obtained from frontal lobe channels AF3, F7, F8, and AF4. Normally the frequency range preferred for EEG signals is 8-30Hz, corresponding to Alpha and Beta wavebands [19]. However, there are opinions out there that Delta and Theta bands can be used for control applications which are generally realized

using MI EEG signals [20-23]. Also, while gamma wavebands can be confused with muscle activity, they can represent sensory processing, movement control, memory, and attention besides emotions [24]. Thus, we filtered the signals between 0.5 and 100 Hz using a bandpass filter.

Table 2. Feature list used in the study.

Feature Types	Features	Statistical Measures
Time	Signal Amplitude	Mean, Standard Deviation, Skewness, Kurtosis, Entropy
Time	TK Energy Operator	Mean, Standard Deviation, Skewness, Kurtosis, Entropy
Frequency	PSD	
Time-Frequency	WD	
Time-Frequency	VMD	
Time-Frequency	HHT	
Nonlinear	HE	-
Nonlinear	MSE	-
Nonlinear	DFA	-
Nonlinear	CD	-
Nonlinear	Hjorth params	-

After preprocessing, time, frequency, time-frequency, and nonlinear features of EEG signals belonging to four channels were extracted. Statistical measurements of signal amplitudes and Teager-Keiser(TK) energy values: mean, standard deviation, skewness, kurtosis, and entropy values form the time properties of signals. Statistical measures of the signal's Power Spectral Density (PSD) values were extracted for frequency features. Wavelet Decomposition (WD) [25], Hilbert-Huang Transform (HHT) [26], and Variational Mode Decomposition (VMD) [27] methods were applied to the signals to obtain time-frequency features. Finally, the nonlinear features of the signals were extracted to define irregularities and long-range dependencies because of the EEG signals' nonlinear nature. Hurst Exponent (HE), Detrended Fluctuation Analysis (DFA), Multiscale Sample Entropy (MSE), Correlation Dimension (CD), and Hjorth Parameters are the extracted nonlinear features [28-30]. The total feature amount was 844 for four channels: 40 time features,

140 frequency features, 620 time-frequency features, and 44 nonlinear features. The features used in this study to represent MI EEG signals are given in Table 2.

2.3. Classification Schemes

After feature extraction, the classifications were realized using Ensemble Subspace Discriminant (EnsSubDisc) with 5-fold Cross Validation. Ensemble learning improves the performance of known classifiers using random subspace (randomizes the learning over a random subspace), bagging (trains several networks over random data and takes the average of the prediction results), or boosting (changes the weights of several trained networks based on their performance) methods [31]. The signals were classified based on four classification schemes: subject-independent, subject-specific, subject-adaptive, and BCI-dependent.

Subject-Specific: In this classification scheme, the network is trained and tested for each subject using only the same subject's data.

Subject-Independent: Subject-Independent is the scheme where all the data belonging to the subjects except one is used for training. The remaining subject's data is tested using the trained network. This is called the leave-one-subject-out (LOSO) paradigm for evaluation [10].

Subject-Adaptive: In this classification scheme, the data obtained from all the subjects are mixed and separated as train and test sets. Thus, the data is evaluated as a whole, and the performance changes due to subjects can be eliminated. The data are divided randomly, so we used the average results of 5 iterations to generalize the performance of the scheme.

BCI-Dependent: The network is trained using the data belonging to the subject, familiar with a BCI system. The other subjects' data are tested using this trained network. Thus, the effects of BCI familiarity on other subjects can be evaluated.

As it is understood, subject-independent and BCI-dependent classification schemes use transfer learning, meaning that the patterns learned from a subject can be transferred to another [32]. After all the classification schemes were used, the extracted features were analyzed for the best-performed scheme based on the different types of features. The whole feature space was analyzed using a feature selection algorithm called Neighborhood Component Analysis (NCA) to find their ranks based on their effectiveness. NCA changes the feature weights by maximizing the pairwise distance of prediction accuracies and assigning a penalty parameter to all the features causing misclassifications. It is a highly accurate algorithm [33]. The EEG signals were classified using 844, 800, 750, 700, 650, 600, 550, 500, 450, 400, 350, 300, 250, 200, 150, 100, and 50 features based on their rank to find the most effective minimum feature space. The flowchart of the study is given in Figure 2 for a better understanding of the procedure.
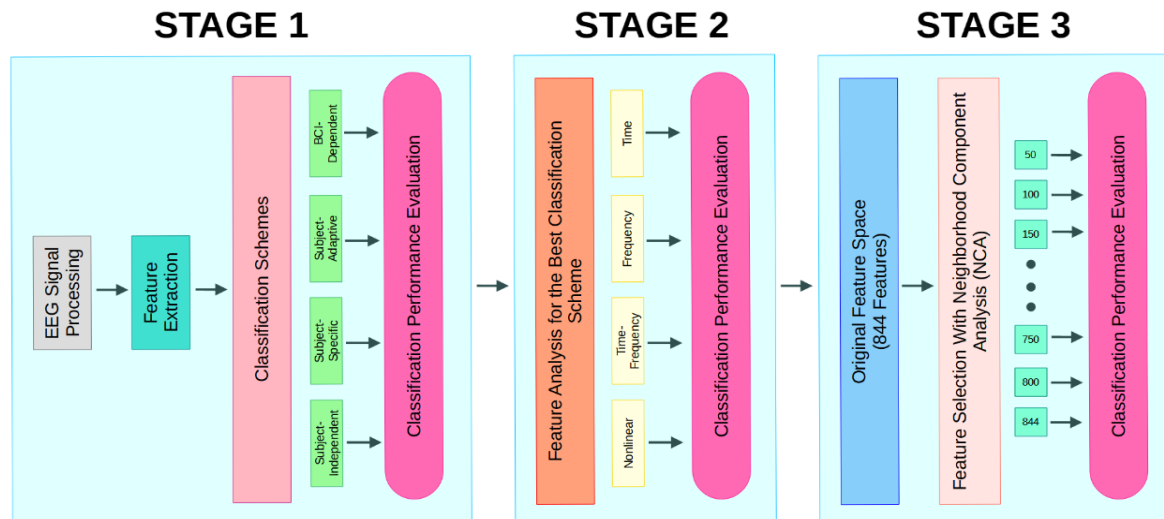
Figure 2 The flowchart of the study indicating the performances of classification schemes and feature selection.

3. RESULTS AND DISCUSSION

The performances of classification schemes are given in Table 3. From the results, it can be surmised that the subject-specific scheme is more accurate than the others for this dataset with %78.3 average accuracy. Interestingly, the third subject's classification results are equivalent to the BCI familiar subject's results. However, when we look at the subject-independent results, it is obvious that a BCI-familiar subject's data can be classified successfully with a network trained with the data of other subjects unfamiliar with a BCI system. A subject-adaptive classification is the next successful classification scheme after subject-specific. Also, the standard deviation is very small for all the iteration

results. The BCI-dependent scheme is the least successful one, with an average accuracy of 55.8%. This low accuracy means that the trained network cannot recognize the patterns of the subjects because they are unfamiliar with a BCI system. The samples can be inconsistent. Only the results of the four subjects were used to calculate the average testing accuracy. The first subject's classification result is the trained network's validation performance.

The next procedure was about the effectiveness of the feature types on the classification performance. Thus, we chose the best classification scheme, which is subject-specific.

Table 3 Test accuracies obtained for all the classification schemes. (S1-S5: Subjects, Acc: Accuracy, Std. Dev.: Standard Deviation, Val: Validation)

Classification Scheme	Test Acc (%) for Each Participant					Average Acc (%)	Std. Dev.
	S1	S2	S3	S4	S5		
Subject-Specific	95.7	58.3	95.8	70.8	70.8	78.3	15.0
Subject-Independent	99.5	56.9	58.8	57.5	60.0	66.5	16.5
Subject-Adaptive	72.3	75.9	75.9	71.7	74.1	74.0	1.8
BCI-Dependent	94.7(Val)	60.6	65.0	51.2	46.3	55.8	7.4

Table 4 gives the classification results belonging to different types of features. It is seen from the results that time features are more effective for the first three subjects.

Frequency features are the most effective, with an average accuracy of 75.7%. The standard deviation is 5.4, meaning that all subjects have consistent frequency features.

Time-frequency features are especially effective for the first subject and are the second best, with a 73.3% average accuracy. Nonlinear features are the least discriminant features, with a 66.9% average accuracy. However, they are consistent for all subjects with a standard deviation value of 5.0.

Table 4 Test accuracies obtained for all feature types belonging to the subject-specific classification scheme. (S1-S5: Subjects, Acc: Accuracy, Std. Dev.: Standard Deviation)

Feature Type	Test Acc (%) for Each Participant (Subject-Specific)					Average Acc (%)	Std. Dev
	S1	S2	S3	S4	S5		
Time	91.3	68.8	75.0	58.3	50.0	68.7	14.2
Frequency	78.3	66.7	75.0	75.0	83.3	75.7	5.4
Time-Frequency	97.8	68.8	75.0	66.7	58.3	73.3	13.4
Nonlinear	73.9	68.8	70.8	58.3	62.5	66.9	5.0

We determined the effects of feature types on the subject-specific right-hand and left-hand MI EEG classification. Nevertheless, they did not reach the highest accuracy of 78.3% obtained from a subject-specific classification using all the features. Also, it is not enough to evaluate the feature types in themselves. For example, a feature among the nonlinear features can be more effective than one among the frequency features. Thus, we applied the NCA feature selection algorithm to the whole feature space. After determining the ranks of all features, we have classified the signals using 844, 800, 750, 700, 650, 600, 550, 500, 450, 400, 350, 300, 250, 200, 150, 100, and 50 features, to find the most effective minimum feature space. The best classification average accuracy of 80.4% was obtained using 250 features, which can be seen in Figure 3. The results are generally close to each other and over 72% until the classification accuracy drops to 69.1% and 66.1%, with 100 and 50 features, respectively. Table 5 shows the true positive rates and the classification accuracies for all subjects with 250 features. As expected, the best classification accuracy belongs to the BCI familiar subject, while the least classification accuracy belongs to the fourth subject. The more accurate classified direction is the left one, with an 82.1% true positive rate.

Table 5 Classification accuracies and true positive rates of the classes obtained using 250 features found more discriminant after the NCA application. (S1-S5: Subjects, R: Right-direction, L: Left-direction, Acc: Accuracy, Std. Dev.: Standard Deviation)

Classes	Test Acc (%) for Each Participant (250 Features)					Average Acc (%)	Std. Dev.
	S1	S2	S3	S4	S5		
R	92.3	69.2	84.6	78.6	66.7	78.3	
L	100.0	86.4	90.9	50.0	83.3	82.1	
Acc	95.7	77.1	87.5	66.7	75.0	80.4	10.1

In Table 6, a comparison of our study with other studies in the literature is given. As seen, the majority of the studies are about the subject-specific scheme. For the subject-specific scheme, in terms of accuracy, our study comes second after [17], which also has the least standard deviation value. Our study has given the best performance with a subject-specific scheme for our dataset, in which the paradigm is not related to any limb movement but movement directions. However, [9], who tried two classification schemes, and [10], who tried three classification schemes, obtained the maximum average accuracies with subject-independent and subject-adaptive schemes, respectively.
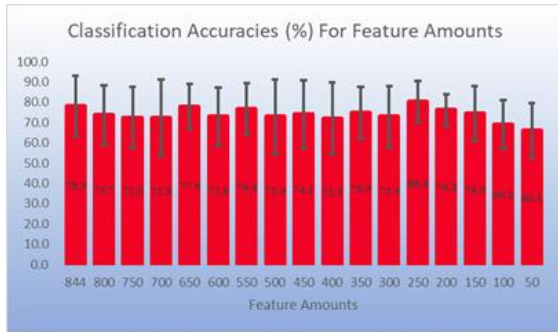
Figure 3 Test accuracies for different amounts of features of which ranks were determined using the feature selection algorithm NCA.

On the other hand, our study is not successful enough with subject-independent and subject-adaptive schemes. On the positive side, our subject-adaptive scheme yielded over 70% accuracy, which the studies in the literature generally obtained, and the standard deviation value is the least among the other studies. The BCI-dependent scheme has the least average accuracy, with 55.8%, but there are no other studies for comparison purposes.

Table 6. Comparison with the other studies in the literature.

Classification Scheme	Study	Method	Average Acc	Std. Dev.
Subject-Specific	[13]	TLCSD	74.9	15.4
	[14]	TSSM-LDA	75.5	13.2
	[15]	FBCSP-CNN	74.5	14.5
	[16]	CSP-RLDA	77.0	12.9
	[4]	CSP-CNN	73.0	-
	[5]	STFT-CNN	74.2	-
	[6]	3D CNN	75.0	7.3
	[7]	STFT-Capsule	77.0	-
	[17]	FAWT-MDS	85.3	3.7
	[18]	MFTL	72.5	10.0
	[8]	ELM	78.5	14.3
	[9]	CNN-Feature Fusion	71.3	15.9
	[10]	CNN	63.5	14.3
	Our Study	EnsSubDisc-NCA	80.4	10.1
Subject-Independent	[9]	CNN-Feature Fusion	74.2	15.8
	[10]	CNN	84.2	10.0
	[11]	EEGSym CNN	84.7	11.7
	[12]	MS-En-CNN	85.4	10.2
	Our Study	EnsSubDisc	66.5	16.5
Subject-Adaptive	[10]	CNN	86.8	11.4
	Our Study	EnsSubDisc	74.0	1.8
BCI-Dependent	Our Study	EnsSubDisc	55.8	7.4

4. CONCLUSION

In this study, we have examined different classification schemes to determine their effects and performances while training networks to classify right-direction and left-direction MI EEG signals. The best classification performance belongs to the subject-specific scheme, unlike in the literature where subject-independent and

subject-adaptive schemes were more successful. The minimum feature space was found using NCA with 250 features for maximum accuracy of 80.4%. Our study was most successful using the subject-specific scheme, while the others were not. The subject-adaptive scheme was the next successful one. There are very few studies in the literature that use classification schemes other than the subject-specific scheme. Our

study was the first one that uses BCI-dependent classification scheme. The result will be more meaningful if there are more studies about BCI dependency. For a more effective BCI system, more classification schemes must be examined and the studies about other existing classification schemes must be increased. Also, feature spaces can be chosen for each subject separately and simultaneously to create a more adaptive BCI system.

Authors' Contribution
The authors contributed equally to the study.

The Declaration of Conflict of Interest/ Common Interest
No conflict of interest or common interest has been declared by the authors.

The Declaration of Ethics Committee Approval
For the data used in the study, the approval of the Ethics Committee of Selcuk University Faculty of Medicine was obtained with the decision numbered 2020/146 by applying to the Noninvasive Clinical Research Ethics Committee.

The Declaration of Research and Publication Ethics
The authors of the paper declare that they comply with the scientific, ethical and quotation rules of SAUJS in all processes of the paper and that they do not make any falsification on the data collected. In addition, they declare that Sakarya University Journal of Science and its editorial board have no responsibility for any ethical violations that may be encountered, and that this study has not been evaluated in any academic publication environment other than Sakarya University Journal of Science.

REFERENCES

[1] S. Kumar, A. Sharma, T. Tsunoda, "An improved discriminative filter bank selection approach for motor imagery EEG signal classification using mutual information," BMC bioinformatics, vol. 18, no. 16, pp. 125-137, 2017.

[2] L. Yang, Y. Song, K. Ma, L. Xie, "Motor imagery EEG decoding method based on a discriminative feature learning strategy," IEEE Transactions on Neural Systems and Rehabilitation Engineering, vol. 29, pp. 368-379, 2021.

[3] D. Y. Lee, J. H. Jeong, B. H. Lee, S. W. Lee, "Motor Imagery Classification Using Inter-Task Transfer Learning via a Channel-Wise Variational Autoencoder-Based Convolutional Neural Network," IEEE Transactions on Neural Systems and Rehabilitation Engineering, vol. 30, pp. 226-237, 2022.

[4] X. Zhu, P. Li, C. Li, D. Yao, R. Zhang, P. Xu, "Separated channel convolutional neural network to realize the training free motor imagery BCI systems," Biomedical Signal Processing and Control, vol. 49, pp. 396-403, 2019.

[5] G. Xu, X. Shen, S. Chen, Y. Zong, C. Zhang, H. Yue, M. Liu, F. Chen, W. Che, "A deep transfer convolutional neural network framework for EEG signal classification," IEEE Access, vol. 7, pp. 112767-112776, 2019.

[6] X. Zhao, H. Zhang, G. Zhu, F. You, S. Kuang, L. Sun, "A multi-branch 3D convolutional neural network for

EEG-based motor imagery classification," IEEE transactions on neural systems and rehabilitation engineering, vol. 27, no. 10, pp. 2164-2177, 2019.

[7] K. W. Ha, J. W. Jeong, "Decoding two-class motor imagery EEG with capsule networks," in 2019 IEEE International Conference on Big Data and Smart Computing, 2019: IEEE, pp. 1-4.

[8] Z. Jin, G. Zhou, D. Gao, Y. Zhang, "EEG classification using sparse Bayesian extreme learning machine for brain–computer interface," Neural Computing and Applications, vol. 32, no. 11, pp. 6601-6609, 2020.

[9] O. Y. Kwon, M. H. Lee, C. Guan, S. W. Lee, "Subject-independent brain–computer interfaces based on deep convolutional neural networks," IEEE transactions on neural networks and learning systems, vol. 31, no. 10, pp. 3839-3852, 2019.

[10] K. Zhang, N. Robinson, S. W. Lee, C. Guan, "Adaptive transfer learning for EEG motor imagery classification with deep Convolutional Neural Network," Neural Networks, vol. 136, pp. 1-10, 2021.

[11] S. Pérez-Velasco, E. Santamaria-Vazquez, V. Martinez-Cagigal, D. Marcos-Martinez, R. Hornero, "EEGSym: Overcoming Inter-Subject Variability in Motor Imagery Based BCIs With Deep Learning," IEEE Transactions on Neural Systems and Rehabilitation Engineering, vol. 30, pp. 1766-1775, 2022.

[12] I. Dolzhikova, B. Abibullaev, R. Sameni, A. Zollanvari, "Subject-Independent Classification of Motor Imagery Tasks in EEG Using Multisubject Ensemble CNN," IEEE

Access, vol. 10, pp. 81355-81363, 2022.

[13] H. Raza, H. Cecotti, Y. Li, G. Prasad, "Adaptive learning with covariate shift-detection for motor imagery-based brain–computer interface," Soft Computing, vol. 20, no. 8, pp. 3085-3096, 2016.

[14] X. Xie, Z. L. Yu, H. Lu, Z. Gu, Y. Li, "Motor imagery classification based on bilinear sub-manifold learning of symmetric positive-definite matrices," IEEE Transactions on Neural Systems and Rehabilitation Engineering, vol. 25, no. 6, pp. 504-516, 2016.

[15] S. Sakhavi, C. Guan, S. Yan, "Learning temporal information for brain-computer interface using convolutional neural networks," IEEE transactions on neural networks and learning systems, vol. 29, no. 11, pp. 5619-5629, 2018.

[16] R. Fu, Y. Tian, T. Bao, Z. Meng, P. Shi, "Improvement motor imagery EEG classification based on regularized linear discriminant analysis," Journal of medical systems, vol. 43, no. 6, pp. 1-13, 2019.

[17] Y. You, W. Chen, T. Zhang, "Motor imagery EEG classification based on flexible analytic wavelet transform," Biomedical Signal Processing and Control, vol. 62, p. 102069, 2020.

[18] Y. Liang, Y. Ma, "Calibrating EEG features in motor imagery classification tasks with a small amount of current data using multisource fusion transfer learning," Biomedical Signal Processing and Control, vol. 62, p. 102101, 2020.

[19] S. Afrakhteh, M. R. Mosavi, "Applying an efficient evolutionary algorithm for EEG signal feature

selection and classification in decision-based systems," in Energy efficiency of medical devices and healthcare applications: Elsevier, 2020, pp. 25-52.

[20] D. R. Edla, M. F. Ansari, N. Chaudhary, S. Dodia, "Classification of facial expressions from eeg signals using wavelet packet transform and svm for wheelchair control operations," Procedia computer science, vol. 132, pp. 1467-1476, 2018.

[21] K. W. Ha, J. W. Jeong, "Motor imagery EEG classification using capsule networks," Sensors, vol. 19, no. 13, p. 2854, 2019.

[22] M. Z. Yusoff, N. Kamel, A. Malik, M. Meselhy, "Mental task motor imagery classifications for noninvasive brain computer interface," in 2014 5th International Conference on Intelligent and Advanced Systems, 2014: IEEE, pp. 1-5.

[23] S. Tiwari, S. Goel, A. Bhardwaj, "MIDNN-a classification approach for the EEG based motor imagery tasks using deep neural network," Applied Intelligence, pp. 1-20, 2021.

[24] S. D. Muthukumaraswamy, "High-frequency brain activity and muscle artifacts in MEG/EEG: a review and recommendations," Frontiers in human neuroscience, vol. 7, p. 138, 2013.

[25] M. H. Alomari, E. A. Awada, A. Samaha, K. Alkamha, "Wavelet-based feature extraction for the analysis of EEG signals associated with imagined fists and feet movements," Computer and Information Science, vol. 7, no. 2, p. 17, 2014.

[26] N. E. Huang, Z. Wu, "A review on Hilbert-Huang transform: Method and its applications to geophysical studies," Reviews of geophysics, vol. 46, no. 2, 2008.

[27] K. Dragomiretskiy, D. Zosso, "Variational mode decomposition," IEEE transactions on signal processing, vol. 62, no. 3, pp. 531-544, 2013.

[28] B. Hjorth, "EEG analysis based on time domain properties," Electroencephalography and clinical neurophysiology, vol. 29, no. 3, pp. 306-310, 1970.

[29] J. Istas, G. Lang, "Quadratic variations and estimation of the local Hölder index of a Gaussian process," in Annales de l'Institut Henri Poincare (B) probability and statistics, 1997, vol. 33, no. 4: Elsevier, pp. 407-436.

[30] Y. Ma, W. Shi, C. K. Peng, A. C. Yang, "Nonlinear dynamical analysis of sleep electroencephalography using fractal and entropy approaches," Sleep medicine reviews, vol. 37, pp. 85-93, 2018.

[31] A. S. Ashour, Y. Guo, A. R. Hawas, G. Xu, "Ensemble of subspace discriminant classifiers for schistosomal liver fibrosis staging in mice microscopic images," Health information science and systems, vol. 6, no. 1, pp. 1-10, 2018.

[32] I. Hossain, A. Khosravi, S. Nahavandhi, "Active transfer learning and selective instance transfer with active learning for motor imagery based BCI," in 2016 International Joint Conference on Neural Networks, 2016: IEEE, pp. 4048-4055.

[33] The Mathworks Inc. (2022, Oct. 10). Feature Selection [Online].

Available:https://www.mathworks.co
m/discovery/feature-selection.html

Title: Examining the Success of Information Gain, Pearson Correlation, and Symmetric Uncertainty Ranking Methods on 3D Hand Posture Data for Metaverse Systems

Authors: Cüneyt YÜCELBAŞ, Şule YÜCELBAŞ

Examining the Success of Information Gain, Pearson Correlation, and Symmetric Uncertainty Ranking Methods on 3D Hand Posture Data for Metaverse Systems

Cüneyt YÜCELBAŞ*[1] , Şule YÜCELBAŞ[1]

Abstract

Metaverse is a hardware and software interface space that can connect people's social lives as in the real-natural world and provide the feeling of being there at the maximum level. In order for metaverse systems to be efficient, many independent accessories have to work holistically. One of these accessories is wearable gloves called meta gloves and equipped with sensors. Thanks to it, an important stage of metaverse systems is completed with the detection of 3-dimensional (3D) hand postures. In this study, the success of Information Gain, Pearson's Correlation, and Symmetric Uncertainty ranking methods on 3D hand posture data for metaverse systems were investigated. For this purpose, various preprocessing was performed on the 3D data, and a dataset consisting of 15 features in total was created. The created dataset was ranked by 3 different methods mentioned and the features that the methods determined effectively were classified separately. Obtained results were interpreted with various statistical evaluation criteria. According to the experimental results obtained, it has been seen that the Symmetric Uncertainty ranking algorithm produces successful results for metaverse systems. As a result of the classification made with the active features determined using this method, there has been an increase in statistical performance criteria compared to other methods. In addition, it has been proven that time loss can be avoided in the classification of big data similar to the data used.

Keywords: Machine learning, metaverse systems, 3D hand posture, information gain, symmetric uncertainty ranking

1. INTRODUCTION

Metaverse is a software and hardware interface platform that can connect people's social lives as in the real-natural world and provide the feeling of being there at the maximum level. The expression metaverse is formed by the combination of the words meta and universe [1]. Here, while the meta means exceeding the limits; the universe is defined as a virtual environment associated with real life [1]. As authors, we would like to define the metaverse as a '*physical reality with high sensibility in the virtual environment*'.

* Corresponding author: cuneytyucelbas@tarsus.edu.tr (C. YÜCELBAŞ)
[1]Tarsus University
E-mail: suleyucelbas@tarsus.edu.tr
ORCID: https://orcid.org/0000-0002-4005-6557, https://orcid.org/0000-0002-6758-8502

In the last 10 years, important developments have emerged in metaverse systems due to the rapid attack of the internet and related technologies. Especially since the whole world has passed and is going through a very dangerous deadly pandemic process, all business areas and people have had to be confined to closed environments [2]. Although this situation was not welcomed, created a disadvantage for many business areas, and caused financial losses, it was observed that especially internet and technology-based companies increased their turnover much more than in the past [2]. The

leading of these is the world's big technology companies such as Microsoft and Facebook [3]. In addition to these, when we look at the investment platforms of other similar technology giants in recent years, it is seen that metaverse systems come first.

Although metaverse systems have been seen as the prominent subject of the last few years, they have actually entered the field of interest of researchers and companies with the active use of the internet. The historical stages of this process are given in Figure 1 [3] below.
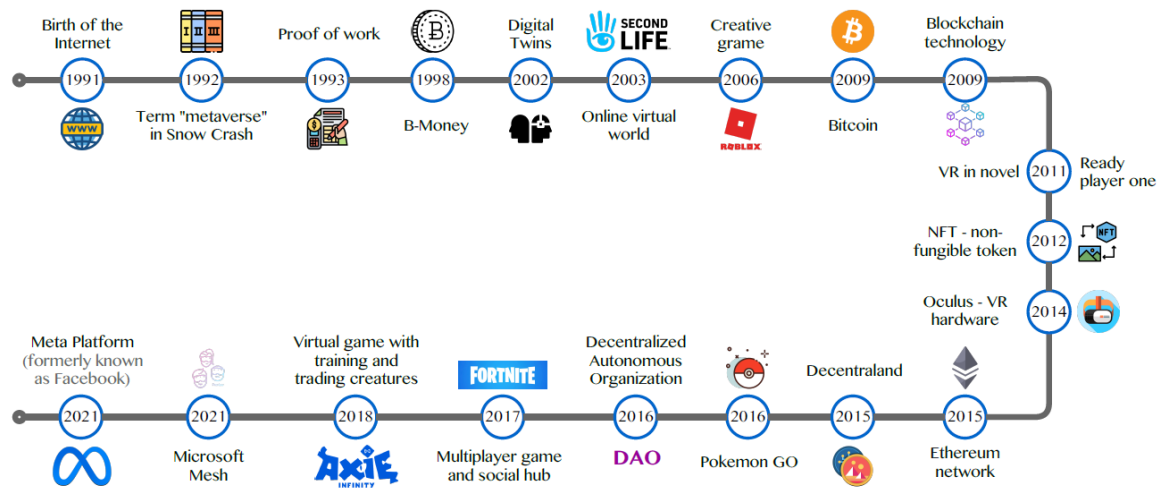
Figure 1 Historical development of Metaverse [3]

As can be seen in Figure 1, the metaverse journey, which started with the internet in 1991, continued until 2021, depending on the development of technology, and today it has been actively used in some areas (especially in the game industry). Metaverse has the potential to apply in every sector of life, from education to entertainment, from health to travel, and e-marketing. In the future, it will be possible to hold business meetings and scientific conferences through metaverse systems without the need to be physically present in the same environment [4]. However, although it is aimed to give the feeling of fully experiencing the real world virtually, the fact that the system is mostly used through hand gestures is proof that this area needs much development.

In the metaverse, the connection between the user and the extended reality (XR), which includes virtual reality (VR), augmented reality (AR), and mixed reality (MR) components, is possible with wearable devices [5]. In addition to these hardware components, it is more important that the software infrastructure is strong and a solution-maker. Currently, it is possible to integrate wearable gloves equipped with sensors, which are most actively used, into the system by using the correct solver software. As a result, it is possible with artificial intelligence algorithms to process and make sense of the data detected from the sensors in the glove and to produce an output that can move toward the virtual world.

In these systems, the first focus on gloves, among the wearable tools, is related to the fact that we mostly use our hands and fingers in daily life, high 3D posture recognition, and matching compatibility [6, 7]. In addition, it is possible for non-speaking people to express themselves through their hands and fingers. The fact that researchers turn to wearable gloves and do their analysis on them can both reach a wider audience in the real world and contribute to an important stage of the system going forward. For example, in one of these studies, a system that can recognize 15 different hand postures through machine learning algorithms has been proposed [8]. In research [9], it has been tried to detect multidimensional gesture movements by using sensor-equipped gloves to provide more realistic experiences to people in the VR environment. In another paper, it has been tried to identify 5 different hand postures for low-cost and hand prosthesis control by using an electromyogram (EMG), which are muscle signals of people [10]. In [11], researchers have proposed convolutional deep averaging Networks for hand posture detection. Nayak, et al. [12] presented the Lightboost-based Gradient boosting model for the same purpose and compared the results obtained with some machine learning algorithms. In another research study, the authors tried many machine learning algorithms, including multilayer perceptrons, where the highest performance was obtained for the detection of 3D hand postures [13]. In addition, the feature selection process was applied to the data, but it was briefly stated in the paper that no improvement effect was observed in the results [13]. In [14], a detailed literature review has been made on many topics such as the techniques, advantages and limitations of metaverse in the computer field. Within the scope of [15], research on metaverse systems of the last 20 years has been discussed and its methods and results have been examined in detail. In this respect, a research has emerged that can provide researchers with a preliminary idea about where the subject has come from and where it will go [15]. In another study that can be used in metaverse systems, the authors tried to detect 5 different finger movements by means of machine learning algorithms over the features obtained by processing the relevant signals, thanks to the wearable EMG system they put forward [16]. In a similar-purpose study that can be used in human-computer interactive applications, the researchers tried to detect 14 different hand movements through 2D images [17]. The authors of this study [18], which can enable metaverse systems to be used by speech impaired individuals, focused on detecting sign language characters through the images of hand movements.

Briefly, as can be understood from these studies mentioned in the literature, the procedures and purposes are circulating around similar phenomena. The general purpose is to detect hand posture movements with high accuracy. In order to achieve this, machine learning algorithms are also applied to reach a conclusion by evaluating the sensor data recorded from wearable gloves equipped with sensors. Although there are studies on the evaluation of meta-gloves data developed for metaverse systems with artificial intelligence in the literature, the performances of the sorting algorithms in which the features in these data are evaluated in detail have not been tested. The most prominent and generally high-performance sorting algorithms mentioned are Information Gain, Pearson's Correlation, and Symmetric Uncertainty ranking methods. In the literature, there are many studies in which these sorting techniques are applied to different data. In one of them, researchers proposed a semi-supervised system based on the Information Gain technique and they were successful [19]. A new model using in reference [20] principal component analysis and the Information Gain algorithm as a hybrid is presented. As a result of the application of this proposed model, the required features were selected along with the reduction in data size, and a high

Cüneyt YÜCELBAŞ, Şule YÜCELBAŞ

Examining the Success of Information Gain, Pearson Correlation, and Symmetric Uncertainty Ranking Met...

classification rate was obtained by reducing the training time [20]. Performance evaluation was made by applying three different feature sorting-selection techniques, including this ranking method [21, 22].

One of the studies in which Pearson's Correlation technique is applied is the research in [23]. Here, the effect of correlation coefficients between features on the classification accuracy of Alzheimer's disease was realized by applying three different techniques [23]. In [24], this technique was applied to the data for the classification of skin segmentation. The authors in their study [25-27] applied the method to different datasets, except for hand posture data.

Finally, when the studies in which Symmetric Uncertainty was applied are examined; in [28], a different attribute subset selection technique was introduced to analyze the symmetric uncertainty between feature-feature and feature-class. As a result, it was seen that the proposed algorithm performed better [28]. In another large-scale research study, the authors investigated the performance of 24 feature selection methods on some ready-made datasets, and it was seen that the specified method performed slightly better than the others [29]. In [30], Symmetric Uncertainty-based Maximal independent classification information and minimal redundancy feature selection techniques were proposed. In another study using this ranking algorithm, the authors developed a hybrid feature selection system [31]. The Symmetric Uncertainty method in the correlation-based system proposed here was used to detect the features to be deleted [31].

The above-mentioned feature sorting-selection techniques have been applied to some fixed-ready data sets and performance outputs that can be considered successful have been obtained. From this point of view,

it is important that these methods have not been applied to the 3D sensor data [13, 32] of meta gloves suitable for metaverse systems before. In this study, the success of Information Gain, Pearson's Correlation, and Symmetric Uncertainty ranking methods on 3D hand posture data for metaverse systems were investigated. For this purpose, various preprocessing was performed on the 3D data, and a dataset consisting of 15 features in total was created. The created dataset was ranked by three different methods mentioned and the features that the methods determined effectively were classified separately. Obtained results were interpreted with various statistical evaluation criteria. According to the experimental results obtained, it has been seen that the Symmetric Uncertainty ranking algorithm produces successful results for metaverse systems. As a result of the classification made with the active features determined using this method, there has been an increase in statistical performance criteria compared to other methods. In addition, it has been seen that the loss of time in the classification of large data similar to the data used can be prevented.

The main novelty and contributions of this research are highlighted as follows: (1) it is important that this feature sorting-selection technique, which has generally proven successful, has not been applied before on 3D hand posture data obtained from meta-gloves. (2) Thanks to this study, different application methods have already been applied to the data to be obtained from metaverse systems, which are intended to facilitate work and operation in many sectors in the future. Thus, a new path has been drawn and different perspectives have been presented to young scientists who will turn to this field. (3) It is an expected handicap that in the sectors where metaverse systems will be used, there will be intense data flow in the future and accordingly the response times of the systems will be prolonged. For

this reason, it is important that the techniques that will ensure the elimination of this situation, which is highly likely to occur in the future, are applied in this paper.

The remainder of this paper is organized as follows. Section 2 introduces preparing the dataset, explanations about Information Gain, Pearson's Correlation, and Symmetric Uncertainty ranking methods. This section also gives classification and evaluation processes. Obtained numerical results, tables, graphical representations, and comments are given in section 3. The discussion and conclusion are presented in section 4.

2. MATERIALS AND METHODS

Gloves that are compatible with metaverse systems and equipped with sensors are known as meta gloves. Thanks to the machine learning algorithms in which the 3D hand posture data obtained from these gloves are presented as input, automatic detection of the determined movements can be made. Thanks to these applications, it will be possible for metaverse systems, which will become widespread in every sector in the future, to produce results with higher accuracy and speed.

2.1. Preparing the Dataset

The data used in this study were created from [13, 32] references. The data in [13, 32] consist of 3D (X, Y, and Z) values of 12 markers placed at certain points of the left-hand glove. In addition, there are three-dimensional marker values of 5 different hand signals, shown in Figure 2, belonging to 12 different subjects in the dataset.

Class information in the dataset is labeled as 1, 2, 3, 4, and 5. These label values are fist with thumb out, stop with hand flat, point-1 with pointer finger, point-2 with pointer and middle fingers, and grab, respectively [13, 32]. One of these 12 markers is placed on the

back of the glove, while the others are fixed on the thumb and fingers [13, 32].
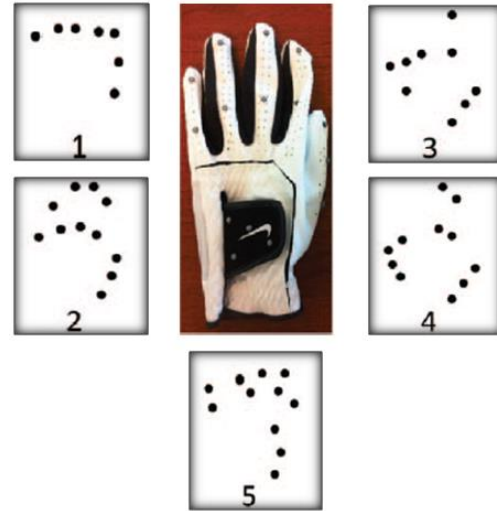
Figure 2 Glove used, and postures in the XY plane belonging to the 5-class [13, 32]

The places indicated by the '?' sign in the data set file represent the missing value [13, 32]. When the file is examined, most of the X, Y, and Z coordinates of 7 markers between 5 and 11 are given as '?'. Therefore, these markers have been ignored by us. In addition, since the same situation exists in the markers of some subjects, these parts were also removed from the data. Thus, the number of attributes, which was 12 x 3 = 36 in total, was taken as 5 x 3 = 15 (X0, Y0, Z0, X1, Y1, Z1, X2, Y2, Z2, X3, Y3, Z3, X4, Y4, Z4) and the research was carried out. Apart from this, the number of data, which is 78095 in total, has been arranged as 74975 due to missing values. As a result, the whole data set was transformed into a 74975x15 matrix, and the next steps of the study were started.

2.2. Information Gain Ranking

The Information Gain ranking is an evaluation algorithm based on entropy [33] and is frequently used in machine learning applications [34]. The Information Gain, which takes a value between 0 and 1, is calculated based on the number of attributes and classes [34]. Higher information gain is needed if a researcher wants better

Cüneyt YÜCELBAŞ, Şule YÜCELBAŞ

Examining the Success of Information Gain, Pearson Correlation, and Symmetric Uncertainty Ranking Met...

discriminating power for decision-making. Determining the relationship of features with classification is the main purpose of this method [35]. While calculating the information gain, all the data in the data set and specific data that are required to be calculated are studied. The specific data to be calculated is called "sampling data" and the calculation of this sampling data is made over the whole data set. The Information Gain calculation formula [34] is given below:

$$G(D,t) = -\sum_{i=1}^{m} P(C_i) \log P(C_i)$$
$$+ P(t) \sum_{i=1}^{m} P(C_i|t) \log P(C_i|t) + \qquad (1)$$
$$+ P(\bar{t}) \sum_{i=1}^{m} P(C_i|\bar{t}) \log P(C_i|\bar{t})$$

In Formula 1, the C notation refers to the dataset array. C_i is the i th data and $P(C_i)$ is the conditional probability of the same data. $P(C_i|t)$ and $P(C_i|\bar{t})$ represent the probabilities that the first category includes and does not include feature t, respectively [34].

2.3. Pearson's Correlation Coefficient Ranking

The Pearson correlation test is a statistical analysis that investigates the linearity of the relationship between related measures [36]. In addition, if there is a relationship, its direction and severity can be determined thanks to it. This analysis technique can be preferred if the data to be studied has a normal distribution. The correlation coefficient takes values between -1 and 1 [36]. The fact that this calculated value is less than zero means that as one of the two data increases, the other decreases [37]. If this coefficient is greater than zero, it means that both variables increase in the same way [37]. If this calculated coefficient is greater than 0.8, it is interpreted that there is a very high correlation. The Pearson's correlation coefficient formula is as follows:

$$r = \frac{n(\sum xy) - (\sum x)(\sum y)}{\sqrt{\left[n \sum x^2 - (\sum x)^2 \right]\left[n \sum y^2 - (\sum y)^2 \right]}} \qquad (2)$$

Here x and y denote the value of the first and second variables, respectively. In addition, n represents how many x or y there are, and r represents the calculated correlation coefficient. In this study, the ranking was performed by calculating the correlation between each trait and the target class [38, 39].

2.4. Symmetric Uncertainty Ranking

Symmetric uncertainty is a value calculated between features and target classes and is used to determine which features are suitable for classification [40]. This method uses an information-theoretic measure to evaluate the value of constructed solutions [41]. Features with high calculated uncertainty values are considered more effective for classification than others [40]. The formula for calculating the symmetric uncertainty is as follows. In Equation 3, $H( )$, A, and B denote entropy, any feature and class label, respectively [40].

Symmetric Uncertainty:

$$U(A,B) = 2\frac{H(A) + H(B) - H(A,B)}{H(A) + H(B)} \in [0,1] \qquad (3)$$

2.5. Classification and Evaluation Processes

In this study, Random Forest (RF) of supervised classification algorithms was used as a classifier. This method, which is frequently used in both classification and regression processes, briefly performs the classification step over multiple decision trees it produces in order to achieve better classification performance [42]. This algorithm has been adopted and spread faster by different application areas due to its advantages such as being adaptable to the solution of many problems, being easy and flexible [42].

Cüneyt YÜCELBAŞ, Şule YÜCELBAŞ

Examining the Success of Information Gain, Pearson Correlation, and Symmetric Uncertainty Ranking Met...

In the evaluation phase, the classification accuracy (ACC) parameter was primarily taken as the basis. This parameter is calculated by the ratio of the data we guessed correctly as a result of the classification to the total data set. In addition, interpretations were made by considering the Kappa coefficient and the areas under the ROC (Receiver Operating Characteristic) curve in each classification. Cohen's Kappa coefficient is a statistical method that measures the reliability of comparative agreement between two raters [43]. This coefficient, which is frequently used to prove classification accuracy in machine learning studies, takes values between -1 and +1. It can be said that success and reliability are very high in classifications where a value of 0.81 and above is calculated for the Kappa coefficient [44]. The ROC curve is a statistical method frequently used in machine learning as it defines the accuracy of the classifier itself and allows a reliable comparison between classifiers. The graphical approach of the ROC curve makes it easy to understand the relationships between the sensitivity and specificity of the measurements. The area under the ROC curve determines the accuracy of the classifier in separating instances from different labels. This area takes values between 0 and 1. When the area under the ROC curve is calculated, this value indicates a very high classification success if it is 0.9 and above [45].

3. RESULTS

In this study, the success of Information Gain, Pearson's Correlation, and Symmetric Uncertainty ranking methods on 3D hand posture data for metaverse systems was investigated. For this purpose, various pre-processes were performed on the 3D data, and a dataset consisting of 15 columns (features) and 74975 rows in total was created by using [13, 32] references. The created dataset was sorted by 3 different ranking methods and the features that the methods determined effectively were classified separately. Obtained results were interpreted with various statistical evaluation criteria. In this section, the details of the mentioned stages will be mentioned.

The generated data set was first sorted by the Information Gain method and then by Pearson's Correlation and Symmetric Uncertainty values, respectively. The obtained values of the features according to ranking methods are shown in Table 1.

Table 1 The obtained values of the features according to ranking methods

Information Gain Ranking		Pearson's Correlation		Symmetric Uncertainty	
Feature	Ranking Value	Feature	Ranking Value	Feature	Ranking Value
Y0	0.453	Z4	0.1643	Y0	0.0987
Y2	0.433	Z3	0.1596	Y2	0.0981
Y3	0.428	Z2	0.1491	Y1	0.0969
Y1	0.427	Z1	0.1353	Y3	0.0967
Y4	0.421	Z0	0.1244	Y4	0.0949
Z4	0.286	Y2	0.0695	Z4	0.0770
Z0	0.285	Y0	0.0674	Z0	0.0724
Z3	0.275	Y3	0.0664	Z3	0.0716
Z1	0.274	X3	0.0663	Z1	0.0715
Z2	0.269	Y1	0.0658	Z2	0.0710
X0	0.203	X2	0.0597	X0	0.0474
X2	0.184	Y4	0.0564	X2	0.0452
X3	0.182	X4	0.0558	X4	0.0447
X4	0.181	X1	0.0545	X3	0.0447
X1	0.180	X0	0.0529	X1	0.0433

Cüneyt YÜCELBAŞ, Şule YÜCELBAŞ

Examining the Success of Information Gain, Pearson Correlation, and Symmetric Uncertainty Ranking Met...

Table 1 shows the values calculated for the properties according to the three ranking methods specified. According to the Information Gain and Symmetric Uncertainty methods, it is seen that the first 5 features whose effectiveness is specified are the same. As can be seen, only the order of the first five features has changed according to these methods. However, it is seen that the 5 features that were determined to be effective by the Pearson's Correlation ranking method are completely different. RF algorithm was used to prove which algorithm can perform statistically more accurate feature ranking on 3D posture data. According to the ranking values obtained as a result of applying the specified 3 ranking methods to the data, the first 5 features were given to the RF algorithm by one. The obtained ACC, Kappa and ROC values are shown in Table 2.

Table 2 The performance outputs obtained as a result of the classification of the first 5 features obtained according to the ranking methods by adding them one by one with RF

Information Gain Ranking				Pearson's Correlation Ranking				Symmetric Uncertainty Ranking			
Feature	ACC%	Kappa	ROC	Feature	ACC%	Kappa	ROC	Feature	ACC%	Kappa	ROC
Y0	36.1	0.201	0.695	Z4	28.8	0.110	0.617	Y0	36.1	0.201	0.695
Y0, Y2	67.7	0.596	0.895	Z4, Z3	47.98	0.349	0.781	Y0, Y2	67.7	0.596	0.895
Y0, Y2, Y3	73.69	0.671	0.931	Z4, Z3, Z2	61.88	0.523	0.797	Y0, Y2, Y1	75.83	0.698	0.940
Y0, Y2, Y3, Y1	77.95	0.724	0.949	Z4, Z3, Z2, Z1	67.93	0.599	0.907	Y0, Y2, Y1, Y3	77.95	0.724	0.949
Y0, Y2, Y3, Y1, Y4	79.73	0.746	0.956	Z4, Z3, Z2, Z1, Z0	73.25	0.665	0.932	Y0, Y2, Y1, Y3, Y4	79.73	0.746	0.956

As seen in Table 2, the results obtained showed that the Symmetric Uncertainty ranking algorithm was better in ranking the features of 3D posture data. Although the results are similar when the Information Gain and Symmetric Uncertainty ranking algorithms are compared, the performance difference between them is clearly seen, especially when the red line of Table 2 is examined. When the line indicated in red is examined, the Symmetric Uncertainty ranking algorithm was 2% more successful than the Information Gain algorithm. In addition, when the Kappa coefficient and the area under the ROC curve were examined, it was seen that the Symmetric Uncertainty ranking algorithm was more successful. The graphical representation of the Kappa coefficient and ROC area values of the methods is shown in Figure 3.

If Figure 3 is examined, the most unsuccessful ranking algorithm among these methods was the Pearson Correlation method. When the results of this method are examined, it is seen that its success is almost 10% lower than the others. Performance results have proven that this method is not successful in determining effective features for 3D hand posture data.

Cüneyt YÜCELBAŞ, Şule YÜCELBAŞ

Examining the Success of Information Gain, Pearson Correlation, and Symmetric Uncertainty Ranking Met...
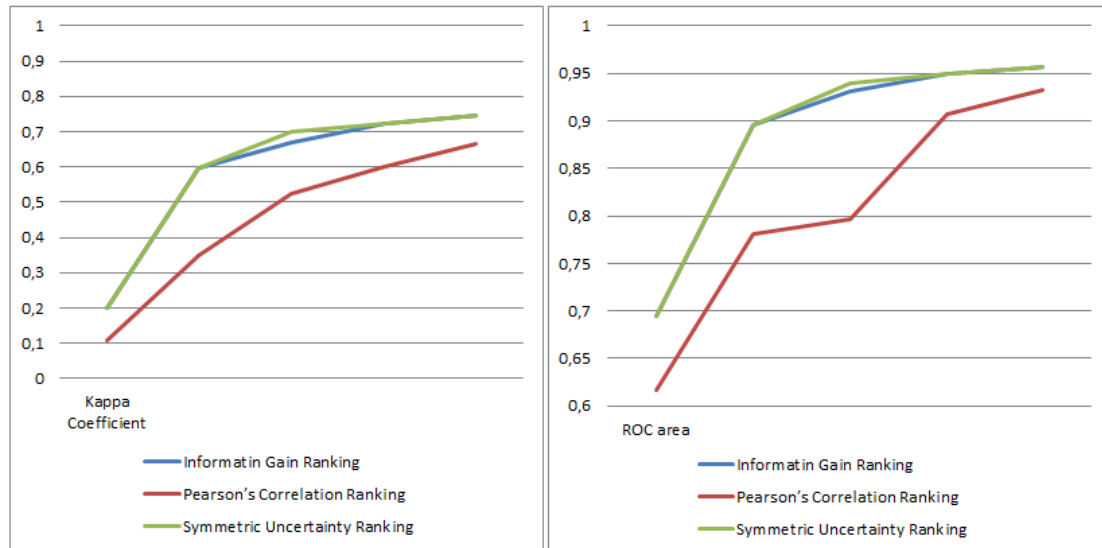
Figure 3 Graphical representation of Kappa coefficient and ROC area values of methods according to feature groups in Table 2

Table 3 The performance outputs obtained as a result of classification with RF of features determined to have different priorities according to Information Gain and Symmetric Uncertainty ranking algorithms

Feature	ACC%	Kappa	ROC
Y3	34.08	0.176	0.675
Y1	34.84	0.185	0.684
X3	25.84	0.073	0.582
X4	26.34	0.079	0.587

Finally, when Tables 1 and 2 are analyzed in detail in terms of prominent Information Gain and Symmetric Uncertainty ranking algorithms, it is seen that there is only a difference in ranking of "Y3 vs. Y1" and "X3 vs. X4" features. The results in Table 3 are obtained as proof that the Symmetric Uncertainty ranking algorithm performs a more successful ranking for the features in the specified data set. According to Table 3, when the Y1 and X4 features, which the Symmetric Uncertainty ranking algorithm determined to have higher priority, are classified separately by RF, it is seen that they achieve higher performance outputs than the Y3 and X3 attributes.

4. DISCUSSION AND CONCLUSION

In many sectors where metaverse systems will be applied, meta gloves are thought to be one of the most compatible hardware devices. However, it is extremely important that the 3D hand posture data obtained from the meta gloves is detected and transferred to the system with high accuracy as a result of the necessary processes. Because if the movement reflected on the glove is perceived as wrong at first, it will inevitably cause problems chaining in the whole system. In this study, the success of Information Gain, Pearson's Correlation, and Symmetric Uncertainty ranking methods on 3D hand posture data for metaverse systems was investigated in order to avoid possible problem chains in these systems, which are thought to have very common areas of use in the future. For this purpose, various pre-processes were performed on the 3D data and the created dataset was ranked by three different methods. Then, the features that the methods determined effectively were classified by the RF algorithm separately. Obtained results were interpreted and it has been proven that the Symmetric Uncertainty ranking algorithm is more successful than the others. On the other hand, it was seen that Pearson's Correlation ranking method was the most unsuccessful among the methods specified in ordering the effectiveness of the features of these data.

Cüneyt YÜCELBAŞ, Şule YÜCELBAŞ

Examining the Success of Information Gain, Pearson Correlation, and Symmetric Uncertainty Ranking Met...

As with other similar studies in this area, this study also has some limitations. One of them is data diversity. Today, the active use of machine learning algorithms in daily life, increasing the current success rates and reliability is possible by presenting many data from different sources to the systems. This is a common and general limitation of all sectors and research areas where artificial intelligence algorithms are used, not only for posture data. Another limiting factor for similar studies is meta gloves. These are important for metaverse systems because they collect and regularly transfer the 3D hand posture data of the relevant movements to the system and start and execute the processes over these data. For this reason, the wrong position of the sensors placed in the glove and the incomplete/incorrect quality of data detection and transmission are seen as limiting factors.

Apart from the ones mentioned above, it is certain that the noise level of the data transferred in current and future research will also affect the accuracy of the evaluations. Therefore, in the future, different studies can be carried out on noise detection, noise removal, and application of various filtering techniques on different data and comparative evaluation of the results. Another research that can contribute to this field may be on eliminating the missing data, which is not very intensive, by various methods and investigating its effects.

Authors' Contribution
The authors contributed equally to the study.

The Declaration of Conflict of Interest/ Common Interest
No conflict of interest or common interest has been declared by the authors.

The Declaration of Ethics Committee Approval
This study does not require ethics committee permission or any special permission.

The Declaration of Research and Publication Ethics
The authors of the paper declare that they comply with the scientific, ethical and quotation rules of SAUJS in all processes of the paper and that they do not make any falsification on the data collected. In addition, they declare that Sakarya University Journal of Science and its editorial board have no responsibility for any ethical violations that may be encountered, and that this study has not been evaluated in any academic publication environment other than Sakarya University Journal of Science

REFERENCES

[1]   A. Tlili, R. Huang, B. Shehata, D. Liu, J. Zhao, A. H. S. Metwally, H. Wang, M. Denden, A. Bozkurt, L. Lee, D. Beyoglu, F. Altinay, R. C. Sharma, Z. Altinay, Z. Li, J. Liu, F. Ahmad, Y. Hu, S. Salha, M. Abed, D. Burgos, "Is Metaverse in education a blessing or a curse: a combined content and bibliometric analysis," Smart Learning Environments, vol. 9, pp. 1-31, 2022.

[2]   F. Almeida, J. D. Santos, J. A. Monteiro, "The challenges and opportunities in the digitalization of companies in a post-COVID-19 World," IEEE Engineering Management Review, vol. 48, no. 3, pp. 97-103, 2020.

[3]   T. Huynh-The, Q.-V. Pham, X.-Q. Pham, T. T. Nguyen, Z. Han, D.-S. Kim, "Artificial Intelligence for the

Cüneyt YÜCELBAŞ, Şule YÜCELBAŞ

Examining the Success of Information Gain, Pearson Correlation, and Symmetric Uncertainty Ranking Met...

Metaverse: A Survey," arXiv preprint arXiv:2202.10336, 2022.

[4] M. Milanesi, S. Guercini, A. Runfola, "Let's play! Gamification as a marketing tool to deliver a digital luxury experience," Electronic Commerce Research, pp. 1-18, 2022.

[5] S. Tayal, K. Rajagopal, V. Mahajan, "Virtual Reality based Metaverse of Gamification," in 2022 6th International Conference on Computing Methodologies and Communication (ICCMC), 2022, pp. 1597-1604.

[6] Y. Xia, W. Li, S. Duan, W. Lei, J. Wu, "Low-cost, Light-weight Scalable Soft Data Glove for VR Applications," in 2022 5th International Conference on Circuits, Systems and Simulation (ICCSS), 2022, pp. 202-205.

[7] F. Wen, Z. Sun, T. He, Q. Shi, M. Zhu, Z. Zhang, L. Li, T. Zhang, C. Lee, "Machine learning glove using self-powered conductive superhydrophobic triboelectric textile for gesture recognition in VR/AR applications," Advanced science, vol. 7, pp. 2000261, 2020.

[8] S. Duan, Y. Lin, C. Zhang, Y. Li, D. Zhu, J. Wu, W. Lei, "Machine-learned, waterproof MXene fiber-based glove platform for underwater interactivities," Nano Energy, vol. 91, pp. 106650, 2022.

[9] M. Zhu, Z. Sun, Z. Zhang, Q. Shi, T. Chen, H. Liu, C. Lee, "Sensory-Glove-Based Human Machine Interface for Augmented Reality (AR) Applications," in 2020 IEEE 33rd International Conference on Micro Electro Mechanical Systems (MEMS), 2020, pp. 16-19.

[10] M. Cognolato, M. Atzori, D. Faccio, C. Tiengo, F. Bassetto, R. Gassert, H. Muller, "Hand gesture classification in transradial amputees using the Myo armband classifier," in 2018 7th IEEE International Conference on Biomedical Robotics and Biomechatronics (Biorob), 2018, pp. 156-161.

[11] A. Gardner, N. Elhami, R. R. Selmic, "Classifying unordered feature sets with convolutional deep averaging networks," in 2019 IEEE International Conference on Systems, Man and Cybernetics (SMC), 2019, pp. 3447-3453.

[12] J. Nayak, B. Naik, P. B. Dash, A. Souri, V. Shanmuganathan, "Hyper-parameter tuned light gradient boosting machine using memetic firefly algorithm for hand gesture recognition," Applied Soft Computing, vol. 107, p. 107478, 2021.

[13] A. Gardner, C. A. Duncan, J. Kanno, R. Selmic, "3d hand posture recognition from small unlabeled point sets," in 2014 IEEE International Conference on Systems, Man, and Cybernetics (SMC), 2014, pp. 164-169.

[14] K. G. Nalbant, Ş. Uyanık, "Computer vision in the metaverse," Journal of Metaverse, vol. 1, no. 1, pp. 9-12, 2021.

[15] O. Güler, S. Savaş, "All Aspects of Metaverse Studies, Technologies and Future," Gazi Journal of Engineering Sciences, vol. 8, no. 2, pp. 292-319, 2022.

[16] İ. Aydoğan, E. A. Aydın, "Wearable Electromyogram Design for Finger Movements Based Real-Time Human-Machine Interfaces," Journal of Polytechnic, pp. 1-1, 2022.

[17] O. Güler, İ. Yücedağ, "Hand gesture recognition from 2D images by using convolutional capsule neural networks," Arabian Journal for Science and Engineering, vol. 47, no. 2, pp. 1211-1225, 2022.

[18] P. Kirci, B. B. Durusan, B. Ozsahin, "Detecting Sign Language from Hand Gestures and Translating it into Text," European Journal of Science and Technology, vol. 36, pp. 32-35, 2022.

[19] W. Shu, Z. Yan, J. Yu, W. Qian, "Information gain-based semi-supervised feature selection for hybrid data," Applied Intelligence, pp. 1-16, 2022.

[20] E. O. Omuya, G. O. Okeyo, M. W. Kimwele, "Feature selection for classification using principal component analysis and information gain," Expert Systems with Applications, vol. 174, p. 114765, 2021.

[21] A. Sharma, P. K. Mishra, "Performance analysis of machine learning based optimized feature selection approaches for breast cancer diagnosis," International Journal of Information Technology, vol. 14, pp. 1949-1960, 2022.

[22] S. F. Sari, K. M. Lhaksmana, "Employee Attrition Prediction Using Feature Selection with Information Gain and Random Forest Classification," Journal of Computer System and Informatics (JoSYC), vol. 3, pp. 410-419, 2022.

[23] Z. Jiao, S. Chen, H. Shi, J. Xu, "Multi-modal feature selection with feature correlation and feature structure fusion for MCI and AD classification," Brain Sciences, vol. 12, p. 80, 2022.

[24] U. Kaya, M. Fidan, "Parametric and nonparametric correlation ranking based supervised feature selection methods for skin segmentation," Journal of Ambient Intelligence and Humanized Computing, vol. 13, pp. 821-833, 2022.

[25] W. Qian, Y. Xiong, J. Yang, W. Shu, "Feature selection for label distribution learning via feature similarity and label correlation," Information Sciences, vol. 582, pp. 38-59, 2022.

[26] P. Gaur, K. McCreadie, R. B. Pachori, H. Wang, G. Prasad, "An automatic subject specific channel selection method for enhancing motor imagery classification in EEG-BCI using correlation," Biomedical Signal Processing and Control, vol. 68, p. 102574, 2021.

[27] Y. Shi, M. Liu, A. Sun, J. Liu, H. Men, "A fast Pearson graph convolutional network combined with electronic nose to identify the origin of rice," IEEE Sensors Journal, vol. 21, pp. 21175-21183, 2021.

[28] X. Gu, J. Guo, "A feature subset selection algorithm based on equal interval division and three-way interaction information," Soft Computing, vol. 25, pp. 8785-8795, 2021.

[29] K. Zhao, Z. Xu, M. Yan, T. Zhang, D. Yang, W. Li, "A comprehensive investigation of the impact of feature selection techniques on crashing fault residence prediction models," Information and Software Technology, vol. 139, p. 106652, 2021.

[30] L. Zhang, X. Chen, "Feature selection methods based on symmetric uncertainty coefficients and

Cüneyt YÜCELBAŞ, Şule YÜCELBAŞ

Examining the Success of Information Gain, Pearson Correlation, and Symmetric Uncertainty Ranking Met...

independent classification information," IEEE Access, vol. 9, pp. 13845-13856, 2021.

[31] X. F. Song, Y. Zhang, D. W. Gong, X. Z. Gao, "A fast hybrid feature selection based on correlation-guided clustering and particle swarm optimization for high-dimensional data," IEEE Transactions on Cybernetics, 2021.

[32] A. Gardner, J. Kanno, C. A. Duncan, R. Selmic, "Measuring distance between unordered sets of different sizes," in Proceedings of the IEEE conference on computer vision and pattern recognition, 2014, pp. 137-143.

[33] J. Ding, L. Fu, "A Hybrid Feature Selection Algorithm Based on Information Gain and Sequential Forward Floating Search," Journal of Intelligent Computing, vol. 9, no. 3, pp. 93, 2018.

[34] S. Lei, "A feature selection method based on information gain and genetic algorithm," in 2012 international conference on computer science and electronics engineering, 2012, pp. 355-358.

[35] S. Jadhav, H. He, K. Jenkins, "Information gain directed genetic algorithm wrapper feature selection for credit rating," Applied Soft Computing, vol. 69, pp. 541-553, 2018.

[36] S. Ciklacandir, S. Ozkan, Y. Isler, "A Comparison of the Performances of Video-Based and IMU Sensor-Based Motion Capture Systems on Joint Angles," in 2022 Innovations in Intelligent Systems and Applications Conference (ASYU), 2022, pp. 1-5.

[37] A. Aytaç, M. Korkmaz, "An Analysis of the World Paper Industry with a Focus on Europe and Trade Perspective," Studia Universitatis Vasile Goldiş Arad, Seria Ştiinţe Economice, vol. 32, pp. 24-40, 2022.

[38] J. Adler, I. Parmryd, "Quantifying colocalization by correlation: the Pearson correlation coefficient is superior to the Mander's overlap coefficient," Cytometry Part A, vol. 77, pp. 733-742, 2010.

[39] J. Biesiada, W. Duch, "Feature selection for high-dimensional data—a Pearson redundancy based filter," in Computer recognition systems 2, ed: Springer, 2007, pp. 242-249.

[40] B. Singh, N. Kushwaha, O. P. Vyas, "A feature subset selection technique for high dimensional data using symmetric uncertainty," Journal of Data Analysis and Information Processing, vol. 2, p. 95, 2014.

[41] S. I. Ali, W. Shahzad, "A feature subset selection method based on symmetric uncertainty and ant colony optimization," in 2012 International Conference on Emerging Technologies, 2012, pp. 1-6.

[42] L. Breiman, "Random forests," Machine learning, vol. 45, pp. 5-32, 2001.

[43] J. Cohen, "A coefficient of agreement for nominal scales," Educational and psychological measurement, vol. 20, no. 1, pp. 37-46, 1960.

[44] J. L. Fleiss, "Measuring nominal scale agreement among many raters," Psychological bulletin, vol. 76, no. 5, pp. 378, 1971.

[45] J. A. Hanley, B. J. McNeil, "The meaning and use of the area under a

Cüneyt YÜCELBAŞ, Şule YÜCELBAŞ

Examining the Success of Information Gain, Pearson Correlation, and Symmetric Uncertainty Ranking Met...

receiver operating characteristic (ROC) curve," Radiology, vol. 143, no. 1, pp. 29-36, 1982.

Title: Investigation of Vitamins, Glutathione and Stress Biomarkers in Blood Serum of Patients with Breast Cancer

Authors: Fikret KARATAŞ, Awat Hamad AWLA IBRAIM, Dursun ÖZER, Sinan SAYDAM

Investigation of Vitamins, Glutathione and Stress Biomarkers in Blood Serum of Patients with Breast Cancer

Awat Hamad AWLA IBRAIM[2] (iD), Dursun ÖZER[1] (iD), Fikret KARATAS[1*] (iD),
Sinan SAYDAM[1] (iD)

Abstract

Breast cancer is a genetic disease caused by the accumulation of mutations in neoplastic cells and is responsible for the highest morbidity and mortality. In this study, blood serum samples from 45 breast cancer patients and 32 healthy individuals (control group) were used. The amounts of vitamins (A, E, β-carotene, C, B_1, B_2, B_3, B_5, B_6, B_9 and B_{12}), glutathione (GSH, GSSG) stress biomarkers (4-HNE, MDA) were determined by HPLC. A significant difference was found between the breast cancer patients and the control group in terms of age and body mass index (BMI) ($p < 0.05$). In the breast cancer group, fat-soluble vitamins, A, E and β-carotene decreasing highly significant ($p < 0.001$), decreasing water-soluble vitamins was found to be significant ($p < 0.05$). No statistically significant difference was observed between the groups that received and did not receive treatment except vitamin B2 ($p > 0.05$) with in the cancer patients. Likewise, no significant difference was observed between the serum vitamin levels of breast cancer patients who breastfeed and not breastfeed, except for vitamins B_2 and B_3 ($p > 0.05$). A high level of significant difference was observed between GSH, GSSG, MDA and 4-HNE in the breast cancer patient and control groups ($p < 0.001$). There was no significant difference found in GSSG, MDA and HNE values according to the treatment status of breast cancer patients, on the other hand, a significant difference was observed in GSH and GSH/GSSG values ($p < 0.05$). While there was no significant difference in GSH, GSSG, MDA and 4-HNE values according to the breastfeeding status of patients, a significant difference was observed in GSH/GSSG values ($p < 0.05$).

Keywords: Breast cancer, vitamins, reduced glutathione, oxidised glutathione, 4-hydroxy neoneal, malondialdehyde.

1. INTRODUCTION

Cancer is the uncontrolled and abnormal growth of the body's cells. Arising from a series of molecular events that fundamentally alter the cells' normal properties. The normal control systems which prevent cell overgrowth and invasion of other tissues in cancer cells are disabled. Such altered cells divide and expand in an

---

KARATAŞ et al.

Investigation of Vitamins, Glutathione and Stress Biomarkers in Blood Serum of Patients with Breast C...

uncontrolled way, and sometimes metastasis by dividing and increasing cells in the presence of signals that normally inhibit cell growth. Cancer cell disorders typically result from mutations in protein-encoding genes that control cell division. With time, more genes are mutated, because the genes that produce the proteins which commonly repair DNA damage do not function normally [1]. Breast is very important for women, growth, development and differentiation take place throughout their lives. The obvious purpose of the breast is to secrete milk for babies [2]. Breast cancer is a genetic disease caused by the accumulation of mutations in neoplastic cells and is responsible for the highest morbidity and mortality [3]. The etiology of breast cancer is multifactorial and several risk factors related to breast cancer may exert their effects by creating an oxidative stress state. Oxidative stress is very effective in the pathogenesis of various chronic diseases such as cancer, diabetes and cardiovascular diseases [4]. Oxidative stress can generally be defined as an oxidant/antioxidant imbalance that can lead to damage. If the amount of reactive species is high and defeats the antioxidant defense mechanisms of the human body, oxidative damage to lipids, proteins or DNA can occur, and this damage is considered to play an important role in the progress of many carcinogenesis-onset diseases, including breast cancer [5]. The measurement of oxidative stress biomarkers in breast cancer patients has a significant interest. There are several markers of oxidative stress, such as malondialdehyde (MDA) and 4-hydroxynonenal (4-HNE), which have been applied broadly as markers of lipid peroxidation, and protein carbonyl that is the biomarker of protein oxidation mostly used in epidemiological and clinical studies [6]. Cells are preserved from oxidative stress through antioxidant detoxification pathways that are containing non-enzymatic antioxidants like reduced glutathione (GSH) and various antioxidant enzymes. Glutathione has been frequently used as a

biomarker of oxidative stress which is a reducing agent that is widely spread in cells. In a patient suffering from breast cancer, it is becoming extremely important to identify possible modifiable factors affecting oxidative stress [4]. In addition, vitamins play an important role as coenzymes or enzymes in many important processes for the proper functioning of the body to necessary for human metabolism. In recent years, due to the large number of studies examining this relationship, vitamins have emerged as important for health and human disease [7, 8], so it is important to know the relationship of vitamins with breast cancer. The study aims to determine the water and fat-soluble vitamins together with the stress biomarkers (MDA, 4-HNE, GSH/GSSG), in the blood serum of women with breast cancer and compare them with the control group.

2. MATERIAL AND METHODS

2.1. Material

In the study, blood samples were taken from a total of 77 individuals aged 20-65 who applied to Hiwa Cancer Hospital between September 2019 and October 2019, 45 with breast cancer patients diagnosed by specialist doctors and 32 healthy controls. Among the 32 of breast cancer patients who did not receive pretreatment, 13 received pretreatment. While 15 of the cancer patients were breastfeeding, 30 did not breastfeed at all. A personal interview was conducted with all patients using a specially designed full history questionnaire with accurate information.

2.2. Exclusion criteria

These criteria include Patients with diabetes mellitus, pre-diabetes, chronic liver or renal disease, and malignancy other than breast cancer and smoking, and alcohol consumption. 5 mL of a blood sample from the individuals was taken into a tube and centrifuged at 3500 rpm for 10 minutes. The

separated serum samples were taken into Eppendorf tubes and transported to the chemistry laboratory of Fırat University by cold chain and stored at -20 °C until analysis. The study was carried out with the approval of the ethics committee of Northern Iraq Hiwa Cancer Hospital dated September-2019 and the approval of the ethics committee at Fırat University with the date and number of 22/10/2019-355284.

2.3. Determination of Body Mass Index (BMI)

Measured height to the nearest 0.5 cm and weight to the nearest 0.1 kg.
BMI is calculated as: BMI = Mass(kg) / [Height m^2] BMI ($<$ 16-18.5) is underweight (18.5-24.9) is normal, (25-29.9) is overweight, ($>$ 30-35) is moderately obese, ($>$ 35-40) is obese severely [9].

2.4. Determination of vitamins A, E, β-carotene and 4-HNE

0.3 mL of serum sample was taken into a tube, 4.0 mL of C_2H_5OH was added, vortexed and centrifuged at 7500 rpm for 10 minutes. Then, the supernatant was transferred and 1.0 mL n-hexane was added, vortexed and centrifuged under the same conditions and the upper n-hexane phase was taken into a glass tube, and this process was repeated twice. The collected n-hexane was dried under a vacuum and the residue in the tube was dissolved in 1.0 mL of methanol and taken into HPLC vials for analysis. Samples were analyzed by HPLC (Shimadzu Prominence-I LC-2030C 3D by PDA detector) using a Supelcosil LC-18 column (25.0 cm x 4.6 mm x 5.0 μm) with a mixture of methanol: acetonitrile: water (63:33: 4.0 v/v) as the mobile phase [10, 11].

2.5. Determination of B, C vitamins, glutathione and MDA

0.7 mL of 0.5 M perchloric acid was added to 0.3 mL of serum sample and vortexed,

then the total volume was completed to 3.0 mL by adding distilled water. The mixture was then centrifuged at 7500 rpm for 10 minutes. The supernatant was taken into HPLC vials and B vitamins were analyzed using a Supelcosil LC-18-DB column (150 mm x 4.6 mm ID, 5 μm) [10, 12]. Vitamin C, Glutathione and MDA amounts were determined in HPLC using Utisil-XB-C-8 (25 cm, 4.6 mm ID, 5 μm) column [10, 13]

3. RESULTS AND DISCUSSION

This study included 77 volunteers divided into two groups; The first group consist 45 volunteer patients with breast cancer and the second group consists of 32 healthy individuals from the same demographic region, as the control group. Some characteristics of the groups such as age, body mass index, family history, marital status, parious and breastfeeding are given in Table 1. Differences in breast cancer risk factors are genetic and epidemiological risk factors such as age, family history, childbirth, breastfeeding, and environmental factors. The distribution of demographic characteristics of participants and the relation between identified and suspected factors in the development of breast cancer is presented in Table 1. It reveals that 15% of the patient group were in the age group of 30-39 years, 38% were lies in 40-49 years, 40% of them belong to more than 50 years of age and only 7% of them were <30 years. This indicates that the majority (78%) of breast cancer patients were over 40 years age group. The risk of occurrence of breast cancer increases in middle-aged (after 40 years) and elderly women compared to young women [14]. Human cancer is mainly an age-related disease that involves a person 50 years old or older as our cells change over time and are more susceptible to genetic damage and less able to deal with damage when it occurs.

This problem is thought to be large to a reduction in our immune system's ability to

KARATAŞ et al.

Investigation of Vitamins, Glutathione and Stress Biomarkers in Blood Serum of Patients with Breast C...

detect and destroy abnormal cells as they occur, the decreased immune response gives those cells time to develop into potentially lethal cancer [15]. It is well known that breast cancer is associated with weight gain, especially in postmenopausal women as depicted in Table 1. Subjects in both groups were observed to range from normal weight, overweight to obese regardless of their diagnosis. In the present study, the maximum number of cancer patients are in the range of obesity group (44%), 31% are overweight (31%) while the lowest (25%) were in the normal group. The result of this study is confirmed by a direct association between BMI and the risk of the disease developing [16]. Because obesity changes hormone levels in postmenopausal women, such as estrogen, the extra fat cells make estrogen, which can cause hormone receptor-positive breast cancer risk [17]. The distribution of marital status and family history of patients with breast cancer is illustrated in Table 1 that 44% of patients had positive family cancer history. Pal et al. reported that about 3-10% of breast cancers are hereditary cancers. It is estimated that about 85% of these are associated with BRCA1 and BRCA2 mutations. The majority of hereditary breast cancers are accepted as "hereditary breast and ovarian cancer syndrome" due to BRCA1 and BRCA2 mutations [18].

Table 1 General characteristics of all studied groups

Characteristics	Study groups		P-Value
	Breast cancer (n=45)	Control (n=32)	
Age (yrs.) Mean±SD	47.26±11.41	38.81±11.61	0.002[a]
Age distribution (%)			
<30 yrs.	3 (7.0%)	8 (25.0%)	0.113[b]
30-39	8 (15.0%)	7 (22.0%)	
40-49	16 (38.0%)	8 (25%)	
≥50	18(40.0%)	9 (28.0%)	
BMI (kg/m^2) Mean±SD	29.62±5.43	25.43±5.47	0.001[a]
BMI distribution (%)			
Normal weight	11 (25.0%)	18 (56.0%)	0.016[b]
Overweight	14 (31.0%)	7 (22.0%)	
Obese	20(44.0%)	7(22.0%)	
Family history of BC (%)			0.027[b]
Yes	20 (44.0%)	6 (19.0%)	
No	25 (56.0%)	26 (81.0%)	
Marital Status (%)			0.024[b]
Married	36 (80.0%)	17(53.0%)	
single	9 (20.0%)	15 (47.0%)	
Parous (%)			0.353[b]
Parent	18(40.0%)	15(47.0%)	
Nulliparous	27 (60.0%)	17(53.0%)	
Breastfeeding (%)			0.244[b]
Yes	15(33.0%)	14(44.0%)	
No	30(67.0%)	18(56.0%)	

[a] One-way anova test and [b] Pearson Chi-squared test were performed for statistical analyses

KARATAŞ et al.

Investigation of Vitamins, Glutathione and Stress Biomarkers in Blood Serum of Patients with Breast C...

Table 2 Amounts of vitamins in breast cancer patients and healthy control groups

Biochemical parameters	Study groups (Mean µg/mL ± SD)		P-Value
	Breast cancer (n=45)	Control (n=32)	
Vitamin A	0.49±0.12	1.89±0.65	0.000**
Vitamin E	4.27±1.04	9.18±4.10	0.000**
β-Carotene	0.54±0.17	0.89±0.20	0.000**
Vitamin C	20.20±4.46	22.70±5.44	0.031*
Vitamin B_1	3.19± 0.83	3.83±1.11	0.007*
Vitamin B_2	3.43±1.10	4.45 ±1.36	0.002*
Vitamin B_3	2.32±0.53	2.63±0.47	0.014*
Vitamin B_5	0.77±0.16	0.85±0.12	0.017*
Vitamin B_6	1.03±0.33	1.26±0.43	0.013*
Vitamin B_9	18.45±7.06	23.34±9.77	0.017*
Vitamin B_{12}	0.12±0.06	0.15±0.06	0.013*

One-way ANOVA test were performed for statistical analyses. *$p<0.05$ was significant and **$p<0.001$ was highly significant

Women, especially those who are younger or, who have a child are less likely to get breast cancer. In this study parous of breast cancer patients 60% have a child and 40% of the patient is nulliparous. Women who are single and nulliparous reported a strong elevated risk of breast cancer in most research relative to multi-parous women at the same age. The marital status itself is not a contributing factor for an increased or decreased risk of breast cancer [19]. Breastfeeding among patients with breast cancer is 33% shown in Table 1. It is not clear how breastfeeding decreases the risk of breast cancer. The biological basis for an inverse relation between breastfeeding and breast cancer risk has not been adequately explained. Although various mechanisms have been postulated, one assumption is that lactation causes long-term endogenous hormone changes, possibly decreased estrogen, and increased production of prolactin, which can reduce the cumulative exposure of a woman to estrogen, thus inhibiting the formation or growth of breast cancer cells [20]. The experimental findings of vitamin for the breast cancer patients and healthy control groups are given in Table 2.

In this study, patients with breast cancer had highly significant $p<0.001$ lower serum levels of β-carotene, vitamin A, and vitamin E than healthy control subjects (Table 2).

Few studies have investigated the serum levels of vitamins A, E, and β-carotene, in breast cancer patients. In a study conducted by Wald et al. [21] it was shown that low serum levels of vitamins A, E, β-carotene, and retinol precede the development of different cancer types. Results of previous research on vitamin A and E in the serum with breast cancer have provided compelling support for the theory that vitamin A and its precursors prevent mammary carcinogenesis [21, 22]. The findings obtained suggest an association between vitamins and antioxidants and an inverse association with breast cancer. Our research confirms the findings of previous studies that serum concentrations of selected vitamins and carotenoids of patients with other cancers are lowered compared with healthy control groups [23, 24]. Antioxidation functions of β-carotene, vitamins A and E have been reported to reduce DNA damage and maling change [25]. The number of water-soluble vitamins (C, B_1, B_2, B_3, B_5, B_6, B_9 and B_{12}) in cancer patients showed a significant decrease in vitamins compared to the control group ($p<0.05$) (Table 2). Vitamin C acts as a prooxidant, promoting the formation of ROS, such as hydrogen peroxide, hydroxyl radicals, and many others. ROS, generated in response to the high concentration of vitamin C, interacts with critical cellular

KARATAŞ et al.

Investigation of Vitamins, Glutathione and Stress Biomarkers in Blood Serum of Patients with Breast C...

molecules and organelles and results in oxidative degradation of these compounds in cancer cells, impairing their viability. Vitamin C acts selectively on tumor cells because they show a decrease of several antioxidant enzymes compared to normal ones [26]. Hussain and Ashafaq [27] stated in their study that the amount of vitamin C in the blood serum of patients with breast cancer is lower than in the control group. Water-soluble vitamins maybe have a complex role in protecting or inhibiting cancer. There are several concerns about the quantities required for their biological functions, and about their beneficial and toxic effects on human health [28]. Vitamin B_1 deficiency has been reported in advanced cancer patients [29]. Vitamin B_2 deficiency has been shown as a risk factor for cancer, but some studies show that riboflavin deficiency increases the risk of cancer in certain regions, while some studies point to a possible weakening effect of riboflavin in the presence of carcinogens [7].

The deficiency of riboflavin has been linked with numerous diseases including cancer and cardiovascular disorders, and there are some indications that the treatment of riboflavin may be effective against oxidative stress-related diseases such as breast cancer [30]. It has been reported that vitamins B_3 and B_6 may be a protective factor against cancer that these vitamins were found to be lower in cancer patients [7, 31]. In a wide range of metabolic functions, vitamin B_5 plays an important role. It is required to form coenzyme A, which is essential for the synthesis of fatty acids, amino acids, steroid hormones, and other significant compounds [32]. Vitamin B_9 is generally reported to be inversely associated with breast cancer risk [33]. Zhang et al. [34] reported that the amount of vitamins B_6 and B_9 in the plasma of patients with breast cancer decreased, but the amount of vitamin B_{12} did not change compared to the control. Vitamins deficiency in the metabolism of patients with breast cancer can be explained in various ways. Reduced levels of vitamins in breast cancer patients can also be due to the eating habit of patients. Lower plasma vitamin levels can be explained by higher oxidative stress caused by lipid peroxidation, and mutations that contribute to higher breast cancer risk [23]. The serum vitamin levels of the groups treated and untreated with breast cancer patients are given in Table 3.

Table 3 Mean concentration of vitamins parameters in breast cancer women considering taking treatments

Biochemical parameters	Breast cancer patients group (Mean µg/mL ± SD)		P-Value
	Untreated (n=32)	Treated (n=13)	
Vitamin A	0.49±0.12	0.48±0.12	0.819
Vitamin E	4.49±1.41	4.14±0.75	0.285
β-Carotene	0.53±0.14	0.55±0.19	0.737
Vitamin C	20.01±2.85	20.30±5.22	0.842
Vitamin B_1	2.88±0.69	3.38±0.87	0.061
Vitamin B_2	2.85±0.68	3.79±1.16	0.007 *
Vitamin B_3	2.29±0.47	2.35±0.58	0.732
Vitamin B_5	0.71±0.12	0.80±0.17	0.054
Vitamin B_6	1.04±0.31	1.01±0.35	0.850
Vitamin B_9	16.74±4.06	19.48±8.27	0.239
Vitamin B_{12}	0.12±0.06	0.11±0.05	0.774

One-way ANOVA test were performed for statistical analyses. *$p<0.05$ was significant and **$p<0.001$ was highly significant

KARATAŞ et al.

Investigation of Vitamins, Glutathione and Stress Biomarkers in Blood Serum of Patients with Breast C...

The experimental result given in Table 3, shows that there is no statistically significant difference was observed between the patient who has the treatment and has not treatment, except for vitamin B_2, in the blood serum of women with breast cancer ($p > 0.05$). Vitamins levels of patients who have breastfed and didn't breastfed that are illustrated in Table 4. There was no significant difference observed between the serum vitamin levels except for vitamins B_2 and B_3 ($p > 0.05$).

The amounts of glutathione (GSH, GSSG), MDA and 4-HNE in the serum of breast cancer patients and control groups were given in Table 5. A high level of significant difference was observed between the breast cancer patients and the control group ($p<0.001$). The amount of oxidative damage is not only depending on ROS rates but also on the cellular antioxidant defense mechanisms. One of the cellular antioxidant defenses is glutathione that functions as the first line of defence against free radicals. GSH levels decrease significantly ($p<0.001$) in patients with breast cancer compared to the healthy control groups while GSSG levels increased significantly ($p<0.001$). These results were agreeing with the research conducted by Yeh et al. [35] that a low level of GSH and increase GSSG levels in breast cancer patients than in control groups. The ratio of GSH/GSSG may be used as an oxidative stress marker, which is maintained at a high ratio under physiological conditions. GSH is oxidized to GSSG under oxidative stress, and the ratio of GSH/GSSG decreases. In the present study, it was found that the GSH/GSSG ratio in breast cancer patients was significantly ($p<0.05$) lower, compared to control groups. There is a similar report that patient with breast cancer has a lower level of GSH/GSSG ratio in their blood serum [35, 36]. GSH level of serum among participants have a statistically significantly correlating with each of MDA, HNE, and GSSG. GSH has an inverse relationship with oxidative stress due to the antioxidant properties of GSH that is equalized free radical by oxidation to GSSG [37]. It has been reported that while the amount of MDA in the blood of gastric cancer patients increases, GSH levels decrease [38]. The serum GSH, GSSG, MDA and 4-HNE levels of the groups who treated and untreated from patients with breast cancer are given in Table 6.

Table 4 Vitamin concentrations in the serum of women with breast cancer by breastfeeding status

Biochemical parameters	Breast cancer patients group (Mean μg/mL ± SD)		P-Value
	Have breastfeeding (n=15)	Didn't have breastfeeding (n=30)	
Vitamin A	0.51±0.13	0.48±0.12	0.424
Vitamin E	4.42±0.59	4.21±1.17	0.552
β-Carotene	0.59±0.19	0.52±0.17	0.274
Vitamin C	21.19±3.99	19.83±4.64	0.372
Vitamin B_1	2.98 ±0.87	3.26 ±0.82	0.335
Vitamin B_2	2.79±0.68	3.68±1.14	0.021*
Vitamin B_3	1.97±0.29	2.46±0.55	0.008*
Vitamin B_5	0.73±0.13	0.78±0.17	0.336
Vitamin B_6	0.94±0.31	1.06±0.34	0.300
Vitamin B_9	19.11±5.62	18.20±7.61	0.720
Vitamin B_{12}	0.14±0.07	0.11±0.05	0,190

One-way ANOVA test were performed for statistical analyses. *$p<0.05$ was significant and **$p<0.001$ was highly significant

KARATAŞ et al.

Investigation of Vitamins, Glutathione and Stress Biomarkers in Blood Serum of Patients with Breast C...

Table 5 Glutathione (GSH, GSSG), MDA and 4-HNE amounts in the serum of breast cancer patients and control groups

Biochemical parameters	Study groups (Mean µg/mL ± SD)		P-Value
	Breast cancer (n=45)	Control (n=32)	
GSH	140.55±42.29	262.09±55.94	0.000**
GSSG	57.33±16.44	30.08±7.56	0.000**
GSH/GSSG	3.68±2.38	8.95±1.17	0.000**
MDA	4.91±1.33	0.33±0.06	0.000**
4-HNE	8.99±2.57	4.75±1.91	0.000**

One-way ANOVA test were performed for statistical analyses. *p<0.05 was significant and **p<0.001was highly significant.

Table 6 Mean GSH, GSSG, MDA and 4-HNE concentrations of breast cancer patients by treatment status

Biochemical parameters	Breast cancer patients group (Mean µg/mL ± SD)		P-Value
	Untreated (n=32)	Treated (n=13)	
GSH	88.83±47.30	148.50±73.50	0.006*
GSSG	59.32±41.78	47.22±36.73	0.323
GSH/GSSG	2.55±2.00	4.34±2.33	0.019*
MDA	5.10±1.11	4.79±1.44	0.457
4-HNE	9.33±2.93	8.79±2.37	0.524

One-way ANOVA test were performed for statistical analyses. *p<0.05 was significant and **p<0.001was highly significant

There was no significant difference in GSSG, MDA and HNE values according to the treatment status of breast cancer patients, a significant difference was observed in GSH and GSH/GSSG values (Table 6). GSH, GSSG, MDA and 4-HNE level which classified according to who have breastfeeding and who didn't breastfeed between breast cancer women that are illustrated in Table 7.

There was no significant difference in GSH, GSSG, MDA and 4-HNE values according to the breastfeeding status of patients with breast cancer, a significant difference was observed in GSH/GSSG values (Table 7).

Table 7 Mean concentration of GSH, GSSG, MDA and 4-HNE in women with breast cancer by breastfeeding status

Biochemical parameters	Breast cancer patients' group (Mean µg/mL ± SD)		P-Value
	Have breastfeeding (n=15)	Didn't have breastfeeding (n=30)	
GSH	148.13±39.83	136.20±67.60	0.587
GSSG	39.60±24.45	63.30±38.70	0.067
GSH/GSSG	4.89±2.54	3.21±2.19	0.046 *
MDA	4.85±1.40	5.06±1.18	0.638
4-HNE	8.87±2.50	9.28±2.84	0.649

One-way ANOVA test were performed for statistical analyses. *p<0.05 was significant and **p<0.001was highly significant.

KARATAŞ et al.

Investigation of Vitamins, Glutathione and Stress Biomarkers in Blood Serum of Patients with Breast C...

4. CONCLUSION

As a result, it can be concluded that the risk of breast cancer increases with age and BMI increase. There was a decrease in the amount of water and fat-soluble vitamins and GSH in the serum of breast cancer patients, and an increase in the amount of stress markers (MDA, 4-HNE) and GSSG. From these results, it can be said that a serum-based screening test may be useful for the diagnosis of breast cancer. There was a negative association between the participants in the oxidative stress biomarker (4-HNE, MDA, GSSG) and GSH of breast cancer patients. A weak antioxidant protection mechanism might increase oxidative stress in breast cancer patients. The low levels of water-soluble vitamins in breast cancer patients indicate that the demand for B vitamins has been increased for these patients due to accelerated energy metabolism. To validate the change in parameters and determine whether breast cancer patients require supplement B vitamins, more research needs to be done.

The Declaration of Conflict of Interest/ Common Interest
The authors declared that there are no potential conflicts of interest with respect to the research, authorship, and/or publication of this article.

Authors' Contribution
Under this title, "First author contributed 40%, second and third authors 25%, and last author10%."

The Declaration of Ethics Committee Approval
The study was carried out with the approval of the ethics committee of Northern Iraq Hiwa Cancer Hospital dated September-2019 and the approval of the ethics committee at Fırat University with the date and number of 22/10/2019-355284.

The Declaration of Research and Publication Ethics
The authors of the paper declare that they comply with the scientific, ethical and quotation rules of SAUJS in all processes of the paper and that they do not make any falsification on the data collected. In addition, they declare that Sakarya University Journal of Science and its editorial board have no responsibility for any ethical violations that may be encountered, and that this study has not been evaluated in any academic publication environment other than Sakarya University Journal of Science.

REFERENCES

[1] G. M. Cooper, R. E. Hausman, "The development and causes of cancer," The cell: a molecular approach (2nd ed.), Sinauer Associates, Sunderland pp. 725-766, 2000.

[2] A. Javed, L. Aida, "Development of the Human Breast," Seminars in Plastic Surgery, vol. 27, no.1, pp 5-12, 2013.

[3] E. A. Rakha, A. R. Green, "Molecular classification of breast cancer: what the pathologist needs to know," Pathology, vol. 49, no. 2, pp 111-119, 2017.

[4] A. R. Nourazarian, P. Kangari, A. Salmaninejad, "Roles of oxidative stress in the development and progression of breast cancer," Asian Pacific Journal of Cancer Prevention, vol. 15, no. 12, pp 4745-4751, 2014.

KARATAŞ et al.

Investigation of Vitamins, Glutathione and Stress Biomarkers in Blood Serum of Patients with Breast C...

[5] F. Hecht, C. F. Pessoa, L. B. Gentile, D. Rosenthal, D. P. Carvalho, R. S. Fortunato, ″The role of oxidative stress on breast cancer development and therapy,″ Tumour Biology, vol. 37, no. 4, pp 4281-4291, 2016.

[6] A. Ayala, M. F. Muñoz, S. Argüelles, ″Lipid peroxidation: production, metabolism, and signaling mechanisms of malondialdehyde and 4-hydroxy-2-nonenal,″ Oxidative Medicine and Cellular Longevity, vol. 2014, pp 1-31, 2014.

[7] A. C. Mamede, S. D. Tavares, A. M. Abrantes, J. Trindade, J. M. Maia, M. F. Botelho, ″The Role of Vitamins in Cancer: A Review,″ Nutrition and Cancer, vol 63, no. 4, pp 479-94, 2011.

[8] K. M. Fairfield, R. H. Fletcher, ″Vitamins for chronic disease prevention in adults: clinical applications," The Journal of the American Medical Association, vol. 287, no. 23, pp 3116-3126, 2002.

[9] M. Pierobon, C. L. Frankenfeld, ″Obesity as a risk factor for triple-negative breast cancers: a systematic review and meta-analysis,″ Breast Cancer Research Treatment, vol. 137, no. 1, pp 307-314, 2013.

[10] M. S. Ibrahim, Y. I. Ibrahim, Z. G. Mukhtar, F. Karatas, ″Amount of Vitamin A, Vitamin E, Vitamin C, Malondialdehyde, Glutathione, Ghrelin, Beta-Carotene, Lycopene in Fruits of Hawthorn, Midland (Crataegus laevigata),″ Journal of Human Nutrition and Food Science, vol. 5, no. 3, pp 1112-118, 2017.

[11] M. Ligor, T. Ligor, R. Gadzała-Kopciuch, B. Buszewski, ″The chromatographic assay of 4-hydroxynonenal as a biomarker of diseases by means of MEPS and HPLC technique,″ Biomedical Chromatography, vol. 29, no. 4, pp 584-589, 2015.

[12] R. Amidžić, J. Brborić, O. Čudina, S. Vladimirov,″Rp-HPLC determination of vitamins, folic acid and B12 in multivitamin tablets,″ Journal of Serbian Chemical Society, vol. 70, no. 10, pp 1229–1235, 2005.

[13] P. Dawes, E. Dawes, ″SGE Choromatography Products Catalog,″ pp: 182, 2000.

[14] A. B. Miller, C. Wall, C. J. Baines, P. Sun, T. To, S. A. Narod, ″Twenty five year follow-up for breast cancer incidence and mortality of the Canadian National Breast Screening Study: randomised screening trial,″ British Medical Journal, vol. 348, pp 1-10, 2014.

[15] N. Howlader, A. Noone, M. Krapcho, D. Miller, K. Bishop, C. Kosary, M. Yu, J. Ruhl, Z. Tatalovich, A. Mariotto, ″SEER cancer statistics review,″ 1975-2014, Bethesda, MD: National Cancer Institute, 2018.

[16] H. D. Nelson, B. Zakher, A. Cantor, R. Fu, J. Griffin, E. S. O'Meara, D. S. Buist, K. Kerlikowske, N. T. van Ravesteyn, A. Trentham-Dietz, ″Risk factors for breast cancer for women aged 40 to 49 years: a systematic review and meta-analysis,″ Annals of Internal Medicine, vol. 156, no. 9, pp 635-48, 2012.

[17] M. P. Cleary, M. E. Grossmann, ″Obesity and breast cancer: the estrogen connection″ Endocrinology, vol. 150, no. 6, pp 2537–2542, 2009.

[18] T. Pal, S. T. Vadaparampil, ″Genetic risk assessments in individuals at high

KARATAŞ et al.

Investigation of Vitamins, Glutathione and Stress Biomarkers in Blood Serum of Patients with Breast C...

risk for inherited breast cancer in the breast oncology care setting," Cancer Control, vol. 19, no. 4, pp 255-66, 2012.

[19] A. A. Zouré, A. H. Bambara, A. Y. Sawadogo, A. K. Ouattara, M. Ouédraogo, S. S. Traoré, Y. Bakri, J. Simporé, "Multiparous and breast cancer risk factor among women in Burkina Faso ", Asian Pacific journal of cancer prevention, vol. 17, no. 12, pp 5095-5099, 2016.

[20] S. Tessaro, J. U. Béria, E. Tomasi, C. G. Victora, "Breastfeeding and breast cancer: a case-control study in Southern Brazil," Cadernos Saúde Coletia, Rio de Janeiro, vol. 19, no.6, pp 1593-1601, 2003.

[21] N. J. Wald, A. Nicolaides-Bouman, G. A. Hudson, "Plasma retinol, beta-carotene and vitamin E levels in relation to the future risk of breast cancer," British Journal of Cancer, vol. 57, no. 2, pp 235, 1988.

[22] T. J. Hartman, D. Albanes, P. Pietinen, A. M. Hartman, M. Rautalahti, J. A. Tangrea, P. R. Taylor, "The association between baseline vitamin E, selenium, and prostate cancer in the alphatocopherol, beta-carotene cancer prevention study," Cancer Epidemiology, Biomarkers and Prevention, vol. 7, no. 4, pp 335-340, 1998.

[23] K. M. Terlikowska, B. Dobrzycka, M. Kinalski, S. J. Terlikowski, "Serum Concentrations of Carotenoids and Fat-Soluble Vitamins in Relation to Nutritional Status of Patients with Ovarian Cancer," Nutrition and Cancer, vol 73, no. 8, pp 1480-1488, 2021.

[24] D. Talwar, T. Ha, H. R. Scott, J. Cooney, G. S. Fell, D. S. O'Reilly, M. Lean, D. C. McMillan, "Effect of inflammation on measures of antioxidant status in patients with non-small cell lung cancer," The American Journal of Clinical Nutrition, vol. 66, no. 5, pp 1283-1285, 1997.

[25] E. Cho, D. Spiegelman, D. J. Hunter, W. Y. Chen, S. M. Zhang, G. A. Colditz, W. C. Willett, "Premenopausal intakes of vitamins A, C and E, folate and carotenoid and risk of breast cancer," Cancer Epidemiol Biomarkers and Prevention, vol. 12, no. 8, pp 713-720, 2003.

[26] Q. Chen, M. G. Espey, A. Y. Sun, J. H. Lee, M. C. Krishna, E. Shacter, P. L. Choyke, C. Pooput, K. L. Kirl, G. R. Buettner, M. Levine, "Ascorbate in pharmacologic concentrations selectively generates ascorbate radical and hydrogen peroxide in extracellular fluid in vivo," Proceedings of the National Academy of Sciences of the United States of America, vol. 104, no. 21, pp. 8749-8754, 2007.

[27] S. Hussain, M. Ashafaq, "Oxidative Stress and Anti-oxidants in Pre and Post-operative Cases of Breast Carcinoma," Turkish Journal of Pharmaceutical Sciences, vol. 15, no. 3, pp 354-359, 2018.

[28] R. I. Inculet, J. A. Norton, G. E. Nichoalds, M. M. Maher, D. E. White, M. F. Brennan, "Water-soluble vitamins in cancer patients on parenteral nutrition: a prospective study," Journal of Parenteral and Enteral Nutrition, vol. 11, no. 3, pp 243-249, 1987.

KARATAŞ et al.

Investigation of Vitamins, Glutathione and Stress Biomarkers in Blood Serum of Patients with Breast C...

[29] M. Cascante, J. J. Centelles, R. L. Veech, W. N. Lee, L. G. Boros, ″Role of thiamin (vitamin B-1) and transketolase in tumor cell proliferation,″ Nutrition and Cancer, vol. 36, no. 2, pp.150-154, 2000.

[30] C. T. Peterson, D. A. Rodionov, A. L. Osterman, S. N. Peterson, ″B Vitamins and Their Role in Immune Regulation and Cancer,″ Nutrients, vol. 12, no. 11, pp 1-23, 2020.

[31] A. Buqué, N. Bloy, G. Kroemer, L. Galluzzi, ″Possible mechanisms of cancer prevention by nicotinamide,″ British Journal of Pharmacology, vol. 178, no. 10, pp 2034–2040, 2021.

[32] L. Bellows, R. Moore, ″Water-soluble vitamins: B-complex and vitamin C,″ (Colorado State University. Extension). Food and nutrition series; Health, Fact Sheet No. 9. 312, pp 1-5, 2012.

[33] K. Durda, K. Jaworska-Bieniek, K. Kąklewski, J. Lubiński, A. Jakubowska, ″Folic acid and breast cancer risk,″ Hereditary Cancer in Clinical Practice. 10, no. 4, pp 1-2, 2012.

[34] S. M. Zhang, W. C. Willett, J. Selhub, D. J. Hunter, E. L. Giovannucci, M. D. Holmes, G. A. Colditz, S. E. Hankinson, ″Plasma Folate, Vitamin B6, Vitamin B12, Homocysteine, and Risk of Breast Cancer,″ Journal of the National Cancer Institute, vol. 95, no. 5, pp 373-80, 2003.

[35] C. C. Yeh, M. F. Hou, S. H. Wu, S. M. Tsai, S. K. Lin, L. A. Hou, H. Ma, L. Y. Tsai, ″A study of glutathione status in the blood and tissues of patients with breast cancer,″ Cell Biochemistry and Function, vol. 24, no. 6, pp 555-559, 2006.

[36] J. Navarro, E. Obrador, J. Carretero, I. Petschen, J. Avino, P. Perez, J. M. Estrela, ″Changes in glutathione status and the antioxidant system in blood and in cancer cells associate with tumour growth in vivo,″ Free Radical Biology and Medicine, vol. 26, no. 3-4, pp 410-418, 1999.

[37] D. Srivastava, R. Mittal, ″Free radical injury and antioxidant status in patients with benign prostate hyperplasia and prostate cancer,″ Indian Journal of Clinical Biochemistry, vol. 20, no. 2, 162-165, 2005.

[38] A. Güven, S. Kısaçam, ″Gastrit ve Mide Kanseri Hastalarında Kan Malondialdehit (MDA) ve Redükte Glutatyon(GSH) Düzeylerinin Araştırılması,″ Caucasian Journal of Science, vol. 7, no. 1, pp1-8, 2020.

Title: The Application of Rain Water and Solar Energy System on Green Roof One of the Building in the Sakarya University

Authors: Esra DEMİRHAN, Yasemin DAMAR ARİFOĞLU

The Application of Rain Water and Solar Energy System on Green Roof One of The Building in Sakarya University

Yasemin Damar Arifoglu*[1] iD , Esra Demirhan[1] iD

Abstract

In our present day, consuming water and energy sources at a rapid rate, losing green areas, air pollution which is caused by gas emissions, global warming and actions that damage the balance in the ecosystem have made it necessary to take precautions. In this perspective, using water and energy sources sufficiently, finding new energy sources and using ecofriendly roofs are crucial for the world's future. Green roof systems, built for the purpose of preventing global warming, and stopping climate change, are the eco-friendly systems that reduce the heat in a city, prevent air pollution, and eliminate too much water accumulation in the city's infrastructure by holding rain water. In this study, decreasing the climate change by holding carbon emissions with green roof, finding the solutions for problems of water scarcity by saving water with the rain harvest system, saving the electricity by lightening the street lamps with stocking the energy coming from the solar system have been aimed. It has been tried to decrease the negative effects of climate change to the environment. The appropriate building has been determined for the inclination and height of roof where a green roof can be built by analyzing some buildings' roofs in Sakarya University in the study. In the scope of experimental study, an extensive green roof system has been designed on the roof of boiler room building. By gathering the rain water on green roof, green places have been watered regularly. The garden has been lightened by producing electricity with solar energy. The contributions have been added to sustainability owing to these sensitive systems for environment.

Keywords: Green roof, water and energy resources, climate change, global warming

1. INTRODUCTION

In the world where water and energy resources are declining, 42% of water and 50% of energy are consumed in building construction. The most important issue on a global scale is due to global warming, 50% of greenhouse gases, 24% of air pollution, chlorofluorocarbon (CFC), 50% of hydro chlorofluorocarbon (HCFC) emissions are building related activities [2]. Green buildings and green roofs have been started to be designed due to the population increase, the use of the average half of the energy resources of the buildings, air pollution, the disappearance of nature and green areas over time [3].

* Corresponding author: ydamar@sakarya.edu.tr
[1] Sakarya University, Department of Environmental Engineering
E-mail: esraademirhann96@gmail.com
ORCID: https://orcid.org/0000-0003-1281-0847, https://orcid.org/0000-0002-5859-7271

While roofs are a building material that absorbs heat, green roofs have been designed and turned into a building material that contributes to the ecosystem with the development of technology and building materials. Green roofs are systems that improve the energy use of the building, air quality and city ecology and provide solutions to the problem of water scarcity by using rain water effectively. At the same time, green roofs provide green space that they can use as an activity. Therefore, the concept of green roof is very important ecologically and socially [1].

In recent studies, it has been observed that green roof shave serious ecological, technical and social benefits in buildings and cities. These benefits are the protection of environment and biodiversity, shelter in wildlife, reuse of water, reducing the impact of urban heat island, reducing electromagnetic radiation, helping exchange of carbon dioxide and oxygen, reducing noise pollution, impacting the lifetime of the roof membrane, filtering airborne particles, energy efficiency and cooling effect [1].

The rise in the world's population, climate changes, urbanization and industrialization have a negative impact on natural resources. In the case of increased water needs, the lack of water due to unconsciousness use and global warming has made water the first issue on the international agenda [4].

The rain water collected by pipes from the rooftops of buildings is filtered and collected in the tank and the water collected is used for needs such as garden irrigation, car washing, cleaning and pool filling. It is also used as drinking water when the collected rain water is purified. When the drinking water has reached its quality, it can also be used when taking a shower, cooking and washing dishes. The potential for rain water harvesting is proportional to the amount of rain and varies according to regions in Turkey. The potential savings in rain water collected from the green roofs are around 30 to 60% of a household's drinking water needs, depending on the area of water collection. The collection and storage of rain water and use for needs both protect water resources and save on the water bill. Thus, rain water collection systems play an important role in the creation of sustainable cities [5].

There are some examples of rain water harvesting technologies from green roofs in Turkey. For example, the Bursa Hilton Hotel is a Green Star concept that improves energy efficiency and is found in the category of environmentally conscious hotels. The Green Star concept includes the use of rain water or purified waste water in garden irrigation and toilet reservoirs. Designed with the green building concept, 20 m^3 of rain water is stored by collecting and filtering rain water on the terrace of the Bursagaz General Directorate building and drainage water around the structure, stored rain water is used in the watering of green areas and in toilet reservoirs [6]. One of the most useful and environmentally friendly energy sources in renewable energy sources is solar energy. Solar panels are elements that convert solar energy into electrical energy. There are also equipment such as charge control pen, accumulator, inverter that can work with solar panels in generating electricity from solar energy. It has benefits such as lighting and heating in buildings. Increasing environmental awareness has made this system widespread [7].

The purpose of this study is to stress the positive effects of green roofs to the environment, to annihilate the climate change problems that are caused by drought and greenhouse gas emissions by using natural sources effectively such as rain and sun. The use of tap water and fossil fuels will be in minimum level and decreasing the carbon footprint has been aimed.

Esra DEMİRHAN, Yasemin DAMAR ARİFOĞLU

The Application of Rain Water and Solar Energy System on Green Roof One of the Building in the Sakary...

2. MATERIAL, METHOD AND FINDINGS

2.1. Research Area

The research area is the roof of the boiler room building in Sakarya University Esentepe Campus (Figure 1). This building was chosen because the slope and height of the roof are suitable for designing a green roof system. The building is located in side area of Engineering Faculty Deanship and Engineering Faculty class block. It is one-storey and reinforced concrete building. Building height is 4,25 meter, roof area is 273 m², the inclination of roof is 8,5%. Shingle has been used for roof coating. Experiments, observations and measurements were made between 14 December 2020 and 14 July 2021 with a 1,5 m² green roof, rain water and solar energy system designed on a part of the roof of the boiler room building.
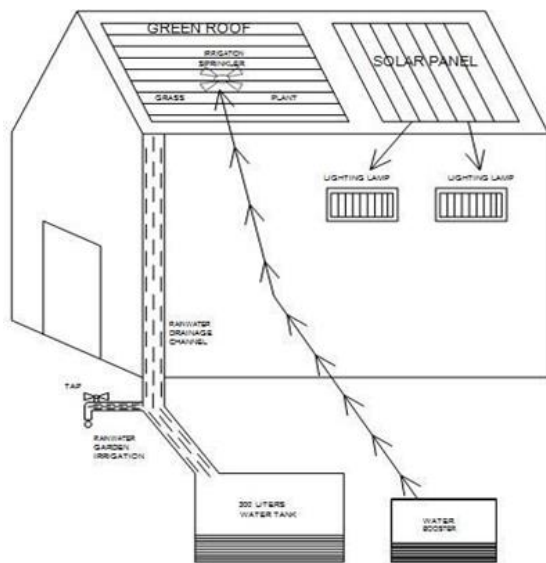
Figure 1 Research area

Approximately 2 and 6,2 mm rain fell in Sakarya/Serdivan where the research site was set between 14 December 2020 and 14 July 2021. This amount is approximately the same as the general average of Sakarya, which has a monthly average precipitation of 3,13 mm. When the monthly average temperature values are examined, it is seen that the monthly average air temperature of

Serdivan is 13,78 °C, and the average monthly air temperature of Sakarya in general is 14,66 °C. Thus, it has been determined that the monthly average air temperature of Sakarya is 0,88°C higher. It was observed that the highest air temperature in the region where the research area is located in the 8 month study period was in July with 33,3 °C, and the lowest air temperature was in January with 1,5 °C. During the experimental period, 634.8 mm of precipitation fell in the region where the research area is located. A total of 52,4 mm of precipitation fell in the research area. The highest amount of precipitation falling at the location of the research area was in July with 50,1 mm, and the lowest amount of precipitation was in May, when 0 mm of precipitation was the highest. The longest consecutive rainy days were observed between 18 – 27 March 2021. The number of days without precipitation is 110. The longest consecutive days without precipitation were observed from 26 June to 3 July 2021. Drought, which occurs as a result of consecutive days without precipitation, negatively affects the growth of plants on the green roof. In this period, the plants on the green roof are irrigated with the rain water accumulated in the tank so that the plants can continue to develop. When the monthly total precipitation data measured throughout the study is examined, it can be concluded that the climates have begun to change since the highest precipitation was measured in July.

When the 8-month meteorological data taken from the General Directorate of Meteorology and covering the years 2020-2021 are examined, the region where the research area is located is normal humid with humidity rates varying between 53% - 58% for 3 months between December 2020 - February 2021, March 2021 - July 2021. It has high humidity according to the humidity rates varying between 65% and 81% in the 4-month period between Sakarya in general has high humidity in the 8-month period between December 2020 - July 2021.

Esra DEMİRHAN, Yasemin DAMAR ARİFOĞLU

The Application of Rain Water and Solar Energy System on Green Roof One of the Building in the Sakary...

2.2. Material

Within the scope of the research, first of all, interviews were held with companies working on green roof systems, solar energy systems and water installation systems and an agreement was reached. In the construction of the green roof; 3 egger osb for floor preparation for water proofing, 2 wooden pallets for mounting egger osb to the pallet, 2 weber polyurethane sealants to ensure sealing and adhesion at the joints of the wooden pallet, 3 polyfin agoc-plan ecb 1015 geomembranes for waterproofing, by creating an uninterrupted drainage channel, 2 florax balls were used to prevent ponding in the soil layer, 9 aluminum pressure bars to prevent water from flowing through the wall and passing between the wall and the membrane, and 3 geotextile felt moisture traps to protect the water and heat insulation materials on the roofs. 1 water tank of 300 liters to collect and store rain water, 1 pump to use the water in the tank for green roof and garden irrigation, 1 pipe to deliver the rain water from the green roof's gutter to the tank, 1 fittings for connecting the pipes and 1 valve used. 1 solar panels measuring 38 cm x 44 cm in 30 watts are used to absorb sunlight and convert it into electrical energy and power the gel battery. 1 gel batteries are used to store solar energy and use it as electrical energy. It is gel because sulfuric acid and silica are produced by homogeneous mixing. 1 charge control pens are used to regulate the voltage from the solar panel, prevent and compensate for high voltage. Two 7 watt lamps are used to provide garden lighting.

2.3. Method

An environmentally friendly green roof consisting of various layers has been designed on the roof of the boiler room building which is located at Sakarya University Esentepe Campus. Rain water coming from the pipe on the green roof was collected and stored in a 300 liter water tank. The rain water collected in this tank was used to irrigate the plants on the roof, the lawn and the garden. Generally, irrigation was done every 15 days, and once a week in the summer season when the weather was hot and dry. Solar panels and equipment placed on the roof helped plants and grass grow, and the garden was illuminated by generating electrical energy from the solar panel and placing two 7-watt lamps on the wall of the building. Rain water falling on the green roof and accumulating in the warehouse and the energy accumulated in the solar panel were observed monthly. The potential of the rain water to be collected in meeting the water requirement outside the building and the amount of savings achieved by generating electrical energy from the energy to be collected were investigated.

The following are the calculations for rain water to be collected from the roof surface [6].

Rain water yield = rain collection area x precipitation amount x roof coefficient x filter efficiency coefficient [6].

Rain collection area; total area of the roof [6].

Precipitation; total annual rainfall determined by the General Directorate of Meteorology [6].

Roof coefficient; this is the coefficient specified by German standards as 0,8 in DIN (1989). It states that all rain falling on the roof cannot be recycled [6].

Filter efficiency coefficient; this is the coefficient specified by German standards as 0,9 in DIN (1989). This coefficient is the efficiency coefficient of the first filter passed to separate rain water from solids from the roof. It is the coefficient given by calculating that some of the rain water cannot pass through here [6].

Esra DEMİRHAN, Yasemin DAMAR ARİFOĞLU

The Application of Rain Water and Solar Energy System on Green Roof One of the Building in the Sakary...

Roof rain water amount (m^3) = roof area (m^2) x 0,9 x 0,8 x rainfall amount (annual, mm) [6].

Figure 2 has a structure trait to hold humidity, it protects the below materials by being used on insulating plates owing to resistant to be unctured (Figure 2). Figure 3 is used for water proofing (Figure 3). Figure 4 protects the geomembranes from being punctured, being torn due to friction based and damages (Figure 4). Figure 5 has higher capacity of vertical drainages than holes (Figure 5). Therefore it blockes ponding on ground plate. It annihilates the weight on the filtration geotextile due to unidirectional bubble structure. It is furnished by making the bubbles get on each. It creates continuous drainage channel under the filtration plus by blocking the plates' moving. Figure 6 is used to protect the water isolation applications owing to the effect of spreading pressure (Figure 6).

of grass on green roof and plants. Grass creates habitat for animals and cleans the air. Figure 8's caring is simple because of rarely planted green roof and it doesn't weight on (Figure 8). Figure 9; pipes make the rain water coming from green roof reach water tank (Figure 9). Figure 10; the general view of green roof, rain and solar energy has been given (Figure 10). Figure 11; the energy which has been picked from sun by solar energy has been used to lighten the garden (Figure 11)

Figure 4 Second geotextile felt moisture trap placed on ecb geomembrane

Figure 2 Geotextile felt moisture trap

Figure 5 Root holder plate

Figure 3 Ecb geomembrane

Figure 6 The third geotextile felt moisture trap placed on the root retaining layer

Figure 7; ground plate makes the rain water reach substratum by absorbing a little part of it (Figure 7). It meets the needs of nutrition

Esra DEMİRHAN, Yasemin DAMAR ARİFOĞLU

The Application of Rain Water and Solar Energy System on Green Roof One of the Building in the Sakary...

Figure 7 Soil and grass

Figure 8 Extensive green roof

Figure 9 Water tank and pipes

Figure 10 Green roof, rain water and solar energy system

Figure 11 Green roof system, solar energy system and garden lighting

3. RESULTS

The amount of stored rain water falling on the green roof surface of the building and the amount of electricity generation from solar panels and equipment are given below:

3.1. December Rain Water, Solar And Electric Power Data

3.1.1. Stormwater data for December 14-31, 2020.

The amount of rain falling in Serdivan district of Sakarya between 14-31 December 2020: 52,2 mm = 0.0522 m

Between 14-31 December 2020, amount of rain water falling on the green roof of the boiler room at Sakarya University:

1,5 m^2 x 0,9 x 0,8 x (0,0522 m) = 0,056376 m^3 = 56,376 liter

Amount of rain accumulated in the water tank at Sakarya University between 14-31 December 2020: 55,37 liter = 0,05537 m^3

Rain water remaining in the tank for irrigation of the green roof for 1 minute: 58,337 liter – 15 liter = 40,37 liter = 0,04037 m^3

Amount of rain water remaining in the tank in garden irrigation for 1 minute: 40,37 liter − 20 liter = 20,37 liter = 0,02037 m^3

Esra DEMİRHAN, Yasemin DAMAR ARİFOĞLU

The Application of Rain Water and Solar Energy System on Green Roof One of the Building in the Sakary...

Solar energy data between 14-31 December 2020

In 1 day: 30 watts x 9 hours = 270 watts

In 10 days: 270 watts x 10 days = 2700 watts

10 days between 14-31 December 2020 are sunny.

Electricity data between 14-31 December 2020

A light bulb in the garden consumes 7 watts of energy in 5 days.

Over 1 night: (7 watts / 5) = 1.4 watts

1,4 watts x 2 = 2,8 watts

2.8 watts x 14 hours = 39,2 watts
At 18 nights: 39,2 watts x 18 nights = 705,6 watts

3.2. January Rain Water, Solar And Electric Power Data

3.2.1. Stormwater data for January 1-15, 2021.

The amount of rain falling in Serdivan district of Sakarya between 1-15 January 2021: 69,9 mm = 0,0689 m
Between 1-15 January 2021, amount of rain water falling on the green roof of the boiler room at Sakarya University:

1.5 m^2 x 0,9 x 0,8 x (0,0689 m) = 0,074412 m^3 = 74,412 liter

Amount of rain accumulated in the water tank at Sakarya University between 1-15 January 2021: 73,41 liter = 0,07341 m^3

The amount of rain water remaining in the water tank at Sakarya University between 14 – 31 December 2020 + the amount of rain water accumulated in the water tank at Sakarya University between 1-15 January 2021: 20,37 liter + 73,41 liter = 93,78 liter =

0,09378 m^3

Rain water remaining in the tank for irrigation of the green roof for 1 minute: 93,78 liter – 15 liter = 78,78 liter = 0,07878 m^3

Amount of rain water remaining in the tank in garden irrigation for 1 minute: 78,78 liter – 20 liter = 58,78 liter = 0,05878 m^3

Solar energy data between 1-15 January 2021

In 1 day: 30 watts x 9 hours = 270 watts

In 9 days: 270 watts x 9 days = 2430 watts

9 days between 1-15 January 2021

Electricity data between 1-15 January 2021

1,4 watts x 2 = 2,8 watts

2,8 watts x 14 hours = 39,2 watts

At 15 nights: 39,2 watts x 15 nights = 588 watts

3.2.2. Stormwater data for January 16-31, 2021.

The amount of rain falling in Serdivan district of Sakarya between 16-31 January 2021: 69,3 mm = 0,0693 m

Between 16-31 January 2021, month of rain water falling on the green roof of the boiler room at Sakarya University:

1,5 m^2 x 0,9 x 0,8 x (0,0693 m) = 0,074844 m^3 = 74,844 liter

Amount of rain accumulated in the water tank at Sakarya University between 16-31 January 2021: 73,84 liter = 0,07384 m^3

The amount of rain water remaining in the water tank at Sakarya University between 1-

15 January 2021 + the amount of rain water accumulated in the water tank at Sakarya University between 16-31 January 2021: 58,78 liter + 73,84 liter = 132,62 liter = 0,13262 m^3

Rain water remaining in the tank for irrigation of the green roof for 1 minute: 132,62 liter – 15 liter = 117,62 liter = 0,117562 m^3

Amount of rain water remaining in the tank in garden irrigation for 1 minute: 117,62 liter – 20 liter = 97,62 liter = 0,09762 m^3

Solar energy data between 16-31 January 2021

In 1 day: 30 watts x 9 hours = 270 watts

In 9 days: 270 watts x 9 days = 2430 watts

9 days between 16-31 January 2021

Electricity data between 16-31 January 2021

1,4 watts x 2 = 2,8 watts

2,8 watts x 14 hours = 39,2 watts

At 15 nights: 39,2 watts x 16 nights = 627,2 watts

3.3. February Rain Water, Solar And Electric Power Data

3.3.1. Stormwater data for February 1-14, 2021.

The amount of rain falling in Serdivan district of Sakarya between February 1-14, 2021: 7,3 mm = 0,0073 m

Between 1-14 February 2021, amount of rain water falling on the green roof of the boiler room at Sakarya University:

1,5 m^2 x 0,9 x 0,8 x (0,0073 m) = 7,884 x 10^{-3} m^3 = 7,884 liter

Amount of rain accumulated in the water tank at Sakarya University between 1-14 February 2021: 6,88 liter = 0,00688 m^3

The amount of rain water remaining in the water tank at Sakarya University between 16-31 January 2021 + the amount of rain water accumulated in the water tank at Sakarya University between 1-14 February 2021: 97,62 liter + 6,88 liter = 104,5 liter = 0,1045 m^3

Rain water remaining in the tank for irrigation of the green roof for 1 minute: 104,5 liter – 15 liter = 89,5 liter = 0,0895 m^3

Amount of rain water remaining in the tank in garden irrigation for 1 minute: 89,5 liter − 20 liter = 69,5 liter = 0,0695 m^3

Solar energy data between 1-14 February 2021

In 1 day: 30 watts x 10 hours = 300 watts

In 8 days: 300 watts x 8 days = 2400 watts

8 days between 1-14 February 2021

Electricity data between 1-14 February 2021

1,4 watts x 2 = 2,8 watts

2,8 watts x 13 hours = 36,4 watts

At 14 nights: 36,4 watts x 14 nights = 509,6 watts

3.3.2. Stormwater data for February 15-28, 2021.

The amount of rain falling in Serdivan district of Sakarya between February 15-28, 2021: 49,4 mm = 0,0494 m

Between 15-28 February 2021, amount of rain water falling on the green roof of the boiler room at Sakarya University: 1,5 m^2 x 0,9 x 0,8 x (0,0494 m) = 0,053352 m^3 =

53,352 liter

Amount of rain accumulated in the water tank at Sakarya University between 15-28 February 2021: 52,35 liter = 0,05235 m^3

The amount of rain water remaining in the water tank at Sakarya University between 1-14 February 2021 + the amount of rain water accumulated in the water tank at Sakarya University between 15-28 February 2021: 69,5 liter + 52,35 liter = 121,85 liter = 0,12185 m^3

Rain water remaining in the tank for irrigation of the green roof for 1 minute: 121,85 liter − 15 liter = 106,85 liter = 0,10685 m^3

Amount of rain water remaining in the tank in garden irrigation for 1 minute: 106,85 liter – 20 liter = 86,85 liter = 0,08685 m^3

Solar energy data between 15-28 February 2021

In 1 day: 30 watts x 10 hours = 300 watts

In 6 days: 300 watts x 6 days = 1800 watts
6 days between 15-28 February 2021

Electricity data between 15-28 February 2021

1,4 watts x 2 = 2,8 watts

2,8 watts x 11 hours = 30,8 watts

At 14 nights: 30,8 watts x 14 nights = 431,2 watts

In figure 12, the most rainfall was seen between 1-7 July 2021, the last rainfall was seen between 1-15 May 2021.
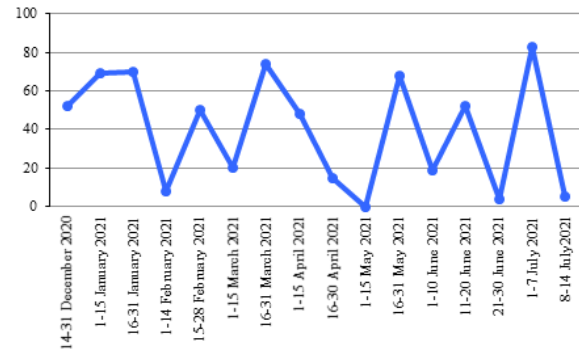
Figure 12 Amount of rain falling on Serdivan between 14 December 2020 – 14 July 2021

In figure 13, the most rainfall on green roof was seen between 1-7 July 2021, the least was seen between 1-15 May 2021.
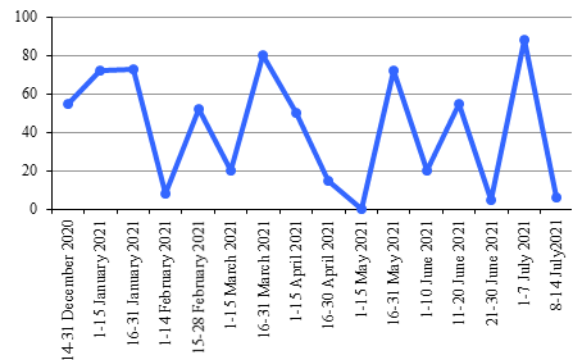
Figure 13 Amount of rain water falling on green roof between 14 December 2020 – 14 July 2021

In figure 14, the most save rain water in tank was between 1-7 July 2021, the least was between 1-15 May
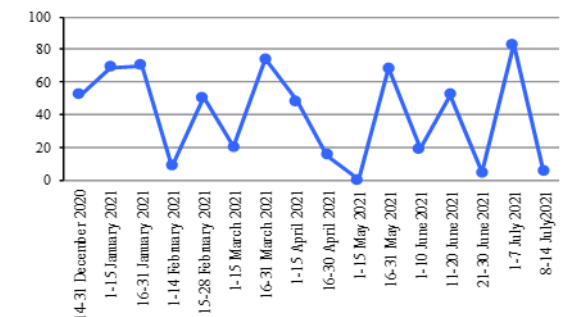
Figure 14 Amount of rain water accumulated in the water tank between 14 December 2020 – 14 July 2021

Esra DEMİRHAN, Yasemin DAMAR ARİFOĞLU

The Application of Rain Water and Solar Energy System on Green Roof One of the Building in the Sakary...

In figure 15, the most saved rain water in tank was seen between 21-30 July 2021 and 1-7 July 2021, the least was seen on 14-31 December 2020.
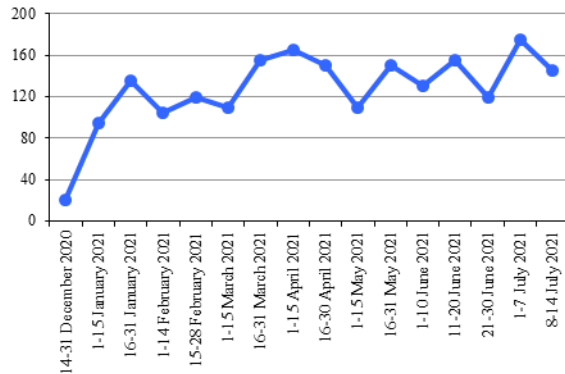
Figure 15 Amount of rain water remaining and accumulated in the water tank between 14 December 2020 – 14 July 2021

In figure 16, after watering the green roof and garden, the most saved rain water in tank was observed between 1-7 July 2021, the least was observed between 14-31 December 2020.
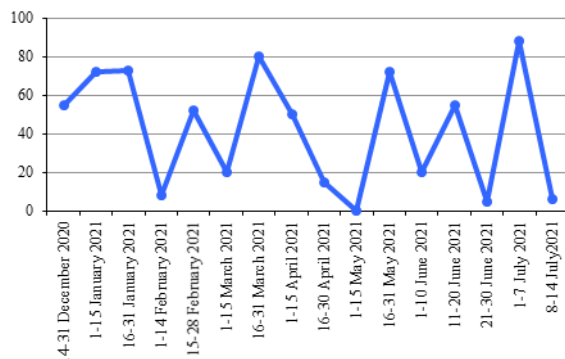
Figure 16 Amount of rain water remaining in the tank after watering the green roof and garden between 14 December 2020 – 14 July 2021

3.4. Comparison Of Monthly Water Amount In Rain Collection Tanks And Precipitation Amounts

The precipitation between 14-31 December 2020 is 52,2 mm. Supply of rainfall saved in tank is 56,376 liter.

The precipitation between 1-15 January 2021 is 68,9 mm. Supply of rainfall saved in tank is 73,41 liter. The precipitation between 16-31 January 2021 is 69,3 mm. Supply of rainfall saved in tank is 73,84 liter.

The precipitation between 1-14 February 2021 is 7,3 mm. Supply of rainfall saved in tank is 6,88 liter. The precipitation between 15-28 February 2021 is 49,4 mm. Supply of rainfall saved in tank is 52,35 liter.

The precipitation between 1-15 March 2021 is 19,8 mm. Supply of rainfall saved in tank is 20,38 liter. The precipitation between 16-31 March 2021 is 74,2 mm. Supply of rainfall saved in tank is 79,13 liter.

The precipitation between 1-15 April 2021 is 47,1 mm. Supply of rainfall saved in tank is 49,86 liter. The precipitation between 16-30 April 2021 is 15,5 mm. Supply of rainfall saved in tank is 15,74 liter.
The precipitation between 1-15 May 2021 is 1 mm. Supply of rain fall saved in tank is 0,08 liter. The precipitation between 16-31 May 2021 is 67,4 mm. Supply of rainfall saved in tank is 71,79 liter.

The precipitation between 1-10 June 2021 is 18,7 mm. Supply of rainfall saved in tank is 19,19 liter. The precipitation between is 11-20 June 2021 is 53 mm. Supply of rainfall saved in tank is 56,24 liter. The precipitation between 21-30 June 2021 is 4,2 mm. Supply of rainfall saved in tank is 3,53 liter.

The precipitation between 1 to 7 July 2021 is 81,86 mm. Supply of rainfall saved in tank is 87,12 liter. The precipitation between 8-14 July 2021 is 5,2 mm. Supply of rainfall saved in tank is 4,61 liter.

When the data is analyzed, it has been determined that monthly precipitation and supply of rainfall saved in tank are proportional.

In figure 17, the most saved solar energy was observed between 1-14 February 2021, the least was observed between 16-31 March

Esra DEMİRHAN, Yasemin DAMAR ARİFOĞLU

The Application of Rain Water and Solar Energy System on Green Roof One of the Building in the Sakary...
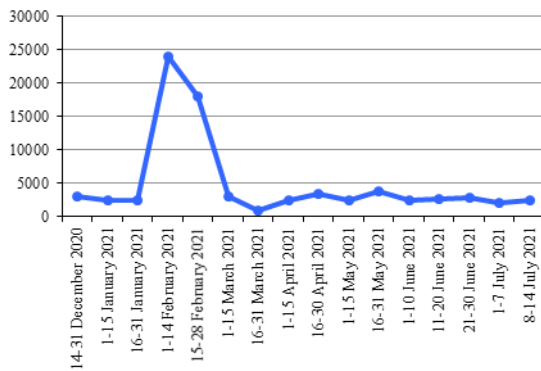
2021.

Figure 17 Solar energy data between 14 December 2020 – 14 July 2021

In figure 18, the most produced electricity was seen between 14-31 December 2020, the least was seen between 1-14 July.
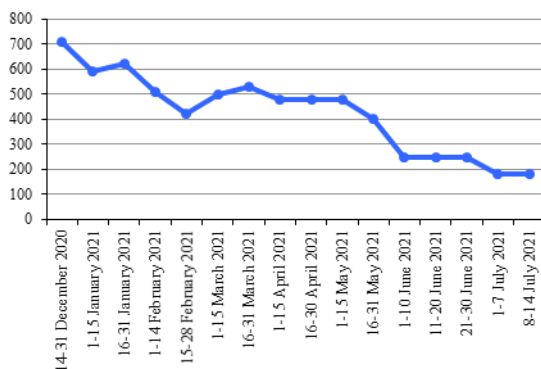
Figure 18 Data of electrical energy between 14 December 2020 – 14 July 2021

3.5. Comparison Of Solar Energy / Electric Energy Datas

Between 14-31 December 2020, 2700 watts of energy was stored. The stored energy enabled 2 lamps to illuminate the garden for 18 nights. 705,6 watts of electrical energy was used.

Between 1-15 January 2021, 2430 watts of energy was stored. The stored energy enabled 2 lamps to illuminate the garden for 15 nights. 588 watts of electrical energy was used. Between 16-31 January 2021, 2430 watts of energy was stored. The stored energy enabled 2 lamps to illuminate the garden for 16 nights. 627,2 watts of

electrical energy was used.

Between 1-14 February 2021, 2400 watts of energy was stored. The stored energy enabled 2 lamps to illuminate the garden for 14 nights. 509,6 watts of electrical energy was used. Between 15-28 February 2021, 1800 watts of energy was stored. The stored energy enabled 2 lamps to illuminate the garden for 14 nights. 431,2 watts of electrical energy was used.

Between 1-15 March 2021, 2640 watts of energy was stored. The stored energy enabled 2 lamps to illuminate the garden for 15 nights. 504 watts of electrical energy was used. Between 16-31 March 2021, 990 watts of energy was stored. The stored energy enabled 2 lamps to illuminate the garden for 16 nights. 537,6 watts of electrical energy was used.

1800 watts of energy was stored between 1-15 April 2021. The stored energy enabled 2 lamps to illuminate the garden for 15 nights. 462 watts of electrical energy was used. 2730 watts of energy was stored between 16-30 April 2021. The stored energy enabled 2 lamps to illuminate the garden for 15 nights. 462 watts of electrical energy was used.

Between 1-15 May 2021, 4320 watts of energy was stored. The stored energy enabled 2 lamps to illuminate the garden for 15 nights. 462 watts of electrical energy was used. 3780 watts of energy was stored between 16-31 May 2021. The stored energy enabled 2 lamps to illuminate the garden for 16 nights. 403,2 watts of electrical energy was used.

1800 watts of energy was stored between 1-10 June 2021. The stored energy enabled 2 lamps to illuminate the garden for 10 nights. 252 watts of electrical energy was used. Between 11-20 June 2021, 2250 watts of energy was stored. The stored energy enabled 2 lamps to illuminate the garden for 10 nights. 252 watts of electrical energy was used. Between 21-30 June 2021, 3150 watts

of energy was stored. The stored energy enabled 2 lamps to illuminate the garden for 10 nights. 252 watts of electrical energy was used.

1350 watts of energy was stored between 1-7 July 2021. The stored energy enabled 2 lamps to illuminate the garden for 7 nights. 176,4 watts of electrical energy was used. Between 8-14 July 2021, 2250 watts of energy was stored. The stored energy enabled 2 lamps to illuminate the garden for 7 nights. 176,4 watts of electrical energy was used.

Generally, the electrical energy used is directly proportional to the stored energy. However, this rate changes according to how many nights the garden lighting is in that month.

4. WATER AND ENERGY SAVİNG CALCULATİON

Water saving

Sakarya province Serdivan district 1 ton water unit price: 4,89 TL

Amounts of used rain water between December 14 2020 and July 14 2021

Amount of used rain water in December: 20 liter + 15 liter = 35 liter = 0,035 tons

Amount of used rain water in January: 35 liter x 2 = 70 liter = 0,07 tons

Amount of used rain water in February: 35 liter x 2 = 70 liter = 0,07 tons

Amount of used rain water in March: 35 liter x 2 = 70 liter = 0,07 tons

Amount of used rain water in April: 35 liter x 2 = 70 liter = 0,07 tons

Amount of used rain water in May: 35 liter x 2 = 70 liter = 0,07 tons

Amount of used rain water in June: 35 liter x 3 = 105 liter = 0,105 tons
Amount of used rain water in July: 35 liter x 2 = 70 liter = 0,07 tons

Amount of saved water between December 14 2020 and July 14 2021: 35 liter + 70 liter + 70 liter + 70 liter + 70 liter + 70 liter + 105 liter + 70 liter = 560 liter = 0,56 tons

Price of saved water between December 14 2020 and July 14 2021: 4,89 TL (SASKİ mains water price) x 0,56 tons = 2,7384 TL

The amount of water which is saved during the 7-month experimental period from December 14 2020 to July 14 2021 was calculated as 0,56 tons. The price of water that purchased from Sakarya Water and Sewerage Administration (SASKİ) is 4,89 TL. According to these analysis 2,7384 TL of water were saved in 7 months.

Energy saving

Sakarya province Serdivan district Electricity Unit Price: 0,4743 TL/kWh

Amounts of used electricity between December 14 2020 and July 14 2021

Amount of used electricity in December: 705,6 watt = 0,7056 kW

Amount of used electricity in January: 588 watt + 627,2 watt = 1215,2 watt = 1,2152 kW

Amount of used electricity in February: 509,6 watt + 431,2 watt = 940,8 watt = 0,9408 kW

Amount of used electricity in March: 504 watt + 537,6 watt = 1041,6 watt = 1,0416 kW

Amount of used electricity in April: 462 watt + 462 watt = 924 watt = 0,924 kW

Amount of used electricity in May: 462 watt

Esra DEMİRHAN, Yasemin DAMAR ARİFOĞLU

The Application of Rain Water and Solar Energy System on Green Roof One of the Building in the Sakary...

+ 403,2 watt = 865,2 watt = 0,8652 kW

Amount of used electricity in June: 252 watt + 252 watt + 252 watt = 756 watt = 0,756 kW

Amount of used electricity in July: 176,4 watt + 176,4 watt = 352,8 watt = 0,3528 kW

Amount of saved electricity between December 14 2020 and July 14 2021: 705,6 watt + 1215,2 watt + 940,8 watt + 1041,6 watt + 924 watt + 865,2 watt + 756 watt + 352,8 watt = 6801,2 watt = 6,8012 kW

Price of saved electricity between December 14 2020 and July 14 2021: 0,4743 TL/kWh x 6,8012 kW = 3,2258 TL
Working time of two 7 watt lamps between December 14 2020 and July 14 2021: W = P x t

6,8012 kW = 0,014 kW x t

t = 485,8 hours = ~ 20 days

Electricity amounts used from December to July were calculated monthly. The total electricity amounts used for 7-month were found. The saved electricity amount has been found by multiplying the electricity unit price taken from Sepaş by these found values.

5. EVALUATION AND DISCUSSION

During the experiment period from December to July, data was collected by making measurements and observations of 15 days, in some months, 10 days and 1 week. Rainfall data on the region where the pilot plant is located were obtained from Sakarya Meteorology Station Directorate. About 1% of the rainfalling on the green roof is absorbed, the rest is transferred to the warehouse. 15 liters of the water in the tank was used for 1 minute to irrigate the green roof, and 20 liters for garden irrigation. The maximum amount of water was collected between 1-7 July 2021 with 87,12 liters, and

the minimum amount of water 0,08 liters between 1-15 May 2021. At the end of the experiment, 560 liters of water were saved. In addition, 2,7384 TL economic gain was obtained. During the experiment, the data of the number of sunny days in each month was collected. Accordingly, electricity is produced with the energy stored in the solar panel. Maximum solar energy was stored with 4320 watts between 1-15 May 2021, minimum solar energy was stored between 16-31 March 2021 with 990 watts. The maximum electricity was produced between 14-31 December 2020 with 705,6 watts, the minimum electricity was produced between 1-7 July 2021 and 8-14 July 2021 with 176,4 watts. At the end of the experiment, 6801,2 watts of electricity was saved. 3,2258 TL economic gain was achieved.

According to the literature, rain water collected from the roof; it can be used in car washing, cleaning, filling pools and toilets. It can also be used for washing dishes, showering and cooking if purified. In the experimental application, rain water collected from the green roof has been used to irrigate the grass, plants and garden on the roof. It was not used inside the building because it was not treated. Solar energy systems are used to meet the electricity needs in bus stops, agricultural irrigation, residences, park and garden lighting. Solar energy systems are used for both indoor and garden lighting in residences; they reduce emissions and save electricity. In the experimental application, the solar energy system designed on the roof of the building has been used in garden lighting, preventing greenhouse gas emissions and saving electricity.

5.1. Cost Analysis

5.1.1. Cost analysis of green roof, rain water, and solar energy system

Cost analysis; it includes equipment which is used in the construction of green roof, rain water and solar energy systems. These

Esra DEMİRHAN, Yasemin DAMAR ARİFOĞLU

The Application of Rain Water and Solar Energy System on Green Roof One of the Building in the Sakary...

equipment; it is classified as consumables and machinery- equipment. According to the number of materials, the amount was determined at the unit price. The total cost is calculated as 9117,96 TL (Table 1).

Table 1 Cost Analysis

Budget Type	Name	Quantity	Unit Price	Cost
Consumables	Eggerosb	3	100,00 TL	300,00 TL
Consumables	Wooden pallet	2	100,00 TL	200,00 TL
Consumables	Weber polyurethane mastic poliyfin agoc-plan ecb 1015	2	80,00 TL	160,00 TL
Consumables	Gomembran	3	200,00 TL	600,00 TL
Consumables	Florax top	2	100,00 TL	200,00 TL
Consumables	Aliminium pressure bar	9	30,00 TL	270,00 TL
Consumables	Geotextile felt moisture trap	3	20,00 TL	60,00 TL
Machinery andequipment	Water tank (300 lt.)	1	750,00 TL	750,00 TL
Machinery andequipment	Hydrophore pump	1	1000,00 TL	1000,00 TL
Consumables	Pipe, fittings, valve	1	2000,00 TL	2000,00 TL
Machinery andequipment	Solar panel	1	1500,00 TL	1500,00 TL
Consumables	Small battery	1	600,00 TL	600,00 TL
Machinery andequipment	Power test light	1	350,00 TL	350,00 TL
Consumables	Grass, ivy plant, soil	1	600,00 TL	600,00 TL
Consumables	Garden light lamp	2	89,99 TL	179,98 TL
Consumables	Bulb	2	23,99 TL	47,98 TL
Machinery andequipment	Crane	1	300,00 TL	300,00 TL

6. CONCLUSION

Turkey is a country with a rapid growth potential and needs to meet its energy needs from natural resources. Measures that can save energy consumption are very important for the future of the country. Due to climate change, natural water resources are decreasing day by day. For this reason, ecological measures should be taken for the formation of sustainable and environmentally sensitive cities. In addition, non-ecological approaches will not be economical in the long run. Within the scope of these measures, green roofs are a positive option [8].

Green roof systems are spreading rapidly in the world as they provide environmental, ecological, social and economic benefits. Green roofs; biodiversity plays an important role as a pioneer of sustainability in terms of environmental and ecological reasons, such as being effective in accumulating rain water, reducing air pollution, reducing urban heat island effects, effecting carbon dioxide oxygen exchange, reducing noise pollution, increasing the amount of green space [1].

In researches on green roofed structures, it has been seen that energy savings of 24-50% and 13% savings in maintenance fees can be achieved compared to traditional roofed structures. Thanks to green roofs, it is possible to create an energy efficient and nature-friendly environment [1].

Thinks to do in order for the roof of the structure examined within the scope of the research to have a green roof feature was evaluated in terms of water, energy efficiency and ecological effects. By reconnoitering in the building, do's to use rain water efficiently and save energy within the scope of water and energy efficiency was determined. The aim of the study is to protect and use natural resources efficiently.

The role of rain water which is harvested on the roof of the boiler room building in Sakarya University in meeting the outdoor water needs and the role of the solar energy

Esra DEMİRHAN, Yasemin DAMAR ARİFOĞLU

The Application of Rain Water and Solar Energy System on Green Roof One of the Building in the Sakary...

system in providing outdoor lighting were investigated. For this purpose, the amount of rain water to be collected from the green roof of the building was calculated by using the monthly rainfall data of Serdivan district of Sakarya province. The water needs used to water the harvested rain water and plants in the roof, lawn and garden was calculated regularly by watering every month twice a month. The energy which is stored on sunny days has also been used on days and seasons when there is no sun. With this energy generates electricity and light the garden.

Thus, it has been determined that water and electricity will be saved thanks to the green roof, rain harvest and solar energy systems and will play an important role in reducing the effects of climate change.

Thanks to the acquired findings in the research, it can be said that a extensive green roof system is a sustainable option in the conditions of Sakarya province.

The Declaration of Conflict of Interest/ Common Interest
No conflict of interest or common interest has been declared by the authors

Authors' Contribution
The authors contributed equally to the study.

The Declaration of Ethics Committee Approval
This study does not require ethics committee permission or any special permission.

The Declaration of Research and Publication Ethics
We declare that we comply with the scientific, ethical and citation rules of SAUJS in all processes of the article and that

we do not falsify the collected data. In addition, we declare that Sakarya University Journal of Science and its editorial board have no responsibility for ethical violations that may be encountered, and that this study has not been evaluated in any academic publication environment other than Sakarya University Journal of Science.

REFERENCES

[1] E. Akpınar. Külekçi, "A research on green roof systems from past to present and determination of quality standards in green roofs," ATA Journal of Planning and Design, vol. 1, no. 1, pp. 35-53, 2017.

[2] B. Kılıç. Turan, A. Gülten, "Analysis of the effect of green roofs on the heating and cooling load of buildings for different building forms and degree day regions," Fırat University Journal of Engineering Sciences, vol. 32, no.1, pp. 105-118, Feb 2020.

[3] N. Şensy, A. Pakoğlu, R. Kara, "Evaluation of structural features of some roof gardens in Ankara," Duzce University Faculty of Forestry Journal of Forestry, vol. 13, no. 2, pp. 58-74, Dec 2017.

[4] E. Kalıpcı, V. Başer, N. Genç, "Evaluation of rain water harvesting using geographic information system: Giresun University Campus Example," Gaziosmanpasa Journal of Scientific Research, vol. 10, no. 1. pp. 49-58, Apr 2021.

[5] G. E. Üstün, T. Can, G. Küçük, "Rain water harvesting in the buildings," Journal of Uludag University Faculty of Engineering, vol. 25, no. 3, pp. 1593-1610, Dec 2020.

[6] M. Yalılı. Kılıç, M. N. Abuş, "Rain water harvesting in a garden house sample," International Journal of

Agricultural and Wildlife Science, vol. 4, no. 2, pp. 209-215, June 2018.

[7] S. Rüstemli, F. Dinçer, "Current situation and future of solar energy in electric power generation in van province," Journal Of The Institute of Natural and Applied Sciences, vol. 16, no. 1, pp. 22-33, June 2011.

[8] E. Yalçınalp, A. Öztürk, D. Bayrak, "Economical effects of green roof and grey water systems in housing scale," Turkish Journal of Agricultural and Natural Sciences, vol 5., no.1, pp. 71-80, Dec 2017.

Sakarya University Journal of Science
SAUJS

Title: Enhanced Tunicate Swarm Algorithm For Big Data Optimization

Authors: Emine BAŞ

New submission to SAUJS
http://dergipark.gov.tr/journal/1115/submission/start

Enhanced Tunicate Swarm Algorithm for Big Data Optimization

Emine BAŞ [*1] iD

Abstract

Today, with the increasing use of technology tools in daily life, big data has gained even more importance. In recent years, many methods have been used to interpret big data. One of them is metaheuristic algorithms. Meta-heuristic methods, which have been used by very few researchers yet, have become increasingly common. In this study, Tunicate Swarm Algorithm (TSA), which has been newly developed in recent years, was chosen to solve big data optimization problems. The Enhanced TSA (ETSA) was obtained by first developing the swarm action of the TSA. In order to show the achievements of TSA and ETSA, various classical benchmark functions were determined from the literature. The success of ETSA has been proven on these benchmark functions. Then, the successes of TSA and ETSA are shown in detail on big datasets containing six different EEG signal data, with five different population sizes (10, 20, 30, 50, 100) and three different stopping criteria (300, 500, 1000). The results were compared with the Jaya, SOA, and SMA algorithms selected from the literature, and the success of ETSA was determined. The results show that ETSA has sufficient success in solving big data optimization problems and continuous optimization problems.

Keywords: TSA, tunicate, meta-heuristic, big data

1. INTRODUCTION

Various institutions and organizations have recently emphasized the importance of collecting data from users, customers or participants and using this data to make various decisions [1]. The greater the amount of data collected, the higher the accuracy of the operations performed on the data. With the widespread use of technology tools, huge amounts of data are growing, including hundreds, sometimes even thousands, of variables. Thus, the importance of analyzing various sources with their outputs in a fast and short time increases [1]. Such data has frequently grown to sizes that conventional analytical techniques cannot handle. As a result, a new term, big data, has been introduced into the computational and information sciences literature to describe such data [2-4]. When a data chunk is considered big data, its 4V characteristics (volume, velocity, diversity, accuracy) should be examined. The volume property is used to describe how large the amount of data is. The speed feature represents the data collection rate. The diversity of resources is expressed by the diversity feature. Accuracy refers to the quality of data sources data [2-4]. They also

* Corresponding author: ebas@ktun.edu.tr (E.BAŞ)
[1] Konya Technical University
ORCID: https://orcid.org/0000-0003-4322-6010

contain a large number of decision variables, objective functions, or functions with mathematical properties, such as variables, and sometimes require real-time solutions. One of today's problems is to analyze big data and make it meaningful. It is almost impossible to examine these data in a reasonable time with classical mathematical methods. Therefore, researchers have started to search for different methods to analyze and interpret this huge data faster. One of the methods they found was heuristic algorithms.

Many researchers have expressed interest in a recent big data optimization problem introduced by Goh et al., which has been investigated using a few meta-heuristic algorithms. They separated the EEG signals into two sections. The first part is similar to the source signal in that it provides the necessary information. The second part is accompanied by artifacts or noise [5]. EEG signal data are grouped into six different data sets named EE4, EE4N, EE12, EE12N, EE19, and EE19N, with reference to the number of interconnected time series. Each time series has a length of 256. While the EE4 problem example has four interconnected time series, the EE12 and EE19 problem examples have twelve and nineteen interconnected time series, respectively. There have been many studies in the literature that have solved the mentioned problem. Zhang et al. pioneered the literature by solving the aforementioned problem with metaheuristics. They solved the aforementioned problem with the variant they created by using crossover and mutation operators named MOME/D [6]. Elsayed and Sarker proposed the ADEF approach, which is based on a DE algorithm, and solved the related problem [7]. Majdouli et al. used the Fireworks algorithm (FW) to solve big data optimization problems [8]. Cao et al. proposed and solved big data optimization problems using a new metaheuristic called Phase Based Optimization (PBO) [9]. Aslan and Karaboga tested the success of the genetic

Artificial Bee Colony algorithm in a big data optimization problem [1].

Kaur et al. proposed a new bio-inspired meta-heuristic algorithm [10]. Tunicate Swarm Algorithm (TSA) was inspired by sea creatures called Tunicates. Tunicates are marine creatures capable of locating food sources in the seas. Tunicates rely on two key behaviors in navigation and foraging for food: jet propulsion and swarm intelligence. Thanks to these two movements, it performs exploration and exploitation operations. Algorithms with swarm behavior are successful to the extent that they balance these two abilities well. In this study, herd behavior has been updated and Enhanced TSA (ETSA) has been proposed to increase the success of TSA. In TSA, only the individual with the best resource was taken into account and the population was searched locally, while in ETSA, the individual with the worst resource was also considered. Thus, it is planned to increase the success of TSA. The balance between exploration and exploitation is better maintained.

Two sets of two problems were used to test the success of TSA and ETSA. In the first problem set, 23 unimodal, multimodal and fixed-dimensional multi-modal test functions were selected from the literature. Descriptions of these test functions are provided in the appendix. In these test functions of TSA and ETSA, parameter analysis was performed for the population sizes (10, 20, 30, 50, and 100), and the most appropriate population size was determined as 30. The performances of TSA and ETSA were tested in detail for population size=30, maximum iteration=500, and dimension=30 on 23 test functions. The results were shown according to the standard deviation, mean, best, and time comparison criteria for TSA and ETSA. The convergence graphs were shown. ETSA achieved better results than TSA in all benchmark functions except F8 and F20. In order to prove the success of ETSA, the results were compared with

various heuristic algorithms selected from the literature in recent years. These algorithms are Jaya Algorithm [11], Skill Optimization Algorithm (SOA) [12], and Slime Mould Algorithm (SMA) [13]. According to the results, ETSA achieved better results than Jaya. ETSA was the most successful algorithm after SMA and SOA. It was proved by Wilcoxon signed test that there was a significant difference on the results.

In the second problem, big datasets containing six different EEG signals (EE4, EE4N, EE12, EE12N, EE19, and EE19N) were selected from the literature. The performances of TSA and ETSA were tested in detail for five different population sizes (10, 20, 30, 50, and 100) and three different maximum iterations (300, 500, 1000) on big datasets containing six different EEG signals. These datasets contain large dimensions (EE4 and EE4N for 1024, EE12 and EE12N for 3072, EE19 and EE19N for 4868). That is why it is called the big data optimization problem. The results were tested according to the standard deviation, mean, best, and time comparison criteria for TSA and ETSA, and convergence graphs were shown. The results have been compared. TSA and ETSA results were compared with new metaheuristic algorithms (Jaya, SOA, and SMA) selected from the literature and developed in recent years, and their success was demonstrated. Convergence graphs were drawn. According to the results, ETSA achieved better results than TSA. Thus, it has been proven that In terms of working time, TSA worked in a shorter time than ETSA. The reason for this is the codes added for the development of ETSA. It is not a significant time difference. When compared with various algorithms selected from the literature, it achieved the best results after SOA. The results obtained were subjected to the Wilcoxon sign test, which is a statistical test, and it was shown that there was a semantic difference between the results obtained.

The results showed that ETSA achieved better results than TSA and showed preferable success for continuous optimization problems. The motivations and contributions of this study can be summarized as follows:

- ETSA was proposed for the first time in this study by improving the local search capability of TSA. In ETSA, not only the best source information, but also the worst source information was used to change the position of the population.

- TSA and ETSA were tested on two different problem sets (a-) twenty-three classic test functions, b-) big data optimization problem). The results showed that ETSA achieved better results than TSA. The success of ETSA was proven by applying the Wilcoxon signed test on the results.

- For the big data optimization problem, TSA and ETSA were tested for the first time in this study and their results were presented to the literature.

- The performances of TSA and ETSA were tested in detail for five different population sizes (10, 20, 30, 50, and 100) and three different maximum iterations (300, 500, 1000) on big datasets containing six different EEG signals.

- The success of ETSA has been compared with various heuristic algorithms (Jaya, SOA, and SMA) selected from the literature and proposed in recent years. ETSA managed to enter the top three in the classical test functions and the top two in the big data optimization problem.

The remainder of this work is structured as follows: TSA is explained in detail in Section 2. ETSA is detailed in Section 3. In Section 4, the big data optimization problem is defined. In Section 5, performance tests of

TSA and ETSA algorithms on classical 23 test functions and on big data optimization problem datasets are performed and compared with each other. Convergence graphs were drawn.

2. MATERIALS AND METHODS

2.1. Standard Tunicate Swarm Algorithm

The Tunicate Swarm Algorithm (TSA) is a recent bio-inspired meta-heuristic algorithm. TSA was inspired by tunicates. Tunicates are marine creatures capable of locating food sources in the seas. Tunicates navigate and forage for food using two key behaviors: jet propulsion and swarm intelligence. In the mathematical model of jet propulsion, a tunicate moves towards the position of the best population individual and stays close to the best population individual, while avoiding conflicts between population members. In herd behavior, population members update their positions according to the best population individual [10].

Mathematical Model of Jet Propulsion:

This behavior was developed to ensure the social balance of power among tunicates and to prevent collisions between them. It is shown by Equations 1-5.

$$\vec{A} = \frac{\vec{G}}{\vec{M}} \tag{1}$$

$$\vec{G} = r_2 + r_3 - \vec{F} \tag{2}$$

$$\vec{F} = 2.r_1 \tag{3}$$

$$\vec{M} = \lfloor X_{min} + r_1.X_{max} - X_{min} \rfloor \tag{4}$$

X_{min} and X_{max} values are taken as 1 and 4, respectively. Necessary parameter analyzes were made by Kaur et al. [10]. In this study, a parameter analysis was not performed for these values.
The movement of the population members towards the best neighbor direction is shown by Equation 5.

$$\overrightarrow{T_{distance}} = \left| \overrightarrow{T_{source}} - r.\overrightarrow{T(x)} \right| \tag{5}$$

where $\overrightarrow{T_{distance}}$ represents the distance between the food source and the population individual, and x represents the current iteration, $\overrightarrow{T_{source}}$ is the location of food source (the location of best tunicate), $\overrightarrow{T(x)}$ indicates the location of tunicate and r is a random number between [0, 1].

$$\overrightarrow{T(x')} = \begin{cases} \overrightarrow{T_{source}} + \vec{A}.\overrightarrow{T_{distance}}, & if\ r \geq 0.5 \\ \overrightarrow{T_{source}} - \vec{A}.\overrightarrow{T_{distance}}, & if\ r < 0.5 \end{cases} \tag{6}$$

where $\overrightarrow{T(x')}$ is the updated $\overrightarrow{T(x)}$ (location of tunicate) with respect to $\overrightarrow{T_{source}}$ (the location of food source) and r is a random number between [0, 1].

Mathematical Model of Swarm Behavior

The herding behavior of a tunicate is illustrated by the following equation:

$$T(\vec{x} + 1) = \frac{\overrightarrow{T(x')} + T(\vec{x} - 1)}{2 + r1} \tag{7}$$

Algorithm 1 depicts the TSA algorithm's pseudocode.

Algorithm 1: Tunicate Swarm Algorithm

Input: Tunicate population T_i (i=1, 2, 3, ... pop)
Output: Optimal tunicate individual
1:   **Procedure:** TSA
2:   Initialize parameters X_{min}, X_{max}, etc.
3:   Calculate the fitness value of each tunicate
4:   $\overrightarrow{T_{source}}$ identify the best tunicate individual
5:     **While** (iteration< $Mak_{iterations}$) **do**
6:       **for** i=1 **to** pop **do**
7:         Update the position of each tunicate individual using Eq. (7).
8:       **end for**
9:       Update parameters ($\vec{A}, \vec{G}, \vec{F},$ and $\vec{M}$)
10:      Check tunicate populations
11:      Update T_i if there is a better solution than the previous optimal solution
12:        iteration ⟵ iteration +1
13:    **end while**
14: Return T_i
15: **end procedure**

Algorithm 1 can be detailed as follows:

Step 1: The procedure for the TSA is created.

Step 2: The initial parameters for TSA are defined.

Step 3: The fitness function is calculated for each individual of the tunicate population.

Step 4: The population individual with the minimum value is determined from the fitness values obtained. This individual is registered as a $\overrightarrow{T_{source}}$.

Step 5: A while loop is set up for the maximum iteration cycle (steps 5-13). The iteration variable loops from zero to the maximum iteration.

Steps 6-8: Position update was performed for each individual of the tunicate population using Equation 7. Thus, new tunicate candidates are created.

Step 9: The parameter settings used in TSA ($\vec{A}$, $\vec{G}$, $\vec{F}$, $\vec{M}$) have been updated using Equations 1-4.

Step 10: Tunicate population individuals are checked to see if they exceed the search space limits.

Step 11: The solutions of the new tunicate candidates are compared with solutions of the existing turnicate individuals. Better new individuals are updated to replace old individuals.

Step 12: The iteration variable is incremented by one.

Step 13: while loop end

Step 14: Tunicate population is returned.

Step 15: end of procedure

2.2. Enhanced Standard Tunicate Swarm Algorithm

In the standard TSA algorithm, only the positions of the best-tunicate are considered in behaviors of the jet propulsion and swarm intelligence. The position of the worst-tunicate individual was not taken into account. In the Enhanced TSA (ETSA) algorithm, the worst tunicate position was taken into account in behaviors of the jet propulsion and swarm intelligence. Equations 5 - 7 have been updated again as Equations 8 - 10. While updating tunicates' new positions, tunicate individuals try to move away from the worst search agent while approaching the best search agent, which provides further development of local search capabilities in the search space. The ETSA and TSA working steps are the same, except for the updated equations. The flowchart of ETSA is shown in Figure 1.

$$\overrightarrow{T_{distance\_w}} = \left| \overrightarrow{T_{worst}} - r.\overrightarrow{T(x)} \right| \qquad (8)$$

$$\overrightarrow{T(x'')} = \begin{cases} \overrightarrow{T_{worst}} + \vec{A}.\overrightarrow{T_{distance\_w}}, & if\ r \geq 0.5 \\ \overrightarrow{T_{worst}} - \vec{A}.\overrightarrow{T_{distance\_w}}, & if\ r < 0.5 \end{cases} \qquad (9)$$

where $\overrightarrow{T(x')}$ is the updated $\overrightarrow{T(x)}$ (location of tunicate) with respect to $\overrightarrow{T_{worst}}$ (the location of worst tunicate) and r is a random number between [0, 1].

$$T(\vec{x} + 1) = \frac{\overrightarrow{T(x\prime)} + T(\vec{x}-1) + \overrightarrow{T(x\prime\prime)}}{2 + r1} \qquad (10)$$

2.3. Definitions of Big Data Problems on the EEG datasets

Because of the unique characteristics of big data, such as volume, speed, variety, and accuracy, big data optimization problems differ from classical optimization problems. They also contain a large number of decision variables, objective functions, or functions with varying mathematical properties, and they occasionally necessitate real-time solutions. A major data optimization

problem have recently emerged, attracting the attention of researchers who wish to solve it using swarm intelligence-based and evolutionary algorithms. Big data has specific properties such as volume, speed, variety and accuracy, so the big data optimization problem is different from the classical optimization problems. They also contain a large number of decision variables, objective functions, or functions with mathematical properties, such as variables, and sometimes require real-time solutions. In recent years, Goh et al. have defined a big data optimization problem and tried to solve this problem with swarm intelligence-based evolutionary algorithms.

EEG signals were collected by Goh et al. for big data optimization problems [5, 11]. EEG signal data are grouped into six different data sets named EE4, EE4N, EE12, EE12N, EE19, and EE19N, with reference to the number of interconnected time series. Each time series has a length of 256. While the EE4 problem example has four interconnected time series, the EE12 and EE19 problem examples have twelve and nineteen interconnected time series, respectively. For problem examples EE4N, EE12N, and EE19N, there are also four, twelve, and nineteen-time series. However, as the name implies, they have been slightly modified with the addition of an extra noise component [5, 14, 15].

Suppose D is a matrix of size $K \times L$ representing the transformed problem example. For matrix E, K corresponds to the number of time series and L is equal to the length of each time series. Suppose E is a matrix of size $K \times K$ representing the transformed problem example. The problem definition is shown in Equations 11-17.

$$X = E \times D \tag{11}$$

$$D = D_1 + D_2 \tag{12}$$

$$X = E \times D_1 + E \times D_2 \tag{13}$$

$$C = \frac{covar(E, \ E \times D_1)}{var(E) \times var(E \times D_1)} \tag{14}$$

$$Minimize \qquad f_1 = \frac{1}{(K^2 - K)} \sum_{i \neq j}(C_{ij})^2 + \frac{1}{K}\sum_i(1 - C_{ij})^2 \tag{15}$$

$$Minimize \qquad f_2 = \frac{1}{K \times L} \sum_{ij}(D_{ij} - D1_{ij})^2 \tag{16}$$

$$Minimize \qquad f_1 + f_2 \tag{17}$$
$$Subject \ to \quad -8 \leq D_1 \leq 8$$
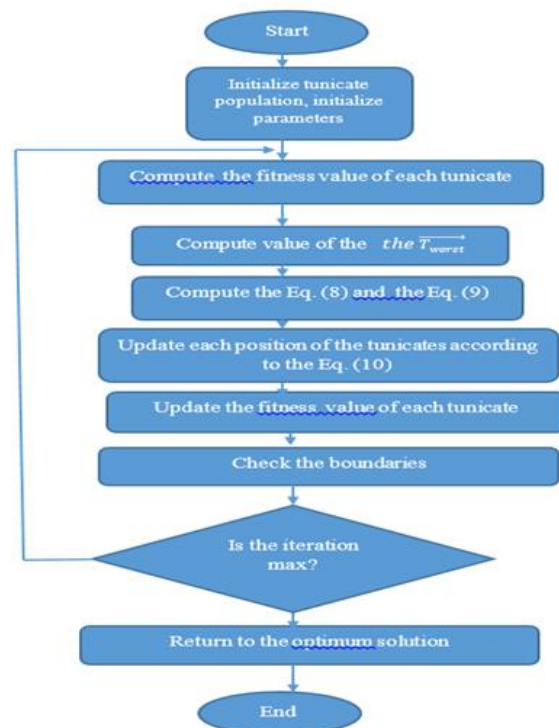
Figure 1 The flowchart of ETSA

3. CONCLUSIONS AND DISCUSSION

All the applications in this section are coded on the Matlab program, and a PC with a Corel i5 processor and 12 GB ram has been chosen for their performance.

3.1. Parameter Analyzes

X_{min} and X_{max} values are taken as 1 and 4, respectively. Necessary parameter analyzes were made by Kaur et al. [10].

In order to show the effect of population size on ETSA, five different values (10, 30, 50, 80, and 100) were chosen randomly. In the

tests performed, the maximum iteration value was taken as 500 and the problem size as 30. Thirteen different unimodal and multimodal benchmark test functions have been selected. The details of the benchmark test functions used for the test are given in the appendix. Each test function was run 20 times independently, and the mean (MN)

and standard deviation values (SDD) of the obtained results were calculated. The best results are marked in bold. The means and standard deviations of the results are shown in Table 1. Looking at the results, it is seen that the population size has an increasing proportion of the results.

Table 1 The mean (MN) and standard deviation (SDD) results of the ETSA for different population sizes (P=population size)

F	ETSA									
	P=10		P=30		P=50		P=80		P=100	
	MN	SDD	MN	SDD	MN	SDD	MN	SDD	MN	SDD
F1	3.23E-207	**0.0000**	1.48E-233	**0.0000**	2.13E-242	**0.0000**	6.72E-250	**0.0000**	**7.55E-253**	**0.0000**
F2	4.39E-110	**0.0000**	8.60E-124	**0.0000**	1.24E-128	**0.0000**	2.25E-132	**0.0000**	**1.75E-134**	**0.0000**
F3	5.61E-187	**0.0000**	3.74E-205	**0.0000**	1.27E-210	**0.0000**	1.60E-215	**0.0000**	**1.65E-216**	**0.0000**
F4	1.96E-98	**0.0000**	2.03E-107	**0.0000**	4.28E-110	**0.0000**	3.33E-112	**0.0000**	**5.53E-113**	**0.0000**
F5	2.87E+01	**0.2862**	2.86E+01	0.3534	2.87E+01	0.3092	2.87E+01	0.3055	**2.85E+01**	0.3587
F6	5.21E+00	0.6730	4.67E+00	0.6206	4.48E+00	0.6550	**3.95E+00**	**0.5485**	3.98E+00	0.6433
F7	2.85E-04	0.0002	8.17E-05	0.0001	5.72E-05	0.0001	**1.96E-05**	**0.0000**	2.59E-05	**0.0000**
F8	-3.40E+03	458.6395	-3.44E+03	464.1231	-3.41E+03	**312.9168**	**-3.81E+03**	422.5721	-3.35E+03	380.1744
F9	**0.00E+00**	**0.0000**	**0.00E+00**	**0.0000**	**0.00E+00**	**0.0000**	**0.00E+00**	**0.0000**	**0.00E+00**	**0.0000**
F10	**4.44E-15**	**0.0000**	**4.44E-15**	**0.0000**	**4.44E-15**	**0.0000**	**4.44E-15**	**0.0000**	**4.44E-15**	**0.0000**
F11	4.81E-03	0.0119	2.98E-03	0.0081	2.61E-03	0.0069	1.03E-03	0.0032	**8.87E-04**	**0.0027**
F12	9.20E-01	0.2522	6.33E-01	0.2362	5.69E-01	0.1960	5.40E-01	0.1592	**4.90E-01**	**0.1264**
F13	2.87E+00	**0.0792**	2.64E+00	0.1873	2.72E+00	0.1514	2.70E+00	0.1343	**2.61E+00**	0.1867

3.2. Comparison of TSA and ETSA

TSA and ETSA were compared on various unimodal, multi-modal, and fixed-dimensional benchmark test functions in terms of five different comparison criteria (mean, standard deviation, time, best, and worst). The details of the benchmark test functions used for the test are given in the appendix. TSA and ETSA were run 20 times for each benchmark function. The parameter settings used in the comparisons are shown in Table 2. Comparison results are shown in Table 3 and Table 4.

According to the average results, ETSA achieved better results than TSA in all

benchmark functions except F8 and F20. The standard deviation results show a parallel success with the average results. According to the time results, TSA works in a shorter time on average. According to Best results, ETSA achieved better results than TSA in 18 of 23 test functions.

Table 2 Parameter settings

Parameter	Value
Population size	30
Dimension	{30, 2, 3, 4, 6}
Maximum iteration	500
X_{min}	1
X_{max}	4

Table 3 The mean (MN), standard deviation (SDD), and Time (T) results
of the TSA and ETSA

F	TSA			ETSA		
	MN	SDD	T	MN	SDD	T
F1	7.84E-19	**0.000000**	**2.87E-01**	**1.48E-233**	**0.000000**	9.21E-01
F2	1.41E-99	5.5E-99	**3.09E-01**	**8.60E-124**	**1.3E-123**	9.68E-01
F3	1.71E-18	**0.000000**	**1.02E+00**	**3.74E-205**	**0.000000**	1.49E+00
F4	5.49E-92	1.56E-91	**3.18E-01**	**2.03E-107**	**5.3E-107**	9.54E-01
F5	2.87E+01	**0.296845**	**3.68E-01**	**2.86E+01**	0.353399	1.15E+00
F6	6.09E+00	0.685039	**3.31E-01**	**4.67E+00**	**0.620591**	1.20E+00
F7	8.38E-05	7.01E-05	**4.56E-01**	**8.17E-05**	**6.94E-05**	1.45E+00
F8	**-3.49E+03**	**440.0958**	**3.73E-01**	-3.44E+03	464.1231	1.24E+00
F9	8.68E+00	24.42137	**3.64E-01**	**0.00E+00**	**0.000000**	1.29E+00
F10	**4.44E-15**	**7.89E-31**	**3.85E-01**	**4.44E-15**	**7.89E-31**	1.00E+00
F11	5.42E-03	0.010736	**3.71E-01**	**2.98E-03**	**0.0081**	1.25E+00
F12	1.10E+00	0.408235	**7.03E-01**	**6.33E-01**	**0.236177**	1.36E+00
F13	2.65E+00	0.235752	**6.93E-01**	**2.64E+00**	**0.187306**	1.42E+00
F14	1.16E+01	4.802528	**1.16E+00**	**7.54E+00**	**4.61054**	2.25E+00
F15	3.77E-03	0.007128	**2.73E-01**	**2.58E-03**	**0.005938**	1.20E+00
F16	-1.02E+00	0.014488	**2.32E-01**	**-1.03E+00**	**0.009485**	9.17E-01
F17	**3.99E-01**	**0.001661**	**2.12E-01**	3.99E-01	0.002015	1.03E+00
F18	1.52E+01	24.87551	**2.22E-01**	**7.45E+00**	**19.40461**	8.95E-01
F19	**-3.86E+00**	**0.002301**	**3.43E-01**	**-3.86E+00**	0.002816	1.18E+00
F20	**-3.19E+00**	**0.080977**	**3.50E-01**	-3.07E+00	0.196455	1.18E+00
F21	-7.32E+00	1.349929	**3.92E-01**	**-7.40E+00**	**1.254483**	1.20E+00
F22	-5.25E+00	2.34319	**4.23E-01**	**-5.74E+00**	**1.180463**	1.31E+00
F23	-4.50E+00	2.962034	**5.06E-01**	**-5.97E+00**	**2.21391**	1.41E+00

Table 4 The best and worst results of the TSA and ETSA

F	TSA		ETSA	
	Best	Worst	Best	Worst
F1	1.43E-203	1.45E-192	**4.21E-238**	1.37E-232
F2	1.43E-104	2.55E-98	**1.98E-125**	5.31E-123
F3	4.20E-188	1.42E-182	**6.76E-210**	3.35E-204
F4	1.22E-96	6.44E-91	**2.06E-109**	2.44E-106
F5	**2.81E+01**	2.89E+01	**2.81E+01**	2.90E+01
F6	4.83E+00	7.25E+00	**3.39E+00**	6.01E+00
F7	3.44E-06	2.50E-04	**1.63E-06**	2.47E-04
F8	-4.33E+03	-2.81E+03	**-4.60E+03**	-2.50E+03
F9	**0.000000**	1.05E+02	**0.000000**	0.000000
F10	**4.44E-15**	4.44E-15	**4.44E-15**	4.44E-15
F11	**0.000000**	3.74E-02	**0.000000**	3.35E-02
F12	3.73E-01	1.70E+00	**3.39E-01**	1.34E+00
F13	**1.87E+00**	2.90E+00	2.23E+00	2.90E+00
F14	2.98E+00	1.83E+01	**1.99E+00**	1.27E+01
F15	3.17E-04	2.09E-02	**3.14E-04**	2.04E-02
F16	**-1.03E+00**	-1.00E+00	**-1.03E+00**	-1.00E+00
F17	**3.98E-01**	4.04E-01	**3.98E-01**	4.06E-01
F18	**3.00E+00**	8.41E+01	**3.00E+00**	9.20E+01
F19	**-3.86E+00**	-3.85E+00	**-3.86E+00**	-3.85E+00
F20	**-3.31E+00**	-3.06E+00	-3.30E+00	-2.45E+00
F21	**-9.78E+00**	-4.98E+00	-8.79E+00	-4.89E+00
F22	**-9.04E+00**	-9.11E-01	-7.98E+00	-3.25E+00
F23	**-1.03E+01**	-1.62E+00	-9.97E+00	-1.80E+00

3.3. Comparison of ETSA With Other Algorithms

ETSA and some heuristic algorithms selected from the literature were compared in 23 benchmark functions in terms of four different comparison criteria (mean, standard deviation, time, and best). These algorithms are Jaya Algorithm [11], Skill Optimization Algorithm (SOA) [12], and Slime Mould Algorithm (SMA) [13]. All algorithms were run 20 times for each benchmark function. The parameter settings used in the comparisons are shown in Table 5. Comparison results are shown in Tables 6-9.

According to the results, ETSA achieved better results than Jaya. However, it could not pass SMA and SOA in many functions. ETSA was the most successful algorithm after SMA and SOA. The results show that ETSA can be preferred for continuous optimization problems in the literature.

The Wilcoxon statistical test is a test of significance used to test whether there is a difference between measurements of the same individuals at two different times or situations. Wilcoxon test results for ETSA and other algorithms (Jaya, SOA SMA, and TSA) are shown in Table 10. Convergence plots of the ETSA and other algorithms for various benchmark functions show in Figure 2 and Figure 3.

Table 5 Parameter settings

Parametre	Değer
Population size	30
Dimension	{30, 2, 3, 4, 6}
Maximum iteration	500
(X_{min}, X_{max}) for TSA and ETSA	1,4
z for SMA	0.03

Table 6 The comparisons of the mean (MN) results of the ETSA and other algorithms

F	TSA	Jaya	SOA	SMA	ETSA
F1	7.84E-19	3.79E+02	1.28E-219	**6.74E-303**	1.48E-233
F2	1.41E-99	5.70E+00	9.33E-112	**1.82E-152**	8.60E-124
F3	1.71E-18	1.29E+05	1.47E-186	**1.31E-300**	3.74E-205
F4	5.49E-92	6.34E+01	3.40E-107	**7.54E-166**	2.03E-107
F5	2.87E+01	4.61E+05	**0.000000**	3.88E+00	2.86E+01
F6	6.09E+00	2.95E+02	**0.000000**	6.64E-03	4.67E+00
F7	8.38E-05	7.14E+00	**6.37E-05**	1.82E-04	8.17E-05
F8	-3.49E+03	-5.19E+03	-6.49E+03	**-1.26E+04**	-3.44E+03
F9	8.68E+00	1.28E+02	**0.00E+00**	**0.000000**	**0.000000**
F10	4.44E-15	1.88E+01	**8.88E-16**	**8.88E-16**	4.44E-15
F11	5.42E-03	3.78E+00	**0.000000**	**0.000000**	2.98E-03
F12	1.10E+00	9.74E+05	**1.57E-32**	6.50E-03	6.33E-01
F13	2.65E+00	1.24E+06	**1.35E-32**	5.02E-03	2.64E+00
F14	1.16E+01	3.16E+00	2.43E+00	**9.98E-01**	7.54E+00
F15	3.77E-03	7.02E-04	**3.22E-04**	6.53E-04	2.58E-03
F16	-1.02E+00	**-1.03E+00**	**-1.03E+00**	**-1.03E+00**	**-1.03E+00**
F17	3.99E-01	NAN	**3.98E-01**	**3.98E-01**	3.99E-01
F18	1.52E+01	9.79E+00	**3.00E+00**	**3.00E+00**	7.45E+00
F19	**-3.86E+00**	**-3.86E+00**	**-3.86E+00**	**-3.86E+00**	**-3.86E+00**
F20	-3.19E+00	-3.22E+00	**-3.31E+00**	-3.26E+00	-3.07E+00
F21	-7.32E+00	-4.74E+00	-9.64E+00	**-1.02E+01**	-7.40E+00
F22	-5.25E+00	-5.66E+00	-1.01E+01	**-1.04E+01**	-5.74E+00
F23	-4.50E+00	-5.85E+00	**-1.05E+01**	**-1.05E+01**	-5.97E+00
Rank	**5**	**4**	**2**	**1**	**3**

Table 7 The comparisons of the standard deviation (SDD) results of the ETSA and other algorithms

F	TSA	Jaya	SOA	SMA	ETSA
F1	**0.000000**	477.6474	**0.000000**	**0.0000000**	**0.000000**
F2	5.5E-99	6.714119	3.3E-111	**7.9E-152**	1.3E-123
F3	**0.000000**	37118.06	**0.000000**	**0.000000**	**0.000000**
F4	1.56E-91	5.932388	1.2E-106	**0.000000**	5.3E-107
F5	0.296845	644275.3	**0.000000**	8.109989	0.353399
F6	0.685039	202.2773	**0.000000**	0.004869	0.620591
F7	7.01E-05	6.692799	**5.38E-05**	0.000156	6.94E-05
F8	440.0958	2145.906	1033.639	**0.313121**	464.1231
F9	24.42137	42.94716	**0.000000**	**0.000000**	0.000000
F10	7.89E-31	1.349448	**0.000000**	**0.000000**	7.89E-31
F11	0.010736	3.181002	**0.000000**	**0.000000**	0.0081
F12	0.408235	2146562	**5.47E-48**	0.008084	0.236177
F13	0.235752	2289017	**2.74E-48**	0.004642	0.187306
F14	4.802528	3.146973	1.854209	**5.11E-13**	4.61054
F15	0.007128	0.000577	**1.95E-05**	0.00033	0.005938
F16	0.014488	0.003009	**1.89E-10**	7.93E-10	0.009485
F17	0.001661	NAN	**5.19E-09**	3.5E-08	0.002015
F18	24.87551	11.42437	**8.95E-10**	9.47E-09	19.40461
F19	0.002301	**6.65E-15**	1.19E-05	1.83E-07	0.002816
F20	0.080977	0.04338	**0.031431**	0.0593	0.196455
F21	1.349929	2.56062	1.52937	**0.00024**	1.254483
F22	2.34319	3.555628	1.158411	**0.000315**	1.180463
F23	2.962034	3.530381	**8.61E-05**	0.000274	2.21391
Rank	**4**	**5**	**1**	**2**	**3**

Table 8 The comparisons of the time (T) results of the ETSA and other algorithms

F	TSA	Jaya	SOA	SMA	ETSA
F1	2.87E-01	2.04E+00	**2.50E-01**	2.98E+00	9.21E-01
F2	3.09E-01	2.18E+00	**2.40E-01**	3.66E+00	9.68E-01
F3	**1.02E+00**	1.06E+01	1.26E+00	3.43E+00	1.49E+00
F4	**3.18E-01**	2.34E+00	3.48E-01	3.40E+00	9.54E-01
F5	3.68E-01	2.54E+00	**2.72E-01**	3.13E+00	1.15E+00
F6	3.31E-01	1.93E+00	**2.58E-01**	3.13E+00	1.20E+00
F7	**4.56E-01**	3.19E+00	6.83E-01	3.12E+00	1.45E+00
F8	**3.73E-01**	2.62E+00	4.02E-01	3.10E+00	1.24E+00
F9	3.64E-01	2.50E+00	**3.12E-01**	3.36E+00	1.29E+00
F10	**3.85E-01**	2.81E+00	3.93E-01	3.36E+00	1.00E+00
F11	3.71E-01	2.94E+00	**3.40E-01**	3.29E+00	1.25E+00
F12	**7.03E-01**	6.15E+00	9.64E-01	3.55E+00	1.36E+00
F13	**6.93E-01**	6.86E+00	8.14E-01	3.77E+00	1.42E+00
F14	**1.16E+00**	1.31E+01	1.65E+00	1.30E+00	2.25E+00
F15	**2.73E-01**	2.06E+00	4.22E-01	7.92E-01	1.20E+00
F16	**2.32E-01**	2.07E+00	3.38E-01	6.10E-01	9.17E-01
F17	**2.12E-01**	NAN	2.18E-01	5.92E-01	1.03E+00
F18	**2.22E-01**	1.68E+00	3.16E-01	5.76E-01	8.95E-01
F19	**3.43E-01**	2.77E+00	4.72E-01	8.16E-01	1.18E+00
F20	**3.50E-01**	2.77E+00	5.64E-01	1.01E+00	1.18E+00
F21	**3.92E-01**	6.49E+00	5.70E-01	1.21E+00	1.20E+00
F22	**4.23E-01**	7.56E+00	6.34E-01	8.63E-01	1.31E+00
F23	**5.06E-01**	8.23E+00	7.44E-01	1.02E+00	1.41E+00
Rank	**1**	**5**	**2**	**4**	**3**

Table 9 The comparisons of the best results of the ETSA and other algorithms

F	TSA	Jaya	SOA	SMA	ETSA
F1	1.43E-203	9.27E+00	1.25E-242	**0.00E+00**	4.21E-238
F2	1.43E-104	7.23E-01	1.35E-121	**3.95E-267**	1.98E-125
F3	4.20E-188	7.04E+04	1.55E-210	**0.00E+00**	6.76E-210
F4	1.22E-96	4.51E+01	2.46E-118	**3.52E-293**	2.06E-109
F5	2.81E+01	8.42E+03	**0.000000**	3.90E-03	2.81E+01
F6	4.83E+00	5.15E+01	**0.000000**	1.50E-03	3.39E+00
F7	3.44E-06	5.63E-01	**6.14E-07**	3.77E-05	1.63E-06
F8	-4.33E+03	-8.21E+03	-8.66E+03	**-1.26E+04**	-4.60E+03
F9	**0.000000**	6.68E+01	**0.00E+00**	**0.000000**	**0.000000**
F10	4.44E-15	1.51E+01	**8.88E-16**	**8.88E-16**	4.44E-15
F11	**0.000000**	1.17E+00	**0.00E+00**	**0.000000**	**0.000000**
F12	3.73E-01	4.89E+01	**1.57E-32**	3.26E-05	3.39E-01
F13	1.87E+00	7.25E+00	**1.35E-32**	6.31E-05	2.23E+00
F14	2.98E+00	**9.98E-01**	9.98E-01	9.98E-01	1.99E+00
F15	3.17E-04	3.08E-04	**3.07E-04**	3.08E-04	3.14E-04
F16	**-1.03E+00**	**-1.03E+00**	**-1.03E+00**	**-1.03E+00**	**-1.03E+00**
F17	**3.98E-01**	NAN	**3.98E-01**	**3.98E-01**	**3.98E-01**
F18	**3.00E+00**	**3.00E+00**	**3.00E+00**	**3.00E+00**	**3.00E+00**
F19	**-3.86E+00**	**-3.86E+00**	**-3.86E+00**	**-3.86E+00**	**-3.86E+00**
F20	-3.31E+00	**-3.32E+00**	**-3.32E+00**	**-3.32E+00**	-3.30E+00
F21	-9.78E+00	**-1.02E+01**	**-1.02E+01**	**-1.02E+01**	-8.79E+00
F22	-9.04E+00	**-1.04E+01**	**-1.04E+01**	**-1.04E+01**	-7.98E+00
F23	-1.03E+01	**-1.05E+01**	**-1.05E+01**	**-1.05E+01**	-9.97E+00
Rank	5	3	1	2	4

Table 10 The Wilcoxon test results of the ETSA and other algorithms

| F	ETSA-Jaya		ETSA-SOA		ETSA-SMA		ETSA-TSA	
	p-value	h-value	p-value	h-value	p-value	h-value	p-value	h-value
F1	0.000248	1	2.92E-05	1	0.00047	1	0.000248	1
F2	0.000248	1	0.000248	1	0.000248	1	0.000248	1
F3	0.000248	1	6.67E-06	1	0.000365	1	0.000248	1
F4	0.000228	1	0.000758	1	6.80E-08	1	0.000248	1
F5	0.000218	1	7.72E-09	1	1.61E-07	1	0.6747	0
F6	0.000248	1	0.000212	1	0.000248	1	0.000475	1
F7	0.000248	1	0.350702	1	0.003639	1	0.7353	0
F8	0.1264	0	7.90E-08	1	6.80E-08	1	0.7764	0
F9	8.01E-09	1	NaN	0	NaN	0	3.31E-06	1
F10	7.68E-09	1	4.68E-10	1	4.68E-10	1	NAN	0
F11	1.96E-08	1	0.080631	0	0.080631	0	0.4162	0
F12	6.80E-08	1	8.01E-09	1	6.80E-08	1	7.58E-04	1
F13	6.47E-08	1	7.51E-09	1	6.47E-08	1	0.8815	0
F14	7.98E-04	1	8.59E-06	1	6.89E-09	1	0.0121	1
F15	0.8392	0	1.81E-05	1	1	0	0.7557	0
F16	0.0499	1	8.01E-09	1	1.13E-08	1	0.2616	0
F17	NAN	0	3.46E-08	1	6.76E-08	1	0.7150	0
F18	1.21E-06	1	1.13E-08	1	1.51E-08	1	0.0018	1
F19	8.01E-09	1	6.80E-08	1	6.79E-08	1	0.1333	0
F20	4.16E-04	1	1.43E-07	1	2.60E-05	1	0.0114	1
F21	6.15E-04	1	9.56E-06	1	6.61E-08	1	0.5975	0
F22	0.3648	0	2.56E-07	1	6.80E-08	1	0.6359	0
F23	0.6750	0	6.80E-08	1	6.80E-08	1	0.0601	0
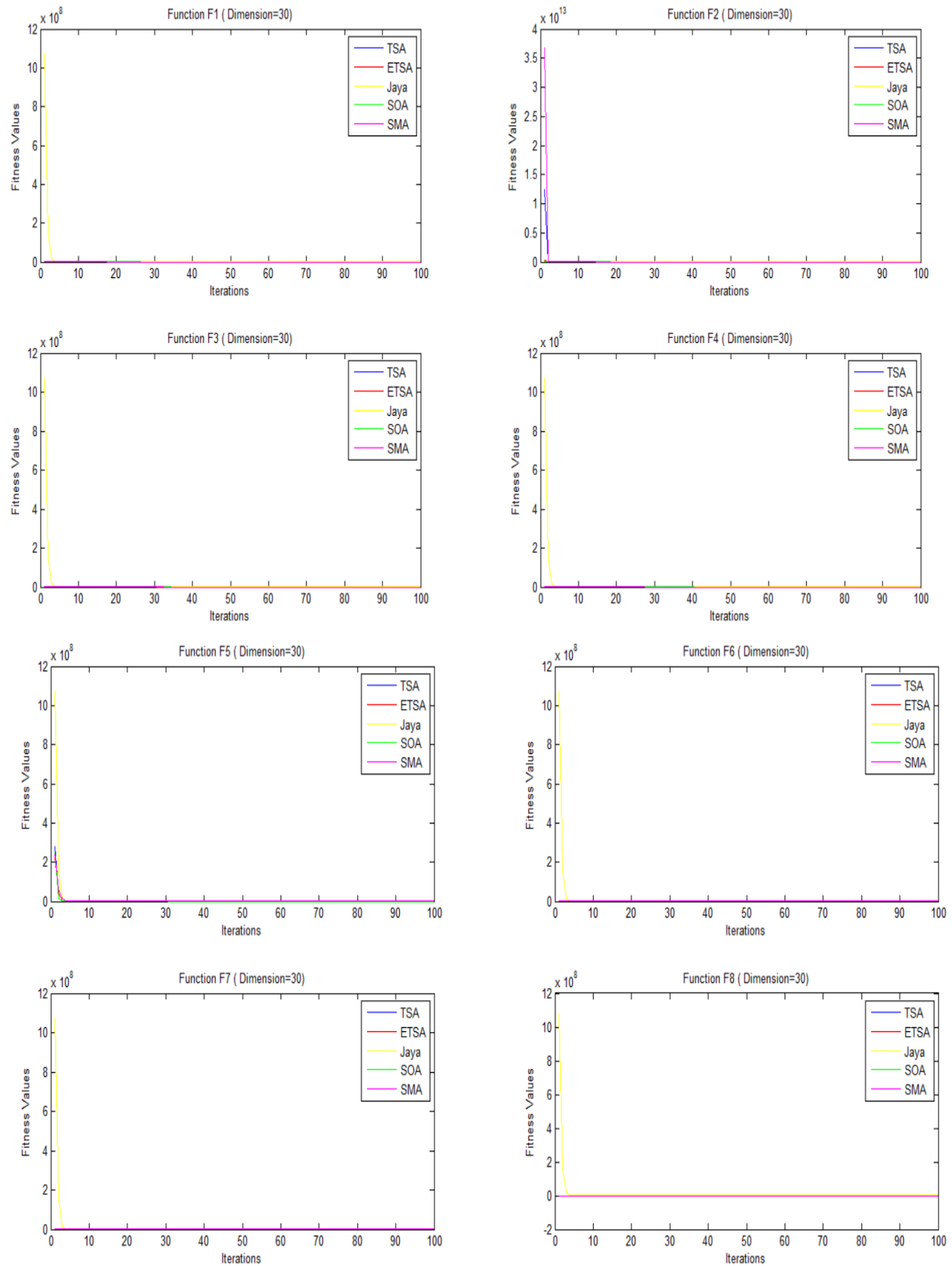
Figure 2 Convergence plots of the ETSA and other algorithms for various benchmark functions (F1, F2, F3, F4, F5, F6, F7, and F8) in dimension=30
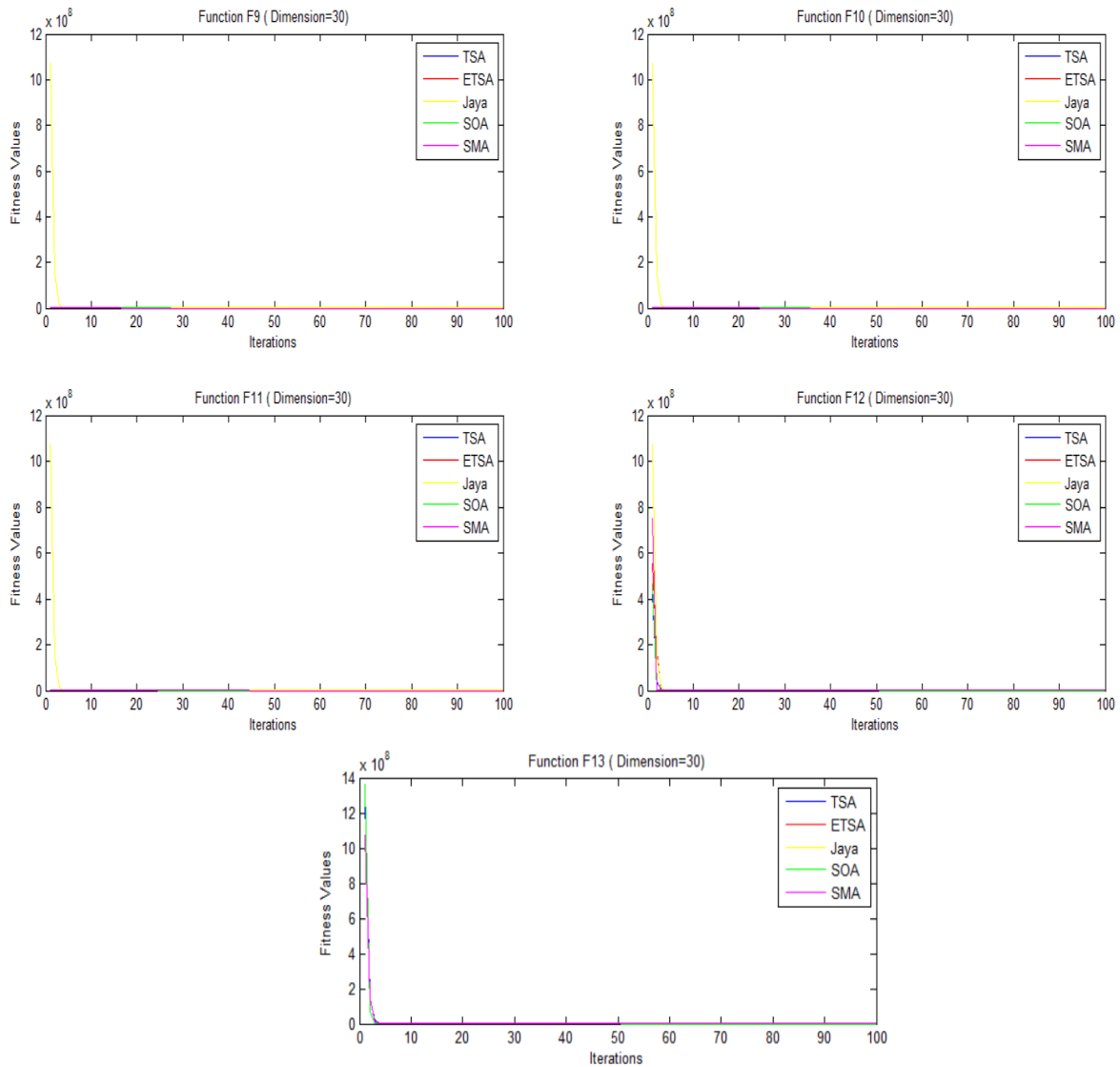
Figure 3 Convergence plots of the ETSA and other algorithms for various benchmark functions (F9, F10, F11, F12, and F13) in dimension=30

3.4. ETSA For Big Data Optimization

The success of TSA and ETSA was tested in detail on six different big data sets. During these tests, five different population sizes (10, 20, 30, 50, 100) were determined with three different maximum iteration values (300, 500, 1000). TSA and ETSA algorithms were run in 20 independent studies on each big data set. Obtained results were compared according to four different criteria (best, mean (MN), standard deviation (SDD), and time (T)). In addition, the results were compared with some heuristic algorithms selected from the literature and proposed in recent years. These algorithms are Jaya Algorithm [11], Skill Optimization Algorithm (SOA) [12], and Slime Mould Algorithm (SMA) [13]. The parameter settings used in the comparisons are shown in Table 11.

Comparison results of TSA and ETSA for maximum iteration={300, 500, 1000} are shown in Tables 12-17. Comparison results of ETSA and other algorithms are shown in Table 18. Wilcoxon test results for ETSA and other algorithms (TSA, Jaya, SOA, and SMA) are shown in Table 19.

According to the results, ETSA achieved better results than TSA. Thus, it has been

proven that In terms of working time, TSA worked in a shorter time than ETSA. The reason for this is the codes added for the development of ETSA. It is not a significant time difference. ETSA has been developed. When compared with various algorithms selected from the literature, it achieved the best results after SOA. The results obtained were subjected to the Wilcoxon sign test, which is a statistical test, and it was shown

that there was a semantic difference between the results obtained.

Table 11 Parameter settings

Parameters	Values
Population size (P)	10, 20, 30, 50, 100
Dimension	1024, 3072, 4868
Maximum iteration	300, 500, 1000
(X_{min}, X_{max}) for TSA and ETSA	1,4
z for SMA	0.03

Table 12 The results of the TSA in big data datasets for maximum iteration=300 (P=population size)

Datasets		P=10	P=20	P=30	P=50	P=100
EE4						
	Best	1.41E+00	1.36E+00	1.37E+00	1.35E+00	**1.33E+00**
	MN	1.47E+00	1.43E+00	1.43E+00	1.41E+00	**1.39E+00**
	SDD	3.40E-02	3.86E-02	3.02E-02	3.27E-02	**2.59E-02**
	T	0.9165	1.6946	3.5140	4.8225	7.3009
EE4N						
	Best	1.42E+00	1.40E+00	1.39E+00	1.35E+00	**1.32E+00**
	MN	1.48E+00	1.46E+00	1.42E+00	1.41E+00	**1.38E+00**
	SDD	3.71E-02	3.16E-02	3.04E-02	2.95E-02	**2.87E-02**
	T	0.9149	1.6457	2.3803	3.7127	7.2040
EE12						
	Best	1.56E+00	1.56E+00	1.54E+00	1.52E+00	**1.48E+00**
	MN	1.63E+00	1.59E+00	1.58E+00	1.56E+00	**1.53E+00**
	SDD	2.87E-02	**1.66E-02**	2.75E-02	2.03E-02	2.32E-02
	T	2.0750	5.8661	5.7513	9.4226	20.1355
EE12N						
	Best	1.57E+00	1.56E+00	1.54E+00	1.52E+00	**1.51E+00**
	MN	1.63E+00	1.60E+00	1.59E+00	1.56E+00	**1.54E+00**
	SDD	2.79E-02	2.57E-02	2.67E-02	2.11E-02	**1.94E-02**
	T	2.0703	5.5020	5.8107	11.8639	35.1981
EE19						
	Best	1.60E+00	1.58E+00	1.57E+00	1.53E+00	**1.51E+00**
	MN	1.66E+00	1.63E+00	1.61E+00	1.58E+00	**1.57E+00**
	SDD	2.68E-02	**2.09E-02**	2.58E-02	2.99E-02	3.12E-02
	T	6.0403	11.4253	17.6720	33.0520	53.9655
EE19N						
	Best	1.60E+00	1.59E+00	1.57E+00	**1.54E+00**	**1.54E+00**
	MN	1.66E+00	1.63E+00	1.61E+00	1.60E+00	**1.57E+00**
	SDD	2.74E-02	2.25E-02	3.20E-02	2.48E-02	**2.09E-02**
	T	4.6871	12.8426	19.2210	33.0938	64.8880

Table 13 The results of the TSA in big data datasets for maximum iteration=500 (P=population size)

Datasets		P=10	P=20	P=30	P=50	P=100
EE4						
	Best	1.41E+00	1.37E+00	1.36E+00	1.35E+00	**1.32E+00**
	MN	1.46E+00	1.43E+00	1.42E+00	1.40E+00	**1.36E+00**
	SDD	2.80E-02	3.73E-02	2.94E-02	2.82E-02	**1.97E-02**
	T	2.2915	4.2904	6.2368	9.4524	18.6667
EE4N						
	Best	1.37E+00	1.36E+00	1.36E+00	1.36E+00	**1.35E+00**
	MN	1.45E+00	1.43E+00	1.42E+00	1.40E+00	**1.38E+00**
	SDD	3.61E-02	3.79E-02	2.85E-02	**2.56E-02**	2.61E-02
	T	1.5895	4.1892	6.4027	10.1032	22.2316
EE12						
	Best	1.56E+00	1.53E+00	1.52E+00	1.51E+00	**1.49E+00**
	MN	1.62E+00	1.58E+00	1.57E+00	1.54E+00	**1.53E+00**
	SDD	2.72E-02	2.63E-02	**1.93E-02**	1.98E-02	2.10E-02
	T	5.6007	11.1384	14.5790	24.7584	55.0372
EE12N						
	Best	1.55E+00	1.53E+00	1.50E+00	1.50E+00	**1.49E+00**
	MN	1.61E+00	1.58E+00	1.57E+00	1.55E+00	**1.53E+00**
	SDD	2.32E-02	**2.06E-02**	2.26E-02	2.29E-02	2.23E-02
	T	3.5387	10.5012	14.5954	25.9696	52.1192
EE19						
	Best	1.61E+00	1.54E+00	1.57E+00	1.56E+00	**1.52E+00**
	MN	1.65E+00	1.62E+00	1.60E+00	1.58E+00	**1.57E+00**
	SDD	2.70E-02	2.52E-02	2.04E-02	**1.91E-02**	2.76E-02
	T	11.4051	21.0422	31.0650	38.1544	85.7928
EE19N						
	Best	1.61E+00	1.57E+00	1.58E+00	**1.54E+00**	**1.54E+00**
	MN	1.66E+00	1.62E+00	1.61E+00	1.58E+00	**1.57E+00**
	SDD	2.38E-02	2.20E-02	2.19E-02	2.64E-02	**1.97E-02**
	T	13.4974	14.2832	38.5597	106.2589	151.6567

Table 14 The results of the TSA in big data datasets for maximum iteration=1000 (P=population size)

Datasets		P=10	P=20	P=30	P=50	P=100
EE4						
	Best	1.37E+00	1.36E+00	1.38E+00	1.35E+00	**1.31E+00**
	MN	1.43E+00	1.41E+00	1.43E+00	1.39E+00	**1.36E+00**
	SDD	3.27E-02	2.75E-02	3.70E-02	2.66E-02	**2.54E-02**
	T	6.8589	12.2524	13.4907	29.1908	39.8686
EE4N						
	Best	1.39E+00	1.37E+00	1.35E+00	**1.32E+00**	1.34E+00
	MN	1.44E+00	1.42E+00	1.42E+00	1.38E+00	**1.37E+00**
	SDD	3.91E-02	3.19E-02	4.17E-02	**2.81E-02**	2.83E-02
	T	6.4894	12.1303	19.6702	20.3234	24.5076
EE12						
	Best	1.55E+00	1.53E+00	1.50E+00	1.49E+00	**1.48E+00**
	MN	1.59E+00	1.57E+00	1.58E+00	1.54E+00	**1.52E+00**
	SDD	2.46E-02	2.11E-02	3.74E-02	2.10E-02	**2.01E-02**
	T	12.7430	31.1192	56.5263	34.6869	66.9431

Table 14 The results of the TSA in big data datasets for maximum iteration=1000 (P=population size) (Continue)

Datasets	P=10	P=20	P=30	P=50	P=100
EE12N					
Best	1.56E+00	1.53E+00	1.54E+00	1.49E+00	**1.47E+00**
MN	1.60E+00	1.56E+00	1.58E+00	1.54E+00	**1.52E+00**
SDD	2.43E-02	**1.99E-02**	2.24E-02	2.01E-02	2.48E-02
T	7.3831	14.0870	35.5943	33.4560	67.7289
EE19					
Best	1.59E+00	1.57E+00	1.58E+00	1.52E+00	**1.50E+00**
MN	1.63E+00	1.59E+00	1.62E+00	1.56E+00	**1.56E+00**
SDD	2.63E-02	2.28E-02	3.17E-02	2.59E-02	**2.21E-02**
T	15.6217	24.2274	65.7384	59.4652	118.7629
EE19N					
Best	1.59E+00	1.57E+00	1.55E+00	1.53E+00	**1.51E+00**
MN	1.63E+00	1.61E+00	1.60E+00	1.57E+00	**1.55E+00**
SDD	2.17E-02	2.15E-02	2.74E-02	**2.00E-02**	2.64E-02
T	21.6556	44.0970	100.3609	102.0027	216.4222

Table 15 The results of the ETSA in big data datasets for maximum iteration=300 (P=population size)

Datasets	P=10	P=20	P=30	P=50	P=100
EE4					
Best	1.42E+00	1.41E+00	1.39E+00	1.38E+00	**1.37E+00**
MN	1.50E+00	1.46E+00	1.44E+00	1.43E+00	**1.41E+00**
SDD	3.92E-02	3.18E-02	3.23E-02	3.45E-02	**2.96E-02**
T	1.4530	4.0206	5.4442	15.5729	31.3489
EE4N					
Best	1.45E+00	1.41E+00	1.38E+00	1.37E+00	**1.35E+00**
MN	1.52E+00	1.47E+00	1.45E+00	1.43E+00	**1.40E+00**
SDD	4.17E-02	3.35E-02	3.39E-02	**2.78E-02**	2.92E-02
T	1.7041	3.9030	5.4782	7.5168	23.8819
EE12					
Best	1.61E+00	1.57E+00	1.52E+00	1.54E+00	**1.53E+00**
MN	1.66E+00	1.62E+00	1.59E+00	1.59E+00	**1.57E+00**
SDD	2.33E-02	2.62E-02	2.94E-02	3.02E-02	**1.95E-02**
T	3.7527	10.4922	17.7711	34.0430	84.6269
EE12N					
Best	1.59E+00	1.56E+00	1.55E+00	1.53E+00	**1.51E+00**
MN	1.65E+00	1.62E+00	1.60E+00	1.58E+00	**1.56E+00**
SDD	2.94E-02	2.85E-02	2.52E-02	**2.49E-02**	3.54E-02
T	4.8291	8.7621	16.4479	35.4610	95.6271
EE19					
Best	1.61E+00	1.59E+00	1.60E+00	1.55E+00	**1.52E+00**
MN	1.67E+00	1.65E+00	1.64E+00	1.61E+00	**1.60E+00**
SDD	3.18E-02	**2.90E-02**	2.96E-02	3.21E-02	3.39E-02
T	8.2209	16.9738	34.4714	70.4807	190.8606
EE19N					
Best	1.61E+00	1.57E+00	1.58E+00	1.57E+00	**1.52E+00**
MN	1.68E+00	1.64E+00	1.64E+00	1.62E+00	**1.59E+00**
SDD	4.04E-02	3.58E-02	**2.86E-02**	3.36E-02	3.36E-02
T	8.8840	18.5949	32.2787	75.0291	148.0824

Table 16 The results of the ETSA in big data datasets for maximum iteration=500 (P=population size)

Datasets		P=10	P=20	P=30	P=50	P=100
EE4						
	Best	1.42E+00	1.42E+00	1.39E+00	1.37E+00	**1.35E+00**
	MN	1.50E+00	1.47E+00	1.44E+00	1.41E+00	**1.39E+00**
	SDD	4.24E-02	3.05E-02	2.75E-02	**2.28E-02**	2.56E-02
	T	2.7479	3.7079	5.5867	12.0395	27.0730
EE4N						
	Best	1.42E+00	1.41E+00	1.36E+00	1.36E+00	**1.35E+00**
	MN	1.48E+00	1.46E+00	1.43E+00	1.42E+00	**1.40E+00**
	SDD	3.33E-02	2.92E-02	3.10E-02	2.73E-02	**2.71E-02**
	T	1.9530	3.7568	5.5512	12.1127	29.3235
EE12						
	Best	1.56E+00	1.56E+00	1.54E+00	1.53E+00	**1.50E+00**
	MN	1.64E+00	1.61E+00	1.59E+00	1.57E+00	**1.56E+00**
	SDD	3.16E-02	**2.34E-02**	3.08E-02	2.70E-02	2.82E-02
	T	11.2345	25.0109	35.9231	39.8899	142.1579
EE12N						
	Best	1.56E+00	1.55E+00	1.56E+00	1.53E+00	**1.51E+00**
	MN	1.63E+00	1.60E+00	1.60E+00	1.58E+00	**1.55E+00**
	SDD	3.53E-02	3.15E-02	**1.68E-02**	2.71E-02	2.22E-02
	T	5.5528	11.9986	19.6726	41.4899	110.5248
EE19						
	Best	1.59E+00	1.59E+00	1.57E+00	1.56E+00	**1.53E+00**
	MN	1.65E+00	1.65E+00	1.63E+00	1.61E+00	**1.58E+00**
	SDD	4.06E-02	3.20E-02	3.29E-02	**2.88E-02**	3.23E-02
	T	13.1811	28.8617	51.5975	93.6329	330.7623
EE19N						
	Best	1.60E+00	1.57E+00	1.56E+00	1.56E+00	**1.54E+00**
	MN	1.66E+00	1.63E+00	1.62E+00	1.61E+00	**1.59E+00**
	SDD	3.27E-02	3.08E-02	**2.86E-02**	3.30E-02	3.38E-02
	T	8.9610	18.9731	37.0469	70.5432	196.8537

Table 17 The results of the ETSA in big data datasets for maximum iteration=1000 (P=population size)

Datasets		P=10	P=20	P=30	P=50	P=100
EE4						
	Best	1.40E+00	1.35E+00	1.37E+00	1.36E+00	**1.35E+00**
	MN	1.46E+00	1.42E+00	1.41E+00	1.42E+00	**1.40E+00**
	SDD	3.42E-02	3.69E-02	**2.62E-02**	2.64E-02	3.08E-02
	T	4.3305	7.9714	18.1214	23.2406	56.0005
EE4N						
	Best	1.42E+00	1.42E+00	1.36E+00	1.36E+00	**1.34E+00**
	MN	1.47E+00	1.45E+00	1.41E+00	1.41E+00	**1.38E+00**
	SDD	2.90E-02	2.39E-02	**2.98E-02**	3.09E-02	2.31E-02
	T	4.2536	7.9278	11.6828	34.8273	53.0632
EE12						
	Best	1.59E+00	1.55E+00	1.50E+00	1.51E+00	**1.49E+00**
	MN	1.62E+00	1.60E+00	**1.54E+00**	1.56E+00	**1.54E+00**
	SDD	**1.80E-02**	2.51E-02	2.14E-02	2.56E-02	2.21E-02
	T	9.8815	21.1255	46.0445	73.9346	568.3986

Table 17 The results of the ETSA in big data datasets for maximum iteration=1000 (P=population size) (Continue)

Datasets		P=10	P=20	P=30	P=50	P=100
EE12N						
	Best	1.55E+00	1.55E+00	1.51E+00	1.51E+00	**1.48E+00**
	MN	1.62E+00	1.60E+00	1.55E+00	1.57E+00	**1.54E+00**
	SDD	3.36E-02	3.14E-02	**2.30E-02**	2.60E-02	3.07E-02
	T	9.1114	36.2446	29.3428	71.2533	2685.8105
EE19						
	Best	1.58E+00	1.56E+00	1.56E+00	**1.54E+00**	**1.54E+00**
	MN	1.65E+00	1.62E+00	1.59E+00	1.59E+00	**1.58E+00**
	SDD	3.87E-02	**2.83E-02**	1.84E-02	3.11E-02	3.05E-02
	T	18.0155	47.6943	55.7210	186.7582	790.6452
EE19N						
	Best	1.57E+00	1.58E+00	1.56E+00	**1.52E+00**	1.53E+00
	MN	1.65E+00	1.63E+00	1.59E+00	1.59E+00	**1.57E+00**
	SDD	3.64E-02	2.41E-02	2.29E-02	2.74E-02	**2.28E-02**
	T	20.5374	36.7440	59.0029	192.0792	373.6314

Table 18 The comparisons results of the ETSA and other algorithms in big data datasets for maximum iteration=1000 and population size=30

Datasets		Jaya	SOA	SMA	TSA	ETSA
EE4						
	Best	1.17E+01	**1.33E+00**	1.87E+00	1.38E+00	1.37E+00
	MN	1.29E+01	**1.36E+00**	1.92E+00	1.43E+00	1.41E+00
	SDD	6.35E-01	2.38E-02	**2.26E-02**	3.70E-02	2.62E-02
	T	4.00E+01	**4.58E+00**	1.24E+02	13.4907	18.1214
EE4N						
	Best	1.19E+01	**1.27E+00**	1.85E+00	1.35E+00	1.36E+00
	MN	1.30E+01	**1.31E+00**	1.90E+00	1.42E+00	1.41E+00
	SDD	6.49E-01	**2.83E-02**	3.11E-02	4.17E-02	2.98E-02
	T	3.04E+01	**3.94E+00**	1.59E+02	19.6702	11.6828
EE12						
	Best	1.30E+01	**1.43E+00**	1.93E+00	1.50E+00	1.50E+00
	MN	1.39E+01	**1.53E+00**	1.95E+00	1.58E+00	1.54E+00
	SDD	3.37E-01	3.47E-02	**1.39E-02**	3.74E-02	2.14E-02
	T	7.06E+01	**1.13E+01**	4.86E+02	56.5263	46.0445
EE12N						
	Best	1.34E+01	**1.50E+00**	1.93E+00	1.54E+00	1.51E+00
	MN	1.38E+01	**1.55E+00**	1.95E+00	1.58E+00	**1.55E+00**
	SDD	2.44E-01	4.28E-02	**1.41E-02**	2.24E-02	2.30E-02
	T	6.05E+01	**1.14E+01**	3.07E+02	35.5943	29.3428
EE19						
	Best	1.36E+01	**1.53E+00**	1.93E+00	1.58E+00	1.56E+00
	MN	1.40E+01	**1.58E+00**	1.96E+00	1.62E+00	1.59E+00
	SDD	2.14E-01	2.39E-02	1.64E-02	3.17E-02	**1.84E-02**
	T	1.01E+02	**1.57E+01**	2.22E+02	65.7384	55.7210
EE19N						
	Best	1.36E+01	1.56E+00	1.92E+00	**1.55E+00**	1.56E+00
	MN	1.41E+01	1.60E+00	1.96E+00	1.60E+00	**1.59E+00**
	SDD	2.87E-01	2.35E-02	**1.84E-02**	2.74E-02	2.29E-02
	T	1.02E+02	**1.92E+01**	2.37E+02	100.3609	59.0029
Rank		5	1	4	3	2

Table 19 The Wilcoxon test results of the ETSA and other algorithms

Datasets	ETSA-TSA		ETSA-Jaya		ETSA-SOA		ETSA-SMA	
	p-value	h-value	p-value	h-value	p-value	h-value	p-value	h-value
D4	0.1478	0	6.80E-06	1	9.13E-07	1	6.72E-08	1
D4N	0.2853	0	6.80E-06	1	1.66E-07	1	6.70E-08	1
D12	0.0036	1	6.80E-06	1	8.36E-04	1	6.46E-08	1
D12N	1.16E-04	1	6.80E-06	1	0.0043	1	6.61E-08	1
D19	0.0114	1	6.80E-06	1	8.36E-04	1	6.70E-08	1
D19N	0.3942	0	6.80E-06	1	0.9676	0	6.70E-08	1

4. CONCLUSION

Tunicate Swarm Algorithm (TSA) is proposed by Kaur et al. in 2020. Tunicate Swarm Algorithm (TSA) was inspired by sea creatures called Tunicates. Tunicates are marine creatures capable of locating food sources in the seas. Tunicates adopted two fundamental movements in exploration and exploitation behavior: jet propulsion and herd intelligence. Thanks to these two movements. it performs exploration and exploitation operations. In this study. herd behavior has been updated and Enhanced TSA (ETSA) has been proposed to increase the success of TSA. Two sets of two problems were used to test the success of TSA and ETSA. In the first problem set. twenty-three unimodal. multimodal. and fixed-dimensional multi-modal test functions were selected from the literature. Secondly. the big data optimization problem involving EEG signals is chosen. The results were tested according to the best. mean. standard deviation. and time comparison criteria for TSA and ETSA. and convergence graphs were shown. The performances of TSA and ETSA were tested in detail for five different population sizes (10. 20. 30. 50. and 100) and three different maximum iterations (300. 500. and 1000) on big datasets containing six different EEG signals. TSA and ETSA results were also compared with Jaya. SOA. and SMA algorithms. The results showed that ETSA achieved better results than TSA and showed preferable success for continuous optimization problems.

In further studies. it is expected that the binary form of TSA will be obtained and the feature selection problem will be solved and its success will be demonstrated.

Authors' Contribution
The authors contributed equally to the study.

The Declaration of Conflict of Interest/ Common Interest
No conflict of interest or common interest has been declared by the authors.

The Declaration of Ethics Committee Approval
This study does not require ethics committee permission or any special permission.

The Declaration of Research and Publication Ethics
The authors of the paper declare that they comply with the scientific. ethical. and quotation rules of SAUJS in all processes of the paper and that they do not make any falsification of the data collected. In addition. they declare that Sakarya University Journal of Science and its editorial board have no responsibility for any ethical violations that may be encountered

and that this study has not been evaluated in any academic publication environment other than Sakarya University Journal of Science.

REFERENCES

[1] S. Aslan, D. Karaboga, "A genetic Artificial Bee Colony algorithm for signal reconstruction based big data optimization," Applied Soft Computing, vol. 88, pp. 106053, 2020.

[2] V. N. Gudivada, R. Baeza-Yates, V. V. Raghavan, "Big data: Promises and problems," Computer, vol. 48, no. 3, pp. 20–23, 2015.

[3] C. W. Tsai, C. -F. Lai, H. -C. Chao, A. V. Vasilakos, "Big data analytics: a survey," Journal Big Data, vol. 2, no. 1, pp. 21, 2015.

[4] M. Hilbert, "Big data for development: A review of promises and challenges," Development Policy Review, vol. 34, no. 1, pp. 135–174, 2016.

[5] S. K. Goh, K. C. Tan, A. Al-Mamun, H.A. Abbass, "Evolutionary big optimization (BigOpt) of signals," In: 2015 IEEE congress on evolutionary computation (CEC), IEEE, 2015, pp. 3332–3339.

[6] Y. Zhang, J. Liu, M. Zhou, Z. Jiang, "A multi-objective memetic algorithm based on decomposition for big optimization problems," Memetic Computing, vol. 8, no. 1, pp. 45–61, 2016.

[7] S. Elsayed, R. Sarker, "An adaptive configuration of differential evolution algorithms for big data," in: IEEE Congress on Evolutionary Computation (CEC), IEEE, 2015, pp. 695–702.

[8] M. A. El Majdouli, I. Rbouh, S. Bougrine, B. El Benani, A. A. El Imrani, "Fireworks algorithm framework for Big Data optimization," Memetic Computing, vol. 8, no. 4, pp. 333–347, 2016.

[9] Z. Cao, L. Wang, X. Hei, Q. Jiang, X. Lu, X. Wang, "A phase based optimization algorithm for big optimization problems," in: 2016 IEEE Congress on Evolutionary Computation (CEC), IEEE, 2016, pp. 5209–5214.

[10] S. Kaur, L. K. Awasthi, A.L. Sangal, G. Dhiman, "Tunicate Swarm Algorithm: A new bio-inspired based metaheuristic paradigm for global optimization," Engineering Applications of Artificial Intelligence, vol. 90, pp. 103541, 2020.

[11] R. Rao, "Jaya: A simple and new optimization algorithm for solving constrained and unconstrained optimization problems," International Journal of Industrial Engineering Computations, vol. 7, no. 1, pp. 19-34, 2016.

[12] H. Givi, M. Hubalovska, "Skill optimization algorithm: a new human-based metaheuristic technique," Computers Materials & Continua, vol. 74, no.1, pp. 179–202, 2023.

[13] S. Li, H. Chen, M. Wang, A. A. Heidari, S. Mirjalili, "Slime mould algorithm: A new method for stochastic optimization," Future Generation Computer Systems, vol. 111, pp. 300–323, 2020.

[14] S. K. Goh, H.A. Abbass, K. C. Tan, A. Al Mamun, "Artifact removal from EEG using a multi-objective independent component analysis model," In: International conference on neural information processing, Springer, 2014, pp. 570–577.

[15] H. A. Abbass, "Calibrating independent component analysis with Laplacian reference for real-time EEG artifact removal," In: International conference on neural information processing, Springer, 2014, pp. 68–75.

Appendix: Benchmark functions

A. Unimodal benchmark functions

F1:

$$F_1(x) = \sum_{i=1}^{d} x_i^2 \qquad -100 \leq x_i \leq 100 \quad f_{min} = 0 \quad d = dimension$$

F2:

$$F_2(x) = \sum_{i=1}^{d} |x_i^2| + \prod_{i=1}^{d} |x_i^2| \qquad -10 \leq x_i \leq 10 \quad f_{min} = 0 \quad d = dimension$$

F3:

$$F_3(x) = \sum_{i=1}^{d} \left(\sum_{j=1}^{i} x_j \right)^2 \qquad -100 \leq x_i \leq 100 \quad f_{min} = 0 \quad d = dimension$$

F4:

$$F_4(x) = \max_i \{|x_i|.1 \leq i \leq d\} \qquad -100 \leq x_i \leq 100 \quad f_{min} = 0 \quad d = dimension$$

F5:

$$F_5(x) = \sum_{i=1}^{d-1} [100(x_{i+1} - x_i^2)^2 + (x_i - 1)^2] \qquad -30 \leq x_i \leq 30 \quad f_{min} = 0 \quad d = dimension$$

F6:

$$F_6(x) = \sum_{i=1}^{d} ([x_i + 0.5])^2 \qquad -100 \leq x_i \leq 100 \quad f_{min} = 0 \quad d = dimension$$

F7:

$$F_7(x) = \sum_{i=1}^{d} i x_i^4 + random[0.1] \qquad -1.28 \leq x_i \leq 1.28 \quad f_{min} = 0 \quad d = dimension$$

B. Multimodal benchmark functions

F8:

$$F_8(x) = \sum_{i=1}^{d} -x_i \sin\left(\sqrt{|x_i|}\right) \qquad -500 \leq x_i \leq 500 \quad f_{min} = -12\,569.5 \quad d = dimension$$

F9:

$$F_9(x) = \sum_{i=1}^{d} [x_i^2 - 10 cos(2\pi x_i) + 10] \qquad -5.12 \leq x_i \leq 5.12 \quad f_{min} = 0 \quad d = dimension$$

F10:

$$F_{10}(x) = -20 exp\left(-0.2 \sqrt{\frac{1}{d} \sum_{i=1}^{d} x_i^2}\right) - exp\left(\frac{1}{d} \sum_{i=1}^{d} cos(22\pi x_i)\right) + 20 + \varepsilon \qquad -32 \leq x_i \leq 32 \quad f_{min} = 0 \quad d = dimension$$

F11:

$$F_{11}(x) = \frac{1}{400} \sum_{i=1}^{d} x_i^2 - \prod_{i=1}^{d} cos\left(\frac{x_i}{\sqrt{i}}\right) + 1 \qquad -600 \leq x_i \leq 600 \quad f_{min} = 0 \quad d = dimension$$

F12:

$$F_{12}(x) = \frac{\pi}{30} \left\{ 10 sin(\pi x_i) + \sum_{i=1}^{d-1} (x_i - 1)^2 [1 + 10 sin^2(\pi x_{i+1})] + (x_d - 1)^2 \right\} + \sum_{i=1}^{d} u(x_i. 10. 100. 4) \qquad -50 \leq x_i \leq 50 \quad f_{min} = 0 \quad d = dimension$$

F13:

$$F_{13}(x) = 0.1 \left\{ sin^2(3\pi x_i) + \sum_{i=1}^{d-1} (x_i - 1)^2 [1 + sin^2(3\pi x_i + 1)] + (x_d - 1)^2 \times [1 + sin^2(2\pi x_d)] \right\} + \sum_{i=1}^{N} u(x_i. 5. 100. 4) \qquad -50 \leq x_i \leq 50. \quad f_{min} = 0 \quad d = dimension$$

$$where. x_i = 1 + \frac{x_i + 1}{4} \qquad u(x_i. a. k. m) = \begin{cases} k(x_i - a)^m & x_i > a \\ 0 & -a < x_i < a \\ k(-x_i - a)^m & x_i < -a \end{cases}$$

C. Fixed-dimension multimodal test functions

F14:

$$F_{14}(x) = \left(\frac{1}{500} + \sum_{j=1}^{25} \frac{1}{j + \sum_{i=1}^{2}(x_i - a_{i,j})^6} \right)^{-1} \qquad -65.536 \leq x_i \leq 65.536. \quad f_{min} \approx 1 \quad d = 2$$

F15:

$$F_{15}(x) = \sum_{i=1}^{11} \left[a_i - \frac{x_i(b_i^2 + b_i x_2)}{b_i^2 + b_i x_3 + x_4} \right]^2 \qquad -5 \leq x_i \leq 5. \quad f_{min} \approx 0.0003075. \quad d = 4$$

F16:

$$F_{16}(x) = 4x_1^2 - 2.1 x_1^4 + \frac{1}{3} x_1^6 + x_1 x_2 - 4 x_2^2 + 4 x_2^4 \qquad -5 \leq x_i \leq 5. \quad f_{min} = -1.0316285. \quad d = 2$$

F17:

$$F_{17}(x) = \left(x_2 - \frac{5.1}{4\pi^2} x_1^2 + \frac{5}{\pi} x_1 - 6\right)^2 + 10\left(1 - \frac{1}{8\pi}\right) cos x_1 + 10 \qquad -5 \leq x_1 \leq 10. \quad 0 \leq x_2 \leq 15. \quad f_{min} = 0.398. \quad d = 2$$

F18:

$$F_{18}(x) = [1 + (x_1 + x_2 + 1)^2 (19 - 14x_1 + 3x_1^2 - 14x_2 + 6x_1 x_2 + 3x_2^2)] \times [30 + (2x_1 - 3x_2)^2 \times (18 - 32x_1 + 12x_1^2 + 48x_2 - 36x_1 x_2 + 27x_2^2)] \qquad -2 \leq x_1 \leq 2. \quad f_{min} = 3. \quad d = 2$$

F19:

$$F_{19}(x) = -\sum_{i=1}^{4} c_i \exp\left(-\sum_{j=1}^{3} a_{i.j}(x_j - p_{ij})^2\right) \qquad 0 \leq x_j \leq 1. \quad f_{min} = -3.86. \quad d = 3$$

F20:

$$F_{20}(x) = -\sum_{i=1}^{4} c_i \exp\left(-\sum_{j=1}^{6} a_{i.j}(x_j - p_{ij})^2\right) \qquad 0 \leq x_j \leq 1. \quad f_{min} = -3.32. \quad d = 3$$

F21:

$$F_{21}(x) = -\sum_{i=1}^{5}[(X - a_i)(X - a_i)^T + c_i]^{-1} \qquad 0 \le x_j \le 10. \qquad f_{min}$$
$$= -10.1532. \qquad d = 4$$

F22:

$$F_{22}(x) = -\sum_{i=1}^{7}[(X - a_i)(X - a_i)^T + c_i]^{-1} \qquad 0 \le x_j \le 10. \qquad f_{min}$$
$$= -10.4028. \qquad d = 4$$

F23:

$$F_{23}(x) = -\sum_{i=1}^{10}[(X - a_i)(X - a_i)^T + c_i]^{-1} \qquad 0 \le x_j \le 10. \qquad f_{min}$$
$$= -10.536. \qquad d = 4$$

$$F_{21}(x) = -\sum_{i=1}^{5}[(X - a_i)(X - a_i)^T + c_i]^{-1} \qquad 0 \le x_j \le 10. \qquad f_{min}$$
$$= -10.1532. \qquad d = 4$$

Title: Comparative Evaluation of Alginate-Gelatin Hydrogel, Cryogel, and Aerogel Beads as a Tissue Scaffold

Authors: Ece BAYIR

Comparative Evaluation of Alginate-Gelatin Hydrogel, Cryogel, and Aerogel Beads as a Tissue Scaffold

Ece BAYIR[*1] iD

Abstract

Hydrogels are frequently used in tissue engineering and regenerative medicine, drug delivery, and environmental remediation. Alginate and gelatin, which are frequently used natural polymers to form hydrogels, were chosen in this study to form a core-shell structured hydrogel. Cryogels and aerogels were obtained by drying hydrogels with different methods, freeze-drying, and the continuous flow of supercritical CO_2, respectively. The potential use of hydrogels, aerogels, and cryogels as a tissue scaffold was evaluated comparatively. Characterizations of materials were determined morphologically by scanning electron microscope and computed-micro tomography, chemically by energy dispersive spectroscopy, and mechanically by the dynamic mechanical analyzer. In addition, the cytotoxic effect of all structures was analyzed by the WST-1 method and the localization of the cells in these structures was determined by microscopic methods. All scaffolds show non-cytotoxic effects. Cryogels have the highest porosity (85.21 %) and mean pore size values (62.3±26.8 µm). Additionally, cryogels show high water retention capacity (782±53.5%) than aerogels (389±2.5%) for 24 h. The elastic modulus values were <10 kPa, which is suitable for brain, bone marrow, spleen, pancreas, fat, kidney, and skin tissue engineering, for all types of beads. It has been determined that cryogel and hydrogel beads are more suitable for cell adhesion and migration in this study.

Keywords: Tissue engineering, scaffold, sodium alginate, gelatin

1. INTRODUCTION

Hydrogels are materials that are composed of hydrophilic polymers, are insoluble in water, and have a high water-holding capacity in their structures. Physical and/or chemical crosslinking methods are used to form hydrogels from polymers [1]. Weak interactions occur between polymer networks during physical gelation, and strong chemical bonds are formed between polymer chains during chemical gelation [2]. For this reason, polymers formed by physical methods are easily degraded, while polymers obtained by chemical methods are not. Hydrogels can be classified as synthetic, semi-synthetic, and natural. Synthetic hydrogels are generally synthesized by

* Corresponding author: ece.bayir@ege.edu.tr
[1] Ege University Central Research Test and Analysis Laboratory Application and Research Center (EGE-MATAL), Ege University, 35100, Izmir, Turkey
E-mail: ece.bayir@ege.edu.tr
ORCID: https://orcid.org/0000-0003-4886-3860

polymerization of vinyl monomers, and natural hydrogels are obtained from natural polymers such as polynucleotides, polypeptides, and polysaccharides [3]. In recent years, studies have been carried out on the use of hydrogels in many different areas such as drug delivery systems, drug encapsulation, tissue engineering, and environmental remediation [4-8]. The most used polymers to obtain hydrogels are natural polymers due to their high biocompatibility.

Sodium alginate, natural water-soluble salt of alginic acid, is an anionic polysaccharide composed of (1-4) linked β-D-mannuronic acid (M) and α-L-guluronic acid (G) obtained from the cell wall of brown algae [9]. It is a highly biocompatible, biodegradable, and relatively cheap biopolymer. The ability to form hydrogels is one of the main properties of alginate. This property of sodium alginate is mainly due to the replacement of Na^+ in the guluronic acid residues with different divalent cations (Ca^{2+}, Sr^{2+}, Ba^2+, etc.) [10].

Gelatin is a cheap, easily obtainable biopolymer with high biocompatibility, which is the denatured collagen of animals such as porcine, bovine, and fish. It is non-immunogenic, biodegradable, and easily soluble in water at 37°C [11]. Because of that its mechanical and chemical properties can be modified easily, cells can adhere easily to gelatin, and it promotes cell proliferation; it can be used as a tissue engineering scaffold and drug delivery agent for biomedical applications [12]. There are many studies performed with alginate-gelatin based 3D tissue scaffolds. In the most of these studies, tissue scaffolds are obtained by 3D printer. Chawla et al. used alginate-gelatin based hydrogel and MG63 osteoblast cells as bioink, and thus the entire hydrogel and cell mixture was bioprinted [13]. In the study of Pan et al., after the alginate-gelatin based scaffold was 3D-printed, it was lyophilized, and mouse bone mesenchymal stem cells were seeded in both hydrogel and

cryogel form of the scaffolds, and the effects of the physical and physicochemical properties of the scaffolds on tissue regeneration were investigated [14]. Baldino et al., different from the other researchers, obtained aerogels by mixing alginate and gelatin in a container, and after supercritical gel drying, their usability for tissue engineering was evaluated [15].

Hydrogels can be dried by various methods to obtain structures with different properties. The pores usually collapse when the solvent evaporates in the hydrogel, which is dried under atmospheric conditions (xerogel). Hydrogels dried with the freeze-drying method and drying with a continuous flow of supercritical CO_2 are called cryogel and aerogel, respectively [16]. The pore structures of hydrogels dried by these two methods are preserved, and therefore their use for biomedical and environmental purposes is more common.

In recent researches, alginate-gelatin based hydrogels, cryogels, and aerogels have been studied by obtaining various methods; however, the use of these structures produced by the same technique as tissue scaffolds has not been examined comparatively. This study aims to compare the physical, chemical, biological, and mechanical properties of alginate-gelatin hydrogel, cryogel, and aerogel beads and to evaluate their suitability for tissue engineering scaffold.

2. MATERIALS AND METHODS

2.1. Alginate-Gelatin Hydrogel, Cryogel and Aerogel Bead Synthesis

Alginic acid sodium salt (71238, Sigma-Aldrich, USA), type A gelatin (G2500, Sigma-Aldrich, USA), and $CaCl_2$ (223506, Sigma-Aldrich, USA) powders were used for the synthesis of alginate-gelatin hydrogel beads. Alginic acid sodium salt was stirred in the ultra-pure water (UPW) at 1.25% (w/v) concentration until dissolving and pH

was adjusted to 7.4 with NaOH (S5881, Sigma-Aldrich, USA). Gelatin (%10 (w/v)) was dissolved in UPW in another bottle at 50°C for overnight, and $CaCl_2$ (1.5% (w/v)) was added and stirred for 1 h. Since sodium alginate cross-linked by divalent cations, $CaCl_2$ was added into gelatin solution for internal Ca^{+2} source for alginate coating.

Alginate solution was poured into the beaker and stirred with a magnetic stirrer. The syringe was filled with gelatin solution and dripped into the alginate solution (Figure 1). This production procedure was adapted from Baruch and Machluf's work [17]. Alginate-gelatin beads were rinsed with UPW three times. To produce cryogel and aerogel, hydrogel beads were dried with two different methods (freeze-drying and critical point drying).
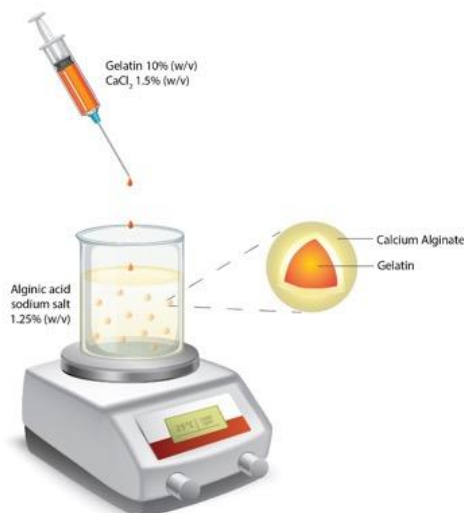
Figure 1 Alginate-gelatin bead production scheme.

Beads were frozen at -20°C before the freeze-drying process and kept in the freeze-dryer (1.2 D Alpha Plus, Martin Christ, Germany) for 24 h. For supercritical CO_2 drying method, hydrogel beads were placed into the sample holder of the critical point drier (CPD, Leica EM CPD300, Germany) in absolute ethanol for 2 h.

2.2. Characterization of Beads

2.2.1. Morphological Observation and Elemental Analysis

Cryogels and aerogels were analyzed with the scanning electron microscopy (SEM) technique for evaluating their morphology. Before the observation, the beads were cross-sectioned and, both beads and sectioned parts were sputter-coated with 7 nm Au-Pd. The observations were performed by Thermo Scientific Apreo S, at 5 kV accelerating voltage. Energy dispersive X-rays detector (EDS) of SEM was used to perform elemental analysis of the samples. Both core and shell structures were analyzed.

2.2.2. Mechanical Analysis

Compressing test was operated on a dynamic mechanical analyzer (DMA, Q800, TA Instruments) to determine the mechanical properties of hydrogels, cryogels, and aerogels. Samples were placed between compression clamps. Tests were performed at 0.5 N/min ramp force to 18 N and 37°C. Hydrogels were analyzed with DMA in wet form, while cryogels and aerogels were analyzed in dry form.

2.2.3. Porosity and Thickness Distribution

The average pore size, porosity, and thickness distribution of the beads were analyzed with Micro Computed Tomography (Micro-CT) device (μCT50, Scanco Medical, Switzerland). Samples were scanned at 70 kVp energy, 114 μA intensity, 20 μm voxel size, and 300 ms integration time. After the scanning process, the samples were analyzed with an evaluation program (Scanco Medical, Switzerland). Porosity was calculated according to the following formulae.

$$Porosity\ (\%) = \frac{Total\ volume - Solid\ volume}{Total\ volume} \times 100$$

2.2.4. Hydration Degree

Cryogel and aerogel beads were weighed separately with three replicates. All beads were weighed after keeping in UPW for 3 h and 24 h at 37°C. Hydration degree was calculated with formulae below.

$$Hydration\ degree\ (\%) = \frac{Wet\ weight - Dry\ weight}{Wet\ weight} \times 100$$

2.3. Biological Analysis

2.3.1. Cell Culture

In order to examine the use of produced alginate-gelatin hydrogels, cryogels, and aerogels as tissue scaffolds, in vitro cytotoxicity tests were performed on the scaffolds within the scope of BS EN ISO 10993-5-2009 standard [18], and cell images were taken under an inverted fluorescence microscope (Zeiss Axio Vert A1, Germany) to determine the localization of the cells seeded in the scaffolds. L929 mouse fibroblast cell line (CCL-1, ATCC, USA), recommended in the standard, was used for the cytotoxicity test.

Cells were cultivated in Minimum Essential Medium Alpha Modification (MEMA-RXA, Capricorn Scientific, Germany) supplemented with 10% (v/v) fetal bovine serum (FBS, 10500-064, Gibco, Germany), 2 mM L-Glutamine (25030-024, Gibco, Germany), 1 mM sodium pyruvate (S8636, Sigma Aldrich, Germany), and 10 µg/mL gentamicin (GEN-10B, Capricorn Scientific, Germany). Cells were incubated in 5% CO_2 and 95–98% humidified atmosphere at 37°C. Cells were trypsinized (25200-056, Gibco, Germany) and passaged until reaching desired cell number.

2.3.2. Cytotoxicity

The cytotoxicity of scaffolds on L929 cells was analyzed with the WST-1 assay (05015944001, Cell Proliferation Reagent WST-1, Merck, Germany). For this purpose, a calibration chart was drawn first to optimize the incubation time of cells with WST-1 and to find the absorbance values corresponding to certain cell numbers. Cells were trypsinized and counted with a Neubauer Hemocytometer and seeded into a 96-well plate at certain concentrations between 1×10^3 - 1×10^5 cells/well and incubated for 4 h. At the end of the incubation time, 10 µL of WST-1 was added to the wells and analyzed in a 450 nm/630 nm microplate reader at different times in the range of 0.5 - 4 h.

To perform the cytotoxicity test, scaffolds were sterilized overnight in 70% (v/v) Ethanol. After the scaffolds were rinsed 3 times with PBS, scaffolds were extracted in culture medium at a concentration of 0.2 g/mL for 24 h at 37°C. Extraction ratio (0.2 g/mL) was selected according to the "Standard surface areas and extract liquid volumes" table in *ISO 10993-12:2009 Biological evaluation of medical devices, Sample preparation and reference materials*. L929 cells were seeded at 1×10^4 cells/well in a 96-well plate and incubated for 24 h. At the end of the incubation period, the medium on the cells was removed and the extracted medium was added in a volume of 100 µL (n=3). After the cells were incubated for 24 h, 10 µL of WST-1 was added to the cells and analyzed after 60 min in a 450/630 nm microplate reader (ELx800, BioTek, USA).

2.3.3. Monitoring Cell Localization in the Scaffolds

Cells were counted and seeded in the scaffolds at 1×10^6 cells/scaffold after the scaffolds were conditioned in a culture medium for 24 h. Cells were seeded with a 1 mL syringe in a volume of 100 µL. After 24 h incubation time, cell nuclei were stained with 4',6-Diamidino-2-phenylindole dihydrochloride (DAPI, D9542, Sigma-Aldrich, Germany). DAPI (0.1 µg/mL) was diluted in PBS, and all scaffolds were

incubated in DAPI solution in the dark after the rinsing with PBS. The cells were monitored under an inverted fluorescent microscope [19].

2.3.4. Statistical analysis

All quantitative experiments were performed in at least three replicates (n=3). For statistical analysis, the Shapiro Wilk test was used to determine whether the data fit the normal distribution, and One-Way Analysis of Variance (ANOVA) was applied (95% confidence interval) for the data sets that fit the normal distribution. Tukey was chosen as the post-hoc method to determine the different groups.

2. RESULTS AND DISCUSSION

3.1. Characterization of Beads

3.1.1. Morphological Observation and Elemental Analysis

All three types of scaffolds are in the form of ellipses, and the average dimensions of hydrogels are $5.014\pm0.123 \times 5.621\pm0.085$ mm (W×L), cryogels are $2.789\pm0.152 \times 2.951\pm0.105$ mm (W×L), and aerogels are $2.213\pm0.201 \times 2.623\pm0.074$ mm (W×L).

Both cryogel and aerogel beads were observed with SEM in order to analyze the morphological difference. Hydrogel beads were not observed with the SEM device because of contained water. It is clearly seen that the size of cryogel beads was larger, and the core structure of the cryogel beads has wider pores than aerogel beads (Figure 2).

Since the cryogels are frozen before the drying process, the volume of the hydrogel increases as the water freezes. Ice crystals between the pores of the hydrogel also expands the pores. For this reason, the morphological structures of cryogel and aerogel scaffolds are different from each other, and this result is in line with previous studies [20, 21].
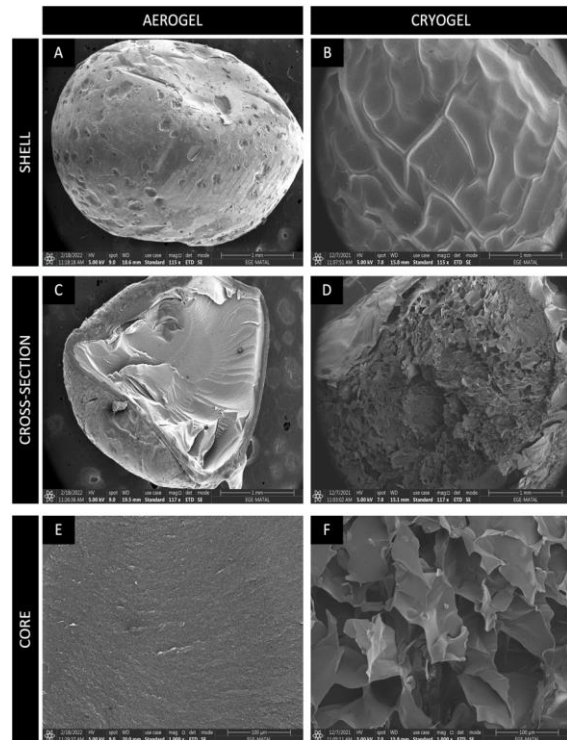
Figure 2 SEM images of aerogel and cryogel beads. A-B. Shell structure of aerogel and cryogel beads, respectively. Scale bars correspond to 1 mm. C-D. Cross-sections of aerogel and cryogel beads, respectively. Scale bars correspond to 1 mm. E-F. Core structure of aerogel and cryogel beads, respectively. Scale bars correspond to 100 μm.

When the cross-section of aerogel beads is observed in more detail, it can be seen the beads have morphologically three different layers (Figure 3). The elemental analysis of outer layer (shell) results shows that the outer wall of aerogels consists of C, H, O and Ca. Na^+ in alginic acid sodium salt solution was replaced by the Ca^{2+} in the gelatin-$CaCl_2$ solution in the core structure and formed calcium alginate ($CaC_{12}H_{14}O_{12}$). The EDS results of the core structure show that it consists of C, H, O, and N elements in the molecular formula of gelatin ($C_{102}H_{151}N_{31}O_{39}$). However, Ca^{2+} was also found in the intersection of core and shell structures.
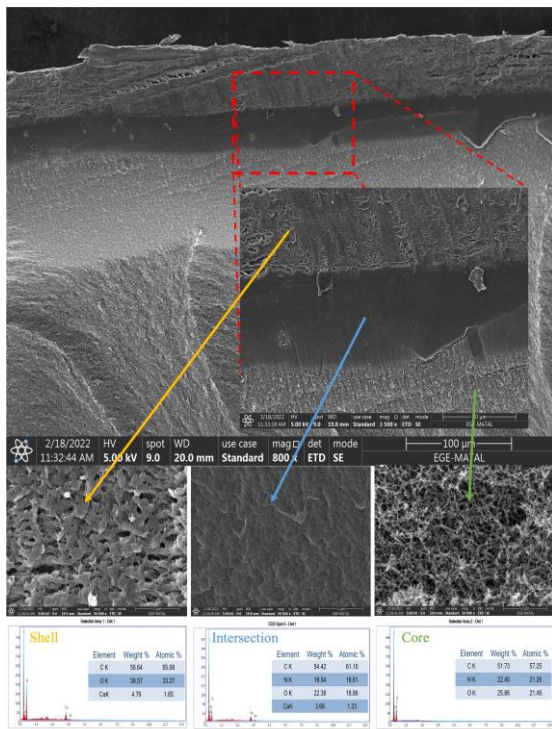
Figure 3 SEM images and EDS results of aerogel cross-section. The outer wall of the aerogel is calcium alginate, and the inner wall is gelatin structured. There is an intersection area, and this part contains both gelatin and calcium alginate properties.
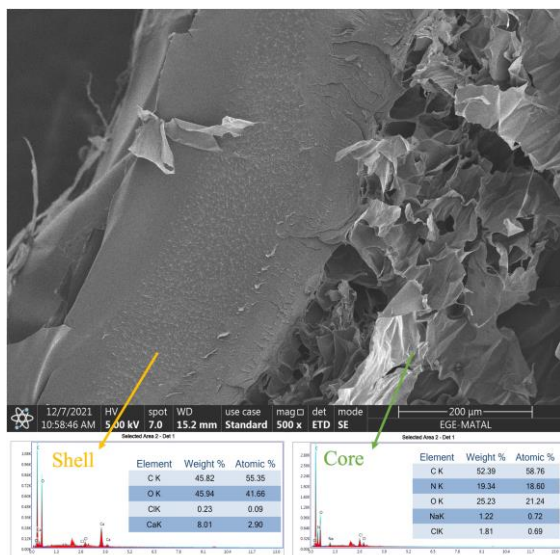

Figure 4 SEM images and EDS results of cryogel cross-section. Contrary to the aerogel, a sharp transition is observed between the core-shell structure in the cryogel. According to EDS results, the core structure consists of gelatin, and the shell structure consists of calcium alginate.

EDS results of cryogel show that the core consist of Na^+ and Ca^{2+} as well as the elements in the molecular formula of gelatin (Figure 4). It is thought that Na^+ originates from alginic acid sodium salt ($NaC_6H_7O_6$) and Cl^- originates from $CaCl_2$ salt. The shell structure consists of C, H, O, Cl and Ca, and it indicates that calcium alginate is formed similarly to aerogel beads.

3.1.2. Mechanical Analysis

The compression tests of scaffolds were performed on DMA device and the stress-strain graph obtained is given in Figure 5. The elastic moduli of the beads were calculated from the linear slope on the stress/strain curves. The elastic moduli of hydrogel, cryogel and aerogel were found 7.1 kPa, 4.2 kPa, and 3.8 kPa, respectively.

It is known that the elastic modulus of the scaffolds affects the behavior of cells [22]. Therefore, researchers try to choose a scaffold whose mechanical properties match those of the tissue being formed. Since the elastic modulus values of beads are <10 kPa, the tissue scaffolds produced are suitable for tissue engineering of brain, bone marrow, spleen, pancreas, fat, kidney and skin [23, 24].
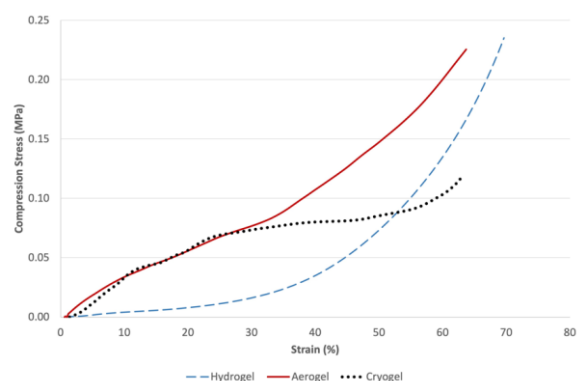
Figure 5 Compression Stress - Strain graph of hydrogel, aerogel, and cryogel.

Mechanical properties of hydrogels, cryogels, and aerogels can be changed by changing different parameters such as the concentration of divalent cations that play a role in the gelation of sodium alginate, the

concentration of crosslinking agents such as glutaraldehyde, treatment time, and production methods [10]. For this reason, it should not be considered that the tissue engineering materials produced are limited to their use only for the specified tissues because mechanical properties of beads can be easily changed for desired tissue.

3.1.3. Porosity and Thickness Distribution

The 2D images obtained after scanning the scaffolds in the Micro-CT device were transformed into 3D models with the Evaluation Program. Figures 6, 7 and 8 show hydrogel, cryogel and aerogel models, respectively. 3D models of beads are given in A and B, pore size distributions are given in C and D, and thickness distributions are given in E and F. The core-shell structure can be seen in these models. The pore sizes and the wall thickness of the scaffold are colored according to the size. The smallest pores are dark blue, and the largest pores are red in the color scale (C-D). Similarly, in the thickness distribution, the thinnest part appears in dark blue and the thickest part in red (E-F).

When the hydrogel and aerogel models are examined, a distinctive shell structure can be seen (Figure 6 and 8). In both models, the porosity of the shell structure is quite low compared to the core structure. The wall thicknesses are higher in the calcium alginate shell than in the gelatin core. For this reason, the use of these structures for drug delivery can also be considered. However, unlike the other two models, a distinct shell structure is not observed in the cryogel. In addition, there are larger diameter pores in the core structure compared to other models (Figure 7).
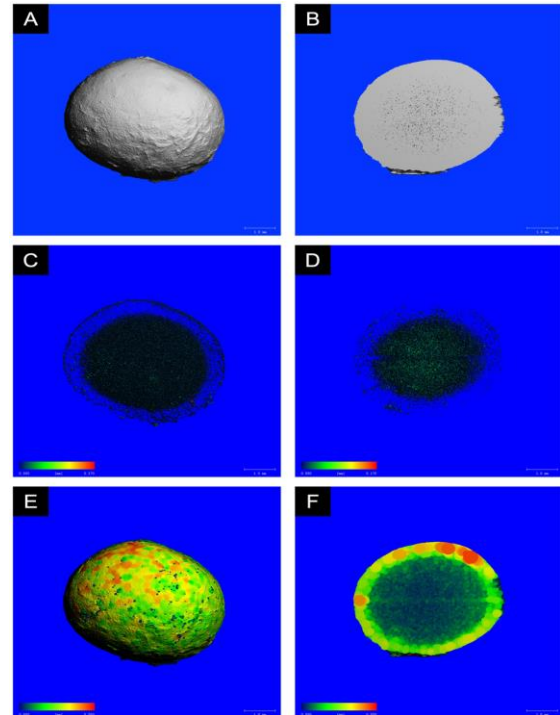
Figure 6 3D models of hydrogel beads. A. Overall 3D model, B. Cross-section of 3D model, C. Overall pore size distribution model, D. Cross-section of pore size distribution model, E. Overall thickness distribution model, F. Cross-section of thickness distribution model of the bead. Scale bars correspond to 1 mm.

The porosity results were determined as 5.18%, 57.46%, and 85.21% for hydrogel, aerogel, and cryogel, respectively. Hydrogel has a nanoporous structure as well as micro and macroporous structures. Nanopores are preserved while hydrogel is dried with supercritical CO_2 and the same structures observed in aerogels. Nanopores in the core structure of aerogels can be observed in SEM results. Since it is not possible to determine the nanopores with Micro-CT, porosity values were obtained as a result of the evaluation of only the micro and macropore structures as a result of the Micro-CT analysis. It is thought that the reason for obtaining low porosity of the hydrogel is that almost all pores in its structure are filled with water, and due to the inability of the Micro-CT device to distinguish well enough the radiopacity of gel structure and water.
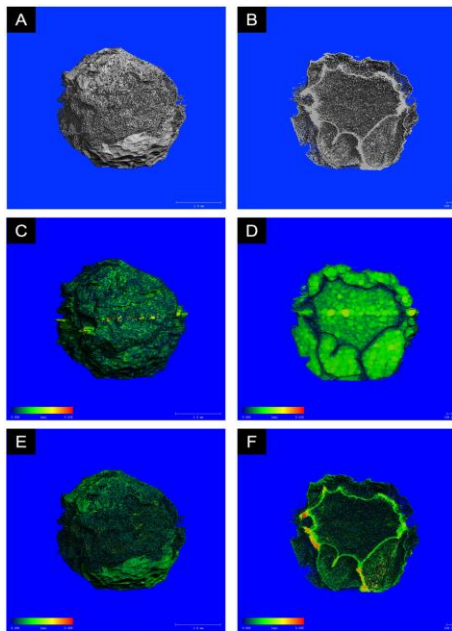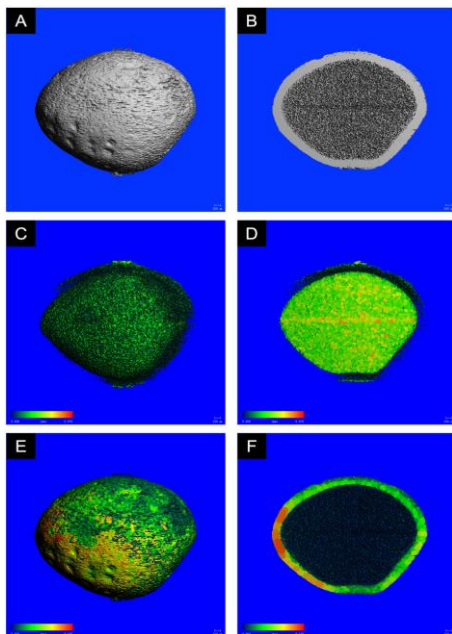
Figure 7 3D models of cryogel beads.
A. Overall 3D model,
B. Cross-section of 3D model,
C. Overall pore size distribution model,
D. Cross-section of pore size distribution
model, E. Overall thickness distribution model,
F. Cross-section of thickness distribution
model of the bead. Scale bars correspond
to 1 mm.

Figure 8 3D models of aerogel beads.
A. Overall 3D model, B. Cross-section of 3D
model, C. Overall pore size distribution model,
D. Cross-section of pore size distribution
model, E. Overall thickness distribution model,
F. Cross-section of thickness distribution
model of the bead. Scale bars correspond
to 100 µm.

When the pore size distribution graphs are examined, it is seen that it is distributed in a wide pore size range in cryogel (Figure 9). The highest mean pore diameter (62.3±26.8 µm), and the lowest wall thickness (85 µm) were seen in the cryogel (Table 1). It is an expected result that the highest pore diameter is in the cryogel due to the expansion of water while freezing. In addition, these results obtained from Micro-CT support the SEM results.
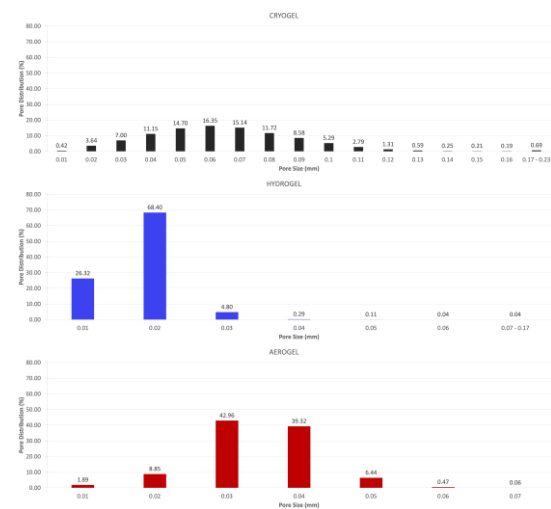
Figure 9 Pore size distribution of
hydrogel, cryogel, and aerogel beads.

Table 1 Mean and maximum pore size and thickness values of hydrogel, cryogel, and aerogel.

	Pore Size (µm)		Thickness (µm)	
	Mean (±SD)	Max	Mean (±SD)	Max
Hydrogel	18±6.3	170	191.1 ±132.5	550
Cryogel	62.3 ±26.8	230	24.9±15.1	85
Aerogel	31.5 ±7.9	70	59.6±4.1	165

3.1.4. Hydration Degree

Hydration degree measurement was carried out in cryogels and aerogels in 3 hours and 24 hours. There was no statistical difference in the water holding capacity of aerogels for 3 and 24 hours, but a significant difference was observed in the water holding capacity of cryogels in 24 hours compared to 3 hours. In addition, in the results obtained in both

time zones, it was determined that the water holding capacity of cryogels was statistically higher than aerogels (p<0.05). While the aerogels held 334±19% water in 3 h, this value was determined as 389±2.5% in 24 h. On the other hand, the cryogels hold 563±55% in 3 h and 782±53.5% in 24 h (Figure 10). Since cryogels are characterized by their high water retention abilities, they are suitable candidates for use in soft tissue engineering and regenerative medicine, and the data obtained in this study also support these results [25].
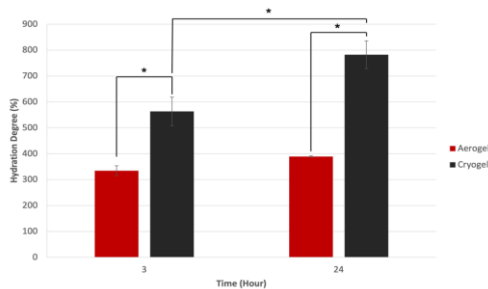
Figure 10 Hydration degree graph of aerogel and cryogel in 3 h and 24 h. The water holding capacity of cryogel is statistically higher than aerogel in both times. Also, the significant difference is observed in the water holding capacity of cryogels in 24 h compared to 3 h (p<0.05).

3.2. Biological Analysis

3.2.1. Cytotoxicity

It is necessary to determine the optimum incubation time to be applied on different cells to get the best results in the WST-1 cell proliferation test method. A calibration graph was obtained both to determine the optimum incubation time of WST-1 for L929 cells and to convert the absorbance data obtained as a result of the cytotoxicity test to the number of cells (Figure 11). After the cells were seeded in different concentrations between 1×10^3 - 1×10^5 cells/well, they were incubated for 4 h for their attachment and four different incubation times of 30 min, 1 h, 2 h and 4 h were tested for WST-1 analysis. The trendline R^2 value obtained was obtained in

the highest on 1 h results (unpublished data). For this reason, a calibration chart for 1 h was used to determine the number of cells corresponding to absorbance.
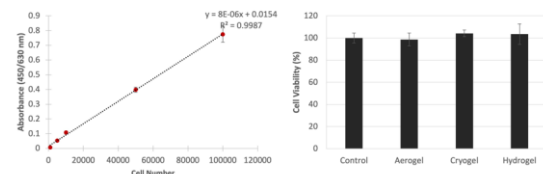
Figure 11 Calibration graph of WST-1 test on L929 cell line and cytotoxicity results of aerogel, cryogel, and hydrogel. There is no significant difference between all groups for cell viability (p<0.05).

The cytotoxic effects of aerogel, cryogel, and hydrogel beads on L929 cells were examined with the WST-1 analysis, and there was no statistically significant difference between viability of control and experimental groups at the end of the 24 h (p<0.05). According to the BS EN ISO 10993-5-2009 standard, the material has a cytotoxic effect when the cell viability is below 70% [18]. In this case, all potential scaffolds show non-cytotoxic effects. It has also been shown in previous studies that alginate and gelatin, which are natural polymers, do not have a cytotoxic effect [26, 27].

3.2.2. Monitoring cell localization in the scaffolds

In order to determine the localization of the cells in the scaffold, which were conditioned overnight in culture medium, after 24 h incubation time, the cells were monitored both under an inverted microscope and under a fluorescence microscope after staining with DAPI. It was observed that the cells were best distributed on the cryogel scaffold, and the number of cells was highest in these scaffolds. It was determined that the least number of cells and the worst distribution in the scaffold were in the aerogel. Although the number of cells in hydrogels is higher than in aerogel, the distribution of cells is not homogeneous as in cryogel (Figure 12-14).
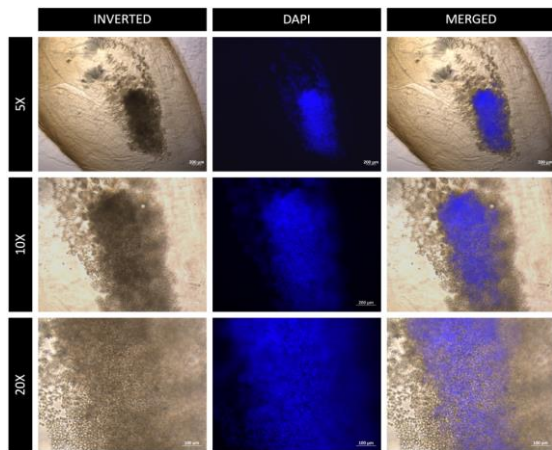
Figure 12 Cell localization in hydrogel tissue scaffolds. The first column shows inverted microscopy images of cells on 5X, 10X, and 20X magnifications, respectively. The second column shows DAPI stained cells on 5X, 10X, and 20X magnifications, respectively. The third column shows merged images of inverted microscopy images and fluorescent microscopy images on 5X, 10X, and 20X magnifications, respectively.
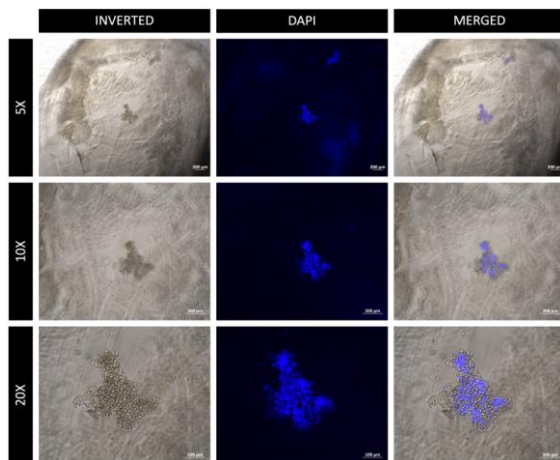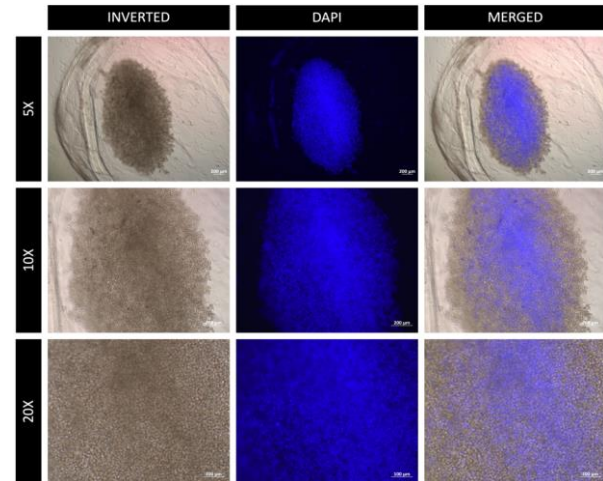

Figure 13 Cell localization in aerogel tissue scaffolds. The first column shows inverted microscopy images of cells on 5X, 10X, and 20X magnifications, respectively. The second column shows DAPI stained cells on 5X, 10X, and 20X magnifications, respectively. The third column shows merged images of inverted microscopy images and fluorescent microscopy images on 5X, 10X, and 20X magnifications, respectively.

It is thought that the reason for this situation is that the pore sizes in the cryogel are larger than the other scaffolds and cells can distribute more homogeneously. In this way,

cells can migrate more easily within the scaffold, and thanks to the increased mass transfer due to the porous structure, they can reach the nutrient medium and oxygen more easily [28].

Figure 14. Cell localization in cryogel tissue scaffolds. The first column shows inverted microscopy images of cells on 5X, 10X, and 20X magnifications, respectively. The second column shows DAPI stained cells on 5X, 10X, and 20X magnifications, respectively. The third column shows merged images of inverted microscopy images and fluorescent microscopy images on 5X, 10X, and 20X magnifications, respectively.

Different methods can be used for cell seeding into the scaffold. It has been shown that the seeding of cells during the formation phase of hydrogels gives more successful results for cell distribution in the scaffold [29]. In addition, cell and scaffold materials can be mixed and used as bioink in bioprinters [13], in this method the cells are also distributed homogenously within the scaffold. Apart from these methods, cells can be directly seeded on the scaffold after the scaffold is formed. When this method is used, the porosity of the scaffold should be high, and the pore diameters should be suitable for cell migration. Thus, even if cells are seeded on the surface of the scaffold, they can migrate into the scaffold. In this study, a different cell seeding strategy was chosen from all these techniques. This is because if cells are mixed with hydrogel during scaffold fabrication, cells would die

during aerogel and cryogel formation. In order to do a comparative evaluation of hydrogel, cryogel, and aerogel scaffolds in terms of cell distribution, the same cell seeding procedure should be used for all scaffolds. For this reason, it was preferred to use post-production cell seeding methods instead of mixing the cells directly into the alginate-gelatin hydrogel. However, it was decided that direct cell seeding on the scaffold, which is a classical method, is not a correct strategy within the scope of this study. Because, especially in aerogels and hydrogels, the pore diameters of the shell are considerably lower than the core of the scaffolds. Since cells were not thought to migrate to the core of the scaffold when they were seeded on the scaffold surface, the cells were seeded by injecting them directly into the core with a syringe.

As a result of this study, it was decided that cryogel is the most suitable structure to be used as tissue scaffold among these three forms since it has higher pore diameters, higher porosities, and therefore the cell distribution within the scaffold is more homogeneous compared to other scaffold types. Although it seems more appropriate to use cryogels as tissue scaffolds in terms of cell distribution and adhesion, the use of hydrogels is also quite suitable. As mentioned above, more successful results can be obtained when cells are seeded during hydrogel formation. Aerogels, on the other hand, do not seem appropriate for 3D tissue culture inside of the bead due to the nano-sized pores in their structure, low hydration degree, and low cell adhesion. However, by attaching cells to the surface of aerogels, these scaffolds can be used as micro/macro carriers in bioreactors.

4. CONCLUSION

In this study, cryogels and aerogels were obtained by drying alginate-gelatin hydrogel beads with different methods (freeze-drying and critical point drying). The physical, chemical, biological, and mechanical properties of hydrogels, cryogels, and aerogels for their use as a tissue scaffold were comparatively investigated. According to the results obtained, all potential scaffolds are non-cytotoxic and their mechanical properties are suitable for soft tissue engineering. It was seen that cryogels with the highest pore diameter gave the most suitable results for cell adhesion and distribution. However, it is known that different cell seeding methods also give successful results for hydrogels. On the other hand, aerogel beads are not satisfactory for cultivating cells inside the bead due to their nanoporous structure. It can be used as a micro/macro carrier in bioreactors by cell adhesion to the surface of these structures or as a drug delivery agent because of the thick shell structure.

The Declaration of Conflict of Interest/ Common Interest

No conflict of interest or common interest has been declared by the authors.

Author's Contribution

E.B: Conceptualization, literature review, formal analysis, data collection, designing and drawing the figures, writing, reviewing, and editing.

The Declaration of Ethics Committee Approval

This study does not require ethics committee permission or any special permission.

The Declaration of Research and Publication Ethics

The author of the paper declare that I comply with the scientific, ethical and quotation

rules of SAUJS in all processes of the paper and that I do not make any falsification on the data collected. In addition, I declare that Sakarya University Journal of Science and its editorial board have no responsibility for any ethical violations that may be encountered, and that this study has not been evaluated in any academic publication environment other than Sakarya University Journal of Science.

REFERENCES

[1] R. Parhi, "Cross-Linked Hydrogel for Pharmaceutical Applications: A Review," Advanced pharmaceutical bulletin, vol. 7, no. 4, pp. 515-530, 2017.

[2] M. F. Akhtar, M. Hanif, N. M. Ranjha, "Methods of synthesis of hydrogels … A review," Saudi Pharmaceutical Journal, vol. 24, no. 5, pp. 554-559, 2016.

[3] I. M. El-Sherbiny, M. H. Yacoub, "Hydrogel scaffolds for tissue engineering: Progress and challenges," Global Cardiology Science and Practice, p. 38, 2013.

[4] A. C. Daly, L. Riley, T. Segura, J. A. Burdick, "Hydrogel microparticles for biomedical applications," Nature Reviews Materials, vol. 5, no. 1, pp. 20-43, 2020.

[5] C. A. Dreiss, "Hydrogel design strategies for drug delivery," Current Opinion in Colloid & Interface Science, vol. 48, pp. 1-17, 2020.

[6] X. Qi, L. Wu, T. Su, J. Zhang, W. Dong, "Polysaccharide-based cationic hydrogels for dye adsorption," Colloids and Surfaces B: Biointerfaces, vol. 170, pp. 364-372, 2018.

[7] C. D. Spicer, "Hydrogel scaffolds for tissue engineering: the importance of polymer choice," Polymer Chemistry, vol. 11, no. 2, pp. 184-219, 2020.

[8] V. Van Tran, D. Park, Y. C. Lee, "Hydrogel applications for adsorption of contaminants in water and wastewater treatment," Environmental Science and Pollution Research, vol. 25, no. 25, pp. 24569-24599, 2018.

[9] W. Jiao, W. Chen, Y Mei, Y. Yun, B. Wang, Q. Zhong, H. Chen, W. Chen "Effects of Molecular Weight and Guluronic Acid/Mannuronic Acid Ratio on the Rheological Behavior and Stabilizing Property of Sodium Alginate," Molecules, vol. 24, no. 23, 2019.

[10] F. Abasalizadeh, S. V. Moghaddam, E. Alizadeh, E. Akbari, E. Kashani, S. M. B. Fazljou, M. Torbati, A. Akbarzadeh, "Alginate-based hydrogels as drug delivery vehicles in cancer treatment and their applications in wound dressing and 3D bioprinting," Journal of biological engineering, vol. 14, no. 8, pp. 1-22, 2020.

[11] P. Jaipan, A. Nguyen, R. J. Narayan, "Gelatin-based hydrogels for biomedical applications," MRS Communications, vol. 7, no. 3, pp. 416-426, 2017.

[12] S. Afewerki, A. Sheikhi, S. Kannan, S. Ahadian, A. Khademhosseini, "Gelatin-polysaccharide composite scaffolds for 3D cell culture and tissue engineering: Towards natural therapeutics," Bioengineering and Translational Medicine, vol. 4, no. 1, pp. 96-115, 2018.

[13] D. Chawla, T. Kaur, A. Joshi, N. Singh, "3D bioprinted alginate-gelatin based scaffolds for soft tissue

engineering," International Journal of Biological Macromolecules, vol. 144, pp. 560-567, 2019.

[14] T. Pan, W. Song, X. Cao, Y. Wang, "3D bioplotting of gelatin/alginate scaffolds for tissue engineering: influence of crosslinking degree and pore architecture on physicochemical properties," Journal of Materials Science & Technology, vol. 32, no. 9, pp. 889-900, 2016.

[15] L. Baldino, S. Cardea, E. J. C. E. T. Reverchon, "Natural aerogels production by supercritical gel drying," Chemical Engineering Transactions, vol. 43, pp. 739-744, 2015.

[16] R. Rodríguez-Dorado, C. López-Iglesias, C. A. García-González, G. Auriemma, R. P. Aquino, P. Del Gaudio, "Design of aerogels, cryogels and xerogels of alginate: Effect of molecular weight, gelation conditions and drying method on particles' micromeritics," Molecules, vol. 24, no. 6, p. 1049, 2019.

[17] L. Baruch, M. Machluf, "Alginate–chitosan complex coacervation for cell encapsulation: Effect on mechanical properties and on long-term viability," Biopolymers: Original research on biomolecules, vol. 82, no. 6, pp. 570-579, 2006.

[18] Biological evaluation of medical devices, 10993-5, ISO, 2009.

[19] W. Y. Leong, C. F. Soon, S. C. Wong, K. S. Tee, S. C. Cheong, S. H. Gan, M. Youseffi, "In vitro growth of human keratinocytes and oral cancer cells into microtissues: an aerosol-based microencapsulation technique," Bioengineering, vol. 4.2, no. 43, pp. 1-14, 2017.

[20] C. S. Bento, S. Alarico, N. Empadinhas, H. C. de Sousa, M. E. Braga, "Sequential scCO2 Drying and Sterilisation of Alginate-Gelatine Aerogels for Biomedical Applications," The Journal of Supercritical Fluids, p. 105570, 2022.

[21] Q. Chen, X. Tian, J. Fan, H. Tong, Q. Ao, X. Wang, "An interpenetrating alginate/gelatin network for three-dimensional (3D) cell cultures and organ bioprinting," Molecules, vol. 25, no. 3, p. 756, 2020.

[22] C. M. Murphy, A. Matsiko, M. G. Haugh, J. P. Gleeson, F. J. O'Brien, "Mesenchymal stem cell fate is regulated by the composition and mechanical properties of collagen–glycosaminoglycan scaffolds," Journal of the mechanical behavior of biomedical materials, vol. 11, pp 53-62, 2012.

[23] A. M. Handorf, Y. Zhou, M. A. Halanski, W.-J. Li, "Tissue stiffness dictates development, homeostasis, and disease progression," Organogenesis, vol. 11, no. 1, pp. 1-15, 2015.

[24] J. Liu, H. Zheng, P. S. Poh, H.-G. Machens, A. F. Schilling, "Hydrogels for engineering of perfusable vascular networks," International journal of molecular sciences, vol. 16, no. 7, pp. 15997-16016, 2015.

[25] A. Barros, S. Quraishi, M. Martins, P. Gurikov, R. Subrahmanyam, I. Smirnova, A. R. C. Duarte, R. L. Reis, "Hybrid Alginate-Based Cryogels for Life Science Applications," Chemie Ingenieur Technik, vol. 88, no. 11, pp. 1770-1778, 2016.

[26] T. P. Nguyen, B. T. Lee, "Fabrication of oxidized alginate-gelatin-BCP hydrogels and evaluation of the

microstructure, material properties and biocompatibility for bone tissue regeneration," Journal of Biomaterials Applications, vol. 27, no. 3, pp. 311-21, 2012.

[27] L. Yuan, Y. Wu, J. Fang, X. Wei, Q. Gu, H. El-Hamshary, S. S. Al-Deyab, Y. Morsi, X. Mo, "Modified alginate and gelatin cross-linked hydrogels for soft tissue adhesive," Artificial cells, nanomedicine, and biotechnology, vol. 45, no. 1, pp. 76-83, 2017.

[28] F. Dehghani, N. Annabi, "Engineering porous scaffolds using gas-based techniques," Current opinion in biotechnology, vol. 22, no. 5, pp. 661-666, 2011.

[29] W. Aljohani, L. Wenchao, M. Ullah, X. Zhang, G. Yang, "Application of sodium alginate hydrogel,", vol. 3, no. 3, pp. 19-31, 2017.

Title: Basic Larval Structural Composition of Thaumetopoea Pityocampa (Denis & Schiffermüller, 1775) (Lepidoptera:Notodontidae) During Feeding Inhibition Due to Some Natural Chemicals

Authors: Beran FERİDUN, Nurver ALTUN

Basic Larval Structural Composition of *Thaumetopoea Pityocampa (Denis & Schiffermüller, 1775)* (Lepidoptera:Notodontidae) During Feeding Inhibition Due to Some Natural Chemicals

Beran FERİDUN[1] Nurver ALTUN[2*]

Abstract

Thaumetopoea pityocampa (Denis & Schiffermüller, 1775) (Lepidoptera:Notodontidae) is the most important defoliating insect for several pine species and cedars. In this study, body nutrient composition of *T. pityocampa* larvae were analyzed under feeding inhibition caused by natural chemical agents. In no-choice assays, larvae were fed ponderosa pine needles treated with oleic acid and chlorogenic acid solutions, respectively, at each of four concentrations, 0%, 25%, 50% and 75%. The neetles were as given to separate test groups. At the end of feeding experiments, antifeedant index (AFI) was calculated for each solutions with different concentrations. Then, rates of protein, lipid, glycogen and water of larvae were calculated for control and test groups. It was determined that there had been a strong relation between concentrations of solution and AFI values regarding oleic acid (r= 0.998, P < 0.05). However, there was no significant relationship between concentrations of solution and AFI values regarding chlorogenic acid (r= 0.663, P > 0.5). The most remarkable finding was a sharp decline in the level of larval glycogen during starvation period in accordance with rising concentrations of both oleic and chlorogenic acid in its food. The glycogen level of the larvae was also affected by both chemical applications

Keywords: Antifeedant index, chlorogenic acid, feeding inhibition, oleic acid, pine processionary caterpillar

1. INTRODUCTION

Plant chemicals have antibacterial, antitumor, cytotoxic to human [1] and antifeedant effects for insects. The effects of plant chemicals used in pest control (or antifeedant) occurs in a variety of ways such as feeding inhibition [2-4] and developmental delay [5]. Antifeedant chemicals play a major role in the unsuitability of host plants as food for insects. Unsuitable plants are avoided by detection of other chemical cues; such [chemical substances may have repellent or toxic properties against insects [6]. These compounds have not any negative effect to humans and environment. Moreover, pests do not develop resistance against these compounds [7]. At this point, a question comes to mind: how chemical composition

* Corresponding author: nurver.altun@erdogan.edu.tr (N. ALTUN)
[1] Gazi University, Faculty of Gazi Education, Department of Science Education, Ankara, TURKEY
[2] Recep Tayyip Erdoğan University, Arts and Sciences Faculty, Department of Biology, Rize, TURKEY
E-mail: beranfiridin@gazi.edu.tr
ORCID: https://orcid.org/0000-0002-2103-6147, https://orcid.org/0000-0002-2657-9263

Beran FERİDUN, Nurver ALTUN

Basic Larval Structural Composition of Thaumetopoea Pityocampa (Denis & Schiffermüller, 1775) (Lepido...

of the pest's body changes because of mentioned effects of these chemicals? Detecting the changes of this chemical composition is important in terms of nutritional value of pest for its natural enemies. Because, insects are significant protein resources for mammals and birds living in number of ecosystems [8]. Relationship between feeding inhibition and body components of pests such as the percentage of protein, glycogen, lipid and water, provide important clues about biological control. Chlorogenic acid as one of the plant chemical has antioxidant effect and insect repellent properties. This compound also causes delay in growth and development when consumed by insects [9]. In addition, it has been shown that chlorogenic acid has a reducing effect on the bioavailability of amino acids and reduces nutrient assimilation in Lepidopteran larvae [10], Coleopterans [11], Cicadellids [12] and small sap-sucking insects [13]. One of the most familiar fatty acids, oleic acid, released from dead members of species, has removal function to other members in American cockroaches [14-15] and two caterpillars [16]. Also, oleic acid exhibited potent feeding deterrent activity *Helicoverpa zea,* (Boddie,1850) (Lepidoptera:Noctuidae), *Lymantria dispar* (Linaaeus, 1758) (Lepidoptera:Erebidae)*, Orgyia leucostigma* (J. E. Smith, 1797) (Lepidoptera:Erebidae), and *Malacosoma disstria* (Hübner, 1820) (Lepidoptera: Lasiocampidae) [17].

The pine processionary caterpillar, *Thaumetopoea pityocampa*, (Denis & Schiffermüller, 1775), is the most important defoliating insect for several pine species [18-20]. It is one of the most destructive species to pines and cedars in central Asia, North Africa, Mediterranean countries and southern Europe [21]). It is also deleterious in Anatolia due to attacks to mentioned pine species [22-23]. Pesticides used to control pests cause water and soil pollution [24].

This study focuses on the antifeedant activity, body nutritional composition of larvae against oleic acid and chlorogenic acid. Because, insecticidal activities of oleic acid and chlorogenic acid are known. It is not known whether it has antifeedant effects on *T. pityocampa*, which is such a harmful forest pest. Therefore, body nutritional composition of *T. pityocampa* has been analyzed during the last larval stage under feeding inhibition caused by natural chemical agents.

2. MATERIAL AND METHODS

2.1. Collection of Test Insects

Larvae of *T. pityocampa* were collected from Ankara province, Beypazarı district, Turkey, from Ponderosa pine (*Pinus brutia*) (Lambert, Aylmer Bourke, 1761-1842) (Pinales:Pinaceae) trees in December 2016. The larvae were brought to laboratory and larvae to feed on Ponderosa pine needles. When the larvae reached 4th instar, they were separated and placed in a growth chambers for feeding experiment. Head capsules of the larvae were distinctively evaluated to determine the developmental stages [25]. 4th instar larvae were chosen for antifeeding activity because they were appropriate to achieve the bioassays.

2.2. Antifeedant Test

Antifeedant tests were done during the 4th larval stage. Experimental design was set up as a non-choice test with 30 larvae for each test and control groups. Each test and control group were set up with perforated 30 plastic boxes (10×15×5 cm) that include 1 larva (4th instar). Thin layer of wet sponge pieces were placed into the boxes before putting the larvae. Untreated group was formed with Ponderosa needles placed in the boxes. Test groups were separately set up with Ponderosa needles treated with oleic acid (Sigma- Aldrich, CAS Number:112-80-1) and chlorogenic acid

(Cayman, CAS Number: 327-97-9) solutions. The weight of each needle was measured before the experiment. Needles of control group were only immersed in the solvent (50% ethanol in H_2O). The solutions of test groups were prepared from chlorogenic acid powder and liquid oleic acid (Sigma- Aldrich) in different concentrations 25%, 50%, 75% using the same solvent (50% ethanol in H_2O). Then, all needles were incubated to let evaporate the solvent at 30 °C for 5 minutes before presenting the needles to larvae. Feeding experiments were conducted in a growth chambers (Caron 6015) (15±5 °C and L10: D14 Photophase). Each daily feeding experiment took 5 hour for all groups. At the end of the fifth hours, remnant of the leaves were collected and weighed. This test procedure was continued for 4 days. Amount of food consumed by larvae was calculated using initial fresh weight of needles and fresh weight of residual needles. The antifeedant index (AFI) was calculated to [26].

$$AFI = [(C-T) / (C+T)] \times 100$$

The meaning of the letters in the formula as follows, "C" is the consumption of control needles and "T" is the consumption of treated needles. Total and average consumptions were separately determined daily using thirty larvae for treated groups but the average consumption of thirty larvae of control group was also calculated. Finally, the AFI values were used in data analysis as average of 4 days for all treatments.

2.3. Determination of Protein, Glycogen, Lipid and Water Levels of Larvae

Extraction of glycogen was carried out using the method of [27] and quantification of glycogen was carried out using the method of [28]. Samples were homogenized with 10% TCA (Sigma- Aldrich, CAS

Number:76-03-9) in ice for analysis of glycogen. After filtration of the obtained extracts, it was waited for precipitation of glycogen by adding ethyl alcohol (Sigma-Aldrich) into homogenates at 35-40 °C in water bath for an overnight. Then, the tubes containing the mixtures were centrifuged at 3500 rpm and the glycogen was allocated from supernatant. Alcohol was also removed at 35 °C. All samples were retained adding 10 ml. anthrone reagent (Sigma- Aldrich, CAS Number:90-44-8) for 30 min. at 80 °C water bath [29]. Blind and standard samples (0.1 mg/ ml glycogen) were prepared in appropriate procedures. Absorbance of the samples were determined at 620 nm as spectrofotometrically (Shimadzu UV-1700). Values of glycogen of the larvae were calculated as fresh weight (mg / 100 mg) with the aid of data obtained from samples using the formula that specified in terms of procedures referred above. Determination of protein levels of the larvae were achieved using the method of [30]. The regression equation was obtained thanks to the spectrophotometric readings at 750 nm in different concentrations of standard solutions prepared from 1% albumin (Biological Industries) stock solution. Protein content of samples was calculated by substituting the absorbance values in the equation. Lipid extraction and determination of total lipid of the larvae were ensured using the method of [31]. Firstly, it was ensured that lipids transfer from the samples to the organic solvent for the determination of lipids. For this transaction, samples were homogenized in chloroform (Sigma- Aldrich) / methanol (Sigma- Aldrich) mixture (2:1, v/v) using ultrasonic homogenizer (Bandelin-2450) rotating 24000 times for a minute. The homogenate was separated from the solvent using rotary evaporator (Bibby- RE 300) and the amount of lipid was determined. The amount of water was detected by calculating differences between fresh

Beran FERİDUN, Nurver ALTUN

Basic Larval Structural Composition of Thaumetopoea Pityocampa (Denis & Schiffermüller, 1775) (Lepido...

weight and dry weight of the larvae. Homogenized larvae were dried in a sterilizer (Elektromag- M5040 P) at 50 °C for 4 hours during this process.

2.4. Data Analysis

Glycogen, protein, lipid and water levels of larvae were evaluated using variance analysis followed by SNK test for determination of significant difference among the parameters. Pearson correlation test was preferred to define the relations between antifeedant index (AFI) and concentrations of treatments. All analysis were performed using the software SPSS version 17.0 for Windows (SPSS Inc., 2008).

3. RESULTS

3.1. Anti-feedant Index of Natural Chemical Agents

The relation between AFI and treatment concentrations of chemicals is very important. Because the determination of AFI values for different concentrations of chemicals give important clues about the relationship between chemicals and the pests. In this context, the relation between AFI values and the concentrations of oleic acid was found very strong ($r = 0.998*$, $P < 0.05$; Fig. I). On the other hand, a strong relation was not found between AFI values and the concentration of chlorogenic acid ($r = 0.663\sim$, $P > 0.5$; Fig. II). At this point, a specific finding was remarkable, when the chlorogenic acid concentration rise to fifty percent from a quarter, the value of AFI was not affected from this increase. Even if this rising reached to 75 percent, the value of AFI showed unexpectedly a slight decrease ($P > 0.5$, 2-tailed, Fig. II). Briefly, these results showed that oleic acid had clearly caused a feeding inhibition but it was not possible to suppose same effect for chlorogenic acid in this experiment.
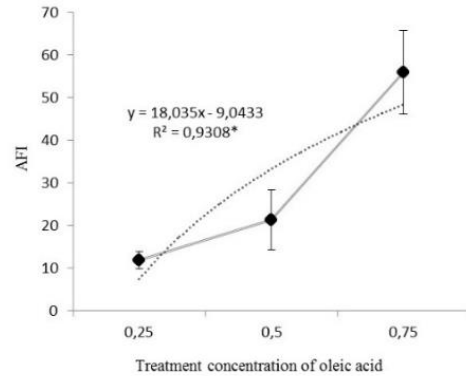

Fig 1 Relation between averages values of AFI of *Thaumetopoea pityocampa* and concentration of oleic acid. *Correlation is significant at the level of $P \leq 0.05$ (2-tailed)
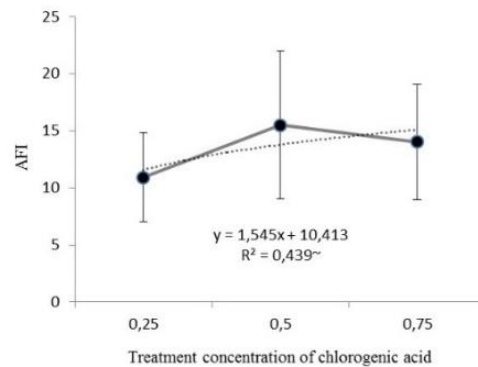

Fig. 2 Relation between averages values of AFI of *Thaumetopoea pityocampa* and concentration of chlorogenic acid. *Correlation is significant at the level of $P > 0.5$ (2-tailed)

3.2. Body Nutritional Composition of Larvae

Any differences was not determined statistically in protein, lipid and water levels of the larvae for different oleic acid concentration ($P < 0.05$, Table 1). However, the larval glycogen levels decreased in accordance with the increase in the concentration of oleic acid. Especially, when the concentration of oleic acid raised to 50 percent, glycogen level of larvae decreased by more than half ($P < 0.05$, Table 2). Similar results was determined for the larvae in experimental group of chlorogenic acid. When the concentration of chlorogenic acid raised to twofold,

glycogen level of the larvae decreased by half ($P < 0.05$, Table 2). As a result of experimental studies, the glycogen level of the larvae was also affected by both chemical applications but the applications did not affect other analyzed body components

Table 1 Protein, lipid, glycogen and water ratio of *Thaumetopoea pityocampa* fed on fresh needle of pine   added different concentrations of oleic acid. Protein, lipid, glycogen and water ratios are the average ± standard deviation of 3 replicates of measurements. Letters refers the difference between the averages as horizontal *(P < 0.05)*

Structural Substance (%)	Concentrations (%)		
	25	50	75
Protein	14,41 ± 1.53[a]	15.87 ± 3.68[a]	15.02 ± 2.43[a]
Lipid	8.02 ± 1.74[a]	8.65 ± 1.01[a]	8.14 ± 1.45[a]
Glycogen	0.86 ± 0.13[a]	0.30 ± 0.06[b]	0.22 ± 0.06[b]
Water	68.12 ± 8.33[a]	61.98 ± 5.04[a]	57.45 ± 6.27[a]

Table 2 Protein, lipid, glycogen and water ratio of *Thaumetopoea pityocampa* fed on fresh needle of pine added different concentrations of chlorogenic acid. Protein, lipid, glycogen and water ratios are the average ± standard deviation of 3 replicates of measurements. Letters refer the difference between the averages as horizontal (*P<0.05*)

Structural Substance (%)	Concentrations (%)		
	25	50	75
Protein	12.44 ± 2.34[a]	14.36 ± 1.47[a]	14.67 ± 0.64[a]
Lipid	7.01 ± 1.51[a]	6.32 ± 0.57[a]	6.48 ± 0.70[a]
Glycogen	1.14 ± 0.16[a]	0.58± 0.09[b]	0.51 ± 0.12[b]
Water	70.56 ± 3.27[a]	62.93 ± 4.53[a]	66.10 11.4[a]

4. DISCUSSION

Relationships between the tested concentrations and AFI values were analyzed at the first stage of the present study. Quantification of antifeedant effect is important for insect pest management. From an ecological point of view, antifeedants are very important since they never kill the target insects directly and allow them to be available to their natural enemies and help in the maintenance of natural balance. Higher antifeedant index normally indicate decreased rate of feeding. Antifeedant is a chemical that inhibits the feeding without killing the insect pests directly, while it remains near the treated foliage and dies through starvation [6]. It is more important to focus on the reactions of pests to different concentrations of the same solution than comparing the AFI values of the different solutions with each other. These relations were important in order to determine the level of solution deterrence. In general, antifeedants have profound adverse effects on insect feeding behavior [32]. A familiar study was carried by [33] regarding the antifeedant effect of chlorogenic acid. These researchers found the important findings about the antifeedant properties of chlorogenic acid against various leaf beetles. They identified that chlorogenic acid had antifeedant property on three leaf beetles but excluding *Plagiodera versicolora* ssp. *distincta*. The results of the study are remarkable in terms of differences in the level of deterrence of chlorogenic acid among the same family of insects. For all that, chlorogenic acid had not an antifeedant effect against the larvae of *T. pityocampa* in this study. [34] transferred the second - fifth instar larvae of

Beran FERİDUN, Nurver ALTUN

Basic Larval Structural Composition of Thaumetopoea Pityocampa (Denis & Schiffermüller, 1775) (Lepido...

cabbage butterfly *Pieris rapae* from cabbage to garden nasturtium, *Tropaeolum majus* (Tropaeolaceae). They observed that the larvae refused to feed and died after this transfer due to starvation. They also thought that this refusal can be stemmed from chlorogenic acid found in nasturtium leaves. However, we can easily express that chlorogenic acid has not any negative effect on the feeding of the larvae of *T. pityocampa*, because this determination was directly based on my observations on the larval feeding behavior. [35] stated that chlorogenic acid was mild stimulant at intermediate concentrations but deterrent at higher concentrations for japanese beetle *Popillia japonica* in artificial diets. In this study, when the concentration of cholorogenic acid was raised double, antifeedant index values changed from 10.95 to 15.52 (Fig 2). Even the concentration was increased tripled, AFI values changed from 10.95 to 14.04 (Fig 1). These results revealed that larvae of *T. pityocampa* were insensitive to higher concentration of chlorogenic acid. Similarly, [36] found that *Lochmaea capreae* was only affected from pure chlorogenic acid among four tested leaf beetle species. It is understood that the defensive effect of pure chlorogenic acid was very limited against willow leaf beetles compatible with the findings of my study on pine processionary caterpillar [37] showed that *P. rapae* caterpillars, reared on artificial diet, did not distinguish between leaf discs treated with chlorogenic acid and solvent, whereas cabbage-reared caterpillars avoided chlorogenic acid-treated leaf material. The results of mentioned study showed that the sensitivity of neonate larvae decreased over time against some secondary chemicals if the larvae were not encountered them in the natural foods or the development of sensitivity against deterrents may be directly related to larval stage as mentioned by [34]. In Lepidoptera larvae, taste neurons are located on the ventral surface of the labrum, maxillary palps, and galea. Insects that have been exposed to deterrent compounds in particular show reduced susceptibility. Sensitivity can change with habitutation [34]. Therefore, the reason why the chlorogenic acid AFI values of *T. pityocampa* larvae did not change depending on the dose may be due to habituation. If the feeding deterrent property is evaluated in terms of oleic acid, the results of present study are exactly different regarding the chlorogenic acid. Because, the relation between AFI and concentration of oleic acid was found to be very strong compatible with the study of [16] where used social caterpillars, *Hyphantria cunea* and *Malacosoma americanum*. The agreement between the results of two studies are very remarkable, because Pine processionary caterpillars also exhibits social life. The fact that oleic acid showed a strong feeding deterrent on the larvae of *T. pityocampa* was not obviously a surprise. Because there is a tight relationship between monofag-oligofag species and smell-taste of their host plants. Any external factors that disrupt this relationship can negatively affect to feeding behavior of the species [38]. In this context, it may be considered a repellent feature of oleic acid, but not such a feature of chlorogenic acid on feeding performance of *T. pityocampa*. [39] also demonstrated that oleic acid is produced by *Monosteria unicostata* and its predator *Piocoris luridus* as seen in most animals, although almond tissues provide very little oleic acid to the herbivore *P. luridus*. This finding supported the idea that oleic acid has some metabolic [40-41] and ecological [14-16] tasks in insects.

Another important point was the body nutrient composition of the larvae during feeding experiment period on this study. The most statistically remarkable findings about this issue were a sharp decline (from

Beran FERİDUN, Nurver ALTUN

Basic Larval Structural Composition of Thaumetopoea Pityocampa (Denis & Schiffermüller, 1775) (Lepido...

0.86% to 0,22%) in the level of larval glycogen of *T. pityocampa* with increasing concentrations of oleic acid and relatively soft decline (from 1.14 to 0.51%) with increasing concentrations of chlorogenic acid in their food. For all that, other parameters (protein, lipid, water) were not affected from rising concentrations of these chemical. These results differ from those of [42]. When *H. cunea* larvae were fed on different foods, the highest amount of pupal protein was determined in the pupae of larvae fed with mulberry leaves containing the least chlorogenic acid. Another difference is that the highest amount of lipid was detected in pupae of individuals fed with plum leaves containing the highest chlorogenic acid [42]. In addition, increasing the dose of oleic acid does not affect the amount of lipid in our study (Table 2). Administration of lufenuron to *Xanthogaleruca luteola* individuals showed no significant change in storage macromolecules at LC_{30} concentration [43]. This result is similar to our study. Hovewer, [43]. an increase in the amount of storage macromolecules was observed at the LC_{50} dose. It is known that important energy sources are also glycogen and fat tissue in insects such as other organisms. At the same time, the first energy sources is glycogen in the execution of metabolic and physical activity in insects [44-46]. Probably, glycogen was primarily used by the larvae during emerged starvation after the deterrent effect due to oleic acid. Especially, at the end of the fourth day of the experiment with the solution of oleic acid (75%), We clearly observed that a disease state occur in the larvae. Nutrient composition of insects's body is definitely important for their predators. It brings to mind the idea that pine processionary caterpillars developed several adaptations against predation risks with respect to life characteristics such as to be nocturnal and social. These life features of caterpillars may be associated with being a nourishing prey. How body nutrient composition of the larvae will change while the state of starvation. As a result of this study, It was found that there is not any significant change in the body nutritional composition of the larvae, except glycogen.

As a conclusion, *T. pityocampa* is an important forest pest. Although many studies have been carried out on the species, an effective control method has not been determined. Antifeedant index value is important for insect management. In this study, chlorogenic acid had not an antifeedant effect against the larvae of *T. pityocampa*. When the concentration of chlorogenic acid was raised double, AFI values raised. Even the concentration was increased triple, the increase in value was less. It was determined that there had been a strong relation between concentrations of solution and AFI values regarding oleic acid. The most remarkable finding was a sharp decline in the level of larval glycogen during starvation period in accordance with rising concentrations of both oleic and chlorogenic acid in its food.

In future studies, more comprehensive and analytical assessment can be made about conversion of organic and inorganic matters of the caterpillars by incorporation specific feces analysis during starvation periods in this concept. Besides deterrence effects of the solutions, it should not be overlooked that reverse effect of the solutions on chemical digestion as stated that [47]. This is important in terms of nutritional composition of the insect's body.

The Declaration of Conflict of Interest/ Common Interest

No conflict of interest and common interest has been declared by the authors.

Authors' Contribution

"The first author contributed 60%, the second author 40%." expressions such as should be included.

The Declaration of Ethics Committee Approval

This study doesn't require ethics committee approval and any special permission

The Declaration of Research and Publication Ethics

In the writing process of this study, international scientific, ethical and citation rules were followed, and no falsification was made on the collected data. Sakarya University Journal of Science and its editorial board have no responsibility for all ethical violations. All responsibility belongs to the responsible author and this study has not been evaluated in any academic publication environment other than Sakarya University Journal of Science.

REFERENCES

[1] A. Kaplan, "Phytochemical Screening of Bioactive Components of Medicinal Plant *Ajuga chamaepitys subsp. laevigata* (Banks & Sol.) P.H.Davis and *Ajuga bombycina* Boiss.by GC-MS Analysis", Sakarya University Journal of Science 24(5), pp. 1053-1064, 2020.

[2] K. D. Klepzig, F. Schlyter, "Laboratory evaluation of plant derived antifeedants against the pine weevil *Hylobius abietis* (Coleoptera: Curculionidae)", Journal of Economic Entomology, vol. 92, pp. 644-650, 1999.

[3] D. A. Wheeler, M. B. Isman, "Antifeedant and toxic activity of *Trichilia americana* extract against the larvae of *Spodoptera litura*", Entomologia Experimentalis et Applicata, vol. 98, pp. 9 –16, 2001.

[4] O. Koul, "Phytochemicals and Insect Control: An Antifeedant Approach", Critical Reviews in Plant Sciences, vol. 27, pp. 1-24, 2008.

[5] M. Breuer, G. H. Schmidt, "Influence of a short period treatment with *Melia azedarach* extract on food intake and growth of the larvae of *Spodoptera frugiperda* (J. E. Smith) (Lep., Noctuidae)", Journal of Plant Disease and Protection, vol. 102, number 8, pp. 633 – 654, 2014.

[6] S. Arivoli, S. Tennyson, "Antifeedant activity, developmental indices and morphogenetic variations of plant extracts against *Spodoptera litura* (Fab) (Lepidoptera: Noctuidae)", Journal of Entomology and Zoology Studies, vol. 1, no. 4, pp. 87-96, 2013.

[7] A. Prakash, J. Rao, "Botanical pesticides in agriculture", CRC Press Inc, USA, 46, 1997.

[8] Z. S. Zhang, X. G. Lu, Q. C., Wang, D. M. Zheng, "Mercury, cadmium and lead biogeochemistry in the soil plant-insect in Hulado City", Bulletin Environmental Contamination Toxicology, vol. 83, pp. 255-259, 2009.

[9] E. N. Matu, "*Solanum incanum* L. PROTA (Plant Resources of Tropical

Beran FERİDUN, Nurver ALTUN

Basic Larval Structural Composition of Thaumetopoea Pityocampa (Denis & Schiffermüller, 1775) (Lepido...

Africa)" Wageningen Netherlands, Protabase, 2008.

[10] N. Mallikarjuna, K. R. Kranthi, D. R. Jadhav, S. Kranthi, S. Chandra S, "Influence of foliar chemical compounds on the development of *Spodoptera litura* (Fab.) in interspecific derivatives of groundnut", Journal of Applied Entomology, vol. 128, no. 5, pp. 321-328, 2004.

[11] A. R., Jassbi, "Secondary metabolites as stimulants and antifeedants of *Salix integra* for the leaf beetle *Plagiodera versicolora*. Verlag der Zeitschrift für Naturforschung, vol. 58, pp. 573-9, 2003.

[12] P. F. Dowd, F. E. Vega, "Enzymatic oxidation products of allelochemicals as a basis for resistance against insects: effects on the corn leafhopper *Dalbulus maidis*". Natural Toxins, vol. 4, pp. 85-91, 1996.

[13] P. W. Miles, J. J. Oertli, "The significance of antioxidants in the aphid-plant interaction: the redox hypothesis". Entomologia Experimentalis et Applicata, vol. 67, pp. 275-83, 1993.

[14] C. D. Rollo, E. Czvzewska, J. H. Borden, "Fatty acid necromones for cockroaches". Naturwissenschaften, vol. 81, number 9, pp. 409-410, 1994.

[15] C. D. Rollo, J. H. Borden, I. B. Casey, "Endogenously produced repellent from American cockroach (Blattaria: Blattidae): Function in death recognition". Environmental Entomology, vol. 24, number 1, pp. 116-124, 1995.

[16] M. Yao, J. Rosenfeld, S. Attridge, S. Sidhu, V. Aksenov, C. D. Rollo, "The ancient chemistry of avoiding risks of predation and disease." Evolutionary Biology, vol. 36, pp. 267- 281, 2009.

[17] R. S. Ramsewac, M. G. Nair, S. Murugesan, W. J. Mattson, J. Zasada, "Insecticidal fatty acids and triglycerides from *Dirca palustris*". Journal of Agricultural and Food Chemistry, vol. 49, pp. 5852-5856, 2001.

[18] J. A. Hodar, R. Zamora, "Herbivory and climatic warming: a Mediterranean outbreaking caterpillar attacks a relict, boreal pine species". Biodiversity & Conservation, vol. 13, pp. 493–500, 2004.

[19] P. A. Arnaldo, L. M. Torres, "Spatial distribution and sampling of *Thaumetopoea pityocampa* (Den.&Schiff) (Lep. Thaumetopoeidea) populations on *Pinus pinaster* Ait. in Montesinho N. Portugal". Forest Ecology and Management, vol. 210, pp. 1–7, 2005.

[20] C. Pimentel, T. Calvao, M. Santos, C. Ferreira, M. Neves, J. A. Nilsson, "Establishment and expansion of a *Thaumetopoea pityocampa* (Den.& Schiff.) (Lep: Notodontidae) population with a shifted life cycle in a production pine forest, Central-Coastal Portugal. Forest Ecology and Management, vol. 233, pp. 108–115, 2006.

[21] C. Kerdelhué, L. Zane, M. Simonato, P. Salvato, J. Rousselet, A. Roques, A. Battisti, "Quaternary history and contemporary patterns in a currently expanding species". BMC Ecology and Evolution, vol. 9, number 1 pp. 1-14, 2009.

Beran FERİDUN, Nurver ALTUN

Basic Larval Structural Composition of Thaumetopoea Pityocampa (Denis & Schiffermüller, 1775) (Lepido...

[22] A. Durkaya, B. Durkaya, I. Dal, The effects of the pine processionary moth on the increment of crimean pine trees in Bartın, Turkey. African Journal of Biotechnology, vol. 8, number 10, pp. 2356-2361, 2009.

[23] M. Kanat, H. Alma, F. Sivrikaya , "Effect of defoliation by *Thaumetopoea pityocampa* (Den. & Schiff.) (Lepidoptera: Thaumetopoeidae) on annual diameter increment of *Pinus brutia* Ten. in Turkey. Annals of Forest Science, vol. 62, pp. 91-94, 2005.

[24] H. S. Canbay, S. Öğüt, "Organik ve organik olmayan elmalar ile çiftçilerde pestisit kalıntıları ve toplam antioksidan kapasiteleri", Sakarya Üniversitesi Fen Bilimleri Enstitüsü Dergisi, 21 (6), 1558~1565, 2017.

[25] C. C. Daiber, "A study of the biology of the false codling moth *Cryptophlebia leucotreta* (Meyr.): The larva". Phytophylactica 11: 141-144, 1979.

[26] A. C. Lewis, H. F. Van Emden, "Assays for insect feeding, In: Insect–Plant Interactions (J. R. Miller and T. A. Miller eds.), Springer Verlag, New York, pp. 95–119, 1986.

[27] J. H. Roe, J. M. Bailey, R. R. Gray, J. N. Robinson, "Complete removal of glycogen from tissues by extraction with cold trichloroacetic acid solution". Journal of Biological Chemistry, vol. 236, pp. 1244-1246, 1961.

[28] N. V. Carroll, R. W. Longley, J. H. Roe, "The determination of glycogen in liver and muscle by use of anthrone reagent". Journal of Biological Chemistry, vol. 220, pp. 583–93, 1956.

[29] D. T. Plummer, "An introduction of practical biochemistry". McGraw-Hill Book Companies, London, United Kingdom, 1971.

[30] O. H. Lowry, N. J. Rosebrough, A. L. Farr, R. J. Randall, "Protein measurement with the Folin phenol reagent". Journal of Biological Chemistry, vol. 193, number 1, pp. 265–275, 1951.

[31] J. Folch, M. Lees, G. H. Sloane Stanley, "A simple method for the isolation and purification of total lipids from animal tissues". Journal of Biological Chemistry, vol. 226, pp. 497–509, 1957.

[32] L. A. Hummelbrunner, M. B. Isman, "Acute, sublethal, antifeedant and synergestic effects of monoterpenoid essential oil compounds on the tobacco cutworm *Spodoptera litura* (Lepidoptera: Noctudiae)". Journal of Agricultural and Food Chemistry, vol. 49, pp. 715-720, 2001.

[33] K. Matsuda, S. Senbo , "Chlorogenic acid as a feeding deterrent for Salicaceae-feeding leaf beetles *Lochmaeae caprae cribrata* (Coleoptera: Chrysomelidae) and other species of leaf beetles". Applied Entomology and Zoology (Japan), vol. 21, pp. 411-416, 1986.

[34] J. A. A. Renwick, X. P. Huang, "Rejection of host plant by larvae of cabbage butterfly: diet-dependent sensitivity to an antifeedant". Journal of Chemical Ecology, vol. 21, pp. 465–475, 1975.

[35] A. F. Fulcher, T. G. Ranney, J. D. Burton, J. F. Walgenbach, D. A. Danehower, "Role of foliar phenolics in host plant resistance of *Malus taxa* to adult Japanese beetles". Hortical Science, vol. 33, number 5, pp. 862-865, 1998

[36] A. Ikonen, J. Tahvanainen, H. Roininen, Chlorogenic acid as an antiherbivore defence of willows against leaf beetles". Entomologia Experimentalis et Applicata, vol. 99, pp. 47–54, 2001.

[37] D. S. Zhou, C. Z. Wang, J. J. A. van Loon, "Chemosensory basis of behavioural plasticity in response to deterrent plant chemicals in the larva of the small cabbage white butterfly *Pieris rapae*". Journal of Insect Physiology, vol. 55, number 9, pp. 788-792, 2009.

[38] J. B. Harborne, Introduction to Ecological Biochemistry. Academic Press. 3rd Edt., 1982.

[39] O. Cakmak, M. Bashan, H. Bolu, "The fatty acid compositions of predator *Piecoris luridus* (Heteroptera: Lygaidea) and its host *Monosteria unicostata* (Heteroptera: Tingidae) reared on almond". Insect Science, vol. 14, pp. 461-466, 2007.

[40] V. A. Bennett, N. L. Pruitt, Jr. R. E. Lee, "Seasonal changes in fatty acid composition associated with cold-hardening in third instar larvae of *Eurosta solidaginis*". Journal of Comparative Physiology B, vol. 167, number 4, pp. 249-255, 1997.

[41] M. Bashan, O. Cakmak, "Changes in phosholipid and triacylglycerol fatty acids prepared from prediapausing and diapausing individuals of *Dolycoris baccarum* and *Piezodorus lituratus* (Heteroptera: Pentatomidae). Annals of Entomological Society of America, vol. 98, number 4, pp. 575-579, 2005.

[42] E. F. Topkara, "Effects of Selected Plant Secondary Metabolites in Mulberry, Apple, Plum, and Walnut on the Pupal Parameters of *Hyphantria cunea* Drury, 1773 (Lepidoptera: Arctiidae) Larvae Infected by *Bacillus thuringiensis subsp. kurstaki*". Journal of Entomological Research Society, vol. 24, number 1, pp. 75-87, 2022.

[43] B. Mohammadzadeh Tamam, M. Ghadamyari, E. Shafiei Alavijeh, "Biological and biochemical effects of lufenuron on *Xanthogaleruca luteola* (Muller, 1766) (Coleoptera: Chrysomelidae)". Acta Agriculturae Slovenica, vol. 118, number 4, pp. 1–8, 2022.

[44] M. A. N. Akpinar, N. Akpinar, L. Gencer, S. Türkoğlu, "Fatty acid composition of *Gryllus campestris* L. (Orthoptera: Grillidae) during its various development stage". Biologia (Bratislava), vol. 58, number 6,pp. 1053-1059, 2003.

[45] M. W. Lorenz MW, A. N. Anand, "Changes in the biochemical composition of fat body stores during adult development of female crickets, *Gryllus bimaculatus*". Archiev of Insect Biochemistry and Physiology, vol. 56, pp. 110-119, 2004.

[46] B. Firidin, "Pamuk yaprak kurdu *Spodoptera littoralis* (Boisduval) (Lepidoptera: Noctuidae) larvalarının gelişim evrelerinde protein, glikojen ve su oranındaki değişim". Tekirdağ

Beran FERİDUN, Nurver ALTUN

Basic Larval Structural Composition of Thaumetopoea Pityocampa (Denis & Schiffermüller, 1775) (Lepido...

Ziraat Fakültesi Dergisi, vol. 13, pp. 34-39, 2016.

[47] P. Feeny, "Plant apparency and chemical defense". Recent Advances in Phytochemistry, vol. 10, pp. 1-40, 1976.

Sakarya University Journal of Science
SAUJS

Title: Parameter Estimation of Induction Motors using Hybrid GWO-CS Algorithm

Authors: Selcuk EMİROGLU

Parameter Estimation of Induction Motors using Hybrid GWO-CS Algorithm

Selçuk EMİROĞLU *1 iD

Abstract

This study investigates a hybrid algorithm between Grey Wolf Optimization (GWO) and Cuckoo Search (CS) algorithms to find the parameters of induction motors. The parameters of the induction motor have been estimated by using the data supplied by the manufacturer. The problem for parameter estimation of the induction motor is formulated as an optimization problem. Then, the optimization problem is solved by using GWO and hybrid algorithm based on GWO and CS algorithms for the estimation of induction motor parameters. Numerical results show that both algorithms are capable of solving the optimization problem for finding the parameters of induction motor. Also, two algorithms and other algorithms such as Differential Evolution (DE), Genetic Algorithm (GA), Particle Swarm Optimization (PSO), Shuffled Frog-Leaping Algorithm (SFLA), and Modified Shuffled Frog-Leaping Algorithm (MSFLA) are compared for the problem. The results show that the hybrid GWO-CS algorithm gives a smaller objective value and closer torque value to the manufacturer's data than the GWO algorithm and several algorithms for motor 1. Hybrid GWO-CS algorithm gives nearly the same results with GWO algorithm for motor 2.

Keywords: Parameter estimation, induction motors, grey wolf optimization, cuckoo search optimization, hybrid algorithm

1. INTRODUCTION

Induction motors are widely used in many applications due to their simple construction, ease of use, low cost of maintenance, and durability [1].

Equivalent circuit parameters for induction machines are necessary for control, design of the controller, dynamic simulations, etc. [2]. The circuit parameters for a motor, however, are typically not provided by the manufacturer [3].

The typical values obtained in the literature are frequently not exact enough because the parameters are motor-specific. Therefore, it is preferable to estimate motor equivalent circuit parameters using the information provided by manufacturers in their catalogs, such as full load torque, full load power factor, breakdown torque, etc. It is important to find the parameters correctly for simulations, design, or control, etc. [4]. So, accurate modeling is viewed as a significant issue for induction machines in order to

* Corresponding author: selcukemiroglu@sakarya.edu.tr
1 Sakarya University, Faculty of Engineering, Department of Electrical and Electronics Engineering
ORCID: https://orcid.org/0000-0001-7319-8861

attain the target performance of induction machines. The accurate modeling of induction machines is a significant issue, especially in terms of drives and control of them which affect the efficiency.

Also, various research studies in the literature have made significant efforts to determine the parameters of induction machines. For decades, meta-heuristic algorithms have been used to solve the parameter estimation problems of induction machines, such as Genetic Algorithm (GA), Particle Swarm Optimization (PSO), etc. GA is employed the offline parameter estimation of the induction motors considering magnetic saturation and iron losses in [5]. Also, Grey Wolf Optimization (GWO), Jaya Algorithm, and Cuckoo Search (CS) have been used for the parameter identification of DC motors with dynamic response relations [6]. A global optimum solution can be obtained in less time with these methods, which are easy to implement in the problem of parameter estimation. But hybrid algorithms have been studied in solving the parameter estimation problem in few works. They have been developed for effectively solving optimization problem recently. It has been shown in many studies that hybrid algorithms give good results. In [7], the parameters of poly-phase induction motors are estimated by a hybrid optimization algorithm between PSO and Jaya algorithms. The parameters of double-cage induction motors are also estimated by using a hybrid metaheuristic algorithm with the help of Phasor Particle Swarm Optimization (PPSO) and Gravitational Search Algorithm (GS) [8]. The performance of the hybrid algorithm has been tested on different motors [8].

The parameter estimation of induction motors has been done using GWO and hybrid GWO-CS algorithms and compared with some heuristic-based techniques, including GA, Differential Evolution (DE), PSO, Shuffled Frog-Leaping Algorithm

(SFLA) and Modified Shuffled Frog Leaping Algorithm (MSFLA).

2. PROBLEM DEFINITION

The model of the induction motor can be obtained by using an equivalent circuit under steady state [9]. The parameter of induction motor is estimated based on optimization using the equivalent circuit. So, the problem of parameter estimation for induction motors is formulated as an optimization problem. By minimizing the objective function which corresponds the square of the difference between manufacturer 'data and estimated data, the parameters can be estimated. The optimization problem uses an objective function and some constraints to find the parameters of induction motor. The optimization problem is solved by using GWO and hybrid GWO-CSO algorithms. The motor data provided by manufacturer such as the maximum torque, starting torque, the full load torque and power factor under full load are used in optimization problem. As a result of optimization problem, the rotor and the stator resistances, the rotor, stator, and magnetizing reactance can be estimated.
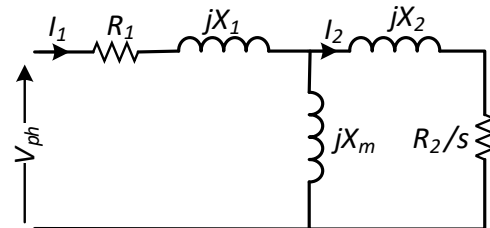

Figure 1 Single-phase steady-state equivalent circuit of a three-phase induction motor

The equivalent circuit model of an induction motor under a steady state is shown in Fig. 1. R_1, R_2, X_1, X_2, and X_m are the stator resistance, rotor resistance transferred to the stator side, stator leakage reactance, rotor leakage reactance transferred to the stator side, and magnetizing reactance, respectively. As can be seen in Fig. 1, the rotor parameters are referred to the stator and

also the core losses are assumed to be negligible.

The aim of the optimization is to find the parameters of the induction motor. An optimization problem is solved by minimizing the objective function satisfying several constraints. Based on the manufacturer's data, the multi-objective function can be written as follows.

$$Objective = F_1^2 + F_2^2 + F_3^2 + F_4^2 \qquad (1)$$

where,

$$F_1 = \frac{T_{st,est} - T_{st,md}}{T_{st,md}} \qquad (2)$$

$$F_2 = \frac{T_{max,est} - T_{max,md}}{T_{max,md}} \qquad (3)$$

$$F_3 = \frac{T_{fl,est} - T_{fl,md}}{T_{fl,md}} \qquad (4)$$

$$F_4 = \frac{p_{fl,est} - p_{fl,md}}{p_{fl,md}} \qquad (5)$$

here, T_{st}, T_{max} T_{fl}, and p_{fl} are the starting torque, maximum torque, full load torque, and power factor at full load, respectively. Subscript *md* and *est* represent the manufacturer and estimated data, respectively. Also, the parameter limits need to be considered as inequality constraints. So, the optimization problem has to satisfy the constraints given below. Eq. 6 contains inequality constraints for the problem.

$$\begin{aligned}
R_{1_{min}} &\leq R_1 \leq R_{1_{max}} \\
R_{2_{min}} &\leq R_2 \leq R_{2_{max}} \\
X_{1_{min}} &\leq X_1 \leq X_{1_{max}} \\
X_{2_{min}} &\leq X_2 \leq X_{2_{max}} \\
X_{m_{min}} &\leq X_m \leq X_{m_{max}}
\end{aligned} \qquad (6)$$

The upper bounds for the parameters of the motors are given as [0.6 0.6 0.5 0.5 11] for

motor 1 and [100 100 100 100 100] for motor 2 and the lower bounds are given as [0.1 0.2 0.1 0.1 4] for motor 1 and [0.001 0.1 0.1 0.1 0.1] for motor 2 corresponding to [R_1 R_2 X_1 X_2 X_m]. The GWO and hybrid GWO-CS algorithms are applied for the estimation of induction motor parameters.

To calculate the torque value of the motor for the solution of the problem in terms of slip, firstly, the stator current needs to be calculated with the following equation [9].

$$\overline{I}_1(s) = \frac{\overline{V}_{ph}}{R_1 + jX_1 + \overline{Z}_p(s)} \qquad (7)$$

where

$$\overline{Z}_p(s) = \frac{1}{\dfrac{1}{jX_m} + \dfrac{1}{\dfrac{R_2}{s} + jX_2}} \qquad (8)$$

Then, the rotor current can be expressed as below.

$$I_2(s) = \frac{\overline{Z}_p(s) \cdot \overline{I}_1(s)}{\dfrac{R_2}{s} + jX_2} \qquad (9)$$

Finally, torque is calculated as

$$T(s) = \frac{3p}{\omega_s} [I_2(s)]^2 \frac{R_2}{s}. \qquad (10)$$

Therefore, the torque at full load and starting is calculated as $T(s_{fl})$ and $T(1)$, respectively. Also, maximum torque $T(s_{max})$ can be obtained using

$$s_{max} = \frac{R_2}{\sqrt{R_{th}^2 + (X_{th} + X_2)^2}} \qquad (11)$$

where

$$Z_{th} = R_{th} + jX_{th} = \frac{1}{\dfrac{1}{R_1 + jX_1} + \dfrac{1}{jX_m}} \qquad (12)$$

Then, the power factor can be calculated as follows [10].

$$pf = \cos\varphi = \cos(\arg(Z_{in})) \qquad (13)$$

where

$$Z_{in} = R_1 + jX_1 + \frac{jX_m\left(\dfrac{R_2}{s} + jX_2\right)}{\dfrac{R_2}{s} + j(X_m + X_2)} \qquad (14)$$

3. HYBRID GWO-CS ALGORITHM

Recently, two or more algorithms have been used together, called a hybrid to find a better solution for the optimization problems [11]. The GWO technique is proposed by Seyedali Mirjalili and Andrew Lewis to solve numerous optimization problems in many disciplines [12]. This algorithm emulates the typical hunting cooperative behavior of grey wolves [13]. The social leadership structure and the hunting behavior of grey wolves in nature serve as the primary driving forces behind this algorithm [12, 14].

Due to its varied lives and aggressive reproduction, the cuckoo bird serves as an inspiration for the CS [11, 15-17].

The traditional GWO has a strong ability to exploit local solutions, while the traditional CS has a strong ability to explore global solutions in the space [18]. Due to a weak ability of global search, GWO can fall into local minimum easier.

So, it is useful to combine GWO and CS algorithms to get the advantages of these two algorithms [19]. CS can update the next positions independently of the search path [17]. Therefore, moving from current place to another is considerably easier in CS algorithm. So, CS is utilized to update the positions of search agents and get new ones for GWO [20]. The flowchart of the hybrid GWO-CS algorithm is depicted in Fig. 2.
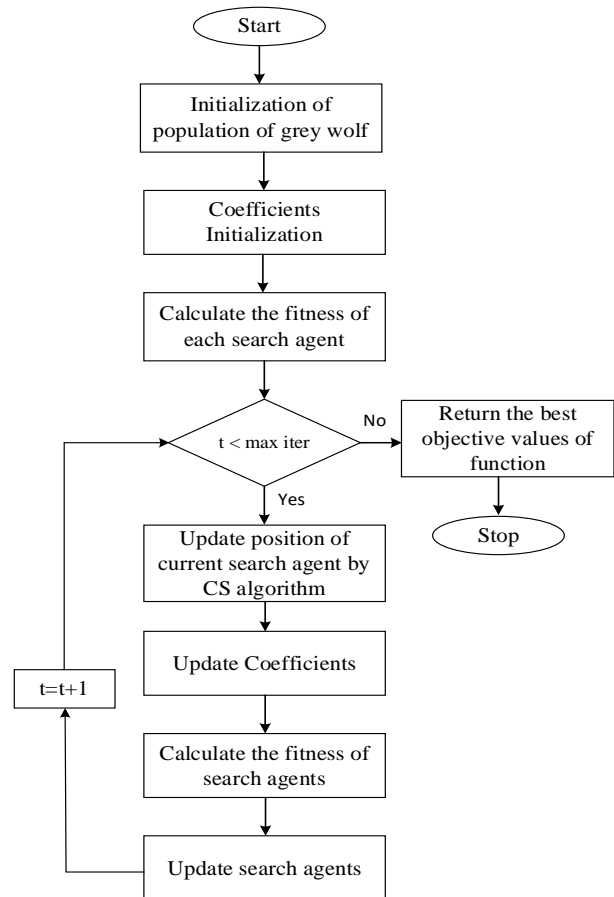

Figure 2 The flowchart of GWO-CS algorithm [11]

4. SIMULATION RESULTS

The hybrid GWO-CS and GWO algorithms have been tested on two motors with 40 HP and 5 HP. The manufacturer data of the two motors are given in Table 1.

Also, proposed hybrid GWO-CS and GWO algorithms are compared with several algorithms such as DE, GA, PSO, SFLA, and MSFLA algorithms.

To show the performance of the proposed approach, two different motors are considered. Tables 2 and 3 show the estimated parameters obtained with the proposed approach and several algorithms for motor 1 and motor 2, respectively. Also, objective function values for proposed approach and other algorithms are given in Tables 2 and 3. Objective values obtained with the proposed approaches for motor 1

are the smallest among all algorithms given in Table 2. In addition, the hybrid GWO-CS algorithm gives a smaller objective value than the GWO algorithm.

As seen in Table 3, the proposed approach has the smallest objective value, but it has an equal objective value with MSFLA algorithm for motor 2. Moreover, hybrid GWO-CS and GWO algorithms give the same objective value with the MSFLA. Besides, the parameters estimated hybrid GWO-CS, GWO and MSFLA are nearly same.

In Tables 4 and 5, starting torque, full load torque, maximum torque, and full load power factor values of the motors obtained from various algorithms and given by the manufacturer are given with the percent error.

Table 1 Manufacturer's data of the induction motors [9]

Parameter	Motor 1	Motor 2
P_n	40 HP	5 HP
V	400 V	400 V
f	50 Hz	50 Hz
p	2	2
T_{st}	260 Nm	15 Nm
T_{fl}	190 Nm	25 Nm
T_{max}	370 Nm	42 Nm
pf_{fl}	0.8	0.8
s_{fl}	0.09	0.07

The errors of starting torque, full load torque, maximum torque, and full load power factor results for motor 1 obtained from the proposed approach GWO-CS and GWO are the smallest among the results of other algorithms in Table 4. Moreover, the results of the hybrid GWO-CS algorithm

compared with the results of GWO are the closest to manufacturer data except for the maximum torque value of motor 1. However, the maximum torque values obtained with GWO-CS and GWO algorithms are very close to each other and manufacturer's data.

The proposed algorithms give the closest value to manufacturer data for motor 2 except maximum torque value as can be seen in Table 5. However, the results of proposed approach for the maximum torque value of motor 2 are close the results of other algorithms.

Fig. 3 and 4 show the curves of the torque versus rotor speed for motor 1 and motor 2, respectively. Both curves shown in Fig. 3 and 4 are obtained with GWO and hybrid GWO-CS algorithm. The red and blue dash line represent the curves obtained with GWO and GWO-CS, respectively.

As shown in Fig. 3, the results obtained with both the GWO-CS and GWO algorithms are close to the manufacturer's data, while the results of the starting and maximum torque values obtained with the GWO-CS appear to be closer to the manufacturer's data than those obtained with the GWO.

One can deduce from Fig. 4 that the results obtained with GWO-CS and GWO algorithms are very similar to each other. The parameters found by GWO-CS and GWO algorithm have already been estimated almost the same. The maximum torque value is estimated with more error regarding the starting torque and power factor for motor 2.

Table 2 Estimated parameters of the induction motor 1 (40 HP) and objective value for several and proposed algorithms

Parameter (Ω)	DE [9]	GA [9]	PSO [9]	SFLA [9]	MSFLA [9]	GWO	GWO-CS
Objective Value	1.0e-04	5.0e-04	1.0e-04	1.0e-05	1.0e-06	**4.53e-08**	**1.196e-08**
R_1	0.4993	0.4875	0.3555	0.3437	0.2707	**0.2783**	**0.2779**
R_2	0.3264	0.3264	0.3455	0.3360	0.3573	**0.3609**	**0.3611**
X_1	0.3510	0.3556	0.4353	0.4345	0.4773	**0.4793**	**0.4796**
X_2	0.3510	0.3556	0.4353	0.4345	0.4773	**0.4793**	**0.4796**
X_m	5.6967	6.0718	6.4223	6.2629	7.5432	**7.5940**	**7.6014**

Table 3 Estimated parameters of the induction motor 2 (5 HP) and objective value for several and proposed algorithms

Parameter (Ω)	DE [9]	GA [9]	PSO [9]	SFLA [9]	MSFLA [9]	GWO	GWO-CS
Objective Value	0.0023	0.0045	0.0023	0.0023	0.00228	**0.00228**	**0.00228**
R_1	0.1838	1.1316	0.9872	0.0008	0.003681	**0.0001**	**0.0005**
R_2	2.1009	2.0330	2.0322	2.1330	2.181757	**2.2053**	**2.2058**
X_1	5.6197	5.3750	5.3785	5.5847	5.720209	**5.779**	**5.7794**
X_2	5.6197	5.3750	5.3785	5.5847	5.720209	**5.779**	**5.7794**
X_m	99.1792	87.1944	77.0420	77.9101	94.140145	**95.6469**	**95.5969**

Table 4 Torque – power factor values of the induction motor 1 (40 HP) and error for several and proposed algorithms

	T_{st} (Nm)		T_{fl} (Nm)		T_{max} (Nm)		p_{fl}	
Parameter	Value	Error	Value	Error	Value	Error	Value	Error
Nameplate	260	-	190	-	370	-	0.8	-
DE [9]	263.51	1.35 %	189.3514	-0.34 %	347.2340	-6.15 %	0.8065	0.82 %
GA [9]	265.8385	2.24 %	191.2220	0.64 %	351.2145	-5.08 %	0.8170	2.13 %
PSO [9]	261.1978	0.46 %	188.9053	-0.58 %	360.8307	-2.48 %	0.7883	-1.46 %
SFLA [9]	260.3347	0.13 %	193.5212	1.85 %	365.0454	-1.34 %	0.7860	-1.75 %
MSFLA [9]	259.5611	-0.17 %	190.6352	0.33 %	370.8140	0.22 %	0.7995	-0.06 %
GWO	**260.0361**	**0.0139%**	**190.018**	**0.0095%**	**370.0263**	**0.0071%**	**0.79991**	**-0.0109%**
GWO-CS	**260.0212**	**0.0082%**	**189.9856**	**-0.0076%**	**370.0405**	**0.0109%**	**0.79996**	**-0.0052%**

Table 5 Torque – power factor values of the induction motor 2 (5 HP) and error for several and proposed algorithms

| Parameter	T_{st} (Nm)		T_{fl} (Nm)		T_{max} (Nm)		p_{fl}	
	Value	Error	Value	Error	Value	Error	Value	Error
Nameplate	15		25		42		0.8	
DE [9]	15.2351	1.57 %	26.3582	5.43 %	40.7443	-2.99 %	0.8110	1.38 %
GA [9]	15.3856	2.57 %	25.7210	2.88 %	38.9606	-7.24 %	0.8101	1.26 %
PSO [9]	15.3465	2.31 %	25.5692	2.28 %	39.0047	-7.13 %	0.7888	-1.40 %
SFLA [9]	15.4939	3.29 %	25.6484	2.59 %	40.7390	-3.00 %	0.7710	-3.63 %
MSFLA [9]	15.2725	1.82%	25.5541	2.22%	40.3870	-3.84%	0.7991	-0.11%
GWO	**15.2553**	**1.702%**	**25.5110**	**2.044%**	**40.3347**	**-3.965%**	**0.79997**	**-0.0038%**
GWO-CS	**15.2553**	**1.702%**	**25.504**	**2.016%**	**40.3281**	**-3.9807%**	**0.7999**	**-0.0125%**
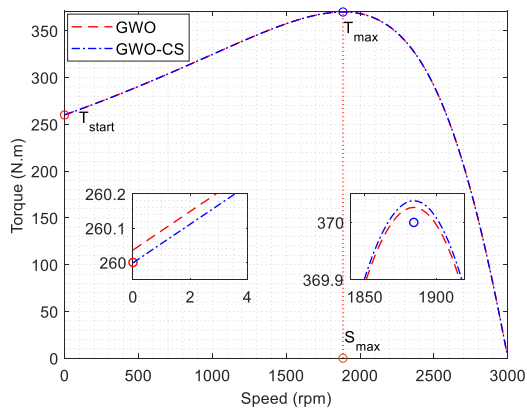
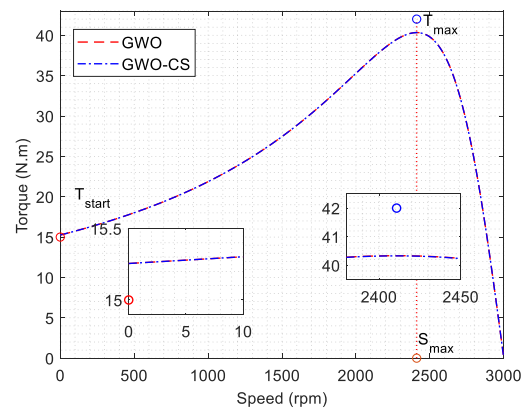Figure 3 Torque–Speed curve of induction motor 1

Figure 4 Torque–Speed curve of induction motor 2

5. CONCLUSION

In this paper, the parameter estimation of induction machines is made by using a hybrid algorithm based on GWO and CS algorithms. The hybrid GWO-CS algorithm are compared with GWO and other algorithms. The results show that GWO-CS is generally gives better results compared to conventional GWO algorithm. Also, the hybrid GWO-CS algorithm provides better results than several algorithms. Simulation results with the lowest values of the objective demonstrate the efficiency and robustness of the proposed GWO-CS and GWO algorithms.

Funding

The Declaration of Conflict of Interest/ Common Interest

No conflict of interest or common interest has been declared by the authors.

The Declaration of Ethics Committee Approval

This study does not require ethics committee permission or any special permission.

The Declaration of Research and Publication Ethics

The authors of the paper declare that they comply with the scientific, ethical and quotation rules of SAUJS in all processes of the paper and that they do not make any falsification on the data collected. In addition, they declare that Sakarya University Journal of Science and its editorial board have no responsibility for any ethical violations that may be encountered, and that this study has not been evaluated in any academic publication environment other than Sakarya University Journal of Science.

REFERENCES

[1] K. Chayakulkheeree, V. Hengsritawat, P. Nantivatana, "Particle swarm optimization based equivalent circuit estimation for on-service three-phase induction motor efficiency assessment," Engineering Journal, vol. 21, no. 6 Special Issue, pp. 101–110, Oct. 2017.

[2] M O. Gülbahçe, M E. Karaaslan, "Estimation of Induction Motor Equivalent Circuit Parameters from Manufacturer's Datasheet by Particle Swarm Optimization Algorithm for Variable Frequency Drives," Electrica, vol. 22, no. 1, pp. 16–26, Jan. 2022.

[3] A I. Çanakoğlu, A G. Yetgin, H. Temurtaş, M. Turan, "Induction motor parameter estimation using metaheuristic methods," Turkish Journal of Electrical Engineering and Computer Sciences, vol. 22, no. 5, pp. 1177–1192, 2014.

[4] H R. Mohammadi, A. Akhavan, "Parameter Estimation of Three-Phase Induction Motor Using Hybrid of Genetic Algorithm and Particle Swarm Optimization," Journal of Engineering, vol. 2014, no. 148204, pp. 1–6, 2014.

[5] A. Accetta, F. Alonge, M. Cirrincione, F. D'Ippolito, M. Pucci, A. Sferlazza, "GA-Based Off-Line Parameter Estimation of the Induction Motor Model Including Magnetic Saturation and Iron Losses," IEEE Open Journal of Industry Applications, vol. 1, no. July, pp. 135–147, 2020.

[6] O. Rodríguez-Abreo, J. Rodríguez-Reséndiz, J. M. Álvarez-Alvarado, A. García-Cerezo, "Metaheuristic Parameter Identification of Motors Using Dynamic Response Relations," Sensors, vol. 22, no. 11, pp. 1–22, 2022.

[7] M I. Abdelwanis, R. A. Sehiemy, M A. Hamida, "Hybrid optimization algorithm for parameter estimation of poly-phase induction motors with experimental verification," Energy and AI, vol. 5, p. 100083, 2021.

[8] J. Vukasinovic, M. Milovanovic, N. Arsic, J. Radosavljevic, S. Statkic, "Parameters estimation of double-cage induction motors using a hybrid metaheuristic algorithm," 2022 21st International Symposium INFOTEH-JAHORINA, 2022, pp. 16–18, 2022.

[9] I. Perez, M. Gomez-Gonzalez, F. Jurado, "Estimation of induction motor parameters using shuffled frog-leaping algorithm," Electrical Engineering, vol. 95, no. 3, pp. 267–275, Sep. 2013.

[10] M. Averbukh, Efim Lockshin, "Estimation of the Equivalent Circuit Parameters of Induction Motors by Laboratory Test," Machines, vol. 9, no. 340, pp. 1–12, 2021.

[11] H Y. Mahmoud, H M. Hasanien, A H. Besheer, A Y. Abdelaziz, "Hybrid cuckoo search algorithm and grey wolf optimiser-based optimal control strategy for performance enhancement of HVDC-based offshore wind farms," IET Generation, Transmission and Distribution, vol. 14, no. 10, pp. 1902–1911, May 2020.

[12] S. Mirjalili, S M. Mirjalili, A. Lewis, "Grey Wolf Optimizer," Advances in Engineering Software, vol. 69, pp. 46–61, Mar. 2014.

[13] W. Long, S. Cai, J. Jiao, M. Xu, T. Wu, "A new hybrid algorithm based on grey wolf optimizer and cuckoo search for parameter extraction of solar photovoltaic models," Energy Convers Manag, vol. 203, p. 112243, Jan. 2020.

.

[14] R K. Khadanga, A. Kumar, S. Panda, "A modified Grey Wolf Optimization with Cuckoo Search Algorithm for load frequency controller design of hybrid power system," Applied Soft Computing, vol. 124, Jul. 2022.

[15] R N. Kalaam, S. M. Muyeen, A. Al-Durra, H. M. Hasanien, K. Al-Wahedi, "Optimisation of controller parameters for grid-tied photovoltaic system at faulty network using artificial neural network-based cuckoo search algorithm," IET Renewable Power Generation, vol. 11, no. 12, pp. 1517–1526, Oct. 2017.

[16] M. Mareli, B. Twala, "An adaptive Cuckoo search algorithm for optimisation," Applied Computing and Informatics, vol. 14, no. 2. Elsevier B.V., pp. 107–115, Jul. 01, 2018.

[17] X. S. Yang, S. Deb, "Cuckoo search via Lévy flights," 2009 World Congress on Nature and Biologically Inspired Computing, NABIC, 2009, pp. 210–214.

[18] P H. Kumar, M. Rudramoorthy, "Distribution network reconfiguration considering DGs using a hybrid CS-GWO algorithm for power loss minimization and voltage profile enhancement," Indonesian Journal of Electrical Engineering and Informatics, vol. 9, no. 4, pp. 880–906, 2021.

[19] H. Xu, X. Liu, J. Su, "An improved grey Wolf optimizer algorithm integrated with Cuckoo Search," in Proceedings of the 2017 IEEE 9th International Conference on Intelligent Data Acquisition and Advanced Computing Systems: Technology and Applications, IDAACS 2017, Nov. 2017, vol. 1, pp. 490–493.

[20] A. Bouaddi, R. Rabeh, M. Ferfra, "Load Frequency Control of Autonomous Microgrid System Using Hybrid Fuzzy logic GWO-CS PI Controller," in 2021 9th International Conference on Systems and Control, ICSC 2021, 2021, pp. 554–559.

Title: Dealing with Aspects of Performance and Environmental Impact of Aircraft Engine with Thermodynamic Metrics

Authors: Hakan AYGÜN

Dealing with Aspects of Performance and Environmental Impact of Aircraft Engine with Thermodynamic Metrics

Hakan AYGUN [*1] ID

Abstract

The limited energy source indicates the necessity of efficient energy consumption in every field of life. Especially, the prompt growth in aviation sector makes this issue more important. In this study, effects of power settings on several thermodynamic indicators regarding low by-pass turbofan engine (LBP-TFE) are investigated. For this aim, the energy and exergy analyses are implemented to the system of turbofan engine for eighteen operating points. According to performance analysis, thrust value of the LBP-TFE changes from 10.77 kN to 71.8 kN throughout RPM values. According to exergetic findings, relative exergy losses from Fan outlet decreases from 52.34 % to 30.58 % whereas exergy efficiency of the LBP-TFE increases from 10.9 % to 30.1 %. Considering improved exergy efficiency, it changes 25.03 % and 41.03 % at the same RPM intervals. As for environmental assessments, environmental effect factor (EEF) of LBP-TFE diminishes from 5.8 to 1.32 while ecological effect factor decreases from 9.16 to 3.31. Finally, specific irreversibility production of LBP-TFE decreases from 0.4811 MW/kN and 0.2716 MW/kN. Considering these outcomes, behaviour of the investigated metrics regarding main components is different from each other. Therefore, the results of these parameters calculated for the whole engine could help understanding optimum running point in terms of exergetic and environmental sustainability.

Keywords: Low by-pass turbofan, ecological effect factor, environmental effect factor, exergy

1. INTRODUCTION

In aviation sector, the dependency on fossil fuel consumption has increased in recent years due to an increasing aircraft fleet. It is estimated that the annual growth of aviation is approximately 5-6 % [1]. According to aviation authorities, the number of passengers conveyed with airline was figured out 3.53 billion in 2015 whereas it increased to 4.5 billion in 2019 [2]. This case corresponds to 27.4 % increment at four years. Therefore, this situation has triggered several issues such as environmental pollution, thereby global warming. Admittedly, CO_2 emissions from aviation activities are proportional with the

* Corresponding author: haygun@firat.edu.tr (H.AYGUN)
[1] Firat University
E-mail: haygun@firat.edu.tr
ORCID: https://orcid.org/0000-0001-9064-9644

quantity of fossil fuel consumption. To mitigate aircraft emissions, several policies have been brought forward by many foundations. The leading measure implemented in several countries is mitigation of CO_2 emissions with carbon taxes. To generate thrust or power is key role of propulsion system, however fuel efficiency of these systems while producing this power is affected from several factors such as design, weight and material of the engine. Commercial airline transportation is highly related to developments of the aviation sector [3]. However, compared with the earlier of invention of gas turbines, the current engines have undoubtedly designed more efficiently [4]. However, these developments could not eliminate impacts of emissions from air traffic [3, 5].

To alleviate effects of gas turbine engines on environment, these systems have been dealt with several approaches such as thermodynamic and optimization. The main challenge pertaining to aircraft system is to minimize environmental impact of engine by keeping system efficiency at the desired level [6]. To overcome this depends on finding optimum running point as well as lowering wasted exergy as possible. To design a competitive gas turbine engine in terms of environmental and performance could increase the interest of the users of this technology. Investigation of these systems under different conditions allows the designer to make decision more efficiently and economically. To meet the design requirements of novel aircraft missions, several elaborated studies along with many projects have been brought to light day by day. On the other hand, the main focusing point of the scientists is to improve energetic and exergetic performance of energy consuming systems due to the rising concern about the limited sources for two decades. For this aim, thermodynamics approaches which are significant tools are necessary for assessment

of thermal systems. Comparison of similar systems is made by applying first and second laws of thermodynamics to the thermal systems. Considering the open literature, a number of studies involving exergy approach have existed. Especially, this method has commonly been implemented to gas turbine engine due to using many fields. In the present study, it is tried that the recent performed works about exergy of gas turbine engines are presented. Akdeniz and Balli [1] investigated the bypass effects on thermodynamic performance for JT3D-3B engine. They stated that exergy efficiency of the engine increases from 25.39 % (BPR:1.3) to 26.23 % (BPR:1.45) whereas energy efficiency of JT3D engine from 26.97% to 27.93% at the specified BPR values. Dinc et al. [7] conducted thermodynamic-based analyses for turboprop engine at several flight phase points. The authors stated that the combustor has the highest exergetic improvement potential ratio with 88.756% whereas for the intermediate pressure turbine, it is calculated lowest with 0.492% at phase point 3. Tuzcu et al. [8] searched turbofan engine in terms of efficiency and emission. Overall efficiency of the engine is found as 19.7%. CO_2 emission per day cyle was produced as 358.9 $tonCO_2$/day whereas its environmental damage cost is determined as 5742.52 US$/day. Moreover, Turan [9] dealt with exergetic parameters of JT9D engine producing thrust of 206 kN. According to the author, exergy efficiency of the engine was calculated as 29.6 % while its environmental effect factor was measured as 0.675. Furthermore, Balli et al. [10] implemented exergetic approach to TF33 low by-pass turbofan engine. The authors expressed that exergy efficiency of TF33 was gauged as 34.86% whereas its environmental effect factor was found as 1.868. On the other hand, Dinc et al. [11] examined three-spool turboprop engine with exergetic method at different flight points. They stated that exergy efficiency of the engine was computed as

29.11% at take-off and 34.69% at cruise phase. Balli and Caliskan [12] was investigated of JTD15 turbofan engine generating thrust of 9.79 kN in terms of energetic and exergetic. According to the authors, exergy efficiency of the whole engine was estimated as 19.91%, whereas environmental effect factor of JTD15 was found as 4.02. According to the studies about exergy analysis of gas turbine engines considered, the most of studies about gas turbine engine in the literature are performed at one-point. This study differs from this aspect. Namely, exergetic parameters are calculated for eighteen running points instead of one case. Thus, exergy and environmental behaviour of the engine against to RPM variations can be observed and compared with each other. This comparison is of high importance since the engine is not operated at only one point in the real world. On the other hand, exergetic and environmental indicators are computed for both the whole engine and its six components. Main novelty of the study is that specific irreversibility production (SIP) index is firstly calculated for the engine which is very similar to JT8D engine. As a conclusion, the current study has differences from following points:

- To calculate exergetic metrics involving exergy efficiency, wasted exergy ratio, fuel exergy waste ratio, improved exergy, exergetic improvement potential for turbofan and its six components
- To compute environmental parameters incorporating environmental effect factor, exergetic sustainability index ecological effect factor and sustainable efficiency factor
- To measure firstly specific irreversibility production for LBP-TFE

- To compare exergetic and environmental indicator for eighteen running points.

2. SYSTEM DESCRIPTION

In this study, gas turbine engine that is the very similar to JT8D engine is dealt with so as to be analyzed. JT8D engine has proven durability and reliability by flying more than 673 million hours since starting operation. However, nowadays, these engines are known as 'the old engines'. Up to date, the number of JT8D engines used exceeds to 14,750. According to the literature, 2400 of these engines are still employing in the aircraft. There are the eight models of JT8D family [13]. Thrust range of these engines are between 62 kN and 96 kN. JT8D engines have been installed in B-727/737, DC-9 and MD-80. These engines have front-mounted fan with two stages, low pressure compressor with four stages, combustor, high pressure compressor with seven stage combustor, high-pressure turbine with one stage and low-pressure turbine with three stages [14]. Overall pressure ratio for JT8D family engines has ranges from 15.8 to 21 whereas their by-pass ratio varies between 1 and 1.7.
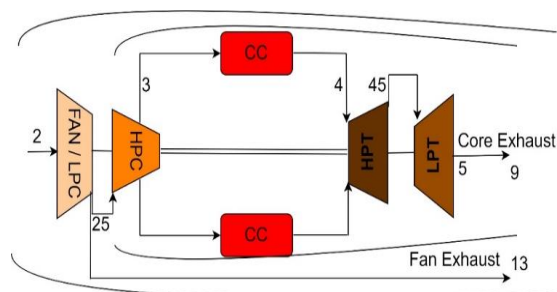

Figure 1 Cross section of JT8D engine

The representative drawing for typical low bypass turbofan engine is illustrated in Figure 1. Table 1 presents several versions of JT8D engine with their key features.

Table 1 Several models and features of the JT8D low by-pass turbofan engine [15]

Versions	By-pass ratio	Overall pressure ratio	Rated thrust	General Applications
JT8D-11	1	17.17	66.72	
JT8D-15	1.03	16.81	68.94	Boeing 727
JT8D-17	1.02	17.01	71.17	Boeing 737-100
JT8D-209	1.8	18.3	85.6	Boeing 737-100
JT8D-217	1.73	19.66	92.74	Boeing MD-80
JT8D-219	1.7	20.27	96.52	DC-9
JT8D-7 series	1.05	15.82	62.27	
JT8D-9 series	1.04	15.88	64.5	

Table 2 The engine input parameters for performing exergy analysis throughout eighteen RPM values

RPM (%)	Fan air mass flow (kg/s)	Core air mass flow (kg/s)	Fuel flow (kg/s)	Fan exhaust velocity (m/s)	Core exhaust velocity (m/s)
50.29	64.824	28.266	0.179	160.103	173.126
55.32	74.628	32.808	0.222	182.525	203.323
59.93	83.271	36.833	0.266	202.003	231.316
64.3	90.98	40.591	0.31	218.555	257.43
68.4	98.056	44.076	0.354	233.486	282.049
71.99	104.605	47.401	0.4	246.75	305.66
75.25	110.699	50.571	0.445	258.65	327.812
78.18	116.466	53.64	0.492	269.52	349.892
80.77	121.919	56.612	0.539	279.439	371.075
83.05	127.079	59.501	0.587	288.438	392.602
85.13	131.976	62.323	0.636	296.623	413.148
87.09	136.622	65.063	0.686	304.124	433.452
89.02	141.035	67.72	0.738	311.04	453.094
90.92	145.156	70.282	0.792	317.262	473.554
92.76	149.016	72.736	0.848	322.901	483.445
94.75	152.591	75.086	0.91	328.045	488.983
97.19	155.726	77.256	0.983	332.741	495.849
100	158.392	79.197	1.066	337.029	504.257

3. METHODOLOGY BACKGROUND

Once performing exergy analysis, potential improvements and environmental impacts of the system considered can be estimated. However, first law of thermodynamics could not gain comprehensive point of view. Therefore, second law of the thermodynamics is required so as to quantify environmental impacts and sustainability level. Namely, the irreversibility of processes can be assessed by means of the exergy approach that includes computation of these irreversibilities. Magnitudes of wastes, destructions and losses of energy occurred in the system are measured

with this approach [7]. Table 2 gives air and fuel mass flows as well as fan and core velocity, which is obtained from parametric cycle equations [16, 17].

3.1. Exergy Analysis

Fuel-Product law is employed so as to compute exergy destruction occurred in the system or the component [18].

$$\sum \dot{E}x_F - \sum \dot{E}x_{Pr} = \sum \dot{E}x_D \qquad (1)$$

where F represents 'fuel' whereas Pr denotes 'product'. Also, D specifies 'destruction'.

Kinetic exergy or product exergy obtained from the engine is calculated as:

$$\dot{Ex}_{PR,engine} = (\dot{m}_F + \dot{m}_a)\frac{V^2_{exhaust}}{2} \qquad (2)$$

Exergy rates for air and exhaust gases are found from following equation. However, specific heat value is separately computed for air and gases [19].

$$\dot{Ex} = \dot{m}\left[c_{p(T)}\left[T - T_0 - T_0 ln\left(\frac{T}{T_0}\right)\right] + RT_0 ln\left(\frac{P}{P_0}\right)\right] \qquad (3)$$

For air and gases, specific heat value is calculated from [20]:

$$C_{p,air}(T) = 1.04841 - 0.000383719(T)$$
$$+ \frac{9.45378(T^2)}{10^7} - \frac{5.49031(T^3)}{10^{10}} + \frac{7.92981(T^4)}{10^{14}} \qquad (4)$$

$$C_{p,gas}(T) = 0.9910 + \frac{3.606(T)}{10^5}$$
$$+ \frac{1.552(T^2)}{10^7} - \frac{6.76(T^3)}{10^{11}} \qquad (5)$$

Fuel exergy is calculated from:

$$\dot{Ex}_F = \dot{m}_F \dot{Q}_{LHV}\xi_F \qquad (6)$$

where ξ_F represents liquid fuel exergy grade function [21]. For liquid fuels (C_aH_b), its formula is:

$$\xi_F \cong 1.04224 + 0.011925\frac{b}{a} - \frac{0.042}{a} \qquad (7)$$

Wasted exergy of turbofan engine is computed from difference between fuel

exergy and product exergy of the engine. It is written as:

$$\dot{Ex}_{WE,engine} = (\dot{Ex}_F + \dot{Ex}_I) - \dot{Ex}_{PR,engine} \qquad (8)$$

Total exergy destruction consists exergy destruction of fan, low pressure compressor, high pressure compressor, combustor, high pressure turbine and low pressure turbine. It is written as:

$$\dot{Ex}_{D,engine} = \sum \dot{Ex}_D = \dot{Ex}_{D,components} \qquad (9)$$

There are several ways that exergy efficiency is formulated for thermal systems. These can be seen in detail elsewhere. In the current study, exergy efficiency is expressed as the ratio of product exergy to fuel exergy [12, 22].

$$\eta_{ex} = \frac{\dot{Ex}_{Pr}}{\dot{Ex}_F} \qquad (10)$$

Waste exergy ratio is calculated by dividing wasted exergy in the kth component to total wasted exergy occurred in overall system. It is written as:

$$WExR_k = \frac{\dot{Ex}_{WE,k}}{\dot{Ex}_{WE,engine}} = \frac{\dot{Ex}_{D,k} + \dot{Ex}_{L,k}}{\dot{Ex}_{WE,engine}} \qquad (11)$$

Fuel exergy waste ratio is computed by dividing wasted exergy in the kth component to fuel exergy entering the system. It is written as [23]:

$$FExWR_k = \frac{\dot{Ex}_{WE,k}}{\dot{Ex}_{F,engine}} = \frac{\dot{Ex}_{D,k} + \dot{Ex}_{L,k}}{\dot{Ex}_{F,engine}} \qquad (12)$$

Moreover, exergetic improvemental potential is found from exergy destruction and exergy efficiency. It means how much exergy destruction could be recovered in the any system. It is expressed as [24]:

$$ExIP_k = (1-\eta_{ex})\dot{Ex}_{D,k} \qquad (13)$$

Improved exergy efficiency is firstly proposed by Balli [25]. It is determined by inserting exergetic improvemental potential to exergy efficiency. This metric means that how much exergy efficiency increases due to recovering exergy destruction. It is presented as:

$$\Psi = \frac{\dot{Ex}_{Pr}}{\dot{Ex}_F - \dot{ExIP}} \qquad (14)$$

3.2. Environmental and Sustainability Parameters

The term sustainability means the usage of energy sources with the lowest negative environmental impacts as possible. Therefore, to consume energy efficiently is of high importance for sustainability [26]. Also, the higher the energy efficiency, the lower the environmental damage. In this context, gas turbine engines have a key role so as to quantify the sustainability of aircraft. For this aim, four different parameters that are commonly used in the literature are dealt with in the present study.

Ecological effect factor is computed by taking the reciprocal of the exergy efficiency. This parameter is adversely proportional with exergy efficiency. It is written as:

$$EcoEF_k = \frac{\dot{Ex}_F}{\dot{Ex}_{Pr}} = \frac{1}{\eta_{ex,k}} \qquad (15)$$

Environmental effect factor (EEF) is computed by dividing fuel exergy waste ratio to exergy efficiency. It means damage of environmental of the engine or the component. It is expressed as [27]:

$$EEF_k = \frac{FExWR_k}{\eta_{ex,k}} \qquad (16)$$

Besides, exergetic sustainability index is found by taking the reciprocal of the EEF. This metric shows the level of sustainability of the engine or the component. It is presented as [27]:

$$ExSI_k = \frac{1}{EEF_k} \qquad (17)$$

On the other hand, sustainable efficiency factor (SEF) is determined from exergy efficiency. Namely, its value depends on exergy efficiency. It is written as[12]:

$$SEF_k = \frac{1}{1-\eta_{ex,k}} \qquad (18)$$

Finally, specific irreversibility production is firstly implemented to the low by-pass turbofan in the present study. It is computed by dividing total exergy destruction to net thrust of the engine. Thanks to this metric, irreversibility performance of the gas turbine engine could be gauged at any operation conditions. Namely, different running points could be compared in terms of irreversibility. It is expressed as follows:

$$SIP_{engine} = \frac{\sum \dot{Ex}_D}{\tau_{engine}} \qquad (19)$$

where τ_{engine} denotes net thrust of the engine.

4. RESULTS AND DISCUSSION

This section covers the outcomes of exergetic and environmental for low by-pass turbofan and its six components. These computations are carried out for eighteen relative RPM values starting from 50.29 % to 100 %. To clearly be understood, this section could be divided to three subsections. Firstly, variations of performance metrics such as thrust and specific fuel consumption (SFC) against RPM values are presented in Figure 2. Secondly, exergetic parameters pertaining to

LBP-TFE and its components are evaluated in Figures 3-8. Thirdly, environmental parameters of the system along with its components are evaluated with Figures 9-13.

Table 3 Exergy destruction of main components throughout eighteen RPM values

RPM (%)	FAN (MW)	LPC (MW)	HPC (MW)	CC (MW)	HPT (MW)	LPT (MW)
50.29	0.194	0.129	0.432	3.621	0.633	0.172
55.32	0.251	0.167	0.516	4.16	0.809	0.249
59.93	0.309	0.204	0.595	4.677	0.987	0.325
64.3	0.366	0.239	0.672	5.163	1.167	0.388
68.4	0.423	0.273	0.744	5.631	1.346	0.444
71.99	0.47	0.3	0.807	6.093	1.52	0.512
75.25	0.506	0.321	0.868	6.544	1.691	0.578
78.18	0.534	0.337	0.928	6.995	1.863	0.639
80.77	0.555	0.348	0.991	7.435	2.036	0.697
83.05	0.567	0.354	1.054	7.876	2.211	0.751
85.13	0.573	0.359	1.117	8.311	2.38	0.811
87.09	0.578	0.363	1.18	8.748	2.548	0.866
89.02	0.585	0.368	1.243	9.182	2.716	0.918
90.92	0.598	0.377	1.304	9.63	2.888	0.966
92.76	0.613	0.388	1.363	10.087	3.058	1.01
94.75	0.657	0.413	1.425	10.567	3.234	1.045
97.19	0.782	0.477	1.497	11.072	3.416	1.093
100	0.984	0.577	1.583	11.604	3.604	1.145

Table 3 presents exergy destruction for six different components. According to this, the lowest exergy destruction takes place in LPC whereas the combustor has the highest irreversibility value. ExD of components increases when RPM is elevated. However, it does not mean that the higher RPM value leads to deteriorate exergetic performance of the engine. To make decision for this, exergetic parameters are calculated for eighteen running points. In this regard, the ExD of the combustor increases from 3.621 MW to 11.604 MW whereas that of the whole engine raises from 5.18 MW to 19.5 MW throughout RPM values.

Table 4 gives the results of exergetic improvement potential for each component. These outcomes indicate that the combustor amongst the components has the highest potential to be enhanced. The second highest potential belongs to the HPT unit.

Considering total improvement rate, it is observed to vary from 1.098 MW to 2.331 MW when RPM is increased from the lowest value to the highest one. Additionally, the combustor consists 84.51 % at 50.29 % RPM and 64.82 % at 100 % RPM of total exergetic improvement potential.

Fuel exergy and product exergy of components are tabulated in Table 5. The term fuel exergy means input exergy whereas the term product exergy represents output exergy. The difference between fuel exergy and output exergy gives exergy destruction.
Table 6 gives exergy losses of Fan outlet and exhaust outlet. This exergy loss is calculated from between wasted exergy and exergy destruction. Considering relative exergy losses, it decreases from 52.34 % to 30.58 % at Fan outlet whereas it increases from 47.65 % to 69.41 % at exhaust outlet when RPM is varied from 50.29 % to 100 %. At 50.29 %

RPM, the difference between losses of Fan outlet and exhaust outlet is calculated as 0.042 MW while it is computed as 5.707 MW at 100%. Considering these findings, to determine the lowest exergy losses depends on determining optimum RPM value.

Table 4 Exergetic improvement potential of main components throughout eighteen RPM values

RPM (%)	FAN (MW)	LPC (MW)	HPC (MW)	CC (MW)	HPT (MW)	LPT (MW)
50.29	0.035	0.018	0.036	0.928	0.067	0.013
55.32	0.04	0.021	0.04	0.963	0.086	0.019
59.93	0.045	0.024	0.044	1.003	0.107	0.024
64.3	0.05	0.026	0.049	1.039	0.129	0.028
68.4	0.055	0.029	0.052	1.076	0.152	0.03
71.99	0.058	0.03	0.055	1.115	0.173	0.035
75.25	0.058	0.03	0.058	1.153	0.195	0.039
78.18	0.057	0.03	0.061	1.193	0.217	0.042
80.77	0.056	0.029	0.064	1.231	0.24	0.045
83.05	0.053	0.028	0.068	1.27	0.263	0.048
85.13	0.049	0.026	0.071	1.308	0.284	0.052
87.09	0.047	0.025	0.074	1.347	0.306	0.055
89.02	0.044	0.024	0.078	1.385	0.327	0.058
90.92	0.043	0.024	0.081	1.425	0.35	0.06
92.76	0.043	0.024	0.084	1.468	0.372	0.062
94.75	0.047	0.025	0.087	1.511	0.395	0.063
97.19	0.063	0.032	0.09	1.551	0.416	0.065
100	0.094	0.044	0.095	1.588	0.438	0.068

Table 5 The outcomes of fuel and product exergy for six components throughout eighteen RPM values

RPM (%)	FAN F (MW)	FAN Pr (MW)	LPC F (MW)	LPC Pr (MW)	HPC F (MW)	HPC Pr (MW)	CC F (MW)	CC Pr (MW)	HPT F (MW)	HPT Pr (MW)	LPT F (MW)	LPT Pr (MW)
50.29	1.077	0.883	0.935	0.805	5.179	4.747	14.132	10.51	5.956	5.322	2.27	2.097
55.32	1.567	1.316	1.321	1.153	6.597	6.081	17.964	13.804	7.562	6.753	3.25	3.001
59.93	2.102	1.792	1.723	1.519	7.92	7.325	21.799	17.121	9.052	8.064	4.29	3.964
64.3	2.652	2.286	2.13	1.89	9.223	8.55	25.636	20.473	10.52	9.352	5.341	4.952
68.4	3.228	2.804	2.542	2.269	10.463	9.719	29.465	23.834	11.918	10.571	6.416	5.971
71.99	3.803	3.333	2.947	2.647	11.667	10.86	33.303	27.209	13.292	11.771	7.473	6.96
75.25	4.374	3.867	3.344	3.022	12.841	11.973	37.13	30.586	14.634	12.942	8.521	7.942
78.18	4.943	4.408	3.735	3.397	14.005	13.076	41.015	34.02	15.966	14.102	9.568	8.928
80.77	5.507	4.952	4.116	3.768	15.159	14.168	44.899	37.463	17.271	15.235	10.602	9.904
83.05	6.057	5.49	4.487	4.132	16.312	15.258	48.831	40.955	18.563	16.352	11.609	10.857
85.13	6.594	6.021	4.85	4.491	17.47	16.352	52.79	44.478	19.877	17.497	12.578	11.767
87.09	7.122	6.543	5.207	4.844	18.627	17.447	56.801	48.053	21.19	18.642	13.526	12.66
89.02	7.642	7.056	5.56	5.191	19.786	18.543	60.861	51.678	22.503	19.787	14.461	13.543
90.92	8.146	7.548	5.907	5.529	20.954	19.649	65.044	55.414	23.814	20.926	15.368	14.401
92.76	8.632	8.019	6.244	5.856	22.112	20.749	69.299	59.211	25.115	22.056	16.248	15.237
94.75	9.126	8.468	6.593	6.18	23.327	21.901	73.872	63.304	26.48	23.245	17.158	16.112
97.19	9.67	8.887	6.988	6.511	24.67	23.173	79.022	67.949	28.004	24.588	18.149	17.055
100	10.257	9.272	7.422	6.844	26.136	24.553	84.765	73.161	29.62	26.015	19.225	18.08

Table 6 Exergy losses from Fan outlet and exhaust outlet

RPM (%)	Fan outlet losses (MW)	Exhaust outlet losses (MW)	Fan Relative exergy losses (%)	Exhaust Relative exergy losses (%)
50.29	0.468	0.426	52.34	47.65
55.32	0.696	0.682	50.5	49.49
59.93	0.947	0.992	48.83	51.16
64.3	1.203	1.355	47.02	52.97
68.4	1.471	1.767	45.42	54.57
71.99	1.741	2.232	43.82	56.17
75.25	2.011	2.741	42.31	57.68
78.18	2.281	3.313	40.77	59.22
80.77	2.549	3.934	39.31	60.68
83.05	2.811	4.631	37.77	62.22
85.13	3.064	5.373	36.31	63.68
87.09	3.309	6.176	34.88	65.11
89.02	3.546	7.027	33.53	66.46
90.92	3.768	7.969	32.1	67.89
92.76	3.976	8.599	31.61	68.38
94.75	4.17	9.085	31.45	68.54
97.19	4.343	9.618	31.1	68.89
100	4.497	10.204	30.58	69.41

To evaluate energetic performance of the engine, thrust and specific fuel consumption metrics regarding LBP-TFE are employed. These parameters are presented in Figure 2. As seen in Figure 2, when the relative RPM is increased from 50.2 % to 100 %,
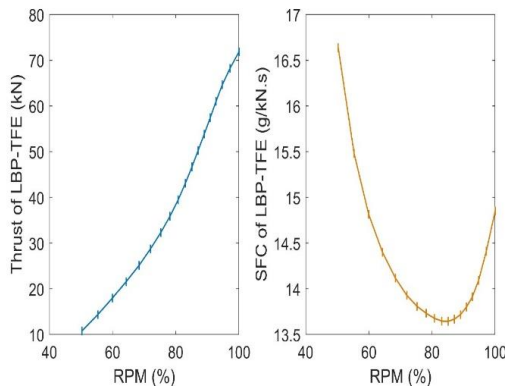
Figure 2 Variation of thrust and SFC regarding LBP-TFE against RPM values

the thrust of LBP-TFE raises from 10.7 kN to 71.8 kN whereas the SFC does not continuously decreases with rising RPM. Namely, it diminishes from 16.63 g/kN.s (at 50.2 % RPM) to 13.644 g/kN.s (at 85.13 %

RPM). After that point, it increases up to 14.85 g/kN.s at 100% RPM.
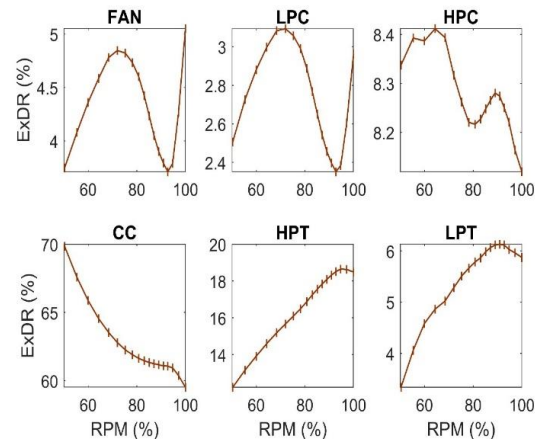
Figure 3 Variation of exergy destruction ratio pertaining to six components against RPM values

Figure 3 shows how exergy destruction ratio (ExDR) of major components changes according to RPM value. As seen in, the ExDR of Fan, LPC and HPC fluctuate throughout RPM values. Therefore, effect of power setting on this metric may not be distinct. However, the trend of ExDR of the combustor is apparent and it amongst other components has highest ratio changing from

69.85% to 59.51% owing to rising RPM. One can infer from this finding is that exergy destruction of the combustor accounts for highest share of total irreversibility. When regarding maximum RPM, ExDRs of the Fan, LPC and HPC are figured out as 5.05%, 2.96% and 8.12% while those of CC, HPT and LPT are estimated as 59.51%, 18.49% and 5.87%, respectively.
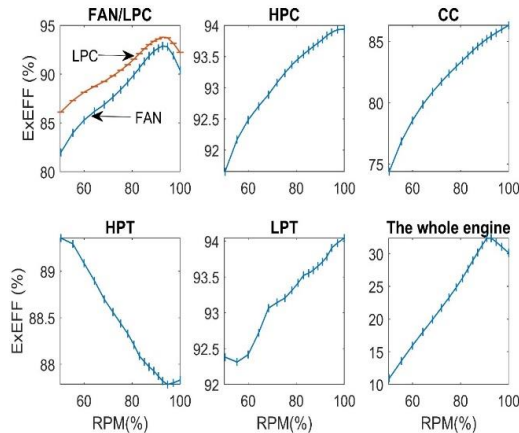
Figure 4 Variation of exergy efficiency pertaining to six components against RPM values

To measure exergetic performance of LBP-TFE and its components, several exergetic parameters are computed for eighteen throttle settings. Firstly, exergy efficiency of the system is presented in Figure 4. As can be understood, variations of exergy efficiency of Fan and LPC have similar trend by an increase in the RPM. Considering only component exergy efficiency, effects of power setting could not be understood. Therefore, exergy efficiency is also examined for the whole engine. This approach is implemented for the other metrics regarding LBP-TFE. Except HPT unit, exergy efficiency of components generally increases due to rising RPM. The lowest exergy efficiency belongs to the combustor, which raises from 74.31% to 86.37%. The highest exergy efficiency for the whole engine is calculated as 32.4% at 92.76 % RPM. In this context, this parameter regarding LBP-TFE varies from 10.91% to 30.14% throughout all RPM values.
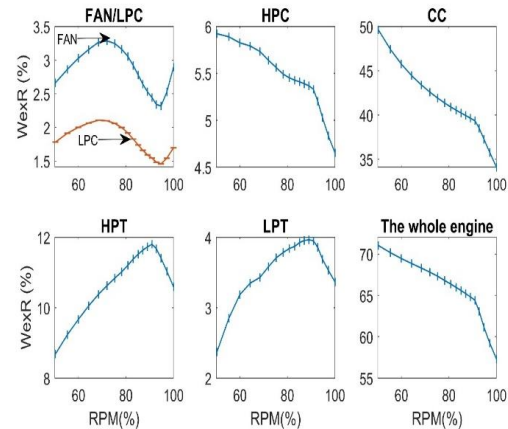
Figure 5 Variation of wasted exergy ratio pertaining to six components against RPM values

As for another significant indicator, wasted exergy ratio of LBP-TFE and its components are given in Figure 5, It is desired that WExR becomes the lowest value. In terms of environmental sustainability, this parameter related to the whole engine is favorably affected at elevated RPM values. Namely as the relative RPM is increased it decreases from 71.04% to 57.31%. This important decrement proves that operation points close to idle RPM lead to inefficiently consume fuel. Furthermore, significant part of this wasted exergy originates from the combustor. As seen in, the decrement curve of WExR of the combustor is similar with that of the whole engine. In this context, WExR of the combustor decreases from 49.62% to 34.1% throughout RPM values. The decrement curve of WExR regarding LBP-TFE is less susceptible to variations of power setting from 50.52% up to 90.92% RPM. This could be attributed to increment in WExRs of HPT and LPT at the specified ranges.
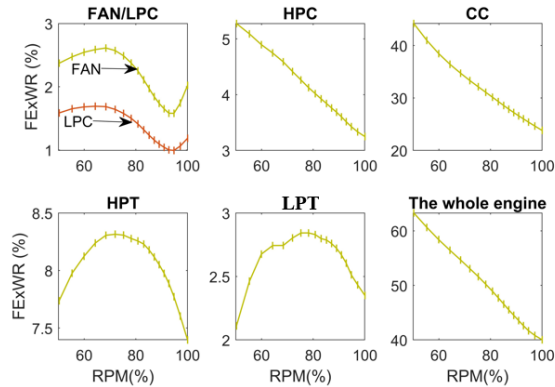
Figure 6 Variation of fuel exergy waste ratio pertaining to six components against RPM values

Variations of Fuel exergy waste ratio of the components are presented in Figure 6. This metric measures wasted exergy rate per unit fuel exergy. As understood in, FExWR of the Fan is higher than that of the LPC. However, their responds against to RPM variation bear resemblance. In this context, the FexWR of the LBP-TFE decreases from 63.28% to 40.02 % whereas that of the combustor diminishes from 44.2% to 23.81% due to rising RPM from 50.2% to 100%.
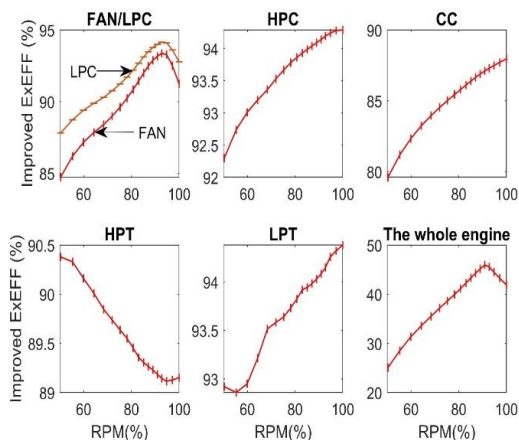
Figure 7 Variation of improved exergy efficiency pertaining to six components against RPM values

Figure 7 presents improved exergy efficiency (IMPExEFF) pertaining to LBP-TFE and its components. This indicator means that if exergetic improvement for each component is achieved, it specifies how much exergy efficiency of the considered unit enhances.

When compared with real exergy efficiency, variation curve of improved exergy efficiency against to RPM is same, but its magnitude is higher than real one for each component as expected. In this sense, the IMPExEFF of the combustor increases from 79.6% to 87.96%. The increment averagely occurs 2.64% whereas the IMPExEFF related to the whole engine is computed to vary from 25.03% to 41.88%. Compared with real exergy efficiency, the increase takes place about 14.25% throughout the whole RPM values.
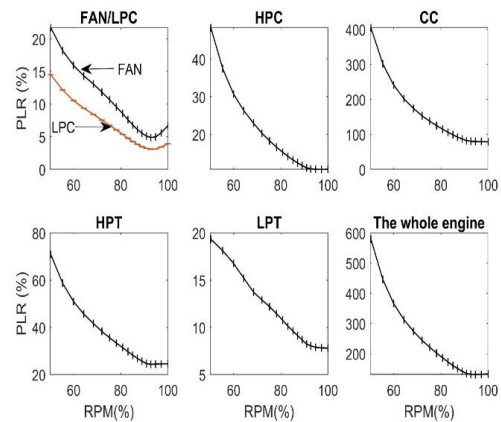
Figure 8 Variation of productivity lack ratio pertaining to six components against RPM values

To investigate exergetic performance in detail, productivity lack ratio of components are also calculated in Figure 8. It gauges exergy destruction per unit product (or useful) exergy. Except the combustor, PLR values of the other components are less than 100 %. It means that magnitude of product exergy is lower than that of exergy destruction. However, it does not hold for the combustor and the whole engine. Moreover, increment of power setting highly affects this metric. Namely, PLR of the combustor decreases from 404.74 % to 78.93 %. Similarly, the PLR of the whole engine diminishes from 560.13 % to 124.84 % as the RPM increases from 50.2 % to 100 %. As seen in, the PLRs of all components demonstrate similar trend by increase in the RPM.
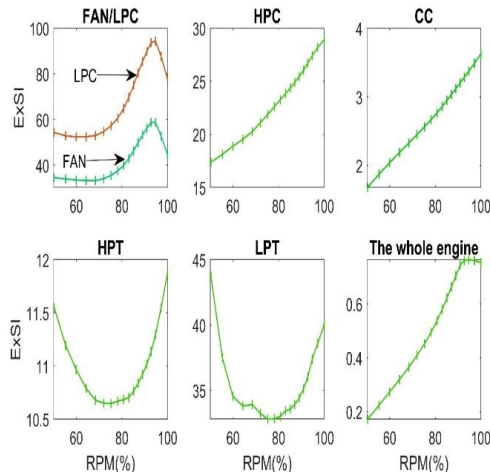
Figure 9 Variation of exergetic sustainability index pertaining to six components against RPM values

In the present study, well-known two parameters are dealt with for evaluating the engine sustainability. Firstly, curves of exergetic sustainability index against RPM variation are obtained in Figure 9. To measure high ExSI, two conditions that are high exergy efficiency and low WExR are necessary. Increasing RPM value leads to enhance ExSI of the whole engine. Namely, its value is found to be 0.1724 at 50.2 % RPM and 0.7533 at 100% RPM. Moreover, the ExSI of the combustor varies from 1.68 to 3.62 throughout RPM values. As seen in Figure 9, ExSI values of Fan, LPC, HPT and LPT fluctuate with variation of RPM. To make decision which point is suitable for sustainability, the ExSI of the whole engine plays key role for determining optimum power setting.

As for another index pertaining to sustainability shown in Figure 10, sustainable efficiency factor is proposed in the open literature. This parameter is associated with exergy efficiency. As the exergy efficiency increases, the SEF is found to be higher. Up to 92.76 % RPM, the SEF of LBP-TFE increases from 1.1225 to 1.4793. At 100 % RPM, its value is computed as 1.4315. The reason for this decrement could be decrement of the SEF

of Fan and LPC. Besides, the SEF of combustor is observed to vary from 3.902 to 7.304 due to rising RPM.
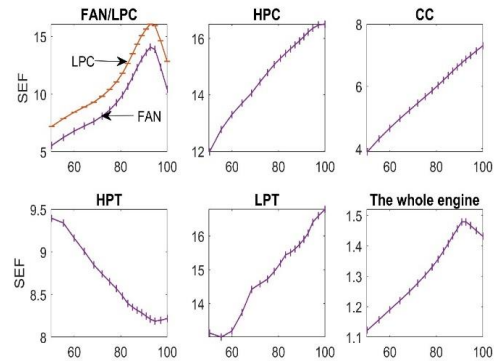
Figure 10 Variation of sustainable effect factor pertaining to six components against RPM values
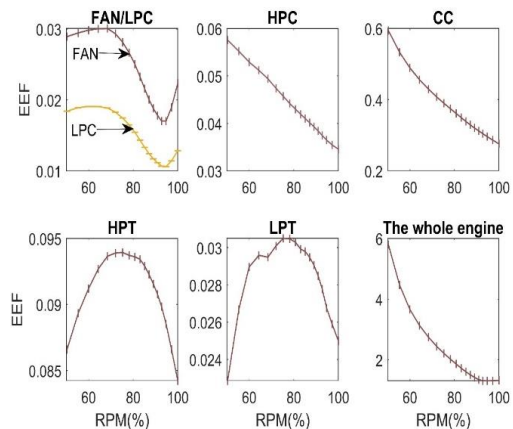
Figure 11 Variation of environmental effect factor pertaining to six components against RPM values

In the current study, there are exergetic indicators related to environmental impact. Firstly, environmental effect factor regarding the engine and its components is investigated for eighteen RPM values in Figure 11. Similar to the previous comments made, EEF value of the overall engine should be considered so as to clearly understand effect of throttle setting. In this context, the EEF of LBP-TFE is estimated to change from 5.8 to 1.32 whereas that of the combustor varies from 0.594 to 0.275 by an increase in the RPM. Moreover, as seen in figure 11, the EEF of LPC is lower than that of the Fan. It can be partly attributed

that exergy destruction of Fan is higher than that of LPC.
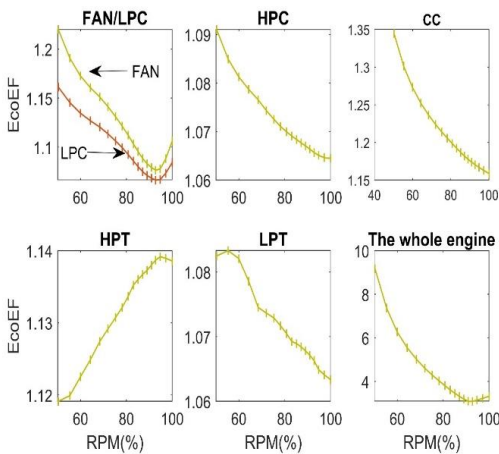

Figure 12 Variation of ecological effect factor pertaining to six components against RPM values

Figure 12 demonstrates how EcoEF regarding components vary according to RPM value. As can be understood, there are non-linear EcoEF curves. Effect of power setting on this index is very obvious. Namely, the EcoEF value pertaining to overall engine decreases from 9.16 to 3.31 while that the combustor is observed to change from 1.344 to 1.158 owing to the elevated RPM step by step.
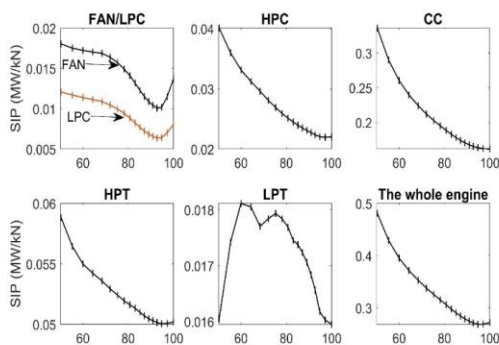
Figure 13 Variation of specific irreversibility index pertaining to six components against RPM values

Finally, specific irreversibility index for each component is calculated for eighteen operating points in Figure 13. This parameter measures exergy destruction per unit thrust. The SIP of the LBP-TFE decreases from 0.481 MW/kN to 0.271 MW/kN. It corresponds 43.6 % decrement. Furthermore, the SIP of the combustor is observed to decrease from 0.336 MW/kN to 0.161 MW/kN. As can seen in, the general trend of SIP for each component is prone to diminish with rising RPM.

5.CONCLUSION

This study dealt with exergetic and environmental metrics regarding low by-pass turbofan engine at several RPM values. The main aim is to evaluate effects of power settings for LBP-TFE and its six components. For this goal, specific code related to exergetic relations was written so as to calculate these parameters for each RPM value at MATLAB environment. Thermodynamic performance of the engine considered is measured with a set of exergetic and exergo-sustainability parameters for the LBP-TFE and its six components. Exergetic metrics evaluated in this study involve exergy efficiency, exergy destruction ratio, wasted exergy ratio, fuel exergy waste ratio, improved exergy efficiency and productivity lack ratio whereas environmental metrics incorporate exergetic sustainability index, environmental effect factor, sustainable efficiency factor and ecological effect factor. The main contribution of this study is to observe behaviours of performance, exergetic and environmental throughout eighteen RPM values. This analysis involving different running points can help understanding optimum RPM value for environmental sustainability. Additionally, firstly, the index 'specific irreversibility production' was computed for the LBP-TFE. Thanks to this metric, irreversibility of the engine per unit thrust is measured. Several significant findings can be highlighted from the current study as following:

i. The thrust of the LBP-TFE non-linearly increases throughout RPM values. Namely, the thrust value of the engine changes from 10.77 to 71.8 kN throughout RPM values.

ii. Exergy efficiency of the LBP-TFE is favourably affected from increase in RPM. Its value increases from 10.91 % to 30.14 % throughout RPM values. However, the highest exergy efficiency is computed as 32.4 % at 92.76 % RPM.

iii. Fuel exergy waste ratio of the engine decreases from 63.28 % to 40.02 % when the relative RPM is increased from 50.29 % to 100 %. This means that irreversibility per unit fuel exergy significantly diminishes.

iv. Improved exergy efficiency of the LBP-TFE is observed to change from 25.03 % to 41.88 %. It can deduced that compared with real exergy efficiency, exergy efficiency can be improved between 11.73 % and 15.55 % throughout RPM values.

v. Environmental efffect factor of the LBP-TFE decreases from 5.8 to 1.32 with increment of power setting. However the lowest value is 1.30 at 92.76 % RPM. It means that determining optimum RPM value leads to find the point where minimum environmental damage occurs.

vi. Finally, the results of specific irreversibility production for the engine verify findings of exergetic parameters. Namely, SIP value decreases due to rising RPM. It means that the engine produces less irreversibility at elevated RPMs.

As a conclusion, to find minimum and maximum points of exergetic values, the engine should be operated at relatively the lowest and the highest points. This study could guide the researchers to detect optimum RPM values in terms of environmental impact of the gas turbine engine. As a next study, exergetic and environmental parameters regarding LBP-TFE could be estimated with several prediction methods such as long-short term memory and supported vector machine. The modeling of performance parameters depending on RPM value could be performed. Also, effects of power settings on exergo-economic analysis metrics can be researched.

The Declaration of Conflict of Interest/ Common Interest
No conflict of interest or common interest has been declared by the authors.

The Declaration of Ethics Committee Approval
The author declare that this study does not require an ethics committee approval or any special permission.

The Declaration of Research and Publication Ethics
The authors of the paper declare that they comply with the scientific, ethical and quotation rules of SAUJS in all processes of the paper and that they do not make any falsification on the data collected. In addition, they declare that Sakarya University Journal of Science and its editorial board have no responsibility for any ethical violations that may be encountered, and that this study has not been evaluated in any academic publication environment other than Sakarya University Journal of Science.

REFERENCES

[1] H.Y. Akdeniz, O. Balli. "Effects of Bypass Ratio Change Trend on Performance in a Military Aircraft Turbofan Engine With Comparative Assessment". Journal of Energy Resources Technology. vol.143 no.12, pp. 120905, 2021.

[2] https://www.icao.int/sustainability/pages/factsfigures.aspx. (Last accessed 05 11 2022)

[3] K. Kayaalp, S. Metlek, S. Ekici, Y. Sohret. "Developing a model for prediction of the combustion performance and emissions of a turboprop engine using the long short-term memory method".Fuel. vol.302, pp. 121202, 2021.

[4] M. Z. Sogut. "New approach for assessment of environmental effects based on entropy optimization of jet engine".Energy. vol.234, pp. 121250, 2021.

[5] A. Dinc, I. Elbadawy. "Global warming potential optimization of a turbofan powered unmanned aerial vehicle during surveillance mission" . Transportation Research Part D: Transport and Environment. vol.85: pp. 102472, 2020.

[6] O. Balli. "Advanced exergy analyses of an aircraft turboprop engine (TPE)".Energy. vol.124, pp. 599-612, 2017.

[7] A. Dinc, H. Caliskan, S. Ekici, Y. Sohret. "Thermodynamic-based environmental and enviroeconomic assessments of a turboprop engine used for freight aircrafts under different flight phases".Journal of Thermal Analysis and Calorimetry. vol.147 no.22, pp. 12693-12707, 2022.

[8] H. Tuzcu, Y. Sohret, H. Caliskan. "Energy, environment and enviroeconomic analyses and assessments of the turbofan engine used in aviation industry".Environmental Progress & Sustainable Energy. vol.40 no.3,pp. e13547, 2020.

[9] O. Turan. "An exergy way to quantify sustainability metrics for a high bypass turbofan engine".Energy. vol.86, pp. 722-736, 2015.

[10] O. Balli, S. Ekici, T.H. Karakoc. "TF33 Turbofan engine in every respect: Performance, environmental, and sustainability assessment". Environmental Progress & Sustainable Energy. vol.40 no.3, pp. e13578, 2021.

[11] A. Dinc, Y. Sohret, S. Ekici. "Exergy analysis of a three-spool turboprop engine during the flight of a cargo aircraft".Aircraft Engineering and Aerospace Technology.vol.92 no.10,pp.1495-1503, 2020.

[12] O. Balli, H. Caliskan. "Turbofan engine performances from aviation, thermodynamic and environmental perspectives".Energy. vol.232, pp. 121031, 2021.

[13] https://prattwhitney.com/products-and-services/products/commercial-engines/jt8d. (Last accessed 09 11 2022)

[14] O. Turan, H. Aydin. "Exergy-based sustainability analysis of a low-bypass turbofan engine: A case study for JT8D". Energy Procedia. vol.95, pp. 499-506, 2016.

[15] https://www.easa.europa.eu/domains/environment/icao-aircraft-engine-emissions-databank. (Last accessed 01 12 2022)

[16] J. D. Mattingly, Elements of propulsion: gas turbines and rockets. 2006: American Institute of Aeronautics and Astronautics.

[17] A. F. El-Sayed, Aircraft propulsion and gas turbine engines. 2008: CRC press.

[18] O. Balli, H. Caliskan. "On-design and off-design operation performance assessmentsof an aero turboprop engine used on unmanned aerial vehicles (UAVs) in terms of aviation, thermodynamic, environmental and sustainability perspectives". Energy Conversion and Management. vol.243, pp. 114403, 2021.

[19] H. Aygun, O. Turan. "Exergetic sustainability off-design analysis of variable-cycle aero-engine in various bypass modes". Energy. vol.195, pp. 117008, 2020.

[20] Y. A. Cengel, M. A. Boles, Thermodynamics: An Engineering Approach 6th Editon (SI Units). 2007: The McGraw-Hill Companies, Inc., New York.

[21] T. J. Kotas, The exergy method of thermal plant analysis. 1995: Krieger.

[22] H. Aygun. "Investigation of effects of several design parameters on exergo-sustainability metrics for twin-spool turbojet engine at different flight conditions". International Journal of Exergy. vol.37 no.2, pp. 200-213, 2022.

[23] H. Aygun. "Thermodynamic and environmental considerations of small turbojet engine under different design variables".Energy Sources, Part A: Recovery, Utilization, and Environmental Effects, 2021. https://doi.org/10.1080/15567036.2021.1985019

[24] W. Van Gool, "Energy Policy: Fairy Tales and Factualities". Innovation and Technology — Strategies and Policies, O.D.D. Soares, A.M. da Cruz, G.C. Pereira, I.M.R.T. Soares, and A.J.P.S. Reis, Editors., Springer Netherlands: Dordrecht. 1997, pp. 93-105.

[25] O. Balli. "Exergy modeling for evaluating sustainability level of a high by-pass turbofan engine used on commercial aircrafts". Applied Thermal Engineering. vol.12, pp. 138-155, 2017.

[26] G. P. Hammond. "Energy and sustainability in a complex world: Reflections on the ideas of Howard T. Odum".International Journal of Energy Research. vol.31 no.12, pp. 1105-1130, 2007.

[27] H. Aydin, O. Turan, T. H. Karakoc, A. Midilli. "Exergetic sustainability indicators as a tool in commercial aircraft: a case study for a turbofan engine".International journal of green energy. vol.12 no.1, pp. 28-40, 2015.

Title: Electrospun PVDF Membranes Incorporated with Functionalized Carbon-based Material for Removal of Cationic Dyes

Authors: Fatma DEMİRCİ, Burçak KAYA ÖZSEL

Electrospun PVDF Membranes Incorporated with Functionalized Carbon-based Material for Removal of Cationic Dyes

Fatma DEMIRCI [*1] iD, Burcak KAYA OZSEL[1] iD

Abstract

In this study, polyvinylidene fluoride (PVDF) polymeric membranes with addition of functionalized carbon-based material (CBM) were fabricated by using electrospinning technique for the removal of cationic dyes from wastewater. CBM was prepared through a two-step carbonization process from cotton linter as an agricultural waste biomass. The characterization of CBM was performed by using Brunauer–Emmett–Teller (BET) surface analysis, fourier transform infrared spectrometry (FTIR) and elemental analysis. The morphologies of electrospun membranes were observed by scanning electron microscope (SEM) which clearly revealed that nanofibers with a smooth surface were produced by incorporation of CBM. According to the results obtained from FTIR and differential scanning calorimetry (DSC), crystallization behavior of PVDF membranes was promoted by increasing the percentage of CBM in the membrane. PVDF membrane prepared with the addition of 3 wt % CBM exhibited the highest water flux performance with a dye rejection of 74.6 % in comparison with the pure PVDF one.

Keywords: Electrospinning, membrane, carbon-based material, dye removal

1. INTRODUCTION

Water, which is vital for sustaining life, is becoming an increasingly scarce resource due to the constantly increasing industrialization and rapid population growth globally. Namely, billions people do not have access to water and sanitation. One of the most important problem in front of sanitation is organic dyes used in many industries such as textile, food, leather, paper and plastic [1]. It is stated that 100.000 different types of paint are commercially produced for use in these industries, and 10-15% of the paints, which reach an annual production amount of 1.6 million tons, are discharged into the water without being specifically treated [1-3]. Many of these paints mixed with water are toxic and difficult to degrade, thus creating serious problems for aquatic organisms and humans. Therefore, many studies have been carried out to remove these pollutants from water such as advanced oxidation processes [4], membrane filtration [5], photocatalytic oxidation reaction [6], and adsorption [7]. Although membrane technologies are the most preferred method in water applications,

Fatma DEMİRCİ, Burçak KAYA ÖZSEL

Electrospun PVDF Membranes Incorporated with Functionalized Carbon-based Material for Removal of Cati...

the adsorption method is considered the most promising method for the removal of organic dyes [2, 8, 9]. In this sense, membrane applications containing adsorbent additives have been studied in the literature recently [10-12].

Electrospinning membranes with high surface area and pore ratio are thought to offer great advantages in environmental applications. PVDF polymer, which is frequently preferred in membrane applications due to its high mechanical strength, thermal and chemical stability, can be easily processed in electrospinning, making the electrospinning process even more usable in membrane applications for water treatments [13-15]. An adsorbent additive to be made into the PVDF membrane will provide a significant efficiency in the removal of dyestuffs in water. In the literature, there are membrane studies in which various adsorbents such as metal-organic frameworks (MOFs) [16, 17], magnetic particles [18], inorganic metal oxides [19], carbon nanotubes [20]. are used. Adding carbon-based materials used as adsorbent into the membrane as an additive will be effective in removing the dyestuff in the water.

Thermal (inert atmosphere, generally $\leq 600\,°C$) and hydrothermal (in water, generally $180–300\,°C$) carbonization are known as the common carbonization methods especially to produce biomass-derived carbon materials [21]. The characteristics of biomass-derived carbon structures are directly affected by the carbonization method due to the differences in reaction mechanism during the different carbonization methods. For instance, specific surface areas are generally low for hydrothermally treated biomass-derived carbon materials. There are many reports in the literature about the carbon materials produced by only using a single carbonization method [22, 23]. In the first part of the study, two carbonization processes were applied consecutively to produce carbon structure with superior physical and chemical properties. In both carbonization processes relatively low temperatures were applied to prepare carbon structure with a higher density of acid sites because biomass components are not completely hydrolysed at low temperatures, thus leading to the formation of surface functional groups onto the carbon surface. Also in the thermal carbonization process if the temperature increases, sulfonic functional groups can decompose decreasing the acidic functionalization [24]. Here, sulfamic and citric acid were used in order to accelerate the decomposition of cellulosic biomass and acidic functionalization of carbon structure to improve dye adsorption capacity. Sulfamic acid is a strong (pKa $\approx$ 1), low-cost, low-corrosive, non-toxic acid for functionalization and citric acid is like a catalyst that leads to higher carbon content during carbonization. The acid-functionalized carbon-based material was characterized by using Brunauer–Emmett–Teller (BET) surface analysis, fourier transform infrared spectrometry (FTIR) and elemental analysis.

In the second part of the study, electrospun PVDF membranes were produced by addition of various amounts of the produced CBM. The CBM addition effect on crystallization behavior of PVDF was investigated by FTIR and DSC analyses. It has been demonstrated by SEM images that CBM addition supports nanofiber formation by regulating jet formation. The effect of the additive on the water flux and cationic dye (methylene blue) rejection ratio of the membrane were investigated.

2. MATERIALS and METHOD

2.1. Materials

Cotton linter as a carbon precursor was provided from a local supplier in Adana, Turkey. It has a cellulose content of 83.4 % (w/w) determined by using the method described in the literature [25]. Sulfamic

acid (≥ 99.0 %, Merck, Germany) and citric acid (≥ 99.5 %, Sigma-Aldrich, Germany) were used for effective carbonization and functionalization of carbon-based material. Polyvinylidene fluoride (PVDF) (Solef® 1015- Solvay, Mw=516,000, Alpharetta, GA, USA) powder was used as a base polymer to prepare electrospun membranes. N,N-Dimethylacetamide (DMAc) (Sigma-Aldrich, Germany), acetone and methanol (Merck, Germany) were used as solvents. Methylene Blue (MB) (Sigma, Italy) was used as a model cationic dye.

2.2. Production of Carbon-based Material

Before the hydrothermal carbonization process alkali treatment was carried out to purify linter biomass [26]. 25.0 g raw linter was treated with 5% (w/v) aqueous NaOH solution for 1 h at 70 °C under stirring. Cold distilled water was added to the mixture to stop the reaction and then the mixture was filtered until to reach pH 6. The dried alkali treated linter biomass was bleached with a 1:20 (g/ml) solution of H_2O_2 30% (v/v) for 1 h at 50 °C under constant stirring. Cold distilled water was added to the mixture in order to stop the reaction and then the mixture was vacuum filtered until to reach pH 6. The bleached fibers were dried in an oven for 48 h at 60 °C.

Carbon-based material was prepared by successive hydrothermal and thermal carbonization of cotton linter. In hydrothermal carbonization process, 1.5 g biomass, 1.5 g sulfamic acid and 0.5 g citric acid were mixed with 20 mL water and the mixture pretreated with high power ultrasound for 10 min by using an ultrasonic probe sonicator. Then the slurry was subjected to heat treatment in a teflon sealed autoclave at 180 °C for 20 h. The semi-carbonized solid was washed by DI water and methanol to remove impurities and dried at 100 °C for 24 h. In the thermal carbonization process, hydrothermally treated-solid was transferred in a tube fixed

furnace then heated to 300 °C at 5°C/min and held for 3 hours under nitrogen atmosphere. After the tube furnace was cooled to room temperature the solid sample was washed with distilled water and dried at 105 °C for 24 h in an oven. Prepared carbon-based material was labeled as 'CBM'. The CBM was sieved at the particle size below 40 mesh prior to use. For comparison a raw carbon-based material was also prepared without using any acids in the hydrothermal carbonization process, labeled as 'CBM0'. All produced carbon-based materials were stored in a desiccator until use.

2.3. Production of CBM Added Electrospun Membranes

To obtain spinning solution firstly, 18 wt% PVDF was dissolved in a mixed solvent of DMAc and acetone with a weight ratio of 1:1, by stirring at 50 °C for 24 h. Then, various amounts of CBM (1 wt%, 2 wt%, and 3 wt%) were added into the solution and stirring was continued for 1 more hour at room temperature to properly disperse the CBM into the solution. The produced membranes were labeled as M-0 (0 wt% CBM), M-1 (1 wt% CBM), M-2 (2 wt% CBM), and M-3 (3 wt% CBM) depending on the amount of the CBM they contain. 20 mL of the prepared solution was taken in a plastic syringe and electrospun on aluminum sheets at 23-27 kV through an electrospinning device (İnovenso – Nanospinner24). The tip and collector distance was 20 cm and the solution fed ratio was 6 mL/h from a diameter capillary tip 20 mL syringe with 1.36 cm inner diameter.

2.4. Characterization of Carbon-based Material

The total surface area and pore size of the CBM and CBM0 were determined by N_2 adsorption–desorption at 77 K using a Micrometrics TriStar II instrument and prior to the analysis the samples were out gassed for 20 h at 473 K. The C,N,H content of carbon-based materials were determined by

Fatma DEMİRCİ, Burçak KAYA ÖZSEL

Electrospun PVDF Membranes Incorporated with Functionalized Carbon-based Material for Removal of Cati...

using a Thermo Scientific FlashSmart Elemental Analyzer. Identification of the functional groups on the surface of samples was performed by FTIR spectroscopy (Perkin Elmer Spectrum Two FTIR ATR System). The total acidity of carbon-based materials was determined by the titration method [27].

2.5. Characterization of CBM Added Membranes

The produced membranes were characterized with FTIR (Thermo Nicolet, iS50 with an attenuated total reflectance (ATR) accessory) analyses. The FTIR spectra of the samples were recorded in the wavenumber range 400 to 4,000 cm^{-1} with 16 scans at 4 cm^{-1} resolutions.

Thermal properties of the produced membranes and the effect of the additive on crystallization behavior of the membranes were characterized with differential scanning calorimeter (DSC) (TA Instrument/DSC25) analyses. Membrane samples of 7-8 mg were heated to 200 °C from -90 °C at a heating rate of 10 °C/min under nitrogen atmosphere.

The water flux and MB rejection performances of the produced membranes were measured with a stirred cell (effective area, 14.6 cm^2, HP4750 Sterlitech) at 1 bar pressure. The produced membranes pure water flux values (J_w) (L/m^{2}h.bar) were calculated by the following equation:

$$J_w = \frac{V}{A \times t} \tag{1}$$

where V (L) is the permeated water volume at in the operation time t (h), and A (m^2) is the effective membrane area.

The same cell was used for the MB rejection measurements of the produced membranes. 10 ppm MB was used as feed solution. The concentration of the MB in the feed and permeate were determined with UV-Visible spectrometer (Scinco-NEOSYS200) at 665 nm wavelength. The MB rejection percentage $(R, \%)$ of the produced membranes were determined with following equation:

$$R(\%) = \frac{A_f - A_p}{A_f} \times 100 \tag{2}$$

where the A_f and A_p were the absorbance value of the feed and permeate MB solutions, respectively. The pure water flux and MB rejection tests were replicated for at least three membrane samples and average values were given with standard deviations.

The surface morphology of the produced membranes was observed by scanning electron microscopy (SEM – Carl Zeiss / Gemini 300). Samples were coated with 15 nm gold palladium and coated samples images were observed with 500 x and 5000 x magnifications.

3. RESULTS AND DISCUSSION

3.1. Characterization of Carbon-based Material

The elemental contents of CBM0 and CBM were listed in Table 1. As expected, CBM has a higher N content than CBM0 since it was functionalized by a nitrogen-containing acid. The higher C content of CBM could be attributed to the higher carbonization degree of CBM due to the presence of acids used in hydrothermal carbonization process.

The specific surface area, pore volume and pore size of the CBM0 and CBM obtained based on the N$_2$ adsorption-desorption datas were also given in Table 1. The specific surface area of CBM was expanded from 19.0 to 258.0 m^2/g (Table 1). This huge increase in the surface area of the CBM could attributed the presence of the acids in the hydrothermal carbonization of this sample. It is known from the literature the presence of such acids in the hydrothermal

Fatma DEMİRCİ, Burçak KAYA ÖZSEL

Electrospun PVDF Membranes Incorporated with Functionalized Carbon-based Material for Removal of Cati...

Table 1 Textural properties and elemental compositions of carbon materials

	BET surface area (m^2/g)	Pore Volume (cm^3/g)	Pore width (nm)	Total acid sites (mmol/g)	C	H	N	O *
					(wt. %)			
CBM0	19.0	0.004	0.91	0.04	61.5	4.2	-	34.3
CBM	258.0	0.01	1.31	0.30	67.4	4.1	2.8	25.7

Calculated by difference, approximately value O% = 100 − [C% + H% + N%]

carbonization promote the dehydration reaction, decrease carbon aggregation thus resulted in a significant increase in specific surface area [28-30]. The CBM could be classified as mesoporous material with average pore size in fall in the range of 2–50 nm.

The FTIR analysis was used to reveal possible functional groups of CBM0 and CBM. The broad peaks located between 3000–3600 cm^{-1} were related to O–H stretching modes of the carboxyl and phenolic hydroxyl groups. The peaks at 2921 and 812 cm^{-1} corresponded to the stretching vibration of aliphatic and aromatic C–H bond [24, 31]. The band at 1700 cm^{-1} was related to the absorption of C=O bonds from -COOH groups. The peak located at 1600 cm^{-1} corresponded to the C=C stretching in the aromatic ring skeleton and this band strength of the CBM was higher than CBM0 which could be ascribed to an increase in aromaticity [21]. A distinct band at 1400 cm^{-1} was assigned to the O=S=O stretching vibration in –SO$_3$H group. And, a new broad band appeared between 1060 to 1262 cm^{-1} could be attributed to -SO$_3$ symmetric vibration which could also be ascribed to the substitute of acidic –SO$_3$H groups [32].

3.2. Characterization of CBM Added Membranes

3.2.1. Morphological Characteristics of the Produced Membranes

It is known in the literature that the acetone ratio used in the DMF/acetone solution system is effective in the formation of nanofibers while obtaining the nanofiber surface from PVDF. If the volatile organic solvent ratio in the solvent mixture is low, film formation takes place instead of the nanofiber surface [33]. Although the weight ratio of acetone to DMF ratio was kept 1:1 in this study, no fibrous surface formation occurred in the undoped sample. Carbon-based materials are known to increase conductivity [15, 34, 35]. When CBM was added to the electrospinning solution, it increased the conductivity and regulated the jet behavior, and thus fiber formation occurred in the doped structures. In Figure 1, surface images of M-1 and M-3 membranes are given with 500x and 5000x magnifications. While M-0 formed a completely flat film surface, a structure consisting of fiber and film mixture was obtained after the addition of 1% CBM as seen in Figure 1. When the additive ratio is further increased, a smooth jet formation is achieved and a nanofiber surface consisting of finer fibers is provided with diameter of 592±114 nm. These results were also confirmed by flux tests.
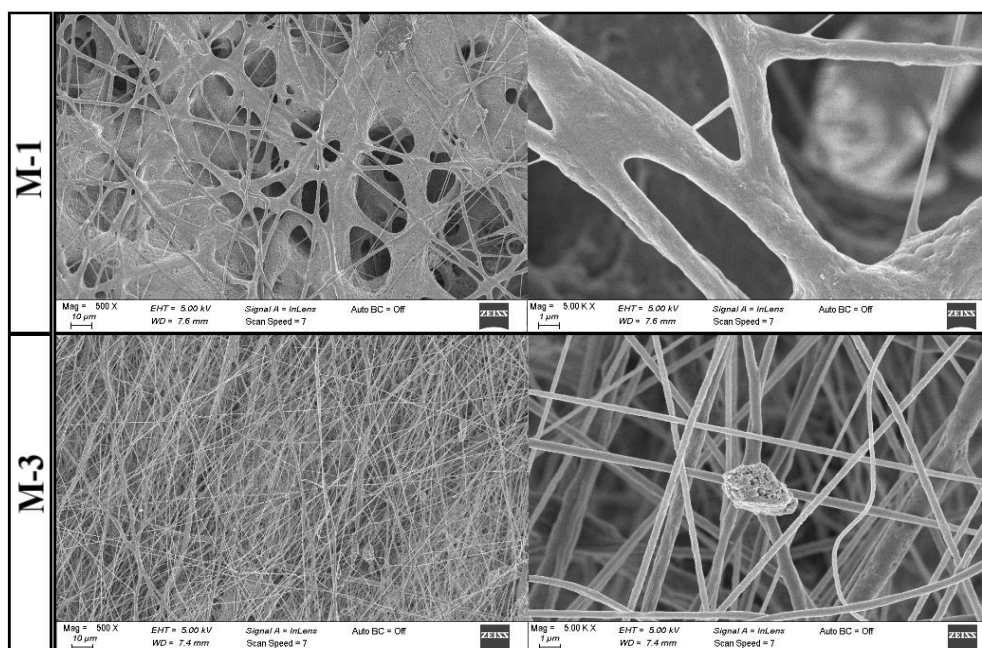
Fatma DEMİRCİ, Burçak KAYA ÖZSEL

Electrospun PVDF Membranes Incorporated with Functionalized Carbon-based Material for Removal of Cati...

Figure 1 SEM images of the produced membranes

3.2.2. FTIR Characterization of the Produced Membranes

FTIR spectra of neat PVDF and CBM added PVDF membranes were given in Figure 2. The addition of the CBM did not cause an additional band formation, but changed the crystallization behavior of the membrane. In order to determine the variation of the specific crystalline phases of the produced membranes, the spectra were examined in the region between 400 cm^{-1} to 1000 cm^{-1}. While the bands at 840, 509, and 473 cm^{-1} were characteristic for β phase, the bands at 974, 795, 762, 613, and 531 cm^{-1} were associated with α phase crystals of the PVDF. It was observed that the M-3 demonstrated the highest band intensities for β phase bands and also it has the second highest band intensities for α phase associated bands. This showed that the most crystallization occurred in M-3, which was also confirmed by DSC analysis. The band at 473 cm^{-1} associated with the β phase was observed only in M-3 and M-2. This result showed that CBM addition to the membrane structure increases the formatın of the β phase crystals. The relative amount of β phase was quantified using Lambert-Beer law [36] by considering the relative intensity of absorption bands at 762 cm^{-1} (α phase)

and 840 cm^{-1} (β phase). The $F(\beta)/F(\alpha)$ was calculated by the following equation,

$$\frac{F(\beta)}{F(\alpha)} = \frac{A_\beta^{840}}{1.26\, A_\alpha^{762}} \tag{3}$$

where A_α and A_β are the absorbed intensity at 762 and 840 cm^{-1}, respectively. β/α phase ratio of the M-0, M-1, M-2, and M-3 were calculated as 0.845, 1.0248, 1.752, and 1.496, respectively. The addition of CBM increased the beta phase of the membrane, but the β/α phase ratio of M-3 was lower than that of M-2, as the alpha phase fraction was also increased when the addition amount was increased to 3%.
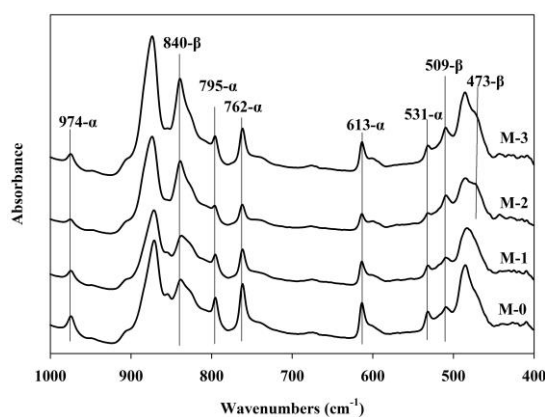

Figure 2 FTIR spectra of produced membranes

3.2.3. Thermal Properties and Crystallinity of the Produced Membranes

The DSC thermograms of the neat PVDF and CBM added PVDF membranes were given in Figure 3. All membranes demonstrated a similar melting temperature at approximately 168°C, indicating the CBM addition did not cause disruption in the thermal transition of the PVDF. Melting peaks of the α- and β-crystals appear to be superimposed at that temperature, in all membrane thermograms. However, the crystallinity of the membranes differed with the addition of the CBM. The degree of crystallinity of the produced membranes were calculated by the fusion enthalpy of the PVDF crystal ($\Delta H_f°=105$ J/g). The melting temperature and crystallinity of the produced membranes were summarized in Table 2. It is know in literature, the structure, dimension of the nanoparticle and the addition amount of this material to the solution can cause difference of the obtain fiber crystallinity [15, 37]. As seen in the table, while 1% CBM additive did not affect the crystallization behavior of the membrane, when the additive rate was increased to 2%, the crystallization rate of the membrane decreased from 64% to 58.13%, although CBM further increased conductivity and so facilitated fiber drawing. This can be explained by the fact that the conductivity increase provided by the CBM additive did not reach the level to orient the fibers. As a result of further increase in the additive ratio, the orientation of the fibers increased with the increased conductivity and thus the highest crystallization was observed in M-3 (82.68%). Similar results are also found in the literature, Nasır et al [15] produced carbon black/PVDF copolymer nanocomposites, 5% carbon black added PVDF nanofibers showed more crystallization than 1% carbon black added fibers.
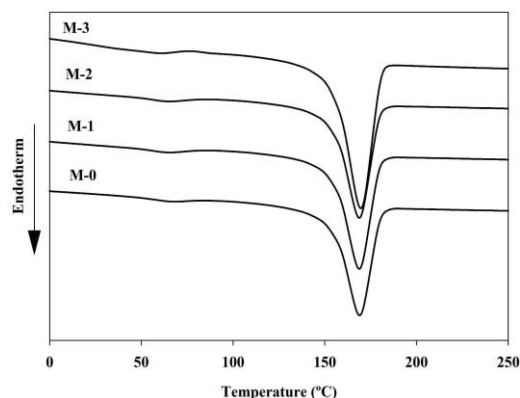

Figure 1 DSC thermogram of the produced membranes

Table 2 Thermal properties and crystallinity of the produced membranes

	Tm (°C)	Crystallinity (%)
M-0	168.98	64.01
M-1	168.76	64.98
M-2	168.76	58.13
M-3	169.17	82.68

3.2.4. Permeability Properties of the Produced Membranes

The pure water flux and MB dye rejection performances of the neat and CBM added membranes were given in Figure 4. As explained in the SEM results (Figure 1), M-0 formed a flat film surface. Therefore, permeation tests could not be applied to this membrane. The addition of CBM to the electrospinning solution increased the electrical conductivity, regulated the jet behavior and made it possible to obtain nanofiber surfaces as seen in the SEM images. More importantly, it thus created a porous surface structure, making the resulting structure suitable for membrane applications. As can be seen in the SEM images, a complete nanofiber structure has not yet been obtained at the 1% CBM contribution. For this reason, as seen in Figure 4, the M-1 membrane gives a very low pure water flux value of 22.1 L/m^{2}h. It is known in the literature, the addition of carbon based materials improve the water flux performance of the electrospun PVDF membranes [38, 39]. Similar to literature, when the CBM additive ratio was increased to 2%, a surface consisting entirely of

Fatma DEMİRCİ, Burçak KAYA ÖZSEL

Electrospun PVDF Membranes Incorporated with Functionalized Carbon-based Material for Removal of Cati...

nanofibers were obtained, and thus a great increase in flux performance was obtained with the increase in porosity. However, as can be seen in Figure 4, the MB rejection performance of the M-2 decreased from 100% to 64% compared to M-1, since the film part of the M-1 is also effective in rejection of the dye. By increasing the CBM additive ratio, the pure water flux performance of the membrane increased further, as a surface consisting of more nano fibers was achieved. At the same time, a significant increase was achieved in the dye rejection performance as the dye adsorber additive ratio was increased.
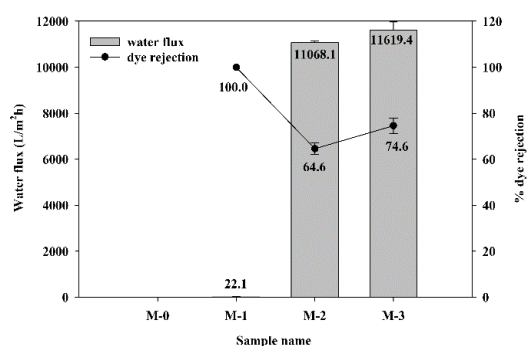
Figure 2 Water flux and dye rejection performances of the produced membranes

4. CONCLUSION

Acid functionalized CBM with high adsorption capacity were produced from cellulosic biowaste by a two-step carbonization process. Electrospun PVDF membranes, in which the produced CBM is doped in various ratios, were produced successfully. It was observed that the CBM additive increasing the conductivity during electrospinning supports nanofiber drawing. While flat film structures were formed in M-0 and M-1 membranes, nanofibrous membrane structures were obtained in M-2 and M-3 with the increase in the additive ratio. This was confirmed by SEM images, water flux and dye rejection results. M-0 and M-1, which form a flat film surface, showed very low water flux values. The M-3 showed the highest water flux performance, while the MB rejection rate also increased by 10% compared to the M-2. This result showed

that the CBM addition promotes finer fiber spinning and the additive works actively in the adsorption of cationic dyestuffs. In addition, FTIR and DSC results showed that the CBM addition supports the formation of regular crystals in the membrane structure, thus enabling the production of more durable membranes.

Authors' Contribution
The authors contributed equally to the study.

The Declaration of Conflict of Interest/ Common Interest
No conflict of interest or common interest has been declared by the authors.

The Declaration of Ethics Committee Approval
This study does not require ethics committee permission or any special permission.

The Declaration of Research and Publication Ethics
The authors of the paper declare that they comply with the scientific, ethical and quotation rules of SAUJS in all processes of the paper and that they do not make any falsification on the data collected. In addition, they declare that Sakarya University Journal of Science and its editorial board have no responsibility for any ethical violations that may be encountered, and that this study has not been evaluated in any academic publication environment other than Sakarya University Journal of Science.

REFERENCES

[1]   E. Santoso, R. Ediati, Y. Kusumawati, H. Bahruji, D. O. Sulistiono, D. Prasetyoko, "Review on recent advances of carbon based adsorbent for methylene blue removal from

Fatma DEMİRCİ, Burçak KAYA ÖZSEL

Electrospun PVDF Membranes Incorporated with Functionalized Carbon-based Material for Removal of Cati...

wastewater," Materials Today Chemistry, vol. 16, no. 100233, 2020.

[2] J. Li, L. Huang, X. Jiang, L. Zhang, X. Sun, "Preparation and characterization of ternary Cu/Cu$_2$O/C composite: An extraordinary adsorbent for removing anionic organic dyes from water," Chemical Engineering Journal, vol. 404, no. 127091, 2021.

[3] K. B Tan, M. Vakili, B. A. Horri, P. E. Poh, A. Z. Abdullah, B. Salamatinia, "Adsorption of dyes by nanomaterials: recent developments and adsorption mechanisms," Separation and Purification Technology, vol. 150, pp. 229-242, 2015.

[4] P. Verma, S. K. Samanta, "Microwave-enhanced advanced oxidation processes for the degradation of dyes in water," Environmental chemistry letters, vol. 16, no. 3, pp. 969-1007, 2018.

[5] J. Zhao, H. Liu, P. Xue, S. Tian, S. Sun, X. Lv, "Highly-efficient PVDF adsorptive membrane filtration based on chitosan@ CNTs-COOH simultaneous removal of anionic and cationic dyes," Carbohydrate Polymers, vol. 274, no. 118664, 2021.

[6] H. D. Bouras, Z. Isik, E. B. Arikan, N. Bouras, A. Chergui, H. C. Yatmaz, N. Dizge, "Photocatalytic oxidation of azo dye solutions by impregnation of ZnO on fungi," Biochemical Engineering Journal, vol. 146, pp. 150-159, 2019.

[7] A. Nasar, F. Mashkoor, "Application of polyaniline-based adsorbents for dye removal from water and wastewater—a review," Environmental Science and Pollution Research, vol. 26, no. 6, pp. 5333-5356, 2019.

[8] F. Demirci, A. Aydın, M. Orhan, H. B. Koçer, "Production of ultrafiltration membranes exhibiting antibacterial properties by the incorporation of novel N-halamine copolymers," Journal of Applied Polymer Science, vol. 139, no. 31, no. e52727, 2022.

[9] J. Wang, Q. Zhang, X. Shao, J. Ma, G. Tian, "Properties of magnetic carbon nanomaterials and application in removal organic dyes," Chemosphere, vol. 207, pp. 377-384, 2018.

[10] F. Baskoro, S. R. Kumar, S. J. Lue, "Grafting thin layered graphene oxide onto the surface of nonwoven/PVDF-PAA composite membrane for efficient dye and macromolecule separations," Nanomaterials, vol. 10, no. 4, pp. 792, 2020.

[11] L. Zhou, Y. He, H. Shi, G. Xiao, S. Wang, Z. Li, J. Chen, "One-pot route to synthesize HNTs@ PVDF membrane for rapid and effective separation of emulsion-oil and dyes from waste water," Journal of hazardous materials, vol. 380, no. 120865, 2019.

[12] Y. Song, Y. Wang, N. Zhang, X. Li, X. Bai, T. Li, "Quaternized carbon-based nanoparticles embedded positively charged composite membranes towards efficient removal of cationic small-sized contaminants," Journal of Membrane Science, vol. 630, no. 119332, 2021.

[13] F. Liu, N. A. Hashim, Y. Liu, M. M. Abed, K. Li, "Progress in the production and modification of PVDF membranes," Journal of Membrane Science, vol. 375, no. 1-2, pp. 1-27, 2011.

[14] S. Mohamadi, N. Sharifi-Sanjani, "Crystallization of PVDF in graphene-filled electrospun PVDF/PMMA

Fatma DEMİRCİ, Burçak KAYA ÖZSEL

Electrospun PVDF Membranes Incorporated with Functionalized Carbon-based Material for Removal of Cati...

nanofibers processed at three different conditions," Fibers and Polymers, vol. 17, no. 4, pp. 582-592, 2016.

[15] M. Nasir, R. I. Sugatri, P. P. P. Asri, F. Dara, "Nanostructure and surface characteristic of electrospun carbon black/PVDF copolymer nanocomposite," Journal of Silicate Based and Composite Materials, vol. 70, no. 209-213, 2018.

[16] G. Yang, D. Zhang, G. Zhu, T. Zhou, M. Song, L. Qu, K. Xiong, H. Li, "A Sm-MOF/GO nanocomposite membrane for efficient organic dye removal from wastewater," RSC Advances, vol. 10, no. 14, pp. 8540-8547, 2020.

[17] S. Tahazadeh, T. Mohammadi, M. A. Tofighy, S. Khanlari, H. Karimi, H. B. M. Emrooz, "Development of cellulose acetate/metal-organic framework derived porous carbon adsorptive membrane for dye removal applications," Journal of Membrane Science, vol. 638, no. 119692, 2021.

[18] M. A. Lalabadi, H. Peyman, H. Roshanfekr, S. Azizi, M. Maaza, "Polyethersulfone nanofiltration membrane embedded by magnetically modified MOF (MOF@ Fe3O4): fabrication, characterization and performance in dye removal from water using factorial design experiments," Polymer Bulletin, pp. 1-21, 2022.

[19] A. K. Shukla, J. Alam, F. A. A. Ali, M. Alhoshan, "Efficient soluble anionic dye removal and antimicrobial properties of ZnO embedded-Polyphenylsulfone membrane," Water and Environment Journal, vol. 35, no. 2, pp. 670-684, 2021.

[20] S. Gholami, J. L. Llacuna, V. Vatanpour, A. Dehqan, S. Paziresh, J.

L. Cortina, "Impact of a new functionalization of multiwalled carbon nanotubes on antifouling and permeability of PVDF nanocomposite membranes for dye wastewater treatment," Chemosphere, vol. 294, pp. 133699, 2022.

[21] M. M. Fu, C. H. Mo, H. Li, Y. N. Zhang, W. X. Huang, M. H. Wong, "Comparison of physicochemical properties of biochars and hydrochars produced from food wastes," Journal of Cleaner Production, vol. 236, no. 117637, 2019.

[22] X. Zhang, Y. Zhang, H. H. Ngo, W. Guo, H. Wen, D. Zhang, C. Li, L. Qi, "Characterization and sulfonamide antibiotics adsorption capacity of spent coffee grounds based biochar and hydrochar," Science of the Total Environment, vol. 716, no. 137015, 2020.

[23] A. Jain, R. Balasubramanian, M. P. Srinivasan, "Hydrothermal conversion of biomass waste to activated carbon with high porosity: A review," Chemical Engineering Journal, vol. 283, pp. 789-805, 2016.

[24] R. O. Araujo, J. da Silva Chaar, L. S. Queiroz, G. N. da Rocha Filho, C. E. F. da Costa, G. C da Silva, R. Landers, M. J. Costa, A. A. Gonçalves, L. K. de Souza, "Low temperature sulfonation of acai stone biomass derived carbons as acid catalysts for esterification reactions," Energy Conversion and Management, vol 196, pp. 821-830, 2019.

[25] T. Foyle, L. Jennings, P. Mulcahy, "Compositional analysis of lignocellulosic materials: Evaluation of methods used for sugar analysis of waste paper and straw," Bioresource Technology, vol. 98, no. 16, pp. 3026-3036, 2007.

[26] M. M. A. D. Maciel, K. C. C Benini, H. J. C. Voorwald, M. O. H. Cioffi, "Obtainment and characterization of nanocellulose from an unwoven industrial textile cotton waste: Effect of acid hydrolysis conditions," International Journal of Biological Macromolecules, vol. 126, pp. 496-506, 2019.

[27] C. Samori, A. Parodi, E. Tagliavini, P. Galletti, "Recycling of post-use starch-based plastic bags through pyrolysis to produce sulfonated catalysts and chemicals," Journal of Analytical and Applied Pyrolysis, vol. 155, no. 105030, 2021.

[28] R. F. Susanti, A. A. Arie, H. Kristianto, M. Erico, G. Kevin, H. Devianto, "Activated carbon from citric acid catalyzed hydrothermal carbonization and chemical activation of salacca peel as potential electrode for lithium ion capacitor's cathode", Ionics, vol. 25, pp. 3915-3925, 2019.

[29] H. Simsir, N. Eltugral, S. Karagoz, "Effects of acidic and alkaline metal triflates on the hydrothermal carbonization of glucose and cellulose," Energy & Fuels, vol. 33, no. 8, pp. 7473-7479, 2019.

[30] Z. Hoseinabadi, S. A. Pourmousavi, "Synthesis of Starch Derived Sulfonated Carbon-based Solid Acid as a Novel and Efficient Nanocatalyst for the Synthesis of Dihydropyrimidinones," Warasan Khana Witthayasat Maha Witthayalai Chiang Mai, vol. 46, no. 1, pp. 132-143, 2019.

[31] Z. Liu, Z. Liu, "Comparison of hydrochar-and pyrochar-based solid acid catalysts from cornstalk: Physiochemical properties, catalytic activity and deactivation behavior," Bioresource Technology, vol. 297, no. 122477, 2020.

[32] R. S. Salama, S. M. El-Bahy, M. A. Mannaa, "Sulfamic acid supported on mesoporous MCM-41 as a novel, efficient and reusable heterogenous solid acid catalyst for synthesis of xanthene, dihydropyrimidinone and coumarin derivatives," Colloids and Surfaces A: Physicochemical and Engineering Aspects, vol. 628, no. 127261, 2021.

[33] Y. J. Hwang, S. Choi, H. S. Kim, "Structural deformation of PVDF nanoweb due to electrospinning behavior affected by solvent ratio," e-Polymers, vol. 18, no. 4, pp. 339-345, 2018.

[34] J. Hwang, J. Muth, T. Ghosh, "Electrical and mechanical properties of carbon-black-filled, electrospun nanocomposite fiber webs," Journal of Applied Polymer Science, vol. 104 no. 4, pp. 2410-2417, 2007.

[35] E. Tarasova, A. Byzova, N. Savest, M. Viirsalu, V. Gudkova, T. Maertson, A. Krumme, "Influence of preparation process on morphology and conductivity of carbon black-based electrospun nanofibers," Fullerenes, Nanotubes and Carbon Nanostructures, vol. 23, no. 8, pp. 695-700, 2014.

[36] M. M. Tao, F. Liu, B. R. Ma, L. X. Xue, "Effect of solvent power on PVDF membrane polymorphism during phase inversion," Desalination, vol. 316, pp. 137-145, 2013.

[37] R. Moradi, J. Karimi-Sabet, M. Shariaty-Niassar, M. A. Koochaki, "Preparation and characterization of polyvinylidene fluoride/graphene superhydrophobic fibrous films",

Fatma DEMİRCİ, Burçak KAYA ÖZSEL

Electrospun PVDF Membranes Incorporated with Functionalized Carbon-based Material for Removal of Cati...

Polymers, vol. 7, no. 8, pp. 1444-1463, 2015.

[38] N. Mehranbod, M. Khorram, S. Azizi, N. Khakinezhad, "Modification and superhydrophilization of electrospun polyvinylidene fluoride membrane using graphene oxide-chitosan nanostructure and performance evaluation in oil/water separation", Journal of Environmental Chemical Engineering, vol. 9, no. 5, pp. 106245, 2021.

[39] J. A. Park, A. Nam, J. H. Kim, S. T. Yun, J. W. Choi, S. H. Lee, "Blend-electrospun graphene oxide/Poly (vinylidene fluoride) nanofibrous membranes with high flux, tetracycline removal and anti-fouling properties", Chemosphere, vol. 207, pp. 347-356, 2018.

Title: Length-Weight, Length-Length Relationships, and Condition Factor of Red Mullet (Mullus barbatus Linnaeus, 1758) Inhabiting Mersin Bay

Authors: Seda KONTAŞ

Length-Weight, Length-Length Relationships, and Condition Factor of Red Mullet (*Mullus barbatus* Linnaeus, 1758) Inhabiting Mersin Bay

Seda KONTAŞ YALÇINKAYA *1 iD

Abstract

This study reports the condition factor, length-weight, and length-length relationships in females, males, and all samples of *Mullus barbatus* inhabiting Mersin Bay. A total of 152 individuals were sampled. The mean weight (W) was 18.01 ± 0.573 g, and the mean total length (TL), fork length (FL), and standard length (SL) were 12.0 ± 0.094 cm, $11.0 \pm 0,086$ cm, and 9.9 ± 0.080 cm for all *M. barbatus*, respectively. The total length-weight relationship was determined as $W=0.0033TL^{3.444}$ ($R^2=0.90$). The *b* value was calculated as 3.444 and it showed positive allometric growth for all *M. barbatus* inhabiting Mersin Bay. The LLRs were calculated as $TL=1.0706FL+0.1386$ ($R^2=0.95$), $TL=1.1634SL+0.371$ ($R^2=0.97$), and $FL=1.0541SL+0.543$ ($R^2=0.96$) for all individuals, respectively. The mean value of the condition factor was calculated as $1.00 \pm 0,0093$ for all *M. barbatus* samples. The values of the condition factor in *M. barbatus* ranged from 0.740 to 1.274. There are few studies about *M. barbatus* population inhabiting Mersin Bay. In this study, condition factor, length-weight and length-length relationships were determined for *M. barbatus* inhabiting this region (the northeastern Mediterranean Sea).

Keywords: Condition factor, length-weight relationship, length-length relationship, *Mullus barbatus*, Mersin Bay

1. INTRODUCTION

The length-weight relationship (LWR) data can be used in fish biology, fish ecology, fish physiology, and fisheries. WLR studies in fisheries research provide useful information in stock assessment models, biomass, and, estimation of fish condition [1-2]. In addition, the length-weight relationship provides morphological comparisons between populations inhabiting different habitats [3-4]. The

equation of the length-weight relationship is also used to explain the allometric or isometric growth pattern of fish species. The length-length relationships are very important parameters in fisheries management and especially in comparative growth studies where is preferred one size type [5]. It also allows the estimation of total, fork, and standard lengths using equations [6].

The condition factor is one of the population parameters and is used as a good indicator of

---

* Corresponding author: sedakontas@gmail.com (S. KONTAŞ YALÇINKAYA)
[1] Ordu University, Fatsa Faculty of Marine Sciences
E-mail: sedakontas@odu.edu.tr
ORCID: https://orcid.org/0000-0002-6582-6722

Seda KONTAŞ

Length-Weight, Length-Length Relationships, and Condition Factor of Red Mullet (Mullus barbatus Linna...

the general health of fish populations and water quality living in a particular habitat or ecosystem [7]. It is possible to have information about the physiological state of the fish by using the condition factor [8]. Age, sex, gonad development, and fatness affect the condition factor [9].

Mullus barbatus (Red mullet) is a demersal and marine fish species. It is found on gravel, sand, and mud bottoms of the continental shelf and lives usually in 100 - 300 m depth ranges [10]. Its distribution is Eastern Atlantic, Mediterranean, and Black Sea [11]. It was also reported in the Sea of Marmara [12] and the Aegean Sea [13].

There are many studies conducted on Red mullets in Turkish seas and other seas. The previous studies were made on the length-weight relationship of *M. barbatus* in the Mediterranean Sea [4, 14-16], in the Black Sea [2, 17-20], in the Sea of Marmara [12, 21-22], and in Aegean Sea [5, 13, 23], the length-length relationships of Red mullet in Aegean Sea [5], and condition factor of *M. barbatus* in Black Sea [8, 24], and Egyptian Mediterranean coast [25]. Whereas there were many studies on the length-weight relationship, there was no study on the length-length relationship for *M. barbatus* inhabiting the northeastern Mediterranean Sea. Although there are many studies on this species on the coast of the Black Sea, Aegean Sea, and Sea of Marmara, there are limited studies in Mediterranean waters [26-29]. This study aimed to determine length-length (LLRs), length-weight (LWRs) relationships, and condition factors of *M. barbatus* from Mersin Bay in the northeastern Mediterranean Sea.

2. MATERIALS AND METHODS

Mullus barbatus samples were obtained from fish market in March 2021 from Mersin Bay (the northeastern Mediterranean Sea). The weight of fish individuals (W) was recorded (± 0.1 g). The total length (TL), fork length (FL), and standard length (SL)

were measured to the nearest ± 0.1 cm. The gender of *M. barbatus* samples was determined by macroscopic investigation of the gonads.

Length-weight relationship (LWR) was calculated from the formula: $W = a \times TL^b$, where W is weight, TL is total boy, *a* and *b* are constants [30]. The %95 confidence interval of *b* values of females, males, and all samples were calculated. "*a*" and "*b*" parameters were estimated from linear regression applied to the log-transformed variables, and the formula "$\log W = \log a + b \log L$" was used for calculations. When *b* is equal to 3, the fish grows isometrically. When the *b* value is less than or greater than 3, it means negative or positive allometric growth. The growth status of the individuals was determined by the t-test according to the *b*=3 isometric growth hypothesis [31]. Length-length relationships (LLRs) such as total length-fork length, total length-standard length, and standard length-fork length were calculated from the following formula: $y = ax + b$. The coefficient of determination (R^2) was used to determine the degree of relationship between the variables. Fulton condition factor (K) was calculated from the formula: $K=(W/L^3) \times 100$ [9]. Whether there was a statistical difference between the length and weight values of females and males was tested using the t-test. The Minitab 16 software was used for all statistical analyses.

3. RESULTS AND DISCUSSION

In this study, a total of 152 *Mullus barbatus* samples were evaluated. The female rate of the total individuals was 29% (n=43) and the male rate of the total individuals was 71% (n=109).

The mean total length, fork length, and standard length were determined as 12.1 ± 0.211 cm, 11.3 ± 0.185 cm, 10.2 ± 0.183 cm for females; 11.9 ± 0.104 cm, 10.9 ± 0.096 cm, 9.9 ± 0.086 cm for males and 12.0± 0.094 cm, 11.0 ± 0.086 cm, 9.9 ± 0.080 cm

Seda KONTAŞ

Length-Weight, Length-Length Relationships, and Condition Factor of Red Mullet (Mullus barbatus Linna...

for all individuals, respectively. The mean weight was determined as 19.8 ± 1.22 g for females; 17.4 ± 0.634 g for males and 18.0 ± 0.573 g for all *M. barbatus* individuals. The length and weight values were statistically different between male and female individuals (t-test; P<0.05). For this reason, the calculations were made for females, males, and all individuals. The condition factor was 1.04 ± 0.0155 for females, 0.98 ± 0.0111 for males, and 1.00 ± 0.0093 for all *M. barbatus*, respectively. The descriptive statistics of total length, fork length, standard length, weight, and condition factor were given in Table 1.

Table 1 The descriptive statistics of variables for *Mullus barbatus* inhabiting Mersin Bay (TL: Total length (cm), FL: Fork length (cm), SL: Standard length (cm), W: Weight (g), K: Condition factor, S.E.: Standard error, Min: Minimum, Max: Maximum)

	Mean±S.E. (Min. - Max.)		
	♀	♂	♀+♂
TL (cm)	12.1 ± 0.211 (10.2 - 15.2)	11.9 ± 0.104 (10.0 - 15.0)	12.0 ± 0.094 (10.0 - 15.2)
FL (cm)	11.3 ± 0.185 (9.6 - 14.0)	10.9 ± 0.096 (9.5 - 14.1)	11.0 ± 0.086 (9.5 - 14.1)
SL (cm)	10.2 ± 0.183 (8.5 - 12.9)	9.9 ± 0.086 (8.5 - 12.5)	9.9 ± 0.080 (8.5 - 12.9)
W (g)	19.8 ± 1.22 (9.20 - 38.80)	17.4 ± 0.634 (9.60 - 38.60)	18.0 ± 0.573 (9.20 - 38.80)
K	1.04 ± 0.0155 (0.87 - 1.23)	0.98 ± 0.0111 (0.74 - 1.27)	1.00 ± 0.0093 (0.74 - 1.27)

This study provided a new reference on length-weight relationships (LWRs), length-length relationships (LLRs), and condition factor (K) of females and males of *M. barbatus* inhabiting the Mersin Bay (Mediterranean Sea). The length-weight relationships of *M. barbatus* (♀, ♂, all samples) were shown in Figure 1. In the present study, the LWRs were determined as $W=0.0049TL^{3.299}$, $W=0.0029TL^{3.490}$, $W=0.0033TL^{3.444}$ for females, males, and all individuals of *M. barbatus*. In a previous study, LWRs were indicated as $W=0.0145TL^{2.949354}$ for females, $W=0.0397TL^{2.544816}$ for males, and $W=0.0211TL^{2.798398}$ for all individuals of *Mullus* sp. in Mersin Bay [26]. [24] reported that LWRs were $W=0.0065TL^{3.17}$, $W=0.0055TL^{3.25}$, and $W=0.0059TL^{3.21}$ for females, males, and all individuals of *M. barbatus barbatus* from the western Black Sea. [32] reported that LWR was $W=0.0121SL^{2.939}$ for *M. barbatus* in the western Mediterranean Sea. [13] reported that LWR was $W=0.0049TL^{3.273}$ for *M. barbatus* inhabiting Gökceada Island. The length-weight relationship is affected by several abiotic and biotic factors [33]. In addition, the length-weight relationship parameters can be affected by locality differences, and biological and ecological factors [34-35].
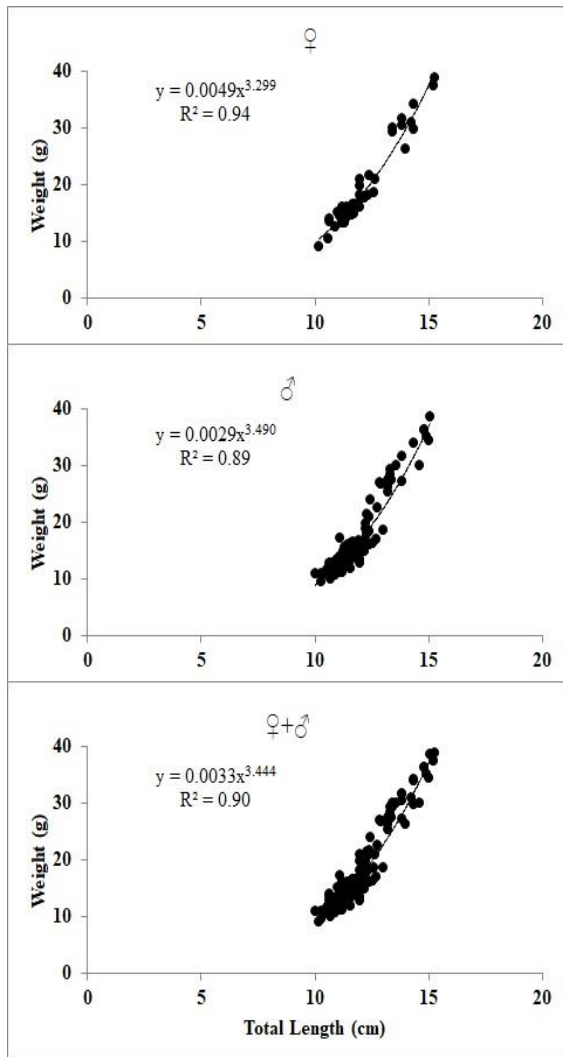
Seda KONTAŞ

Length-Weight, Length-Length Relationships, and Condition Factor of Red Mullet (Mullus barbatus Linna...

Figure 1 The length-weight relationships (LWRs) of *Mullus barbatus* (♀, ♂, ♀+♂) inhabiting Mersin Bay

Generally, the *b* values for all fish species were reported between 2.5-3.5 [33]. *b* values may range from 2 to 4 according to [30]. In the present study, the *b* value was 3.444±0.042, and 95% C.I. of *b* ranged between 3.437 - 3.451 for all *M. barbatus* from Mersin Bay. The *b* value was 3.299±0.035 for females and 3.490±0.043 for males, respectively. The growth was positive allometric (*b*>3) in *M. barbatus* (♀, ♂, all samples) inhabiting Mersin Bay (P<0.001). Similarly, the *b* values were reported as 3.17 for females, 3.25 for males, and 3.21 for all *M. barbatus barbatus* individuals in the western Black Sea, and the females, males, and all individuals of *M. barbatus barbatus* had positive allometric growth in the western Black Sea [24]. [8]

reported that *b* values of *M. barbatus* were 3.0855 for females, 3.0688 for males, and 3.1267 for all individuals and the growth type was positive allometric for all samples. [16] were determined as positive allometric for all specimens of *M. barbatus* in Babadilli Bight (the northeastern Mediterranean Sea). However, [13] determined as isometric for males (b=3.171) and as positive allometric for females (b=3.361) and all samples (b=3.273) of *M. barbatus* in Gökceada Island (northern Aegean Sea), respectively. [20] reported isometric growth type (b=3.045) for *M. barbatus* inhabiting the eastern Black Sea Turkey. In another study, the *b* values were 2.993 for males, 3.134 for females, and 3.119 for all *M. barbatus* individuals in the southern Black Sea. While the growth type was isometric in males, it was reported as positive allometric in females and all individuals [36]. The sampling methods, the number of samples, and length ranges may cause a difference in *b* values [13]. In addition, the difference in *b* values can originate from the hydrographical differences among the Mediterranean Sea, Aegean Sea, Black Sea, and Sea of Marmara [20].

The obtained *b* values from other studies were determined as 3.060 for *M. barbatus* in the Mediterranean Sea [4], 2.949354 (♀), 2.544816 (♂), and 2.798398 (♀+♂) for *Mullus* sp. in Mersin Bay [26], 3.16 in Antalya Bay [37], 3,128 in Babadillimani Bight [16], 3.16 in İskenderun Bay [38], 3.12 in the Black Sea [2], 3.24 in the southeastern Black Sea [17], 3.23 in the eastern Black Sea [39], 3.12 in the eastern and central Black Sea [40], 3.139 in the eastern Black Sea [19], 3.36 in the western Black Sea [41], 3.326 in Sea of Marmara [12], 3.004 in Sea of Marmara [21], 2.873 in Sea of Marmara [22], 3.17 in İzmir Bay [42], 3.10 in the north Aegean Sea [23], 2.832 in the Aegean Sea [5]. The *b* value is characteristic for each species and, in general, it does not change significantly throughout the year [3, 12]. The *b* value of the length-weight relationship is affected by

Seda KONTAŞ

Length-Weight, Length-Length Relationships, and Condition Factor of Red Mullet (Mullus barbatus Linna...

habitat, seasons, temperature, salinity, sex, gonad maturity, length range, health, and diet differences [30, 33]. Thus, these values can vary from species to species and population to population. The *b* value for *M. barbatus* in this study was slightly higher than the obtained from the other studies in the Mediterranean Sea [4, 16]. It may be differences between the fish specimens and populations that grew in the same region [43]. The number of samples and the differences in the length ranges of the individuals affect the *b* values for the same species [13]. These differences may also be appeared due to temporal variations in the sampling sites [39].

The LLRs of *M. barbatus* (♀, ♂, all samples) were shown in Figure 2-4. The LLRs of females were determined as TL=1.1277FL-0.5864, TL=1.1434SL+0.5291, FL=0.9991SL+1.1403 and the LLRs of males were determined as TL=1.0523FL+0.3676, TL=1.1807SL+0.2154, FL=1.0818SL+0.2544, respectively. The LLRs of all individuals were determined as TL=1.0706FL+0.1386, TL=1.1634SL+0.371, and FL=1.0541SL+0.543, respectively. In the present study, it was determined that the total length, fork length, and standard length values of *M. barbatus* showed strong linear relations with each other (Table 2). The LLRs were reported as FL=−1.78+0.96TL, SL=−1.25+0.87TL, and SL=0.40+0.90FL for *M. barbatus* (n=15) in the Aegean Sea (Greece), respectively [5]. The length-length relationships are important and they use in comparative growth studies. The fish tails can break for various reasons. This makes it difficult to accurately measure the total length. If the standard length or fork length is known, they allow the determination of the total length.
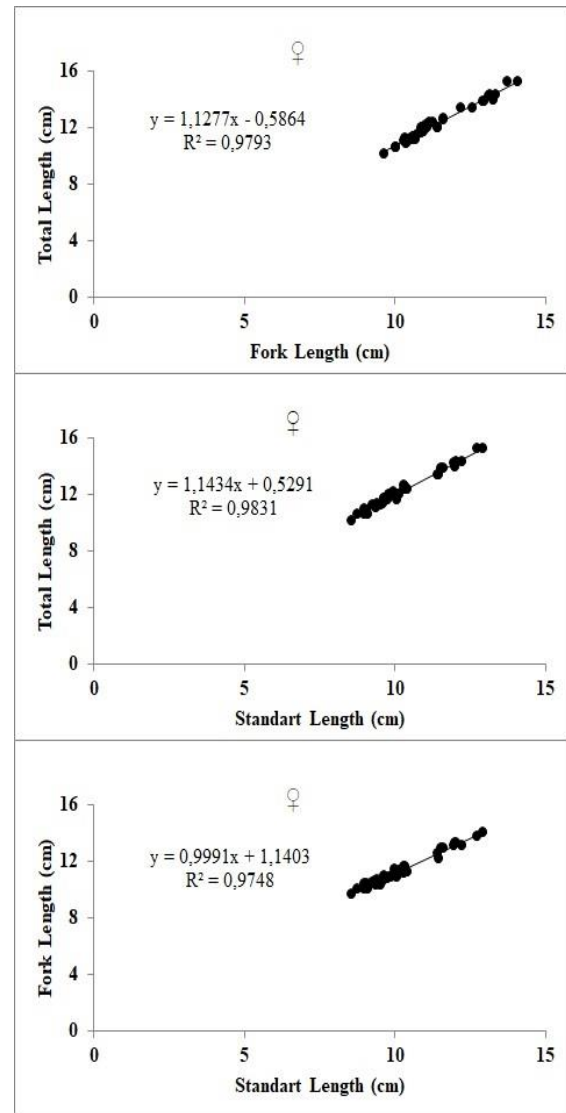

Figure 2 The length-length relationships (LLRs) for females of *Mullus barbatus*

Seda KONTAŞ

Length-Weight, Length-Length Relationships, and Condition Factor of Red Mullet (Mullus barbatus Linna...
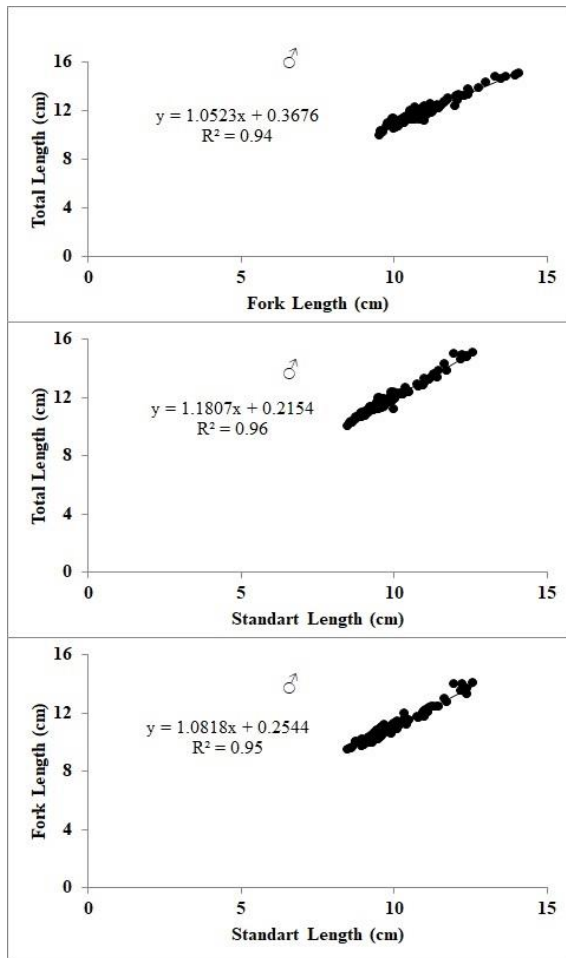
Figure 3 The length-length relationships (LLRs) for males of *Mullus barbatus*
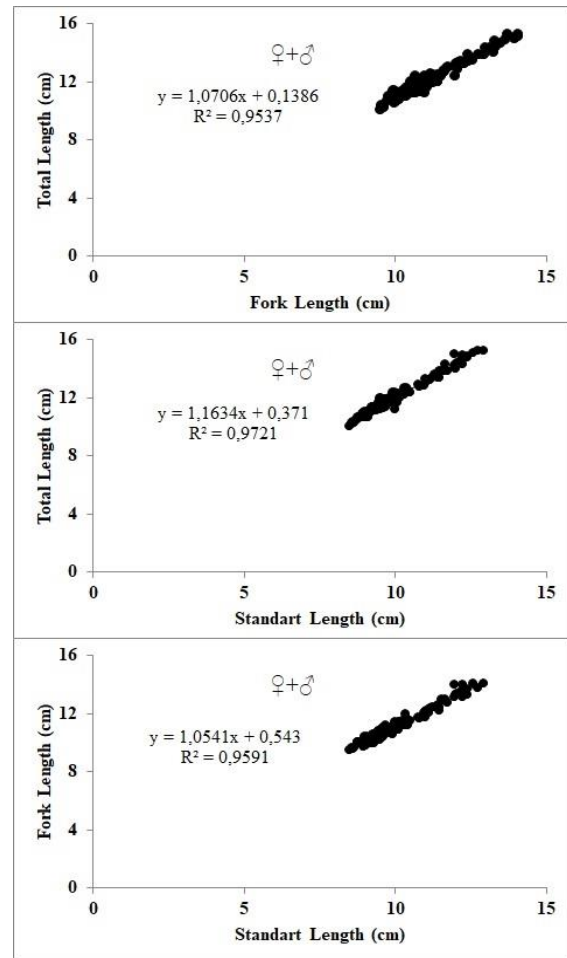

Figure 4 The length-length relationships (LLRs) for all individuals of *Mullus barbatus*

Table 2 The length-length (LLRs) relationships for *Mullus barbatus* inhabiting Mersin Bay (TL; total length (cm), FL; fork length (cm), SL; standard length (cm), R^2; Determination Coefficient)

	The Length-Length Relationships	R^2
♀	TL = 1.1277FL - 0.5864	0.97
♂	TL = 1.0523FL + 0.3676	0.94
♀+♂	TL = 1.0706FL + 0.1386	0.95
♀	FL = 0.9991SL + 1.1403	0.97
♂	FL = 1.0818SL + 0.2544	0.95
♀+♂	FL = 1.0541SL + 0.543	0.95
♀	TL = 1.1434SL + 0.5291	0.98
♂	TL = 1.1807SL + 0.2154	0.96
♀+♂	TL = 1.1634SL + 0.371	0.97

The condition factor was an important parameter for the assessment of fish stock and it was used in fish biology. [25] reported that the condition factor was 0.894 for *M. barbatus* along the Egyptian Mediterranean coast. The condition factor was determined as 1.375 (♀), 1.292 (♂), and 1.3195 (♀+♂) for *Mullus* sp. in Mersin Bay [26]. [24] determined that the condition factors of females, males, and all *M. barbatus barbatus* samples inhabiting the western Black Sea were 0.968, 0.970, and 0.974, respectively and it showed insignificant variation between sexes in the western Black Sea (P>0.05). In the present study, the condition factors were determined as 1.04 for females, and 0.98 for males, and the condition factor showed statistically significant variation between females and males of *M. barbatus* (P<0.001).

Seda KONTAŞ

Length-Weight, Length-Length Relationships, and Condition Factor of Red Mullet (Mullus barbatus Linna...

The condition factor in fish can vary from species to species, as well as within the species. Differences in size, growth, sex, gonad development, age, stomach contents, and seasons can change the condition factor values of fish populations [9, 33].

4. CONCLUSION

This research has new data and it ensures new contributions on condition factors and relationships of length-length and length-weight for *Mullus barbatus* from the northeastern Mediterranean Sea. The length-length relationships for females, males, and all *M. barbatus* individuals in the northeastern Mediterranean Sea (Mersin Bay) are also presented for the first time. If the mean, minimum, and maximum variables of the weight and length of fish and the relationships between these variables are known, it helps the sustainable use of natural resources. Therefore, the results of the present study will contribute to the stock assessment and management of fisheries in this region. It is expected that the scientists and fishermen benefit from the outcomes of future studies as part of their stock conservation and management programs. In addition, the study was evaluated according to gender. The results that may vary by gender can apply to other studies as well. The results obtained from this present study will also allow comparison with populations from other regions. The related studies on LWRs of other populations caught in the Mediterranean Sea should be also evaluated and developed in the future.

Authors' Contribution
All process of the study was done by the author.

The Declaration of Conflict of Interest/ Common Interest
No conflict of interest or common interest has been declared by the author.

The Declaration of Ethics Committee Approval
This study does not require ethics committee permission or any special permission.

The Declaration of Research and Publication Ethics
The authors of the paper declare that they comply with the scientific, ethical, and quotation rules of SAUJS in all processes of the paper and that they do not make any falsification of the data collected. In addition, they declare that Sakarya University Journal of Science and its editorial board have no responsibility for any ethical violations that may be encountered and that this study has not been evaluated in any academic publication environment other than Sakarya University Journal of Science.

REFERENCES

[1] K. I. Stergiou, D. K. Moutopoulos, "A review of length-weight relationships of fishes from Greek Marine Waters," Naga, The ICLARM Quarterly, vol. 24, pp. 23-39, 2001.

[2] O. Samsun, O. Akyol, T. Ceyhan, Y. Erdem, "Length-weight relationships for 11 fish species from the Central Black Sea, Turkey," Ege Journal of Fisheries and Aquatic Sciences, vol. 34, no. 4, pp. 455-458, 2017.

[3] M. N. Santos, M. B. Gaspar, P. Vasconcelos, C. C. Monteiro, "Weight-length relationships for 50 selected fish species of the Algarve (Southern Portugal," Fisheries Research, vol. 59, no. 1-2, pp. 289-295, 2002.

[4] L. Sangun, E. Akamca, M. Akar, "Weight-length relationships for 39

Seda KONTAŞ

Length-Weight, Length-Length Relationships, and Condition Factor of Red Mullet (Mullus barbatus Linna...

fish species from the north-eastern Mediterranean coast of Turkey," Turkish Journal of Fisheries and Aquatic Sciences, vol. 7, pp. 37-40, 2007.

[5] D. K. Moutopoulos, K. I. Stergiou, "Length–weight and length–length relationships of fish species from the Aegean Sea (Greece)," Journal of Applied Ichthyology, vol 18, no. 3, pp. 200-203, 2002.

[6] S. Yedier, "Estimation of some population parameters of *Squalius cephalus* (Linnaeus 1758) in Tabakhane Stream (Ordu-Turkey)," Sakarya University Journal of Science, vol. 26, no. 1, pp. 14-23, 2022.

[7] M. Tsoumani, R. Liasko, P. Moutsaki, I. Kagalou, I. Leonardos, "Length-weight relationships of an invasive cyprinid fish (*Carassius gibelio*) from 12 Greek lakes in relation to their trophic states," Journal of Applied Ichthyology, vol. 22, no. 4, pp. 281-284, 2006.

[8] A. Van, A. Gümüş, S. Süer, "Length-weight relationships and condition factors of 15 fish species from Kizilirmak-Yesilirmak shelf area, the southeastern Black Sea," NESciences, vol. 4, no. 1, pp. 21-27, 2019.

[9] C. D. Le Cren, "The Length-weight relationship and seasonal cycle in gonad weight and condition in perch, *Perca fluviatilis*," Journal of Animal Ecology, vol. 20, no. 2, pp. 201-219, 1951.

[10] B. J. Muus, J. G. Nielsen, Sea fish: Scandinavian Fishing Year Book, Hedehusene, Denmark, 340 p, 1999.

[11] J. C. Hureau, "Mullidae," in Fishes of the north-aestern Atlantic and the Mediterranean, P. J. P. Whitehead, M. L. Bauchot, J. C. Hureau, J. Nielsen, E. Tortonese Eds. UNESCO, Paris, 1986, pp. 877-882.

[12] T. D. Bok, D. Gokturk, A. E. Kahraman, T. Z. Alicli, T. Acun, C. Ates, "Length-weight relationships of 34 fish species from the Sea of Marmara, Turkey," Journal of Animal and Veterinary Advances, vol. 10, no. 23, pp. 3037-3042, 2011.

[13] F. S. Karakulak, H. Erk, B. Bilgin, "Length–weight relationships for 47 coastal fish species from the northern Aegean Sea, Turkey," Journal of Applied Ichthyology, vol. 22, no. 4, pp. 274-278, 2006.

[14] E. Taskavak, M. Bilecenoglu, "Length-weight relationships for 18 Lessesian (Red Sea) immigrant fish species from the Mediterranean coast of Turkey," Journal of the Marine Biological Association of the United Kingdom, vol. 81, no. 5, pp. 895-896, 2001.

[15] G. Morey, J. Moranta, E. Massuti, A. Grau, M. Linde, F. Riera, B. Morales-Nin, "Weight–length relationships of littoral to lower slope fishes from the western Mediterranean,". Fisheries Research, vol. 62, no. 1, pp. 89-96, 2003.

[16] E. Cicek, D. Avsar, H. Yeldan, M. Ozutok, "Length–weight relationships for 31 teleost fishes caught by bottom trawl net in the Babadillimani Bight (northeastern Mediterranean),". Journal of Applied Ichthyology, vol. 22, no. 4, pp. 290-292, 2006.

[17] S. A. Demirhan, M. F. Can, "Length–weight relationships for seven fish species from the southeastern Black Sea," Journal of Applied Ichthyology, vol. 23, no. 3, pp. 282-283, 2007.

Seda KONTAŞ

Length-Weight, Length-Length Relationships, and Condition Factor of Red Mullet (Mullus barbatus Linna...

[18] F. Kalaycı, N. Samsun, S. Bilgin, O. Samsun, "Length-weight relationship of 10 fish species caught by bottom trawl and midwater trawl from the Middle Black Sea, Turkey," Turkish Journal of Fisheries and Aquatic Sciences, vol. 7, no. 1, pp. 33-36, 2007.

[19] O. Ak, S. Kutlu, İ. Aydın, "Length-weight relationship for 16 fish species from the eastern Black Sea, Turkey," Turkish Journal of Fisheries and Aquatic Sciences, vol. 9, no. 1, pp. 125-126, 2009.

[20] S. Çalık, N. Erdoğan Sağlam, "Length-weight relationships of demersal fish species caught by bottom trawl from Eastern Black Sea (Turkey)," Cahiers de Biologie Marine, vol. 58, pp. 485-490, 2017.

[21] N. Demirel, E. M. Dalkara, "Weight−length relationships of 28 fish species in the Sea of Marmara," Turkish Journal of Zoology, vol. 36, no. 6, pp. 785-791, 2012.

[22] İ. B. Daban, M. Arslan İhsanoğlu, A. İşmen, H. İnceoğlu, "Length-weight relationships of 17 teleost fishes in the Marmara Sea, Turkey," KSU Journal Of Agriculture and Nature, vol. 23, no. 5, pp. 1245-1256, 2020.

[23] G. Gökçe, İ. Aydın, C. Metin, "Length–weight relationships of 7 fish species from the north Aegean Sea, Turkey," International Journal of Natural and Engineering Sciences, vol. 1, pp. 51-52, 2007.

[24] D. Türker, H. Bal, "Length–weight relationship and condition factor of Red mullet (*Mullus barbatus barbatus* Linnaeus, 1758) from the western Black Sea, Turkey," NESciences, vol. 3, no. 2, pp. 120-127, 2018.

[25] E. H. K. Akel, "Length-weight relationships and condition factors for fifteen species caught by experimental bottom trawl along the Egyptian Mediterranean Coast," Acta Velit, vol. 2, no. 4, pp. 15-19, 2016.

[26] H. H. Atar, T. Mete, "Investigating of some biological features of Red mullet (*Mullus* sp. Linnaeus, 1758) distributing in Mersin Bay," Research Journal of Biology Sciences, vol. 2, no. 2, pp. 29-34, 2009.

[27] M. Ok, "Evaluation of the demersal fish assemblages of the northeastern Levant Sea," Ph.D. dissertations, Department of Marine Biology and Fisheries, Middle East Technical Univ., Ankara, 2012.

[28] C. E. Özyurt, E. Çiçek, D. Avşar, H. Yeldan, M. Manaşırlı, "The relationship among spawning period, length at first maturity and depth distribution of *Mullus barbatus* and *Upeneus moluccensis* inhabiting the northeastern Mediterranean coast of Turkey," International Journal of Aquatic Biology, vol. 2, no. 4, pp. 215-222, 2014.

[29] S. Gündoğdu, M. Baylan, "Analyzing growth studies of four Mullidae species distributed in Mediterranean Sea and Black Sea," Pakistan Journal of Zoology, vol. 48, no. 2, pp. 435-446, 2016.

[30] T. E. Bagenal, W. F. Tesch, "Age and growth," in Methods for assessment of fish production in freswater, Bagenal, T. Eds. Blackwell Scientific publications, Oxford and Edinburgh, 1978, pp. 101-136.

[31] R. R. Sokal, F. L. Rohlf, Introduction to biostatistics, Freeman, New York, 363 p, 1987.

Seda KONTAŞ

Length-Weight, Length-Length Relationships, and Condition Factor of Red Mullet (Mullus barbatus Linna...

[32] C. Valle, J. T. Bayle, A. A. Ramos, "Weight-length relationships for selected fish species of the western Mediterranean Sea," Journal of Applied Ichthyology, vol. 19, no 4, pp. 261-262, 2003.

[33] R. Froese, "Cube law, condition factor and weight–length relationships: history, meta-analysis and recommendations," Journal of Applied Ichthyology, vol. 22, no. 4, pp. 241-253, 2006.

[34] W. E. Ricker, Computation and interpretation of biological statistics of fish populations, Bulletin-Fisheries Research Board of Canada, 1975, pp. 1-382.

[35] P. Sparre, "Introduction to Tropical Fish Stock Assessment," in Part I Manual. FAO Fisheries Technical Paper 306/1. Rev 1. Rome, 1992, 376 pp.

[36] T. Yeşilçiçek, F. Kalayci, C. Şahin, "Length-weight relationships of 10 fish species from the southern Black Sea, Turkey," Journal of Fisheries Sciences, vol. 9, no. 1, pp. 19-23, 2015.

[37] Y. Özvarol, "Length–weight relationships of 14 fish species from the gulf of Antalya (northeastern Mediterranean Sea, Turkey)," Turkish Journal of Zoology, vol. 38, no. 3, pp. 342-346, 2014.

[38] E. Çiçek, "Age, growth and mortality parameters of *Mullus barbatus* Linnaeus, 1758 (Perciformes: Mullidae) in İskenderun Bay, northeastern Mediterranean," Iranian Journal of Ichthyology, vol. 2, no. 4, pp. 262-269, 2015.

[39] H. Onay, G. Dalgıç, "Length-weight relationships for fourteen fish species collected by bottom trawl from the Eastern Black Sea coast, Turkey," Marine Science and Technology Bulletin, vol. 10, no. 4, pp. 326-332, 2021.

[40] N. Kasapoğlu, E. Düzgüneş, "Length-weight relationships of marine species caught by five gears from the Black Sea," Mediterranean Marine Science, vol. 15, no. 1, pp. 95-100, 2013.

[41] D. Türker, H. Bal, "Length–weight relationships of 13 fish species from the western Black Sea (Zonguldak-Amasra), Turkey," Journal of Black Sea/Mediterranean Environment, vol. 24, no. 2, pp. 115-127, 2018.

[42] O. Özaydın, E. Taskavak, "Length-weight relationships for 47 fish species from Izmir Bay (eastern Aegean Sea, Turkey)," Acta Adriatica, vol. 47, no. 2, pp. 211-216, 2006.

[43] E. M. Tıraşın, "Investigations of the growth parameters of fish populations," Turkish Journal of Zoology, vol 17, pp. 29-82, 1993.

Title: Production and Characterization of Colon Targeted pH Sensitive Macrospheres and Investigation of Release Kinetics

Authors: Ezgi EREN BELGİN, Cankız Gizem DELİBALTA, Hüseyin ÇİÇEK

Production and Characterization of Colon Targeted pH Sensitive Macrospheres and Investigation of Release Kinetics

Ezgi EREN BELGİN [*1] , Cankız Gizem DELİBALTA[1] , Hüseyin ÇİÇEK[1]

Abstract

The gastrointestinal track has different pH values at different sections. Thus, it is not easy to carry a drug to the colon for absorption. pH sensitive polymeric macrosphere drug carriers have important advantages such as being able to be taken orally, targeting the active ingredient to the desired area and dosing the active ingredient at the desired concentration for a long time in the target area. In this contex pH sensitive sodium alginate-gelatin macrospheres were produced by the dispersion phase gelling and cross-linking (complex coacervation) process method then loaded with *Sternbergia lutea* extract in this study. The macrosphere extract release kinetics were investigated for different pH medias that simulates different sections of the gastrointestinal track. As a result, the produced drug carrier macrospheres released the active ingredient at the colon pH (pH 7.0) while at lower pH values did not show a significant extract release. Therefore, it was reported that the produced macrospheres have potential to be used for colon diseases treatments.

Keywords: Colon targeted drug delivery, macrosphere, controlled release, release kinetics, pH sensitive

1. INTRODUCTION

The colon is a suitable site for the systematic absorption of a drug or active ingredient due to its long drug residence time, less enzyme activity than the upper gastrointestinal tract and pH value of approximately 7.0 [1, 2]. However, it is not always easy to carry the active ingredient up to the colon and absorb it in the colon, due to the different pH values of different sections of the gastrointestinal tract [3]. Polymeric sphere based controlled drug release systems are systems with important advantages such as being able to be taken orally, targeting the active ingredient to the desired area and dosing the active ingredient at the desired concentration for a long time in the target area [4-7]. Thus, orally ingested macrospheres can be used to transport the active ingredient to the colon and provide local treatment in colon diseases [8, 9]. However, macrosphere carriers can be degradate along the gastrointestinal tract leading the active ingredient at the desired dosage cannot reach the colon [10, 11]. Orally available pH sensitive macrospheres are one of the solutions that can be used to overcome this disadvantage [12, 13]. In this

* Corresponding author: ebelgin@mu.edu.tr (E. EREN BELGİN)
[1] Mugla Sitki Kocman University
E-mail: cankizdelibalta@gmail.com, hcicek@mu.edu.tr
ORCID: https://orcid.org/0000-0002-1089-3741, https://orcid.org/0000-0002-3199-3709, https://orcid.org/0000-0001-9719-6481

BELGİN et al.

Production and Characterization of Colon Targeted pH Sensitive Macrospheres and Investigation of Rele...

context, the production of pH sensitive sodium alginate macrospheres in calcium chloride ($CaCl_2$) solution was carried out by electrospray collection method in the study conducted by the Z. Yao et. al. [14] and it was reported that the active ingredient release from the macrospheres was very low at pH 1.7 but increased towards pH 7.0.

In the present study, pH sensitive macrospheres were produced using natural sodium alginate and gelatin polymers. With the use of two polymers, it is aimed to obtain a system with higher targeting performance, thanks to the relatively high interaction between negative and positive charged groups at pH 3.0. Active ingredient of a plant origin was loaded into the produced macrospheres and it was investigated whether the active ingredient could be delivered to the colon at the desired dosage and released long-term in the colon.

2. MATERIALS AND METHODS

2.1. Materials

Sodium alginate (Sigma, medium viscosity) and gelatin (Huaxuan, 80-120 bloom) polymers used for macrosphere production were commercially supplied. *Sternbergia lutea* (*S. lutea*), which is used to obtain herbal active ingredients, from the Aegean Region of Turkey was commercially supplied in dried form. All other reagents used were of analytical grade.

2.2. Methods

2.2.1. Plant extract preparation

Extraction of *S. lutea* flowers was started with shredding the plants into small pieces and placing them in a mouth closed ethanol containing flask. The extraction was carried out three times at room temperature for 48 hours for each extraction. After all extraction steps, the mixture was filtered, and ethanol solution was separated. The total ethanol solution obtained was treated by using a

rotary evaporator for removing ethanol 72 hours at 45 $^{\circ}$C. Then the extract was taken into a beaker and subjected to freeze drying in the lyophilizer. The obtained *S. lutea* extract was stored at -20 $^{\circ}$C until use [15-17].

2.2.2. Macrosphere production

Macrospheres were produced by the dispersion phase gelling and cross-linking (complex coacervation) process method. The method used was created by modification of the literature studies [18-25] and used in our previous studies [16].

First of all, 4% sodium alginate and 1.5% gelatin solutions were prepared and the solutions were homogenized with the help of an ultrasonic homogenizator. Then, these two solutions were mixed and a homogeneous alginate-gelatin mixture was obtained. Pre-prepared 0.035 g of *S. lutea* extract was added to the alginate-gelatin mixture and homogenization was achieved with mechanical mixing and ultrasonic homogenization. The pH value of this mixture was adjusted to pH 7.0 with the use of 0.1 M HCl and 0.1 M NaOH. 5 mL mixture was injected using a disposable plastic syringe with 22-gauge needle. At this stage care was taken that the mixture to be air bubble free. The syringe was placed to a push-pull syringe pump at a speed of 0.1 mLh^{-1} and the mixture was dropped into a beaker that contains 0.20 M $CaCl_2$ (pH=3.0, ionic strength=0.1) as curing solution in it. During the dropping procedure the macrospheres formed instantaneously while $CaCl_2$ solution was continued to be stirred at a speed that is slow enough for not to shred the macrospheres and fast enough for not to allow them stick to each other. The formed macrospheres were filtered and washed with deionized water for 2 times, taken into falcon tubes and kept for 2 days at -80°C for lyophilization. Then the spheres were fiberized in the freeze-drying unit and stored in desiccator.

BELGİN et al.

Production and Characterization of Colon Targeted pH Sensitive Macrospheres and Investigation of Rele...

2.3. Characterization of macrospheres

2.3.1. Morphology studies

The produced macrospheres were first gold-coated in a cryopreparation chamber and morphology of the macrospheres were investigated via scanning electron macroscopy (SEM, Quanta 250) studies.

2.3.2. In vitro extract release kinetics investigation

The release kinetics of the macrospheres were investigated for the buffer solutions that simulate gastrointestinal track's different section pH values (pH of 1.3, 3.0, 5.0, 6.0 and 7.0) since they are produced to be taken orally and targeted to the colon during application.

0.05 g of lyophilized macrosphere were taken into 100 mL of buffer solutions for release kinetics investigation studies. The beakers were placed into an incubator shaker at 200 cpm and 37°C simulating human body temperature. 3 mL of the solutions were taken from the buffer solutions at various time intervals. An UV spectrometer (Shimadzu-UV-1601) was used to record the absorbance values of the solutions in the 200-800 nm wavelength. The cumulative extract release from the macrospheres was calculated by using the calibration equation that is determined by using UV scan results of 15 standard calibration solutions that are prepared in different concentrations. The standard solutions of *S. lutea* extract were prepared with the concentrations in the range of 0.01-0.15 mgmL^{-1}. The absorbance values of the standard solutions were recorded with respect to concentrations and the calibration curve is obtained. The calibration equation was obtained by using the calibration curve and the extract concentrations of the solutions with respect to time were calculated by using the equation and absorbance values.

The results were given in terms of percent cumulative release (CR%) that is defined as the percentage ratio of the instantaneous amount of extract released at a certain time of incubation to the initial amount of extract loadings. The initial amount of loaded extract was accepted as the maximum released amount of the extract.

2.3.3. Swelling behavior investigation

The solution sorption capacity tests of the macrospheres were carried out by using 100 mg of dry macrospheres. The macrospheres were swelled for 24 h to reach equilibrium swelling. The swelled macrospheres were taken from the solutions at different time intervals and blotted with filter paper to take surface liquid before weighted. The swelling tests were carried for for 4 times. The percent swelling (S%) of the macrospheres was then calculated by using Equation 1.

$$S\% = \frac{(W_e - W_0)}{W_0} \times 100\% \qquad (1)$$

where W_e denotes the weight of the gel macrospheres at equilibrium swelling and W_0 is the dry weight of the macrospheres.

3. RESULTS AND DISCUSSION

The sodium alginate aqueous solution electrical charge differs with respect to pH of media. Mainly, below pH 7.0 it has a negative charge while above pH 7.0 it has no charge. Thus, the crosslinking between sodium alginate and gelatin could not be occur at the pH values above 7.0. However, when the mixture is added to the solution with low pH value gelatin was crosslinked with sodium alginate molecules by gaining positive charge. $CaCl_2$ was also used to obtain more stable structure of the macrospheres. Each of the Ca^{2+} cations of the $CaCl_2$ caused ionic interaction with negatively charged alginate anions, causing cross-linking. The produced macrospheres are shown in Figure 1.

BELGİN et al.

Production and Characterization of Colon Targeted pH Sensitive Macrospheres and Investigation of Rele...
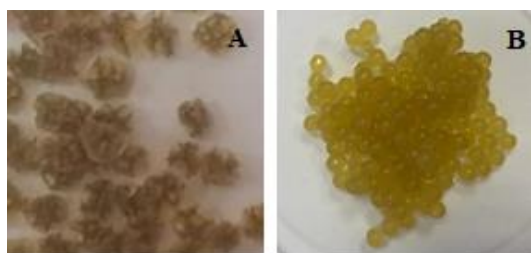
Figure 1 The produced macrospheres (A: Dry, B: Wet)

3.1. Morphology of the macrospheres

The surface morphology of macrospheres was determined by SEM and represented by the particle size and a characteristic shape. The SEM macrographs of loaded and unloaded macrospheres taken at different magnifications are shown in Figure 2.

The macrospheres did not possed proper spherical shape after drying while proper spherical shapes are observed before drying and during swelling. The surfaces of the macrospheres were slightly rough and extract particles were also present on the surface of the macrospheres. The diameter of the macrospheres were in the range of 1.2-1.4 mm.
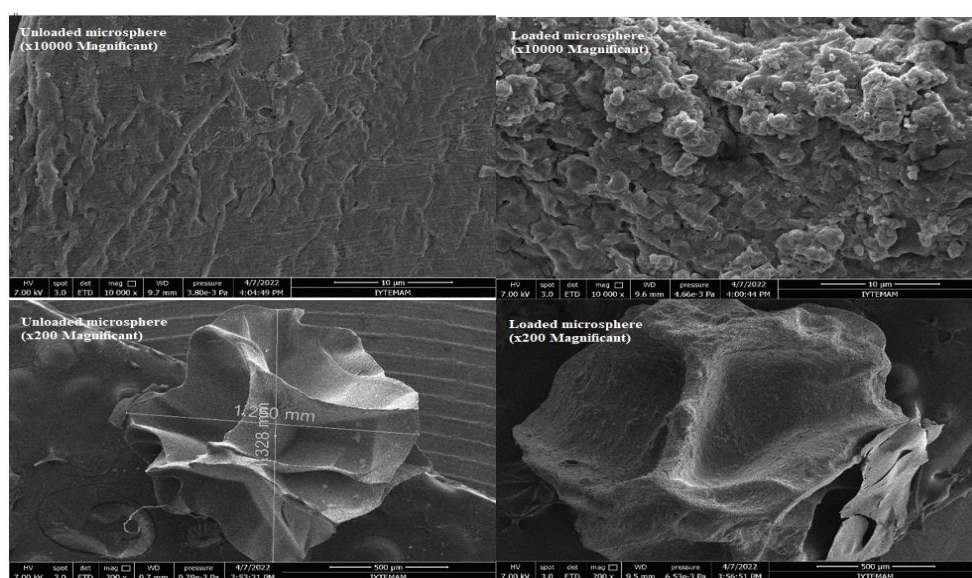
Figure 2 SEM images of produced macrospheres

3.2. In vitro exract release kinetics

In vitro extract release kinetics were investigated for the buffer solutions with differen pH values. The measurements were done for 480 minutes, CR% values were calculated by using pre-prepared calibration curve and results are given in Table 1.

The results are piloted as CR% with respect to time and given in Figure 3. As it is seen from Table 1 and Figure 3 the extract release was very low at the pH values under 7.0 while at pH 7.0 a rapid extract release was observed approximately in 300 minutes. Approximately 60% of the extract content was release in 180 minutes at pH 7.0.

After determination of CR% values with respect to time the kinetic release model of extract release of produced macrospheres were studied by fitting the experimental data to zero-order, first-order, Higuchi, Hixson-Crowell and Korsmeyer-Peppas models at pH 7.0 media. The data was plotted as cumulative amount of drug released versus time for zero-order model, log cumulative percentage of drug remaining versus time for first-order model, cumulative percentage drug release versus square root of time for Higuchi model, cube root of drug percentage remaining in matrix versus time for Hixson-Crowell model and log cumulative drug released versus log time for Korsmeyer-Peppas model [26, 27] and given in Figure 4-8.

BELGİN et al.

Production and Characterization of Colon Targeted pH Sensitive Macrospheres and Investigation of Rele...

Table 1 CR% values of the macrospheres at different pH values

Time (min)	CR %				
	pH 1.3	pH 3.0	pH 5.0	pH 6.0	pH 7.0
5	0.00000000	0.00000049	0.00000052	0.00000139	0.75674259
15	0.00000004	0.00000594	0.00003972	0.00001269	2.22216165
25	0.00000011	0.00000877	0.00005496	0.00001919	4.46037276
35	0.00000033	0.00001129	0.00006607	0.00002817	7.68461721
45	0.00000076	0.00001385	0.00007324	0.00003242	11.30058034
60	0.00000105	0.00001777	0.00008219	0.00003658	14.99282525
90	0.00000200	0.00002322	0.00009266	0.00004164	19.85479550
120	0.00000298	0.00002662	0.00010391	0.00004800	27.78215802
150	0.00000348	0.00003123	0.00011405	0.00005939	39.52295194
180	0.00000440	0.00003425	0.00012663	0.00006879	61.60389020
240	0.00000459	0.00003505	0.00017379	0.00007223	80.15732572
300	0.00000644	0.00003736	0.00025639	0.00008247	98.91430800
360	0.00000755	0.00003874	0.00039552	0.00009375	100.00000000
420	0.00000850	0.00003994	0.00060703	0.00010408	100.00000000
480	0.00000924	0.00004079	0.00090126	0.00012205	100.00000000
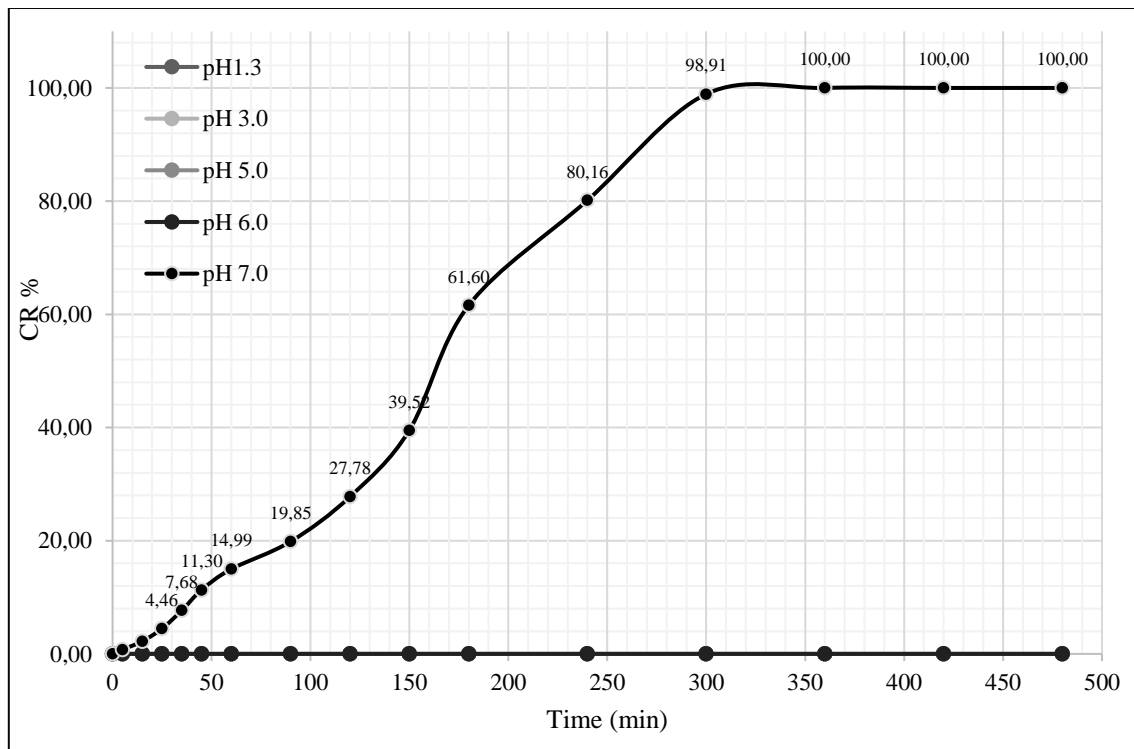
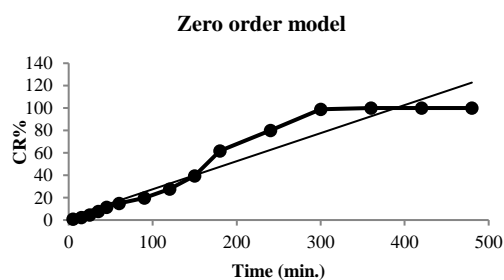Figure 3 CR% values of the macrospheres with respect to time

BELGİN et al.

Production and Characterization of Colon Targeted pH Sensitive Macrospheres and Investigation of Rele...

Zero order model

Figure 4 Kinetic model fitted to the release data of the macrospheres for zero order
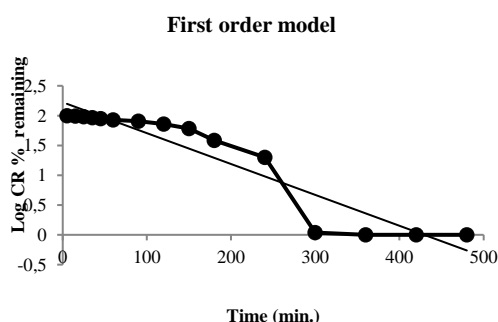
First order model

Figure 5 Kinetic model fitted to the release data of the macrospheres for first order
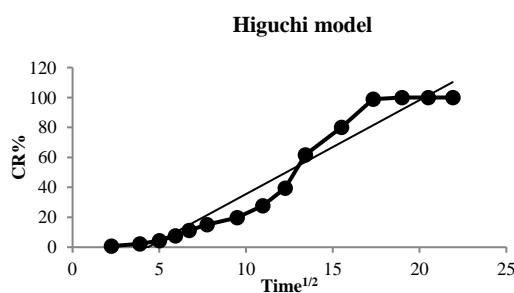
Higuchi model

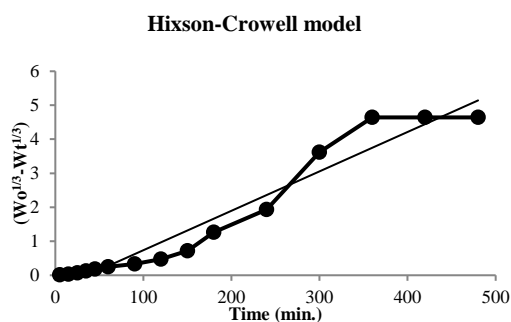Figure 6 Kinetic model fitted to the release data of the macrospheres for Higuchi

Hixson-Crowell model

Figure 7 Kinetic model fitted to the release data of the macrospheres for Hixson-Crowell

Korsmeyer - Peppas Model

Figure 8 Kinetic model fitted to the release data of the macrospheres for Korsmeyer-Peppas

The model plots were fitted to the model equations and the regression coefficients (R^2), release rate constants (K) and release exponent (n) of Korsmeyer-Peppas model are given in Table 2 for pH 7.0 media. The Korsmeyer-Peppas model n value calculation was done for first 60% extract release.

Kinetic model studies showed that the best fit model for extract release at pH 7.0 was Korsmeyer-Peppas model with the regression coefficient of 0.9797 and Hixson-Crowell model was the second-best fit model with the regression coefficient of 0.9447.

The n value is indicative of the mechanism of transport of extract through the polymer and used to characterize the release mechanism of extract from the macrospheres. The n value was 1.2002 for the produced macrospheres which is higher than 1 and indicates drug transport mechanism as Super case II transport and release mechanism as relaxation/erosion. Case-II relaxational release is the drug transport mechanism associated with stresses and state-transition in hydrophilic glassy polymers which swell in water or biological fluids. This term also includes polymer disentanglement and erosion.

BELGİN et al.

Production and Characterization of Colon Targeted pH Sensitive Macrospheres and Investigation of Rele...

Table 2 Release kinetic parameters of the macrospheres

Model	Model Equation	Regression coefficient (R^2)	Release rate constant (K)
Zero Order	$Q_t = Q_0 + K_0 t$ Where; Q_t: Amount of drug dissolved at time Q_0: Initial amount of drug K_0: Zero order release rate constant	0.9268	0.2506 ($mg\,min^{-1}$)
First Order	$\ln(m_0 - m_t) = \ln(m_0) - K_1 t$ Where; C_0: Initial concentration of drug t: Time K_1: First order release rate constant	0.8958	0.0052 (min^{-1})
Higuchi	$Q = K_H t^{1/2}$ Where; Q: Cumulative amount of drug release at time t K_H: Higuchi release rate constant t: Time	0.9430	6.2767 ($mg\,min^{-1/2}$)
Hixson-Crowell	$W_0^{1/3} - W_t^{1/3} = kt$ Where; W_0: Initial amount of drug W_t: Remaining amount of drug at time t K: Release rate constant	0.9447	0.0116 ($mg^{1/3} min^{-1}$)
Korsmeyer–Peppas	$M_t/M = K_m t^n$ Where; M_t: Mass of drug released at time M: Total mass of drug in dosage form K_m: Release rate constant n: Release exponent t: time	0.9797	0.8935 (min^{-n}) n=1.2002

As expected and aimed, the extract release of the macrospheres were insignificantly low at low pH values since the ionic interactions in the structure of macrospheres do not undergo a significant change at low pH values and the deformation of macrospheres remained at minimum levels at low pH values.

With the pH being 7.0, the ionic bonds in the structure disappeared in addition to the conformational structure changes on the macrosphere surface as a result of the displacement of the polymer chains at this pH value. The macrospheres rapidly swelled and the chains forming crosslinks between the main polymer chains have moved and during this movement, the bonds between main chains have been broken and the macrospheres have been degraded in a short time. The amount of extract that macrospheres can release has reached its maximum value after 300 minutes.

3.3. Swelling behavior

Swelling behaviour of the macrospheres were invesigated by using swelling media of pH 7.0 since the significant extract relase was observed at this pH. Figure 9 shows the swelling behaviour of the macrospheres with respect to time. The rapid degredation of the macrospheres in first 500 minutes was compatible with the release kinetics of the macrospheres. The equilibrium percent swelling was determined as aproximately 6500 %.
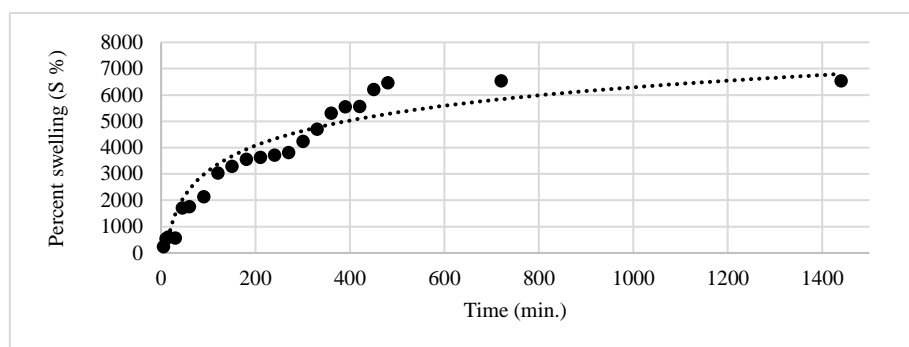
BELGİN et al.

Production and Characterization of Colon Targeted pH Sensitive Macrospheres and Investigation of Rele...

Figure 9 S% values of the macrospheres at pH 7.0

4. CONCLUSION

In this study, the pH sensitive sodium alginate-gelatin macrospheres were produced by the dispersion phase gelling and cross-linking (complex coacervation) process method and the prepared *S. lutea* extract was loaded to the macrospheres. The equilibrium percent swelling of the macrospheres was determined as aproximately 6500 %. Extract release kinetics of the loaded macrospheres were investigated in different solutions with different pH values that represents sections of the gastrointestinal track. When all the results obtained were evaluated, it was understood that the produced drug carrier macrospheres within the scope of the study released the active ingredient at the colon pH while at lower pH values that simulates different sections of the gastrointestinal track did not showed a significant extract release. The amount of extract that macrospheres can release has reached its maximum value after 300 minutes.

Kinetic model studies also showed that the best fit model for extract release at pH 7.0 was Korsmeyer-Peppas model Therefore, they have the potential to be used as colon targeted drug carrier.

The Declaration of Conflict of Interest/ Common Interest
No conflict of interest or common interest has been declared by the authors.

The Declaration of Ethics Committee Approval
This study does not require ethics committee permission or any special permission.

The Declaration of Research and Publication Ethics
The authors of the paper declare that they comply with the scientific, ethical and quotation rules of SAUJS in all processes of the paper and that they do not make any falsification on the data collected. In addition, they declare that Sakarya University Journal of Science and its editorial board have no responsibility for any ethical violations that may be encountered, and that this study has not been evaluated in any academic publication environment other than Sakarya University Journal of Science.

REFERENCES

[1] S. Amidon, J. E. Brown, Dave V. S., "Colon-targeted oral drug delivery systems: design trends and approaches,"An Official Journal of the American Association of Pharmaceutical Scientists, vol. 16, 4, pp: 731-41, 2015.

[2] G. V. D. Mooter, Kinget R., "Oral colon-specific drug delivery: a

BELGİN et al.

Production and Characterization of Colon Targeted pH Sensitive Macrospheres and Investigation of Rele...

review",Drug Delivery,vol. 2, no.2, pp.81-93, 1995.

[3] Z. Vinarov, M., Abdallah, J. A., Agundez, K., Allegaert, A. W., Basit, M., Braeckmans, J., Ceulemans, M., Corsetti, B. T., Griffin, M., Grimm, D., Keszthelyi, M., Koziolek, C. M., Madla, C., Matthys, L. E., McCoubrey, A., Mitra C., Reppas J., Stappaerts, N., Steenackers, N. L., Trevaskis P., Augustijns, "Impact of gastrointestinal tract variability on oral drug absorption and pharmacokinetics: an UNGAP review," European Journal of Pharmaceutical Sciences, vol. 162, 2021.

[4] S. Adepu, Ramakrishna S., "Controlled drug delivery systems: current status and future directions,"Molecules, vol. 26, no. 19, pp. 5905, 2021.

[5] S. Hua, "Advances in oral drug delivery for regional targeting in the gastrointestinal tract - ınfluence of physiological, pathophysiological and pharmaceutical factors," Frontiers in Pharmacology, vol. 11, 2020.

[6] A. Geraili, M. Xing, K. Mequanint, "Design and fabrication of drug-delivery systems toward adjustable release profiles for personalized treatment," View, vol. 2, no. 5, 2021.

[7] U. Nautyal, D. G. Deepak , "Oral sustained release tablets: an overview with a special emphasis on matrix tablet," International Journal of Health and Biological Sciences, vol. 3, no.1, pp. 06-13, 2020.

[8] A. H. Teruel, I. Gonzalez-Alvarez, M., Bermejo, V. Merino, M. D. Marcos, F. Sancenon, M. Gonzalez-Alvarez, R. Martinez-Mañez, "New insights of oral colonic drug delivery systems for inflammatory bowel disease therapy," International Journal of Molecular Sciences, vol. 21, no. 18, pp. 6502, 2020.

[9] K. Ulrich, M. Schwab, "Topical delivery of therapeutic agents in the treatment of ınflammatory bowel disease," Advanced Drug Delivery Reviews, vol. 57, no. 2, pp. 267-79, 2005.

[10] R. Lalani, R. Samant, A. Misra, "Applications of polymers in small intestinal drug delivery,"Applications of Polymers in Drug Delivery (Second Edition), pp. 105-129, 2021.

[11] H. Zhang, C. Yang, W. Zhou, Q. Luan, , W. Li, , Q. Deng, X. Dong, H. Tang, F. Huang, "A pH-responsive gel macrosphere based on sodium alginate and cellulose nanofiber for potential intestinal delivery of probiotics,"ACS Sustainable Chemistry & Engineering, vol. 6,no. 11, pp.13924-13931, 2018.

[12] L. Liu, W. Yao, Y. Rao, X. Lu, J. Gao, "pH-responsive carriers for oral drug delivery: challenges and opportunities of current platforms," Drug Delivery, vol. 24, no. 1, pp. 569-581, 2017.

[13] F. Hsu, D. Yu, C. Huang, "Development of pH-sensitive pectinate/alginate microspheres for colon drug delivery," Journal of Materials Science: Materials in Medicine, vol. 24, no. 2, pp. 317-323, 2013.

[14] Z. Yao, L. Ji, Z. Ahmad, J. Huang, M. Chang, J. Li, "Ganoderma lucidum polysaccharide loaded sodium alginate micro-particles prepared via electrospraying in controlled deposition environments," International Journal of Pharmaceutics, vol. 524, pp. 148–158, 2017.

[15] Ç. Aydın, A. Ermiş, R. Mammadov, "Phenolic contents and antioxidant properties of sternbergia lutea (l.) ker-gawl. ex sprengel ethanol extract," International Journal of Secondary Metabolite, vol. 2, no. 1, pp. 18-26, 2015.

[16] E. Eren Belgin, H. Gönen, H. Çiçek, "Production of ganoderma lucidum extract loaded kıscgelatın-sodium alginate microspheres, investigation of release kinetics at different pH values and evaluation of kinetic models," Mugla Journal Of Science And Technology, vol. 8, no. 1, pp. 41-50, 2022.

[17] N. Bahrin, N. Muhammad, N. Abdullah, B. H. A. Talip, S. Jusoh, S. W. Theng, "Effect of processing temperature on antioxidant activity of Ficus carica leaves extract," Journal of Science and technology, vol. 10, no. 2, 2018.

[18] R. Gong, C. Li, S. Zhu, Y. Zhang, Y. Du, J. Jiang, "A novel pH-sensitive hydrogel based on dual crosslinked alginate/N-α-glutaric acid chitosan for oral delivery of protein," Carbohydrate polymers, vol. 85, no. 4, pp. 869-874, 2011.

[19] Q. Wang, W. Wang, J. Wu, A. Wang, "Effect of attapulgite contents on release behaviors of a pH sensitive carboxymethyl cellulose-g-poly (acrylic acid)/attapulgite/sodium alginate composite hydrogel bead containing diclofenac," Journal Of Applied Polymer Science, vol. 124, no. 6, pp. 4424-4432, 2012.

[20] I. Colinet, V. Dulong, G. Mocanu, L. Picton, D. Le Cerf, "Effect of chitosan coating on the swelling and controlled release of a poorly water-soluble drug from an amphiphilic and pH-sensitive hydrogel," International Journal of Biological Macromolecules, vol. 47, no. 2, pp. 120-125, 2010.

[21] S. Wang, Q. Zhang, B. Tan, L. Liu, L. Shi, "pH-sensitive poly (vinyl alcohol)/sodium carboxymethylcellulose hydrogel beads for drug delivery," Journal of Macromolecular Science, Part B,vol. 50, no. 12, pp. 2307-2317, 2011.

[22] S. Banerjee, S. Singh, S. S. Bhattacharya, P. Chattopadhyay, "Trivalent ion cross-linked pH sensitive alginate-methyl cellulose blend hydrogel beads from aqueous template," International Journal of Biological Macromolecules, vol. 57, pp. 297-307, 2013.

[23] B. Yang, Y. Lu, T. Ren, G. Luo, "One-step synthesis of pH-sensitive poly (acrylamide-co-sodium acrylate) beads with core–shell structure," Reactive and Functional Polymers, vol.73, no. 1, pp. 122-131, 2013.

[24] M. S. M. Eldin, E. A. Kamoun, M. A. Sofan, and S. M. Elbayomi, "L-Arginine grafted alginate hydrogel beads: A novel pH-sensitive system for specific protein delivery," Arabian Journal of Chemistry, vol. 8, no. 3, pp. 355-365, 2015.

[25] L. Li, C. Dong, L. Liu, J. Li, K. Xiao, D. Zhang, X. Li "Preparation and characterization of pH-controlled-release intelligent corrosion inhibitor," Materials Letters,vol. 116, pp. 318-321, 2014.

[26] S. Dash, P. N. Murthy, L. Nath, P. Chowdhury, "Kinetic modeling on drug release from controlled drug delivery systems," Acta Poloniae Pharmaceutica in Drug Research, vol. 67, no. 3, pp. 217-223, 2010.

BELGİN et al.

Production and Characterization of Colon Targeted pH Sensitive Macrospheres and Investigation of Rele...

[27] G. Singhvi, M. Singh, "Review: In-Vitro Drug Release Characterization Models," International Journal of Pharmaceutical Studies and Research, vol. 2, no. 1, pp. 77-84, 2011.

Title: Catalytic Hydrothermal Liquefaction of Artichoke Residues (Cynara Scolymus L.) to Valuable Chemicals

Authors: Dilek SELVİ GÖKKAYA, Mehmet SAĞLAM, Mithat YÜKSEL, Levent BALLİCE

Catalytic Hydrothermal Liquefaction of Artichoke Residues (Cynara Scolymus L.) to Valuable Chemicals

Dilek SELVİ GÖKKAYA [*1] [iD], Mehmet SAĞLAM[1] [iD] Mithat YÜKSEL [*1] [iD],
Levent BALLİCE[1] [iD]

Abstract

Lignocellulosic biomass is accepted to be one of the best sustainable alternatives for overcoming fossil fuel dependence and to reduce environmental pollution. Intensive research studies have been carried out on conversion of this big potential source via chemical and biochemical processes to miscellaneous chemicals. According to one of the present methods of chemical conversion, cellulose and hemicellulose parts of the plant biomass can be converted to platform chemicals by hydrolysis, dehydration and rehydration reactions in the presence of acidic medium. In this study, the efficient conversion conditions of the Artichoke (Cynara Scolymus L.) leaves and stalks to the valuable chemicals (formic acid, acetic acid and 5-hydroxymetilfurfural) were investigated using acid (HCl, HNO_3 and H_2SO_4) catalyzed hydrothermal reaction. Experiments were performed in the temperature range of 150°C - 300°C and at the pH values 2.0 - 3.0 with a reaction time of 1 hour. Evolution of liquid parts and their variations with respect to reaction parameters were determined using HPLC via related analysis.

Keywords: Lignocellulosic biomass, artichoke, catalytic hydrothermal reaction

1. INTRODUCTION

Increasing energy demand, environmental pollution impacts of petroleum and oil prices lead to the search for new technologies to convert biomass into high worth chemicals. As a renewable energy source, plant biomass (e.g., energy crops, aquatic plants, agricultural and forest residues) has a significant potential for the bioenergy production, since it is one of the most available organic compound in the world. From lignocellulosic biomass, bioenergy, which includes liquid fuels (e.g., ethanol, butanol biodiesel), and various platform chemicals (e.g., acetic acid, formic acid, levulinic acid, furfural, 5-hydroxymethylfurfural) can be produced by chemical, thermochemical or biological processes.

A platform chemical is defined as a chemical that can be used as a substrate for the production of various other valuable products. US Energy Department issued the name of the twelve basic chemicals and

---

* Corresponding author: dilek.selvigokkaya@gmail.com (D.GOKKAYA)
[1] Ege University, Izmir, Turkey
E-mail: mehmet.saglam@ege.edu.tr, mithat.yuksel@gmail.com, levent.ballice@ege.edu.tr
ORCID: https://orcid.org/ 0000-0002-3501-562X, , https://orcid.org/0000-0003-1784-4472 https://orcid.org/ 0000-0002-6287-3566, , https://orcid.org/ 0000-0002-3137-1352

more than 300 candidates, which are the basis of the biorefineries that is expected to take place the ordinary petrochemical refineries in the near future. In 2010, the DOE updated the Platform Chemical List which includes e.g. ethanol, furfural, hydroxymethylfurfural, succinic acid, levulinic acid, lactic acid, sorbitol, and xylitol [1]. All these identified platform chemicals can be produced from lignocellulosic biomass. Researches about hydrothermal biomass liquefaction analyzing influence of parameters such as temperature, pressure, catalyst type, pH value, biomass/catalyst ratio, catalytic effects, etc. have been conducted by many research groups [2 - 9]. Also the studies with biomass model compounds are helpful to develop the theoretical decomposition pathway depending on nature of feedstock [10 - 12].

Biobased platform chemicals can be produced effectively by hydrothermal biomass liquefaction in subcritical water (T<374 °C, P<22.1 MPa). The physicochemical properties of the hot compressed liquid water ensure many chemical advantages than the water at ambient conditions (T = 25°C, P = 0.1 MPa). Water at ambient conditions is immiscible with hydrocarbons because it is weak solvent for nonpolar compounds. As water is heated up along its vapor-liquid saturation curve the density decreases. The consequence of the lower density is that the dielectric constant decreases [2]. The reduced dielectric constant increases dissolving capacity of water [3]. In addition subcritical water has higher ion product, high diffusivity and low viscosity. The increased ion product cause to higher levels of hydronium ion in liquid water, which can accelerate the rates of the acid-catalyzed decomposition reactions [3]. All these thermodynamic properties give opportunity to water to decrease the required reaction temperature for the hydrothermal conversion and to increase decomposition efficiency for the hydrolysis of biomass in water.

The aim of this study is to investigate the conversion of Artichoke (Cynara Scolymus L.) leaves and stalks to valuable chemicals using subcritical water in a batch reactor and to support the progress of the subcritical reaction conditions by acid catalysts, to shift the product distribution toward more desirable platform chemicals. As a model lignocellulosic biomass residues of the artichoke was selected, since artichoke has a considerable amount of agricultural crop in Turkey and also in the world. As artichoke producer Turkey is the eleventh country in the world in 2016 according to the data from the FAOSTAT (Food and Agriculture Organization Corporate Statistical Database) [13]. This study can make a great contribution to solving the global bioenergy shortage and can be an effective waste management of the food industry. The efficient conversion conditions of Artichoke leaves and stalk to the valuable chemicals (formic acid, acetic acid and 5-hydroxymetilfurfural) were investigated in the presence of acidic medium. We focused our attention on the effects of HCl, HNO_3 and H_2SO_4 in subcritical water as a function of pH and temperature to shift the product distribution towards desired compounds. Additionally, the results presented in this paper have a novelty due to the examination of the feedstock.

2. EXPERIMENTAL

2.1. Materials

Artichoke leaves and stalks were dried in an oven at 60°C and then, were grounded using a crush mill until the desired particle size was obtained and sieved to get below of 1mm fractions. The values of moisture content, proximate and ultimate analysis for the dried biomass samples are summarized in Table 1. Elemental analysis of the biomass residues were performed via an

elemental analyzer (CHNS-932 by Leco, MI-USA). The composition of artichoke leaves and stalks was determined by the Van Soest method [14] and is given in Table 2.

Table 1 Proximate and ultimate analysis of the artichoke leaves and stalk

	Artichoke Leaves	Artichoke Stalk
Proximate analysis (wt %)		
Moisture	7.73	9.05
Ash	5.54	6.90
Ultimate analysis (dry. wt %)		
C	46.33	41.57
H	5.70	5.85
N	2.16	1.15
S	0.03	0.04
O (from difference)	45.78	51.43

Table 2 The components of the artichoke leaves and stalk

Components (daf. wt %)	Artichoke Leaves	Artichoke Stalk
Cellulose	37.37	31.41
Lignin	4.13	3.30
Hemicellulose	7.92	17.05
Extractives	50.58	48.24

2.2. Experimental Procedure

HTL experiments were performed in a stainless steel batch reactor (SS316) with an internal volume of 100 cm^3. The details about the experimental system used in this study and a schematic diagram of the experimental procedure employed for the products were explained in our previously published work [15]. In the HTL experiments, the reactor was loaded a total mass of 2 g of biomass and 18 ml of deionized water. For the catalytic HTL experiments, the same experimental procedure was applied by the adding catalyst solutions at the pH values 2.0 and 3.0. After loading the reactants, the inside air that was in the reactor was swept out three times by nitrogen and the reactor was heated (~15°C/min) by PID temperature controller (EMKO-ESM XX20) heater to

the reaction temperature. At the end of the reaction time (60 min) the reactor was cooled to ambient temperature (~25°C) by a water bath. After the reactor expanded to ambient pressure, the product gas was measured with a gasometer. Gas-tight analytical syringes were used for the gas chromatography analysis. The solid residue and liquid products in the reactor were separated by filter paper, and then liquid products were analyzed using HPLC. After removal of the products in the reactor, the walls of reactor were rinsed with THF (tetrahydrofuran). The solids remaining on the filter paper were dried (at 105°C) before measuring its carbon content by TOC-SSM apparatus.

2.3. Analyses

Gas chromatography (HP 7890A), which was equipped with Flame ionization (FID) and thermal conductivity detectors, was used for the gas analysis. HPLC device (Shimadzu LC-20A with an Inertsil ODS-4 column) was used for identification of liquid products (aldehydes, ketones, carboxylic acids, furfurals and phenols). The HPLC system was equipped with a DGU-20AS degassing module, LC-20AT gradient pump, CTO-10ASVP chromatography, oven, and an SPD-20 multi wavelength ultraviolet detector. Dried solid residues were analyzed with a TOC-SSM (Solid Sample Module: Shimadzu SSM-5000A) device. Moles of carbon atoms in the liquid phase were calculated by measuring the total organic carbon in the liquid product by using TOC analyzer. And the carbon content of gaseous products was also calculated according to GC reports. So that carbon mass balance (92-97%) was determined using the results obtained for each carbon containing products. All the product analyses were repeated in duplicate or triplicate and their mean values were reported.

3. RESULTS AND DISCUSSION

Some of the important factors that are influencing hydrothermal liquefaction, which are reaction temperature, pH values and acid catalysts are investigated to optimize the reaction conditions. In this regard the experiments were performed at 150, 175, 200, 250 and 300°C and the pH values 2.0 and 3.0 values by using acid catalysts HCl, HNO$_3$ and H$_2$SO$_4$. The efficient liquefaction conditions of artichoke residues for production of high value chemicals were investigated in terms of the yield and chemical composition of the produced aqueous phase at a constant reaction time.

3.1. Effect of experimental parameters of hydrothermal liquefaction on liquid phase

The overall liquid yields were obtained from all the experiments in the range of 25 % to 64 % for the artichoke leaves and in the range of 24 % to 62 % for the artichoke stalks. Due to change of water characteristic properties by increasing temperature, liquid product yields were found to be at the minimum value at the highest reaction temperature (300°C). As the temperature increases hydrocarbons of liquid product decompose into gaseous products easily and carbohydrates at temperatures above 180°C completely decomposes into mono carbohydrates in hot compressed water [10, 16, 17]. So that yields of the liquid and solid products of the artichoke leaves and artichoke stalks were decreased by increasing the temperature from 175°C to 300°C. This effect on the product yields comes from the changing water properties such as the dielectric constant, density, viscosity, and ion product with temperature. Because of these thermodynamic properties solvation power of water increases and starts to dissolve hydrocarbons and salts in higher ratio. The lowest solid product yields 30.8 C% and 33.2 C% were obtained at 150°C by using HNO$_3$ at the pH of 3.0 for the artichoke leaves and stalks, respectively. The highest solid product yields were determined for the without catalyst experiments at the reaction temperature of 200°C, as 59.7 and 57.5 C % for the artichoke leaves and stalks, respectively.

The differences for the artichoke leaves and stalks come from the lignocellosic structure. Lignocellulosic biomass is mainly composed of cellulose, hemicelluloses, lignin, extractives, and ash forming inorganic materials and their compositions vary depending on the source of the plant biomass. These major structural components have rough compositions of (30-50) % cellulose, (20-40)% hemicelluloses, (15-25) % lignin, and (1-3)% extractives. Cellulose ratio for the artichoke leaves (37.37 %) is higher than the artichoke stalks (31.41%) as seen from the Table 2. Cellulose is a complex carbohydrate, consisting of linear chain of d-glucose units and significant structural component of primary cell walls of plants. The structure of hemicellulose is more complex than cellulose which composed of carbohydrate polymers (e.g., pentoses, hexoses, glucuronic acid). Hemicellulose has a lower molecular weight than cellulose and its role is to connect lignin and cellulose fibers. Lignin is a long chain heterogeneous polymer generally contains functional groups including phenolic, hydroxyl, aliphatic and carbonyl groups. Cellulose, lignin, and hemicelluloses, show different chemical reactions in hydrothermal processes. So that important disparities are observed in the product gas composition and the quantity of organics in the liquid product distribution. For example furfural, 5-hydroxymethylfurfural, levulinic acid, xylitol and value added materials can be obtained by hydrolysis of hemicellulose [18].

From the Figures 1-4 liquid, yields from the hydrothermal liquefaction of artichoke leaves and artichoke stalks in the presence of acid catalyst can be seen. Both catalysts

had a positive effect on liquid yields; high yields were obtained with the catalysts than in the non-catalytic experiments. The aims of using catalysts are to increase the liquid product selectivity and to decrease solid residue formation. The highest liquid yields were obtained at 150°C by using HNO_3 at the pH of 3.0 as seen from the Figures 1-4. According to the experimental results, efficiency of the acid catalysts in hydrothermal liquefaction can be ordered as; $HNO_3 > H_2SO_4 > HCl$. The experimental results of this study pointed that liquid phase production pathways are enhanced by HNO_3 at the highest rate.
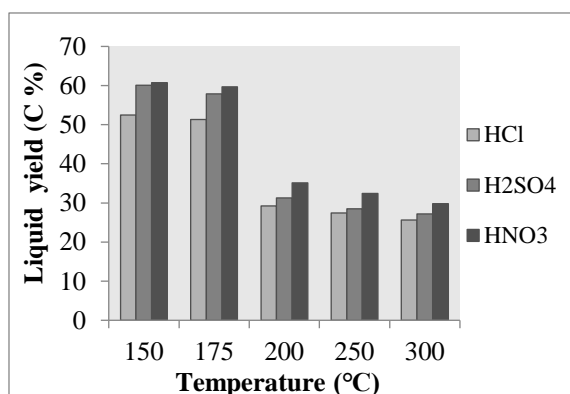
Figure 1 Effects of temperature and catalysts on the liquid yields of artichoke leaves at the pH 2.0.
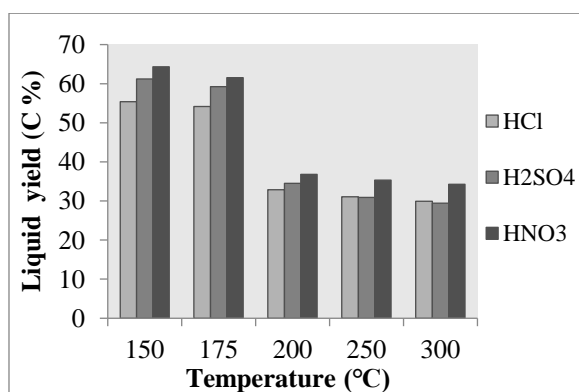
Figure 2 Effects of temperature and catalysts on the liquid yields of artichoke leaves at the pH 3.0.
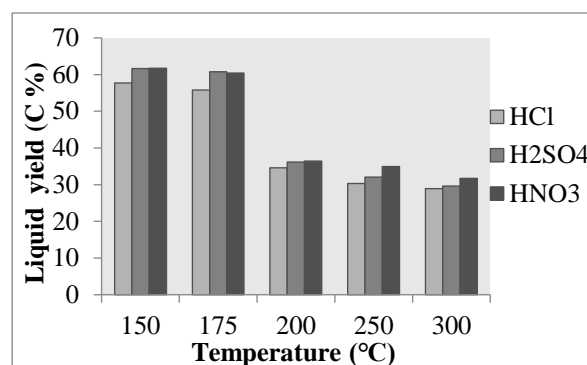

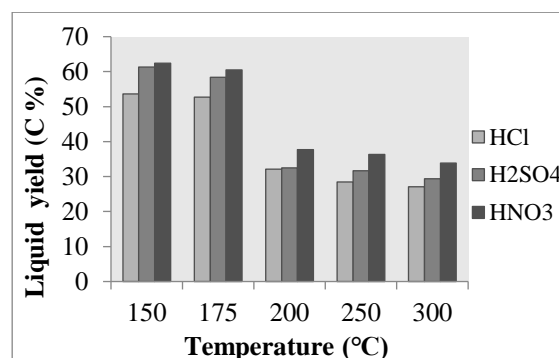Figure 3 Effects of temperature and catalysts on the liquid yields of artichoke stalks at the pH 2.0.

Figure 4 Effects of temperature and catalysts on the liquid yields of artichoke stalks at the pH 3.0.

3.2. Effect of experimental parameters of hydrothermal liquefaction on liquid product distribution

The aqueous products contained major organic compounds, which were carboxylic acids, furfurals, aldehydes and ketones. Their amounts were measured by using HPLC device to interpret the effects of the reaction conditions. Identified major organic compounds in liquid product from the hydrothermal liquefaction of artichoke leaves and stalks without catalyst are given in Figures 5 and 6, respectively, for the reaction temperatures (150°C - 300°C). According to the experimental results, HNO_3 led to highest increase of typical acidic intermediates; carboxylic acids and furfurals. Effects of temperature and HNO_3 on the liquid product yields of artichoke leaves and stalks at the pH 3.0 are given in the Figures 7 and 8, respectively.
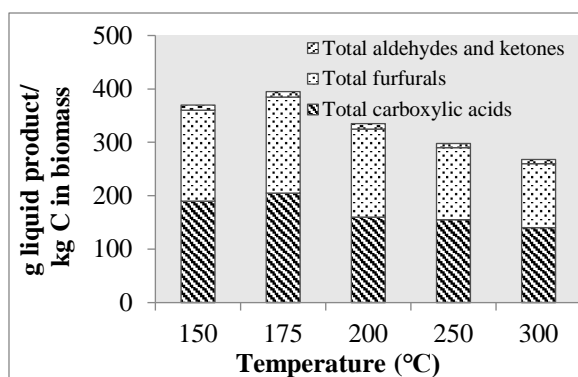
Figure 5 Effects of temperature on the liquid product yields of artichoke leaves.
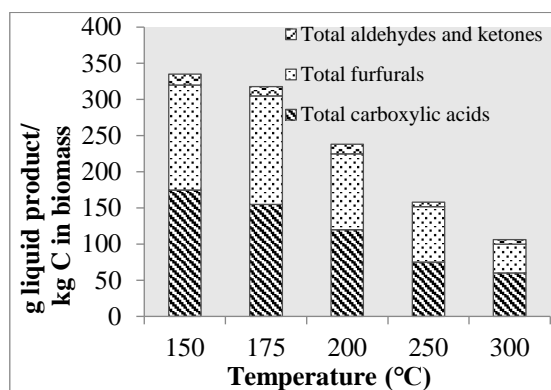

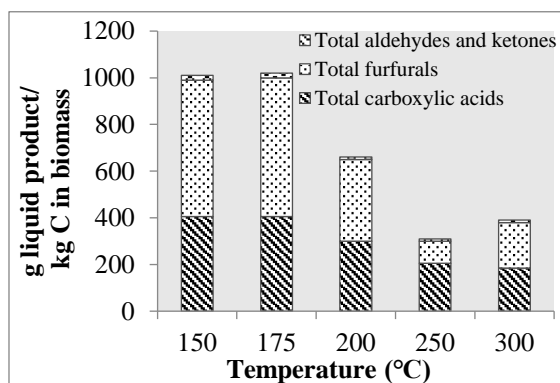Figure 6 Effects of temperature on the liquid product yields of artichoke stalks.

Figure 7 Effects of temperature and HNO_3 on the liquid product yields of artichoke leaves at pH 3.0.

Aqueous product contained high concentrations of carboxylic acids such as acetic acid and formic acid which are degradation products of furfural or 5-HMF. Effects of temperature and catalysts on the main aqueous products, formic acid, acetic acid and 5-HMF yields of artichoke leaves, and stalks at the pH 2 and pH 3 are shown in the Figures 9-14.
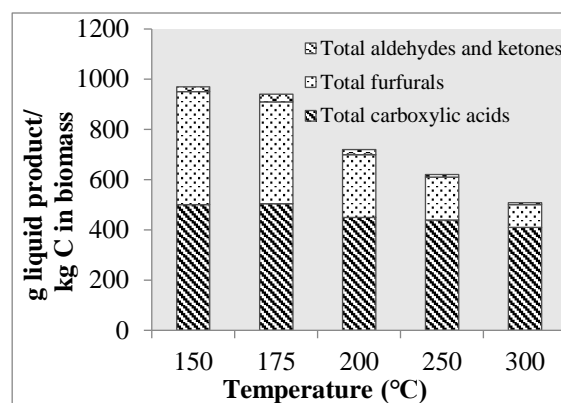

Figure 8 Effects of temperature and HNO_3 on the liquid product yields of artichoke stalks at pH 3.

The main aqueous products acetic acid and formic acid reached maximum value with HNO_3 catalyst at the pH 3. 5-HMF and reached maximum value with HCl catalyst at the pH 3. Especially, the main aqueous products were decreased sharply by increasing the temperature from 175°C to 200°C. Acetic acid was the highest product 268.52 (g aqueous product/kg C in biomass), and decreased to 103.59 (g aqueous product/kg C in biomass) at 300°C by using HNO_3. The highest formic acid was 72.12 (g aqueous product/kg C in biomass) and decreased to 26.82 (g aqueous product/kg C in biomass) at 300°C by using HNO_3. The highest 5-HMF was 176.24 (g aqueous product/kg C in biomass and decreased to 102.59 (g aqueous product/kg C in biomass) at 300°C by using HCl.
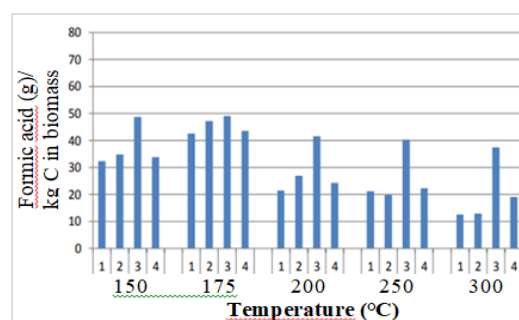

Figure 9 Effects of temperature and catalysts on the formic acid yields of artichoke leaves at pH 2. (1: without catalyst, 2: HCl, 3: HNO_3, 4: H_2SO_4).

Figure 10 Effects of temperature and catalysts on the formic acid yields of artichoke leaves at pH 3. (1: without catalyst, 2: HCl, 3: HNO_3, 4: H_2SO_4).

Figure 11 Effects of temperature and catalysts on the acetic acid yields of artichoke leaves at pH 2. (1: without catalyst, 2: HCl, 3: HNO_3, 4: H_2SO_4).
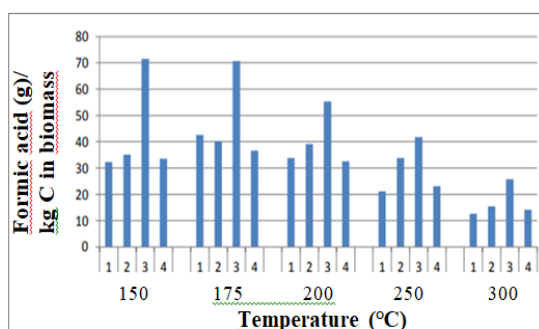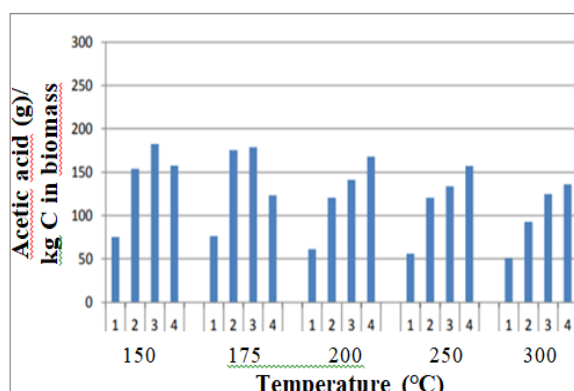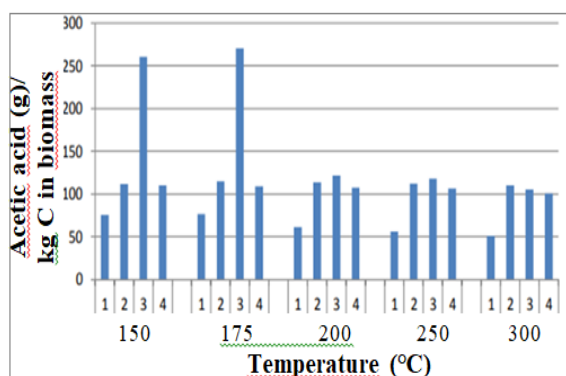

Figure 12 Effects of temperature and catalysts on the acetic acid yields of artichoke leaves at pH 3. (1: without catalyst, 2: HCl, 3: HNO_3, 4: H_2SO_4).
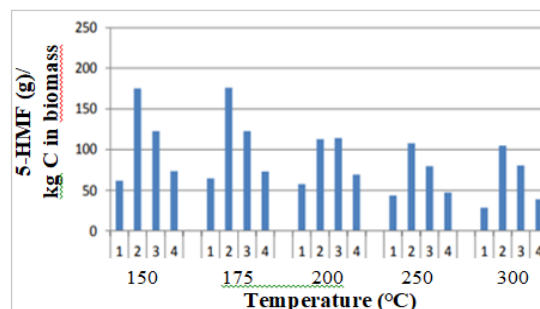

Figure 13 Effects of temperature and catalysts on the 5-HMF yields of artichoke leaves at pH 2. (1: without catalyst, 2: HCl, 3: HNO_3, 4: H_2SO_4).
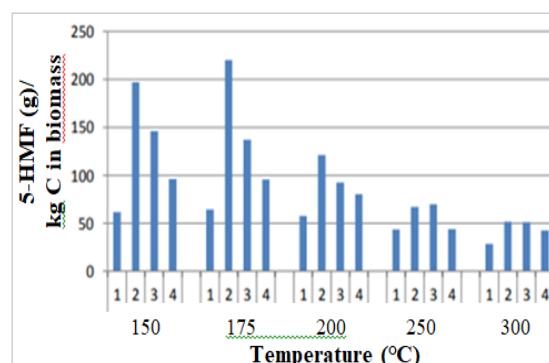

Figure 14 Effects of temperature and catalysts on the 5-HMF yields of artichoke leaves at pH 3. (1: without catalyst, 2: HCl, 3: HNO_3, 4: H_2SO_4).

4. CONCLUSION

This study was aimed to investigate the efficient conversion conditions of Artichoke residues to the valuable chemicals (formic acid, acetic acid and 5-hydroxymetilfurfural) by using acid (HCl, HNO_3 and H_2SO_4) catalyzed hydrothermal reaction as a function of pH and temperature. The experimental results of the hydrothermal liquefaction of the artichoke residues could be an alternative method to the waste management of the food industry. Additionally, the results presented in this paper have a novelty due to the examination of the feedstock. Experimental evolution of liquid parts and their variations with respect to the reaction parameters will be able to give more information about decomposition pathway depending on nature of feedstock. The experimental results of this study pointed that liquid phase production

pathways are enhanced by HNO_3 at the highest rate. According to experimental results, efficiency of the acid catalysts in hydrothermal liquefaction can be ordered as: $HNO_3 > H_2SO_4 > HCl$. The aqueous products contain major organic compounds, which were carboxylic acids, furfurals, aldehydes and ketones. The main aqueous products acetic acid and formic acid reached maximum value with HNO_3 catalyst at the pH 3, at 175ºC and 150ºC, respectively. 5-HMF reached maximum value with HCl catalyst at the pH 3 at 175°C.

The Declaration of Conflict of Interest/ Common Interest
No conflict of interest and common interest has been declared by the authors.

Authors' Contribution
The first author contributed 60%, the other authors 40%.

The Declaration of Ethics Committee Approval
This work does not require ethics committee permission or any special permission.

The Declaration of Research and Publication Ethics
The author of the paper declares that, international scientific, ethical and citation rules were followed for this study, and no falsification was made on the collected data Sakarya University Journal of Science and its editorial board have no responsibility for all ethical violations. All responsibility belongs to the responsible author and this study has not been evaluated in any academic publication environment other than Sakarya University Journal of Science.

REFERENCES

[1] S. Takkellapati,T. Li, M. A. Gonzalez, "An Overview of Biorefinery Derived Platform Chemicals from a Cellulose and Hemicellulose Biorefinery," Clean Technologies and Environmental Policy, vol. 20, no.7, pp. 1615–1630, 2018.

[2] A. Kruse, N. Dahmen, "Water-A magic solvent for biomass conversion," Journal of Supercritical Fluids, vol. 96, pp. 36-45, 2015.

[3] T. M. Yeh, J. G. Dickinson, A. Franck, S. Linic, L. T. Thompson Jr, P. E. Savage, "Hydrothermal catalytic production of fuels and chemicals from aquatic biomass," vol.88, no.1, pp.13-24, 2012.

[4] A. Yüksel Özşen, "Conversion of Biomass to Organic Acids by Liquefaction Reactions Under Subcritical Conditions," Frontiers in Chemistry, vol. 8, no.24, pp. 1-13, 2020.

[5] Y. H. Chan, S. Yusup, A. T. Quitain, Y. Uemura, M. Sasaki, "Bio-oil production from oil palm biomass via subcritical and supercritical hydrothermal liquefaction," Journal of Supercritical Fluids, vol. 95, pp. 407–412, 2014.

[6] N. Shimizu, B. Zeng, "Hydrothermal liquefaction of wood chips under supercritical and subcritical water reaction conditions," SN Applied Sciences, vol. 577, no.3, pp. 6-15, 2020.

[7] A. Kruse, A. Gawlik, "Biomass conversion in water at 330–410 °C and 30–50 MPa. Identification of key compounds for indicating different chemical reaction pathways," Industrial and Engineering Chemistry Research, vol. 42, no.2, pp. 267-279, 2003.

[8] L. M. Cheng, X. P. Ye, R. H. He, S. Liu, "Investigationof rapid conversion of switchgrass in subcritical water," Fuel Processing Technology, vol. 90, no.2, pp. 301–311, 2009.

[9] G. T. Jeong, "Catalytic conversion of Helianthus tuberosus L. to sugars, 5-hydroxymethylfurfural and levulinic acid using hydrothermal reaction," Biomass and Bioenergy, vol. 74, pp. 113-121, 2015.

[10] D. A. Cantero, T. Sánchez Tapia, M. D. Bermejo, M. J. Cocero, "Pressure and temperature effect on cellulose hydrolysis in pressurized water," Journal of Chemical Engineering, vol. 276, pp. 145–154, 2015.

[11] T. Saito, M. Sasaki, H. Kawanabe, Y. Yoshino, M. Goto, "Subcritical water reaction behavior of D-glucose as a model compound for biomass using two different continuous-flow reactor configurations," Chemical Engineering Technology, vol. 32,pp. 527–533, 2009.

[12] P. T. Williams, J. Onwudili, "Subcritical and supercritical water gasification of cellulose, starch, glucose, and biomass waste," Energy Fuels, vol 20, pp. 1259–1265, 2006.

[13] FAOSTAT (Food and Agriculture Organization Corporate Statistical Database), 2016.

[14] H. K. Goering, P. J. Van Soest, Forage fiber analyses, Agriculture Handbook, US Government Printing Office, Washington, D.C., 1970, pp. 829-835.

[15] D. Selvi Gökkaya, G. Akgül, M. Sağlam, M. Yüksel, L. Ballice, "Supercritical conversion of wastes from wine industry: Effects of concentration, temperature and group 1A carbonates" The Journal of Supercritical Fluids, vol. 176, pp.105359, 2021.

[16] A. Kruse, N. Dahmen, "Hydrothermal biomass conversion: Quo vadis?," Journal of Supercritical Fluids, vol.134, no. SI, pp. 114-123, 2018.

[17] C. M. Martínez, D. A. Cantero, M. D. Bermejo, M. J. Cocero, "Hydrolysis of cellulose in supercritical water: reagent concentration as a selectivity factor," Cellulose, vol. 22, pp. 2231–2243, 2015.

[18] F. Peng, N. Jia, J. Bian, P. Peng, R. C. Sun, S. J. Liu, "Isolation and fractionation of hemicelluloses from Salix Psammophila," Cellulose Chem. Technology, vol. 46, pp. 177-184, 2012.

Title: Cancer Risk Analysis in Untreated and Photocatalytic Treated Water Containing THM

Authors: Pınar Nazire TANATTI, Cemil ÖRGEV, Hülya DEMİREL, İsmail Ayhan ŞENGİL

Cancer Risk Analysis in Untreated and Photocatalytic Treated Water Containing THM

Cemil ÖRGEV[1] , N. Pınar TANATTI[*1] , Hülya DEMİREL[1] , İ. Ayhan ŞENGİL[2]

Abstract

In this study, cancer risk analysis was investigated in untreated trihalomethanes (THMs) containing water using synthetic THM solution and after photocatalytic treatment with TiO_2 and ZnO of this water. Trace amounts of disinfection by-products remain in the water. In this study, cancer risk assessment was investigated water containing trihalomethanes (THMs) constituted with synthetic THM solution and after the photocatalytic treatment of this water, the cancer risk was determined depending on the presence of THM in the water. With the photocatalytic treatment method using ZnO and nano TiO_2 particles, THM removal was studied with synthetic water with an initial concentration of 300 µg/L. In the ZnO-catalyzed process chloroform 25 µg/L, BDCM 2.4 µg/L and DBCM 35 µg/L were found. However, in the TiO_2-catalyzed process, chloroform 49 µg/L and DBCM 28 µg/L were obtained. The cancer risk analysis and the hazard index of THMs through oral, dermal and inhalation ingestion from these waters were evaluated. Comparing the three different pathways, humans have a higher risk of cancer through oral ingestion than dermal and inhalation pathways. It has been determined that the cancer risk for ZnO treated water was reduced by 62% and for TiO_2 treated water by 69% when THMs by oral ingestion have examined compared to untreated water in cancer risk analysis. The cancer risks of oral ingestion are determined as acceptable low risk, but the cancer risk of THMs through dermal ingestion from dibromochloromethane plays an essential role in this study.

Keywords: Cancer risk assessment, photocatalytic treatment, trihalomethanes (THMs)

1. INTRODUCTION

Disinfection is a method used to eliminate pathogenic microorganisms in drinking water and prevent waterborne diseases since the early 1900s [1]. Chlorine is the most common chemical used in water disinfection and protects against microbial contamination by keeping minimum chlorine residues along the water distribution line [2, 3]. However, it was determined in the 1970s that it created

* Corresponding author: ptanatti@sakarya.edu.tr
[1] Sakarya University of Applied Science
E-mail: corgev@subu.edu.tr, hsemercioglu@subu.edu.tr
ORCID: https://orcid.org/0000-0003-4199-1915, https://orcid.org/0000-0002-2904-7334, https://orcid.org/ 0000-0002-8128-3043,
[2] Sakarya University
E-mail: asengil@subu.edu.tr
ORCID: https://orcid.org/0000-0002-1858-3369

harmful disinfection by-products that caused health problems in disinfection [4].

During the disinfection of water, chlorine reacts with natural organic substances (NOM) in the water, and various disinfection by-products (DBP) are formed [5, 6]. The hypochlorous acid (HOCl) and hypochlorite (OCl$^-$) ions formed during disinfection with chlorine tend to react with the aromatic parts of the NOM [7]. Trihalomethanes (THM) and haloacetic acids (HAA) are predominantly disinfection by-products that occur as a result of disinfectant reactions with DOM [8]. The four main components of the THM group are Chloroform, Dibromochloromethane (DBCM), Bromodichloromehane (BDCM), and Bromoform and also the most dominant type in surface waters is chloroform [9, 10].

These compounds have negative health effects on humans and many have been classified as possible or possible human carcinogens [11]. USEPA [12] classified chloroform, BDCM, and bromoform as possible carcinogens [13]. Various international regulatory agencies have regulated THM limit values worldwide [14]. EPA has determined the maximum pollutant level (MCL) of THMs as 80 µg / L [2].

People are exposed to THMs in different ways throughout their lives. In addition to using clean water as drinking water, this exposure also occurs during breathing and regular human activities such as cooking, showering, and using swimming pools. Therefore, people have accepted being exposed to THM in three different ways, oral, dermal, and respiratory [14-16]. Many studies have been conducted on the effects of exposure on human health, and THMs have been proven to be associated with bladder, colon, leukemia, stomach, and rectum cancer risks [17-21]. Also, studies have demonstrated that DBPs have negatively affected reproductive and growth abilities, such as growth retardation, infertility, preterm/low birth in humans

[22,23]. In disinfection drinking water/wastewater treatment plants, THM concentrations in water should be determined and compared with EPA (TR) limit values and possible effects (exposure risk) in humans should be determined. While evaluating the health risks of toxic substances, it was accepted that people were exposed to these substances mostly orally in the traditional approach, but in the light of the studies conducted, respiratory and skin contact should be considered in risk determination [14, 16, 24-25].

It was determined that THM concentrations exceed the reference limit values of EPA in disinfection with chlorine in many studies [7]. Therefore, THM treatment has become important. Many literature studies have investigated the removal method of THM precursors, and the research of THMs removal methods has gained speed today. Adsorption [26], coagulation-flocculation [27] and ion exchangers [28] methods have been studied as removal methods of THM precursors. Microfiltration [29] and advanced oxidation processes have been studied as THM removal methods.

In this study, synthetic water containing THMs was first formed, and THMs purification was carried out in this water by photocatalytic oxidation. The health risk of THMs in synthetic waters before and after treatment has been determined. The presence of THMs in the treated waters was investigated due to the use of photocatalytic methods to minimize the disinfection by-products in the waters. Finally, it has been revealed by using the possible health risk (multi-pathway risk assessment) that may occur in people with the discharge of treated water to the receiving environment.

2. MATERIAL AND METHODS

2.1. Measurement method of THMs

THM measurements have been made according to SM 6232 C with the

SHIMADZU brand QP 2010 model GC/MS device. Extraction has done by shaking with a Tert Butyl Methyl Ether (Merck, Extra Pure) in a 1:1 (v:v) ratio for a 5 ml sample containing THM for 1 minute and phase separation has waited. Sodium Sulfate Anhydrous (Merck, Extra Pure Food Grade), which is conditioned at 450 °C for 4 hours to hold water that can remain in the samples, is taken into 4 ml vials and added to the sample after extraction.

Temperature program developed in GC / MS: column temperature is started at 40 °C for 2 minutes, waiting time increases by 8 °C per minute, reaching 220 °C and waiting for 5 minutes. The injection and detector temperature are 225 °C. Nitrogen was used as the carrier gas and the column pressure was 82.5 kPa.

2.2. Photocatalytic reactor design

The batch type of slurry photoreactor used for THM removal is shown in Figure 1. The outer part of the reactor is made of bright chrome steel and is in the shape of a cylinder with a height of 300 mm and a diameter of 100 mm. Six 6 Watt UV lamps are placed on the inner surface of the reactor at equal distances, which can be controlled separately. THM samples were placed in quartz tubes with a volume of 150 ml and placed in the center of the reactor.
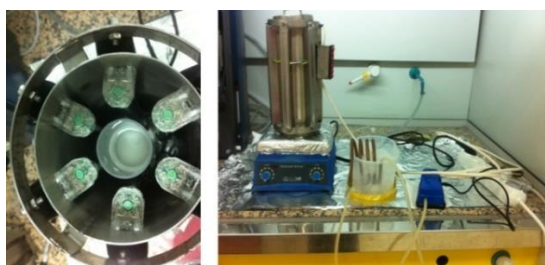

Figure 1 Batch-type slurry photoreactor

In the experiments, synthetic wastewater with an initial concentration of 300 µg/L THMs was obtained using RESTEK brand THMs stock solution. This synthetic was photocatalytically treated for cancer risk analysis. Particle doses, UV light intensity and reaction time parameters were investigated in the wastewater's pH value.

2.3. Health risk assessment

Cancer risk assessment refers to the probability of cancer risk that may occur in an individual because of an individual's (male and female) exposure to THM for life. During cancer risk assessment, data collection and interpretation, possible exposure, the toxicity of the substance (pollutant), risk determination and management stages are considered. During the cancer risk assessment, USEPA [30] guideline and Lee [15] were based on and potential THM exposure was determined based on the THM concentrations of the water samples before and after the two different photocatalytic oxidation methods [23, 31]. Depending on THM concentrations, possible cancer risk was determined by taking a chronic daily dose (CDI), exposure route (dermal, oral, inhalation) and corresponding slope factor (SF) [15,30-32]. Chronic daily doses determined for each exposure route specified in Equations 1-3 were calculated and then possible cancer risk was found using equation a 4 based on three different exposures.

$$CDI_{oral} = \frac{(CW \times IR \times EF \times ED)}{(BW \times AT)} \qquad (1)$$

$$CDI_{dermal} = \frac{(CW \times SA \times PC \times ET \times EF \times ED)}{(BW \times AT)} \qquad (2)$$

$$CDI_{inhalation} = \frac{(CA \times IR \times ET \times EF \times ED)}{(BW \times AT)} \qquad (3)$$

$$Cancer\ Risk\ for\ THMs\ = \sum CDI_i \times SF_i \qquad (4)$$

CW is the chemical concentration in water, mg/L, IR is the ingestion rate, L/day, EF is the exposure frequency (days/year), ED is exposure duration (years), BW is the body weight (kg), AT is the average lifetime (days), SA is a skin-surface area exposed to water (m^2), ET is the exposure time (h/day), CA is the concentration of THMs in the air

(mg/m^3). PC is the chemical-specific dermal permeability constant (cm/h), IR is the inhalation rate (m^3/h) and SF is the corresponding slope factor/potential factor of specific THMs. The statistical distributions and values of parameters are shown in Table S1[33-41].

2.4. Non-cancer risk assessment (Hazard index)

At the same time, the hazard index (HI) of THMs in different exposure routes is calculated to assess for non-carcinogenic risk assessment. The assessment of hazard indexes for ingestion route and dermal absorption is as follows:

$$\text{Hazard index for THMs of oral route } = CDI_{oral} / RfD_{THMs} \quad (5)$$

$$\text{Hazard index for THMs of dermal route } = CDI_{dermal} / RfD_{THMs} \quad (6)$$

RfD is the reference dose for a specific substance, which is given in many experiments [39, 42]. CDI value for inhalation ingestion is lower than the others so inhalation adsorption is neglected and the hazard index is calculated for only oral and dermal ingestion.

3. RESULTS AND DISCUSSION

3.1. Photocatalytic treatment method

Photocatalytic treatment of THMs was investigated by using TiO$_2$ nanoparticles and ZnO in synthetic water containing THMs. Samples have been prepared using the RESTEK brand THM standard. The photocatalytic treatment method determined optimum conditions by studying the particle dose, light intensity, and reaction time of the wastewater containing THM at its pH value. The amount of TTHM in the samples where the experiments are carried out is 300 µg/L.

In order to determine the optimum TiO$_2$ and ZnO dose, experiments have been carried out at pH 6.89, 24 Watt light intensity and 30 min reaction time. Table S2 shows the effect of particle dose on THM removal. Table S1 shows the effect of particle dose on THM removal. With the oxidation of ZnO, THM is reduced below 50 mg/L in THM removal and below 100 µg/L in all other doses. For this reason, 50 mg/L was chosen as the appropriate ZnO dose in ZnO oxidation. In TiO$_2$ oxidation, THM removals below 100 µg/L are obtained at 200 mg/L and above doses.

For this reason, the optimum dose for TiO$_2$ oxidation was chosen as 200 mg/L. The effect of light intensity on THM removal is presented in Table S3. As can be seen from Table S2, high THM removals are obtained at all light intensities between 12 Watt and 36 Watt. 12 Watt light intensity was determined as the optimum value for THM removal by photocatalytic treatment for both processes. The effect of reaction time on THM removal has been investigated from 5 min to 60 min and the results are given in Table S3. THM removal is obtained at values less than 100 µg/L after 30 minutes for both processes.

The optimum conditions for THM removal by photocatalytic treatment for both processes were determined as pH 6.89, 200 mg/L TiO$_2$ dose, 50 mg/L ZnO dose, 12 Watt light intensity and 30 minutes reaction time. THM removals obtained under optimum conditions for THM treatment in photocatalytic treatment using ZnO and TiO$_2$ are given in Table S4. The THM concentrations of the untreated water containing THM and the water treated using two different photocatalytic treatment methods, given in Table S5, were used in the cancer risk analysis.

3.2. Evaluations of lifetime cancer risks for THMs

The cancer risk assessments of THMs through oral, dermal and inhalation ingestion were done using parameters given

in Table S5. Total water ingestion of 2.0 L/day per person was accepted considering the water consumption habits of people in Turkey for evaluation of lifetime cancer risks [33]. The cancer risk was interpreted as follows:

Negligible risk ($CR<10^{-6}$), acceptable low risk ($1\times10^{-6} \leq CR<5.1\times10^{-5}$), acceptable high risk ($5.1\times10^{-5} \leq CR<10^{-4}$), and unacceptable risk ($CR\geq10^{-4}$) [38, 43, 44].

3.3. Oral ingestion

The result of lifetime cancer risk through oral ingestion is shown in Figure 2 for the initial dose and treatment methods. The lifetime cancer risks of chloroform ($CHCl_3$) were higher than 10-6, which is the negligible risk level defined by USEPA. All cancer risks are defined as acceptable low risk for $CHCl_3$. The highest risks are determined for females and males in the initial dose. Also, when photocatalytic oxidation methods are compared, the highest risk is observed at 3.40×10^{-6} for females in the TiO_2 oxidation method. The lifetime cancer risks of bromodichloromethane (BDCM) are higher than 10^{-6} which is the negligible risk level defined by USEPA. All cancer risks are defined as acceptable low risk for BDCM. The cancer risks are observed at 1.7×10^{-6} and 1.65×10^{-6} for females and males the in ZnO oxidation method. The lifetime cancer risks of dibromochloromethane (DBCM) are higher than 5×10^{-5} for initial doses and the risks are stated as acceptable low risk. Cancer risks are negligible for the treatment methods, and the risks range from 2.61×10^{-5} to 3.35×10^{-5}. Bromoform wasn't detected in the waters treated by both photocatalytic treatment methods.

Therefore, no risks can be mentioned for bromoform. When TTHMs are compared in the waters treated by both photocatalytic treatment methods, the highest risk values are observed ZnO oxidation method both in females and males. The average lifetime

cancer risk for THMs from high to low was in the order of $CHBr_2Cl$, $CHCl_3$ and $CHCl_2Br$. Exposure to multiple toxicants results in additive or synergistic effects. Therefore, these compounds, if not alone, have considerable cancer risk [45]. The percentage contribution of average cancer risks through oral ingestion for THMs in the ZnO treatment method indicated that dibromochloromethane made the highest contribution (91%) to total risks, followed by chloroform (5%), and bromodichloromethane (4%). The percentage contribution of average cancer risks through oral ingestion for THMs in the TiO_2 treatment method indicated that dibromochloromethane made the highest contribution (89%) to total risks and chloroform (11%).
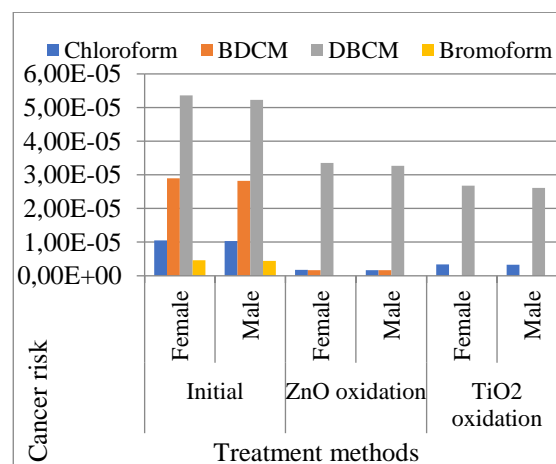
Figure 2 Lifetime cancer risk of THMs through oral ingestion

3.4. Dermal ingestion

Skin contact with water during showering, bathing, and swimming can result in the penetration of contaminants into the body. The different available skin-surface areas for males and females are reported 1.94 m^2 and 1.69 m^2, respectively by USEPA [36]. The cancer risk of THMs lifetime cancer risk of THMs through dermal ingestion exposure for initial dose and treatment methods are shown separately in Figure 3. The lifetime cancer risks of chloroform ($CHCl_3$) except the ZnO treatment method are higher than 10^{-6} which is the negligible risk level defined

by USEPA. All cancer risks are defined as acceptable low risk for $CHCl_3$. On the other hand, the highest risk is observed at 1.34×10^{-6} for males in the TiO_2 oxidation method. The lifetime cancer risks of BDCM are higher than 10^{-6}. Bromoform wasn't detected in the waters treated by TiO_2 photocatalytic treatment method. The cancer risks are observed at 6.45×10^{-7} and 7.52×10^{-7} for females and males in the ZnO oxidation method. The lifetime cancer risks of DBCM range from 1.13×10^{-5} to 1.65×10^{-5} for the treatment methods and the cancer risks are defined as acceptable low risk. When the risks of DBCMs are compared, the highest risk values are observed in the ZnO oxidation method both in females and males.

Figure 3 Lifetime cancer risk of THMs through dermal ingestion

Bromoform, one of the disinfectant by-products, couldn't be detected in the waters treated by both photocatalytic methods. The cancer risks of THM for female and male is determined as 1.54×10^{-5} and 1.79×10^{-5}, respectively in the ZnO oxidation method. The percentage contribution of average cancer risks through oral ingestion for THMs in the ZnO treatment method indicated that dibromochloromethane made the highest contribution (92%) to total risk chloroform by chloroform (4%), and bromodichloromethane (4%). The percentage contribution of average cancer risks through oral ingestion for THMs in the TiO_2 treatment method indicated that dibromochloromethane made the highest contribution (91%) to total risks and chloroform (9%). As a result, the cancer risk
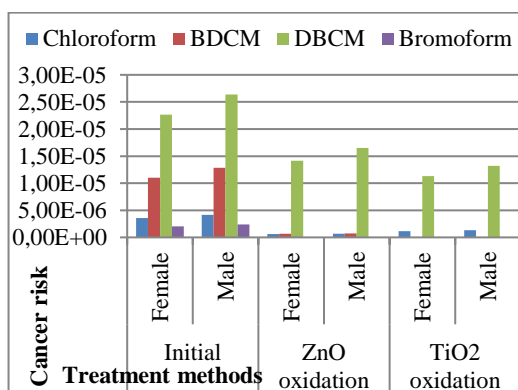
of THMs through dermal ingestion from dibromochloromethane plays an important role in this study. According to risk values, females have been determined to have higher cancer risks compared to males due to skin surface area, body weight and lifetime.

3.5. Inhalation ingestion

Inhalation ingestion occurs when the air contains compounds volatilized during water usage, such as bathing, showering, laundering, and cooking [14, 15, 46]. Showering is the predominant contributor to volatile compounds through inhalation exposure [47]. The cancer risk of THMs through the inhalation route of exposure depends on different treatment methods are shown in Figure 4. The cancer risk assessment of total THMs due to inhalation exposure is lower than 10^{-6} both TiO_2 and ZnO photocatalytic treatment methods. Also, the risks can be identified as negligible risks. The highest cancer risk is observed in chloroform compounds in both initial and TiO_2, ZnO treatment methods.
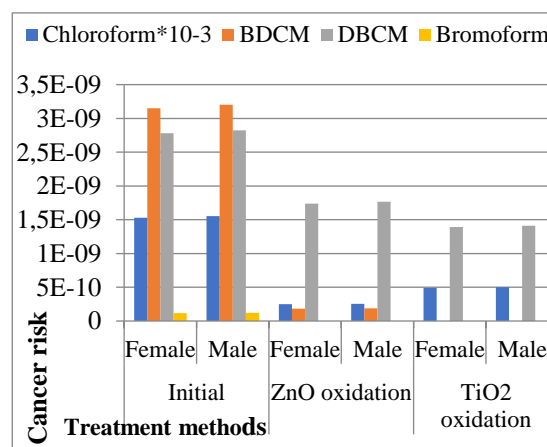
Figure 4 The cancer risk of THMs through the inhalation route of exposure

Because of the boiling point of chloroform at low temperatures, people are exposed to chloroform during bath and shower. So, chloroform is the main contributor to the total cancer risk in inhalation exposure. The major contributor through inhalation is $CHCl_3$ 2.51×10^{-7}, 2.55×10^{-7} in the ZnO method and 4.92×10^{-7}, 5×10^{-7} for females

and males, respectively. $CHCl_3$ has a major contribution (99%), (99.2%) to total risks and dibromochloromethane (1%), (0.8%) both in ZnO and TiO_2 methods. It's stated that males have a higher cancer risk than females, depending on Turkey's living conditions, similar to different studies [14, 15, 31].

3.6. Non-cancer risk assessment

The hazard indexes of THMs through different exposure are calculated to determine the non-carcinogenic risks of disinfection by-products. The potency factor and the reference dose (RfD) values for the four THM compounds were taken from literature based on USEPA [39]. The hazard index values through oral and dermal ingestion for males and females are given in Figure 5 and Figure 6, respectively. The results indicated that the oral route has higher HI values than the dermal route, similar to various studies [39,46-48]. Chloroform has the highest contribution to average total HI values for females and males in TiO_2 and ZnO photocatalytic treatment methods. The hazard index values for THMs from high to low are in the order of $CHCl_3$, $CHBr_2Cl$ and $CHCl_2Br$ for females and males in the treated water.
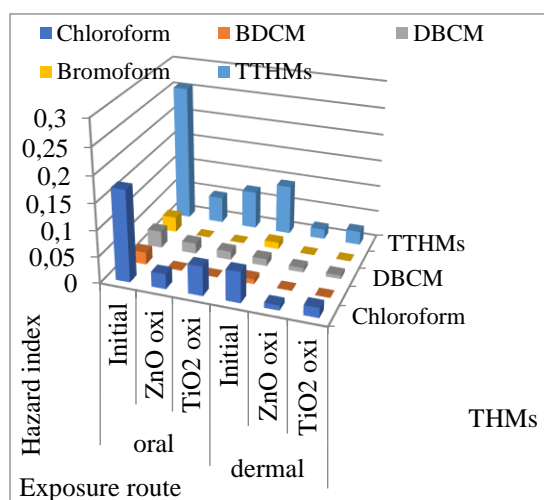
Figure 5 The hazard index values through oral and dermal ingestion for females
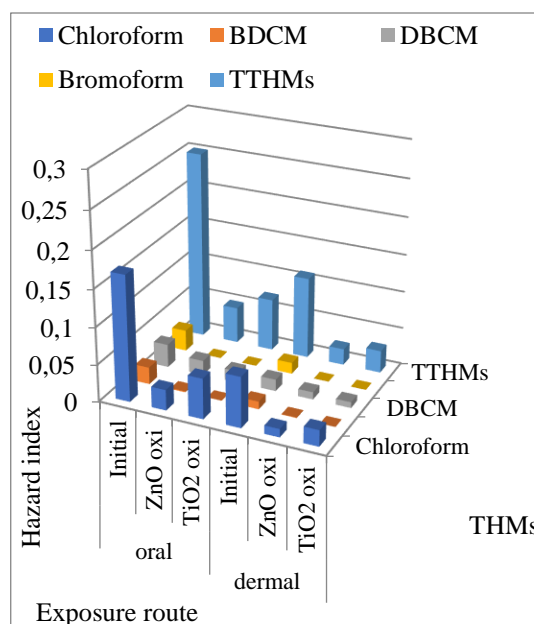
Figure 6 The hazard index values through oral and dermal ingestion for males

4. RESULTS

Three different exposure routes evaluated the association between trihalomethanes (THMs) exposure and lifetime cancer risks. This study evaluates the potential carcinogenic and non-carcinogenic risks of disinfection by-products and provides a primary human health risk categorization for THMs in synthetic water and treated water with TiO_2 and ZnO photocatalytic treatment methods. The results showed that people have a higher risk of cancer through oral ingestion. The lifetime cancer risks through oral ingestion of $CHCl_3$, $CHBrCl_2$, and $CHBr_2Cl$ from treated water are higher than 10^{-6} and the cancer risks are identified as acceptable low risk. Bromodichloromethane has a higher cancer risk to people through dermal exposure than the other THMs. In addition to this, it's found that males have a higher cancer risk than females in exposure to THMs in inhalation digestion. The result of the present study is also good in line with the findings of many studies [46-53]. In a study on THMs removal by advanced oxidation method, the females were found to have a higher cancer risk than males for oral and dermal digestion, similar to this study. The non-carcinogenic risk analysis denoted that the risk is substantially through oral

ingestion in contrast with dermal ingestion, have almost negligible risk.

Authors' contributions
NPT has done all the experiments of the study. HD has done all cancer risk assessments. All parts of the writing belong to CÖ, NPT, HD, and İAŞ.

The Declaration of Conflict of Interest/ Common Interest

No conflict of interest or common interest has been declared by the authors.

The Declaration of Ethics Committee Approval

This study does not require ethics committee permission or any special permission.

The Declaration of Research and Publication Ethics

The authors of the paper declare that they comply with the scientific, ethical and quotation rules of SAUJS in all processes of the paper and that they do not make any falsification on the data collected. In addition, they declare that Sakarya University Journal of Science and its editorial board have no responsibility for any ethical violations that may be encountered, and that this study has not been evaluated in any academic publication environment other than Sakarya University Journal of Science.

Table S1. Effect of particle dose on THM removal

	ZnO					TiO$_2$				
Particle doses (mg/L)	50	100	200	300	500	50	100	200	300	500
Chloroform (µg/L)	21.8	20.37	18.77	16.94	15.48	88.69	69.05	41.78	36.21	34.48
BDCM (µg/L)	1.96	1.71	1.54	1.25	0.99	1.01	0.06	-	-	-
DBCM (µg/L)	29.34	25.44	23.86	20.97	19.38	31.8	27.29	24.11	22.17	19.86
Bromoform (µg/L)	-	-	-	-	-	0.86	-	-	-	-
TTHMs (µg/L)	53.1	47.52	44.17	39.16	35.85	12.36	96.4	65.89	58.38	54.34

Table S2. Effect of light density on THM removal

	ZnO				TiO$_2$			
Light density (Watt)	12	18	24	36	12	18	24	36
Chloroform (µg/L)	25	24.64	21.8	19.23	49	46.69	41.78	37.65
BDCM (µg/L)	2.4	2.27	1.96	1.51	-	-	-	-
DBCM (µg/L)	35	33.8	29.34	25.44	28	26.98	24.11	21.04
Bromoform (µg/L)	-	-	-	-	-	-	-	-
TTHMs (µg/L)	62.4	60.71	53.1	46.18	77	73.67	65.89	58.69

Table S3. Effect of reaction time on THM removal

	ZnO				TiO$_2$			
Reaction time (min)	5	15	30	60	5	15	30	60
Chloroform (µg/L)	73.29	48.87	25	23.89	91.09	65.79	49	41.83
BDCM (µg/L)	15.54	4.56	2.4	1.81	10.73	3.03	-	-
DBCM (µg/L)	38.41	37.12	35	33.26	43.71	35.2	28	19.52
Bromoform (µg/L)	18.34	3.11	-	-	14.69	2.32	-	-
TTHMs (µg/L)	145.58	93.66	62.4	55.91	160.22	106.34	77	61.35

Table S4. THM concentrations

	Chloroform (µg/L)	BDCM (µg/L)	DBCM (µg/L)	Bromoform (µg/L)	TTHMs (µg/L)
Initial	152	41	56	51	300
ZnO oxidation	25	2.4	35	-	62.4
TiO$_2$ oxidation	49	-	28	-	77

Table S5. The statistical distributions and values of parameters

Input parameters	Units	Values	References
Oral ingestion			
The concentration of the chemical in water (CW)	mg/L		This study
Ingestion rate (IR)	L/day	2	[33]
Exposure frequency (EF)	days/year	365	[15]
Exposure duration (ED)	years	30	[34]
Body weight (BW)	kg	Female: 65 Male: 72	[22]
Average time (AT)	days	Female: 29565 Male: 26280*	[35]
Dermal ingestion			
Area of surface skin expose to water (SA)	m^2	Female: 1.69 Male: 1.94	[36]
Chemical-specific dermal permeability constant (PC)	cm/h	Chloroform:0.16 BDCM: 0.18 DBCM:0.2	[37]
Exposure time (ET)	h/day	0.25	[38]
Inhalation ingestion			
The concentration of studied THM species in the air (CA)	mg/m^3	Calculation**	This study
Inhalation rates (IR)	m^3/h	0.83	[15]
Reference doses (RfD)	mg/kg/day	Chloroform:0.01 BDCM: 0.02 DBCM:0.02 Bromoform: 0.02	[39]
Slope factor/ potential factor (SF)	mg/kg/day	Oral Chloroform:0.006 1 BDCM: 0.062 DBCM:0.084 Bromoform: 0.0079	Dermal Chloroform:0.0 81 BDCM: 0.13 DBCM:0.094 Bromoform: 0.0039	[40]

* Exposure duration (ED) was considered 81 years for women on average life and 75 years for men on average life in Turkey according to TUİK [35] data.
** THMs concentration in air CA has been calculated by many studies based on statistical models and experimental datas [23,38,40,41]. The CA for chloroform was calculated by a statistical model based on Legay [38]. For the other three THMs, a volatilization factor of $5 \times 10^{-4} \times 1000$ L/m^3 was used for the estimation of CA.

REFERENCES

[1] W. E. Elshorbagy, H. Abu-Qadais, M. K. Elsheamy, "Simulation of THM species in water distribution systems" Water Research, vol:34, issue 13, pp. 3431- 3439, 2000.

[2] V. Uyak, K. Ozdemir, I. Toroz, "Multiple linear regression modeling of disinfection by-products formation in Istanbul drinking water reservoirs" Science of Total Environmental, vol: 378, pp. 269–280, 2007.

[3] J. Zhang, J. Liu, C. S. He, C, Qian, Y. M, "Formation of iodo-trihalomethanes (I-THMs) during disinfection with chlorine or chloramine: Impact of UV/H_2O_2 pre-oxidation" Science of Total Environmental, pp. 640–641, 2018.

[4] G. Hua, S. Yeats, "Control of trihalomethanes in wastewater treatment" Fla. Water Resource Journal, vol: 4, pp. 6-12, 2010.

[5] A. Marcoux, G. Pelletier, C. Legay, C. Bouchard, M. J. Rodriguez, "Behavior of nonregulated disinfection by-products in water following multiple chlorination points during treatment" Science of Total Environmental, vol: 586, pp. 870–878, 2017.

[6] A. M. Tugulea, R. Aranda-Rodriguez, D. Bérubé, M. Giddings, F. Lemieux, J. Hnatiw, F. Breton, "The influence of precursors and treatment process on the formation of Iodo-THMs in Canadian drinking water" Water Research, vol: 130, pp. 215-223, 2018.

[7] T. Priya, P. Prakash, B. K. Mishra, "Understanding the coagulant activity of zirconium oxychloride to control THMs formation using response surface methodology" Ecotoxicology and Environmental Safety, vol:159, pp. 28-37, 2018.

[8] E. M. Rodríguez, M. V. Gordillo, A. Rey, F. J. Beltrán, "Impact of TiO_2/UVA photocatalysis on THM formation potential" Catalysis Today, vol: 313, pp.167-174, 2018.

[9] S. K. Golfinopoulos, G. B. Arhonditsis, "Multiple regression models: a methodology for evaluating trihalomethane concentrations in drinking water from raw water characteristics" Chemosphere, vol: 47(9), pp.1007-1018, 2002.

[10] V. Uyak, I. Toroz, S. Meric, "Monitoring and modeling of trihalomethanes (THMs) for a water treatment plant in Istanbul" Desalination, vol: 176(1-3), pp.91-101, 2005.

[11] S. W. Krasner, M. J. McGuire, J. G. Jacangelo, N. L. Patania, K. M. Regan, A. E. Marco, "Occurrence of disinfection by-products in US drinking water" Journal Water Works Association, vol: 81, 8, pp. 41–53, 2001.

[12] United States Environmental Protection Agency (USEPA). Guidelines for carcinogen risk assessment. Risk Assessment Forum. Washington DC. NCEA-F-0644 (Revised draft), 1999.

[13] T. Priya, B. K. Mishra, "Enzyme mediated chloroform biotransformation and quantitative cancer risk analysis of trihalomethanes exposure in South East Asia" Exposure and Health, vol:9, 1, pp.61-75. 2017.

[14] V. Uyak, "Multi-pathway risk assessment of trihalomethanes

exposure in Istanbul drinking water supplies" Environmental International, vol: 32, 1, pp.12-21, 2006.

[15] S. C. Lee, H. Guo, S. M. J. Lam, S. L. A. Lau, "Multipathway risk assessment on disinfection by-products of drinking water in Hong Kong" Environmental Research, vol: 94, 1, pp. 47-56, 2004.

[16] A. Siddique, S. Saied, M. Mumtaz, M. M. Hussain, H. A. Khwaja, "Multipathways human health risk assessment of trihalomethane exposure through drinking water" Ecotoxicology, and Environmental Safety, vol: 116, pp. 129-136, 2015.

[17] S. E. Hrudey, L. C. Backer, A. R. Humpage, S. W. Krasner, D. S. Michaud, L. E. Moore, B. D. Stanford, "Evaluating evidence for association of human bladder cancer with drinking-water chlorination disinfection by-products" Journal of Toxicology and Environmental Health, Part B. vol:18, 5, pp. 213-241, 2015.

[18] T. E. Arbuckle, S. E. Hrudey, S. W. Krasner, J. R. Nuckols, "Assessing exposure in epidemiologic studies to disinfection by-products in drinking water: Report from an international workshop" Environmental Health Perspective, vol:110, 1, pp. 53–60, 2002.

[19] R. J. Bull, L. S. Birnbaum, K. P. Cantor, J. B. Rose, B.E. Butterworth, R. Pergram, J. Tuomisto, "Water chlorination: essential process or cancer hazard" Toxicology Science, vol: 28, pp.155–166, 1995.

[20] K. S. Crump, H. A. Guess, "Drinking water and cancer review of recent epidemiological findings and

assessment of risks" Annual Review Public Health, vol: 3, pp. 339–57, 1982.

[21] R. L. Calderon, "The epidemiology of chemical contaminants of drinking water" Food Chemical Toxicology, vol: 38, 12, pp.13–20, 2000.

[22] D. Baytak, A. Sofuoglu, F. Inal, S. C. Sofuoglu, "Seasonal variation in drinking water concentrations of disinfection by-products in Izmir and associated human health risks" Science of the Total Environmental, vol: 407, 1, pp: 286-296, 2008.

[23] Y. Wang, G. Zhu, B. Engel, "Health risk assessment of trihalomethanes in water treatment plants in Jiangsu Province, China" Ecotoxicology and Environmental Safety, vol: 170, pp. 346-354, 2019.

[24] W. Gan, W. Guo, J. Mo, Y. He, Y. Liu, W. Liu, X. Yang, "The occurrence of disinfection by-products in municipal drinking water in China's Pearl River Delta and a multi-pathway cancer risk assessment" Science of the Total Environmental, vol: 447, pp. 108-115, 2013.

[25] C. P. Weisel, H. Kim, P. Haltmeier, J. B. Klotz, "Exposure estimates to disinfection by-products of chlorinated drinking water" Environmental Health Perspective, vol: 107, 2, pp. 103-110, 1999.

[26] T. Sirivedhin, K. A. Gray, "Comparison of the disinfection by-product formation potentials between a wastewater effluent and surface waters, Water Research, vol: 39, 6, pp. 1025-1036, 2005.

[27] D. Zheng, R. C. Andrews, S. A. Andrews, L. Taylor-Edmonds, "Effects of coagulation on the removal

of natural organic matter, genotoxicity and precursors to halogenated furanone, Water Research, vol:70, pp. 118-129, 2015.

[28] B. Bolto, D. Dixon, R. Eldridge, S. King, K. Linge, "Removal of natural organic matter by ion exchange, Water Research, vol: 36, 20, pp. 5057-5065, 2002.

[29] M. M. T. Khan, Z. Lewandowski, S. Takizawa, K. Yamada, H. Katayama, K. Yamamoto, S. Ohgaki, "Continuous and efficient removal of THMs from river water using MF membrane combined with high dose of PAC, Desalination, vol: 249, 2, pp. 713-720, 2009.

[30] United States Environmental Protection Agency (USEPA), Guidelines for carcinogen risk assessment, Risk assessment forum, Washington DC, 2005.

[31] B. Tokmak, G. Capar, F. B. Dilek, U. Yetis, "Trihalomethanes and associated potential cancer risks in the water supply in Ankara, Turkey, Environmental Research, vol: 96, 3, pp. 345-352, 2004

[32] G. S. Wang, Y. C. Deng, T. F. Lin, "Cancer risk assessment from trihalomethanes in drinking water, Science of Total Environment, vol: 387, 1-3, pp. 86-95, 2007.

[33] S. Liu, Z. Zhu, C. Fan, Y. Qiu, J. Zhao, "Seasonal variation effects on the formation of trihalomethane during chlorination of water from Yangtze River and associated cancer risk assessment, Journal Environmental Science, vol:23, 9, pp. 1503–1511, 2011.

[34] N. Wang, Y. Zhu, "Empirical analysis of the factors affecting life expectancy in China" Commercial Economy, vol: 3, pp. 21–23, 2014.

[35] Turkey Statistical Institute (TUIK), New Bulletin 2017, 22 June 2020 [Online], available:http://www.tuik.gov.tr/PreH aberBultenleri.do;jsessionid=DVvxhx qb321PZgscMkXhNKCT7yvnTnWY C2LJSgLGBlkr5WLqFxGp!1247757 447?id=24640.

[36] L. B. Gratt, Air toxic risk assessment and management, New York, NY' Van Nostrand Reinhold, 1996.

[37] X. Xu, T. M. Mariano, J. D. Laskin, C. P. Weisel, "Percutaneous absorption of trihalomethanes, haloacetic acids, and haloketones" Toxicology and Applied Pharmacology, vol:184, 1, pp.19-26, 2002.

[38] C. Legay, M. J. Rodriguez, R. Sadiq, J. B. Sérodes, P. Levallois, F. Proulx, "Spatial variations of human health risk associated with exposure to chlorination by-products occurring in drinking water" Journal of Environmental Management, vol. 92, 3, pp. 892-901, 2011.

[39] H. Amjad, I. Hashmi, M. S. U. Rehman, M. A. Awan, S. Ghaffar, Z. Khan, "Cancer and non-cancer risk assessment of trihalomethanes in urban drinking water supplies of Pakistan" Ecotoxicology and Environmental Safety, vol:91, pp: 25-31, 2013.

[40] J. Lee, E. S. Kim, B. S. Roh, S. W. Eom, K. D. Zoh, "Occurrence of disinfection by-products in tap water distribution systems and their associated health risk" Environmental Monitoring and Assessment, vol:185, 9, pp. 7675-7691, 2013.

[41] M. Okamoto, M. Sato, Y. Shodai, M. Kamijo, "Identifying the physical properties of showers that influence user satisfaction to aid in developing water-saving showers" Water Research, vol:7, 8, pp. 4054-4062, 2015.

[42] The United States Environmental Protection Agency (USEPA), Edition of the drinking water standards and health advisories, Office of water U.S. Environ. Protect. Agency. Washington, DC, 2011.

[43] J. S. Hammonds, F. O. Hoffman, S. M. Bartell, "Environmental restoration program, An introductory guide to uncertainty analysis in environmental and health risk assessment" Senes Oak Ridge, Inc. TN. USA, 1994.

[44] United States Environmental Protection Agency (USEPA). Risk assessment guidance for superfund— Vol. I, Human health evaluation manual (Part D, Standardized planning, reporting and review of superfund risk assessments), Office of emergency and remedial response. Washington, DC, 2001.

[45] C. H. Hsu, W. L. Jeng, R. M. Chang, L. C. Chieng, B. C. Han, "Estimation of potential lifetime cancer risks for trihalomethanes from consuming chlorinated drinking water in Taiwan" Environmental Research, vol: 85, pp.77–82, 2001.

[46] M. Kumari, S. K. Gupta, B. K. Mishra, "Multi-exposure cancer and non-cancer risk assessment of trihalomethanes in drinking water supplies–a case study of Eastern region of India" Ecotoxicology and Environmental Safety, vol: 113, pp. 433-438, 2015.

[47] M. Basu, S. K. Gupta, G. Singh, U. Mukhopadhyay, "Multi-route risk assessment from trihalomethanes in drinking water supplies" Environmental Monitoring and Assessment, vol: 178, 1-4, pp.121-134, 2011.

[48] Z. Karim, M. Mumtaz, T. Kamal, "Health risk assessment of trihalomethanes of tap water in Karachi, Pakistan" Journal Chemical Society, vol:33, pp. 215–219, 2011.

[49] J. K. Mahato, S. K. Gupta, "Advanced oxidation of Trihalomethane (THMs) precursors and season-wise multi-pathway human carcinogenic risk assessment in Indian drinking water supplies" Process Safety and Environmental Protection, vol:159, pp. 996-1007, 2022

[50] E. S. I. Mishaqa, E. K. Radwan, M. B. M.Ibrahim, T. A. Hegazy, M. S. Ibrahim, "Multi-exposure human health risks assessment of trihalomethanes in drinking water of Egypt" Environmental Research, vol:207, 2022.

[51] M. Mosaferi, M. Asadi, H. Aslani, A. Mohammadi, S. Abedi, S. Nemati Mansour, S. Maleki, "Temporospatial variation and health risk assessment of trihalomethanes (THMs) in drinking water (northwest Iran)" Environmental Science and Pollution Research, vol:28-7, pp. 8168-8180. 2021

[52] A. Mohammadi, M. Faraji, A. Ebrahimi, S. Nemati, A. Abdolahnejad, M. Miri, "Comparing THMs level in old and new water distribution systems; seasonal variation and probabilistic risk assessment" Ecotoxicology and Environmental Safety, vol:192, 2020.

[53] M. Kumari, S. K. Gupta, "Cumulative human health risk analysis of trihalomethanes exposure in drinking water systems" Journal of Environmental Management, vol:321, 2022.

Title: A Novel Deep Learning Method for Detecting Defects in Mobile Phone Screen
Surface Based on Machine Vision

Authors: İsmail AKGÜL

New submission to SAUJS
http://dergipark.gov.tr/journal/1115/submission/start

A Novel Deep Learning Method for Detecting Defects in Mobile Phone Screen Surface Based on Machine Vision

İsmail AKGÜL*1 iD

Abstract

With the innovations in technology, the interest in the use of mobile devices is increasing day by day. Any defect that may occur during the production of smart mobile phones, which is among mobile devices, causes significant damage to both the manufacturer and the user. The careful detection of defects that may occur on the screen glass, which is one of the most striking defects among these defects, with the human eye significantly affects the workforce cost. Therefore, it is important to detect defects with the help of software. In recent years, many methods based on machine vision have been developed for the detection of any object or difference in the image.

In this study, a new model structure called Yolo-MSD, based on machine vision and the Yolo-v3 deep learning model, which detects and classifies oil, scratch, and stain defect types on the glass on the touch screen surface used in the design of smart mobile phones, is proposed. The proposed model structure (Yolo-MSD) is obtained by reducing the number of blocks in the Darknet-53 network structure developed in Yolo-v3. As a result of the training, a success rate of 98.50% with the Yolo-v3 model and 98.72% with the Yolo-MSD model was achieved in detecting and classifying defect types. Therefore, it has been observed that the Yolo-MSD model structure is better than the Yolo-v3 model structure by making better feature extraction from the types of defects on the screen glass since it is both faster and has less complexity.

Keywords: Machine vision, deep learning, Yolo-v3, Yolo-MSD, defect detection

1. INTRODUCTION

The use of mobile devices, which play an important role in the development of the world, is increasing day by day with the development of technology. The development of smart mobile phones, which is among mobile devices, and which is one of the most important inventions of our age, has greatly facilitated human life. The development of touch screens in the design of smart mobile phones has provided convenience for all users, and has increased the use, efficiency, and interaction of smart mobile phones, providing a more convenient and faster workflow. The quality and flawlessness of the screen glass in the touch screen design play an important role in the production process of smart mobile phones [1]. Therefore, the slightest defect that may occur on the touch screen surface during the production of smartphones causes more

* Corresponding author: iakgul@erzincan.edu.tr
1 Erzincan Binali Yıldırım University, Department of Computer Engineering
ORCID: https://orcid.org/0000-0003-2689-8675

İsmail AKGÜL

A Novel Deep Learning Method for Detecting Defects in Mobile Phone Screen Surface Based on Machine Vi...

defects or damages during the use of smartphones [2].

For this reason, it is necessary to carefully examine the screen surface with the human eye to detect any defects that may occur on the touch screen surface during the production of smart mobile phones [3-5]. This situation causes both loss of time and slower production for industrial organizations producing smart mobile phones [6-8]. Therefore, a machine vision system is needed to detect the defects in the glass on the touch screen surface of smart mobile phones efficiently and quickly.

Machine vision is a set of systems that reduce the defects in many application processes performed by machines and, accordingly, have the ability to make quick decisions [9-11]. In recent years, in parallel with the developments in the field of technology, many artificial intelligence-based methods for defect detection in the industry have been developed and successful results have been obtained [12-15].

In this study, a new model structure (Yolo-MSD) based on machine vision and Yolo-v3 deep learning is proposed to detect the defects on the glass on the touch screen surface used in the design of smart mobile phones. Yolo-v3 and proposed Yolo-MSD deep learning methods were trained separately using a dataset containing 3 types of screen surface defects (oil, scratch, and stain), and the defects occurring on the smart mobile phone surface were detected and classified. The remainder of the study is organized as follows. In Chapter 2, studies on the detection of defects on the surface of smart mobile phones are examined and discussed. Materials and methods related to the study are presented in Chapter 3, and experimental results and discussions are presented in detail in Chapter 4. In Chapter 5, information about the results of the study and future studies is given.

2. RELATED WORKS

In this section, the studies carried out in recent years in detecting the defects on the surface of mobile phones are examined in detail.

Jian et al. developed an improved fuzzy c-means cluster algorithm to detect defects in mobile phone screen glass. Thanks to the developed algorithm, defects on the screen glass of the mobile phone were detected in 1.6601 seconds, with success rates of 94% sensitivity and 97.33% specificity [1]. In their study, Park & Kweon proposed a multi-class classification model to classify the defects on the screen panel surface used in smartphones. In the proposed model, a new filter method that was successful under various conditions was used and successful results were obtained [16].

Wang et al. proposed a deep learning model based on Faster R-CNN to detect defects on the mobile phone surface. In the proposed model, the feature pyramid network and the ResNet-101 model are combined to detect smaller defects. However, to reduce the quantization deviation, the RoI Pooling layer was replaced with the RoI Align layer and a 99.43% mAP success rate was achieved in detecting defects [17]. Li et al., in their study, proposed a new algorithm to detect and classify mobile phone screen defects. Successful results were obtained by proposing a clustering algorithm to prevent false detection and a classification algorithm that combines multi-layer perceptron and deep learning for classification [18].

Zhang et al., in their study, proposed a method called FDSNet to detect defects on the mobile phone screen in real-time. The proposed method has shown successful results in detecting defects on the mobile phone screen [19].

Wang et al. obtained successful results by using many methods including morphological filter, gamma grayscale,

İsmail AKGÜL

A Novel Deep Learning Method for Detecting Defects in Mobile Phone Screen Surface Based on Machine Vi...

threshold segmentation, and binary tree classifier to classify defects (scratch, bruise, pit, and blister) on the mobile phone screen [20]. Jianguo et al., on the other hand, proposed a method based on machine vision to detect scratches on the mobile phone screen and achieved a success rate of 98.7% [21].

3. MATERIALS AND METHODS

3.1. Dataset and Preprocessing

In the study, a Mobile phone screen Surface Defect (MSD) dataset containing 3 types of surface defects (oil, scratch, and stain) was used to detect and classify the defects on the screen surfaces of smart mobile phones. In this dataset, there are 1200 images in total, 400 images with 1920×1080×3 pixel size for each defect type [19, 22]. 960 images in the Train-Val in the dataset were combined and used for the train, and 240 images in the Test were used for the test. Example images of each defect type in the data set are shown in Figure 1.
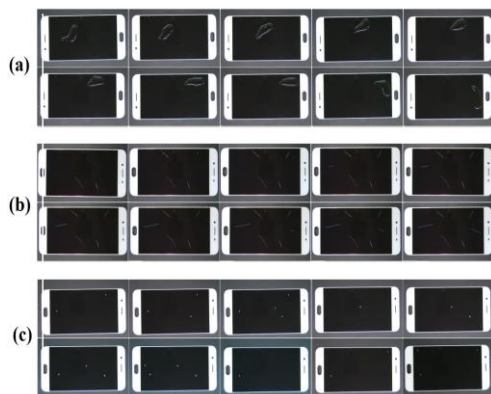
Figure 1 Sample images of defect types in the dataset (a) oil, (b) scratch, (c) stain

The pixel size of each defect type image in the dataset was preprocessed by reducing it by ¼ in a way that the width and height ratio was maintained. As a result of preprocessing, each defect type image is reduced to 480×270×3 pixels. In addition, to train the Yolo models, the coordinates of each defect type were labeled manually with the help of the LabelImg [23] program. The number of labels obtained for each defect type as a result of labeling is given in Table 1.

Table 1 Number of labels for each type of defect in the dataset

Types of defects	Number of defect type labels in the dataset		
	Train	Test	Total
Oil	441	115	556
Scratch	1096	288	1384
Stain	879	247	1126
Total	**2416**	**650**	**3066**

3.2. Yolo-MSD Model Structure

In the study, Yolo-v3 [24] deep learning model is based on to successfully detecting and classifying oil, scratch, and stain defects in the dataset. By changing this model structure, a new model structure (Yolo-MSD) based on Yolo-v3 has been proposed for better feature extraction in defect types. Layer structures used in Yolo-v3 and Yolo-MSD architectures are given in detail in Table 2

When Table 2 is examined, the number of layers is reduced by reducing the number of 7th Block ×4, 9th Block ×4 and 11th Block ×2 repetitions in the Darknet-53 network structure of the proposed Yolo-MSD model. The Yolo-v3 model structure, which has 106 layers, was reduced to 76 layers and the Yolo-MSD model structure was created.

Therefore, by using fewer layers in the Yolo-MSD model, its complexity is reduced compared to the Yolo-v3 model. In this way, both better feature extraction has been achieved and a model structure has been created that can be trained faster.

Table 2 Yolo-v3 and Yolo-MSD model structures

Blok	Type	Filters	Size/Stride	Output	Repeat Yolo-v3	Yolo-MSD
1	Convolutional	32	3×3/1	416×416×32		
2	Convolutional	64	3×3/2	208×208×64		
3	Convolutional	32	1×1/1	208×208×32	×1	×1
	Convolutional	64	3×3/1	208×208×32		
	Residual			208×208×64		
4	Convolutional	128	3×3/2	104×104×128		
5	Convolutional	64	1×1/1	104×104×64	×2	×2
	Convolutional	128	3×3/1	104×104×128		
	Residual			104×104×128		
6	Convolutional	256	3×3/2	52×52×256		
7	Convolutional	128	1×1/1	52×52×128	×8	×4
	Convolutional	256	3×3/1	52×52×256		
	Residual			52×52×256		
8	Convolutional	512	3×3/2	26×26×512		
9	Convolutional	256	1×1/1	26×26×256	×8	×4
	Convolutional	512	3×3/1	26×26×512		
	Residual			26×26×512		
10	Convolutional	1024	3×3/2	13×13×1024		
11	Convolutional	512	1×1/1	13×13×512	×4	×2
	Convolutional	1024	3×3/1	13×13×1024		
	Residual			13×13×1024		
	Detection Layers				82	52
					94	64
					106	76

The training and analysis of the Yolo-v3 and Yolo-MSD model structures were carried out in the Python programming language using the TensorFlow library in the Google Colaboratory [25] environment. Thus, the success of Yolo-v3 and Yolo-MSD models were compared using images containing 3 different defect types in the dataset. To compare the models, the train-test parameters given in Table 3 were used in both models.

4. RESULTS AND DISCUSSION

In the study, Yolo-v3 and the proposed Yolo-MSD deep learning methods were trained and tested using the parameters given in Table 3 to efficiently detect and classify the defects on the glass on the screen surface of smart mobile phones. To determine the validity of the training and testing results of the Yolo-v3 and Yolo-MSD model structures, each model was trained 5 times separately. As a result of training and testing,

the Yolo-v3 model showed a learning success between 98.38% and 98.50%. The Yolo-MSD model, on the other hand, achieved a learning success between 98.45% and 98.72%. Average Loss, mAP@0.50, and Average IoU graphs of the best training and

Table 3 Parameters used in training Yolo-v3 and Yolo-MSD model structures

Parameters	Values
Batch	64
Subdivisions	16
Mini Batch Size	4
Width	416
Height	416
Channels	3
Momentum	0.9
Decay	0.0005
Angle	0
Saturation	1.5
Exposure	1.5
Hue	0.1
Learning Rate	0.001
Burn In	1000
Max Batches	6000
Steps	4800, 5400
Activation Function	Leaky

test result obtained by running 5 times are given in Figure 2. The model was recorded in the epoch with the best result from the training and testing process carried out during 6000 epochs. All analyzes and performance tests were performed according to the best-recorded model and all metric measures obtained are given in Table 4 comparatively.
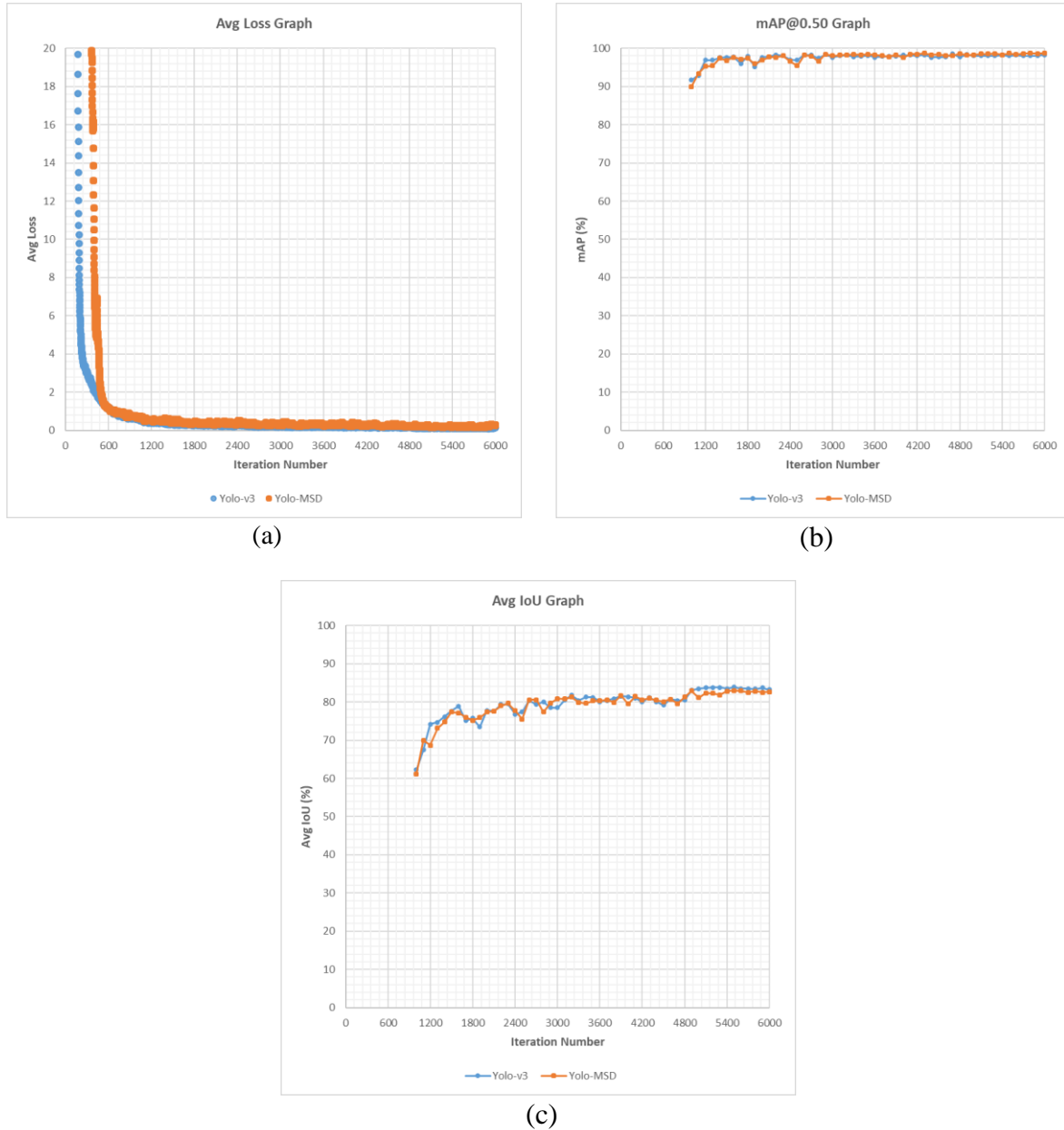

(a)

(b)

(c)

Figure 2 Comparative graphics obtained as a result of training and testing the Yolo-v3 and Yolo-MSD model structures (a) Average Loss, (b) mAP@0.50, (c) Average IoU

İsmail AKGÜL

A Novel Deep Learning Method for Detecting Defects in Mobile Phone Screen Surface Based on Machine Vi...

Table 4 Metric criteria obtained as a result of training and testing Yolo-v3 and Yolo-MSD model structures

Metric Criteria	Models	
	Yolo-v3	Yolo-MSD
Best Epoch	4700	4300
Average Loss	0,145222	0,272315
mAP@0.50	98.50	98.72
Average IoU	80.34	80.93
Precision	1.00	0.99
Recall	0.98	0.98
F1-Score	0.99	0.99
Total Training Time	34,433.124 sec.	26,391.039 sec.
Support	650	650

According to the results obtained in Figure 2 and Table 4, the Yolo-v3 model achieved success values of 98.50% mAP, 80.34% Average IoU, and 0.145222 Average Loss as a result of 4700 epochs. The proposed Yolo-MSD model, on the other hand, achieved success values of 98.72% mAP, 80.93% Average IoU, and 0.272315 Average Loss as a result of 4300 epochs. According to the results obtained, the proposed Yolo-MSD model achieved more successful results as a result of fewer epochs. It is seen that the proposed model is better than the Yolo-v3 model as a result of training and testing.

Therefore, with the proposed Yolo-MSD model, a more advantageous model structure has been obtained compared to the Yolo-v3 model due to its speed and low complexity of the model structure, depending on the number of layers used in training and testing the defect types.

Table 5 Classification rates by defect type as a result of training and testing Yolo-v3 and Yolo-MSD models (AP: Average Precision, mAP: Mean Average Precision)

Dataset Classes	AP	
	Yolo-v3	Yolo-MSD
Oil	98.15%	98.06%
Scratch	98.61%	98.94%
Stain	98.74%	99.16%
mAP@0.50	**98.50%**	**98.72%**

In addition, as a result of the training and testing of the Yolo-v3 and Yolo-MSD models, the classification rates according to the defect type were obtained to determine the rate at which each defect type was classified, and the details are given in Table 5.

4.1. Performance Testing of Yolo-v3 and Yolo-MSD Models

Performance tests were conducted for each model structure to test the validity of the Yolo-v3 and Yolo-MSD models discussed in the study on real-life performance. As a result of the performance tests, sample images of oil, scratch, and stain defect types on the screen glass surface of smart mobile phones are given in Figure 3.

In addition, the proposed Yolo-MSD method for detecting and classifying the defects on the screen surface of smart mobile phones has been compared with different methods in the literature, and the comparison results are given in Table 6 in detail. In the study, it is seen that the proposed Yolo-MSD model structure gives better results than many different model structures when the successful results obtained in the training, testing, and performance testing stages are taken into consideration

İsmail AKGÜL

A Novel Deep Learning Method for Detecting Defects in Mobile Phone Screen Surface Based on Machine Vi...
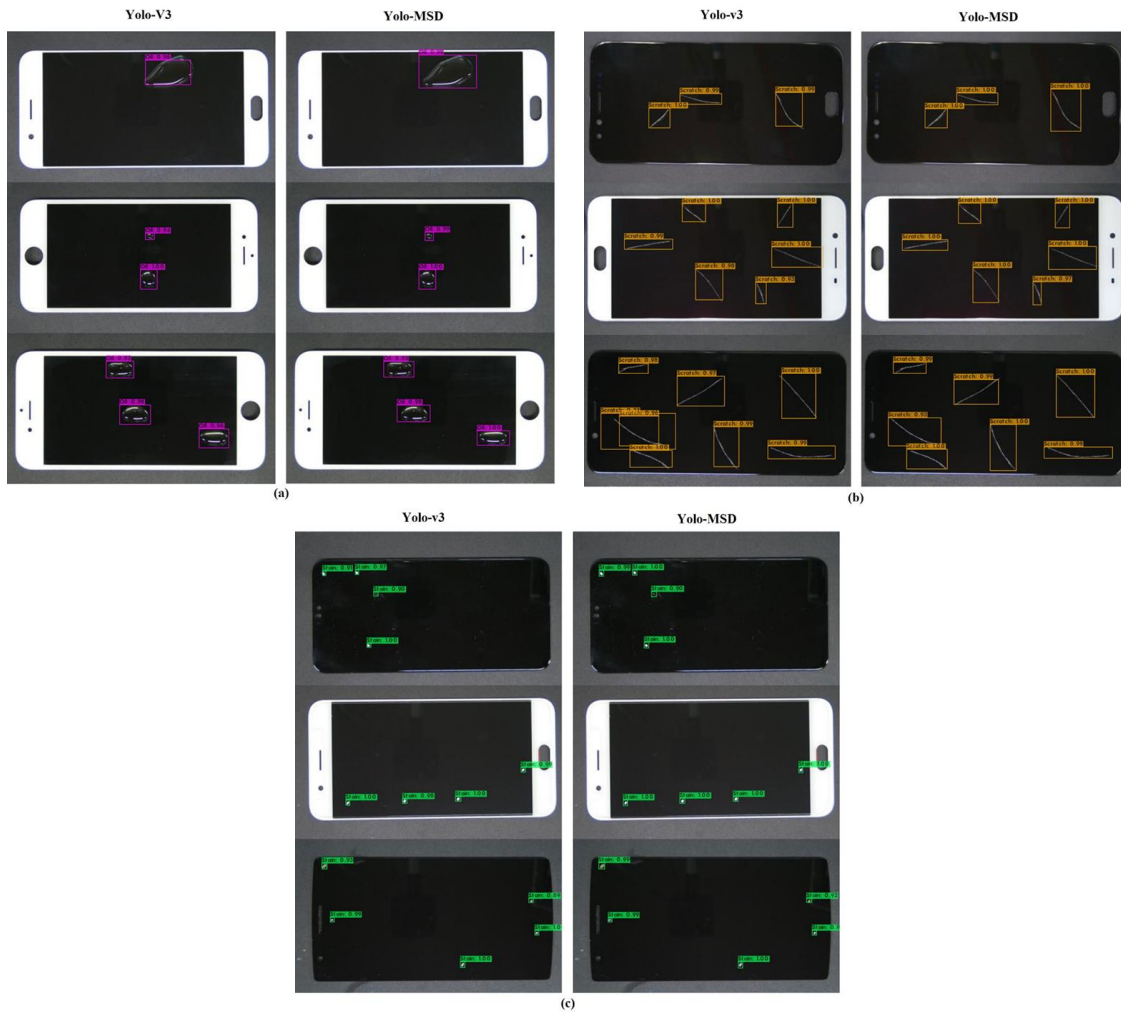
Figure 3 Sample images of performance test results of Yolo-v3 and Yolo-MSD models (a) oil, (b) scratch, (c) stain

Table 6 Comparison of the proposed method with different methods for detecting defects on the screen surface of smart mobile phones

Ref.	Models	Dataset	Success Rate
[7]	HMFCA-Net	MPSSD	83.75%
		DAGM	98.41%
[8]	EU-Net	Dataset consists of scratches and bubbles	70.2%
[13]	GoogLeNet	Dataset consists of the positive sample, point defect, and linear defect	98%
[17]	Faster R-CNN (ResNet101)	Dataset consists of screen scratches, edge defects, point defects, and stripe dents	99.43%
[19]	FDSNet	Magnetic-tile-defect-datasets	63.90%
		NEU-Seg	78.80%
		MSD	90.20%
The proposed method	**Yolo-MSD**	**MSD**	**98.72%**

İsmail AKGÜL

A Novel Deep Learning Method for Detecting Defects in Mobile Phone Screen Surface Based on Machine Vi...

5. CONCLUSION

In this study, a new Yolo-MSD model based on machine vision and Yolo-v3 deep learning model has been developed to detect and classify defects on the glass on the touch screen surface used in the design of smart mobile phones. Yolo-v3 and the developed Yolo-MSD deep learning methods were compared by training-testing 5 times using the same parameters. As a result of the comparisons, the Yolo-v3 model showed a learning success between 98.38% and 98.50%, and the Yolo-MSD model showed a learning success between 98.45% and 98.72%. However, it has been observed that the developed Yolo-MSD model is both faster and less complex than the Yolo-v3 model.

According to the experimental results obtained, Yolo-MSD is the method that detects and classifies the types of oil, scratch, and stain defects that occur on the surface of the smart mobile phone with a success rate of 98.72%. Therefore, it is thought that the Yolo-MSD deep learning method developed in the study provides successful results in detecting and classifying the defects on the surface of smart mobile phones, and accordingly, it will help industrial organizations produce smart mobile phones in terms of both time and higher quality production. It is expected that a real-time method will be realized by using different methods and different datasets for the detection and classification of different types of defects that will occur on the smartphone surface in the future.

Funding

The author has no received any financial support for the research, authorship or publication of this study.

The Declaration of Conflict of Interest/ Common Interest

No conflict of interest or common interest has been declared by the author.

The Declaration of Ethics Committee Approval

This study does not require ethics committee permission or any special permission.

The Declaration of Research and Publication Ethics

The author of the paper declare that they comply with the scientific, ethical and quotation rules of SAUJS in all processes of the paper and that they do not make any falsification on the data collected. In addition, they declare that Sakarya University Journal of Science and its editorial board have no responsibility for any ethical violations that may be encountered, and that this study has not been evaluated in any academic publication envirnment other than Sakarya University Journal of Science.

REFERENCES

[1] C. Jian, J. Gao, Y. Ao, "Automatic surface defect detection for mobile phone screen glass based on machine vision," Applied Soft Computing, vol. 52, pp. 348-358, 2017.

[2] L. Meiju, Z. Rui, G. Xifeng, Z. Junrui, "Application of improved Otsu threshold segmentation algorithm in mobile phone screen defect detection," In 2020 Chinese Control And Decision Conference (CCDC), Hefei, 2020, pp. 4919-4924.

[3] L. Yuan, Z. Zhang, X. Tao, "The development and prospect of surface defect detection based on vision measurement method," In 2016 12th World Congress on Intelligent Control and Automation (WCICA), Guilin, 2016, pp. 1382-1387.

[4] Z. C. Yuan, Z. T. Zhang, H. Su, L. Zhang, F. Shen, F. Zhang, "Vision-based defect detection for mobile phone cover glass using deep neural networks," International Journal of

İsmail AKGÜL

A Novel Deep Learning Method for Detecting Defects in Mobile Phone Screen Surface Based on Machine Vi...

Precision Engineering and Manufacturing, vol. 19, no. 6, 2018.

[5] Y. Lv, L. Ma, H. Jiang, "A mobile phone screen cover glass defect detection model based on small samples learning," In 2019 IEEE 4th International Conference on Signal and Image Processing (ICSIP), Wuxi, 2019, pp. 1055-1059.

[6] J. Jiang, P. Cao, Z. Lu, W. Lou, Y. Yang, "Surface defect detection for mobile phone back glass based on symmetric convolutional neural network deep learning," Applied Sciences, vol. 10, no. 10, pp. 1-13, 2020.

[7] Y. Zhu, R. Ding, W. Huang, P. Wei, G. Yang, Y. Wang, "HMFCA-Net: Hierarchical multi-frequency based Channel attention net for mobile phone surface defect detection," Pattern Recognition Letters, vol.153, pp. 118-125, 2022.

[8] J. Pan, D. Zeng, Q. Tan, Z. Wu, Z. Ren, "EU-Net: A novel semantic segmentation architecture for surface defect detection of mobile phone screens," IET Image Processing, vol. 6, pp. 2568–2576, 2022.

[9] J. Zhang, Y. Li, C. Zuo, M. Xing, "Defect detection of mobile phone screen based on improved difference image method," In 2019 International Conference on Intelligent Informatics and Biomedical Sciences (ICIIBMS), Shanghai, 2019, pp. 86-92.

[10] Z. Ren, F. Fang, N. Yan, Y. Wu, "State of the art in defect detection based on machine vision," International Journal of Precision Engineering and Manufacturing-Green Technology, vol. *9*, pp. 661–691, 2021.

[11] M. Eshkevari, M. J. Rezaee, M. Zarinbal, H. Izadbakhsh, "Automatic dimensional defect detection for glass vials based on machine vision: A heuristic segmentation method," Journal of Manufacturing Processes, vol. 68, pp. 973-989, 2021.

[12] C., Jian, J. Gao, Y. Ao, "Imbalanced defect classification for mobile phone screen glass using multifractal features and a new sampling method," Multimedia Tools and Applications, vol. 76, no. 22, 24413-24434, 2017.

[13] H. Chen, "CNN-based surface defect detection of smartphone protective screen," 3rd International Symposium on Big Data and Applied Statistics, Kunming, China, 2020, pp. 1-7.

[14] S. Qi, J. Yang, Z. Zhong, "A review on industrial surface defect detection based on deep learning technology," In 2020 the 3rd international conference on machine learning and machine intelligence, Hangzhou, China, 2020, pp. 24-30.

[15] W. Huang, C. Zhang, X. Wu, J. Shen, Y. Li, "The detection of defects in ceramic cell phone backplane with embedded system," Measurement, vol. 181 no. 2021, pp. 1-7, 2021.

[16] Y. Park, I. S. Kweon, "Ambiguous surface defect image classification of AMOLED displays in smartphones," IEEE Transactions on Industrial Informatics, vol. 12, no. 2, pp. 597-607, 2016.

[17] T. Wang, C. Zhang, R. Ding, G. Yang, "Mobile phone surface defect detection based on improved faster r-cnn," In 2020 25th International Conference on Pattern Recognition (ICPR), Milan, 2021, pp. 9371-9377.

[18] C. Li, X. Zhang, Y. Huang, C. Tang, S. Fatikow, "A novel algorithm for defect extraction and classification of mobile phone screen based on machine vision," Computers & Industrial Engineering, vol. 146, no. 2020, pp. 1-14, 2020.

[19] J. Zhang, R. Ding, M. Ban, T. Guo, "FDSNeT: An Accurate Real-Time Surface Defect Segmentation Network," In ICASSP 2022-2022 IEEE International Conference on Acoustics, Speech and Signal Processing (ICASSP), Singapore, 2022, pp. 3803-3807

[20] C. Wang, C. Li, Y. Huang, X. Zhang, "Surface defect inspection and classification for glass screen of mobile phone," In Tenth International Conference on Graphics and Image Processing (ICGIP 2018), Chengdu, 2019, pp. 527-536.

[21] Z. Jianguo, L. Ying, Q. Jiakun, J. Tiantian, L. Jun, "Surface scratch detection of mobile phone screen based on machine vision," Journal of Applied Optics, vol. 41, no. 5, pp. 984-989, 2020.

[22] "Github", Nov. 02, 2022. [Online]. Available:https://github.com/jianzhang96/MSD

[23] D. Tzutalin, "LabelImg", Nov. 8, 2022. [Online]. Available: https://github.com/tzutalin/labelImg

[24] J. Redmon, A. Farhadi, "Yolov3: An incremental improvement," arXiv preprint, pp. 1-6, 2018.

[25] Google Colaboratory, "Colab", Nov. 11, 2022. [Online]. Available: https://colab.research.google.com

Title: A Vibrational Spectroscopic Investigation of 2,2'-Bithiophene Using Experimental and DFT Methods

Authors: Semiha BAHÇELİ, Ebru KARAKAŞ SARIKAYA, Ömer DERELİ, Feride Pınar ÖZTURAN

A Vibrational Spectroscopic Investigation of 2,2'-Bithiophene Using Experimental and DFT Methods

Ebru KARAKAŞ SARIKAYA[1] [iD], Ömer DERELİ[2] [iD], Semiha BAHÇELİ*[3] [iD]
Feride Pınar ÖZTURAN[4] [iD]

Abstract

Organic compounds like 2,2'-Bithiophene (with a synonym. 2,2'-bithienyl, 2,2'-dithienyl)-containing bis(dioxaborin) have drawn significant concern in the area of materials science because of their electron affinity and luminescent properties. With this motivation, we have been concentrating on the properties and functions of 2,2'-Bithiophene. The vibrational frequencies of the molecule 2,2'-Bithiophene in the solid phase were recorded using the Fourier Transformed-Infrared (FT-IR) and FT-Raman spectrometers. Meanwhile, the molecular geometric parameters, the spectral wavenumbers, HOMO-LUMO analysis and the molecular electrostatic potential (MEP) of the 2,2'-Bithiophene molecule were computed at the B3LYP/6-311++G (d,p) level of the theory. Furthermore, a comparison between experimental and calculated values for the vibrational frequencies of the 2,2'-Bithiophene molecule exhibits a good agreement.

Keywords: 2,2'-bithiophene, FT-IR and FT-Raman spectroscopies, DFT method, conformational analysis

1. INTRODUCTION

The 2,2'-Bithiophene, ($C_8H_6S_2$), (or briefly BT) molecule which is a typical aromatic dimer gives us a basic knowledge about the aromatic compounds such as thiophene tetramer and higher oligomers. In the past over 30 years, the mentioned aromatic compounds (including thiophene, bithiophene and oligothiophene) have gained a great popularity since they are promising and extensively investigated materials in organic chemistry, medicine, pharmacology, and organic electronics

* Corresponding author: s.bahceli.80@gmail.com (S. BAHÇELİ)
[1] Necmettin Erbakan University, Facultyof Engineering, Department of Basic Sciences, Konya, Turkey
E-Mail: ebrukarakas_84@hotmail.com
[2] Necmettin Erbakan University, Faculty of A.K. Education, Department of Physics, Konya, Turkey.
E-Mail: odereli@erbakan.edu.tr
[3] Turkish Aeronautical Association University, Faculty of Aeronautics and Astronautics, Department of Astronautical Engineering, Ankara, Turkey.
[4] Necmettin Erbakan University, Instutite of Science, Department of Nanoscience And Nanoengineering, Konya, Turkey.
E-Mail: pinar.ozturan2015@gmail.com
ORCID: https://orcid.org/0000-0003-2149-9341, https://orcid.org/0000-0002-9031-8092, https://orcid.org/0000-0002-5614-325X, https://orcid.org/0000-0002-8010-1498

fields. Thus, they can be used for the oligothiophene light-emitting diodes (OLEDs) which are taken places at the mentioned areas above [1-6].

Since the BT molecule, which has a well-known structure in gas and solid phases, forms, one of the most proper model molecules for understanding the structural features for polythiophene is focused on this study [7-14].

In this framework, we are interested with BT compound by considering its conformational analysis and the vibrational spectroscopic features. As a matter of fact, there are a great number of studies related to the main properties of torsion energy of the BT molecule using the semi-empirical and ab-initio calculations on different basis sets such as 3-21 G* and 6-31 G* [15-18]. Furthermore, the effect of external electric field on the potential energy surface of BT molecule was investigated using various basis sets at Hartree-Fock and DFT levels [19].

However, unlike the previous calculations, the conformational analysis results of title molecule in the present study were verified at the B3LYP/ 6-311++G(d,p) level which contain the diffuse and polarization functions of the theory and the computations were extended to a greater number of bond and dihedral angles of BT molecule.
On the other hand, a remarkable interest of the researchers for the vibrational spectrum on thiophene, BT molecule and its derivatives has continued for many years. In this framework, Orza et al. presented the assignments of the thiophene normal modes experimentally [20]. The infrared spectrum of 2,2'-Bithiophene was recorded by Furukawa et al. and Lopez et al.[21, 22]. Likewise, the assignments of the vibrational spectrum of thiophene, 2,2'-Bithiophene and higher oligomers were performed by Zerbi et al. [23]. Hernández et al. investigated the vibrational spectrum and ab-initio DFT calculations of 3,3'- and 4,4'-dimethyl

substituted as the methyl-derivative of 2,2'-Bithiophene [24]. So as to obtain a deeper study for the conformational and geometrical properties and vibrational analysis of the BT molecule, we present here the theoretical and experimental investigations. Furthermore, it is well-known that the long-range intramolecular delocalization of the π-electrons along the adjacent rings which brings about a small HOMO-LUMO gap as a crucial parameter for adjustment to the properties of conducting polyphenes [25-28].

At the present work, unlike the- above mentioned study [23], we report in detail the results of the experimental and simulated vibrational (FT-IR and FT-Raman) spectra, the conformational analysis of the 2,2'-Bithiophene molecule in the solid phase, the optimized molecular geometry, HOMO-LUMO analysis and the electrostatic molecular potential map (MEP) of title molecule.

2. MATERIALS AND METHODS

2.1. Experimental

The 2,2'- Bithiophene compound in powdered form was purchased from the commercial company (Merck, 99.5 %). A Brucker IFS 66/S with PIKE Gladi ATR (Diamond) spectrometer was used at room temperature with 2 cm^{-1} resolutions for recording the FT-IR spectrum of BT molecule at interval 3500-400 cm^{-1}. The prepared sample for the measurement was compressed into self-supporting pellet and then, it was placed into an IR cell equipped with KBr window.

Likewise, a Brucker FRA 106/S spectrometer using 1064 nm excitation from a Nd: YAG laser whose the detector was a Ge-diode cooled to liquid nitrogen temperature was used for the FT-Raman spectrum of the mentioned compound at the interval 3500- 500 cm^{-1}.

2.2. Computational Details

Our calculations were verified by employing the Gaussian 03 program on an individual computer [29]. In order to determine the stable conformers of the 2,2'-Bithiophene molecule, a precise conformational analysis was performed. First, in the framework of the Molecular Mechanics Force Fields method, the conformational space of the title compound was scanned, and then, full geometry optimization for these structures were carried out at the B3LYP/6-311++G(d,p) level whose expansion is Becke–3–Lee Yang Parr (B3LYP) density functional theory method with 6–311++G(d,p) basis set in a ground state [30-32]. Secondly, after the determination of the geometrical optimization for a stable conformer, the vibrational frequency calculations were performed for the optimized structural parameters of this conformer.

It is well-known that the computed positive vibrational wavenumber values indicate that the optimized molecular structure is stable. On the other hand, since the computed wavenumber values at the mentioned level include the well-known systematic errors, they can be prevented by scaling the computed vibrational wavenumbers as 0.967 (under 1800 cm^{-1} for wave numbers) and 0.955 (over 1800 cm^{-1}) at the B3LYP/6-311++G(d,p) level of the theory [33, 34].

Table 1 The calculated at the B3LYP/6-311++G (d,p) level energy values of the conformers for the 2,2'- bithiophene molecule

Conf	E (Hartree)	E (kcal/mol)	ΔE (kcal/mol)	Dip. Mom. (Debye)
anti	-1104.949	-693366.52	0.000	0.288
s-cis	-1104.948	-693365.84	0.001	0.965

As for the attributes of fundamental vibrational modes of title molecule, the total energy distribution (TED) analysis by using VEDA 4 program were performed [35]. Likewise, the HOMO and LUMO analyses

Figure 1 Two conformers of 2,2'-bithiophene molecule.

and molecular electrostatic potentials (MEP) calculations for the 2,2'-Bithiophene molecule were carried out at the B3LYP/6-311++G(d,p) level. Furthermore, by using the same level the plotting of both HOMO

and LUMO orbitals and the map of the molecular electrostatic potential (MEP) in 3-dimensional (3D) were performed at the Gauss View 5 program.

Meanwhile, the Raman activities were converted into Raman intensities in the framework of RaInt program by using the relationship:

$$I_i = 10^{-12} (n_0 - n_i)4 (1/n_i) S_i$$

where I_i is the Raman intensity, S_i is the Raman scattering activities, n_i is the wavenumber of normal modes, and no indicates the wavenumber of the excitation laser [36].

3. RESULTS AND DISCUSSION

3.1. Molecular optimization

The results of molecular geometry were exhibited that the BT molecule in solid-state has two stable conformers as indicated in Fig. 1. Molecular structure and atom numbering scheme of these conformers were
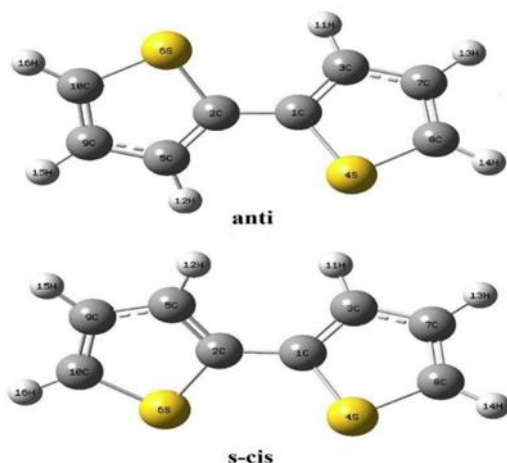
given in Fig. 1. The most stable conformer of the title molecule with a DFT energy of -1104.949 Hartree, called anti conformer, which is given in Table 1.

Therefore, the optimized molecular geometric parameters at the B3LYP/6-

311++G (d, p) level are tabulated in Table 2. A comparison between the calculated and experimental values for the bond lengths and bond angles in thiophene rings was also presented in Table 2.

Table 2 Theoretical geometric values at the B3LYP/6-311++G(d,p) level for anti-conformation of the 2,2'-bithiophene molecule

Bond lengths (Å)	Cal	Exp.*	Dihedral angles (^{0})	Cal
C1,C2	1.451	1.456	C3,C1,C2,C5	153.6
C1,C3	1.376	1.370	C3,C1,C2,S6	-26.7
C1,S4	1.753	1.733	S4,C1,C2,C5	-26.7
C2,C5	1.376	1.370	S4,C1,C2,S6	152.9
C2,S6	1.753	1.733	C2,C1,C3,C7	-179.8
C3,C7	1.423	1.452	C2,C1,C3,H11	-1.2
C3,H11	1.082	1.124	S4,C1,C3,C7	0.5
S4,C8	1.733	1.719	S4,C1,C3,H11	179.1
C5,C9	1.423	1.452	C2,C1,S4,C8	179.5
C5,H12	1.082	1.124	C3,C1,S4,C8	-0.7
S6,C10	1.733	1.719	C1,C2,C5,C9	-179.8
C7,C8	1.366	1.363	C1,C2,C5,H12	-1.2
C7,H13	1.082	1.230	S6,C2,C5,C9	0.5
C8,H14	1.079	1.220	S6,C2,C5,H12	179.1
C9,C10	1.366	1.363	C1,C2,S6,C10	179.5
C9,H15	1.082	1.123	C5,C2,S6,C10	-0.7
C10,H16	1.079	1.122	C1,C3,C7,C8	0.1
Bond angles (^{0})			C1,C3,C7,H13	179.5
C2,C1,C3	129.1	126.3	H11,C3,C7,C8	-178.5
C2,C1,S4	120.8	-	H11,C3,C7,H13	0.9
C3,C1,S4	110.2	111.8	C1,S4,C8,C7	0.8
C1,C2,C5	129.1	126.3	C1,S4,C8,H14	-179.2
C1,C2,S6	120.8	-	C2,C5,C9,C10	0.1
C5,C2,S6	110.2	111.8	C2,C5,C9,H15	179.5
C1,C3,C7	113.5	111.9	H12,C5,C9,C10	-178.5
C1,C3,H11	122.8	123.1	H12,C5,C9,H15	0.9
C7,C3,H11	123.7	-	C2,S6,C10,C9	0.8
C1,S4,C8	91.8	91.7	C2,S6,C10,H16	-179.2
C2,C5,C9	113.5	111.9	C3,C7,C8,S4	-0.6
C2,C5,H12	122.8	-	C3,C7,C8,H14	179.4
C9,C5,H12	123.7	125 .0	H13,C7,C8,S4	180.0
C2,S6,C10	91.8	91.7	H13,C7,C8,H14	0.0
C3,C7,C8	112.9	112.3	C5,C9,C10,S6	-0.6
C3,C7,H13	123.8	123.6	C5,C9,C10,H16	179.4
C8,C7,H13	123.3	-	H15,C9,C10,S6	180.0
S4,C8,C7	111.6	112.3	H15,C9,C10,H16	0.0
S4,C8,H14	119.8	-	C3,C1,C2,C5	153.6
C7,C8,H14	128.6	127.8		
C5,C9,C10	112.9	112.3		
C5,C9,H15	123.8	123.6		
C10,C9,H15	123.3	-		
S6,C10,C9	111.6	-		
S6,C10,H16	119.8	-		
C9,C10,H16	128.6	127.8		

*Experimental values have been taken from Refs [12, 15]

However, the experimental values of the three C_1-C_2 bond distances and the two C_1-S_4 lengths within the thiophene rings are assumed equal [12, 15]. Meanwhile, we must state that the experimental values are valid for solid phase while the theoretical calculations were verified for gaseous phase. By considering our calculations, the largest differences between experimental and calculated bond lengths are about 0.148 Å for the C_7-H_{13} bonds of the rings, which can be based on the low scattering factors of hydrogen atoms in the X-ray diffraction experiment.

Likewise, although some experimental bond angle values are missing in Table 2, the biggest difference for bond angles becomes 2.8° for the C_2-C_1-C_3 bond angles of the rings. As far as our knowledge up to now, the experimental and computed values of the dihedral angles of the BT compound do not exist in the literature. For this reason, we report only calculated dihedral angle values in Table 2.

However, the bond, C_1-C_2, which connects to two thiophene rings in the compound and has the intramolecular delocalization of the molecular π-electrons, was computed as 1.451 Å at the mentioned level and its experimental value was 1.456 Å [15]. As a result, it is clear that a good agreement with the results between the computed and experimental geometric parameters of the 2,2'-Bithiophene compound.

3.2. Vibrational frequencies

For BT molecule, ($C_8H_6S_2$), the experimental and simulated FT-IR and FT-Raman spectra are exhibited in Figs. 2 and 3 at the frequency interval 3500-3000 cm^{-1} and 2000-500 cm^{-1}, respectively. Since BT molecule includes 16 atoms, it has 42 fundamental vibrational modes. In Table 3, the experimental and computed at the B3LYP/6-311++G(d,p) level, the vibrational frequencies and vibrational frequency attributes of the mentioned

molecule are listed. The PED analysis has been used in the assignments of vibrational frequencies.

As for the comparisons between the experimental vibrational wavenumbers of thiophene and BT molecules, first we can present the C-H stretching infrared frequency values of thiophene molecule which are 3126 cm^{-1} and 3098 cm^{-1} [20], whereas these experimental values for BT molecule were registered as 3107 cm^{-1} and 3080 cm^{-1}, respectively [23]
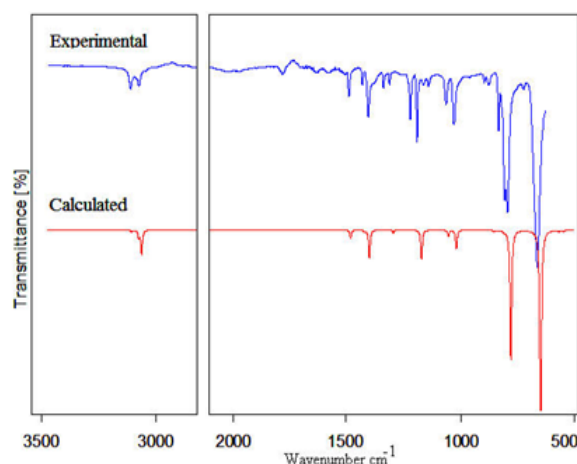

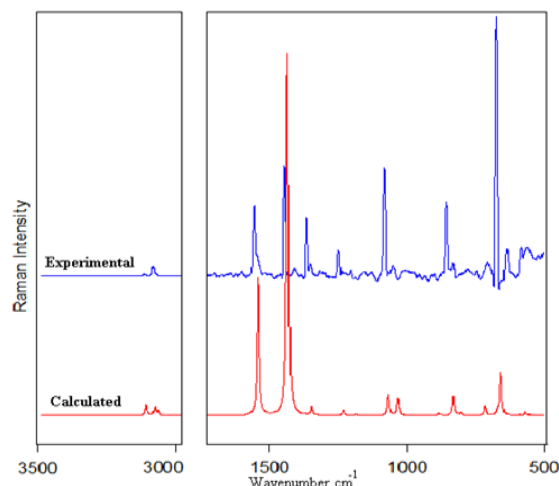Figure 2 Experimental and theoretical FT-IR spectra of the 2,2'-bithiophene molecule

Figure 3 Experimental and theoretical FT-Raman spectra of the 2,2'-bithiophene molecule

Modes	Experimental		Theoretical				TED[c](%)
	IR	Raman	Unscaled[a]	Scaled[b]	I_{IR}	I_{Raman}	
1	-	-	3245	3099	0	4	84 ν(CH)
2	3104	3104	3245	3098	1	0	84 ν(CH)
3	-	3075	3210	3066	0	3	82 ν(CH)
4	-	-	3210	3065	3	0	82 ν(CH)
5	3069	-	3197	3053	11	0	80 ν(CH)
6	-	-	3196	3053	0	2	80 ν(CH)
7	-	1554	1591	1538	0	39	36 ß(CCH)+ 32 ν(CC)+ 10 ß(SCC)
8	1500	-	1544	1493	4	0	48 ß(CCH)+ 25 ν(CC)
9	1441	1443	1481	1432	1	100	34 ν(CC)+ 30 ß(CCH)
10	1416	1368	1460	1412	13	0	44 ß(CCH)+ 34 ν(CC) +10 ß(SCC)
11	1350	1351	1394	1348	0	2	46 ß(CCH)+ 18 ν(CC) +10 ß(CCC)+ 10 ß(SCH)
12	1323	-	1353	1308	2	0	40 ß(CCH)+ 20 ν(CC)
13	1234	1250	1274	1232	0	1	64 ß(CCH)+ 12 ν(CC)+ 10 ß(SCH)
14	1205	-	1226	1186	12	0	54 ß(CCH)
15	-	-	1225	1185	2	0	21 ν(CC) +20 ß(CCC)+ 16 ß(CCH)+14 ß(SCC) +12 ν(CS)
16	1079	-	1107	1070	3	0	64 ß(CCH) +20 ß(SCH)
17	-	1079	1102	1065	0	5	54 ß(CCH) +20 ß(SCH) + 10 ν(CC)
18	1045	-	1071	1035	9	0	50 ß(CCH)+ 20 ν(CC) +10 ß(CCC)
19	-	1046	1067	1032	0	4	52 ß(CCH)+ 16 ν(CC) +10 ß(CCC)
20	-	-	912	882	0	1	34 τ(HCCH)+ 26 τ(CCCH)+ 16 τ(SCCH)
21	914	-	910	880	0	0	36 τ(HCCH)+ 26 τ(CCCH)+ 16 τ(SCCH)
22	895	-	901	871	1	0	18 ß(CCC) +14 τ(HCCH) +14 ß(CCS)+ 12 ß(CCH)+ 12 ν(CS)
23	852	856	858	830	1	4	16 ν(CS) +16 ß(CCS)+ 16 ß(CCC) + 14 ß(CCH)+ 10 τ(CCCH)
24	-	-	839	811	1	0	40 τ(CCCH)+ 18 τ(HCCH)+ 14 τ(SCCH)
25	825	-	828	800	20	1	42 τ(CCCH)+ 20 τ(HCCH)+ 18 τ(SCCH)
26	813	-	826	799	43	0	20 ν(CS) +18 τ(CCCH)+ 12 ß(CCH)+ 10 ß(CCS)
27	-	709	741	716	0	2	28 ν(CS) +20 ß(CCC)+ 17 ß(CCH)
28	-	-	737	713	0	0	40 ν(CS) +20 ß(CCH)+ 18 ß(CCC)
29	-	-	696	673	5	0	40 τ(CCCH)+ 18 τ(CSCH)+ 18 τ(SCCH)+ 16 τ(HCCH)
30	684	-	693	670	100	1	38 τ(CCCH)+ 18 τ(CSCH)+ 16 τ(HCCH)+ 14 τ(SCCH)
31	-	670	681	658	0	10	16 ß(CCC)+ 14 ν(CS) +10 τ(CCCH)
32	-	-	612	592	1	0	14 τ(CCCH)+ 12 τ(CCCS)+ 12 ß(CCS)+ 10 ν(CS)
33	-	588	592	572	1	1	24 τ(CCCS)+ 20 τ(CCCH)+ 12 τ(CCCC)+ 10 τ(HCCH)+ 10 τ(SCCH)+ 10τ(CCSC)
34	-	-	575	556	0	0	22 τ(CCCS)+20 τ(CCCC)+16 τ(CCCH)+12 τ(SCCH)
35	-	-	524	507	2	0	20 τ(CCCC)+20 τ(CCSC)+18 τ(CCCS)+14 τ(CCCH)
36	-	-	468	453	3	1	22 τ(CCCS)+ 16 τ(CCCS)+ 14 τ(CCCH)+ 12 τ(CCCC)+ 12 τ(SCCH)
37	-	-	374	361	0	1	12 ß(CCC)+ 12 ß(CCS)
38	-	-	288	278	0	3	20 ß(CCS)+ 12 τ(CCSC)+ 10 ß(CCC)
39	-	273	280	270	0	1	28 τ(CCSC)+18 τ(CCCH)+18 τ(CCCS)+18 τ(CCCC)
40	-	-	124	120	0	2	16 ß(CCC)+16 τ(CCCS)+14 ß(CCS)+14 τ(CCCC)+12 τ(CCCH)+12 τ(CCCS)
41	-	-	111	107	1	1	29 τ(CCCC)+23 τ(CCCH)+22 τ(CCSC)+10 τ(SCCS)
42	-	-	38	37	0	17	44 τ(CCCS)+22 τ(SCCS)+21 τ(CCCC)

ν, stretching; β, bending; τ, torsion
[a] Unscaled computed values.
[b] In scaled values, the scaling factors 0.967 and 0.955 were used for wave numbers under 1800 cm⁻¹ and above 1800 cm⁻¹, respectively.

[c]Relative intensities of IR normalized with highest peak absorption of 100.
[d]Relative intensities of Raman normalized with highest peak absorption of 100. [e] Only contributions ≥10% are tabulated.

By considering Table 3, the ν (CH) anti-symmetric stretching modes of BT molecule take place at 3104 cm^{-1} (IR/R), 3075 cm^{-1} (R) and 3069 cm^{-1} (IR) while their calculated at the mentioned level wavenumbers were found as 3098, 3066 and 3053 cm^{-1}, respectively [37-42].

The experimental infrared frequencies of thiophene for CCH bending mode were observed 1083 cm^{-1} and 1036 cm^{-1} [20]. In our study, the exp./cal. values for the β (CCH) in-plane bending modes in the rings of title molecule were found in the region (1500-1045) cm^{-1} (IR) and (1554-1046) cm^{-1} (R) / (830-716) cm^{-1}, respectively [37-42]. The experimental IR frequency values for BT molecule were registered in the region (1557- 1446) cm^{-1} [23].

Likewise, the experimental bands at 852, 825 and 813 cm^{-1} (IR) and 856 cm^{-1} and 709 cm^{-1} (R) can be assigned to the C-S stretching mode of the mentioned compound [43, 44]. These mentioned bands were computed at the B3LYP/6–311++G(d,p) level as 830, 800, 799 and 716 cm^{-1}, respectively. However, the mentioned C-S band for thiophene molecule were observed 872 cm^{-1} [20]. Therefore, it can be easily said that the observed values of the ring infrared band for both thiophene and BT molecules exhibit a great similarity.

3.3. HOMO-LUMO analysis

It can be easily stated that the frontier molecule orbitals (FMOs) contain the HOMO and LUMO orbitals, which are deciphered as the highest occupied molecular orbital and the lowest unoccupied molecular orbital, respectively. The HOMO orbital is known as an electron donor while the LUMO is known as an electron acceptor. Therefore, the energy gap between HOMO and LUMO energies is a crucial and critical parameter for the fix of the molecular electrical features [45]. At the same time, for the molecules this energy gap provides the determination of chemical reactivity,

polarizability, chemical hardness and softness, and electronegativity and so on [46]. For instance, if HOMO-LUMO gap is small for any molecule, the molecule becomes soft and reactive in chemical reactions.

In our study, Table 4 summarizes some calculated at mentioned level molecular properties for BT molecule. Furthermore, the 3D plots of HOMO and LUMO orbitals, their shapes and energy gaps of BT are given in Fig. 4.
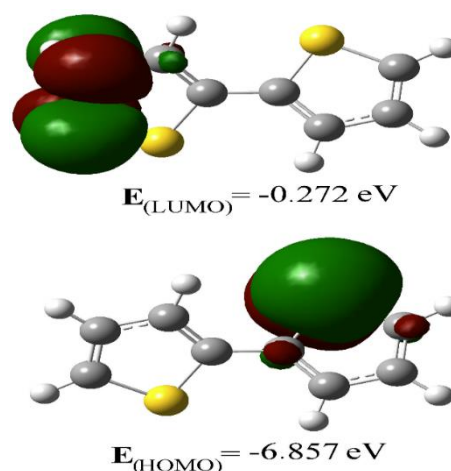
Figure 4 3D plots of HOMO and LUMO of the 2,2'-bithiophene molecule

By considering Table 4, the gap between HOMO and LUMO energy values becomes 6.585 eV. Furthermore, the calculated values at the mentioned level the total dipole moment μ, the chemical hardness η, the absolute electronegativity and the electrophilicity index (or, reactivity index) ω for BT compound were presented in Table 4 [47]. As we mentioned in the Introduction, if the energy gap between HOMO and LUMO orbitals is small because of the existence of the long-range delocalization of the π-systems on neighboring rings (on the intramolecular C1-C2 bond of the title molecule), it can be a tool for tuning conducting polyphenes [19].

3.4. MEP

The electrostatic potential (MEP) can be defined in terms of its relation to the interaction between total charge distribution of the compound and a unit positive test charge. Furthermore, since it is an important device in order to understand for the molecular interactions of a chemical compound and satisfies the correlations among the molecular features such as partial charges, dipole moments, electronegativity and chemical reactivity for molecule [48, 49].
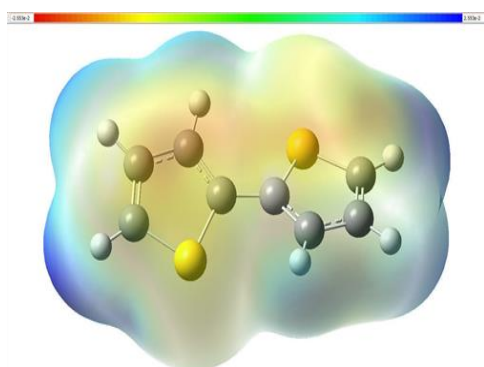

Figure 5 The MEP surface of the 2,2'-bithiophene molecule

Figure 5 exhibits the 3D plot of the MEP of BT compound and computed using the optimized molecular structure of the mentioned compound at the B3LYP/6-311++G(d,p) level. Furthermore, Fig. 5 demonstrates the electrostatic potentials at the surfaces represented by blue, red and green colors. In this content, the regions of negative and positive electrostatic potential are represented with the red and blue colored parts, respectively and the regions with zero potential are indicated by green color. Meanwhile, it can be remained that the electrophilic reactivity is related to the negative regions of molecular electrostatic potential while the nucleophilic reactivity is related to the positive ones. Therefore, in our study Fig. 5 indicates that the negative regions (with red color) are localized on the

S4 and C5 atoms in the thiophene rings but the blue sites (positive regions) are localized

Table 4 The calculated at the B3LYP/6-311++G(d,p) level some molecular properties (in eV) for 2,2'-bithiophene molecule

ET	E_{HOMO}	E_{LUMO}
-30067.453	-6.857	-0.272
μ (Debye)	η	χ
0.288	3.293	3.565

For the calculation the equations were taken from Ref.[47].

on hydrogen atoms in rings of BT compound. On the other hand, the zero potential (green colored) are partly localized in out of rings. Therefore, the positive and negative regions are the localizations for the potential hydrogen bonds of title compound. With this study, a complementary information for the molecular structure, molecular electrostatic potentials (MEPs), and HOMO-LUMO analysis of BT molecule was verified and presented to other researchers of the mentioned compound.

4. CONCLUSION

This work reports a new study about the BT compound, which is a starting agent for polythiophenes and presents an additional investigation in terms of the observed and calculated vibrational spectra. Theoretical examination was carried out at the B3LYP/6-311++G(d,p) level. In our work, the vibrational analysis results present that the relationship between spectroscopic properties such as IR and Raman and theoretical calculations is very useful since it gives basic knowledge of aromatic compounds that can be used for the oligothiophene light-emitting diodes (OLEDs).

Meanwhile, in order to fix the most stable state for BT molecule in solid-state, an examination was verified and the results obtained are confirmed the previous conformational studies, which were performed at the different levels of theory.

(Konya) (Project number: 161710003) (Konya/TURKEY).

Authors' Contribution
Ebru Karakaş Sarıkaya: Conceptualization, Formal analysis, Writing - original draft.
Ömer Dereli: Methodology, Funding acquisition, Resources.
Semiha Bahçeli: Corresponding Author, Writing - review & editing.
Feride Pınar Özturan: Investigation.

The Declaration of Conflict of Interest/ Common Interest
No conflict of interest was declared by the authors.

The Declaration of Ethics Committee Approval
This study does not require ethics committee permission or any special permission.

The Declaration of Research and Publication Ethics
The authors of the paper declare that they comply with the scientific, ethical and quotation rules of SAUJS in all processes of the paper and that they do not make any falsification on the data collected. In addition, they declare that Sakarya University Journal of Science and its editorial board have no responsibility for any ethical violations that may be encountered, and that this study has not been evaluated in any academic publication environment other than Sakarya University Journal of Science.

5. REFERENCES

[1] A. M. Mishra, C. Q. Ma, P. Bauerle, "Functional oligothiophenes: molecular design for multidimensional nanoarchitectures and their applications," Chemical Reviews, vol. 109, no. 3, pp. 1141-1276, 2009.

[2] N. Agarwal, P. K. Nayak, F. Ali, M. P. Patankar, K. Narasimhan, N. Periasamy, "Tuning of HOMO levels of carbazole derivatives: New molecules for blue OLED," Synthetic Metals, vol. 161, no. 5-6, pp. 466-473, 2011.

[3] W.-Y. Hung, L.-C. Chi, W.-J. Chen, Y.-M. Chen, S.-H. Chou, K.-T. Wong, "A new benzimidazole/carbazole hybrid bipolar material for highly efficient deep-blue electrofluorescence,yellow–green electrophosphorescence, and two-color-based white OLEDs," Journal of Materials Chemistry, vol. 20, no. 45, pp. 10113-10119, 2010.

[4] M.-C. Cui, Z.-J. Li, R.-K. Tang, B.-L. Liu, "Synthesis and evaluation of novel benzothiazole derivatives based on the bithiophene structure as potential radiotracers for β-amyloid plaques in Alzheimer's disease," Bioorganic & Medicinal Chemistry Letters, vol. 18, no. 7, pp. 2777-2784, 2010.

[5] Y. Lin, Y. Li, X. Zhan, "Small molecule semiconductors for high-efficiency organic photovoltaics," Chemical Society Reviews, vol. 41, no. 11, pp. 4245-4272, 2012.

[6] Y. Yang, X.-H. Duan, J.-Y. Deng, B. Jin, H.-M. Jia, B.-L. Liu, "Novel imaging agents for β-amyloid plaque based on the N-benzoylindole core," Bioorganic & Medicinal Chemistry Letters, vol. 21, no. 18, pp. 5594-5597, 2011.

[7] A. Almenningen, O. Bastiansen, P. Svendsas, "Electron Diffraction Studies of 2, 2'-Dithienyl Vapour," Acta Chemica Scandinavica, vol. 12, no. 8, 1958.

[8] G. Visser, G. Heeres, J. Wolters, A. Vos, "Disorder in crystals of the dithienyls and β-thiophenicacid," Acta Crystallographica Section B: Structural Crystallography and Crystal

Chemistry, vol. 24, no. 4, pp. 467-473, 1968.

[9] P. Bucci, M. Longeri, C. A. Veracini, L. Lunazzi, "Nematic phase nuclear magnetic resonance investigations of rotational isomerism. III. Conformational preferences and interconversion barrier of 2, 2'-bithienyl," Journal of the American Chemical Society, vol. 96, no. 5, pp. 1305-1309, 1974.

[10] D. Smith, Z. Yu, A. Saxena, R. Martin, A. Bishop, "Molecular Geometry Fluctuation Model for the Mobility of Conjugated Polymers," Physical Review Letters vol. 24, no. 84-4 pp. 721-4, 2000.

[11] C. Alemán, L. Julià, "Characterization of the Quinoid Structure for the 2,2'-Bithiophene and 2,2',5',2''-Terthiophene Dications," The Journal of Physical Chemistry, vol. 100, no. 35, pp. 14661-14664, 1996.

[12] V. Hernandez, J. Lopez Navarrete, "Ab initio study of torsional potentials in 2, 2'-bithiophene and 3,4'-and 3,3'-dimethyl-2, 2'-bithiophene as models of the backbone flexibility in polythiophene and poly (3-methylthiophene)," The Journal of Chemical Physics, vol. 101, no. 2, pp. 1369-1377, 1994.

[13] E. Orti, P. M. Viruela, J. Sanchez-Marin, F. Tomas, "Ab Initio Determination of the Geometric Structure and Internal Rotation Potential of 2,2'-Bithiophene," The Journal of Physical Chemistry, vol. 99, no. 14, pp. 4955-4963, 1995.

[14] N. Di Césare, M. Belletête, G. Durocher, M. Leclerc, "Towards a theoretical design of thermochromic polythiophenes," Chemical Physics Letters, vol. 275, no. 5-6, pp. 533-539, 1997.

[15] S. Samdal, E. J. Samuelsen, H. V. Volden, "Molecular conformation of 2, 2'-bithiophene determined by gas phase electron diffraction and ab initio calculations," Synthetic Metals, vol. 59, no. 2, pp. 259-265, 1993.

[16] G. Distefano, M. Dal Colle, D. Jones, M. Zambianchi, L. Favaretto, A. Modelli, "Electronic and geometric structure of methylthiophenes and selected dimethyl-2, 2'-bithiophenes," The Journal of Physical Chemistry, vol. 97, no. 14, pp. 3504-3509, 1993.

[17] M. Kofranek, T. Kovář, H. Lischka, A. Karpfen, "Ab initio studies on heterocyclic conjugated polymers: structure and vibrational spectra of thiophene, oligothiophenes and polythiophene," Journal of Molecular Structure: Theochem, vol. 259, pp. 181-198, 1992.

[18] G. Raos, A. Famulari, V. Marcon, "Computational reinvestigation of the bithiophene torsion potential," Chemical Physics Letters, vol. 379, no. 3-4, pp. 364-372, 2003.

[19] J. Zhao, P. Li, Y. Li, Z. Huang, "Theoretical investigation on conformational behavior of 2, 2'-bithiophene under the influence of external electric field at ab initio levels," Journal of Molecular Structure: Theochem, vol. 808, no. 1-3, pp. 125-134, 2007.

[20] J. Orza, M. Rico, J. F. Biarge, "Complete quadratic potential function for out-of-plane vibrations of thiophene," Journal of Molecular Spectroscopy, vol. 19, no. 1-4, pp. 188-202, 1966.

[21] Y. Furukawa, M. Akimoto, I. Harada, "Vibrational key bands and electrical conductivity of polythiophene," Synthetic Metals, vol. 18, no. 1-3, pp. 151-156, 1987.

[22] J. L. Navarrete, B. Tian, G. Zerbi, "Chain flexibility in polyheteroaromatic polymers part I. Electronic properties, structure and vibrational spectra of oligomers as models of polypyrrole and polythiophene," Synthetic Metals, vol. 38, no. 3, pp. 299-312, 1990.

[23] G. Zerbi, B. Chierichetti, O. Ingänas, "Vibrational spectra of oligothiophenes as model of polythiophenes," The Journal of Chemical Physics, vol. 94, no. 6, pp. 4637-4645, 1991.

[24] V. Hernández, J. Casado, L. Favaretto, G. Distefano, J. L. Navarrete, "Vibrational spectra and ab initio dft calculations of 3, 3′-and 4, 4′-dimethyl substituted 2, 2′-bithiophene," Synthetic Metals, vol. 101, no. 1-3, pp. 590-591, 1999.

[25] C. Alemán, V. M. Domingo, L. Fajarí, L. Juliá, A. Karpfen, "Molecular and electronic structures of heteroaromatic oligomers: Model compounds of polymers with quantum-well structures," The Journal of Organic Chemistry, vol. 63, no. 4, pp. 1041-1048, 1998.

[26] X. Yin, Y. Li, Y. Zhang, P. Li, J. Zhao, "Theoretical analysis of geometry-correlated conductivity of molecular wire," Chemical Physics Letters, vol. 422, no. 1-3, pp. 111-116, 2006.

[27] R. G. Parr, R. G. Pearson, "Absolute hardness: companion parameter to absolute electronegativity," Journal of the American Chemical Society, vol. 105, no. 26, pp. 7512-7516, 1983.

[28] J. Li, J. K. Tomfohr, O. F. Sankey, "Theoretical study of carotene as a molecular wire," Physica E: Low-dimensional Systems and Nanostructures, vol. 19, no. 1-2, pp. 133-138, 2003.

[29] Gaussian 03, Revision C.02, M. J. Frisch, G. W. Trucks, H. B. Schlegel, et al., Gaussian, Inc., Wallingford CT, 2004.

[30] T. A. Halgren, "The representation of van der Waals (vdW) interactions in molecular mechanics force fields: potential form, combination rules, and vdW parameters," Journal of the American Chemical Society, vol. 114, no. 20, pp. 7827-7843, 1992.

[31] A. Becke, " Density- functional thermochemistry. III. The role of exact exchange," The Journal of Chemical Physics, vol. 98, p. 5648, 1993.

[32] C. Lee, W. Yang, R. G. Parr, "Development of the Colle-Salvetti correlation-energy formula into a functional of the electron density," Physical Review B, vol. 37, no. 2, p. 785, 1988.

[33] R. Johnson, "NIST 101. Computational Chemistry Comparison and Benchmark Database",Computational Chemistry Comparison and Benchmark Database, 1999. [online],http://cccbdb.nist.gov

[34] M. H. Jamróz, Vibrational Energy Distribution Analysis (VEDA).Warsaw. Spectrochimica Acta, Part A: Molecular and Biomolecular Spectroscopy Vol. 114, pp. 220-30, 2013.

[35] G. Keresztury, S. Holly, G. Besenyei, J. Varga, A. Wang, J. Durig,

"Vibrational spectra of monothiocarbamates-II. IR and Raman spectra, vibrational assignment, conformational analysis and ab initio calculations of S-methyl-N, N-dimethylthiocarbamate," Spectrochimica Acta Part A: Molecular Spectroscopy, vol. 49, no. 13-14, pp. 2007-2026, 1993.

[36] D. Michalska, RAINT program. Wroclaw University of Technology, Wroclaw University of Technology, Poland. 2003.

[37] N. Colthup, LH,Daly and S, E Wiberley," Introduction to Infrared and Raman Spectroscopy," Academic Press Inc., New York. pp. 306-307, 1964.

[38] H.-H. Perkampus, L. J. Bellamy: "The Infrared Spectra of Complex Molecules" Berichte der Bunsengesellschaft für physikalische Chemie, vol. 80, no. 1, pp. 99-100, 1976.

[39] J. B. Lambert, H. F. Shurvell, D. A. Lightner, R. G. Cooks, "Introduction to organic spectroscopy." DA Lightner, RG Cooks. Macmillan Publishing Company, 1987.

[40] B. H. Stuart, "Infrared spectroscopy: fundamentals and applications". John Wiley & Sons Ltd., The Atrium, 1-110, 2004.

[41] R. Silverstein, F. Webster, D. Kiemle, "Spectrometric Identification of Organic Compounds, John Willey & Sons, New York. 2005.

[42] L. G. Wade Jr, "Organic Chemistry 6th Edition" Pearson Prentice Hall, Upper Saddle River, N.J., 2006

[43] L.G. Wade, "Organic Chemistry", New Jersey: Pearson Prentice Hall, 2006.

[44] M. Rofouei, E. Fereyduni, N. Sohrabi, M. Sham sipur, J. A. Gharamaleki, N. Sundaraganesan, "Synthesis, X-ray crystallography characterization, vibrational spectroscopic, molecular electrostatic potential maps, thermodynamic properties studies of N, N′-di (p-thiazole) formamidine." Spectrochimica Acta Part A: Molecular Spectroscopy, vol. 78, p. 88, 2011.

[45] R. G. Pearson, "Absolute electronegativity and hardness correlated with molecular orbital theory," Proceedings of the National Academy of Sciences, vol. 83, no. 22, pp. 8440-8441, 1986.

[46] K. Fukui, "Role of frontier orbitals in chemical reactions," Science, vol. 218, no. 4574, pp. 747-754, 1982.

[47] S. Chtita , G., Mounir, L., Majdouline, A. Azeddine, R. Hmammouchi, B., Mohammed, L.Tahar, "Prediction of biological activity of imidazo [1, 2-a] pyrazine derivatives by combining DFT and QSAR results," The International Journal of Innovative Research in Science, Engineering and Technology, vol. 2, no. 12, p. 7962, 2013.

[48] J. S. Murray, K. Das Sen, "Molecular Electrostatic Potentials: Concepts and Applications." Elsevier Science Limited, 1996

[49] A. Pîrnău C. Vasile, O. Ovidiu, L. Nicolae, S., Laszlo, B., Maria, C., Onuc., "Vibrational and DFT study of 5-(3-pyridyl- methylidene) - thiazolidine-2-thione- 4-one," Vibrational spectroscopy, vol. 48, no. 2, pp. 289-296, 2008.

Title: Investigation of Vertical Stiffness of the Front Axle Air Springs for Passenger
Bus by Experimental and Finite Element Analysis

Authors: Hasan KASIM, Erol ÖZKAN

Investigation of Vertical Stiffness of the Front Axle Air Springs for Passenger Bus by Experimental and Finite Element Analysis

Hasan KASIM [*1] , Erol ÖZKAN[2]

Abstract

Air Springs have been used for years, especially in commercial vehicles and buses, to maintain the vehicle's height regardless of the load and increase vehicle comfort. It is complex to experimentally determine the changes (reaction force, extension, strain) caused by loading alone to fully interpret the damping ability of air springs under operating conditions. The air springs are exposed to tension and force in different directions as they are made of a rubber composite structure. Therefore, discussing the damping properties of air springs with only the experimental method is difficult. The study aims to obtain information about the damping behavior of the bellows produced from composite materials, such as bellows under static loads, using both experimental and finite element analysis models. The finite element model of the air springs was obtained by modeling the three parts that provide its integrity. The material definitions required for the composite structure were determined by experimental methods and entered into the FEA program. No material is defined for rigid body members. The results of unidirectional and multidirectional tensile tests performed in a laboratory environment were used for material properties. The characteristics of the air were also entered into the analysis software with the information taken from the literature. The analyzes were carried out in three steps inflating the bellows to the specified pressure values, vertical movement, and compression to the specified displacement value. In this study, it was seen that the cord fabrics in rubber composite structures were affected more by excessive tension than rubber material, and the deviation of the static stiffness value was approximately 5% between the experimental study and the analysis studies. Thanks to FEA studies, it has been determined that more results can be obtained regarding values such as regional stress, force, and displacement in the bellows.

Keywords: Finite element analysis, cord-rubber composites, vertical stiffness, hyper-elastic materials, ride comfort

* Corresponding author: hasan@pegaairsprings.com (H.KASIM)
[1]Pega Automotive Ind. Co. Inc.
[2]Bursa Uludag University, Automotive Engineering, Bursa, Turkey
E-mail: erolozkan149@gmail.com
ORCID: https://orcid.org/0000-0002-3024-5207, https://orcid.org/0000-0002-8382-3461

Hasan KASIM, Erol ÖZKAN

Investigation of Vertical Stiffness of the Front Axle Air Springs for Passenger Bus by Experimental a...

1. INTRODUCTION

Air springs' ability to compress air in a specific volume has enabled them to be used instead of leaf springs in vehicle suspensions. Its outstanding effectiveness in vibration damping increases the use of air suspensions in cars, buses, and heavy commercial vehicles today [1, 2]. The low vibration transmission coefficient of the bellows and their ability to adapt to the load capacity has led to their use as an important vibration isolator in vehicles. It also reduces the impact of vibration on passengers and parts. An air spring's dynamic behavior depending on amplitude and frequency depends on the system's geometric structure [3, 4]. The variation of the air springs internal pressure in the suspension system is the same as the compression of a gas held in a closed container; lateral expansion occurs at the moment of compression. Air springs, which are part of air suspension systems, are the most vital element in the chassis system of operation [5]. The air spring function depends on the load it will carry, its diameter, and the supported air gap area, and the air pressure inside the bellows [6, 7]. The air spring's high flexibility due to the pressure minimizes the harmful effects of the load carried on the vehicle depending on the road conditions [8, 9]. Air suspension systems should have a high damping coefficient for more effective driving, soft and fast damping for comfortable vehicle use. Air spring can give different reactions instantly according to road and driving conditions [10]. It provides a compromise between comfort and safety in vehicles. Depending on the various internal pressure values, the spring coefficient change offers an advantage for air springs. Parts that provide structural integrity in air springs are piston, plate, and cord-rubber composite structures. The internal pressure change in the air spring first affects the rubber layer [11, 12]. Cord-rubber composite structure is a hyperelastic material consisting of two layers of rubber and two cord fabric layers [13]. Rubber material among composite layers is a more flexible and soft material than cord fabric. The part of the air spring subjected to tension is the rubber layer of the composite structure, and the mainframe that carries the load is the cord fabric layers [14]. The cord fibers in the two-layer cord fabric layer are found in the structure of rubber bellows at opposite angles. The air spring is subject to vertical displacement at different frequencies during operation. The stress values and types (compression and tension) occurring in the air spring due to displacement are different. Cord fabric layers prevent deformations caused by stress changes on the bellows. The fatigue life of air springs is affected by many interacting factors, but it is difficult to determine the relationship between these factors using analytical methods [15].

The operating performance of air springs exposed to different loads during driving depends on thermo-mechanical fatigue [16]. It is possible to observe shape change, internal pressure value, and diameter increase of air spring models with experimental studies. However, it is almost impossible to determine regional matters such as tension and reaction force occurring in the air spring in empirical investigations. Observing the regional stress and force values in air springs can be achieved with the Finite Element Analysis (FEA) study [17]. The deviation rate in the results obtained from experimental studies and FEA studies enables us to have clearer information about the working behavior of air springs. Tests determined the rubber and cord fiber's mechanical properties in prototype production for the minimum deviation value. The mechanical data obtained by experimental methods were defined as the material properties of the composite structure of the model we created in the FEA study. The air properties, which provide the change of the air bellows of internal pressure value as a compressible material, are fully defined in the FEA study [18]. Thus, the air spring's vertical reaction force values, static and dynamic stiffness values, the lateral

Hasan KASIM, Erol ÖZKAN

Investigation of Vertical Stiffness of the Front Axle Air Springs for Passenger Bus by Experimental a...

stress, vertical stress, lateral displacement, and vertical displacement values occurring in the rubber composite structure were also obtained [19]. The effect of the piston shape on the stress values on the air spring was interpreted.

The similarity and low deviation rate between the results obtained from the finite element analysis and experimental methods add different originality to the study. The convergence in the amount of deviation between the experimental and FEA studies results will reduce the need for prototype production in the bellows designs, design changes, and product comparisons. The mechanical behavior of the air springs can be easily observed with Finite element analysis [20]. The mathematical model of the air spring created using the correct parameters in FEA will speed up the work both in the development phase and in different areas without increasing production costs.

2. MATERIALS AND METHOD

2.1. An Analytical Examination of Air springs

The prototype and FEA model of the front axle air springs of a bus produced for passenger transport are shown in Figure 1.

The reaction force formed in the air springs depends on the compression and the shape change. The air spring's operation depends on the effective area, volume, pressure, bellows form, hardness, and rubber and cord material thickness. In vehicles with an air suspension system, the vehicle height can be kept constant by changing the air pressure in the bellows regardless of the load [21, 22].

Figure 1 Display of prototype product (A) and FEA model (B)

The level control valves and electronic control unit automatically adjust the relationship between vehicle transport height and pressure. Elastic composite is exposed to compression and tensile stresses at various points due to the force that occurs due to road conditions. The volume change due to compression stresses during the damping of the bellows generally tends to decrease [23]. An air spring movement used in the suspension system changes the internal volume depending on the road conditions. When the volume decreases, the air particles in the bellows compress, and their kinetic energy increases. Accordingly, the internal pressure and temperature of the bellows also increase. Since the gas pressure inside the air spring will change according to the movement, the spring rate also varies as an isothermal, adiabatic, and polytropic process. The air spring's thermodynamic behavior is closer to the state where the temperature does not change and remains constant at low frequency operating speeds and to the position where the temperature changes due to changes in the system's internal energy at high frequency operating speeds. In other words, the minimum spring rate occurs under isothermal compression conditions, and the maximum spring rate occurs under adiabatic compression conditions. If the air spring moves slowly enough to dissipate all the heat generated during compression or expansion, this is an isothermal (constant temperature) process. If the air spring moves fast enough to maintain

Hasan KASIM, Erol ÖZKAN

Investigation of Vertical Stiffness of the Front Axle Air Springs for Passenger Bus by Experimental a...

all the system's heat, this is an adiabatic process. Under real operating conditions, the air spring acts according to neither the isothermal nor the adiabatic process but rather the polytropic state. The polytropic process defines various expansion and compression processes, including heat transfer. The polytropic constant (n) varies between isothermal and adiabatic values $1 < n < \gamma$. The pressure of the gas is directly proportional to the absolute temperature. As the temperature increases, the speed of the gas molecules increases, so the gases in the inner volume of the bellows contact each other more, and the internal pressure increases. This is true for air springs. If the system's compression speed is slow, there is sufficient time for the heat to propagate inside the bellows, creating conditions close to the isothermal (constant temperature) state. The new pressure generated in the air spring under isothermal conditions is calculated according to equation 1.

$$P_1 . V_1 = P_2 . V_2 \tag{1}$$

The variables P1 (bar) and P2 (bar) given in equation 1 are the initial and final absolute pressures of the air springs, V_1 (m^3) and V_2 (m^3), the initial and the final (after compression or expansion) volume. In evaluations according to equation 1, a nonlinear spring rate and an almost constant system frequency occur at system operating pressures. While the vehicle is in driving conditions, the isothermal condition is impossible as the bellows are exposed to variable stresses at high frequencies. Because there is some heat transfer from bellows to the environment due to the increase in pressure during compression, but air springs cannot recover the heat lost during volume increase. It acts according to the adiabatic process due to rapid compression and expansion process in air springs. Equation 2 is used to calculate the pressure change in air springs for the adiabatic state.

$$P_1 . V_1^{\gamma} = P_2 . V_2^{\gamma} \tag{2}$$

The constant γ in equation 2 varies according to the gas type and is a function of the specific temperature for gases. For air;

$$\gamma = C_P / C_V = 1.4 \tag{3}$$

C_P is the specific heat value of air at constant pressure; C_V is the specific heat value of air at constant volume. In summary, the rate of compression or expansion of air has a significant effect on air properties. The high spring rate, high pressure, and fast spring movements occurring in the bellows depending on the road conditions are close to the adiabatic state. Slow and low amplitude spring movements are close to the isothermal state. Since the air suspension's operating conditions are not exactly an adiabatic process, the gamma value can be changed. Usually, the gamma values are used between 1.3 and 1.4.

Equation 4 is used to determine the bellows' internal pressure at any position during the operation of the air spring; P_a is the atmospheric pressure, and P_s gauge pressure. The force (or load) value at any point of the air spring on the working stroke is equal to the effective area multiplied by the gauge pressure. Equation 5 shows the relationship between the pressure force and the effective area.

$$P = P_s + P_a \tag{4}$$

$$F_y = P_s . A_e \tag{5}$$

The relationship between equations 4 and 5 determines the force acting on the system in the vertical direction. The system's vertical spring coefficient expressed by equation 6 is derived by using equations 4 and 5 mentioned above.

$$K_Y = \frac{dF_Y}{dY} = P_s \frac{dA_e}{dY} + \frac{dP_s}{dY} A_e = P_s \frac{dA_e}{dY} + \frac{dP}{dY} A_e \tag{6}$$

Hasan KASIM, Erol ÖZKAN

Investigation of Vertical Stiffness of the Front Axle Air Springs for Passenger Bus by Experimental a...

An expression giving the pressure change in the air spring due to the vertical direction displacement is obtained by deriving equation 2.

$$\frac{d}{dY}(P.V^\gamma) = (P.\gamma.V^{(\gamma-1)})\frac{dV}{dY} + \frac{dP}{dY}V^\gamma = 0 \quad (7)$$

The effective area is shown in equation 8. The sign in front of the effective area varies according to the compression and expansion directions.

$$\frac{dV}{dY} = A_e \quad (8)$$

Equation 9, which is the displacement function of pressure, is used to find the spring rate. For this, equations 7 and 8 are used.

$$\frac{dP}{dY} = \frac{-P.\gamma.V^{(\gamma-1)}}{V^\gamma} = \frac{-P.\gamma.A_e}{V} \quad (9)$$

Different stiffness constants can be obtained depending on the operating frequency of the air springs. Dynamic stiffness can be expressed as shown in equation 10:

$$K_{Y,dyn} = \frac{dP}{dY}A_e = \gamma.(P_s + P_a).\frac{A_e^2}{V} + P_s\frac{dA_e}{dY} \quad (10)$$

The (quasi) static stiffness can be expressed as shown in equation 11:

$$K_{Y,stc} = \frac{dP}{dY}A_e = (P_s + P_a)\frac{A_e^2}{V} + P_s\frac{dA_e}{dY} \quad (11)$$

If the effective area change is very small, it can be assumed that the stiffness constants indicated by equations 10 and 11 are as follows:

$$K_{Y,dyn} = \frac{dP}{dY}A_e = \gamma.(P_s + P_a).\frac{A_e^2}{V} \quad (12)$$

$$K_{Y,stc} = \frac{dP}{dY}A_e = (P_s + P_a)\frac{A_e^2}{V} \quad (13)$$

The value of γ for air is equal to 1.4. Bellows' volume V (m^3). Vertical force F_y (N). $K_{Y,dyn}$ (N/mm) dynamic stiffness. $K_{Y,stc}$ is the static vertical stiffness (N/mm)), P is the absolute pressure (bar), P_s is the gauge pressure (bar), and P_a is the atmospheric pressure (bar)

2.2. Experimental Studies Applies to Air springs

Depending on the pressure change of the bellows at different heights, the reaction force, diameter change, stiffness constants, natural frequency changes can be observed by experimental studies. An air spring; It is obtained by combining basic components such as upper plate, piston, bumper (damping) , rubber-cord composite structure using special process conditions and equipment. The air spring used in this study is the front axle bellows of a bus produced for passenger transport. The aim of choosing the bellows to be used in this study as the bus air springs is to evaluate passenger comfort more critically than other parameters. The top plate of the air springs was attached to the movable plate of the testing machine, the piston base to the stationary plate and was allowed to move only in the vertical direction [24, 25]. There is no restriction on the degree of freedom of the cord-rubber composite structure, which is the most important part of air springs. The cord-rubber composite structure consists of hyper elastic material.

The height values required for the tests of air springs can be characterized by three different dimensions, including minimum, maximum and design height. The actual working height values of the selected air spring were obtained from the vehicle manufacturer and are shown in Table 1.

Table 1 Air springs working heights on the axle

Definition	Test Height (mm)	Total Displacement (mm)
Starting Height	510±1	0
Minimum Height	250±1	260
Design Height	295±1	215
Maximum Height	350±1	160

Hasan KASIM, Erol ÖZKAN

Investigation of Vertical Stiffness of the Front Axle Air Springs for Passenger Bus by Experimental a...

The air pressure inside the bellows is initially zero bar, and the test starting height is 510 mm. In experimental analysis studies, the air spring is automatically brought to the specified working heights, and tests are performed for different pressure values (1, 2, 3, 4 and 5 bar). The measurements were not started before the air pressure given into the bellows became stable. Pressure from 1 to 5 bars was sent into the air springs for three different heights, and the vertical reaction forces were measured. The spring rate in the vertical direction depends on the reaction force obtained, and the displacement applied [26, 27]. Air springs images for experimental testing are shown in Figure 2.
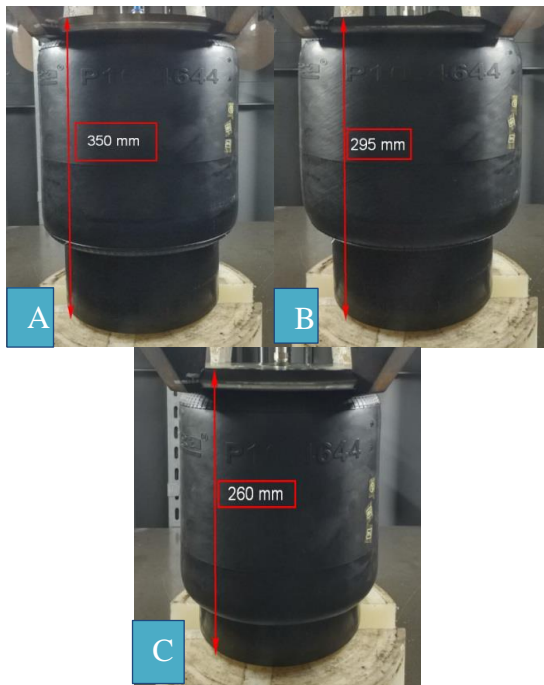

Figure 2 Air springs test heights (A) 250 mm, (B) 295 mm, (C) 350 mm, at 5 bar internal pressure

Shared images are images of different heights of air springs at 5 bar pressure.

Table 2 shows the reaction force values obtained from the experimental studies of the air spring. The gas (air) compression ratio in the air spring increases from maximum height to minimum height. Pressure and reaction forces increase as a result of the compression of the gas. Reaction forces are measured in Newton (N) units.

Table 2 Reaction force values obtained from an experimental study

Pressure (bar)	Assembly Height (mm)		
	250	**295**	**350**
1	3700	3800	3760
2	7980	8010	7420
3	12310	12240	10480
4	16820	16580	14030
5	20950	20670	16780

2.3. Finite element analysis model

The minimum deviation between the reaction force values obtained in the experimental study and the reaction force values obtained in the finite element analysis increases the reliability of the study. The finite element model of the air springs was achieved by modeling three parts that ensure air spring integrity. Air springs basically consist of piston, plate, and cord-rubber composite structures. Air springs components and cord-rubber composite structure are shown schematically in Figure 3. Obtaining a more reliable solution from FEA depends on the correct identification of the interactions between the components that make up the mathematical model of the bellows.

During vertical loading of the air springs, the cord-rubber composite structure between the top plate and the piston is subjected to different stresses. The rubber part of the air spring consists of a layered composite structure. The correct definition of the mechanical interactions between the plies that make up this structure directly affects the accuracy of the analysis results.

Otherwise, the obtained mathematical results may not reflect the actual situation. The up and down movements of the air bellows take place on the piston outer profile of the composite bellows. Thanks to the elastic property of the composite structure, it wraps the piston and takes its shape. For

Hasan KASIM, Erol ÖZKAN

Investigation of Vertical Stiffness of the Front Axle Air Springs for Passenger Bus by Experimental a...

FEA study, there is no need to model auxiliary parts on the product. The piston and top plate, one of the main parts of the air springs, have been accepted as rigid bodies in the FEA study. This means that there will be no stress and force changes in the structures chosen as rigid. The part that will be affected by the pressure change is the bellows part. The rubber layer forming the cord-rubber composite structure is a hyperelastic material that makes the analysis different. The description of a hyperelastic material's mechanical properties is quite different from metallic materials, and its mechanical properties are determined according to the Mooney Rivlin model [14, 28]. The strain energy density function (E_d) for a hyperelastic material is specified in equation 14.

$$E_d = C_{10}(I_1 - 3) + C_{01}(I_2 - 3) + \frac{1}{D}(J^{el} - 1)^2 \quad (14)$$

C_{10}, C_{01}, and D values found in equation 14 are superelastic material constants obtained by testing the material. J^{el} is the elastic volume ratio, I_1 equation 15 and I_2 equation 16 are the first and second strain invariants.

$$I_1 = (\lambda_1)^2 + (\lambda_2)^2 + (\lambda_3)^2 \quad (15)$$

$$I_2 = (\lambda_1\lambda_2)^2 + (\lambda_2\lambda_3)^2 + (\lambda_1\lambda_3)^2 \quad (16)$$

In equation 16 and equation 17, λ_1, λ_2, and λ_3 are stress coefficients in three directions. In the FEA studies, the fibers in the cord fabric layer were modeled similarly to the rebar unit [29]. Cord fibers made of PA66 in the composite structure forming the air bellows model are embedded in the rubber [30]. Polyamid66 fiber cord reinforced rubber composite can be considered as an elastic, orthotropic, and homogeneous material. Cord fibers that increase the resistance against tensions in a composite structure are materials with elastic properties. Elastic modulus, poison rate, and cord fibers' density values were entered into the software as data. The advantage of the cord fabric's elastic structure allows the bellows to return to their original state when the bellows' load and pressure are removed. Thanks to this situation, the bellows structure is not damaged, and the bellows gain strength.
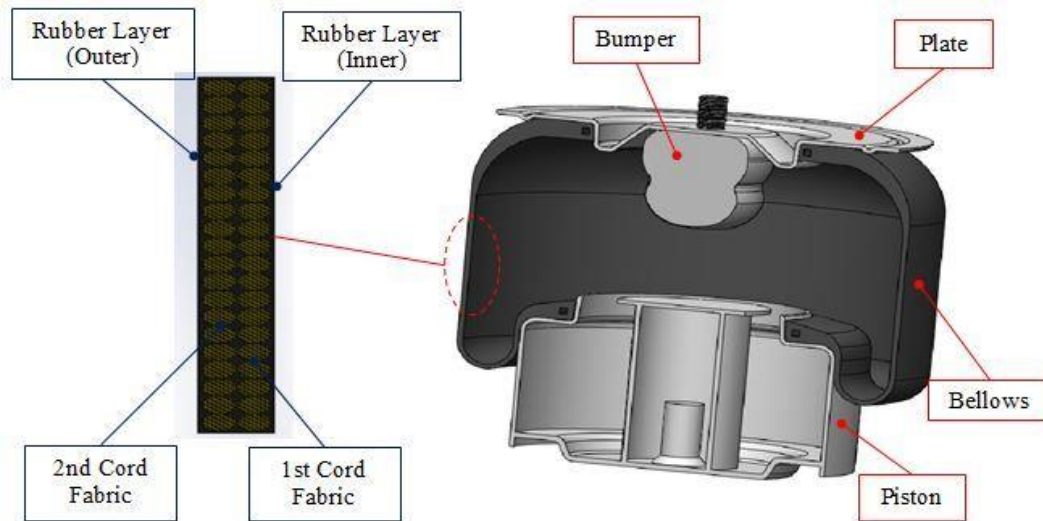
Figure 3 Schematic represantation of the air springs structure

All technical dimensions of the air spring prepared for FEA study are the same as the prototype. The material definitions required for the composite structure were determined by experimental methods and entered into the FEA program. No material is defined for rigid body members. Results data of one-way and multi-directional tensile tests performed in the laboratory environment are placed in the analysis software. The degrees of freedom of the air springs components are the same as to FEA and experimental work. The most critical point of analysis is that the air properties inside the bellows are correctly

Hasan KASIM, Erol ÖZKAN

Investigation of Vertical Stiffness of the Front Axle Air Springs for Passenger Bus by Experimental a...

defined in the FEA program. Air is the primary material that will allow the reaction force to vary due to the bellows' pressure. It is essential to determine the properties of the air correctly. The air in the air springs can be compressed at different rates. For this reason, the air weight and atmospheric pressure values were entered as data after selecting the reference point in the middle of the bellows and the inner surface where the air contacts in the analysis program. Other parameters required for air are absolute temperature and gas constant value [31, 32].

Table 3 Material properties required for air spring FEA study

Material Properties	Unit	Value
Cord Fiber		
Elasticity Module	MPa	4640
Poisson Ratio	-	0.3
Density	T/mm^3	1.16x10^{-9}
Rubber		
C_{10}	-	0.382
C_{01}	-	0.096
D	-	0
Air		
Gas Constant (R)	Kj/kgK	8.317x10^3
Temperature	K	-273.15+25
Molecular Weight	Kg/mol	0.02897

The material properties of the bellows components are also entered into the analysis program as data. The properties of the materials used in the analysis are obtained as a result of the experimental studies and shown in detail in Table 3.

The production parameters of the cord fabric forming the layers of the bellows determine the spring stiffness during the air spring operation, the operating frequency, the friction coefficient between the piston and the rubber surface, the spring rate, and the reaction forces formed in the system [33, 34]. Correct association of the composite structure layers prevents structural deformations from occurring in the air spring and extends the product life. The air spring used in the study is a product that has received design validity as a result of field and laboratory tests. The production

parameters of the layers of bellows are also approved data. The composite part of the air spring parameters used in the experimental studies is available in Table 4. These data were entered as dimensional properties during the composite design in the FEA study [35].

Table 4 Structural features of the cord-rubber composite bellows part

Parameters	Unit	Value
Cord Fabric Layer Count	piece	2
Composite Total Thickness	mm	5
1st Cord Angle	°	55
2nd Cord Angle	°	-55
Distance Between Cords	mm	0.3968
Area per Pressure	mm^2	0.049

2.4. Air springs finite element analysis study

The definition of the FEA model boundary conditions is fixed to the press floor from the lower base of the metal piston of the air spring, and the degree of freedom is set to zero. The upper connection plate of the air spring was defined to move only in the vertical direction, and the degree of freedom was set as one. FE analysis was defined as three steps respectively: inflating the air spring to the specified pressure values, defining motion in the vertical direction, and compressing it to the specified displacement value. Depending on the top cover's vertical movement, the load of the air spring can be determined. In this study, thanks to the FE analysis study, the air spring's vertical stiffness performances are determined by analyzing the load fluctuations caused by the stress values caused by the different internal pressure and displacement of the air spring. Table 5 shows the reaction force values of the air spring obtained from FE analysis studies. As the air spring moves from the maximum height to the minimum height, the reaction forces increase due to the pressure

Hasan KASIM, Erol ÖZKAN

Investigation of Vertical Stiffness of the Front Axle Air Springs for Passenger Bus by Experimental a...

of the gas trapped inside. However, some reaction force values are lower while the air spring is compressing towards the minimum height. The reason for this is that the frictional force due to the if movement on the outer diameter of the piston limits the diameter of the bellows. Reaction forces are measured in units of Newton (N).

Table 5 Reaction force values obtained as a result of FE analysis

Pressure (bar)	Assembly Height (mm)		
	250	295	350
1	3886	3970	3880
2	8020	8320	7460
3	12610	12360	10750
4	17000	17200	14220
5	21280	20800	16380

According to the assembly heights, the changes of reaction force values obtained from FE analysis and experimental studies are shown in Figure 4 comparatively. A deviation value below 5% between the two studies is significant for the study's reliability.The comparative graphs shown in Figure 4 show the relationship between the pressure increase in the air spring and the reaction force change. The reaction force formed in the air spring depends on the air pressure and effective area in the bellows. The deviation values between the reaction forces obtained in FEA study and experimental studies become more in the free position and with increasing pressure.

The lower reaction force values obtained at 350 mm mounting height are due to the less interaction of the cord-rubber composite structure with the piston.

In other words, the composite structure has the freedom to extend laterally and upwards. As the air spring starts to compress from the design height, the interaction between the bellows and the piston increases. The resulting friction force prevents the composite bellows structure from expanding sideways. Thus, the reaction force decreases

a little. However, when the compression is maximum, the deviation value between the FEA study and experimental studies decreases to approximately 1.5%. Tests were performed at vertical compression values of 160 mm, 215 mm, and 260 mm respectively, starting from a height of 510 mm.
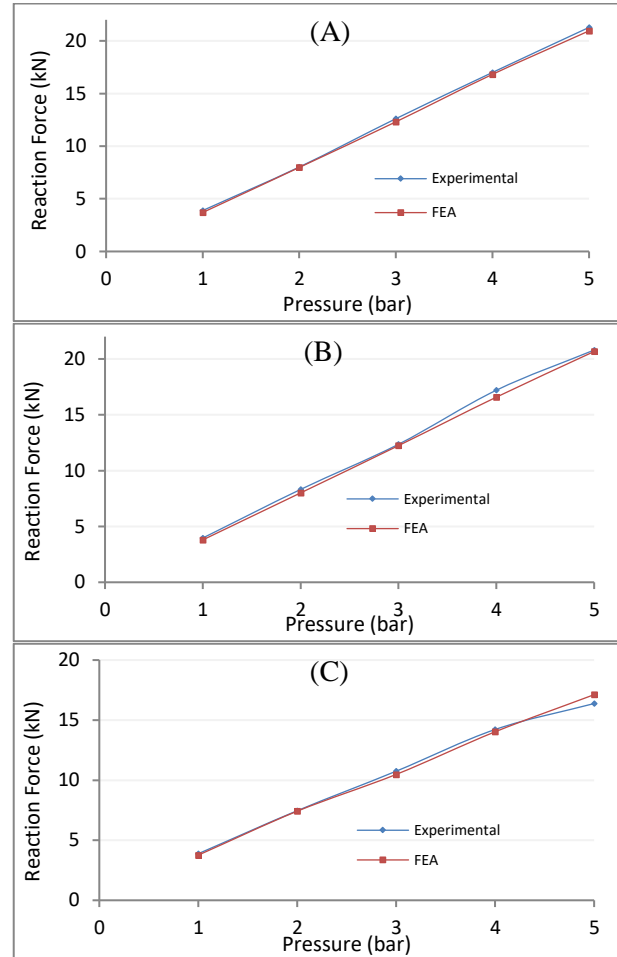

Figure 4 Reaction force comparison graphs depending on assembly heights, (A) 250 mm, (B) 295 mm, (C) 350 mm

Figure 5 shows the displacement values of the air spring in the hyperelastic material structure at different amounts. Since the rubber composite structure movement does not occur linearly, the displacement values at the nodes are different. The maximum displacement value in the rubber composite structure occurs in areas close to the upper plate. The part where the nodes are less displaced is at the base of the rubber composite structure. As the compression amount in the air spring increases, the rubber

Hasan KASIM, Erol ÖZKAN

Investigation of Vertical Stiffness of the Front Axle Air Springs for Passenger Bus by Experimental a...

composite structure moves depending on the shape of the piston. The rubber composite structure takes the piston's shape, while the rubber composite structure folds from the bottom base. The folding movement that occurs at the bottom of the bellows causes the knots to rotate. For this reason, the vertical displacement value is higher in the upper plate part and less in the base part.

Figure 6 shows the bellow's lateral displacement values in the air spring depending on vertical movement and internal pressure. Bellows are composite structures consisting of inner rubber, two layers of cord fabric, and an outer rubber. The system that limits the amount of lateral expansion in the bellows is the cord fabrics, which are opposite to each other. Cord fabrics restrict the growth of bellow's diameter at internal pressure increase. The

higher lateral displacement in the middle part is due to the more remarkable angle change between the cord fibers in this region. Excessive angle variation between cord fabrics increases lateral displacement. The lateral displacement values of the bellows are high in the middle section.

Figure 7 shows the stress values in the vertical direction of rubber bellows due to the displacement of the air spring. The pressure increase in the bellows also increases the stress values in the air spring.

Since the rubber composite structure is hyperelastic, it resists changes in stress values. The main structure affected by the tension changes in the bellows is the cord fabrics. Cord ropes are affected more by high-stress values than rubber material.
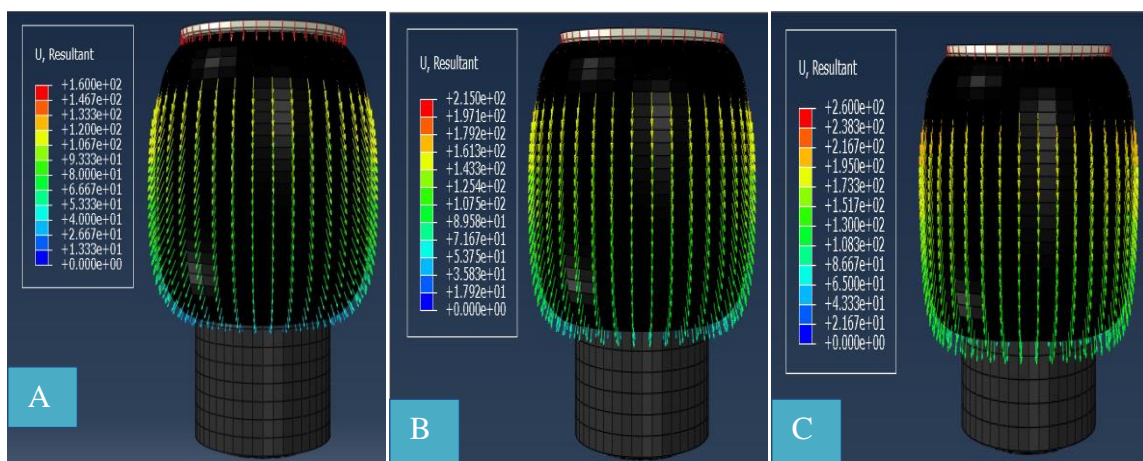

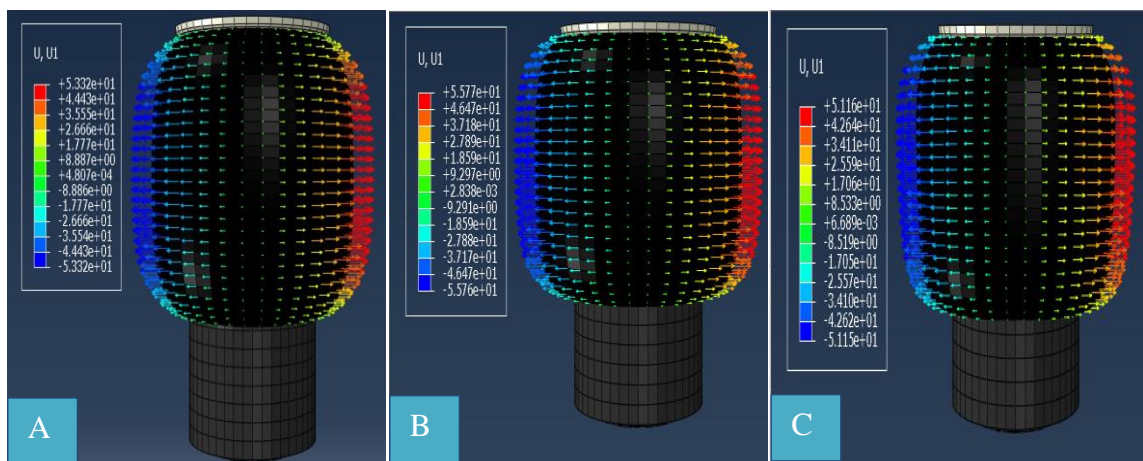Figure 5 The movement of the nodes on the vertical displacements, (A) 160 mm, (B) 215 mm, (C) 260mm

Figure 6 The movement of the nodes undergoing lateral expansion, (A) 160 mm, (B) 215 mm, (C) 260mm

Hasan KASIM, Erol ÖZKAN

Investigation of Vertical Stiffness of the Front Axle Air Springs for Passenger Bus by Experimental a...
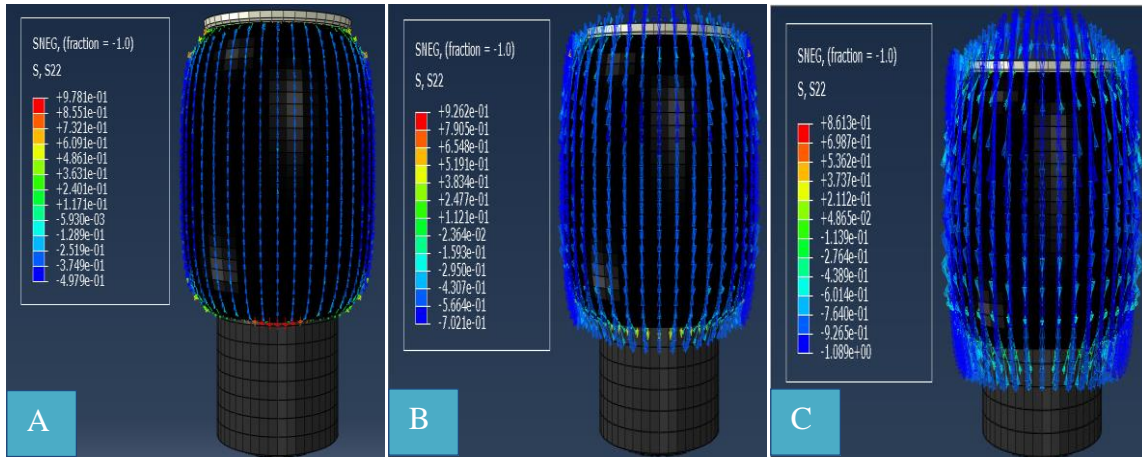
Figure 7 Vector representation of vertical stresses, (A) 160 mm, (B) 215 mm, (C) 260mm

Figure 8 shows the lateral stress values of the air spring due to different displacements. The changes in the lateral stress values change in proportion to the lateral displacement values. Since the lateral displacement values in the middle part of the bellows are high, the stress values are also high. Stress values were observed depending on three different displacements in the study. The increase in the vertical displacement causes the lateral stress values in the bellows to decrease. Because with vertical displacement, bellows contact and curl more on the outer diameter of the piston. When the bellows take the piston's shape, some of the stresses that occur in the bellows are met by the piston. In this case, high displacement reduces the lateral stresses that occur in the bellows.
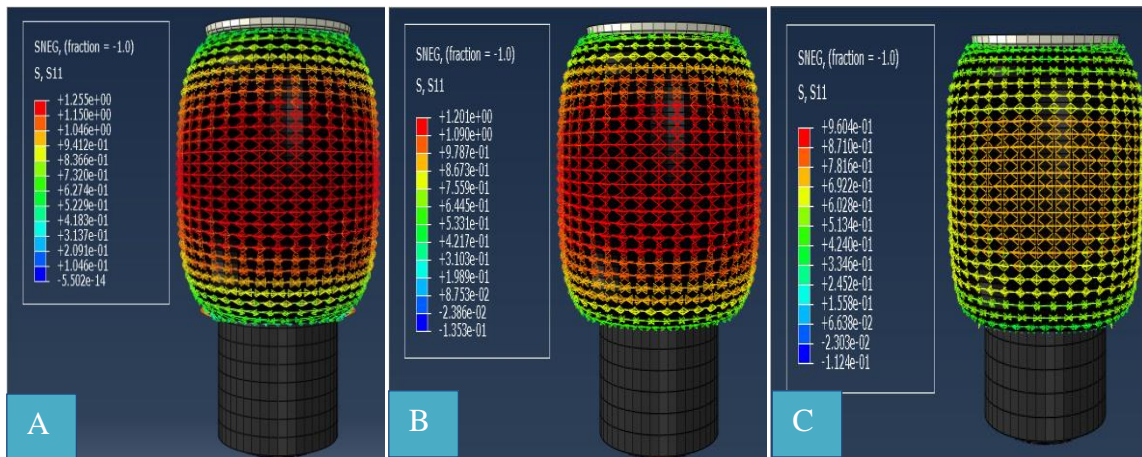

Figure 8 Vector representation of lateral stresses, (A) 160 mm, (B) 215 mm, (C) 260mm

Figure 9 shows the reaction force values caused by the change in the internal pressure of air spring moving in the vertical direction. The bellows vertical stiffness has been analyzed to determine the reaction force we have obtained by finite element analysis. With the finite element study, the air spring differences due to internal pressure variation and displacement are clearly observed. The development of the air spring is possible by knowing more about the changes in the air spring. According to the experimental method, more information about the stress, displacement, and reaction force values in the air spring can be obtained by finite element analysis. Different data can be provided with finite element analysis designed correctly for the air spring, which is difficult to work on

Hasan KASIM, Erol ÖZKAN

Investigation of Vertical Stiffness of the Front Axle Air Springs for Passenger Bus by Experimental a...
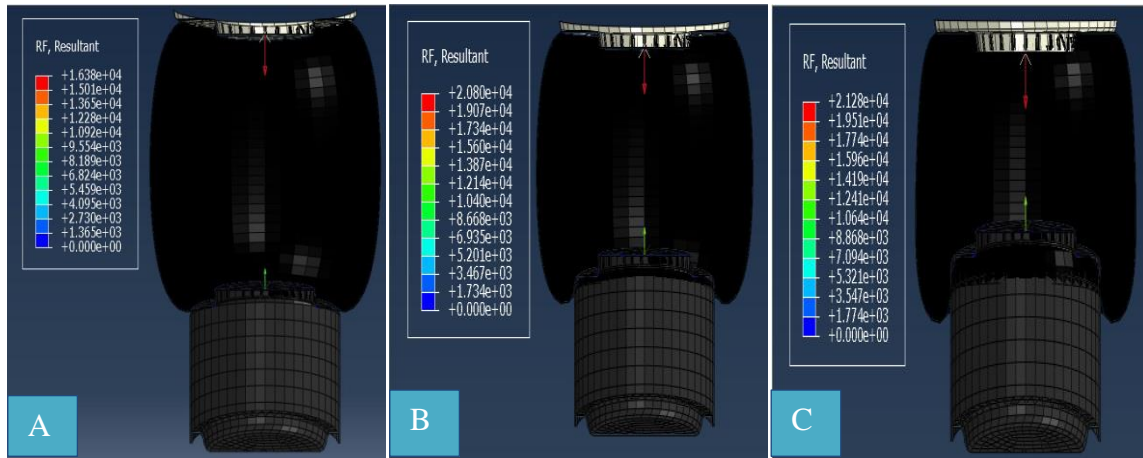
Figure 9 Display of the vertical reaction forces on the air spring, (A) 160 mm, (B) 215 mm, (C) 260mm

3. RESULT AND DISCUSSION

The design features (stiffness, reaction forces, displacements, etc.) of the air springs used in the passenger bus suspension system were determined by FE analysis. FE analysis results with experimental field tests were verified by capturing deviation values below 5%. Air springs are subjected to loads while the vehicle is in motion, but a certain amount of compression occurs in the air springs when the vehicle is not moving and is loaded. Air springs work by mounting on the axle under the chassis and vehicle. Internal pressure and compression ratios vary according to the load and road conditions during operation. The damping properties, stiffness, and frequency of bellows depend on internal pressure and displacement [36]. In the study carried out, considering the vehicle's condition loaded and not being in motion, stiffness properties were obtained depending on the tests performed at different heights and internal pressures. Determining the damping properties of air springs with analytical solutions contributes greatly to the design process. Air springs create a reaction force to the forces coming to the air suspension systems depending on the road conditions. Depending on the vehicle's loading and road conditions, there are constant changes in the internal pressure of

the air springs, and these changes form the reaction forces. By using the reaction force values obtained in experimental and numerical studies, it is possible to calculate the stiffness of the air spring and interpret the damping properties. The spring coefficients calculated with the reaction force values obtained in experimental and analytical studies are given in Table 6. The values obtained are N/mm.

The values in Table 6 were established using the data obtained from the experimental studies in Table 2 and the reaction force values obtained as a result of the FEA studies in Table 5. The results enable interpretation by looking at the deviations between the finite element analysis and experimental study values. The deviation between the stiffness values of experimental and analytical studies varied between 0.5% and 6%. The fact that the percentage deviation values obtained are very close to the experimental data is promising in terms of verifying the design inputs of the bellows with analysis. The closeness between the results obtained depends on the fact that many tests have been carried out between the minimum and maximum working height of the air spring, and the material properties are defined very well. Static stiffness curves obtained as a result of experimental and FEA

Hasan KASIM, Erol ÖZKAN

Investigation of Vertical Stiffness of the Front Axle Air Springs for Passenger Bus by Experimental a...

simulation are compared as shown in Figure 10. It is seen from the studies that FEA

studies can be used effectively in air spring analysis.

Table 6 Damping coefficient values calculated at different pressure and displacement values with experimental and FEA studies

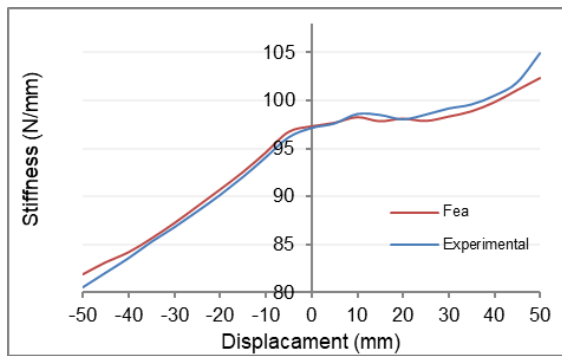| Pressure (bar)	Experimental Results			FEA Results		
	Displacement (mm)			*Displacement (mm)*		
	260 mm	**215 mm**	**160 mm**	**260 mm**	**215 mm**	**160 mm**
1	14 230	17 674	23 500	14 920	18 465	25 031
2	30 692	37 255	46 375	31 000	38 697	46 375
3	47 346	56 930	65 500	48 500	57 488	67 187
4	64 682	77 116	87 687	65 384	80 000	88 875
5	80 576	96 139	108 875	81 846	96 744	102 375

Figure 10 Comparision of static stiffness curves of the air spring

4. CONCLUSION

This study obtained information about the damping behavior of the bellows produced from composite materials such as air bellows under static loads, thanks to both the experimental and finite element analysis models. As a result of the studies, the following information was obtained;

1. The approximate deviation between the static stiffness value obtained from the experimental study and the mathematical study of the bellows was determined as 5%. Values close together indicate that the two study results can be reconciled.

2. Thanks to the FEA study, more results can be obtained regarding values such as regional stress, force, and displacement in the air spring.

3. Analysis studies have shown that the increase in the vertical displacement value of the bellows decreases the lateral stress values. Some of the stresses in the bellows, which take the shape of the piston, are covered by the piston. However, the vertical stress values occurring in the bellows increase proportionally as the displacement value increases.

4. In our study, it has been seen that the cord fabrics in the rubber composite structure are affected by excessive stress more than the rubber material. Cord fibers limit the excessive expansion of the bellows in the event of a sudden pressure increase. It is the main element that carries the loads that occur in instant pressure increases.

5. The effect of air is important in both our work. For analysis studies, it is important to correctly define the characteristics of the air that creates the internal pressure of

Hasan KASIM, Erol ÖZKAN

Investigation of Vertical Stiffness of the Front Axle Air Springs for Passenger Bus by Experimental a...

the bellows, such as pressure, absolute temperature, weight, and effective area.

6. The 5% deviation between the stiffness values obtained by the experimental results of the prototype and the results obtained from FEA studies can be caused by ambient temperature, prototype internal pressure, and errors that can occur in the prototype production process.

Authors' Contribution
The authors contributed equally to the study.

The Declaration of Conflict of Interest/ Common Interest
No conflict of interest or common interest has been declared by the authors.

The Declaration of Ethics Committee Approval
This study does not require ethics committee permission or any special permission.

The Declaration of Research and Publication Ethics
The authors of the paper declare that they comply with the scientific, ethical and quotation rules of SAUJS in all processes of the paper and that they do not make any falsification on the data collected. In addition, they declare that Sakarya University Journal of Science and its editorial board have no responsibility for any ethical violations that may be encountered, and that this study has not been evaluated in any academic publication environment other than Sakarya University Journal of Science.

REFERENCES

[1] S. Oman, M. Fajdiga, M. Nagode, "Estimation of air-spring life based on accelerated experiments," Materials and Design, vol. 31, no. 8, pp. 3859–3868, 2010.

[2] V. Eskandary, V. Khajepour, V. Wong, "Analysis and optimization of air suspension system with independent height and stiffness tuning," International Journal of Automotive Technology, vol. 17, pp. 807-816, 2016.

[3] H. Zhu, J Yang, Y Zhang, X. A. Feng, "A novel air spring dynamic model with pneumatic thermodynamics, effective friction and viscoelastic damping," Journal of Sound and Vibration, vol. 408, pp. 87-104, 2017.

[4] M. W. Holtz, J. L. Nierkerk, "Modelling and design of a novel air spring for a suspension seat," Journal of Sound and Vibration, vol. 329, no. 21, pp. 4354-4366, 2010.

[5] S. Oman, M. Nagode, M. Fajdiga, "The material characterization of the air spring bellow sealing layer," Materials and Design, vol. 30, no. 4, pp. 1141-1150, 2009.

[6] S. Lee, "Development and analysis of an air spring model," International Journal of Automotive Technology, vol. 11, pp. 471-479, 2010.

[7] J. Ye, H. Huang, C. He, G. Liu, "Analysis of Vertical Stiffness of Air Spring Based on Finite Element Method," in MATEC Web of Conferences, vol.153, no. 06006, 2018.

Hasan KASIM, Erol ÖZKAN

Investigation of Vertical Stiffness of the Front Axle Air Springs for Passenger Bus by Experimental a...

[8] S. Razdan, P. J. Awasare, S. Y. Bhave, "Active Vibration Control using Air Spring," Journal of The Institution of Engineers (India): Series C, vol. 100, no. 1, pp. 1–12, 2018.

[9] G. Quaglia, A. Guala, "Evaluation and Validation of an Air Spring Analytical Model," International Journal of Fluid Power, vol. 4, pp. 43-54, 2003.

[10] M. Ber, "A Three–Dimensional Airspring Model with Friction and Orifice Damping," International Journal of Vehicle Mechanics and Mobility, vol. 33, pp. 528-539, 1999.

[11] T. Mankovits, T. Szabo, "Finite element analysis of rubber bumper used in air spring," Journal of Procedia Engineering, vol. 48, pp. 388-395, 2012.

[12] B. Agnew, "A Note on the Design of Air Springs," Proceedings of the Institution of Mechanical Engineers, Part D: Journal of Automobile Engineering, vol. 205, no. 3, pp. 207-209, 1991.

[13] S. Oman, M. Nagode, "On the influence of the cord angle on air-spring fatigue life," Engineering Failure Analysis, vol. 27, pp. 61-73, 2013.

[14] M. Jamshidi, F. Afshar, B. Shamayeli, "Evaluation of cord/rubber adhesion by a new fatigue test method," Journal of Applied polymer Science, vol.101, no.4, pp. 2488-2494, 2006.

[15] W. V. Mars, A. Fatemi, "Literature survey on fatigue analysis approaches for rubber," International Journal of Fatigue, vol. 24, no. 9, pp. 949–961, 2002.

[16] M. Shahzada, A. Kamranb, MZ. Siddiqui, M. Farhan, "Mechanical Characterization and FE Modelling of a Hyperelastic Material," Journal of Material Research, vol. 18, no. 5, pp. 918-924, 2015.

[17] B. Agnew, "A Comparison of Approximate Forms of Air Spring Shells," Proceedings of the Institution of Mechanical Engineers, Part C: Journal of Mechanical Engineering Science, vol. 208, no. 3, pp. 207-210, 1994.

[18] Z. Li, L. Ju, H. Jiang, X. Xu, M. Li, "Experimental and simulation study on the vibration isolation and torsion elimination performances of interconnected air suspensions, "Proceedings of the Institution of Mechanical Engineers, Part D: Journal of Automobile Engineering, vol. 230, no. 5, pp. 679-691, 2016.

[19] H. Fu, Z. Hua, L. Zou, Y. Wang, J. Ye, "Combined stiffness characteristic of metal rubber material under vibration loads," Proceedings of the Institution of Mechanical Engineers, Part C: Journal of Mechanical Engineering Science, vol. 233, no. 17, pp. 6076-6088, 2019.

[20] X. Q. Sun, L. Chen, S. H. Wang, X. Xu, "Vehicle height control of electronic air suspension system based on mixed logical dynamical modeling," Science China Technological Sciences, vol. 58, pp. 1894-1904, 2015.

[21] S. Oman, M. Nagode, "The influence of piston shape on air-spring fatigue life," Fatigue&Fracture of Engineering Materials & Structures, vol.41, no. 5, pp. 1019-1031, 2017.

[22] P. K. Wong, Z. Xie, J. Zhao, T. Xu, F. He, "Analysis of automotive rolling lobe air spring under alternative factors with finite element model,"

Hasan KASIM, Erol ÖZKAN

Investigation of Vertical Stiffness of the Front Axle Air Springs for Passenger Bus by Experimental a...

Journal of Mechanical Science and Technology, vol. 28, no. 12, pp. 5069-5081, 2014.

[23] B. Sarıoğlu, A. Durmuş, "Manufacture and Testing of Air Springs Used in Railway Vehicles," Arabian Journal for Science and Engineering, vol.44, pp. 7967–7977, 2019.

[24] J. J. Chen, Z. H. Yin, S. Rakheja, J. H. He, K.H. Guo, "Theoretical modelling and experimental analysis of the vertical stiffness of a convoluted air spring including the effect of the stiffness of the bellows," Proceedings of the Institution of Mechanical Engineers, Part D: Journal of Automobile Engineering, vol.232, no. 4, pp. 547-561, 2018.

[25] I. Okorn, M. Fajdiga, M. Nagode, "Analysis of a test rig drive for air springs," Proceedings of the Institution of Mechanical Engineers, Part C: Journal of Mechanical Engineering Science, vol.224, no.1, pp. 243-251, 2010.

[26] D. Qu, X. Liu, G. Liu, T. He, "Vibration isolation characteristics and control strategy of parallel air spring system for transportation under abnormal road and eccentric load conditions,"Measurement and Control, vol. 54, no. 3-4, pp. 252-268, 2021.

[27] H. Ding, A. Khajepour, Y. Huang, "A novel tripped rollover prevention system for commercial trucks with air suspensions at low speeds, "Proceedings of the Institution of Mechanical Engineers, Part D: Journal of Automobile Engineering, vol. 232, no. 11, pp. 1516-1527, 2018.

[28] H. Darijani, R. Naghdabadi, M. H. Kargarnovin, "Hyperelastic materials modelling using a strain measure consistent with the strain energy postulates," Proceedings of the Institution of Mechanical Engineers, Part C: Journal of Mechanical Engineering Science, vol. 224, no. 3, pp. 591-602, 2010.

[29] W. Huai, G. RuHai, L. Y. Li, "The influence of meshing density on automobile crashing simulation and the efficiency of calculation," Journal of Jiangsu University of Science and Technology, vol.23, no. 4, pp. 29-33, 2002.

[30] S. Wenku, J. Wan, H. Ying, Y. Weimin, Y. Hao, L. Zubin, "Finite element analysis of an air spring concerning initial pressure and parameters of cord fabric layer," in Asia-Pacific Conference on Computational Intelligence and Industrial Applications (PACIIA), Wuhan, China, 2009, pp. 496-499.

[31] P. J. Mago, S. A. Sherif, "Formulations of thermodynamic properties of supersaturated moist air," Proceedings of the Institution of Mechanical Engineers, Part C: Journal of Mechanical Engineering Science, vol. 217, no. 6, pp. 705-718, 2003.

[32] F. Chang, Z. H. Lu, "Dynamic model of an air spring and integration into a vehicle dynamics model," Proceedings of the Institution of Mechanical Engineers, Part D: Journal of Automobile Engineering, vol. 222, no.10, pp. 1813-1825, 2008.

[33] L. Fang, Y. Wang, "Study on the stiffness property of a variable stiffness joint using a leaf spring,"Proceedings of the Institution of Mechanical Engineers, Part C: Journal of Mechanical Engineering Science, vol. 233, no. 3, pp. 1021-1031, 2019.

Hasan KASIM, Erol ÖZKAN

Investigation of Vertical Stiffness of the Front Axle Air Springs for Passenger Bus by Experimental a...

[34] J. J. Chen, Z. H.Yin, S. Rakheja, J. H. He, K. H. Guo, "Theoretical modelling and experimental analysis of the vertical stiffness of a convoluted air spring including the effect of the stiffness of the bellows,"Proceedings of the Institution of Mechanical Engineers, Part D: Journal of Automobile Engineering, vol. 232, no. 4, pp. 547-561, 2018.

[35] H. W. Lee, S. H. Kim, H. Huh, J. Y. Kim, S. G. Jeong, "Finite Element Analysis of Diaphragm-type Air Springs with Fiber-reinforced Rubber Composites, "Journal of Composite Materials, vol. 37, no. 14, pp.1261-1274, 2003.

[36] G. Taiping, H. Lin, Z. Yinglong, "Composite finite element approach for dynamic stiffness calculation of bellows type air spring," Journal of Vibration and Shock, vol. 29, no.8, pp. 221-223, 2010.

Title: Reinforcement Learning Applications in Cyber Security: A Review

Authors: Emine CENGİZ, Murat GÖK

Reinforcement Learning Applications in Cyber Security: A Review

Emine CENGİZ *1 (iD), Murat GÖK1 (iD)

Abstract

In the modern age we live in, the internet has become an essential part of our daily life. A significant portion of our personal data is stored online and organizations run their business online. In addition, with the development of the internet, many devices such as autonomous systems, investment portfolio tools and entertainment tools in our homes and workplaces have become or are becoming intelligent. In parallel with this development, cyberattacks aimed at damaging smart systems are increasing day by day. As cyberattack methods become more sophisticated, the damage done by attackers is increasing exponentially. Traditional computer algorithms may be insufficient against these attacks in the virtual world. Therefore, artificial intelligence-based methods are needed. Reinforcement Learning (RL), a machine learning method, is used in the field of cyber security. Although RL for cyber security is a new topic in the literature, studies are carried out to predict, prevent and stop attacks. In this study; we reviewed the literature on RL's penetration testing, intrusion detection systems (IDS) and cyberattacks in cyber security.

Keywords: Cyber security, reinforcement learning, penetration testing, IDS, cyberattack.

1. INTRODUCTION

Cybersecurity can be defined as technologies and processes that help protecting the integrity, confidentiality and availability of networks and data in computer systems against cyberattacks or unauthorized access [1]. Cyber security has become one of the most important problems in cyberspace [2]. Recent developments in information technologies, communication networks, the internet of things, cloud technology, increase in mobile internet and development of

hardware of devices have revealed security vulnerabilities and uncertainties. This situation causes systems not to function, economic damage and danger to cyber security.

In favour of maximising the level of security of system assets, it is required to build up innovative and intelligent defense methods that are able to overcome cyber threats [3]. For this, it is necessary to obtain the historical and current security status data of the system and make intelligent decisions that provide

* Corresponding author: emine.cengiz@yalova.edu.tr (E.CENGİZ)
1 Yalova University
E-mail: murat.gok@yalova.edu.tr
ORCID: https://orcid.org/0000-0002-6695-9500, https://orcid.org/0000-0003-2261-9288

security management and control. Machine learning (ML) is a method applied to both attack and defense. This method is used to make the defense mechanism smarter, more durable and more efficient [4]. At the offensive level, however, it complicates the attacks to get through the defensive methods easily.

It is known that simple algorithms are not enough for cyber security software to fulfill their task. Many studies conducted on the Reinforcement Learning (RL) method, which leads today's algorithms, show that its importance in cyber security is increasing. RL is a purposeful ML approach that learns what to do. The RL agent directly relates to the environment to reach a set target, imitating the human learning process [5]. The agent learns by trial and error and uses experience to improve its behavior [6]. RL has been used in numerous disciplines such as robotics [7-9], control systems [10], advertising [11], video games [12-14], autonomous vehicles [15,16], autonomous surgeries [17, 18].

The main goal of this research is to compose a narrative review of studies, which provide an overview of what is known about a particular topic and are often topic based [19], in the field of cyber security using RL. We used selective search method which surveys only that literature and evidence that are readily available to the researchers [20].

The rest of this paper is organized as follows. In Chapter 2, general information about the RL algorithm is given. In Chapter 3, RL applications in cyber security are discussed in detail. The conclusion of the article is summarized in Chapter 4.

2. REINFORCEMENT LEARNING

RL provides a suitable study for modeling complex control problems and solving these models using learning algorithms [21]. Unlike other methods of ML, RL is a reward-based learning method that interacts with the environment [22]. The learning machine, called the agent in RL, reacts to the situations it encounters. In consequence of this response, it receives a numerical reward value. Figure 1 demonstrates the basic structure of the RL.
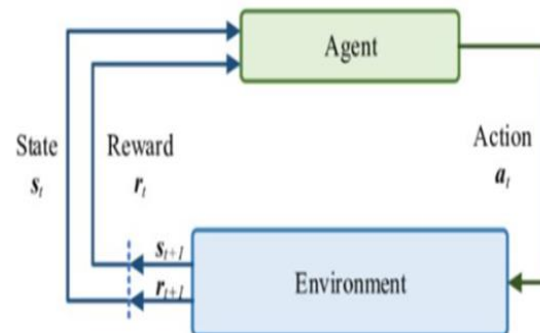
Figure 1 Reinforcement learning

Table 1 RL parameters

Parameters	Definition
s_t	state at time t
$a_t \in A$	a action taken from action space A
$s'_t = s_{t+1}$	new state passed with action a at time t
$r_t = r(s_t, a_t, s'_t)$	in case s_t, the reward obtained by switching to the s'_t state with a_t decision
$\pi(s,a) = P(a_t = a \mid s_t = s)$	probability of the agent making decision a_t in case s_t

The agent, that has no information about the environment, makes a choice of action in accordance with the situation it is in. This choice is evaluated by the environment and the agent moves into a new state. The agent evaluates the reward or punishment it received

from the action it made in the previous situation by its own decision-making mechanism and produces a new action for the new situation. This cycle continues until the agent completes the learning process. The mathematical symbols that are used in the learning process are presented in Table 1.

The goal of RL is to learn which action to take in any given situation. In order to find out this, it is necessary to calculate the quality of movement a. In case s, the quality of action a is defined as the total reward expected when acting within the framework of the decision-making function π. R_t is the summation of all rewards available from time t. The sum of these rewards is shown in Equation 1.

$$R_t = r_{t+1} + \gamma r_{t+2} + \gamma^2 r_{t+3} + \cdots = \sum_{k=0}^{\infty} \gamma^k r_{t+1+k} \qquad (1)$$

The discount rate γ is used when calculating the reward. The discount rate determines the importance of future reward value in decision making and takes a value between 0≤γ<1. In the case of γ=0, the agent makes a decision considering the highest reward value at that moment, while in the case of γ>0, it chooses its actions taking the future rewards into account. The determination of this rate directly affects the learning of the agent.

RL algorithms use an estimation of value functions that shows how important the states are to the agent. Value functions are calculated through systems called policies, which probabilistically determine which actions to choose.

Status value and action value functions are calculated from the status and rewards obtained by the steps taken in line with the policy. The state value function is shown in Equation 2. While the state value function is in state s, it returns the expected value of state s when policy π is fulfilled.

$$V^{\pi}(s) = E[\sum_{k=0}^{\infty} \gamma^k r_{t+1+k} | s_t = s] \qquad (2)$$

When the action value function is in the state of s, it returns the expected value of the state-action pair when it chooses the action a using the policy of π. The action value function is shown in Equation 3.

$$Q^{\pi}(s,a) = E[\sum_{k=0}^{\infty} \gamma^k r_{t+1+k} | s_t = s, a_t = a] \qquad (3)$$

For policy π and state s values, Equation 3 shows the consistency condition among the value of state s and the value of states to be reached from s. This gives Equation 4, the Bellman equation.

$$V^{\pi}(s) = \sum_a \pi(a|s) \sum_{s',r} p(s',r|s,a)[r + \gamma V^{\pi}(s')] \qquad (4)$$

This equation simplifies the calculation of the value function. Because we can find the best solution to a complex problem by dividing it into simpler and iterative sub-problems instead of summing multiple time steps [20].

Deep Reinforcement Learning (DRL)

The integration of deep learning and RL is a breakthrough that Google DeepMind initiated and spearheaded to form an intelligent agent capable of defeating a professional human player in [23] 49 Atari games. DRL is a revolutional technique in RL that can solve complex computational task [24]. The DRL model is given in Figure 2.
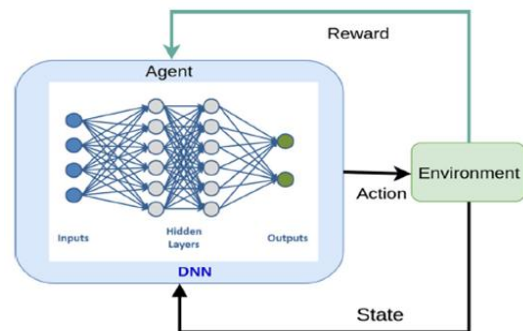

Figure 2 Deep reinforcement learning

The learning system is the same as the RL methods. However, some parts of the system are modeled by deep learning technique. For instance, deep learning is suitable to be used to acquire the amount of reward corresponding to a given state-action pair. In addition, deep learning can increase the intelligence of RL agents and accelerate the agent's ability to optimize policy [25]. DRL has been used in control [26], resource management [27], robotics [28, 29] and many other applications.

3. RL IN CYBER SECURITY

Increasing levels of interaction between cloud computing and machines have resulted in a remarkable increment in the number and complexity of cyberattack cases. Therefore, securing user data, privacy and devices have become an important issue nowadays. Numerous RL models have been presented in the literature for various applications of cybersecurity. This section provides a comprehensive review of RL-powered solutions for penetration testing, intrusion detection systems, and cyberattacks.

3.1 RL in Penetration Testing

Penetration testing (PT) are safety tests performed by "authorized" persons and "legal" entities in order to detect logic errors and vulnerabilities of digital assets (network, website, application, database) to prevent exploitation of security vulnerabilities by malicious people and to make systems more secure [30]. Checking and reporting security vulnerabilities in information systems by a third eye plays an important role in ensuring security. The steps that take place when PT is applied are shown in Figure 3.

Although systems evaluated using PT vary, the same general steps are followed in all cases. When a successful attack is carried out,

a specific set of attack actions is reported. With this report, security vulnerabilities can be minimized or completely avoided by system administrators and developers.

It is possible to automate the discovery, exploitation and identification steps by imitating experts in PT. The need to develop autonomous pentest solutions has become important to ensure that the pentest results implement extensive testing of attack surfaces. Autonomous pentesting is an emerging research area. An important point here is the method to create the attacks. Sarraute et al. [31] simulated the attack planning problem with regard to Partially Observable Markov Decision Processes (POMDP). POMDP allows to evaluate available information and to use scan actions intelligently as a part of the attack. It is recognised that POMDPs are not scalable for many network nodes. In this study, the PT process is divided into four levels using the multi-level architecture called 4AL: individual machines, attacking components, decomposing the network and subnetworks. In this study, the scalability problem of POMDPs has been tried to reduce by separating the network into double link components consisting of more than one subnet. Sarraute et al. [32] designed POMDP in the pentest problem in another study. POMDP has been used to overcome the missing information limitation by creating attack plans when missing information and uncertainties are given to the planner. It has also been observed again that the POMDP-based solution does not scale well for large networks. POMDPs are complex and require large computational resources. As a solution, Hoffmann [33] presented a common platform between POMDPs and classical planning called Markov decision processes (MDP) in his study. Unlike previous studies, actions do not scan. Each action result is assigned by a probability value that is independent from the

estimates of the host configuration, and this value refers to the level of uncertainty in which the attacker initiated the action. It has been observed that Planning Domain Definition Language (PDDL) is not endowed to overcome these uncertainties. For this, he proposed a language which is like PDDL that enables probability values within actions. Schwartz and Kurniawati [34] showed that RL can search to find the cause of the network exploit and the attack policy on all target machines. They used a Network Attack Simulator (NAS) and three different Q-learning algorithms in their study. These are tabular Q-learning using Upper Confidence Bound (UCB) action selection, tabular Q-

learning using ε-greedy action selection (tabular ε-greedy) and deep Q-learning (DQL) using a single layer neural network and ε-greedy action selection. The network created with a NAS consists of elements including connections, subnets, services, hosts and firewalls.These constituents enable the network simulator to run on different systems. Algorithm performance started to decline when there were more than 43 machines in the network. As a result of the study, it was observed that tabular RL algorithms do not scale well in large networks with many machines, whereas DQN does not scale well when the number of actions increases.

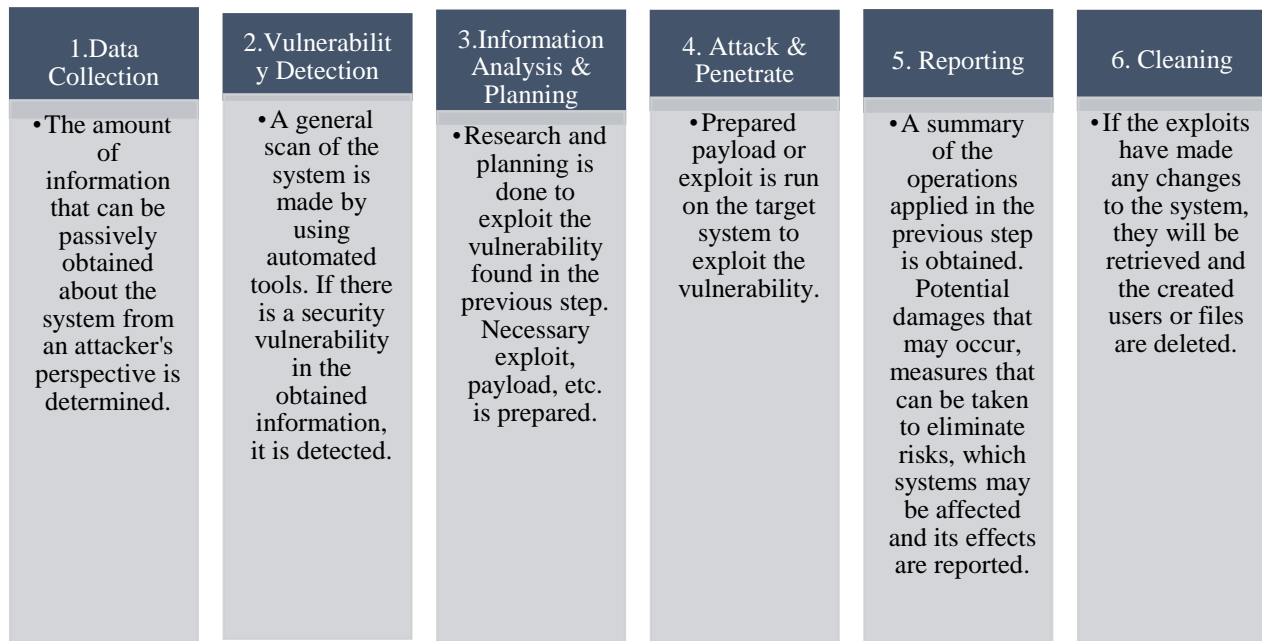| 1.Data Collection	2.Vulnerability Detection	3.Information Analysis & Planning	4. Attack & Penetrate	5. Reporting	6. Cleaning
•The amount of information that can be passively obtained about the system from an attacker's perspective is determined.	•A general scan of the system is made by using automated tools. If there is a security vulnerability in the obtained information, it is detected.	•Research and planning is done to exploit the vulnerability found in the previous step. Necessary exploit, payload, etc. is prepared.	•Prepared payload or exploit is run on the target system to exploit the vulnerability.	•A summary of the operations applied in the previous step is obtained. Potential damages that may occur, measures that can be taken to eliminate risks, which systems may be affected and its effects are reported.	•If the exploits have made any changes to the system, they will be retrieved and the created users or files are deleted.

Figure 3 Main steps of penetration testing

Ghanem and Chen [35] recommend an "Intelligent Automated Penetration Testing System (IAPTS)" that combines with industrial PT frameworks to enhance the performance and accuracy of medium and large network infrastructures. IAPTS targets to save human resources while providing improved outcomes with regard to reliability, test frequency and time. As in previous studies ([30-31, 33]), an environment consisting of

10-100 machines was used in this study. They concluded that RL outperforms the -abilities of any PT specialist concerning attack vectors, time, reliability and accuracy of the outputs.

The complexity and uncertainty of penetration testing can be determined using the RL environment [34]. Previous studies [31-32, 34-35] using the RL method have been

observed to be mostly successful in small networks. Chowdary et al. [36] designed a model to learn efficient pentesting schemes in large networks. They worked on an autonomous security analysis framework which assists in reducing the manual work done on PT. Penetration testing framework (ASAP) was used to generate the attack graph. ASAP creates autonomous attack plans and reveals undetected stealth attack paths in a manual test. In their study, one of the RL algorithms, Deep-Q Network (DQN), was also used to determine the most appropriate policy in PT. It has been observed that the created framework is more scalable on a large network compared to existing studies. Nguyen et al. [37] propose a double-agent architecture (DAA) technique to escalate the size and performance of the network. DAA uses the MDP model to attack environments. The purpose of DAA is to implement PT in entensive network systems with about 1000 machines. It is observed that the ability of DAA to attack hosts successfully is 70% if it reaches 1024 hosts and 100 services, and up to 81% in networks with less than 10 available services and 1024 hosts. The double agent structure presents in this work is shown in Figure 4.
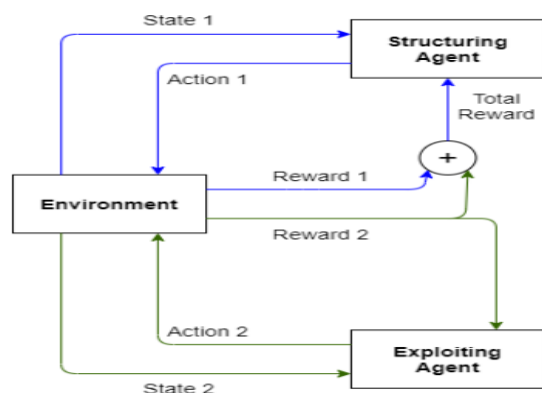

Figure 4 Double-agent structure [37]

Here, as a first step the structuring agent monitors the environment and receives a state1. If the agent considers that the state information is not sufficient, it continues with its structured discovery actions, including scanning of hosts and subnets. Meanwhile, the agent receives a reward1 value from the environment instantly and uses it to evaluate the accuracy of the action. Otherwise, if the agent concludes that it is allowable to gather information or make use of the services because of the lack of service information, it will not make direct decisions and will trigger the exploit agent. The exploiting agent uses the state of the selected host (state2) as the input. If the selected host considersthat the status information is not sufficient for the agent, hosts are continued to scan, otherwise it can take advantage of the host with the suitable service. After its action, the exploiting agent gets the reward 2 value from the environment to update its policy. The structuring agent also uses the sum of reward 1 and reward 2. If the structuring agent's chosen action is to scan hosts or subnets, the reward2 value is taken as 0. Finally, the structuring agent uses the sum of reward 1 and reward 2 to update its policy.

RL has demonstrated its capability to find the optimal way to attack. However, creating a correct model of exploitation and a realistic training simulator for agents are required [34]. Zennaro and Erdori [21] presented a PT approach that uses variable RL techniques in a simulation to obtain the hidden flag in the flag competition and overcome cybersecurity challenges. The primary goal of their research is to see the suitability of using different RL techniques for PT. Neal et al. [38] presented a groundwork for conducting PT steps against Microgrid (MG) control algorithms using RL. MGs are small-scale power systems with their own energy sources, outputs, and loads with certain limits. Within MGs, the digital infrastructure used to transfer data and execute control commands is compromised under a cyber-attack. In a simulated MG, the RL agent is trained to find malicious input that harms the MG controller.

Yang and Liu [39] formulate the Multi-Objective Reinforcement Learning (MORL) model in PT in their study. They used NAS and Cyber Autonomy Gym for Experimentation (CAGE) as the PT simulation platform. In PT, various types of attacks and agents with different behaviors are produced using Chebyshev criticism. A model is presented that increases agents' adaptability to future exploration and reduces their attention to previous actions. In this proposed model, it is shown that more information is collected from the network, thus enhancing the security level of the target network.

3.2 RL in Intrusion Detection Systems

With the universal use of computer and internet technology, the number of websites and web-based applications has increased rapidly. Sharing many important elements such as information, ideas and money through websites and applications provides convenience for people. However, material and nonmaterial losses may occur due to system and security vulnerabilities in applications. Many tools have been developed to prevent this situation and ensure safety. Security solutions were tried to be developed by using software such as firewall and virus programs, but it was not sufficient [40]. For this reason, it is aimed to analyse possible dangers with Intrusion Detection Systems (IDS) in addition to existing software. IDS are software products that are used to identify attacks by controlling the activities of a network or system, provide information about these attacks, and report attack attempts so that security analysts can analyse them better. The general form of the IDS [41] is given in Figure 5.
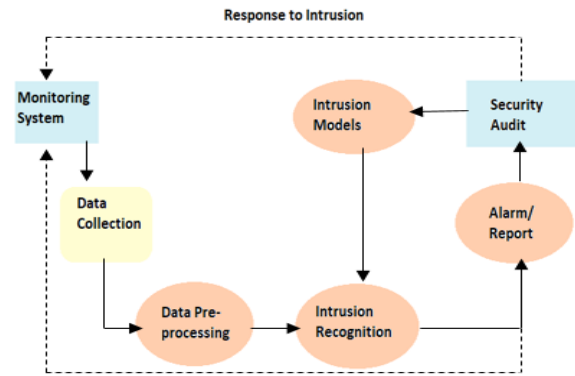

Figure 5 General structure of the IDS system

IDS are classified by two methods according to the installation and the detection mechanisms of the systems. According to the installation of the systems, it is divided into two as network- based IDS and host-based IDS. Network-based IDS is deployed at key points in a network to display the traffic between devices and computers on the network. Host-based IDS, on the other hand, works within a single computer and monitors the traffic coming from the system to the computer and its effects on the system. It is also divided into two, according to the detection mechanism of the system: signature-based IDS and anomaly-based IDS. Signature-based IDS store known attacks in pre-created signature databases and classify incoming samples by checking this database. In anomaly-based IDS, user profiles are created for the user group or for each user separately. A threshold value is determined for these profiles by means of various machine learning methods or mathematical models. If a transaction on the network deviates from this threshold significantly, it is considered an attack and an alarm is triggered.

With the lack of immediate response to dynamic intrusions and the development of attack methods, the RL method has started to be used in IDS. Xu and Xiu [40] proposed the RL method for Host-based IDS implementing the order of system calls. The Markov Reward Process (MRP) was used to model the

behaviour of system calls and the intrusion detection problem. A different learning algorithm that uses linear functions is applied to estimate the value function of the MRP. Xu [42] proposed a new sequential anomaly detection technique based upon temporal difference learning, in that multi-stage intrusion detection of cyber-attacks is considered as an implementation case. An MRP model was created for determining the anomalies and alarming process of the datasets. If the reward function is defined correctly, the anomaly possibilities of the datasets are equivalent to the value function of the MRP. This study was compared with different machine methods. It has been observed that the prediction accuracy can be enhanced even if the number of labelled training data is small.

Deokar and Hazarnis [43] conducted a study on the shortcomings of signature-based and anomaly-based detection methods. The authors proposed an IDS capable of recognizing attacks by combining the features of these two methods by using log files. In the proposed IDS that use the RL method, log correlation techniques and association rule learning are used together. RL is used to reward the system when it chooses log files that have anomalies or signs of attacks and it allows the system to select more suitable log files when looking for traces of attacks. Otoum et al. [44] propose a big data-oriented IDS approach in Wireless Sensor Networks (WSN) by utilizing the RL algorithm in a hybrid IDS framework. The research examines the efficiency of the RL-based IDS. Results are compared with Adaptively Supervised and Clustered Hybrid IDS (ASCH-IDS). Test results indicate that RL-IDS is able to reach 100% success in detection, accuracy and precision-recall rates.

Caminero et al. [45] worked on the first implementation of adversarial reinforcement learning to enable real-time prediction of attacks and detect intrusions. A new application that integrates the behaviour of the environment into the learning process of an improved RL method is provided. In aforementioned study, (NSL-KDD and AWID) datasets were used. The presented model was compared with different ML algorithms and it was observed that it outperformed other models on weighted accuracy (> 0.8) and F1 score (> 0.79) measures.

Sethi et al. [46] presented a context-adaptive IDS that maintains the balance between accuracy and false positive rate (FPR). This system has multiple independent RL agents deployed on the network to detect and classify complex and new attacks accurately. In the study, experiments were carried out using NSL-KDD, UNSW-NB15 and AWID dataset, showing higher accuracy and lower FPR compared to up-to-date solutions. In the model, the resilience of the system against attacks was analysed and only a slight drop in accuracy was observed compared to existing models.

Alavizadeh et al. [47] combined Deep Q-learning-based (DQL) RL with a feedforward neural network to detect and classify attacks. In the presented method, hyperparameters of a DQL agent like discount factor, batch size and the number of learning episodes are analysed to improve learning capabilities. In the study, using the NSL-KDD dataset, they obtained the best performance results in the case of 250 episodes of learning and a discount factor of 0.001. In their study, comparisons were made with other machine learning approaches to detecting different classes of intrusion, and they observed that their proposed model performed better (more than 90%).

Alawsi and Kurnaz [48] proposed a method grounded on measured Quality of Service (QoS) to evaluate the services given in the network to protect the network. QoS is evaluated periodically based on the services provided in the network and is used to calculate the reward value used to train the neural network. Decisions made for packages are reassessed based on their QoS value, as the goal is to increase the value of the collected reward. All decisions made by the neural network are updated when there is a decrease in the QoS value. CICIDS2017 dataset was used in the study. While the F1 score was 0.51 when classification-based neural network was used, an F1 score of 0.96 was obtained in this study.

3.3 RL in Cyber Attacks

Today, cyber-attacks and cyber security are among the most important digital transformation issues. The internet platform being so wide and easily accessible has created positive and negative effects. Cyber-attack is the name given to all of the attack actions made by one or more computers towards the opposite computers or networks, using various methods to steal, change or destroy data. It is possible to prevent these attacks or create defenses.

1) DoS and DDoS:

Denial of Services (DoS) and Distributed Denial of Services (DDoS) are types of attacks that are carried out against a target, hindering the system from functioning and preventing users from accessing the system. Attackers can send numerous requests to a database or website, keeping the system busy and causing systems to crash. DDoS, on the other hand, occurs when these attacks are made from more than one computer.

Xu et al. [49] used Hidden Markov Models (HMM) and RL to separate valid traffic from DDoS attacks based upon the source IP addresses being tracked. To detect DDoS attacks earlier, detection agents are located at network nodes or near DDoS attack sources. HMMs are used to generate regular traffic grounded on the frequencies of new IP addresses. The RL method is proposed to calculate the optimized information exchange between multiple distributed detectors.

Malialis and Kudenko [50] used the multi-agent router throttling method based on the SARSA algorithm for DDoS attacks in their study. They introduced this method by teaching multiple agents to reduce traffic to the server. Agents are placed in routers and learn to throttle or restrict traffic to the victim server. This is observed to work well in small-scale network topologies. However, this technique has limited capability in terms of scalability. To eliminate this disadvantage, Malialis and Kudenko [51] proposed the Coordinated Team Learning (CTL) approach that is a new structure of the multi-agent router throttling method based on the divide-and-conquer paradigm. CTL gives a decentralized coordinated response to the DDoS problem. This technique integrates three mechanisms to coordinate or mitigate DDoS attacks that are hierarchical team-based communication, task separation, and team rewards.

Shamshirband et al. [52] studied multi-agent system design to detect intrusion in WSN. They proposed a game method called Game-Fuzzy Q-learning (G-FQL), which combines game theory and fuzzy Q-learning to detect DDoS attacks in WSN. G-FQL is a three-player strategy game for defending against DDoS attacks composed of sink nodes, a base station and an attacker. The game uses the information of past behaviours in the decision-making process of fuzzy Q-learning to detect attacks.

Simpson et al. [53] offer two agent classes created to act on a per-flow basis for any network topology to mitigate DDoS attacks using the RL method. This method is assisted by profound investigation of the availability of the feature and it proves that there are highly predictive flow characteristics for different traffic classes.

Feng et al. [54] used the RL method as a defense method against Application Layer DDoS attacks (L7 DDoS) in their study. Conventional DDoS solutions are difficult to catch and defend against an L7 DDoS attack because the L7 DDoS attack seems legitimate at the transport and network layers. Therefore, a multi-purpose reward function is provided to guide the RL agent. As a result of the study, it was seen that 98.73% of malicious application messages were mitigable. Table 2 summarizes the DoS and DDoS attack.

Table 2 DoS and DDoS attacks.

Reference	Attack Type	Algorithm/Approach	Explanation
Xu et al. [49]	DDoS	HMM	The goal is to separate valid traffic based on source IP addresses from a DDoS attack.
Malialis and Kudenko [50]	DDoS	SARSA	Presented the multi-agent router throttling method by introducing multiple agents to reduce traffic of the server.
Malialis and Kudenko [51]	DDoS	SARSA	Proposed Coordinated Team Learning design on their multiagent router throttling method.
Shamshirband et al. [52]	DDos	Game-Fuzzy Q Learning	Multi-agent system design for detecting intrusions in wireless sensor networks.
Simpson et al. [53]	DDoS	Semi Gradient Sarsa	Train a two agent classes model to drop packets through the analysis on the source destination pair.
Feng et al. [54]	DDoS	MDP	Introduces a multi-objective reward function to guide an RL agent to learn the most suitable action to detect and mitigate AppDDoS attacks

2) Jamming Attacks:

Jamming is a type of attack that works under the principle of broadcasting noise from another station to disrupt a radio broadcast. It can be regarded as a special condition of DoS attacks [4]. Jamming attack has become a severe threat in wireless networks. Different anti-jamming techniques have been improved lately to eliminate this threat [55]. One of the biggest threats to cognitive radio networks (CNR) is jamming attacks [56]. Studies on jamming/anti-jamming in CNR have been done using the RL method [57-62]. In CNR, there are primary users (PU) and secondary users (SU). While PU refers to the users who own the licensed spectrum, SU refers to the unlicensed users who communicate over the licensed spectrum when the PU is not active. Jamming attacks occur in CRNs due to the emergence of smart jammers that can detect jamming frequencies and signal strengths based on the transmission strategies of SUs. Wang et al. [63] developed a game theory

framework to present the interactions of cognitive radio users during a jamming attack. The SU updates their strategy at every stage by observing the status of the channels and the strategy of the attackers from the status of the congested channels. A minimax-Q learning technique is conducted to obtain the optimal anti-jamming channel selection strategy. Using minimax-Q learning, CRN can solve problems regarding to the number of channels and how they switch between various channels to transmit data and control messages. It can also check packets along with channel switching strategy. Lo and Akyildiz [64] proposed jamming-resilient control channel JRCC game to simulate the interaction between cognitive radio users and attackers under the influence of PU. JRCC used user collaboration to facilitate control channel allocations and Win-or-Learn-Fast scheme for jamming resistance in malicious environments. In this scheme, it adapts to PUs activity with learning rates. The optimal control channel allocation strategy for SU is obtained by multi-agent RL.

Xiao et al. [65] studied the interactions between SUs and a smart jammer using game theory. They studied situations where a smart jammer targets to degrade SUs instead of PUs. The Stackelberg equilibrium of the anti-jamming power control game made of a source node, a relay node and a jammer is derived and compared with the Nash equilibrium of the game. Power control strategies with RL techniques like Q-learning and WoLF-PHC are presented to obtain the optimum forces against jamming for SUs without knowing the network parameters.

Han et al. [66] designed a dynamic anti-jamming communication game for CRNs that improves the signal to interference plus noise ratio (SINR) against intelligent jammers. The game represents an environment made up of multiple jammers sending jamming signals to disrupt the SUs' communication. The RL state is the radio medium made of PUs, SUs, jammers and the serving base station. DQN is used as a frequency-hopping policy to see if the SU will exit from a dense jamming area and defeat smart jammers. As a result of the study, it was seen that the anti-jamming system proposed using the DQN algorithm outperforms the Q-learning algorithm with higher SINR, faster convergence rate, lower defense cost and improved use of SU. Liu et al. [67] aimed to enhance Han et al.'s [66] work by proposing an anti-jamming communication system with different and more comprehensive contributions. Instead of using SINR and PU occupancy as in [66], spectrum waterfall using spectrum information with temporal characteristics is used to describe the environmental state. To deal with the infinite state of the spectrum waterfall, a recursive convolutional neural network (RCNN) is modelled and a DRL algorithm for anti-jamming is proposed. The model has been tested with the scenarios of comb jamming, sweeping jamming, dynamic jamming and intelligent comb jamming. The drawback of the studies in [66] and [67] is that they can only acquire the most appropriate policy for one user.

There have been studies on wideband autonomous cognitive radio (WACR) based jamming prevention using RL [68, 69]. Machuzak and Jayaweera [68] studied the design and implementation of WACR for anti-jamming. WACR can acquire spectrum information to locate and identify the sweeping jammer. In this study, the Q-learning method was used to optimally determine a new sub-band that continues to transmit uninterruptedly for a long time when the existing spectrum sub-band is blocked by a jammer. The agent's reward function was determined while it took for the jammer or interferer to interfere with WACR transmission. The results indicate that the

agent can detect jamming patterns and has successfully learned the optimal sub-band selection policy for jammer avoidance. Aref et al. [69] propose the RL method for anti-jamming communication in WACR in a multi-agent environment. WACRs can detect the states of the radio frequency spectrum and the network and autonomously optimize the corresponding operating mode. The aim of every radio is to avoid broadcasts from other WACRs and the sweeping jammer signal affecting the whole spectrum band. The proposed multi-agent RL method is used to avoid crosstalk and interference from other radios by learning the appropriate sub-band selection policy. Their results demonstrate that the proposed multi-agent RL can provide a significant improvement of the anti-jamming protocol against a random policy. Yao and Jia [70] investigated the anti-jamming defense problem in multi-user cases, in which inter-user coordination is considered. The Markov game structure was used to simulate and analyse the anti-jamming defense problem. A collaborative multi-agent anti-jamming (CMAA) algorithm is presented to find out the optimal anti-jamming strategy. CMAA can both solve the external malicious jamming problem and effectively deal with mutual interference between users.

Anti-jamming methods generally depend on frequency jumping to hide or escape jammers. Aforementioned methods are not useful regarding to bandwidth usage and can cause high congestion. Pourranjbar et al. [71] unlike other studies, used a new anti-jamming technique which redirects the jammer to attack a victim channel while legitimate users are communicating on secure channels. Since jammer's channel information is not recognised by users, an optimal channel selection scheme and a suboptimal power allocation algorithm using RL are presented. The efficiency of the proposed method is evaluated by calculating the statistical lower limit of the total received power (TRP). More than 50% of the highest TRP with no jamming for a given access point is achieved when there are a single user and three frequency channels. The presented anti-jamming technique exceeds the compared RL-based anti-jamming methods and the random search method.

Considering the weaknesses of a wireless environment for vehicle communications, both Vehicular Transportation Networks (VANET) and Unmanned Aerial Vehicular (UAV) networks are vulnerable to jamming attacks [72]. Lu et al. [73] and Xiao et al. [74] studied intelligent jamming attacks in a VANET, where a jammer constantly alters its attack strategy taking advantage of UAV devices. To recover vehicle communications, a UAV was used to transmit data to alternate units when roadside units were under jamming attacks. . A game theory technique is used to illustrate the interactions between the jammer and the UAV. Peng et al. [75] studied a communication system in which the communication between the UAV swarm and the base station in compressed by various interventions. Multiple parameters have been considered so that UAV communications can overcome jamming attacks. This study represents a modified Q-Learning algorithm based on multi-parameter programming to provide a balance between the motion and communication performance of UAVs. Li et al. [76] propose an RL method that uses domain information to improve algorithm speed and shrink the state space that the agent has to search. They used signal attenuation in free space and the law of inertia of aircraft to guide the efficient research of UAVs in state space. The subjective value of the task and the performance indicators of the receiver are added to the reward function.

Lu et al. [77] proposed an RL-based robot relay scheme for smart jamming attacks in

UAVs. In this diagram, RL is combined with a functional approach called tile coding. This case is designed to optimize both the robot's travel distance and relay power to improve UAV transmission quality and save robot energy. Robot mobility and relay policyare selected according to signal quality, jamming power, energy consumption and bit error rate of UAV messages. It uses three deep neural networks to select robot mobility and reduce the complexity of transition policy. The structure of the three networks is modelled with fully connected layers rather than convolutional layers. In the proposed scheme, better performance results were obtained than the existing schemes in the probability of interruption, robot energy consumption and bit error rate. Table 3 summarizes the Jamming attacks.

3) Spoofing and Phishing Attack:

A spoofing attack, especially in network security, is a situation in which a person or program is successfully identified as another identity by illegally distorting data. Xiao et al. [78, 79] conducted research on the authentication at the PHY layer in wireless networks. They used RL to detect the spoofing attack and find the optimum test threshold. The interactions between a legitimate receiver and spoofer are modelled as a zero-sum authentication game. Q-learning and Dyna-Q algorithms were used to find the optimum test threshold for spoofing detection.

Benefit states of the receiver or spoofing are calculated grounded on Bayesian risk that is the expected utility in spoofing detection. The receiver targets to choose the most appropriate test threshold in hypothesis testing in PHY layer spoofing detection. Experimental results show that the presented PHY authentication method with RL can improve authentication performance significantly. As a result of the study, it is shown that the proposed PHY authentication technique with RL can enhance authentication performance. Xiao et al. [80] modelled the protection against attacks in smart programmable radio devices of mobile communication throughout the offloading process. The Nash and Stackelberg equilibriums of the offloading game are derived and a Q-Learning based mobile offloading strategy is proposed to enhance the security of mobile devices during offloading. The results show that the presented offloading model can enhance mobile device usage and reduce the attack rate. Radio-based authentication is a procedure to authenticate the device and avoid spoofing attacks. On the other hand, it is not easy to determine the dynamic time variable channel mode in a real environment.

Liu et al. [81] used RL to obtain time-varying channel information. They proposed active authentication of mobile devices with the RL method. PHY layer information is evaluated to detect spoofing attacks. It is accepted that the signal strength received on the receiver side detects the spoofing attack. The receiver calculates the test statistics of the hypothesis test while receiving a packet. If this value is above the threshold value, the receiver detects the packet as a spoofed packet. Q-learning was used to obtain the optimum testing strategy without knowing the incoming packet's model.

Table 3 Jamming attacks.

Reference	Attack Type	Algorithm/Approach	Explanation
Wang et al. [63]	Jamming	Minimax Q-Learning	They presented a game theory approach to simulate the CRN under jamming attack.
Lo and Akyildiz [64]	Jamming	Win-or-Learn-Fast	The best control channel allocation strategy for SU is derived using multi agent reinforcement learning
Xiao et al. [65]	Jamming	Q-learning and WoLF-PHC	Anti-jamming problem of SU is defined as Stackelberg equilibrium problem.
Liu et al. [67]	Jamming	DQN with CNN	Improved the anti-jamming strategies against dynamic and intelligent jammers
Machuzak and Jayaweera [68]	Jamming	Q-Learning	Q-learning is trained to prevent attacks with a wide range of hundreds of MHz in real time.
Aref et al. [69]	Jamming	Q-Learning	A study of anti-jamming communication in WACR in a multi-agent environment.
Pourranjbar et al. [71]	Jamming	Q-Learning	The goal is to attack the victim channel with a jammer while maintaining users' communications on secure channels.
Lu et al. [73] and Xiao et al., [74]	Jamming	Q-Learning	It is presented to use UAV communications for rerouting traffic from congested areas to alternative RSUs.
Li et al. [76]	Jamming	Q-Learning	Q-learning is modeled to select transport policy to improve SINR with small-scale state space.
Lu et al. [77]	Jamming	Q-learning Safe DDQN	DRL model is proposed to avoid the high interruption hazards of UAV messages using three deep neural networks.

Phishing attacks, on the other hand, is a crime that obtains personal information from users through spoofed websites [82]. In this method, attackers try to obtain people's passwords or credit card information by sending e-mails to individuals as if they are sent from safe sources. Victims who click on the links they send via e-mails are usually directed to spoofed sites and share the information they entered with the attackers. Spoofing is an identity theft in which someone tries to use the identity of a legitimate user. On the other hand, phishing is used to steal a user's sensitive information, such as bank account details. Smadi et al. [83] proposed a phishing detection scheme called a phishing email detection system (PEDS), combining a neural network approach with RL. The proposed model, PEDS, is the first study in this area to use RL to detect zero-day phishing attacks. In

the pre-processing stage, the mail header, email text, URL and HTML content are known as the input to the feature evaluation and reduction algorithm (FERA). The dataset consists of 9118 emails, of which 50% are legitimate and the remainings are phishing emails. It has been observed that the attacks of the proposed system reach high accuracy (98.63%), true positive rate (99.07%) and true negative rate (98.19%) performance levels. In addition, they obtained false positive and false negative rates of 1.81% and 0.93%, respectively. Table 4 summarizes the Spoofing and Phishing attacks.

Table 4 Spoofing and Phishing attacks.

Reference	Attack Type	Algorithm/Approach	Explanation
Xiao et al.[78, 79]	Spoofing	Q-Learning and Dyna-Q	The purpose is selecting the optimum authentication threshold value in wireless networks.
Xiao et al. [80]	Spoofing	Q-Learning	The purpose is to provide security during the offloading process on mobile devices.
Liu et al. [81]	Spoofing	Q-Learning	The purpose is to authenticate mobile devices against attacks.
Smadi et al. [83]	Phishing	Neural network +RL	It is the first study to use RL to determine a zero-day phishing attack.

4) Cross-Site Scripting:

Cross-Site Scripting (XSS) is an attack on a web page through script codes. This attack appears when the developer does not pass the inputs, received from the user, from the necessary HTML and JavaScript filters. When the entries do not pass the necessary filters and at the same time the user is an attacker, it runs malicious codes which are able to harm other users or directly the system. Since HTML, CSS and JavaScript are languages described by XSS, the malicious code can directly harm other users. Fang et al. [84] represent an XSS adversarial attack model based on the RL method (RLXSS). The aim of this study is to optimize the detection of XSS attacks according to adversarial attack models. To achieve this, RL was used to determine the most appropriate escape technique. This RL method demonstrates how detection capabilities against XSS attacks are improved. Tariq et al. [85] used Genetic Algorithms together with RL to deal with XSS attack, which was compared with previous studies. For validation, a real dataset of XSS attacks

was used. The proposed approach achieves 99.75% accuracy in the normal state, while it reaches 99.89% accuracy after loading the attacks. The study showed better results as the number of attacks increased. Caturano et al. [86] used the MORL model to generate attack strings that enable the detection of XSS vulnerabilities in web applications. They designed an intelligent agent called Suggester that suggests learned actions to a human upon possible observations. They have trained this agent to generate attack sequences using the MORL environment and action space.

5) SQL Injection:

Recently, many databases are created to conform to commands written in SQL. Many websites acquire information from users and send these data to SQL databases. Attackers take control of victims' databases by exploiting SQL vulnerabilities. Erdodi et al. [87] worked on expressing the SQL injection vulnerability exploit problem using RL. They modelled their work using MDP. It is represented as an attacker or pentester agent,

and the MDP environment as a vulnerable web page with its associated database. Agents assigned with learning policy were deployed to execute SQL injection into the environment. Agents are designed to learn both a certain method to overcome an individual challenge and a more general principle which can be implemented to perform SQL injection attacks on any system. Table 5 summarizes Cross-Site Scripting and SQL Injection attacks.

Table 5 Cross-site scripting and SQL injection attacks.

Reference	Attack Type	Algorithm/Approach	Explanation
Fang et al. [84]	Cross-Site Scripting	Double DQN	Proposes an XSS adversarial attack model formed on the RL method (RLXSS).
Tariq et al. [85]	Cross-Site Scripting	Genetic algorithm +RL	In order to detect XSS attack, GA was used with RL because it gave good results in static analysis.
Caturano et al. [86]	Cross-Site Scripting	Q-Learning	The purpose is to detect XSS vulnerabilities in web applications.
Erdodi et al. [87]	SQL Injection	Q-Learning	The aim is to express the problem of exploiting SQL injection vulnerability using RL.

4. CONCLUSION

The use of RL in the field of cyber security is increasing day by day. In this study, we gathered RL studies in the literature under three headings: penetration testing, IDS and cyberattacks. POMDP, MDP and DQN types of RL algorithms are widely used in Penetration Tests. Studies show that the POMDP model does not scale well for large networks. MDP and DQN algorithms have been presented in the literature both to overcome this limitation of POMDP and to increase the size and performance of the network. In IDS studies, with the use of deep learning and RL together, attacks were detected with higher accuracy. In this study, we discussed the types of DoS, DDoS, Jamming, Spoofing, Phishing, Cross-Site Scripting and SQL injection cyberattacks in which RL is applied. When we consider the studies in general, it is seen that RL algorithms are used more than DRL algorithms. It is clear that DRL will be used more frequently in the future to solve complex and dynamic intrusion detection problems.

Although machine learning for cyber security is a new topic in the literature, it has been observed that the techniques used give promising results for the detection and prevention of attacks. It is expected that RL will develop cyber defense and attack methods and contribute to the reshaping of cyber risks. We expect the RL examined in this study to deal with cyber security problems and offer solutions, lay the foundations for future studies and guide these studies to a large extent.

The Declaration of Conflict of Interest/ Common Interest
No conflict of interest or common interest has been declared by the author.

REFERENCES

[1] B. von Solms, R. von Solms, "Cybersecurity and information security – what goes where?," Information & Computer Security, vol. 26, no. 1, pp. 2–9, 2018.

[2] Z. Guan, J. Li, L. Wu, Y. Zhang, J. Wu, X. Du, "Achieving efficient and secure data acquisition for cloud-supported internet of things in smart grid," IEEE Internet Things Journal, vol. 4, no. 6, pp. 1934–1944, 2017.

[3] J.-H. Li, "Cyber security meets artificial intelligence: a survey," Frontiers of Information Technology & Electronic Engineering, vol. 19, no. 12, pp. 1462–1474, 2018.

[4] T. T. Nguyen, V. J. Reddi, "Deep reinforcement learning for cyber security," arXiv [cs.CR], 2019.

[5] N. D. Nguyen, T. T. Nguyen, H. Nguyen, D. Creighton, S. Nahavandi, "Review, analysis and design of a comprehensive deep reinforcement learning framework," arXiv [cs.LG], 2020.

[6] N. D. Nguyen, T. Nguyen, S. Nahavandi, "System design perspective for human-level agents using deep reinforcement learning: A survey," IEEE Access, vol. 5, pp. 27091–27102, 2017.

[7] M. Riedmiller, T. Gabel, R. Hafner, S. Lange, "Reinforcement learning for robot soccer," Autonomous Robots, vol. 27, no. 1, pp. 55–73, 2009.

[8] K. Mülling, J. Kober, O. Kroemer, J. Peters, "Learning to select and generalize striking movements in robot table tennis," The International Journal of Robotics Research, vol. 32, no. 3, pp. 263–279, 2013.

[9] T. G. Thuruthel, E. Falotico, F. Renda, C. Laschi, "Model-based reinforcement learning for closed-loop dynamic control of soft robotic manipulators," IEEE Transactions on Robotics, vol. 35, no. 1, pp. 124–134, 2019.

[10] I.Arel, C. Liu, T. Urbanik, A. G. Kohls, "Reinforcement learning-based multi-agent system for network traffic signal control," IET Intelligent Transport Systems, vol. 4, no. 2, p. 128, 2010.

[11] J. Jin, C. Song, H. Li, K. Gai, J. Wang, W. Zhang, "Real-time bidding with multi-agent reinforcement learning in display advertising," in Proceedings of the 27th ACM International Conference on Information and Knowledge Management, 2018.

[12] M. E. Taylor, N. Carboni, A. Fachantidis, I. Vlahavas, L. Torrey, "Reinforcement learning agents providing advice in complex video games," Connection Science, vol. 26, no. 1, pp. 45–63, 2014.

[13] C. Amato, G. Shani, "High-level reinforcement learning in strategy games", In AAMAS Vol. 10, pp. 75-82, 2010.

[14] M. Jaderberg, W.M Czarnecki, I. Dunning, L. Marris, G. Lever, A.G. Castaneda, C. Beattıe, N. C. Rabinowıtz, A.S. Morcos, A. Ruderman, N. Sonnerat, T. Green, L. Deason, J. Z. Leibo, D. Silver, D.Hassabis, K. Kavukcuoglu, T. Graepel, "Human-level performance in 3D multiplayer games with population-based reinforcement learning," Science, vol. 364, no. 6443, pp. 859–865, 2019.

[15] T. Liu, B. Huang, Z. Deng, H. Wang, X. Tang, X. Wang, D. Cao, "Heuristics-oriented overtaking decision making for autonomous vehicles using reinforcement learning," IET Electrical Systems in Transportation, vol. 10, no. 4, pp. 417–424, 2020.

[16] W. Gao, A. Odekunle, Y. Chen, Z.-P. Jiang, "Predictive cruise control of connected and autonomous vehicles via reinforcement learning," IET Control Theory Applications, vol. 13, no. 17, pp. 2849–2855, 2019.

[17] F. Richter, R. K. Orosco, M. C. Yip, "Open-sourced reinforcement learning environments for surgical robotics," arXiv [cs.RO], 2019.

[18] C. Shin, P. W. Ferguson, S. A. Pedram, J. Ma, E. P. Dutson, J. Rosen, "Autonomous tissue manipulation via surgical robot using learning based model predictive control," in 2019 International Conference on Robotics and Automation (ICRA), 2019.

[19] H. Snyder, "Literature review as a research methodology: An overview and guidelines". Journal of business research, 104, 333-339, 2019.

[20] P. Davies, "The relevance of systematic reviews to educational policy and practice", Oxford review of education, 26(3-4), 365-378, 2000.

[21] F. M. Zennaro, L. Erdodi, "Modeling penetration testing with reinforcement learning using capture-the-flag challenges and tabular Q-learning", arXiv preprint arXiv:2005.12632, 2020.

[22] R. S. Sutton, A. G. Barto, "Reinforcement Learning: An Introduction", 2nd ed. Cambridge, MA: Bradford Books, 2018.

[23] V. Mnih, V. Mnih, K. Kavukcuoglu, D. Silver, A. A. Rusu, J. Veness, M. G. Bellemare, A. Graves,

[24] M. Riedmiller, A. K. Fidjeland, G. Ostrovski, S. Petersen, C. Beattie, A. Sadik, I. Antonoglou, H. King, D. Kumaran, D. Wierstra, S. Legg D. Hassabis., "Human-level control through deep reinforcement learning," Nature, vol. 518, no. 7540, pp. 529–533, 2015.

[25] V. François-Lavet, P. Henderson, R. Islam, M. G. Bellemare, J. Pineau, "An introduction to deep reinforcement learning," Foundations and Trends® in

Machine Learning, vol. 11, no. 3–4, pp. 219–354, 2018.

[26] A.Uprety, D. B. Rawat, "Reinforcement learning for IoT security: A comprehensive survey," IEEE Internet of Things Journal, vol. 8, no. 11, pp. 8693–8706, 2021.

[27] S. P. K. Spielberg, R. B. Gopaluni, P. D. Loewen, "Deep reinforcement learning approaches for process control," in 2017 6th International Symposium on Advanced Control of Industrial Processes (AdCONIP), 2017.

[28] H. Mao, M. Alizadeh, I. Menache, S. Kandula, "Resource management with deep reinforcement learning," in Proceedings of the 15th ACM Workshop on Hot Topics in Networks, 2016.

[29] M. Vecerik T. Hester, J. Scholz, F. Wang, O. Pietquin, B. Piot, N. Heess, R. Thomas,T. Rothörl, T. Lampe, M. Riedmiller, "Leveraging demonstrations for deep Reinforcement Learning on robotics problems with sparse rewards," arXiv [cs.AI], 2017.

[30] S. Gu, E. Holly, T. Lillicrap, S. Levine, "Deep reinforcement learning for robotic manipulation with asynchronous off-policy updates," in 2017 IEEE International Conference on Robotics and Automation (ICRA), 2017.

[31] M. C. Ghanem, T. M. Chen, "Reinforcement learning for intelligent penetration testing," in 2018 Second World Conference on Smart Trends in Systems, Security and Sustainability (WorldS4), 2018.

[32] C. Sarraute, O. Buffet, J. Hoffmann, "POMDPs make better hackers: Accounting for uncertainty in penetration testing," Twenty-Sixth AAAI Conference on Artificial Intelligence, vol. 26, no. 1, pp. 1816–1824, 2021.

[33] C. Sarraute, O. Buffet, J. Hoffmann, "Penetration Testing == POMDP Solving?," arXiv [cs.AI], 2013.

[34] J. Hoffmann, "Simulated penetration testing: From 'Dijkstra' to 'Turing Test++,'" Proceedings of the International Conference on Automated Planning and Scheduling, vol. 25, pp. 364–372, 2015.

[35] J. Schwartz, H. Kurniawati, "Autonomous Penetration Testing using Reinforcement Learning," arXiv [cs.CR], 2019.

[36] M. C. Ghanem, T. M. Chen, "Reinforcement learning for efficient network penetration testing," Information (Basel), vol. 11, no. 1, p. 6, 2019.

[37] A.Chowdhary, D. Huang, J. S. Mahendran, D. Romo, Y. Deng, A. Sabur, "Autonomous security analysis and penetration testing," in 2020 16th International Conference on Mobility, Sensing and Networking (MSN), 2020.

[38] H. Nguyen, S. Teerakanok, A. Inomata, T. Uehara, "The proposal of double agent architecture using actor-critic algorithm for penetration testing," in Proceedings of the 7th International Conference on Information Systems Security and Privacy, 2021.

[39] C. Neal, H. Dagdougui, A. Lodi, J. M. Fernandez, "Reinforcement learning based penetration testing of a microgrid control algorithm," in 2021 IEEE 11th Annual Computing and Communication Workshop and Conference (CCWC), 2021.

[40] Y. Yang, X. Liu, "Behaviour-diverse automatic penetration testing: A curiosity-driven multi-objective deep Reinforcement Learning approach," arXiv [cs.LG], 2022.

[41] X. Xu, T. Xie, "A reinforcement learning approach for host-based intrusion detection using sequences of system calls," in Lecture Notes in Computer Science, Berlin, Heidelberg: Springer Berlin Heidelberg, 2005, pp. 995–1003.

[42] S. Aljawarneh, M. Aldwairi, M. B. Yassein, "Anomaly-based intrusion detection system through feature selection analysis and building hybrid efficient model," Journal of Computational Science, vol. 25, pp. 152–160, 2018.

[43] X. Xu, "Sequential anomaly detection based on temporal-difference learning: Principles, models and case studies," Applied Soft Computing, vol. 10, no. 3, pp. 859–867, 2010.

[44] B. Deokar, A. Hazarnis, "Intrusion detection system using log files and reinforcement learning", International Journal of Computer Applications, vol. 45, no. 19, 28-35, 2012.

[45] S. Otoum, B. Kantarci, H. Mouftah, "Empowering reinforcement learning on big sensed data for intrusion detection," in ICC 2019 - 2019 IEEE International Conference on Communications (ICC), 2019.

[46] G. Caminero, M. Lopez-Martin, B. Carro, "Adversarial environment reinforcement learning algorithm for intrusion detection," Computer Networks, vol. 159, pp. 96–109, 2019.

[47] K. Sethi, E. Sai Rupesh, R. Kumar, P. Bera, Y. Venu Madhav, "A context-aware robust intrusion detection system: a reinforcement learning-based approach," International Journal of Information Security, vol. 19, no. 6, pp. 657–678, 2020.

[48] H. Alavizadeh, H. Alavizadeh, J. Jang-Jaccard, "Deep Q-learning based reinforcement learning approach for network intrusion detection," Computers, vol. 11, no. 3, p. 41, 2022.

A. S. S. Alawsi, S. Kurnaz, "Quality of service system that is self-updating by intrusion detection systems using reinforcement learning," Applied Nanoscience, 2022.

[49] X. Xu, Y. Sun, Huang, Z, "Defending DDoS attacks using hidden Markov models and cooperative reinforcement learning", In Pacific-Asia Workshop on Intelligence and Security Informatics (pp. 196-207). Springer, Berlin, Heidelberg, 2007.

[50] K. Malialis, D. Kudenko, "Multiagent Router Throttling: Decentralized coordinated response against DDoS attacks," In Twenty-Fifth IAAI Conference, vol. 27, no. 2, pp. 1551–1556, 2013.

[51] K. Malialis, D. Kudenko, "Distributed response to network intrusions using

multiagent reinforcement learning," Engineering Applications of Artificial Intelligence, vol. 41, pp. 270–284, 2015.

[52] S. Shamshirband, A. Patel, N. B. Anuar, M. L. M. Kiah, A. Abraham, "Cooperative game theoretic approach using fuzzy Q-learning for detecting and preventing intrusions in wireless sensor networks," Engineering Applications of Artificial Intelligence, vol. 32, pp. 228–241, 2014.

[53] K. A. Simpson, S. Rogers, D. P. Pezaros, "Per-host DDoS mitigation by direct-control reinforcement learning," IEEE Transactions on Network and Service Management, vol. 17, no. 1, pp. 103–117, 2020.

[54] Y. Feng, J. Li, T. Nguyen, "Application-layer DDoS defense with reinforcement learning," in 2020 IEEE/ACM 28th International Symposium on Quality of Service (IWQoS), 2020.

[55] K. Grover, A. Lim, Q. Yang, "Jamming and anti-jamming techniques in wireless networks: a survey," International Journal of Ad Hoc and Ubiquitous Computing, vol. 17, no. 4, p. 197, 2014.

[56] Y. Wu, B. Wang, K. J. R. Liu, T. C. Clancy, "Anti-jamming games in multi-channel cognitive radio networks," IEEE journal on selected areas in communications, vol. 30, no. 1, pp. 4–15, 2012.

[57] S. Singh, A. Trivedi, "Anti-jamming in cognitive radio networks using reinforcement learning algorithms," in 2012 Ninth International Conference on Wireless and Optical Communications Networks (WOCN), 2012.

[58] Y. Gwon, S. Dastangoo, C. Fossa, H. T. Kung, "Competing Mobile Network Game: Embracing antijamming and jamming strategies with reinforcement learning," in 2013 IEEE Conference on Communications and Network Security (CNS), 2013.

[59] K. Dabcevic, A. Betancourt, L. Marcenaro, C. S. Regazzoni, "A fictitious play-based game-theoretical approach to alleviating jamming attacks for cognitive radios," in 2014 IEEE International Conference on Acoustics, Speech and Signal Processing (ICASSP), 2014.

[60] F. Slimeni, B. Scheers, Z. Chtourou, V. Le Nir, "Jamming mitigation in cognitive radio networks using a modified Q-learning algorithm," in 2015 International Conference on Military Communications and Information Systems (ICMCIS), 2015.

[61] F. Slimeni, B. Scheers, Z. Chtourou, V. Le Nir, R. Attia, "Cognitive radio jamming mitigation using Markov decision process and reinforcement learning," Procedia Computer Science, vol. 73, pp. 199–208, 2015.

[62] F. Slimeni, B. Scheers, Z. Chtourou, V. L. Nir, R. Attia, "A modified Q-learning algorithm to solve cognitive radio jamming attack," International Journal of Embedded Systems, vol. 10, no. 1, p. 41, 2018.

[63] B. Wang, Y. Wu, K. J. R. Liu, T. C. Clancy, "An anti-jamming stochastic game for cognitive radio networks," IEEE journal on selected areas in communications, vol. 29, no. 4, pp. 877–889, 2011.

[64] B. F. Lo, I. F. Akyildiz, "Multiagent jamming-resilient control channel game for cognitive radio ad hoc networks," in 2012 IEEE International Conference on Communications (ICC), 2012.

[65] L. Xiao, Y. Li, J. Liu, Y. Zhao, "Power control with reinforcement learning in cooperative cognitive radio networks against jamming," The Journal of Supercomputing, vol. 71, no. 9, pp. 3237–3257, 2015.

[66] G. Han, L. Xiao, H. V. Poor, "Two-dimensional anti-jamming communication based on deep reinforcement learning," in 2017 IEEE International Conference on Acoustics, Speech and Signal Processing (ICASSP), 2017.

[67] X. Liu, Y. Xu, L. Jia, Q. Wu, A. Anpalagan, "Anti-jamming communications using spectrum waterfall: A deep reinforcement learning approach," IEEE Communications Letters, vol. 22, no. 5, pp. 998–1001, 2018.

[68] S. Machuzak, S. K. Jayaweera, "Reinforcement learning based anti-jamming with wideband autonomous cognitive radios," in 2016 IEEE/CIC International Conference on Communications in China (ICCC), 2016.

[69] M. A. Aref, S. K. Jayaweera, S. Machuzak, "Multi-agent reinforcement learning based cognitive anti-jamming," in 2017 IEEE Wireless Communications and Networking Conference (WCNC), 2017.

[70] F. Yao, L. Jia, "A collaborative multi-agent reinforcement learning anti-jamming algorithm in wireless networks," IEEE wireless communications letters, vol. 8, no. 4, pp. 1024–1027, 2019.

[71] Pourranjbar, G. Kaddoum, A. Ferdowsi, W. Saad, "Reinforcement learning for deceiving reactive jammers in wireless networks," IEEE Transactions on Communications, vol. 69, no. 6, pp. 3682–3697, 2021.

[72] H. Pirayesh, H. Zeng, "Jamming attacks and anti-jamming strategies in wireless networks: A comprehensive survey," arXiv [cs.CR], 2021.

[73] X. Lu, D. Xu, L. Xiao, L. Wang, W. Zhuang, "Anti-jamming communication game for UAV-aided VANETs," in GLOBECOM 2017 - 2017 IEEE Global Communications Conference, 2017.

[74] L. Xiao, X. Lu, D. Xu, Y. Tang, L. Wang, W. Zhuang, "UAV relay in VANETs against smart jamming with reinforcement learning," IEEE Transactions on Vehicular Technology, vol. 67, no. 5, pp. 4087–4097, 2018.

[75] J. Peng, Z. Zhang, Q. Wu, B. Zhang, "Anti-jamming communications in UAV swarms: A reinforcement learning approach," IEEE Access, vol. 7, pp. 180532–180543, 2019.

[76] Z. Li, Y. Lu, X. Li, Z. Wang, W. Qiao, Y. Liu, "UAV networks against multiple maneuvering smart jamming with knowledge-based reinforcement learning," IEEE Internet of Things Journal, vol. 8, no. 15, pp. 12289–12310, 2021.

[77] X. Lu, J. Jie, Z. Lin, L. Xiao, J. Li, Y. Zhang, "Reinforcement learning based energy efficient robot relay for unmanned aerial vehicles against smart jamming," Science China Information Sciences, vol. 65, no. 1, 2022.

[78] L. Xiao, Y. Li, G. Liu, Q. Li, W. Zhuang, "Spoofing detection with reinforcement learning in wireless networks," in 2015 IEEE Global Communications Conference (GLOBECOM), 2015.

[79] L. Xiao, Y. Li, G. Han, G. Liu, W. Zhuang, "PHY-layer spoofing detection with reinforcement learning in wireless networks," IEEE Transactions on Vehicular Technology, vol. 65, no. 12, pp. 10037–10047, 2016.

[80] L. Xiao, C. Xie, T. Chen, H. Dai, H. V. Poor, "A mobile offloading game against smart attacks," IEEE Access, vol. 4, pp. 2281–2291, 2016.

[81] J. Liu, L. Xiao, G. Liu, Y. Zhao, "Active authentication with reinforcement learning based on ambient radio signals," Multimedia Tools and Applications, vol. 76, no. 3, pp. 3979–3998, 2017.

[82] S. Purkait, "Phishing counter measures and their effectiveness – literature review," Information Management & Computer Security., vol. 20, no. 5, pp. 382–420, 2012.

[83] S. Smadi, N. Aslam, L. Zhang, "Detection of online phishing email using dynamic evolving neural network based on reinforcement learning," Decision Support Systems, vol. 107, pp. 88–102, 2018.

[84] Y. Fang, C. Huang, Y. Xu, Y. Li, "RLXSS: Optimizing XSS detection model to defend against adversarial attacks based on reinforcement learning," Future internet, vol. 11, no. 8, p. 177, 2019.

[85] Tariq, M. A. Sindhu, R. A. Abbasi, A. S. Khattak, O. Maqbool, G. F. Siddiqui, "Resolving cross-site scripting attacks through genetic algorithm and reinforcement learning," Expert Systems with Applications., vol. 168, no. 114386, p. 114386, 2021.

[86] F. Caturano, G. Perrone, S. P. Romano, "Discovering reflected cross-site scripting vulnerabilities using a multiobjective reinforcement learning environment," Computers & Security, vol. 103, no. 102204, p. 102204, 2021.

[87] L. Erdodi, Å. Å. Sommervoll, F. M. Zennaro, "Simulating SQL injection vulnerability exploitation using Q-learning reinforcement learning agents," arXiv [cs.CR], 2021.